

RECENT ADVANCES AND APPLICATIONS OF HYBRID SIMULATION

EDITED BY: Wei Song, Chia-Ming Chang and Vasilis K. Dertimanis
PUBLISHED IN: Frontiers in Built Environment





frontiers

Frontiers eBook Copyright Statement

The copyright in the text of individual articles in this eBook is the property of their respective authors or their respective institutions or funders. The copyright in graphics and images within each article may be subject to copyright of other parties. In both cases this is subject to a license granted to Frontiers.

The compilation of articles constituting this eBook is the property of Frontiers.

Each article within this eBook, and the eBook itself, are published under the most recent version of the Creative Commons CC-BY licence.

The version current at the date of publication of this eBook is CC-BY 4.0. If the CC-BY licence is updated, the licence granted by Frontiers is automatically updated to the new version.

When exercising any right under the CC-BY licence, Frontiers must be attributed as the original publisher of the article or eBook, as applicable.

Authors have the responsibility of ensuring that any graphics or other materials which are the property of others may be included in the CC-BY licence, but this should be checked before relying on the CC-BY licence to reproduce those materials. Any copyright notices relating to those materials must be complied with.

Copyright and source acknowledgement notices may not be removed and must be displayed in any copy, derivative work or partial copy which includes the elements in question.

All copyright, and all rights therein, are protected by national and international copyright laws. The above represents a summary only. For further information please read Frontiers' Conditions for Website Use and Copyright Statement, and the applicable CC-BY licence.

ISSN 1664-8714

ISBN 978-2-88966-380-4

DOI 10.3389/978-2-88966-380-4

About Frontiers

Frontiers is more than just an open-access publisher of scholarly articles: it is a pioneering approach to the world of academia, radically improving the way scholarly research is managed. The grand vision of Frontiers is a world where all people have an equal opportunity to seek, share and generate knowledge. Frontiers provides immediate and permanent online open access to all its publications, but this alone is not enough to realize our grand goals.

Frontiers Journal Series

The Frontiers Journal Series is a multi-tier and interdisciplinary set of open-access, online journals, promising a paradigm shift from the current review, selection and dissemination processes in academic publishing. All Frontiers journals are driven by researchers for researchers; therefore, they constitute a service to the scholarly community. At the same time, the Frontiers Journal Series operates on a revolutionary invention, the tiered publishing system, initially addressing specific communities of scholars, and gradually climbing up to broader public understanding, thus serving the interests of the lay society, too.

Dedication to Quality

Each Frontiers article is a landmark of the highest quality, thanks to genuinely collaborative interactions between authors and review editors, who include some of the world's best academicians. Research must be certified by peers before entering a stream of knowledge that may eventually reach the public - and shape society; therefore, Frontiers only applies the most rigorous and unbiased reviews. Frontiers revolutionizes research publishing by freely delivering the most outstanding research, evaluated with no bias from both the academic and social point of view. By applying the most advanced information technologies, Frontiers is catapulting scholarly publishing into a new generation.

What are Frontiers Research Topics?

Frontiers Research Topics are very popular trademarks of the Frontiers Journals Series: they are collections of at least ten articles, all centered on a particular subject. With their unique mix of varied contributions from Original Research to Review Articles, Frontiers Research Topics unify the most influential researchers, the latest key findings and historical advances in a hot research area! Find out more on how to host your own Frontiers Research Topic or contribute to one as an author by contacting the Frontiers Editorial Office: researchtopics@frontiersin.org

RECENT ADVANCES AND APPLICATIONS OF HYBRID SIMULATION

Topic Editors:

Wei Song, University of Alabama, United States

Chia-Ming Chang, National Taiwan University, Taiwan

Vasilis K. Dertimanis, ETH Zürich, Switzerland

Citation: Song, W., Chang, C.-M., Dertimanis, V. K., eds. (2021). Recent Advances and Applications of Hybrid Simulation. Lausanne: Frontiers Media SA.
doi: 10.3389/978-2-88966-380-4

Table of Contents

- 04 Editorial: Recent Advances and Applications of Hybrid Simulation**
Wei Song, Chia-Ming Chang and Vasilis K. Dertimanis
- 07 Real-Time Hybrid Simulation Analysis of Moat Impacts in a Base-Isolated Structure**
Michael J. Harris and Richard E. Christenson
- 28 Stability Analysis and Verification of Real-Time Hybrid Simulation Using a Shake Table for Building Mass Damper Systems**
Pei-Ching Chen, Meng-Wei Dong, Po-Chang Chen and Narutoshi Nakata
- 39 Advances in Real-Time Hybrid Testing Technology for Shaking Table Substructure Testing**
Yingpeng Tian, Xiaoyun Shao, Huimeng Zhou and Tao Wang
- 57 Robust Model Predictive Control for Dynamics Compensation in Real-Time Hybrid Simulation**
Nikolaos Tsokanas, David Wagg and Božidar Stojadinović
- 74 Online Stability Analysis for Real-Time Hybrid Simulation Testing**
Cristóbal Gálmez and Gastón Fernandois
- 88 Conceptual Study of a Real-Time Hybrid Simulation Framework for Monopile Offshore Wind Turbines Under Wind and Wave Loads**
Wei Song, Chao Sun, Yanhui Zuo, Vahid Jahangiri, Yan Lu and Qinghua Han
- 108 Investigation of Hybrid Simulation With Model Updating Compared to an Experimental Shake Table Test**
Ge Ou, Ge Yang, Shirley Dyke and Bin Wu
- 122 Communication Development and Verification for Python-Based Machine Learning Models for Real-Time Hybrid Simulation**
Elif Ecem Bas and Mohamed A. Moustafa
- 143 Real-Time Aeroelastic Hybrid Simulation of a Base-Pivoting Building Model in a Wind Tunnel**
Moniruzzaman Moni, Youchan Hwang, Oh-Sung Kwon, Ho-Kyung Kim and Un Yong Jeong
- 159 A Reflective Framework for Performance Management (REFORM) of Real-Time Hybrid Simulation**
Amin Maghareh, Yuguang Fu, Herta Montoya, Johnny Condori, Zixin Wang, Shirley J. Dyke and Arturo Montoya
- 172 Towards Data-Driven Real-Time Hybrid Simulation: Adaptive Modeling of Control Plants**
Thomas Simpson, Vasilis K. Dertimanis and Eleni N. Chatzi
- 188 Hybrid Test on a Simply Supported Bridge With High-Damping Rubber Bearings**
Chengyu Yang, Xuesong Cai, Ziqin Lai and Yong Yuan
- 197 Real-Time Hybrid Test Using Two-Individual Actuators to Evaluate Seismic Performance of RC Frame Model Controlled by AMD**
Yoichi Mukai, Ayaka Yokoyama, Kohiro Fushihara, Takashi Fujinaga and Hideo Fujitani



Editorial: Recent Advances and Applications of Hybrid Simulation

Wei Song^{1*}, Chia-Ming Chang² and Vasilis K. Dertimanis³

¹ Department of Civil, Construction and Environmental Engineering, University of Alabama, Tuscaloosa, AL, United States,

² Department of Civil Engineering, National Taiwan University, Taipei, Taiwan, ³ ETH Zurich, Zurich, Switzerland

Keywords: hybrid simulation, real-time hybrid simulation, compensation algorithm, stability analysis, uncertainty

Editorial on the Research Topic

Recent Advances and Applications of Hybrid Simulation

The smooth operation of our built environment and modern society heavily rely on the design and construction of large structural systems. Examples include buildings, bridges, and wind turbines. These systems, which serve important daily functions, such as human habitat, transportation, power generation and transmission, often face complex and demanding operation conditions throughout their service life. To ensure the structural integrity and operation safety of these systems and improve their future design, it is important to reveal their complex behavior in various operation environments, especially doing so through experimentations that can replicate realistic working conditions.

Conventional structural testing platforms alone, such as shake table and wind tunnel, may have difficulties in accommodating the entirety of such large- or full-scale structural systems due to limitations in laboratory space, equipment capacity, or fabrication cost. Hybrid simulation provides an attractive alternative for testing large and complex structural systems. This testing method allows physical testing of only the part of the system that is of interest, usually exhibiting complex behavior or yet to be fully understood, while the rest of the system is simulated simultaneously using numerical models with good accuracy and confidence. Such a substructure technique not only provides cost-savings and insights into detailed local behavior of the physical subsystem, but also offers better understanding of the entire complex structural systems, particularly of those systems with multiple components and complex interactions.

A successful hybrid simulation depends on several key factors, including a well-conceived experimental subsystem closely representing realistic boundary conditions, a high-fidelity yet efficient numerical subsystem, a robust and reliable transfer system interfacing numerical and physical subsystems, and a partitioning configuration promoting stability and accuracy in real-time hybrid simulation. As researchers are pushing the boundaries of new capabilities and better enabling tools for hybrid simulation, its benefit on characterizing complex structural behavior is driving the growth of hybrid simulation in broader engineering fields. This Research Topic on Recent Advances and Applications of Hybrid Simulation aims to deepen the knowledge of novel theories and enabling techniques for hybrid simulation and to broaden the spectrum of hybrid simulation applications and studies. Research works collected through this topic closely represent the advancement in the above fronts and are summarized in this editorial.

This Research Topic opens with new applications of hybrid simulation on revealing the structural behavior of complex systems. In Harris and Christenson, a real-time hybrid simulation (RTHS) campaign is developed to capture the uncertainties in force profiles of moat wall impacts and to analyze the complex interactions between impacts and the dynamics of base-isolated structures during earthquake excitations. It is shown that the use of hybrid simulation fully captures the force-deflection behavior of the moat wall and the uncertainties associated with impact events,

OPEN ACCESS

Edited and reviewed by:

Yao Chen,
Southeast University, China

*Correspondence:

Wei Song
wsong@eng.ua.edu

Specialty section:

This article was submitted to
Computational Methods in Structural
Engineering,
a section of the journal
Frontiers in Built Environment

Received: 02 November 2020

Accepted: 09 November 2020

Published: 27 November 2020

Citation:

Song W, Chang C-M and
Dertimanis VK (2020) Editorial: Recent
Advances and Applications of Hybrid
Simulation.
Front. Built Environ. 6:625197.
doi: 10.3389/fbuil.2020.625197

and illustrates the importance of designing for potential non-linear behavior within the moat wall during impact events. In another application involves building structure, Mukai et al. conduct a RTHS to study the seismic response of a single-story reinforced concrete (RC) frame building with an active mass damper (AMD). In this study, most parts of the RC frame are simulated as a numerical model, while a single column of the first story and a controllable AMD are physically tested as experimental subsystems. To improve the online numerical model based on the measured force responses of the RC column specimen, a high-pass filter (HPF) is applied for a force correction by utilizing its phase-lead property. The RTHS test results demonstrate the control performance of the AMD on increasing the damping of the target RC frame. Hybrid simulation has also been applied to study bridge behavior. In Yang et al., hybrid simulation techniques are used to study the seismic behavior of steel girder bridge supported on high-damping rubber (HDR) bearings. In the hybrid simulation tests, HDR bearings are physically tested, while other structural components including the bridge structure are numerically simulated. The results demonstrate that hybrid simulation is a reliable means to study the seismic performance of HDR bearings.

A hybrid simulation platform is a complex dynamic system by itself. Without a proper control strategy, the transfer system interfacing numerical and physical subsystems will experience amplitude variations and phase delays, cause possible instability of hybrid simulation and eventually lead to experimental failure. This effect is more profound in the case of RTHS where rate dependent behavior is dominant. Therefore, control algorithms that can ensure tracking performance of the transfer system are an essential enabling tool for RTHS. Tsokanas et al. propose a novel transfer system controller for time delay compensation. It consists of a robust model predictive control (MPC) along with a polynomial extrapolation algorithm and a Kalman filter. The tracking performance and robustness of the proposed controller is then verified by two virtual RTHS parametric case studies. The obtained results illustrate that the proposed tracking controller can guarantee very small time delays and tracking errors under uncertainties that may be present in RTHS. In Simpson et al., a data-driven control strategy is developed for RTHS. Unlike conventional controllers, where the control plant (transfer system and experimental subsystem) is modeled by a physics-based analytical model, the proposed approach relies exclusively on data processing for tuning an adaptive inverse controller for RTHS. The efficacy and robustness of the proposed control strategy is assessed via a virtual RTHS study. The obtained results indicate that the proposed approach may form a competitive alternative to conventional controllers in RTHS applications.

For a successful hybrid simulation, it is crucial to analyze the system stability of overall hybrid simulation platform to avoid potential damage to specimen or equipment. Gálmez and Fermandois develop a stability indicator that can be evaluated online during RTHS test. Derived from energy analysis, this indicator allows the detection of unstable behavior before the system reaches large displacements that can damage the experimental subsystem or laboratory equipment. Its effectiveness is demonstrated through a virtual RTHS study

with linear system assumption and different compensation strategies. In Chen et al., a stability analysis is conducted for a RTHS for building mass damper (BMD) systems. In the RTHS design, the experimental subsystem includes the control layer and the superstructure of the BMD system installed on a shake table while the substructure is simulated as numerical subsystem. Through a stability analysis, the stability margin can be obtained as an allowable mass ratio of the experimental subsystem to the entire BMD system. This stability margin is then experimentally verified by a RTHS of a simplified BMD system. This study also represents an example of shake table substructure testing (STST), a technique combining hybrid simulation and shake table testing. Tian et al. provides a comprehensive review on STST based on its development in the past two decades, including hybrid simulation frameworks, time integration algorithms, delay compensation methods, shake table and actuator control schemes and boundary force measurement methods. The key techniques and challenges for future STST studies and applications are also identified and presented in this review.

By leveraging advanced modeling techniques and system analysis tools, new developments on its frameworks are empowering hybrid simulation with capabilities of tackling more complex structural systems and more efficient implementation. During hybrid simulation, response time history measured from an experimental subsystem can be utilized to identify the model associated with the tested specimen. Ou et al. present a detailed investigation on model fidelity improvement using hybrid simulation with model updating. This study is focused on both local and global assessment of the updating results by comparing it to conventional simulation and shake table testing. Using seismic response obtained from a steel building frame under shake table testing, this updating approach is successfully implemented to update both a Bouc-Wen model and a bilinear steel constitutive finite element model. In Maghareh et al., a modular framework is developed to enable a safe, confident, and effective RTHS application with challenging and realistic experiments. This framework, currently in its first phase, serves as a foundation for extending RTHS application to black-box RTHS experiments. The building blocks of the framework are demonstrated and validated using numerical studies on a virtual RTHS. The main goal of Bas and Moustafa is to explore the use of machine learning models for RTHS and verify the necessary communication schemes in doing so. Machine learning techniques have been gaining popularity in modeling complex engineering systems across different disciplines. In this study, deep long short-term memory networks in Python are considered for advanced metamodeling for RTHS tests and the idea of embedding the delay compensators within the machine learning model is also explored. The RTHS tests are validated through comparisons with the pure analytical solutions obtained from finite element models.

Most of the above hybrid simulation research works are related to earthquake engineering. As hybrid simulation evolves with more powerful tools and enabling techniques, more and more researchers start the exploration of hybrid simulation in other engineering fields. Moni et al. introduce a new testing

platform for wind engineering, which combines a numerical simulation and the conventional aeroelastic wind tunnel test through RTHS. The stiffness, damping, and partial mass of a scaled building model are represented as the numerical subsystem, while the rest of the mass, the wind-induced pressure around the model and the wind-structure interaction are represented as the experimental subsystem in a wind tunnel. This RTHS framework is validated and calibrated by a series of preliminary tests and RTHS tests in this study. In Song et al., a RTHS framework for monopile offshore wind turbine (OWT) is proposed to study the structural behavior of OWTs under combined wind-wave loading conditions. To overcome the scaling incompatibilities in OWT scaled model testing, the rotor assembly is replaced by an aerodynamic model simulated in full-scale, representing the numerical subsystem, whereas the experimental subsystem contains a reduced-scale tower structure along with the hydrodynamic loading effects provided by wave tank. A set of sensitivity analyses is conducted to evaluate the feasibility of this RTHS framework and determine possible influence of scaling laws, noises, and delays on its design.

With comprehensive reviews to the past technologies and development of more powerful enabling tools and new applications across broader engineering fields, the authors contributing to this Research Topic not only advance the knowledge of hybrid simulation through their latest research works, but also provide exploratory and inspirational fronts for its future growth and expansion. The collection made through this Research Topic is a timely snapshot of these exciting

technical advancements which may propel hybrid simulation into practice, and more importantly, we hope it could highlight the new research avenues for more to explore.

AUTHOR CONTRIBUTIONS

WS drafted the document. C-MC and VD reviewed and provided revising comments on the document. All authors contributed to the article and approved the submitted version.

ACKNOWLEDGMENTS

The topic editors would like to thank all the contributors to this Research Topic for submitting their valuable research works for consideration. They would also like to extend their sincere appreciation to the reviewers and editorial team of Frontiers for their help and effort to make this collection possible.

Conflict of Interest: The authors declare that the research was conducted in the absence of any commercial or financial relationships that could be construed as a potential conflict of interest.

Copyright © 2020 Song, Chang and Dertimanis. This is an open-access article distributed under the terms of the Creative Commons Attribution License (CC BY). The use, distribution or reproduction in other forums is permitted, provided the original author(s) and the copyright owner(s) are credited and that the original publication in this journal is cited, in accordance with accepted academic practice. No use, distribution or reproduction is permitted which does not comply with these terms.



Real-Time Hybrid Simulation Analysis of Moat Impacts in a Base-Isolated Structure

Michael J. Harris* and Richard E. Christenson

Structures Laboratory, Civil and Environmental Engineering Department, University of Connecticut, Storrs, CT, United States

OPEN ACCESS

Edited by:

Vasilis K. Dertimanis,
ETH Zürich, Switzerland

Reviewed by:

Manolis N. Chatzis,
University of Oxford, United Kingdom
Marco Furinghetti,
University of Pavia, Italy
Bozidar Stojadinovic,
ETH Zürich, Switzerland

*Correspondence:

Michael J. Harris
Michael.harris@uconn.edu

Specialty section:

This article was submitted to
Earthquake Engineering,
a section of the journal
Frontiers in Built Environment

Received: 14 March 2020

Accepted: 02 July 2020

Published: 24 July 2020

Citation:

Harris MJ and Christenson RE
(2020) Real-Time Hybrid Simulation
Analysis of Moat Impacts in a
Base-Isolated Structure.
Front. Built Environ. 6:120.
doi: 10.3389/fbuil.2020.00120

Base isolation is a well-known technique used to reduce accelerations and inertial forces in structures during earthquakes. However, excessive displacements of the structure due to flexibility of the isolation layer bearings may contribute to moat wall impact events. These impact events have the potential to cause substantial structural damage. This impact behavior and the effects on structural dynamics have been shown to be highly complex and difficult to model by means of pure numerical simulation. In this paper, the cyber-physical technique called Real-Time Hybrid Simulation (RTHS) is employed to capture the uncertainties in force profiles of moat wall impacts and to analyze the complex interactions between impacts and the dynamics of base-isolated structures during earthquake excitations. It is shown that RTHS is capable of accurately capturing the interactions between the isolation layer and moat wall during impact events induced by ground motions. In addition, the RTHS technique is used to analyze the role played by moat wall material nonlinearities in reducing the inertial demand on the structure during impact events. Finally, possible extensions of the research to larger scales as well as consideration of additional moat wall variants are proposed.

Keywords: real-time, hybrid, simulation, base-isolated, moat impact

INTRODUCTION

Base Isolation

Base isolation is a widely accepted approach aimed at protecting a structure from seismic excitations. This protection is generally accomplished through the use of flexible rubber bearings placed between the foundation and the bottom story (isolation layer) of the structure (Delfosse, 1977; Kelly, 1981, 1990). The flexible bearings reduce the fundamental frequency of the structure to the point that incoming ground excitations contain energy in a higher bandwidth than the resonance frequency and reduce the absolute acceleration of the structure (Jain and Thakkar, 2004; Warn and Ryan, 2012). This, in turn, reduces the inertial demand on the structure, but the relative displacements between the structure and the ground are substantially increased (Connor, 2003; Chopra, 2006). For this reason, the technique of base-isolation is often combined with additional energy dissipation devices such as viscous and/or magneto rheological dampers (Providakis, 2008; Hussain, 2018). This decreases the relative displacement of the base slab during ground motions, but also decreases the effectiveness of structural isolation while increasing accelerations (Thakkar and Jain, 2004; Chopra, 2006). This energy dissipation has been the focus of prior work using RTHS to analyze base isolation. Studies have focused on the use of smart energy dissipation devices

in conjunction with isolation mechanisms (Lin et al., 2004; Chen et al., 2014; Asai et al., 2015), mid-story isolation techniques (Keivan et al., 2017; Zhang et al., 2017), and examination of the nonlinear characteristics of the base-isolation layer (Furinghetti et al., 2020). Even in the cases where added damping is used, if the relative displacement of the base isolation layer is large enough, the isolation layer may impact the foundation wall. This can cause damage to the foundation due to impact and increase the demand on the superstructure due to increased accelerations and inertial forces. Base-isolated structures are particularly vulnerable to long-period, long-duration earthquakes such as the Tohoku, Japan earthquake which occurred on March 11, 2011 as well as the Kumamoto, Japan earthquake which occurred on April 14, 2016 (Ariga et al., 2006; Takewaki et al., 2013; Hayashi et al., 2018).

Previous Impact Work

In order to predict the effects of moat impacts and general pounding impacts on structures, numerous analytical studies have been conducted. The treatment of impact between structures is typically accomplished through the use of either impact or force methods with the force method being more prevalent because the impulse model is incapable of providing the forces between the impacting entities (Muthukumar and DesRoches, 2006; Polycarpou et al., 2013, 2014). Various numerical models have been developed for use in numerical simulations. Muthukumar and DesRoches (2006) discuss several approaches to numerical impact models based on impact theory including linear spring, Kelvin viscoelastic, Hertz nonlinear spring, and Hertz damp hyperelastic models. These models have been used in a number of analytical studies to investigate the effects of impacts on structures including analyses based on purely linear behavior (Liu et al., 2014, 2017), viscoelastic impact behavior (Kun et al., 2009), and nonlinear impact behavior (Muthukumar and DesRoches, 2006). The models assumed a constant line of action and a lack of torsional forces. The viscous damping of the impact behavior was constructed based on assumed coefficients of restitution. The models also assumed the impacting bodies were lumped masses. However, when studying the response of diaphragms in buildings during pounding events, Cole et al. (2011) asserted that simplified lump mass models of impact behavior may be inadequate when describing the complexities associated with these impact events. This is due to the fact that lumped mass models do not consider the impact geometry and how this geometry will affect contact forces observed during impact events. Indeed, the actual impact geometry contains a large degree of uncertainty. Bamer et al. (2017) noted that contact forces have a profound effect on the interaction forces of impacts and examined the potential for simplifying the representation of these contact forces using techniques such as modal truncation. They concluded that as higher fidelity is introduced to the contact models, there is a notable increase in agreement between time history simulation results for these modal analysis methods, which performed well as compared to the full benchmark solution of the pounding problem being analyzed. In particular, they observed marked agreement between the benchmark solution and their proposed “Hybrid Substructure Truncation” technique. However, this

higher fidelity and accuracy of contact models necessitates the use of increasingly smaller time steps during simulation in order to maintain stability (Bamer et al., 2017). Polycarpou et al. (2013) developed a methodology of treating impact events that helped to alleviate the need for *a priori* knowledge or assumptions regarding the stiffness, damping, and geometry of the region of impact between structures. This need for assumptions regarding the impact geometry underlies the highly uncertain nature of not only this geometry, but the force-displacement behavior of the impacting bodies. In addition to the above-mentioned impact studies, Masroor and Mosqueda (2013) developed a model for the force-displacement behavior of impacts based on empirical results of impact forces of a base-isolated structure during large scale testing. In their experimental results, the impact force time history approximates a half-sine pulse of frequency equal to roughly 8 Hz. On top of this half-sine pulse, there was also higher frequency behavior observed initially, but these higher frequency oscillations damp out rapidly. From their results, they constructed an impact model based on a cantilevered beam with distributed stiffness and damping used to represent soil backfill of the foundation wall. The proposed model showed good agreement with experimental results. All of these impact models attempt to strike a balance between computational efficiency and realism. However, the experimental studies of Masroor and Mosqueda have demonstrated the complexities and uncertainties involved with predicting the force-displacement behavior of the foundation wall.

Scope of Work

The present study proposes the use of the dynamic testing technique, Real-Time Hybrid Simulation (RTHS), as a means of analyzing structural pounding in response to earthquake excitations. By replacing the analytical representation of impacting bodies with the physically measured restoring forces occurring during impact events, this approach eliminates the need to strike a balance between overly simplistic impact models and those that are computationally expensive. The use of a moat wall analog for the physical substructure within the RTHS loop enables the test to capture the uncertainties associated with impact geometry and the force-displacement of the materials by using measured feedback forces in place of a numerical calculation of the impact forces. In addition to alleviating the uncertainties associated with the impact geometry and behavior, RTHS is able to capture the effects of yielding within the moat wall. This phenomenon was shown to have a substantial effect on the dynamic response of the system by both Wolf and Skrikerud (1979) as well as Sarebanha et al. (2017).

Following this introduction, a discussion of the RTHS testing technique is provided, including both the history and implementation procedure. A description of the structure to be analyzed, and the substructuring methodology is also provided. The specialized equipment required to conduct RTHS testing is then discussed, and the specific equipment used for this work is outlined. Next, the experimental techniques used in this work are discussed. This discussion includes the selection of ground motions for testing, the selection and testing of the physical substructure, the technique used to transform full-scale

numerical displacements to the lab scale and back, and the topic of actuator compensation. The results of the tests are presented which include the time histories of impact force behavior for the moment of impact with the physical substructure and the frequency content of this impact behavior. This is followed by time histories of the relative displacement of the isolation layer, the absolute acceleration time histories of the isolation layer, and the time histories of the reaction force of the moat wall acting on the base slab. The force-displacement behavior obtained during RTHS testing is then presented along with the deformation strain rate behavior. The above-mentioned experimental test results are compared with previous results by Masroor and Mosqueda (2013) as well as with results from analytical simulations based on elastic impact models as used by Liu et al. (2014, 2017). Finally, conclusions from this work are drawn and suggestions for future work are proposed.

REAL-TIME HYBRID SIMULATION

History and Description

Real-Time Hybrid Simulation is a testing technique wherein a structure is partitioned or substructured into physical and numerical components which are then coupled in real-time. An excitation is imparted on one or more substructures and the response of the entire structure is analyzed. Typically, the numerical substructure contains components of the structure that can be modeled analytically with great confidence, while the physical substructures are those containing strong nonlinearities, uncertainties, or properties that cannot be modeled in closed form. The first RTHS test was conducted by Hakuno et al. (1969) where a cantilevered structure was excited by base excitations imparted by a shaker. The real-time solutions of the equations of motion were obtained using an analog electronic computer. Due to inadequate control of the actuators, the test was considered unsuccessful (Takanashi and Nakashima, 1987).

Subsequently, the dynamic substructure testing of systems progressed using digital computers and testing was typically conducted on an extended time scale. This new approach to hybrid testing was termed Pseudo-dynamic Testing (PDT) (also known as Online Testing) and used the same hybrid substructuring approach, but coupled physical substructures with numerical substructures using digital means of numerical integration and extended timescales for testing (Mahin and Shing, 1985; Takanashi and Nakashima, 1987). Extending the timescale of testing reduced the burden on required computation power, and lessened the potential for instabilities stemming from inadequate actuator control. During testing, the complete system was partitioned into a physical substructure containing components of the structure that would likely undergo nonlinear deformation while the numerical substructure represented the remainder of the structure from which, boundary conditions to be imposed on the physical substructure were calculated. The solution of the equation of motion was calculated by a computer and this solution was used to define the boundary conditions at the interface between the numerical and physical substructures. Compatibility of the forces and displacement of the structure

at the interface of the numerical and physical substructures are considered. This quasi-static method of structural testing was capable of capturing a number of phenomena associated with seismic excitation such as permanent deformation and hysteretic behavior (Takanashi and Nakashima, 1987). Despite the success of PDT, the extended time scale used for this technique prohibited accurate physical testing of rate-dependent components such as viscoelastic or friction dampers. To this end, a number of techniques have been used or developed to decrease the computational demand during testing including Frequency-Based Substructuring (Gordis, 1994), Convolution Integral Method (Kim et al., 2011), State Space Modeling (Su and Juang, 1994; Abbiati et al., 2019) and Partitioned Time Integration (Abbiati et al., 2019).

The increasing power of digital computers, the development of digital actuator control, and the improvement of D/A converters led to the re-introduction of real-time testing by a number of researchers (Nakashima et al., 1992). Horiuchi et al. (1996) analyzed the effects of hydraulic actuator delay on test setup and stability and proposed methods of compensating for this delay using a polynomial extrapolation technique. Additional compensation techniques were developed by Carrion and Spencer (2007) based on developing Laplace-domain polynomial fraction representation of the actuator dynamics and then multiplying the commanded displacement signal by the reciprocal of this polynomial fraction prior to sending the command signal to the actuator. This latter technique was used for actuator compensation during this study.

This paper discusses the use of RTHS to analyze the effects of moat-wall impacts on a base-isolated structure. The numerical substructure examined was a two degree of freedom (DOF) base-isolated structure which was excited numerically based on time history accelerations of earthquake records. During testing, the numerical displacement of the base isolation layer was computed and the relative displacement between the isolation layer and the ground was calculated. This relative displacement constraint was imposed on the physical substructure consisting of a moat wall analog located in the Structures Laboratory at the University of Connecticut. Imposing the boundary constraint compatibility between the physical and numerical substructures was accomplished through the use of a hydraulic actuator. If the relative displacement of the base slab was large enough, the actuator piston would impact the physical substructure of the moat wall analog. The reaction forces between the actuator piston and the physical substructure were then sensed by a force sensor on the tip of the actuator piston and then fed back into the numerical model as an impact force acting on the base slab. A schematic of the RTHS test is shown in **Figure 1**.

Numerical Substructure

The structure analyzed in this test was a scaled version of a 2DOF base-isolated structure designed to mimic the frequency-domain behavior of the first two modes of the three story structure base isolated structure used moat impact testing by Masroor and Mosqueda (2013). This structure was subdivided into a numerical substructure of the 2DOF base-isolated building and the physical substructure of the foundation wall. The 2DOF base isolated

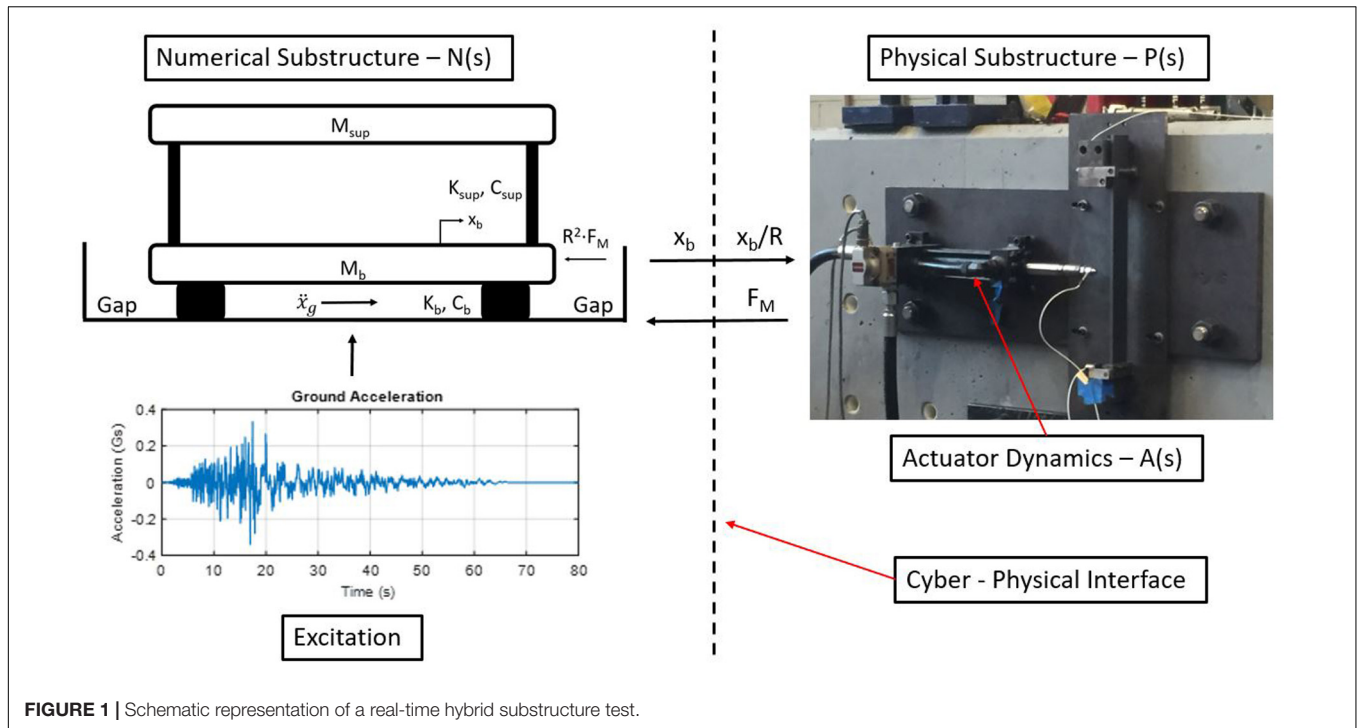


FIGURE 1 | Schematic representation of a real-time hybrid substructure test.

structure can be seen in **Figure 1**. In the Figure, M_{sup} , represents the mass of the superstructure. The stiffness of the superstructure layer, K_{sup} , was tuned to match the fundamental period (0.67 s) of the superstructure tested by Masroor and Mosqueda. The mass and stiffness of the base isolation layer were tuned such that the fundamental frequency of the total structure matched that of the complete structure from the previous experiment (0.32 Hz). Structural damping was defined using Rayleigh damping with the damping ratios of the two modes set to 0.15 and 0.048 for the first and second modes and the mass ratio of the base slab to the mass of the superstructure was held constant at 0.56:1 which was consistent with the structure tested by Masroor and Mosqueda.

During both analytical studies as well as RTHS testing, a state space representation of the structure was used. The equation of motion describing the dynamics of the structure can be seen in Eq. 1 below.

$$M \cdot \ddot{x} + C \cdot \dot{x} + K \cdot x = -\Gamma_g \cdot M \cdot \ddot{x}_g + \Gamma_m \cdot F_m \quad (1)$$

where M , C , and K represent the mass, damping, and stiffness matrices respectively. The vector *Gamma* (Γ) represents the influence vector for the two DOFs of the structure with Γ_g being the influence vector based on the ground excitation which is equal to $[1 \ 1]^T$ and Γ_m being the influence vector from the force of the moat impact which is equal to $[1 \ 0]^T$. Eq. 1 assumes a linear force-displacement (F-D) behavior of both the isolation bearings and superstructure. In regards to the linearity of the F-D behavior of the isolation layer, such viscoelastic behavior with damping ratios of 0.15 could be provided by devices such as High Damping Rubber Bearings (HDRB)s (Oh et al., 2016). By assuming the isolation bearings are linear in this initial study, the effect of the nonlinear behavior of the moat impact on the overall

system response could be observed and analyzed. From, Eq. 1, the dynamics of the structure can be rewritten in state space form as the following:

$$\dot{x} = A_{ss} \cdot x + B_{ss} \cdot u \quad (2)$$

$$y = C_{ss} \cdot x + D_{ss} \cdot u \quad (3)$$

where:

$$x = \begin{bmatrix} x_{base} \\ x_{sup.} \\ \dot{x}_{base} \\ \dot{x}_{sup.} \end{bmatrix} \quad (4)$$

and:

$$u = \ddot{x}_g \quad (5)$$

The matrix A_{ss} was the state matrix, B_{ss} was the input matrix, C_{ss} was the output matrix, and D_{ss} was the direct throughput matrix. These matrices are given as:

$$A_{ss} = \begin{bmatrix} \emptyset & I \\ -M^{-1} \cdot K & -M^{-1} \cdot C \end{bmatrix} \quad (6)$$

$$B_{ss} = \begin{bmatrix} \emptyset \\ M^{-1} \end{bmatrix} \quad (7)$$

$$C_{ss} = [I \ \emptyset] \quad (8)$$

$$D_{ss} = [\emptyset] \quad (9)$$

The output of the state space system y was a vector containing the calculated displacement of the base slab and superstructure as in

Eq. 10. These output signals were used during the development of the figures within the section “Results and Discussion.”

$$y = \begin{bmatrix} x_b \\ x_{sup} \end{bmatrix} \quad (10)$$

The state space model of the structure was used to perform numerical simulations of structural dynamics in Simulink using a Runge-Kutta explicit numerical integration scheme with a fixed sampling time of $4,096^{-1}$ s. Within Simulink, the output signal y provided the signal of the analytically predicted displacement of the base isolation layer and superstructure. In addition, by twice differentiating the components of y , the predicted acceleration of the two stories was obtained.

Physical Substructure

The physical substructure meant to represent the moat wall was comprised of a simply supported beam made of low carbon steel (Right side of **Figure 1**). Steel was chosen to be consistent with studies performed by Masroor and Mosqueda (2013) during experimental analyses of moat impacts with a steel foundation. For this proof-of-concept RTHS test, the impacts of the base slab with one side of the foundation wall will be considered. The effects of single-sided pounding excitations of structures is a well-established field of study in structural dynamics (Wolf and Skrikerud, 1979; Pantelides and Ma, 1996). This type of pounding event tends to occur when a building has an adjacent structure on only one side or when the dynamic characteristics of a structure differ from adjacent structures on one side. Wolf and Skrikerud (1979) examined the time- and frequency-domain responses of dynamic systems where single-sided impacts were observed. They noted a strong amplitude-dependence on the overall dynamic behavior of the structure. They also examined the transient response of impacts between a nuclear reactor structure and an adjacent SDOF structure when subjected to an earthquake excitation. The studies showed the importance of considering pounding forces during the design phase of structures and promoting the beneficial effects of tuned mass damper systems for mitigating pounding damage. Pantelides and Ma (1996) examined the parameterization of single-sided impact events between SDOF systems and infinitely rigid constructs. They considered the effect that separation distance of structures has on the response. In addition, they examined the differences in dynamic response when considering elastic structures as opposed to elastic-perfectly plastic structures. They observed both a decrease in pounding as separation distance was increased as well as a decrease in the acceleration and pounding forces when considering inelasticity of the structure. They noted that this inelasticity may have benefited structural performance for structures in the past even when structural separation was inadequate.

RTHS TEST EQUIPMENT

The equipment required to conduct the RTHS test included sensors to measure the restoring force from the moat impact

events, a real-time controller to calculate the response of the structure to the ground excitation and impact force, a hydraulic actuator system to enforce the calculated displacement of the base slab, and a data acquisition system used to collect response data of the test. These are elaborated upon below.

Force Measurement

The reaction force of the moat wall was measured using a single axis PCB 208C04 piezoelectric force sensor with a maximum capacity of 4.45 kN (1000 lbs). The force sensor was accurate to within $\pm 5\%$ over the frequency range of 0.0003 to 36,000 Hz. A picture of the force sensor mounted to the actuator piston can be seen in **Figure 2**. The force sensor required an input electrical signal of 4 mA which was provided by a PCB 483C28 signal conditioner. A hemispherical attachment was mounted to the force sensor so as to improve the contact between the force sensor and beam during impacts. The mass of the attachment was small and the inertial effects on the force measurement were neglected. In addition, while both comprised of metal, the stiffness of the attachment was very large in comparison to the stiffness of the moat wall substructure. In the context of the RTHS test, this meant that the base slab was very stiff relative to the moat wall.

Real-Time Controller

A dSPACE 1103 real-time controller was used to conduct the RTHS testing. During testing, the controller was used to calculate the response of the 2DOF structure to the inertial force due to the ground excitation and restoring force of the moat impact. The displacement of the structure was calculated at each time step using a state space representation. Once calculated, the displacement of the base slab was then scaled to fit within the stroke limits of the actuator, compensated, and sent to the actuator. The dSPACE controller was running Simulink at a time step of 0.244 ms (4,096 Hz) using a Runge-Kutta explicit integration scheme. The dSPACE controller has 16 multiplexed analog inputs, each with a 16 bit resolution A/D converter as well as 8 analog outputs with 16 bit D/A converters and is capable of interfacing with MATLAB and Simulink. Of the available D/A converters, a total of four were used during testing. The analog signals produced corresponded to the ground acceleration, calculated base slab displacement, calculated superstructure displacement, and the absolute acceleration of the base slab respectively. There were two A/D converters used to collect the measured actuator displacement and the measured restoring force from the moat impacts.

Hydraulic Actuator

The hydraulic actuator used was a Quincy Ortman servo-hydraulic actuator designed for dynamic testing applications. The actuator had a maximum capacity of 8.896 kN (2,000 lbs) with a maximum one-sided stroke limit of 8.5 cm (3.3 in). The frequency bandwidth of actuation for the actuator was 0–40 Hz. The hydraulic actuator was controlled with a Parker Hannifin Corporation analog controller. A Micropulse LVDT internal to the hydraulic actuator provided an analog output signal (± 10 V) corresponding to the measured position of the cylinder. This measured displacement was assumed to correspond to

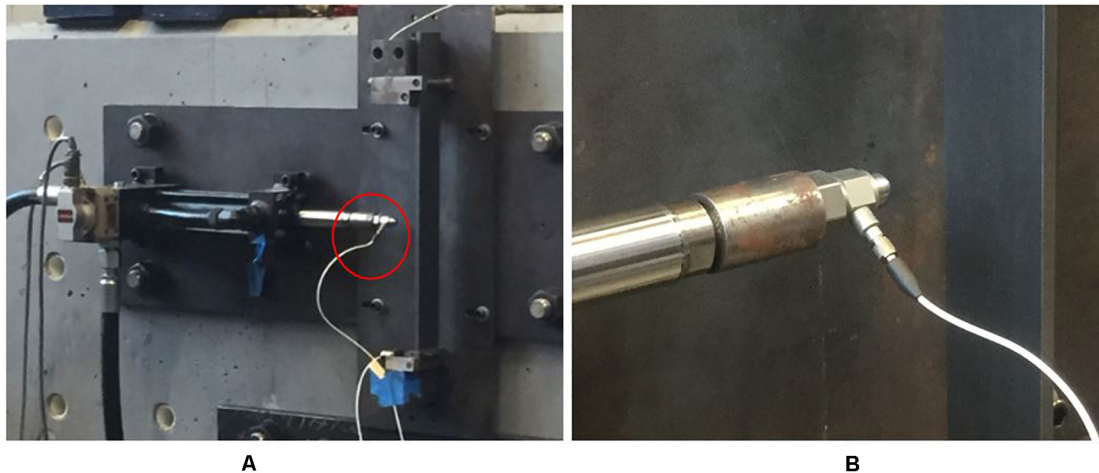


FIGURE 2 | (A) The hydraulic actuator with the force sensor circled and **(B)** a close-up view of the force sensor mounted on the actuator piston.

the displacement of the base slab within the physical scale of the laboratory.

Data Acquisition

During testing, data collected included the ground acceleration input to the building, the displacement time histories of the base slab and superstructure, the measured displacement time history of the actuator, and the restoring force time history signal from the force sensor. The signals were collected with a DataPhysics SignalCalc Mobilyzer Dynamic Signal Analyzer with 32 input channels. This data acquisition unit allowed for adjustable sampling rates for data collection as well as providing anti-aliasing filters that are integrated into the A/D input channels. As the duration of a full time history sample was inversely related to the sample frequency, longer time histories (64.00 s duration) at sampling rates of 2,048 Hz were collected of the structural response over the full duration of the ground motion excitations and shorter time histories (10.67 s duration) at sampling rates of 12,288 Hz were collected to analyze the force profile during impact events.

EXPERIMENTAL PROCEDURE

Ground Motion Selection

The effects of moat impacts on a base-isolated structure during earthquake excitation were tested using the RTHS technique. In order to perform the tests, a total of 3 ground motions were selected from the suite of 50 ground motions put forth in the FEMA P695 document “Quantification of Building Seismic Performance Factors” (Federal Emergency Management Agency [FEMA], 2009). Of the three ground motions selected for testing, one ground motion represented a near-field pulse-like motion, one ground motion represented a near-field non-pulse-like motion, and one ground motion represented a far-field motion. The ground motions selected from each category were those predicted by numerical simulations to

cause the largest absolute acceleration in the base-isolation layer during moat wall impacts. The specific ground motions selected have been identified in **Table 1** and the time histories and frequency content of these ground motions have been plotted in **Figure 3**.

Structural Description

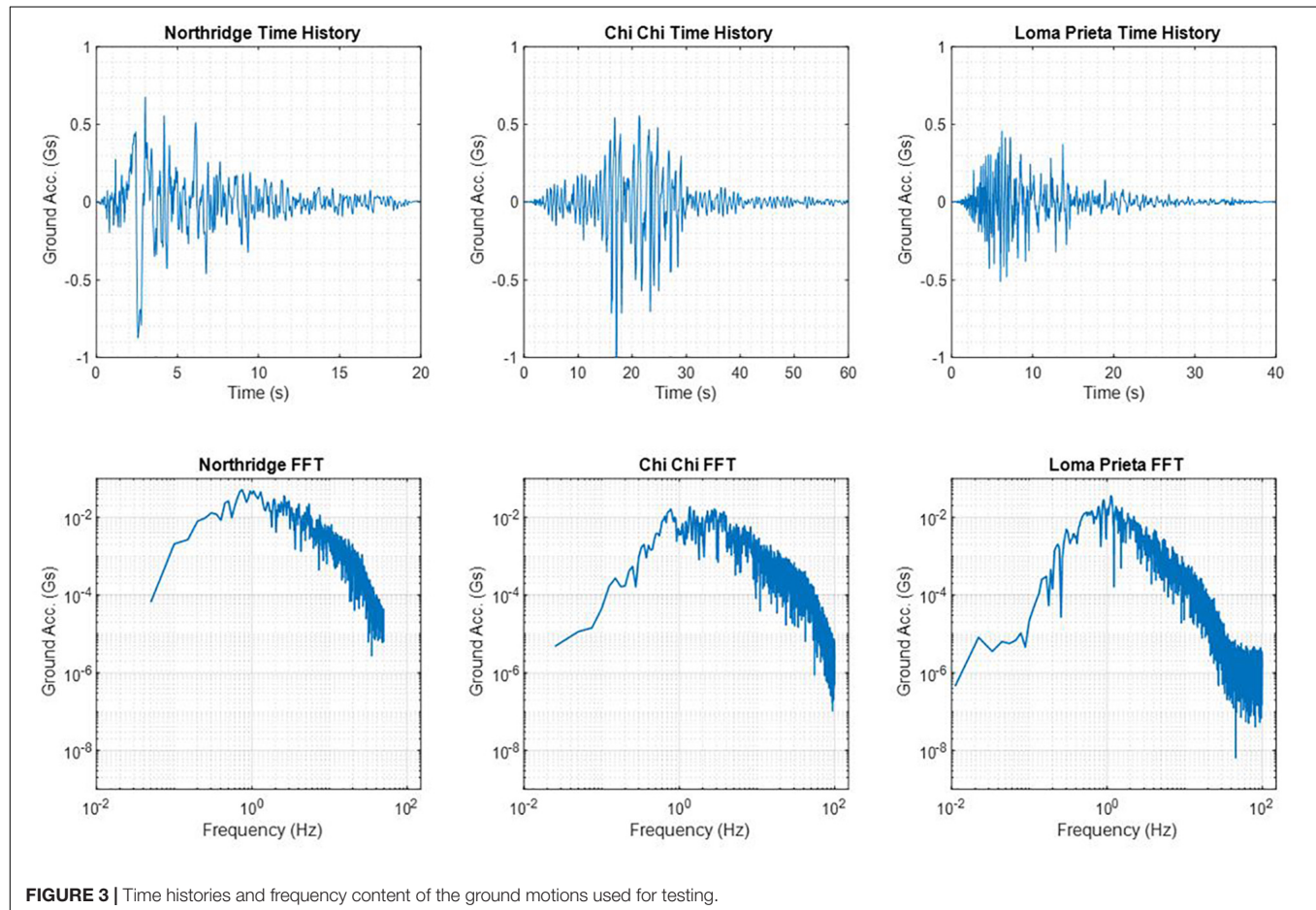
The numerical substructure of the base-isolated structure was designed to exhibit the same response frequencies as the first two modes of the structure analyzed by Masroor and Mosqueda (2013) during laboratory testing of moat impacts of base isolated structures. The resonant frequencies of the structural modes of the numerical substructure were 0.32 and 1.5 Hz. The mass ratio of the base slab to that of the total mass of the superstructure is 0.56:1. These frequencies and mass ratios are consistent with the structure tested by Masroor and Mosqueda. Based on the size limitations imposed by the test setup however, the total mass of the structure needed to be scaled down. A discussion of the scaling of the mass of structure has been provided in following sections.

Physical Substructure Description

The physical substructure used in this work was a simply supported steel beam which would act as the moat wall during RTHS testing. A steel beam was used as the physical substructure during testing in order to facilitate comparisons of RTHS test results with steel moat wall impact results obtained by Masroor and Mosqueda (2013). This comparison of impact force time histories was used to ensure that the RTHS test was accurately capturing impact forces between the structure and moat wall. The steel beams used for the RTHS tests presented here were made of low carbon steel meeting the ASTM A 108 Standard. The dimensions and support conditions of the steel beams were constrained by the specifications of the PCB 208C04 force sensor which had a maximum load capacity of 4.45 kN (1,000 lbs). The steel beam had a span length of 38.74 cm (15.25 in), a width

TABLE 1 | Identifying information for ground motions used in testing.

Event	Classification	Year	Station	PEER database file
Northridge, CA, United States	Near Field Pulse-like	1994	Rinaldi	RSN1063_NORTHR_RRS228.AT2
Chi-Chi, Taiwan	Near Field Non-Pulse-like	1999	TCU084	RSN1517_CHICHI_TCU084-E.AT2
Loma Prieta, CA, United States	Far Field	1989	Capitola	RSN752_LOMAP_CAP000.AT2

**FIGURE 3** | Time histories and frequency content of the ground motions used for testing.

of 5.08 cm (2 in) and thickness of 0.64 cm (0.25 in). A simply supported steel beam with the dimensions listed was predicted to provide the ability to test material nonlinearities within the physical substructure while providing a margin of safety to not exceed the capacity of the force sensor.

Moat Wall Force-Displacement Testing

The physical substructure in the RTHS test was a steel beam used to represent a moat wall on one side of a base isolated structure. During testing, the restoring force provided by this steel beam represented the restoring force of a moat impact event. The force-displacement behavior of the beam when subjected to a point load at midspan can be seen in **Figure 4**. From the initial slope of the force-deflection behavior within the elastic region of the curve, the stiffness of the beam was calculated experimentally as 1.787 kN/cm. This result can be compared to

calculations using Timoshenko beam theory for a pinned-pinned beam (Roylance, 2000). The stiffness of the beam was calculated to be 1.790 kN/cm when assuming pure bending conditions and 1.784 kN/cm including the effects of shear deformation. As the two results differ by 0.34%, it was assumed that pure bending is the predominant mode of deformation within the steel beam. It was also noted that this analytical stiffness prediction based on pure bending differs by 0.17% from the experimentally obtained beam stiffness. Using this pure bending assumption, the strain at the point furthest from the neutral axis can be obtained from Eq. 11 (Beer et al., 2006):

$$\varepsilon = \frac{c}{2} \cdot \frac{1}{\rho} \quad (11)$$

In Eq. 11, c is the thickness of the beam (0.64 cm), and ρ is the radius of curvature for a given strain ε . The radius of curvature

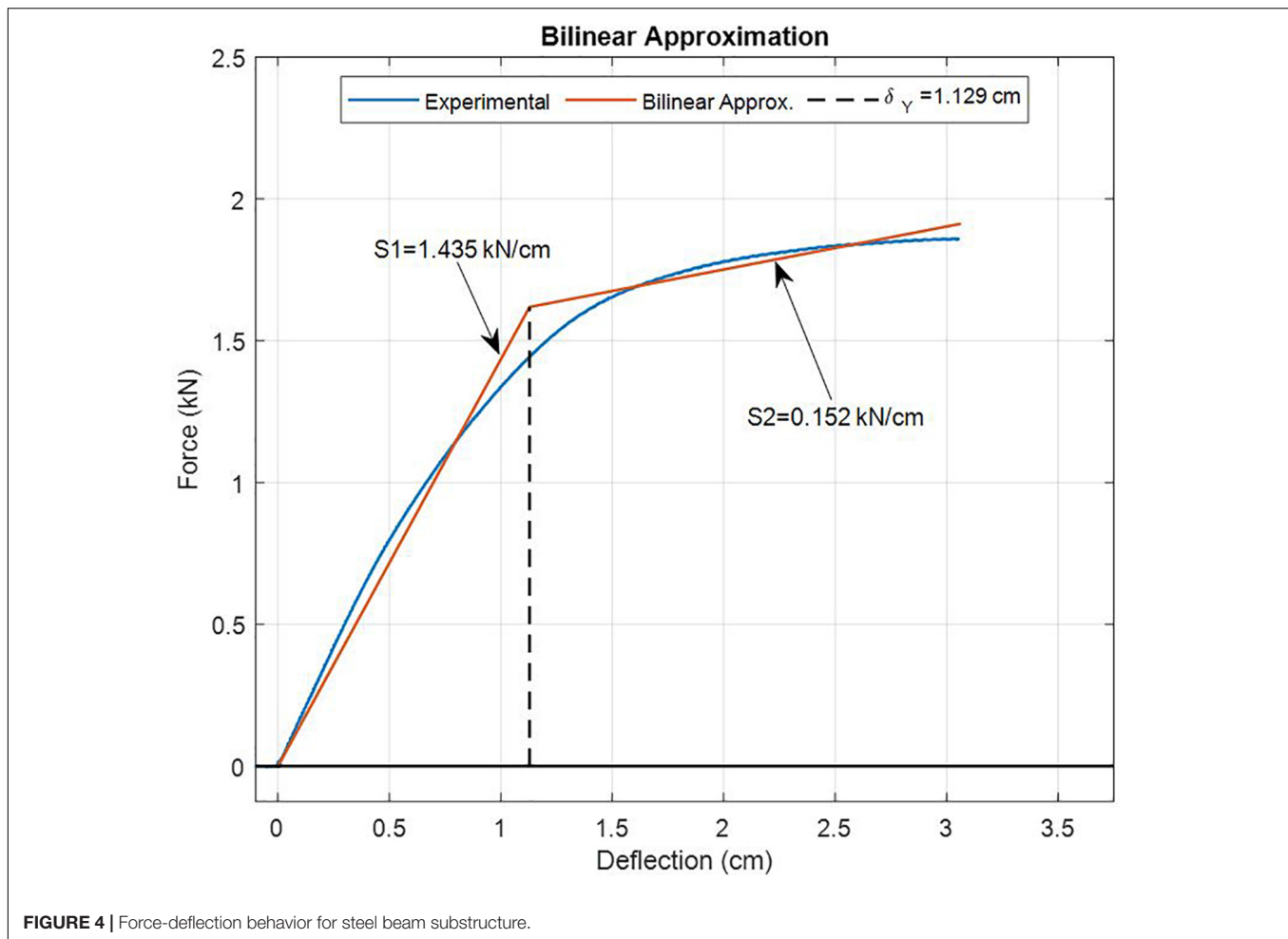


FIGURE 4 | Force-deflection behavior for steel beam substructure.

can be calculated from the geometry of the experimental setup as given by Eq. 12 (Weisstein, 2015).

$$\rho = \frac{\left(\frac{l}{2}\right)^2}{2 \cdot \delta} + \frac{\delta}{2} \quad (12)$$

Where l is the span length of the beam (38.74 cm) and δ is the deflection of the beam at midspan. Eqs. 11 and 12 to calculate the strain allowed for the analysis of how the deformation strain rate affected the stiffness of the physical substructure.

For purposes of numerical simulations, a bilinear representation of this force-displacement curve was constructed. This approximation can also be seen in **Figure 4**. Based on the bilinear approximation of the force-deflection curve, the deflection at the onset of yielding was approximately 1.13 cm (0.5 in); a result which was difficult to verify with calculations due to the complexity of plastic hinge formation. Similar to the work of Masroor and Mosqueda (2013), the bilinear approximation of the F-D behavior was used to develop an impact model for restoring forces acting on the base-isolated structure in response to ground motions. There were two types of impact scenarios examined. In the first scenario termed a “linear” impact scenario, the deflection of the beam substructure

would stay within the deflection region of $0 < \delta < 1.129$ cm. The second type of impact scenario termed a “nonlinear” impact scenario, was a scenario designed to deflect the beam substructure so as to induce yielding, permanent deformation, and dissipate energy during the impact event. During this scenario, the value of δ would exceed the 1.129 cm calculated to be the yielding point of the bilinear approximation. The creation of linear or nonlinear impact scenario conditions was achieved by scaling the total mass of the structure. As the mass of the structure decreases, the total momentum of the structure is reduced, and the impact tends to cause smaller deflections in the moat wall. The mass ratio between the isolation layer and superstructure remained constant when scaling the total mass of the structure. In addition, the frequency response function of the structure was held constant when scaling the total mass of the structure. The procedure for scaling the mass of the total structure is further discussed later within the section “Mass Calibration for Linear and Nonlinear Deflection Testing.”

While in reality moat impacts are characterized by axial and shear forces as well as torques, this work studied a simplified version of an impact event where impacts were assumed to generate forces along the single line of action of the actuator

piston. This force was the restoring force due to imparting bending within the physical substructure. The single line of action simplification has been used extensively to alleviate some of the computation expense of calculating impact forces. A summary of several of these impact models is provided in Muthukumar and DesRoches (2006). In reality, the impacts during RTHS testing undoubtedly contained shear forces and torques acting at the point of impact. However, the use of a single axis PCB 208C04 piezoelectric force sensor allowed for capturing of the restoring forces along the single line of action for feedback into the numerical substructure. In this manner, the physical substructure was treated as a spring acting in a single DOF, similar to the impact model used by Liu et al. (2017, 2014). Unlike the models used by Liu et al. however, use of a physical substructure and RTHS testing allowed for the incorporation of uncertainties in the impact behavior such as friction forces at supports and at the contact point as well as the dynamic characteristics of the moat wall during impact. It is noted, however, that future studies may look to expand the RTHS testing technique to examine more degrees of freedom during impact events through the use of 6DOF shake tables along with multiple 3DOF sensors at the impact interface.

Scaling of Dimensions for Testing

The physical scale of the laboratory equipment used for this work necessitated scaling of either the ground motions used for testing, or the displacements and forces observed during testing. Procedures for scaling ground motions for time history analysis have been well-studied and documented both in research as well as in codes (American Society of Civil Engineers [ASCE], 2010; Wood and Hutchinson, 2012). Typically, scaling of ground motions has been performed during design or analysis of a structure so as to produce a suite of ground motions that match the expected spectral acceleration response at a building site if such ground motions are not available. The validity of the practice of scaling ground motions, while extensively researched, is still largely debated. Studies investigating the effects of scaling on nonlinear time history analyses of SDOF and MDOF systems have shown no appreciable difference in nonlinear deformations when careful scaling of ground motions is performed (Shome et al., 1998; Iervolino and Cornell, 2005) and FEMA has proposed that ground motions should be scaled by normalizing the peak ground velocity (Federal Emergency Management Agency [FEMA], 2009). At the same time, studies have arrived at different conclusions; stating that the scaling of ground motion suites may produce changes in the nonlinear displacement of a structure when compared to selection of an appropriate suite of ground motions that approximate the desired response spectra (Luco and Bazzurro, 2007). During this work, the decision was made to perform the numerical simulations of the structural response to ground motions using the full scale of the ground motion acceleration and not to adjust the ground motion such that the calculated displacement of the base slab would be within the limits of the stroke limits of the hydraulic actuator. Rather, the calculated displacement of the base slab due to the full ground motion was then scaled to accommodate

the stroke limit of the actuator and the restoring force of the moat wall impact was adjusted so as to match the scale of the numerical simulation. This scaling procedure was similar to “Procedure 2” as described by Kumar et al. (1997). The decision to scale displacements and forces rather than ground acceleration was made for several reasons. First, as the main focus of this work sought to illustrate the ability of the RTHS technique to analyze the impact forces that occur during ground excitations, the question of accurate scaling of ground motions was beyond the intended scope of this paper. In addition, ensuring the compatibility and proper enforcement of boundary conditions is of paramount importance during RTHS testing. This work endeavored to illustrate the care that must be taken in order to ensure proper scaling was implemented. Scaling of the forces and displacements required the assumption that all impact forces scaled similarly including the restoring forces due to beam deflection, the contact forces, and any forces stemming from vibrations of the beam.

Energy Conservation During Testing

Due to limitations with the scale of the experiment, it was necessary to scale down the calculated displacement of the base slab as obtained from simulations in order to accommodate the stroke capacity of the hydraulic actuator used for the RTHS test. In simulating the structural response to the ground motions, it was observed that the displacement of the base slab regularly exceeded 0.25 m. The maximum one-sided stroke of the actuator, meanwhile, was only 8.5 cm. It was therefore necessary to scale down the structural response to such an extent that the displacement of the base slab could be accomplished by the actuator. However, scaling down the displacement commanded of the actuator had the effect of altering the apparent kinetic energy of the base slab as it moves in response to the ground motion and impacted the moat wall. Consequently, as the restoring force of a moat impact event was fed back into the simulation, the energy that is absorbed and dissipated by the moat wall must be scaled back up properly such that the kinetic energy losses of the base slab were of the correct magnitude within the simulation. The procedure used for developing the scale factors as well as for converting between simulated and actuator displacements have been outlined in the paragraphs to follow.

The scale of the experiment necessitated a careful analysis to be sure that the change in kinetic energy of the structure within the simulation was equal to the energy absorbed and dissipated by the steel beam during the impact event. In the case of a beam deflecting within the linear regime, the stored potential energy within the beam can be calculated from Eq. 13.

$$E^{\text{potential}} = \int_0^{\delta_f} (K \cdot \delta) d\delta = \frac{K\delta_f^2}{2} \quad (13)$$

Within Eq. 13, K is the stiffness of the beam and δ is the deflection of the beam. The size of the beam substructure as well as the stroke limit of the hydraulic actuator were substantially smaller than a full-scale test of the moat impact and therefore, it was necessary that the calculated displacement of the base slab be

scaled so as to accommodate the stroke limit of the actuator. For testing, a scale factor R was defined as:

$$\text{Scale} = R = \frac{x_{\text{Simulation}}^{\text{Max}}}{x_{\text{Desired}}^{\text{Max}}} \quad (14)$$

where $x_{\text{Desired}}^{\text{Max}}$ was the maximum desired actuator displacement and $x_{\text{Simulation}}^{\text{Max}}$ was the maximum displacement of the base slab as calculated during time history simulations where moat wall impacts were not considered. The analytically obtained maximum displacement of the structure where moat impacts were ignored provided the maximum uncontrolled displacement to be expected from a particular ground motion. Generating a scale factor from this uncontrolled displacement would provide assurance that the actuator would stay within its desired stroke limits. The maximum desired actuator displacement was set to 7.303 cm (2.875 in) based on the maximum one-sided stroke limit of the actuator 8.382 cm (3.3 in). The maximum simulated displacement and scale factor R was determined for each earthquake analyzed. This scale factor was the reduction factor required to stay within the desired stroke limits of the actuator in the case of an uncontrolled test if no moat wall were present. At the same time, the kinetic energy of the isolation layer was given by Eq. 15.

$$E^{\text{kinetic}} = \frac{(m_{\text{slab}} \cdot v_{\text{slab}}^2)}{2} \quad (15)$$

In Eq. 15, v_{slab} represented the velocity of the base slab at the instant of impact with the beam. Eq. 15 implies that when scaling the displacement by the scale factor R the kinetic energy of the base slab scales by R^2 . When scaling the restoring force back into the scale of the numerical simulation, care must be taken such that the restoring force of the beam substructure would be consistent with the scale of the simulation. Knowing that the relationship between the simulation space and laboratory space was given by Eq. 16,

$$\delta_{\text{simulation}} = R \cdot \delta_{\text{Actuator}} \quad (16)$$

and knowing that the potential energy of the beam during impact was proportional to the square of the beam deflection as shown by Eq. 11, the restoring force of the beam must be multiplied by R^2 when transitioning from the actuator to the simulation scale in order for it to be consistent with the scale of the numerical simulation. This has been further derived in Eqs 17 and 18.

$$E_{\text{Simulation}} = \int_0^{\delta_{\text{Desired}}^{\text{Max}}} R^2 \cdot K \cdot \delta_{\text{Act}} = R^2 \cdot \left| \frac{K \cdot \delta_{\text{Act}}^2}{2} \right|_0^{\delta_{\text{Desired}}^{\text{Max}}} \quad (17)$$

$$E_{\text{Simulation}} = \left| \frac{R^2 \cdot K \cdot \delta_{\text{Act}}^2}{2} \right|_0^{\delta_{\text{Act}}^{\text{Max}}} = \left| \frac{K \cdot \delta_{\text{Simulation}}^2}{2} \right|_0^{\delta_{\text{Simulation}}^{\text{Max}}} \quad (18)$$

Mass Calibration for Linear and Nonlinear Deflection Testing

A numerical simulation was constructed using MATLAB/Simulink to analyze the response of the base-isolated structure

to the three earthquake records selected from those outlined in FEMA P695 (Federal Emergency Management Agency [FEMA], 2009) and to calibrate the mass of the base slab such that the impact with the moat impacts would induce either linear or nonlinear deflection within the beam. Initially, the response of the structure was simulated neglecting the effect of moat wall impacts in order to determine the maximum displacement and subsequently define the scale factor R for each individual record. During the next round of simulations, moat wall impacts were simulated based on the bilinear approximation of the F-D behavior of the physical substructure. A description of the F-D behavior as implemented in the numerical simulation can be seen in Eq. 19 where F_m represented the restoring force from the moat wall impact.

$$F_m = \begin{cases} 0 \text{ kN} \cdot \text{cm}^{-1}, & \text{for } x < 3.784 \text{ cm} \\ 1.435 \text{ kN} \cdot \text{cm}^{-1}, & \text{for } 3.784 < x < 5.08 \text{ cm} \\ 0.152 \text{ kN} \cdot \text{cm}^{-1}, & \text{for } x > 5.08 \text{ cm} \end{cases} \quad (19)$$

Within the Simulink model two dead zone blocks were included to simulate bilinear approximation of the moat wall F-D behavior as described above. The dead zone blocks returned a zero value if the displacement of the base slab was within a certain “dead” range defined as the gap distance. Beyond the dead range, the dead zone blocks returned the magnitude by which the displacement of the base slab had exceeded the limits of the dead range. In this manner, scaling the output of a single dead zone block by 1.4345 kN/cm were able to simulate linear elastic impacts similar to the impact model used by Liu et al. (2014, 2017). At the same time, summation of two dead zone blocks were used to simulate the bilinear approximation of the stiffness behavior if the second block as a gap corresponding to the displacement where the approximation takes on the less stiff slope within the bilinear approximation of the restoring force of the moat wall.

Within the simulation, the moat impact events were simulated as if they were occurring within the lab. The structure was excited with a ground acceleration and the calculated isolation layer displacement was divided by R and sent through the dead zone blocks in order to simulate the actuator impacts with the steel beam substructure. The output from the dead zone blocks was then multiplied by R^2 , and fed back into the simulation as negative feedback that was summed with the inertial force acting on the isolation layer due to the ground motion excitation. The moat wall gap distance was set to 3.784 cm (1.875 in) in the (+) displacement direction to match the experimental settings of the laboratory. The gap distance was set to a sufficiently large value in the (−) displacement direction such that the impacts would only occur in the (+) displacement direction. This simulated the experimental setup where only one-sided impacts would be considered and the actuator could extend 3.784 cm prior to impacting the steel beam.

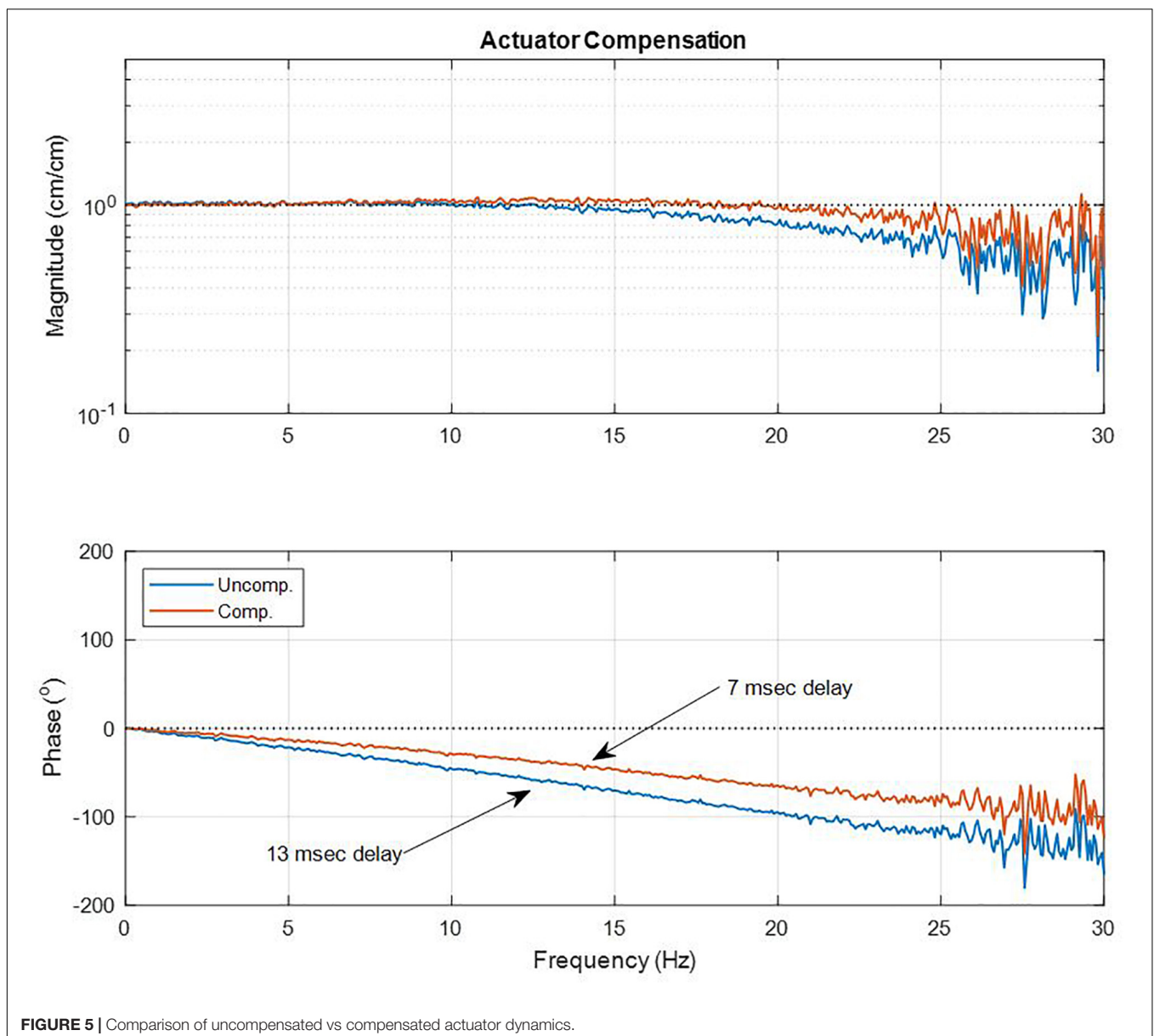
Using the described simulation architecture above, the mass of the structure within the simulation was then scaled and the impact behavior analyzed using the bilinear approximation of the force-deflection behavior of the beam. In order to induce linear deflections in the beam, the mass of the structure was

calibrated such that the maximum simulated deflection of the beam substructure was 0.635 cm (0.25 in). The maximum deflection during nonlinear impacts was 2.477 cm (0.975 in). The calibration of the mass for the linear and nonlinear impacts was performed by recursively increasing or decreasing the mass of the structure such that the maximum simulated deflection of the beam substructure lies within 1% of the desired beam deflection. Limitations of this simulation technique included the assumption that the impact was perfectly elastic, with no energy loss from the system during impacts. During analytical simulations, the only energy dissipation within the system was due to damping within the structure itself. This was not entirely accurate when compared to the experimental setup. The energy dissipation by the friction of the bearings at the supports, as well as contact friction between the base slab and moat wall were neglected.

In addition, energy converted to noise and vibrations within the beam was not considered.

Actuator Compensation

The hydraulic actuators utilized during RTHS testing exhibit inherent dynamics that could potentially affect the accuracy and stability of an RTHS test. These dynamics are observed in **Figure 5** as magnitude attenuations and phase lags between the commanded and measured displacement of the actuator. A phase lag in an RTHS test behaves as an apparent time delay which effectively results in negative damping within the feedback loop of the test setup (Horiuchi et al., 1996). Apparent time delays caused by actuator dynamics have the potential to destabilize the test setup, and thus, actuator compensation is utilized to help ensure test stability.



The experimentally obtained commanded-to-measured displacement transfer function of the actuator was obtained by sending a band-limited displacement commanded displacement signal to the actuator and the collecting the measured displacement from the analog output of the actuator. From these commanded and measured displacement signals, the transfer function of the actuator was calculated. This process of obtaining the transfer function was performed before and after applying a model-based compensator to determine the impact of compensation on the system.

Several compensation techniques exist ranging from prediction of commanded displacement via polynomial extrapolation (Horiuchi et al., 1996, 1999) to feed-forward model-based compensation (Carrion and Spencer, 2007). Feed-forward model-based compensation was used for this study. The compensation procedure involved characterizing the transfer function $A(s)$ of the commanded to measured displacement of the actuator using Laplace-domain polynomial fractions. Development of a compensator for an RTHS test should be tailored to the system being analyzed, but the compensator must satisfy a number of qualities to avoid inaccuracies or instabilities within the RTHS test setup. To develop a compensator, a curve fit representation of the actuator dynamics $A(s)$ must be obtained by fitting a Laplace-domain polynomial fraction to the experimentally obtained transfer function of commanded to measured displacement of the actuator. By taking the reciprocal of this fraction, the actuator compensator $H(s)$ was obtained. Hydraulic actuators typically exhibit a transfer function from commanded to measured displacement that resembles a low-pass filter. However, the reciprocal of the polynomial fraction that represents a low-pass filter approaches an infinite magnitude at high frequencies and will introduce high frequency noise to the commanded actuator displacement signal and potentially destabilize the RTHS test. In order to ensure that the magnitude of the compensator is small enough at high frequencies, the curve fit of the actuator transfer function must include a sufficient number of zeros at higher frequencies such that the magnitude of the compensator does not tend toward infinity at higher frequencies. Once a compensator has been obtained for the system being analyzed, the commanded displacement signal is multiplied by the compensator prior to sending it to the actuator in order to partially alleviate the effects of the actuator dynamics. The actuator compensator $H(s)$ listed in Eq. 20 was constructed to minimize the phase lag of the commanded to measured displacement of the actuator over the bandwidth of 0–3 Hz. The feedforward compensation was implemented using the dSPACE real-time controller as an outer control loop on the Parker Analog Controller.

$$H(s) = \frac{9.870e4 \cdot s^2 + 1.537e7 \cdot s + 1.193e9}{1.1229e4 \cdot s^2 + 1.193e6 \cdot s + 1.213e9} \quad (20)$$

A plot of the commanded to measured displacement transfer functions for the uncompensated and compensated actuator behavior has been provided in **Figure 5**; illustrating the improvement in both the magnitude and phase of the actuator transfer function. As a result of the compensation technique, the

dynamics of the actuator were improved such that the apparent time delay was reduced from 13 to 7 ms over the bandwidth of 0–3 Hz where the majority of the structural dynamics exist.

The compensation process was performed on the actuator alone, while not engaged with the moat wall substructure. This decision was made as the actuator was meant to represent the interface between the base slab and the moat wall. During a majority of the structural response, the actuator was engaged with the moat wall substructure, as was also the case just prior to and just after impact events. Therefore, tailoring the actuator compensation to the response bandwidth of the structure was deemed to be the best strategy. It should be noted that during impacts, the dynamics of the actuator were altered. However, within this work, the physical substructure was relatively flexible and not expected to have altered the actuator dynamics substantially. If larger scale RTHS tests were to be conducted, or if a stiffer physical substructure were used, the effects of dynamic coupling between the actuator and physical substructure should potentially be taken into consideration. This dynamic coupling between the actuator and physical substructure can lead to detrimental effects on actuator performance by a process known as control-structure interaction (Dyke et al., 1995).

RESULTS AND DISCUSSION

Moat Wall Impact Behavior

In order to validate the experimental setup, the time history of the RTHS moat wall impact was collected and compared to force profiles observed during the Masroor and Mosqueda (2013) shake table tests. During the collection of the force profile time history, the restoring force of the moat wall impact was fed back into the system, such that the closed-loop system behaved like a base-isolated structure impacting the wall during an impact event. The time history and frequency content of the impact force obtained using RTHS testing can be seen in **Figure 6**. The force signal was the measured force signal from the piezoelectric sensor during the linear impact and was obtained at a data acquisition sampling rate of 12,288 Hz and is depicted here in the reduced scale of the actuator (laboratory scale). The force profile observed in **Figure 6A** was similar to the impact force profile observed by Masroor and Mosqueda in the case of impacts with a steel moat wall. The similarities between the shake table test and RTHS test force profiles included the shape of the impact force time histories which approximated a half-sine pulse of frequency equal to roughly 8 Hz. Both force profiles also contained higher frequency behavior on top of the half-sine pulse initially, but these higher frequency oscillations damped out rapidly. This similarity between the experimental and RTHS results indicated that the force feedback technique used in RTHS was capable of producing realistic conditions for observing moat wall impacts in base-isolated structures.

In order to ensure accurate capturing of the frequency content of a structural impact with the moat wall substructure must be considered. The PSD of the impact forces as obtained from the linear impact test conducted at 12,288 Hz can be seen in **Figure 6B**. The frequency content of moat impact forces was

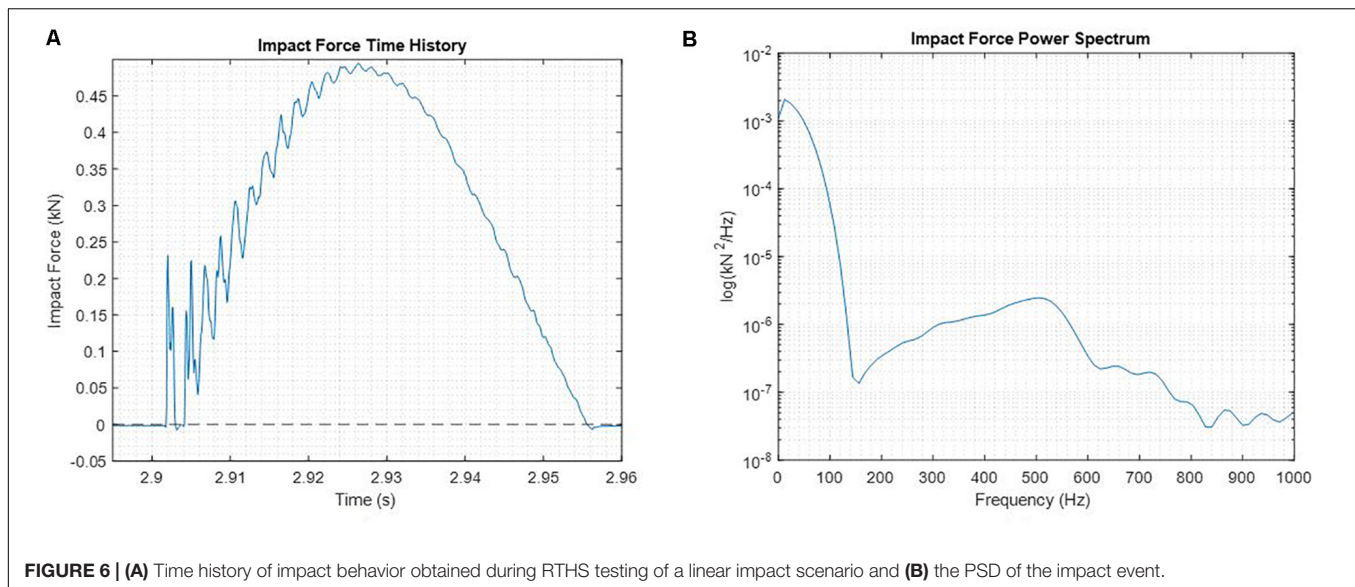


FIGURE 6 | (A) Time history of impact behavior obtained during RTHS testing of a linear impact scenario and **(B)** the PSD of the impact event.

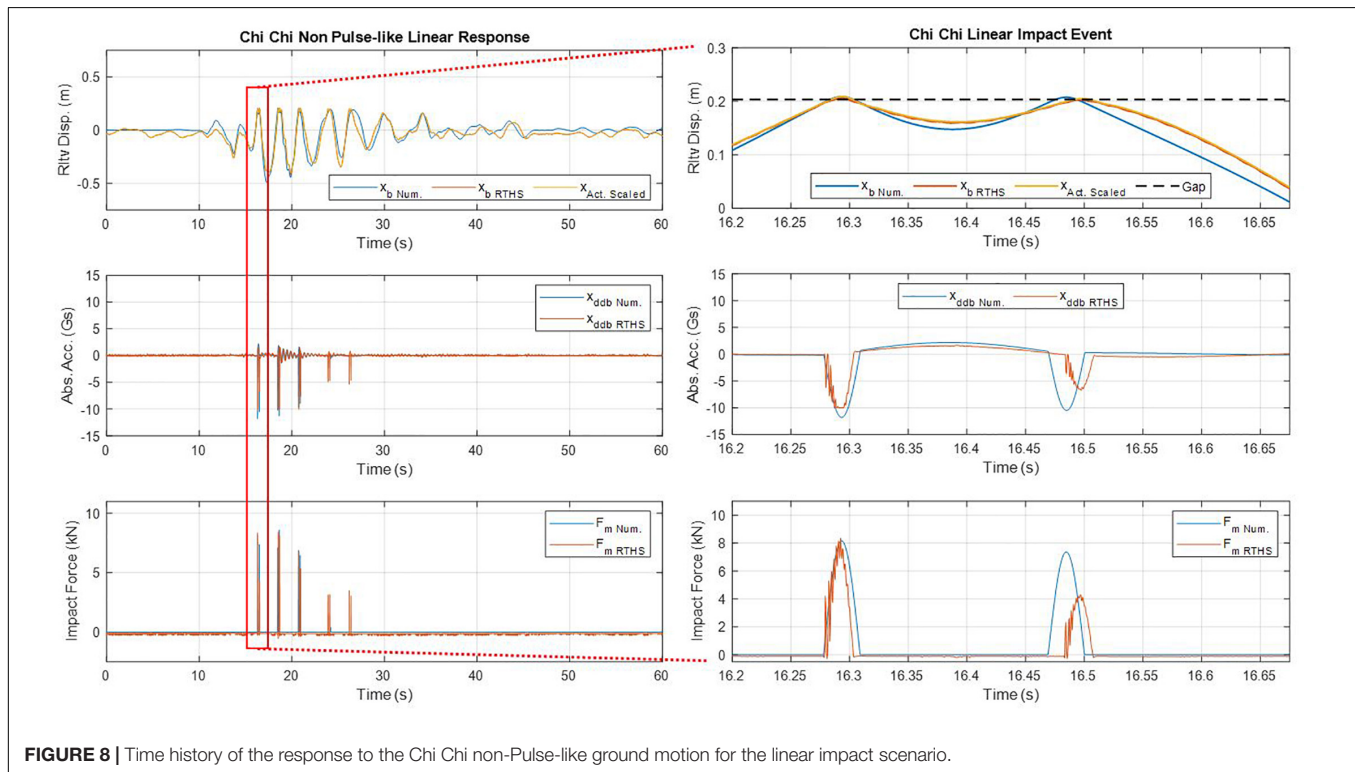
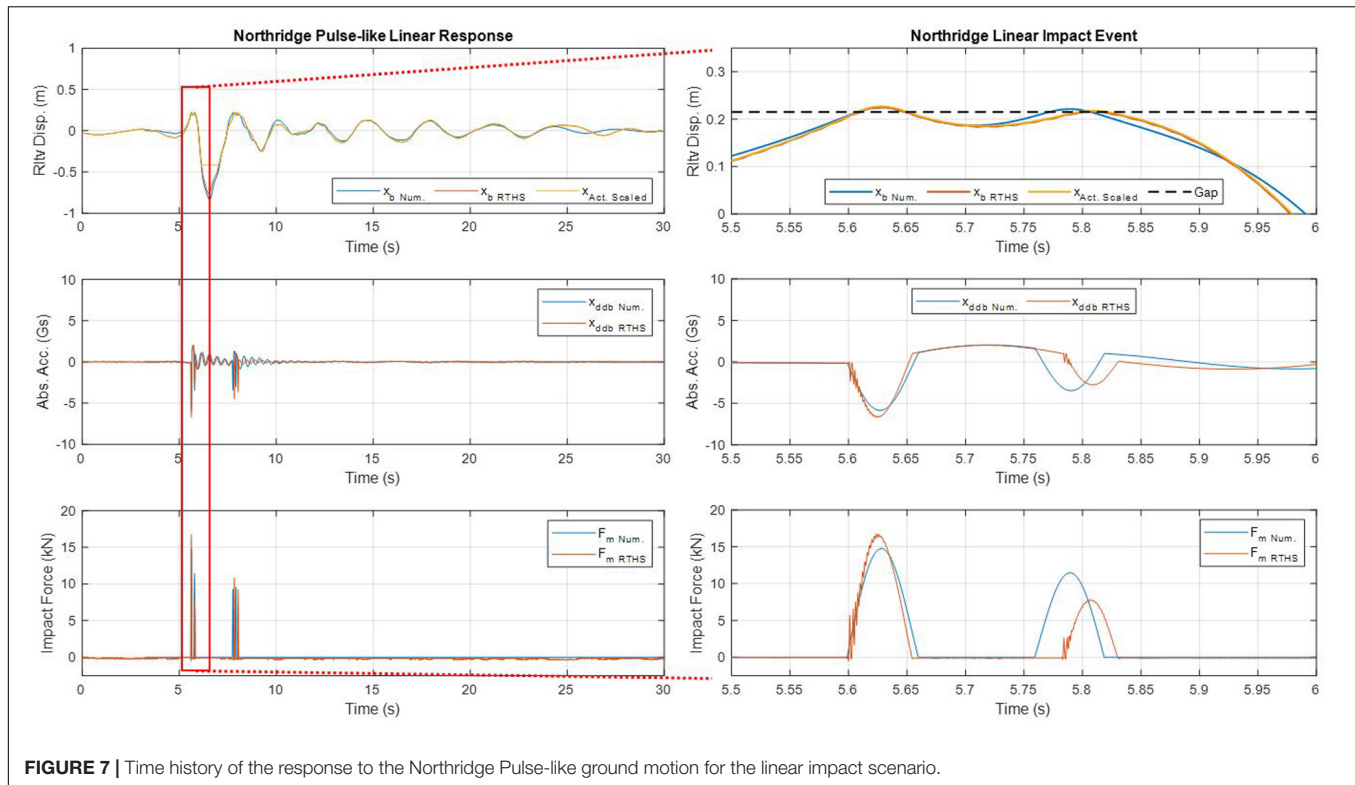
dependent on both the dynamics of the structure as well as the stiffness of the moat wall to resist deformation. Within this test, the impacts occurred along a single line of action or a single degree of freedom, with the physical substructure providing a uniaxial restoring force to be fed back to the numerical substructure. Both the physical substructure and the base-isolated structure representing the numerical substructure were flexible in the axis of the single degree of freedom and would not be expected to contribute to substantial high-frequency content within the impacts. From **Figure 6B** it can be seen that the impact behavior in the system analyzed was predominantly within the bandwidth of 0–50 Hz; dropping to $0.97 \text{ kN}^2/\text{Hz}$ at roughly 46 Hz compared to $1.94 \text{ kN}^2/\text{Hz}$ at 0.2 Hz (a 50% reduction in power/Hz). This signified that a majority of the energy of the impacts was within the bandwidth of the hydraulic actuator. However, if the RTHS technique were to be applied to stiffer moat wall substructures, care should be taken to ensure that the actuator has sufficient bandwidth to capture the dynamics of the impact. In addition, analyses of the experimental setup should ensure that the actuator has sufficient power to avoid the effects of control-structure interaction as described by Dyke et al. (1995). Additionally, high-frequency, high-force actuation capabilities such as those at UC San Diego Blast Simulator (University of California San Diego, 2010) can potentially be leveraged to examine high-frequency, impulsive loading conditions like those of moat-wall impacts or blast loads.

In any experimental testing of system dynamics, it is critical to ensure that the mechanism used to drive the system has sufficient capacity to avoid the phenomenon known as Control-Structure Interaction (Dyke et al., 1995). For the results presented in this paper, the physical substructure was relatively flexible with respect to the force capacity of the actuator, with the maximum dynamic force observed within the actuator scale being equal to 1.903 kN as seen in later time histories of the nonlinear impact scenario. This force represented only 21.39% of the maximum force capacity of the actuator and it is therefore asserted that

Control-Structure Interaction most likely did not affect the ability of the actuator to impose displacement constraints on the physical substructure during testing. Furthermore, as was observed within the time history results presented later in this study, the measured actuator displacement ($x_{\text{Act. Scaled}}$) tracked very closely the commanded displacement ($x_{\text{b RTHS}}$) for all tests conducted. As such, the efficacy of the compensation and the absence of significant Control-Structure interaction was verified. However, if the scale of the experiment were increased, or the stiffness of the moat wall increased, care should be taken to ensure that the actuator possess sufficient force and bandwidth capacity to impose boundary conditions on the physical substructure. This stipulation would extend to actuators imposing displacements in each DOF. Should a 6DOF shake table be used to examine normal, shear, and torsional components of impact forces, it must be ensured that the actuators driving the shake table have sufficient force capacity to impose boundary conditions as prescribed by the numerical substructure.

Ground Motion Response Results

Real-Time Hybrid Simulation testing was utilized to analyze the effects of moat wall impacts on base isolated structures. **Figures 7–9** present the time histories of the relative displacement and absolute acceleration of the base slab as well as the impact force acting on the isolation layer from linear impact scenarios. The time history results of the nonlinear scenario for the Northridge ground motion excitation have been presented in **Figure 10**. All of these time history results were collected at a data acquisition sampling rate of 2,048 Hz and are depicted here within the scale of the numerical substructure (the full structural scale). A zoomed-in view of the first impact event within the time history response has also been provided for each ground motion. Within these figures, the numerical signals were obtained from numerical simulations of the structural response to the ground motions using elastic impact models similar to those used by Liu et al. (2017, 2014). In the case of the nonlinear



impact scenario, the RTHS test results are compared to the numerical results obtained using the bilinear approximation of the F-D behavior of the physical substructure. The RTHS

signals within the time histories were obtained during the RTHS tests of the structural response to ground motions using the physical moat wall substructure. The nonlinear response of

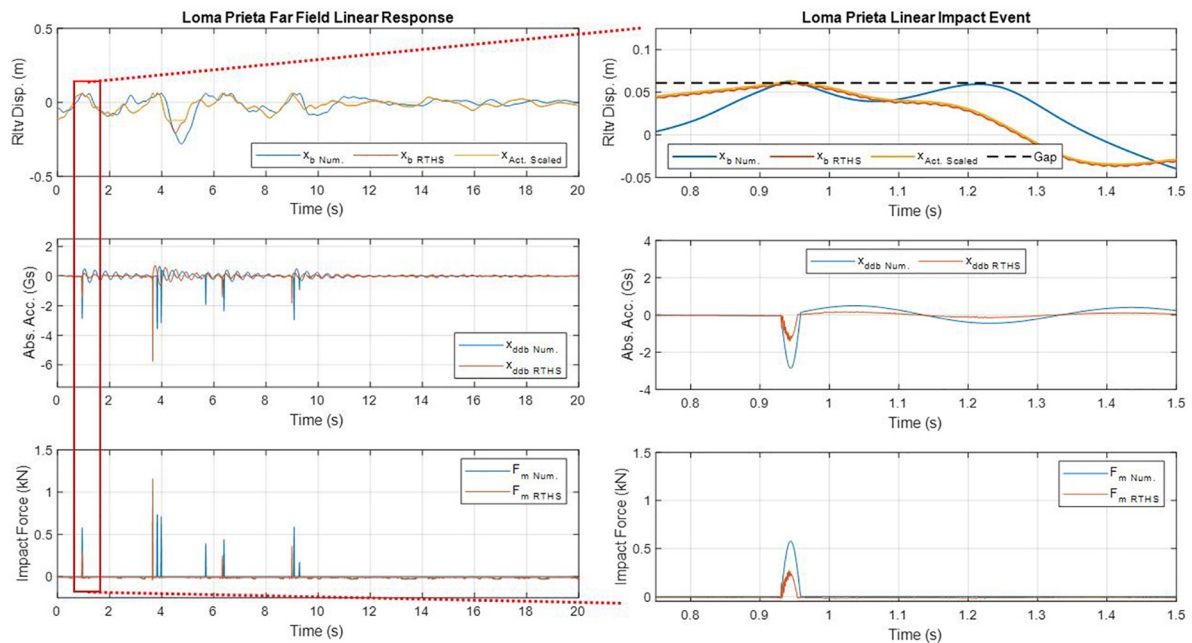


FIGURE 9 | Time history of the response to the Loma Prieta Far Field ground motion for the linear impact scenario.

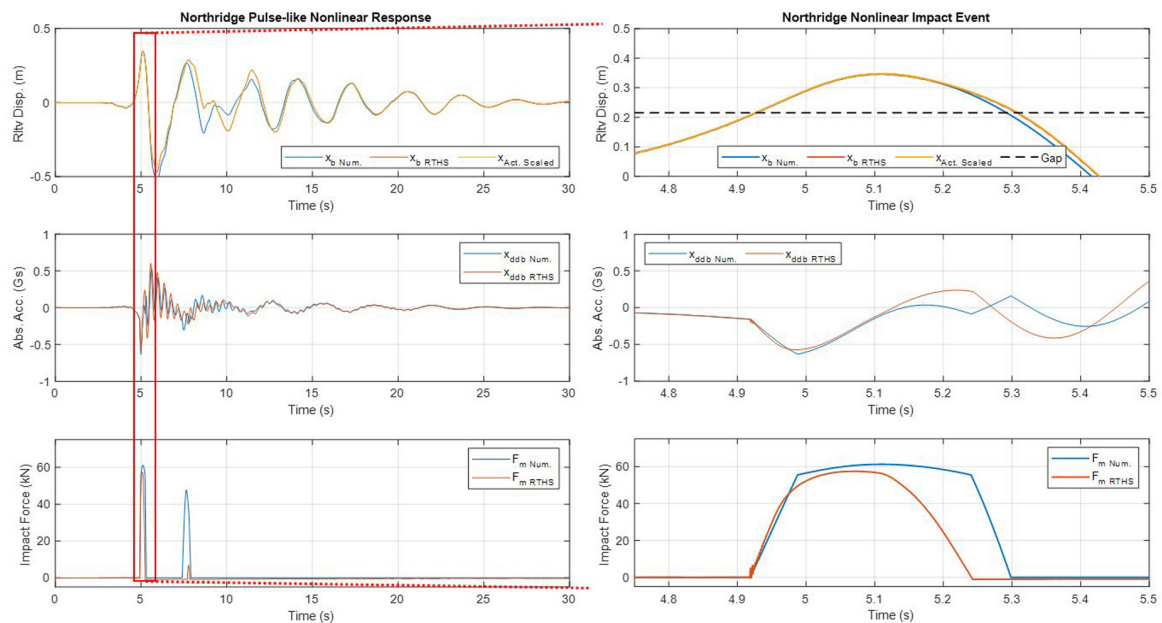


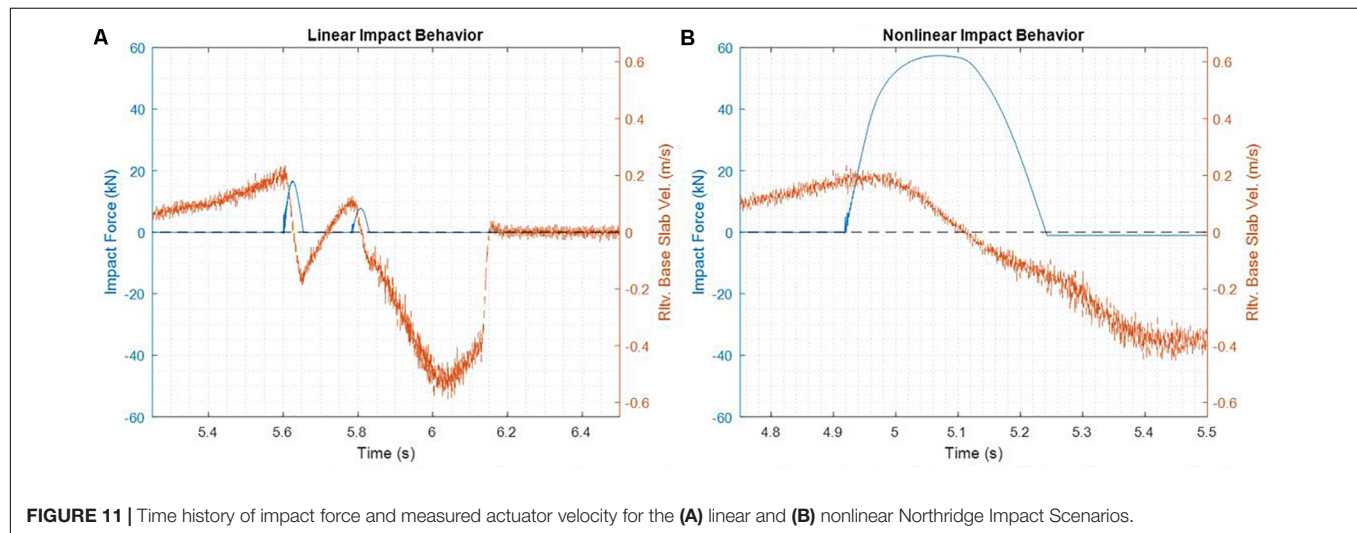
FIGURE 10 | Time history of the response to the Northridge Pulse-like ground motion for the nonlinear impact scenario.

the structure could only be analyzed for one ground motion due to the limited availability of steel beams for testing. The Northridge ground motion was selected as there were noted instances where base-isolated structures impacted the moat wall (Nagarajaiah and Sun, 2001). **Table 2** contains a summary of the signals plotted within the time history graphs from **Figures 7–10**.

Within both the numerical and RTHS time history results depicted in **Figures 7–9**, there were several occasions where impact events were characterized by two rapid impacts. One example of this was in the first impact of the tests for both the RTHS test and numerical simulation of the linear scenario of the Northridge ground motion as seen in **Figure 7**. This phenomenon was due to settling or bouncing of the base

TABLE 2 | Description of signals contained within Results section.

Signal	Description	Analysis method	Origin
x_b Num.	Relative base displacement	Numerical	Simulink output
x_b RTHS	Relative base displacement	RTHS	Simulink output
x_{Act} Scaled	Measured actuator displacement (scaled to match full structural scale)	RTHS	Actuator output
x_{ddb} Num.	Absolute base acceleration	Numerical	Simulink output
x_{ddb} RTHS	Absolute base acceleration	RTHS	Simulink output
F_m Num.	Moat wall impact force	Numerical	Simulink output
F_m RTHS	Moat wall impact force (scaled to match full structural scale)	RTHS	Force sensor output
Gap	A reference line illustrating the gap distance for each time history analysis	N/A	N/A

**FIGURE 11** | Time history of impact force and measured actuator velocity for the (A) linear and (B) nonlinear Northridge Impact Scenarios.

slab at the time of impacting the moat wall. This was verified in **Figure 11A**. This figure depicts the impact force and base slab velocity within the full structural scale as obtained RTHS testing. The relative velocity of the base slab was obtained from the time derivative of the measured actuator displacement. It was believed that this settling behavior was due to the flexibility of the physical substructure coupled with the small mass and momentum of the base-isolated structure. While being driven into the moat wall, the resiliency of the moat wall causes the structure to exhibited a behavior similar to settling or “bouncing” off of the moat wall. Meanwhile, the same phenomenon was not observed for the nonlinear scenario of the Northridge ground motion (**Figure 11B**) as the base slab had more momentum and was able to deform the physical substructure more. Note that for **Figure 11**, a positive force sensed by the force sensor would induce base slab acceleration in the negative x direction as depicted in **Figure 1**. Additionally, the measured actuator displacement was seen to reach the stroke limit in the (–) direction after impacting the moat wall substructure during the linear scenario as opposed to the nonlinear scenario where the structure did not have as much acceleration demand during and after the impact event.

Some discrepancies were observed within the timing and number of impact events within the time histories. For example, there were two additional impact events observed in the RTHS test results of the structural response to the Chi Chi

Non-Pulse-like ground motion (see **Figure 8**). It was believed that these differences between the response time histories were due to both differences in the moat wall F-D behavior of the numerical and RTHS simulations as well as the strength of the ground motion. As stated previously, the analytical simulations modeled the impact as a purely elastic even with the only damping resulting from the inherent damping of the structure itself. Meanwhile, RTHS impact events captured the energy dissipated by the friction of the bearings at the supports, contact friction between the base slab and moat wall, and energy converted to noise and vibrations within the beam. Unless the motion of the structure is dominated largely by its response due to the ground acceleration, it is plausible that differences in the impact behavior between the numerical simulations and RTHS tests could cause some discrepancies in the response time histories observed. Indeed, for large ground accelerations such as those at the beginning of the Northridge and Chi Chi events, there was marked agreement between the impact behavior and timing between the Numerical and RTHS results. As the ground motion decayed to smaller magnitudes, such as in the case of the end of the Chi Chi event as well as the majority of the Loma Prieta event, the applied forces from the ground acceleration are smaller in comparison to the forces due to impact events. This potentially led to discrepancies in the response time histories after impacts. This phenomenon should be studied in more detail. In order to do so, it is possible that a band-limited white noise acceleration

TABLE 3 | Summary of structural response for time history analyses.

Ground motion	Scenario	Max impact force (kN)			Max acc. (Gs)			Max disp. (m)		
		Numerical	RTHS	(%) Error	Numerical	RTHS	(%) Error	Numerical	RTHS	(%) Error
Northridge	Linear	15.03	16.75	11.48	5.841	6.728	15.18	0.8376	0.7668	−8.458
Chi Chi	Linear	8.589	8.417	−2.008	11.81	10.08	−14.7	0.4922	0.4181	−15.06
Loma Prieta	Linear	0.7338	1.159	57.94	3.567	5.767	61.65	0.28	0.2078	−25.81
Northridge	Nonlinear	61.21	57.52	−6.029	0.6343	0.6039	−4.789	0.5288	0.4688	−11.35

could be used in place of the acceleration time history from the ground motion records. In this way, a stochastic impact analysis could be achieved using both analytical and RTHS testing techniques.

Quantitative results from the various time histories obtained through simulation and RTHS are summarized in **Table 3**. The results are presented in the full structural scale.

Within these results, several notable trends can be observed. For the three linear impact analyses, the maximum impact force observed during RTHS testing was, on average, 22.47% greater than the maximum forces observed in Numerical simulations. At the same time, the average acceleration as obtained by RTHS testing of the linear impact scenarios was 20.71% greater than the maximum accelerations as predicted by analytical simulations. These findings are consistent with expectations based on the fact that during RTHS testing, the behavior of the moat wall was stiffer for small deflections than the bilinear approximation of the force-deflection behavior used during numerical simulations. At the same time, the maximum displacement from linear impacts in RTHS testing was 16.44% smaller than that of the maximum displacements from the simulated linear impact scenario. This is also consistent with the fact that the bilinear approximation of the force-displacement behavior of the beam has a lower stiffness than the true force-displacement behavior of the beam for small deflections. Therefore, the simulation using this bilinear approximation would predict a larger displacement than would be observed when using the physical beam. Based on the linear impact scenario results, it appears that RTHS testing is capable of capturing the true force-displacement behavior associated with the physical moat wall analog. It is noted that there was some scattering of the results for the linear impact scenario. This may be due to the respective strength of the individual ground motions. For the Northridge ground motion, the response of the structure was characterized by two large impact events early into the ground motion record. Likewise, the Chi Chi event induced a response in the structure that caused the structure to impact the moat wall in three major impact events followed by two additional minor impact events. These two Near-field ground motions induced a large response in the structure and a comparison between the statistics from Numerical and RTHS results show that the responses are far more consistent than in the case of the Loma Prieta results. As stated previously, the Loma Prieta ground motion did not induce a large response on the structure, and as such, the statistics regarding the impact events are far more disparate. Again, this phenomenon should be studied in more detail by using a stochastic acceleration input to the structure for looking at a larger collection of impact statistics.

Another noteworthy comparison can be made between the results of linear and nonlinear tests in **Table 3**. The dissipation of energy due to the nonlinear impact events had the potential to substantially decrease the inertial demand on the structure substantially when compared to a linear impact scenario. By incorporating material nonlinearity into the impact scenario, the maximum acceleration observed within the isolation layer was reduced by 91.02% as obtained from RTHS test results. This result was very similar to the 89.99% reduction in maximum acceleration observed between numerical simulations of linear and nonlinear impacts. This illustrated the importance of designing the moat wall such that it will safely yield and help to dissipate the energy of the structural vibrations during ground motion events. The result also echoed findings by Wolf and Skrikerud (1979), as well as by Sarebanha et al. (2017) where material nonlinearities during pounding were shown to be an important factor in limiting the demand on structures undergoing pounding events. Overall, the results obtained from RTHS testing showed its ability to effectively capture the complex behavior and uncertainties associated with impacts between base isolated structures and moat walls.

Force-Displacement Behavior Analyses

A comparison of the force-deflection behavior for both analytical and experimental studies can be seen in **Figure 12**. The restoring forces and base displacements have been presented within the scale of the actuator displacement and physical substructure (reduced laboratory scale) such that they can be compared with the F-D behavior depicted in **Figure 4**. The similarity of the force-deflection behavior observed in **Figures 4, 12B** demonstrated the effectiveness of the RTHS technique in capturing the nonlinear force-deflection behavior of the physical substructure during impact events. In addition, there was a significant amount of energy dissipation during actual impact events that was not accounted for by using the linear impact model. The signals used to produce **Figures 12A,C,E** were the relative base slab displacement and impact force signal as obtained from numerical simulations of the Northridge ground motion for both linear and nonlinear impact scenarios. The relative velocity of the base slab was obtained by differentiating the relative displacement signal. The strain was calculated using Eqs 11 and 12 and the amount by which the base slab exceeded the gap distance. The strain rate was obtained as the time derivative of this strain signal. It is noted that within the numerical simulation, the nonlinear impacts were nonlinear in as much as they used the bilinear elastic approximation of the force-deflection behavior of the moat wall substructure, but the simulated impacts of nonlinear scenarios

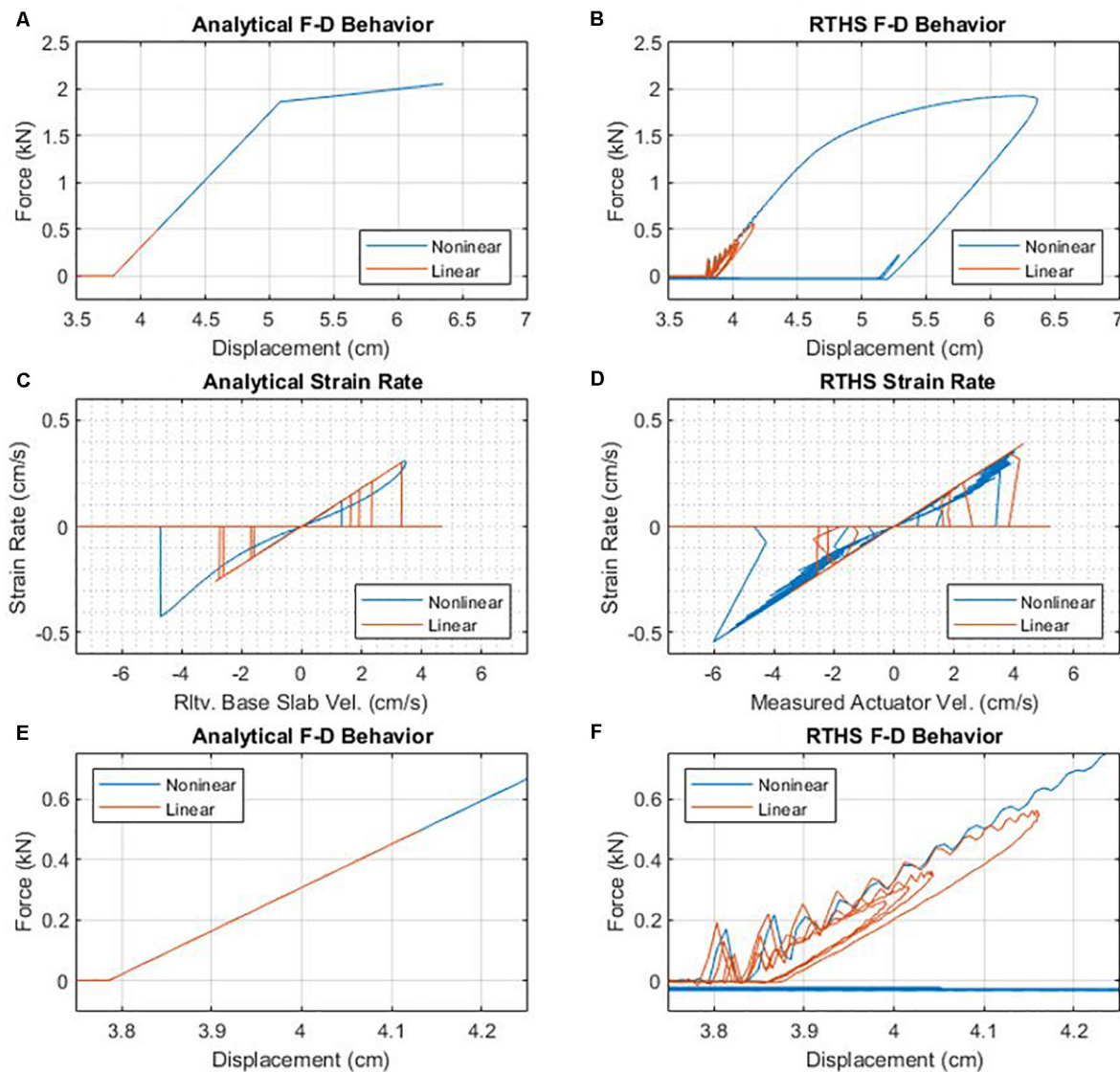


FIGURE 12 | The force displacement behavior as observed during impact by (A) numerical simulation and (B) RTHS testing, the deformation strain-rate dependency obtained by (C) numerical simulation and (D) RTHS testing, and a zoomed-in view of the force-displacement behavior obtained by (E) numerical simulations and (F) RTHS testing.

did not take into account the energy that will be dissipated due to yielding of the moat wall substructure. The signals used to produce **Figures 12B,D,F** were the measured actuator displacement signal and the restoring force signal collected from the piezoelectric force sensor. The measured velocity of the actuator was obtained by differentiating the measured actuator displacement. The strain of the beam during RTHS tests was calculated using Eqs 11 and 12 where δ was taken as the distance by which the measured actuator displacement exceeded the gap distance of 3.784 cm. The strain rate was obtained as the time derivative of this strain vector. Within **Figure 12**, the numerical simulation showed no rate-dependence of impact behavior, and RTHS tests of impacts showed little, if any dependence on strain rate during impacts. While **Figures 12B,C** illustrated that impact

events induced different strain rates on the moat wall, there was no noticeable difference in the stiffness of the steel beam during the impact events (see **Figures 12E,F**). While this finding was to be expected within the numerical simulations, the finding could be justified for the RTHS tests when the relative flexibility of the physical substructure was considered as this would lower strain rates being observed during testing (<0.4 cm/s in both the linear and nonlinear impact scenarios). These strain rates would not be expected to produce an appreciable change in stiffness within the steel beam (Knobloch et al., 2013; Brauer et al., 2019).

Ultimately, the evolution of impact forces is a highly complex phenomenon affected by factors such as the contact surfaces and geometry, friction and other damping methods, material properties and nonlinearities, and rate-dependence

of the impacting bodies. The importance of characterizing nonlinear deflection behavior during impacts is critical for predicting the true inertial demand on the system. The RTHS technique was capable of capturing material nonlinearities within the physical substructure without the use of computationally expensive impact models. The numerical model, while straight forward to implement and computationally inexpensive, was far from accurate when modeling the interaction between the isolation layer and the moat wall. **Figure 12** presented the ability of the RTHS testing technique to capture the complexities and uncertainties of F-D behavior of the physical substructure during impact events without the need for computationally expensive impact modeling and calculations. The determination of impact forces was accomplished using empirically measured forces which were then fed back to the simulation. In this way, RTHS was shown to have the potential to produce more realistic impact force time histories.

CONCLUSION

Real-time hybrid simulation testing was used to analyze a base isolated system impacting a moat wall. The comparison of experimental and analytical results showed that the RTHS technique was able to capture the complexities of impact events between a base isolation layer and a steel foundation wall analog. Structural response predicted by RTHS testing was shown to accurately capture the effects of moat wall impacts based through comparisons of both predicted inertial demand as well as observed force-deflection behavior during impact events. When compared to simulations using a bilinear approximation of the moat wall, for the linear impact scenario, the RTHS testing technique predicted maximum displacements averaging 16.44% lower, while predicting increases in maximum accelerations and impact forces averaging 20.71 and 22.47% respectively. Both of these results are consistent with what would be expected based on comparisons of the experimental and numerical force-deflection analyses. Use of RTHS was shown to be a means of fully capturing the force-deflection behavior of the moat wall as well as the uncertainties associated with impact events while alleviating the need to use a computationally expensive model of impact behavior.

The results also illustrated the importance of designing for nonlinear behavior to occur within the moat wall during impact events. Results of RTHS testing showed that the maximum acceleration observed in the isolation layer was reduced by over 90% when the moat wall yielded during testing. Design of the foundation such that it yields safely during impact events could

help to increase the safety of base-isolated structures during large earthquake events.

Future tests should expand on results presented here by using a larger experimental setup to mitigate the need for scaling of forces and displacements during testing. In addition, examination of moat wall impacts using 6DOF shake tables would enable the consideration of shear and moment contributions to impact event. Additional studies could use RTHS with band-limited white noise (stochastic) input accelerations to the numerical substructure as a different means of analyzing moat wall impact events. The testing of multiple varieties of moat wall designs such as those using reinforced concrete as well as those with soil backfills and other innovative materials and mechanisms would also help to better characterize nonlinear behavior of moat walls and structures during impact events and could ultimately provide insight for safer design practices. Other applications of the RTHS technique to impulsive, high-frequency loading conditions could investigate the effects of blast loads on structures using loading capabilities such as those available at UC San Diego.

DATA AVAILABILITY STATEMENT

The datasets generated for this study are available on request to the corresponding author.

AUTHOR CONTRIBUTIONS

MH conducted numerical simulation and experimental testing, performed the post-test data analysis, and wrote the manuscript. RC provided advice and guidance during the planning, testing, analysis, and writing phases as research advisor for the work. Both authors contributed to the article and approved the submitted version.

FUNDING

This work was supported by a graduate fellowship under US Department of Education GAANN award #P200A140212.

ACKNOWLEDGMENTS

The authors would like to thank the Pacific Earthquake Engineering Research Center (PEER) for providing a database of ground motions that was used to obtain the ground motion time histories for this work.

REFERENCES

- Abbiati, G., Lanese, I., Cazzador, E., Bursi, O. S., and Pavese, A. (2019). A computational framework for fast-time hybrid simulation based on partitioned time integration and state-space modeling. *Struct. Control Health Monit.* 26:e2419. doi: 10.1002/stc.2419
- American Society of Civil Engineers [ASCE] (2010). *Minimum Design Loads for Buildings and Other Structures*. Reston, VA: American Society of Civil Engineers.
- Ariga, T., Kanno, Y., and Takewaki, I. (2006). Resonant behaviour of base-isolated high-rise buildings under long-period ground motions. *Struct. Design Tall Special Build.* 359, 1869–1891.
- Asai, T., Chang, C., and Spencer, B. F. Jr. (2015). Real-time hybrid simulation of a smart base-isolated building. *J. Eng. Mech.* 141:04014128. doi: 10.1061/(asce)em.1943-7889.0000844
- Bamer, F., Shi, J., and Markert, B. (2017). Efficient solution of the multiple seismic pounding problem using hierarchical substructure techniques. *Comput. Mech.* 62, 761–782. doi: 10.1007/s00466-017-1525-x

- Beer, F., Johnson, R., and DeWolf, J. T. (2006). *Mechanics of Materials*, 4th Ed. New York, NY: McGraw-Hill.
- Brauer, S. A., Whittington, W. R., Rhee, H., Allison, P. G., Dickel, D. E., Crane, C. K., et al. (2019). Stress-State, temperature, and strain rate dependence of vintage ASTM A7 steel. *J. Eng. Mater. Technol.* 141, 1–9.
- Carrion, J. E., and Spencer, B. F. Jr. (2007). *Model-based Strategies for Real-Time Hybrid Testing*. Newmark Structural Engineering Laboratory Report Series No. 6 (Urbana, IL: University of Illinois at Urbana-Champaign).
- Chen, P., Tsai, K., and Lin, P. (2014). Real-time hybrid testing of a smart base isolation system. *Earthquake Eng. Struct. Dyn.* 43, 139–158. doi: 10.1002/eqe.2341
- Chopra, A. K. (2006). *Dynamics of Structures*, 3rd Edn. Englewood Cliffs, NJ: Prentice Hall.
- Cole, G., Dhakal, R., Carr, A., and Bull, D. (2011). An Investigation of the effects of mass distribution on pounding structures. *Earthquake Eng. Struct. Dyn.* 40, 641–659. doi: 10.1002/eqe.1052
- Connor, J. J. (2003). *Introduction to Structural Motion Control*. Upper Saddle River, NJ: Prentice Hall.
- Delfosse, G. C. (1977). “The gapec system: a new highly effective aseismic system,” in *Proceedings of the 6th World Conference on Earthquake Engineering*, New Delhi, 1135–1140.
- Dyke, S. J., Spencer, B. F. Jr., Quast, P., and Sain, M. K. (1995). Role of control-structure interaction in protective system design. *ASCE J. Eng. Mech.* 121, 322–338. doi: 10.1061/(asce)0733-9399(1995)121:2(322)
- Federal Emergency Management Agency [FEMA] (2009). *Quantification of Building Seismic Performance Factors*. Redwood City: Applied Technology Council.
- Furinghetti, M., Lanese, I., and Pavese, A. (2020). Experimental assessment of the seismic response of a base-isolated building through a hybrid simulation technique. *Front. Built Environ.* 6:33. doi: 10.3389/fbuil.2020.00033
- Gordis, J. H. (1994). Structural synthesis in the frequency domain, a general formulation. *Shock Vibr.* 1, 461–471. doi: 10.1155/1994/947253
- Hakuno, M., Shidawara, M., and Hara, T. (1969). Dynamic destructive test of a cantilever beam, controlled by an analog-computer (Japanese). *Civil Eng. Rep.* 171, 1–9. doi: 10.2208/jscej1969.1969.171_1
- Hayashi, K., Fujita, K., Tsuji, M., and Takewaki, I. (2018). A simple response evaluation method for base-isolation building-connection hybrid structural system under long-period and long-duration ground motion. *Front. Built Environ.* 4:2. doi: 10.3389/fbuil.2018.00002
- Horiuchi, T., and Nakagawa, M. (1996). “Development of a real-time hybrid experimental system with actuator delay compensation,” in *11th World Conference on Earthquake Engineering*, 660.
- Horiuchi, T., Inoue, M., Konno, T., and Namita, Y. (1999). Real-time hybrid experimental system with actuator delay compensation and its application to a piping system with energy absorber. *Earthquake Eng. Struct. Dyn.* 28, 1121–1141. doi: 10.1002/(sici)1096-9845(199910)28:10<1121::aid-eeq858>3.0.co;2-o
- Hussain, S. (2018). Design Of A Seismic Isolation System With Supplemental Viscous Damping For A Near-Fault Essential Services Facility. Available online at: https://www.iitk.ac.in/nicee/wcee/article/14_S05-02-007.pdf (accessed May 9, 2019).
- Iervolino, I., and Cornell, C. A. (2005). Record selection for nonlinear seismic analysis of structures. *Earthquake Spectr.* 21, 685–713. doi: 10.1193/1.1990199
- Jain, S., and Thakkar, S. (2004). “Application of Base Isolation for Flexible Buildings,” in *Proceedings of the 13th World Conference on Earthquake Engineering*, Vancouver, BC.
- Keivan, A., Zhang, R., Phillips, B., and Ikago, K. (2017). “Protection of inter-story isolated structures through rate-independent linear damping,” in *Proceedings of the 3rd Huixian International Forum on Earthquake Engineering for Young Researchers* (Urbana-Champaign: University of Illinois).
- Kelly, J. M. (1981). “Aseismic base isolation: its history and prospects,” in *Proceedings of the 1st World Congress on Joints and Bearings, ACI-SP-70*, Niagara Falls, NY, 549–586.
- Kelly, J. M. (1990). Base isolation: linear theory and design. *Earthquake Spectra*. 6, 223–244. doi: 10.1193/1.1585566
- Kim, S. J., Christenson, R. E., Wojtkiewicz, S. F., and Johnson, E. A. (2011). Real-time hybrid simulation using the convolution integral method. *Smart Mater. Struct.* 20,
- Knobloch, M., Pauli, J., and Fontana, M. (2013). Influence of the strain-rate on the mechanical properties of mild carbon steel at elevated temperatures. *Materials Design* 49, 553–565. doi: 10.1016/j.matdes.2013.01.021
- Kumar, S., Itoh, Y., Saizuka, K., and Usami, T. (1997). Pseudodynamic Testing of Scaled Models. *J. Struct. Eng.* 123, 524–526. doi: 10.1061/(asce)0733-9445(1997)123:4(524)
- Kun, Y., Li, L., Hongping, Z. (2009). A modified Kelvin impact model for pounding simulation of base-isolated building with adjacent structures. *Earthquake Eng. Eng. Vibr.* 8, 433–446. doi: 10.1007/s11803-009-8045-4
- Lin, P., Roschke, P., Loh, C., and Cheng, C. (2004). “Semi-active controlled base-isolation system with magnetorheological damper and pendulum system,” in *Proceedings of the 13th World Conference on Earthquake Engineering*, Vancouver.
- Liu, Y., Liu, W. G., Wang, X., He, W. F., and Yang, Q. R. (2014). New equivalent linear impact model for simulation of seismic isolated structure pounding against moat wall. *Shock Vibr.* 2014:151237.
- Liu, C., Yang, W., Yan, Z., Lu, Z., and Luo, N. (2017). Base pounding model and response analysis of base-isolated structures under earthquake excitation. *Appl. Sci.* 7:1238. doi: 10.3390/app7121238
- Luco, N., and Bazzurro, P. (2007). Does amplitude scaling of ground motion records result in biased nonlinear structural drift responses. *Earthquake Eng. Struct. Dyn.* 36, 1813–1835. doi: 10.1002/eqe.695
- Mahin, S. A., and Shing, P. B. (1985). Pseudodynamic method for seismic testing. *J. Struct. Eng.* 111, 1482–1503. doi: 10.1061/(asce)0733-9445(1985)111:7(1482)
- Masroor, A., and Mosqueda, G. (2013). Impact model for simulation of base isolated buildings impacting flexible moat walls. *Earthquake Eng. Struct. Dyn.* 42, 357–376. doi: 10.1002/eqe.2210
- Muthukumar, S., and DesRoches, R. (2006). A hertz contact model with non-linear damping for pounding simulation. *Earthquake Eng. Struct. Dyn.* 35, 811–826.
- Nagarajaiah, S., and Sun, X. (2001). Base-Isolated FCC building: impact response in northridge earthquake. *J. Struct. Eng.* 127, 1063–1075. doi: 10.1061/(asce)0733-9445(2001)127:9(1063)
- Nakashima, M., Kato, H., and Takaoka, E. (1992). Development of real-time pseudo dynamic testing. *Earthquake Eng. Struct. Dyn.* 21, 79–92. doi: 10.1002/eqe.4290210106
- Oh, J., Jang, C., and Kim, J. H. (2016). Seismic behavior characteristic of high damping rubber bearing through shaking table test. *J. Vibroeng.* 18, 1591–1601. doi: 10.21595/jve.2016.15973
- Pantelides, C. P., and Ma, X. (1996). “Nonlinear seismic pounding of inelastic structures,” in *Proceedings of the Eleventh World Conference on Earthquake Engineering*, Acapulco.
- Polycarpou, P., Komodromos, P., and Polycarpou, A. (2013). A nonlinear impact model for simulating the use of rubber shock absorbers for mitigating the effects of structural pounding during earthquakes. *Earthquake Eng. Struct. Dyn.* 42, 81–100. doi: 10.1002/eqe.2194
- Polycarpou, P., Papaliozou, L., and Komodromos, P. (2014). An efficient methodology for simulating earthquake-induced 3d pounding of buildings. *Earthquake Eng. Struct. Dyn.* 43, 985–1003. doi: 10.1002/eqe.2383
- Providakis, C. P. (2008). Effect of LRB isolators and supplemental viscous dampers on seismic isolated buildings under near-fault excitations. *Eng. Struct.* 30:1187–1198. doi: 10.1016/j.engstruct.2007.07.020
- Roylance, D. (2000). *Beam Displacements*. New York, NY: Massachusetts Institute of Technology
- Sarebanha, A., Mosqueda, G., Kim, M. K., and Kim, J.H. (2017). “Modeling of moat wall compliance during impact in seismically isolated nuclear power plants,” in *Proceedings of the International Association for Structural Mechanics in Reactor Technology. SMIRT-24* (Busan: BEXCO).
- Shome, N., Cornell, C. A., Bazzurro, P., and Carballo, J. E. (1998). Earthquakes, records, and nonlinear MDOF responses. *Earthquake Spectr.* 14, 469–500. doi: 10.1193/1.1586011
- Su, T. J., and Juang, J. N. (1994). Supplemental energy dissipation: state-of-the-art and state-of-the-practice. *Eng. Struct.* 24, 243–259. doi: 10.1016/s0141-0296(01)00092-x
- Takanashi, K., and Nakashima, M. (1987). Japanese activities on on-line testing. *J. Eng. Mech.* 113, 1014–1032. doi: 10.1061/(asce)0733-9399(1987)113:7(1014)

- Takewaki, I., Fujita, K., and Yoshitomi, S. (2013). Uncertainties in long-period ground motion and its impact on building structural design: Case study of the 2011 Tohoku (Japan) earthquake. *Eng. Struct.* 4, 119–134. doi: 10.1016/j.engstruct.2012.10.038
- Thakkar, S. K., and Jain, S. K. (2004). “Optimal damping in isolation system,” in *Proceedings of the 13th World Conference on Earthquake Engineering*, Vancouver.
- University of California San Diego (2010). *Blast Simulator Specifications*. NHERI at UC San Diego. San Diego, CA: University of California San Diego
- Warn, G. P., and Ryan, K. (2012). A review of seismic isolation for buildings: historical development and research needs. *Buildings* 2, 300–325. doi: 10.3390/buildings2030300
- Weisstein, E. W. (2015). “Circular Segment.” From *MathWorld—A Wolfram Web Resource*. Available online at: <https://mathworld.wolfram.com/CircularSegment.html> (accessed June 12, 2020).
- Wolf, J. P., and Skrikerud, P. E. (1979). Mutual Pounding of Adjacent Structures during Earthquakes. *Nuclear Eng. Design* 57, 253–275. doi: 10.1016/0029-5493(80)90106-5
- Wood, R. L., and Hutchinson, T. C. (2012). Effects of ground motion scaling on nonlinear higher mode building response. *Earthquakes Struct.* 3, 869–887. doi: 10.12989/eas.2012.3.6.869
- Zhang, R., Phillips, B., Taniguchi, S., Ikenaga, M., Ikago, K. (2017). Shake table real-time hybrid simulation techniques for the performance evaluation of buildings with inter-story isolation. *J. Struct. Control Health Monit.* 24:e1971. doi: 10.1002/stc.1971

Conflict of Interest: The authors declare that the research was conducted in the absence of any commercial or financial relationships that could be construed as a potential conflict of interest.

Copyright © 2020 Harris and Christenson. This is an open-access article distributed under the terms of the Creative Commons Attribution License (CC BY). The use, distribution or reproduction in other forums is permitted, provided the original author(s) and the copyright owner(s) are credited and that the original publication in this journal is cited, in accordance with accepted academic practice. No use, distribution or reproduction is permitted which does not comply with these terms.



Stability Analysis and Verification of Real-Time Hybrid Simulation Using a Shake Table for Building Mass Damper Systems

Pei-Ching Chen ^{1*}, Meng-Wei Dong ¹, Po-Chang Chen ¹ and Narutoshi Nakata ²

¹ Advance Experimental Technology Laboratory, Department of Civil and Construction Engineering, National Taiwan University of Science and Technology, Taipei, Taiwan, ² Department of Civil and Environmental Engineering, Tokushima University, Tokushima, Japan

OPEN ACCESS

Edited by:

Chia-Ming Chang,
National Taiwan University, Taiwan

Reviewed by:

Yoichi Mukai,
Kobe University, Japan
Dario De Domenico,
University of Messina, Italy

*Correspondence:

Pei-Ching Chen
peichingchen@mail.ntust.edu.tw

Specialty section:

This article was submitted to
Earthquake Engineering,
a section of the journal
Frontiers in Built Environment

Received: 16 April 2020

Accepted: 12 June 2020

Published: 03 August 2020

Citation:

Chen P-C, Dong M-W, Chen P-C and
Nakata N (2020) Stability Analysis and
Verification of Real-Time Hybrid
Simulation Using a Shake Table for
Building Mass Damper Systems.
Front. Built Environ. 6:109.
doi: 10.3389/fbuil.2020.00109

The building mass damper (BMD) system, which incorporates the concept of a tuned mass damper into a mid-story isolation system, has been demonstrated as an effective system for suppressing structural vibration due to earthquakes. The BMD system separates a building into a substructure, a control layer and a superstructure. By applying well-design parameters, the seismic responses of the superstructure and substructure of a building can be mitigated simultaneously. However, merely limited design parameters have been verified by shaking table testing because it is difficult to construct several sets of specimens with limited research funding. Therefore, real-time hybrid simulation (RTHS) may become an alternative to conduct parametric studies of the BMD system efficiently and economically. In this study, the BMD system is separated into a numerical substructure and an experimental substructure. The experimental substructure includes the control layer and the superstructure of the BMD system installed on a seismic shake table while the substructure is numerically simulated. Then, substructuring method of the BMD system is derived and the stability analysis considering the dynamics of the shake table is performed to realize the potential feasibility of RTHS for BMD systems. The stability margin is represented as an allowable mass ratio of the experimental substructure to the entire BMD system. Finally, RTHS of a simplified BMD system has been conducted to verify the stability margin in the laboratory. Phase-lead compensation and force correction are applied to RTHS in order to improve the accuracy of RTHS for the simplified BMD system.

Keywords: building mass damper, real-time hybrid simulation, shake table, stability, substructuring

INTRODUCTION

A novel structural system named as building mass damper (BMD) system, which combines the advantages of seismic isolation and tuned mass damper design has been proposed and studied. A BMD system is composed of a substructure, a control layer and a superstructure. Conventionally, the mass of the superstructure above the control layer can be designed as a tuned mass, becoming an energy absorber to suppress the response of the substructure. This system is also called partial mass isolation technique, or large-mass ratio tuned mass damper (TMD), and has been extensively

studied by many researchers for the past decades. Matta and De Stefano (2009) developed the concept of the roof-garden TMD and explored the mass ratio effect on the performance of seismic mitigation. De Angelis et al. (2012) performed shake table testing of a large mass ratio TMD and a reduced order model was proposed for optimal design for seismic applications. Anajafi and Medina (2018) analyzed the performance of partial mass isolation and compared it to conventional TMD and base isolation system for different soil conditions through numerical simulation. For special application, De Domenico and Ricciardi (2018b) applied the base isolation incorporated with a large mass ratio TMD located at the basement. Meanwhile, De Domenico and Ricciardi (2018a) proposed an inerter-based vibration absorber combined with base isolation systems and performed parametric optimization considering different objective functions. The aforementioned researches explored the seismic performance of structures with various layout and allocation of isolation system and mass damper.

In recent years, the occupancy of the superstructure has been also considered in the design optimization of a BMD system (Wang et al., 2018). In the optimization process, a BMD system was represented by a simplified three degrees-of-freedom (3DOF) lumped mass structure model, composed of a superstructure, a control layer, and a substructure. By minimizing the sum of differences between each two modal damping ratios, the optimal design parameters of a BMD system can be obtained. After determining the mass and natural frequency of the substructure, a total number of seven parameters can be designed for a BMD system including the frequency ratios of the control layer and superstructure with respect to the fundamental frequency of the substructure, mass ratios of the control layer and superstructure with respect to the mass of the substructure, and the damping ratios of the superstructure, control layer, and substructure. Design parameters of the BMD system were verified by conducting shake table testing. Experimental results indicated that the seismic performance of the BMD system is strongly related to the frequency content of seismic excitation. Unfortunately, further experimental validation considering various design parameters as well as structural non-linearity remain empty because the shake table test was not repeatable as long as the specimen behaved non-linearly. Replacing the steel specimen could be time-consuming and costly. As a result, real-time hybrid simulation (RTHS) could be adopted to investigate the seismic responses of BMD systems when parametric studies are needed with expected non-linear behavior.

RTHS which combines structural testing with numerical simulation is an advanced, efficient and cost-effective experimental method for earthquake engineering studies to explore the structural response due to dynamic excitation. In a RTHS, a structure is separated into at least an experimental substructure and a numerical substructure. The interfacial degrees of freedom between the experimental and numerical substructures are represented by servo-hydraulic actuators and mechanical fixtures. A step-by-step integration algorithm is required to solve the response at the interfacial degrees of freedom of the numerical substructure subjected to excitation.

This response is imposed on the experimental substructure in real time through a servo-hydraulic system. The corresponding response is then measured from the experimental substructure and fed back to numerical substructure to compute the interfacial response for the next time step until the RTHS is completed. In particular, seismic shake tables can be adopted as the interface between numerical and experimental substructures which enables seismic simulation of multi-story shear buildings in a way that the upper part of a building can be experimentally tested on the table while the rest part of the building can be numerically modeled. In this approach, the seismic shake table must track the absolute acceleration at the interfacial degrees of freedom when the numerical substructure is subjected to earthquakes. The inertial forces of the experimental substructure then can be accurately represented. However, significant vibrating mass in the experimental substructure could result in the difficulties of tracking the acceleration computed from the numerical substructure, leading to the so-called control-structure interaction (Dyke et al., 1995). As a result, control analysis and synthesis have been conducted in order to achieve accurate RTHS using seismic shake table (Nakata and Stehman, 2014; Zhang et al., 2016). Currently, limited research topics have been studied by employing RTHS with shake table, such as tuned liquid damper system (Wang et al., 2016), mid-level isolation (Schellenberg et al., 2017), and semi-active mass damper system (Chu et al., 2018).

It is expected that RTHS could become an effective alternative to investigate the seismic performance of a BMD system with numerous structural parameters. During a RTHS, the substructure can be simulated numerically while the control layer and superstructure can be tested physically on a seismic shake table. In this study, substructuring of the equation of motion is derived first and stability analysis procedure is proposed to evaluate the feasibility of reproducing the experimental results of the BMD system that was previously tested on a shake table through RTHS. The stability margin is represented as an equivalent allowable mass ratio of the experimental substructure to the entire BMD system. This stability analysis method provides potential users with a rapid and simple approach to evaluate the feasibility of RTHS using a shake table. The stability analysis results are discussed and summarized. Finally, RTHS of a simplified BMD system is conducted in the laboratory. Phase-lead compensation (PLC) and force correction (FC) methods are applied to RTHS in order to improve the accuracy of RTHS. Finally, experimental results are discussed and compared with a benchmark BMD system. Experimental results demonstrate that the stability analysis is instrumental in understanding the theoretical stability margin of RTHS before it is conducted. Besides, the PLC and FC are effective in improving the RTHS results.

SUBSTRUCTURING OF A BMD SYSTEM

A BMD system can be simplified by a 3DOF structure model in the design stage which includes a superstructure, a control layer, and a substructure as shown in **Figure 1**. When a BMD system

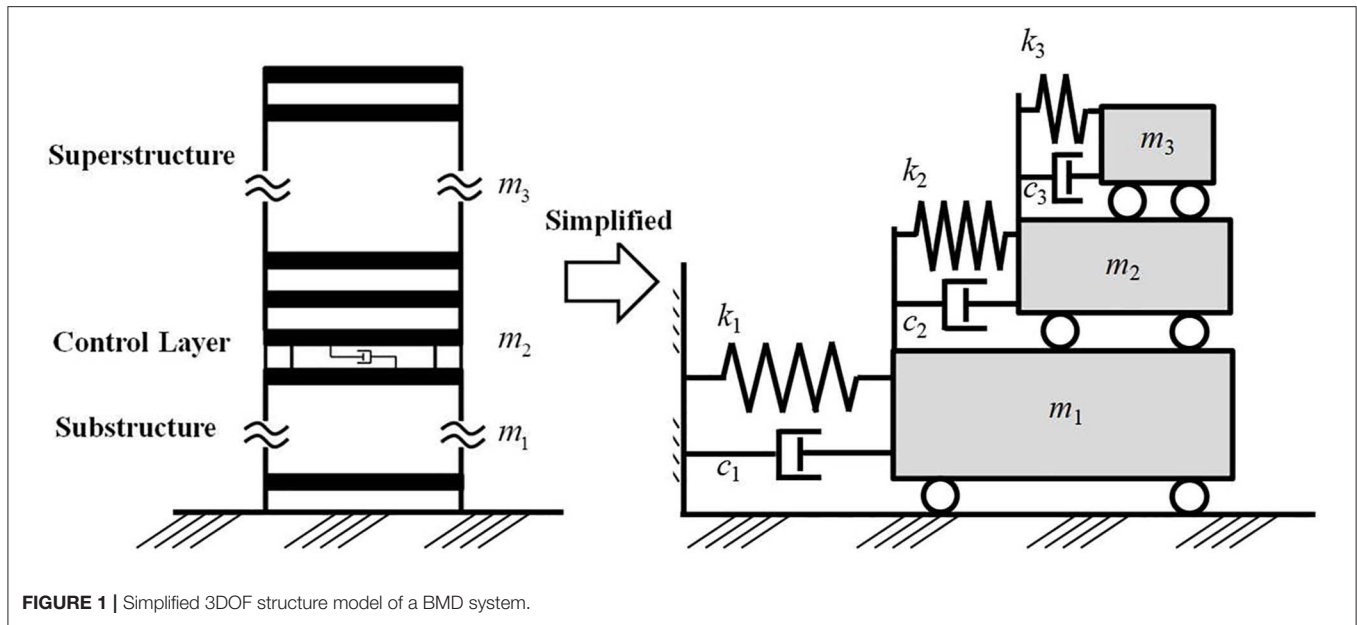


FIGURE 1 | Simplified 3DOF structure model of a BMD system.

is subjected to ground motion, its equation of motion can be expressed as

$$\mathbf{M}\ddot{\mathbf{u}}(t) + \mathbf{C}\dot{\mathbf{u}}(t) + \mathbf{K}\mathbf{u}(t) = -\mathbf{M}\mathbf{l}\ddot{u}_g(t) \quad (1)$$

where \mathbf{M} , \mathbf{C} , and \mathbf{K} are the mass, damping coefficient and stiffness matrices, respectively; \mathbf{u} is the relative displacement vector; \mathbf{l} is the earthquake excitation influence vector in which all elements are unity; and $\ddot{u}_g(t)$ is the ground acceleration. For a BMD system, \mathbf{M} , \mathbf{C} , and \mathbf{K} can be expressed as

$$\mathbf{M} = \begin{bmatrix} m_1 & 0 & 0 \\ 0 & m_2 & 0 \\ 0 & 0 & m_3 \end{bmatrix}; \quad (2)$$

$$\mathbf{C} = \begin{bmatrix} c_1 + c_2 & -c_2 & 0 \\ -c_2 & c_2 + c_3 & -c_3 \\ 0 & -c_3 & c_3 \end{bmatrix}; \mathbf{K} = \begin{bmatrix} k_1 + k_2 & -k_2 & 0 \\ -k_2 & k_2 + k_3 & -k_3 \\ 0 & -k_3 & k_3 \end{bmatrix}$$

where m_1 , m_2 , and m_3 are the mass of the substructure, control layer, and superstructure, respectively; c_1 , c_2 , and c_3 are the damping coefficient of the substructure, control layer, and superstructure, respectively; and k_1 , k_2 , and k_3 are the lateral stiffness of the substructure, control layer, and superstructure, respectively.

During a RTHS, the BMD system can be separated into an experimental substructure and a numerical substructure as depicted in **Figure 2**. The experimental substructure contains the control layer and superstructure that is tested physically on a seismic shake table, while the substructure is numerically simulated. The equation of motion of a BMD system shown in

Equation (1) can be modified by considering the numerical and experimental substructures as

$$\begin{bmatrix} m_1^N & 0 & 0 \\ 0 & m_2^E & 0 \\ 0 & 0 & m_3^E \end{bmatrix} \begin{Bmatrix} \ddot{u}_1^I \\ \ddot{u}_2^E \\ \ddot{u}_3^E \end{Bmatrix} + \begin{bmatrix} c_1^N + c_2^E & -c_2^E & 0 \\ -c_2^E & c_2^E + c_3^E & -c_3^E \\ 0 & -c_3^E & c_3^E \end{bmatrix} \begin{Bmatrix} \dot{u}_1^I \\ \dot{u}_2^E \\ \dot{u}_3^E \end{Bmatrix} + \begin{bmatrix} k_1^N + k_2^E & -k_2^E & 0 \\ -k_2^E & k_2^E + k_3^E & -k_3^E \\ 0 & -k_3^E & k_3^E \end{bmatrix} \begin{Bmatrix} u_1^I \\ u_2^E \\ u_3^E \end{Bmatrix} = - \begin{bmatrix} m_1^N & 0 & 0 \\ 0 & m_2^E & 0 \\ 0 & 0 & m_3^E \end{bmatrix} \begin{Bmatrix} 1 \\ 1 \\ 1 \end{Bmatrix} \ddot{u}_g \quad (3)$$

The superscript N represents the contribution of the numerical substructure; the superscript E represents the contribution of the experimental substructure; and the superscript I represents the interfacial degree of freedom. Only the equation of motion of the numerical substructure is solved by applying step-by-step integration algorithm as

$$m_1^N \ddot{u}_1^I + c_1^N \dot{u}_1^I + k_1^N u_1^I = -m_1^N \ddot{u}_g + f_1^I \quad (4)$$

where f_1^I represents the shear force transmitted from the experimental substructure to the numerical substructure at the interfacial degree of freedom. Since the platen of shake table can be regarded as the interfacial degree of freedom, the response of the control layer and the superstructure is relative to the platen of shake table. By letting $\hat{u}_2^E = u_2^E - u_1^I$ and $\hat{u}_3^E = u_3^E - u_1^I$, the equation of motion of the experimental substructure can be expressed as

$$\begin{bmatrix} m_2^E & 0 \\ 0 & m_3^E \end{bmatrix} \begin{Bmatrix} \ddot{\hat{u}}_2^E \\ \ddot{\hat{u}}_3^E \end{Bmatrix} + \begin{bmatrix} c_2^E + c_3^E & -c_3^E \\ -c_3^E & c_3^E \end{bmatrix} \begin{Bmatrix} \dot{\hat{u}}_2^E \\ \dot{\hat{u}}_3^E \end{Bmatrix} + \begin{bmatrix} k_2^E + k_3^E & -k_3^E \\ -k_3^E & k_3^E \end{bmatrix} \begin{Bmatrix} \hat{u}_2^E \\ \hat{u}_3^E \end{Bmatrix} = - \begin{bmatrix} m_2^E & 0 \\ 0 & m_3^E \end{bmatrix} \begin{Bmatrix} 1 \\ 1 \end{Bmatrix} (\ddot{u}_1^I + \ddot{u}_g) \quad (5)$$

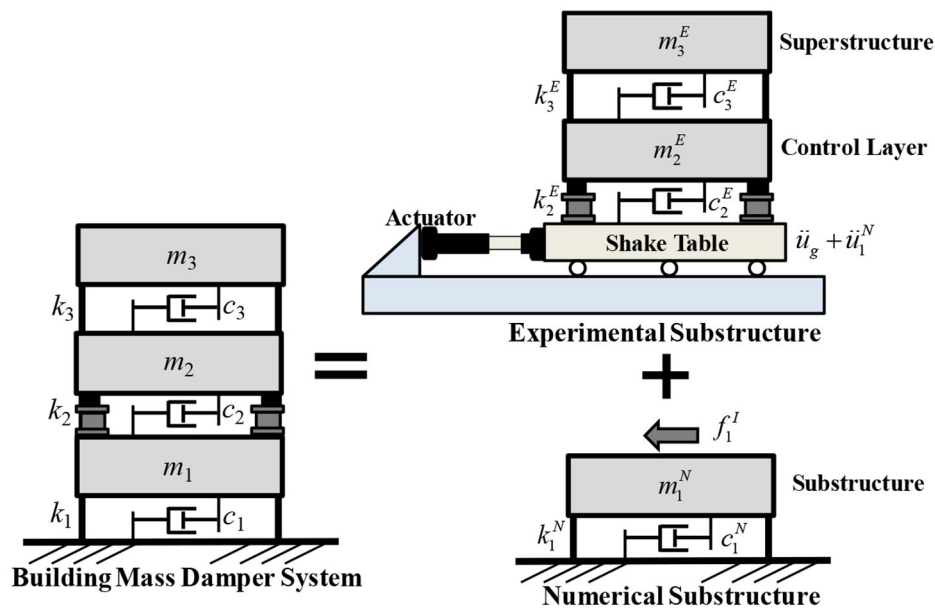


FIGURE 2 | Illustration of the substructuring for RTHS of a BMD system.

Finally, the transmitted shear force f_1^I can be derived as:

$$\begin{aligned} f_1^I &= -m_2^E (\ddot{u}_2^E + \ddot{u}_1^I + \ddot{u}_g) - m_3^E (\ddot{u}_3^E + \ddot{u}_1^I + \ddot{u}_g) \\ &= -m_2^E (\ddot{u}_2^E + \ddot{u}_g) - m_3^E (\ddot{u}_3^E + \ddot{u}_g) \end{aligned} \quad (6)$$

It is obvious that the transmitted shear force can be obtained by the inertial force of the experimental substructure. In practice, the measurement of accelerometers could contain noise. Therefore, Kalman filter can be applied to estimate the absolute acceleration at each floor of the experimental substructure. The inertial force at each floor can be obtained by multiplying the estimated absolute acceleration by the lumped mass. Then, the transmitted shear force can be calculated by summing the inertial force of each floor. Alternatively, load cells can be installed between the control layer and the shake table to measure the transmitted shear force directly.

STABILITY ANALYSIS METHOD

In the study, RTHS of a BMD system forms a closed loop between the numerical substructure, seismic shake table, and experimental substructure. Figure 3 illustrates the linking between each component in the RTHS. The ground motion \ddot{u}_g is input to the numerical substructure and the transmitted absolute acceleration response $(\ddot{u}_1^I + \ddot{u}_g)$ at the interfacial degree of freedom needs to be reproduced by the shake table. In other words, the experimental substructure is subjected to the transmitted absolute acceleration. Inevitably, the achieved acceleration of the shake table $(\ddot{u}_{1m}^I + \ddot{u}_g)$ is different from the desired acceleration due to the dynamics of the shake table. The shear force f_1^I is then measured by load cells or

calculated by a Kalman filter, and fed back to the numerical substructure and complete the RTHS closed loop. Noted that a Kalman filter may be necessary for the RTHS loop in order to prevent measurement noise from being introduced to the numerical substructure and leading to spurious command to the shake table.

The stability of a RTHS loop can be investigated from the perspective of transfer function as shown in Figure 4 in which s is the Laplace complex number. From Equation (4), it can be seen that the acceleration relative to the ground \ddot{u}_1^I is contributed from the ground acceleration and the transmitted shear force from the experimental substructure. Therefore, the transfer function from the ground acceleration to the absolute acceleration at interfacial degree of freedom is denoted as $G_{au}^N(s)$. Meanwhile, the relative acceleration at the top of the numerical substructure due to the transmitted shear force is denoted as \ddot{u}_s . The desired absolute acceleration $(\ddot{u}_1^I + \ddot{u}_g)$ is obtained and sent to the seismic shake table $G_s(s)$. The achieved acceleration $(\ddot{u}_{1m}^I + \ddot{u}_g)$ excites the experimental substructure and the corresponding shear force f_1^I can be obtained. Therefore, the transfer function from the input excitation of the experimental substructure to the shear force at the interfacial degree of freedom can be represented as $G_{fa}^E(s)$. This shear force is converted to the relative acceleration \ddot{u}_s to the numerical substructure by the transfer function $G_{af}^N(s)$. Finally, the corresponding closed-loop transfer function of the RTHS from the ground acceleration to the achieved acceleration of the shake table becomes:

$$G_{RTHS}(s) = \frac{G_{au}^N(s)G_s(s)}{1 + G_{af}^N(s)G_{fa}^E(s)G_s(s)} \quad (7)$$

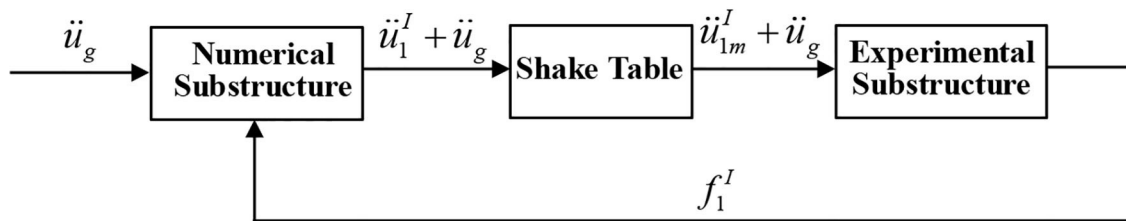


FIGURE 3 | Block diagram of RTHS for a BMD system.

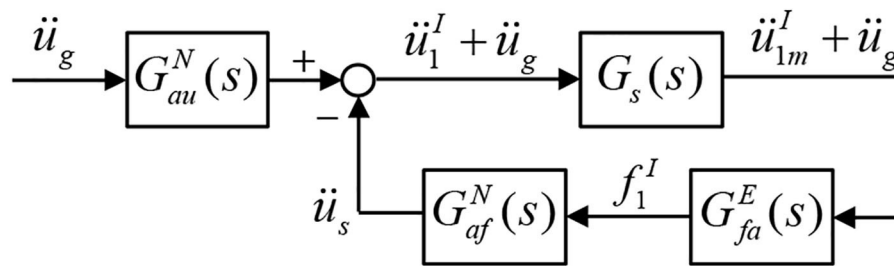


FIGURE 4 | Closed loop transfer function of RTHS for a BMD system.

The RTHS stability can be investigated by solving the characteristic equation in the denominator. Noted that the effect of integration algorithm and system uncertainty of shake table are not considered in the stability analysis in this study. It can be found in Equation (7) that the transfer functions related to the experimental and numerical substructures are dependent on the structural parameters, i.e., mass, damping coefficient, and stiffness. Since the interaction between the experimental and numerical substructures is the transmitted shear force f_1^I , which is associated with the mass of the experimental substructure as indicated in Equation (6). As a result, the allowable mass ratio is adopted as a stability index for RTHS of BMD systems which is defined as:

$$\rho = \frac{m_E}{m_N + m_E}, 0 \leq \rho \leq 1 \quad (8)$$

where m_E and m_N are the effective modal mass of the dominant mode of the experimental and numerical substructures, respectively. With determined modal frequencies and damping ratios of the experimental and numerical substructures, the allowable mass ratio of the closed-loop RTHS can be obtained.

DEMONSTRATIVE EXAMPLE

Experimental Setup

In the first stage, the stability analysis regarding the mass ratio of the experimental substructure to the entire BMD structural system was performed. The BMD system for demonstrative purposes is identical to one of the BMD systems tested by Wang et al. (2018). The entire BMD specimen was an 8-story steel structure model with single-bay widths of 1.1 and 1.5 m in the longitudinal and lateral directions, respectively.

The substructure contained the three stories from the bottom and the superstructure included the four stories from the top. The control layer was located at the fourth floor. It is noted that the experimental substructure for the RTHS merely consisted of the control layer and the superstructure. Each floor was 1.1 m high, and each slab was 20 mm thick. The columns and beams were wide flange with a sectional dimension of $100 \times 100 \times 6 \times 8$ (mm). Four elastomeric bearings with a diameter of 180 mm and two linear fluid viscous dampers were installed at the control layer. Two sets of steel blocks with a mass of $0.25 \text{ kN-s}^2/\text{m}$ were installed regularly at each floor to simulate the mass. Considering the mass contribution from the columns and slab, the lumped mass for the control layer and each story of the superstructure was 0.76 and $0.8 \text{ kN-s}^2/\text{m}$, respectively. The experimental substructure was installed on a uni-axial shake table in the structural laboratory of the National Center for Research on Earthquake Engineering (NCREE) in Taiwan. The uni-axial shake table was operated by using a FlexTest GT controller manufactured by MTS Systems Corporation with well-tuned proportional and integral gains. The maximum stroke and force capacity of the actuator were $\pm 250 \text{ mm}$ and $\pm 500 \text{ kN}$, respectively. Two linear-position sensors, Temposonics, were installed in the longitudinal direction of the shake table. The displacement of the shake table was obtained by taking the average of the two measurements. Furthermore, six accelerometers were installed on the shake table and each floor of the experimental substructure to measure the corresponding absolute accelerations. A dSPACE MicroLabBox, an integrated system which has more than 100 input/output channels of different types was utilized to run the numerical substructure as it can be simply interfaced with MATLAB and Simulink. The Simulink-based equation of motion of the numerical substructure can be converted to



FIGURE 5 | Experimental setup of the experimental substructure of the 8-story BMD system.

real-time C code, compiled and downloaded to the MicroLabBox, achieving real-time measurement data collection and integration algorithm computation. Meanwhile a commercial graphical user interface software, ControlDesk was implemented to monitor the responses online during RTHS. The experimental setup is shown in **Figure 5**.

Stability Analysis

In the RTHS, the substructure was numerically modeled using a non-linear real-time structural analysis software “RTFrame2D” (Castaneda-Aguilar et al., 2012). The first modal natural frequency of the numerical substructure, denoted as ω_N , was 35.43 rad/s. The modal damping ratio of the numerical substructure was assumed 2%. On the other hand, system identification was conducted in order to identify the structural parameters of the experimental substructure. The root-mean-square of accelerometer measurement noise was 0.0524 m/s^2 . The first modal natural frequency of the experimental substructure was 17.72 rad/s, and the damping ratio was 2.8%. Noted that the mass ratio indicated in Equation (8) for this 8-story BMD system was 0.65 for this BMD system. The dynamics of the shake table with the experimental substructure can be also identified by conducting system identification testing. The identified transfer function between the acceleration command to the achieved acceleration is

$$G(s) = \frac{1.1768 \cdot 10^{10}(s^2 + 1.186s + 3051)(s^2 + 4.739s + 1.06 \cdot 10^4)}{(s + 64.95)(s^2 + 1.108s + 2995)(s^2 + 97.46s + 8960)(s^2 + 4.567s + 1.049 \cdot 10^4)(s^2 + 21.07s + 2.13 \cdot 10^4)} \quad (9)$$

Figure 6 shows the transfer function of the shake table with experimental substructure and the corresponding identified

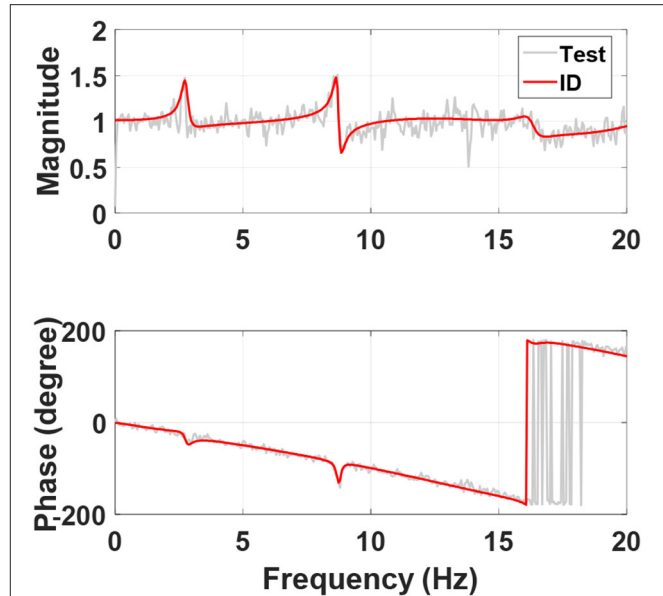


FIGURE 6 | System identification of the shake table with the experimental substructure.

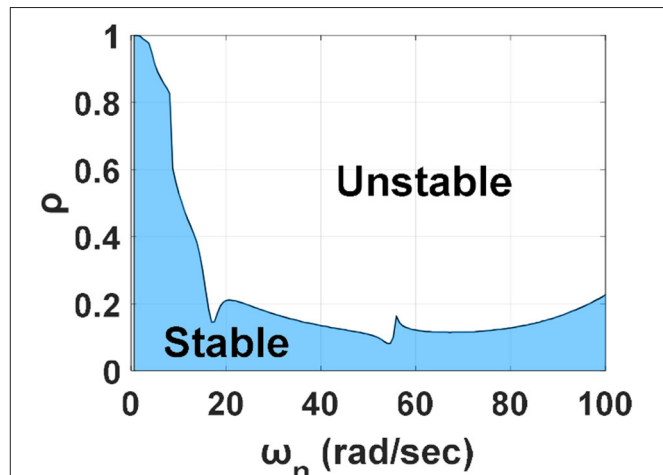


FIGURE 7 | Stable margin considering shake table dynamics for RTHS of the 8-story BMD system.

model. It can be seen that both the magnitude and phase of the model fit the transfer function well within the frequency of interest. Meanwhile, there is strong interaction at 8.98 Hz which is the 2nd modal frequency of the experimental substructure. By considering the dynamics of the shake table $G(s)$, the stability margin in terms of the allowable mass ratio can be obtained as shown in **Figure 7**. Since ω_N was 35.43 rad/s and the mass ratio

for the 8-story BMD substructuring was 0.65, RTHS for this BMD system was unstable if compensation methods were not applied.

Delay Compensation

Generally, delay compensation is essential to completing successful RTHS as time delay between the desired and achieved response at the interfacial degree of freedom introduce negative damping into RTHS, which would result in inaccuracies and potential instabilities. The discrete phase-lead compensator (PLC) proposed by Chen and Tsai (2013) was adopted to compensate the dynamics of the shake table in the demonstrative example which can be expressed as

$$C(z) = \frac{[W_1 + (W_1 + W_2 + 1)\alpha]z^2 + [W_2 - (W_1 + W_2 + 1)\alpha]z + 1}{W_1 z^2 + W_2 z + 1} \quad (10)$$

where W_1 and W_2 are the weightings which has to be located in the stable regions; and z is a complex number in the z transform. In the demonstrative example, both W_1 and W_2 were set 2. Meanwhile, the delay constant α can be determined by the phase plot as shown in **Figure 6**. The phase lag can be approximated to a constant delay time of 26 ms, which is equal to 5 time steps when the sampling rate of RTHS was 200 Hz ($\alpha = 5$).

For the BMD substructuring, perfect compensation leads to accurate achieved acceleration of the shake table. Due to the sequential architecture of RTHS as shown in **Figure 3**, perfect compensation results in shear force response from the experimental substructure with one-step time delay that is fed back to the numerical substructure. By assuming that the acceleration tracking control of the shake table was perfect but with one step of delay (0.005 s for example), the corresponding stability margin in terms of the allowable mass ratio can be obtained as shown in **Figure 8**. It can be seen that the mass ratio of the 8-story BMD system (0.65) is very close to the stable margin which was obtained by assuming a perfect shake table that was able to reproduce the absolute acceleration at the top of the numerical substructure. However, this allowable mass ratio drops significantly when the dynamics of the shake table is considered as shown in **Figure 7**. Conclusively, it was considered extremely difficult to conduct RTHS of the 8-story BMD system even appropriate delay compensation was applied. Moreover, RTHS of the 8-story BMD system was only stable when the shear force fed back to the numerical substructure was reduced to 30% or less in this demonstrative example. In other words, the mass ratio in Equation (8) was changed from 0.65 to 0.2 or less. From the stability margin shown in **Figure 7**, the allowable mass ratio considering the shake table dynamics without compensation is around 0.15. It indicates that the PLC was helpful to increasing the allowable mass ratio for the BMD system (from 0.15 to 0.2); however, the improvement was considered limited. In summary, it was extremely difficult to complete stable RTHS for the BMD system which was identical to the one tested by Wang et al. (2018). As a result, a simplified BMD system became an alternative for RTHS demonstration in which the mass ratio was smaller than but close to the allowable mass ratio.

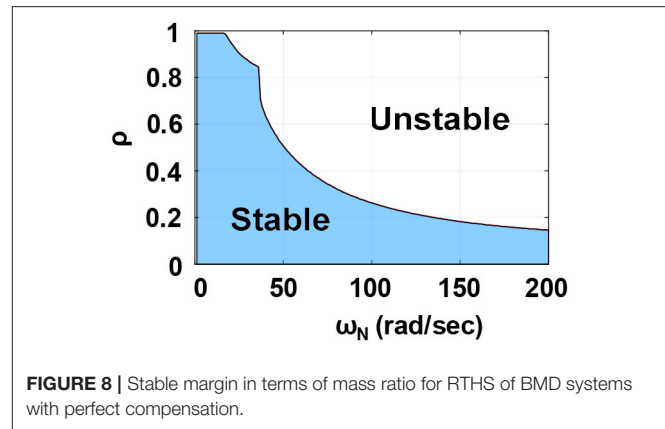


FIGURE 8 | Stable margin in terms of mass ratio for RTHS of BMD systems with perfect compensation.

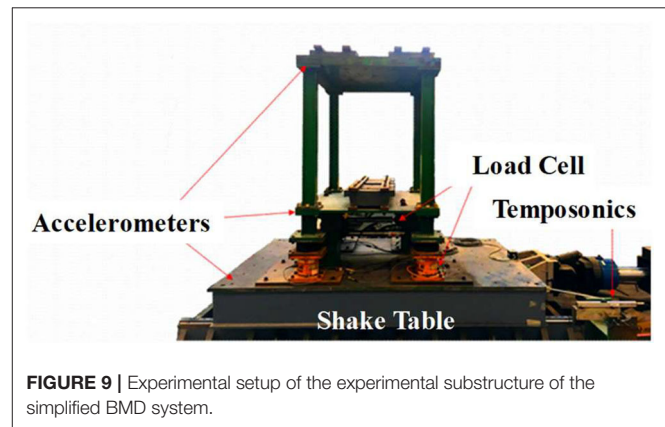


FIGURE 9 | Experimental setup of the experimental substructure of the simplified BMD system.

RTHS OF A SIMPLIFIED BMD SYSTEM

Design Parameters

The simplified BMD system was a 3DOF structure which was identical to the illustration as shown in **Figure 2**. After removing three stories from the experimental substructure of the 8-story BMD system, the experimental substructure of the simplified BMD system only contained the control layer and one-story superstructure while the one-story substructure was numerically simulated. The experimental setup is shown in **Figure 9**. The identified natural frequencies of the experimental substructure were 5.94 and 19.21 Hz. The damping ratio of the first two modes were 2.14 and 1.24%. The structural parameters of the experimental substructure are shown in **Table 1**. The transfer function of the shake table with the experimental substructure is depicted in **Figure 10**. The update rate of the RTHS was 200 Hz. It can be found that the phase lag can be approximated to a constant delay time of 25 ms which is equal to 5 time steps. In other words, the PLC in the RTHS of the simplified BMD system was identical to the one used for the 8-story BMD system previously.

According to the design suggestions for BMD systems from Wang et al. (2018), the substructure was designed with a natural frequency of 14.98 Hz (94.09 rad/s) and a damping ratio of 1.67%. Accordingly, the natural frequency of the substructure was about 2.5 times of the first modal frequency of the experimental

substructure. By following the aforementioned procedure, the stability margin in terms of the allowable mass ratio can be obtained as shown in **Figure 11**. It can be found that the allowable mass ratio of RTHS for the simplified BMD was 0.2 because ω_N was 94.09 rad/s. The effective modal mass of the experimental substructure was 1.53 kN-s²/m, which can be calculated based on the identified structural parameters. Accordingly, the mass of the numerical substructure was set as 8 kN-s²/m, which gave a mass ratio close to the stability margin of RTHS.

Force Correction Method

In addition to delay compensation, a force correction method is proposed in this study in order to improve the accuracy of RTHS. In the architecture of RTHS for BMD systems as shown in **Figure 3**, the response at the interfacial degree of freedom at the i -th time step is obtained by solving the equation of motion of the numerical substructure and becomes the input to the experimental substructure. The resulted base shear measured from the experimental substructure is input to the numerical substructure at the $i + 1$ -th step. As mentioned previously, there is one-step delay between the numerical and experimental substructures inevitably even perfect acceleration tracking is achieved. In fact, the equation of motion is not satisfied due to the imperfect interfacial connection between the experimental and numerical substructures in real practice including the dynamics of shake table, experimental boundary condition, modeling error and etc. Thus, the unbalanced force at each time step leads to

significant inaccuracy of RTHS which is generally referred to as error propagation. As a result, the force correction method compares the force balance at each time step and the unbalanced force is corrected at the next time step to prevent the RTHS from error propagation. The force correction method calculates the correction force f_c as

$$f_c = m_1^N (\ddot{u}_1^I + \ddot{u}_g) + c_1^N \dot{u}_1^I + k_1^N u_1^I - f_1^I \quad (11)$$

The correction force is used to correct the transmitted shear force error due to the difference between the desired and achieved acceleration at the interfacial degree of freedom. **Figure 12**

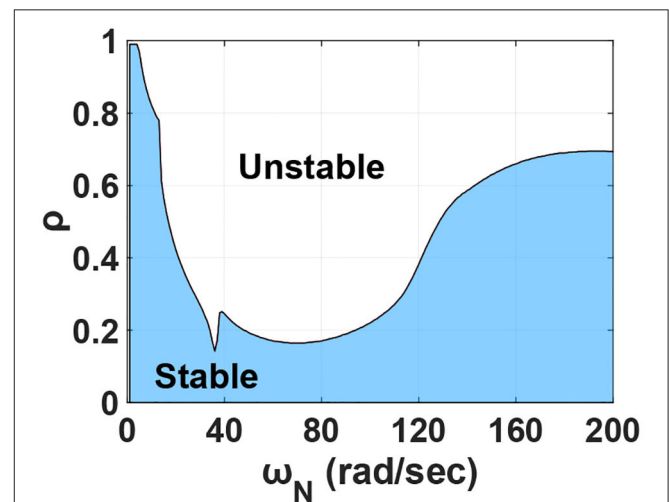


FIGURE 11 | Stable margin considering shake table dynamics for RTHS of the simplified BMD system.

TABLE 1 | Identified structural parameters of the experimental substructure.

Story	Mass (N-s ² /m)	Stiffness (N/m)	Damping coefficient (N-s/m)
Control layer	760	2,495,320	3,330
Superstructure	800	4,941,700	78

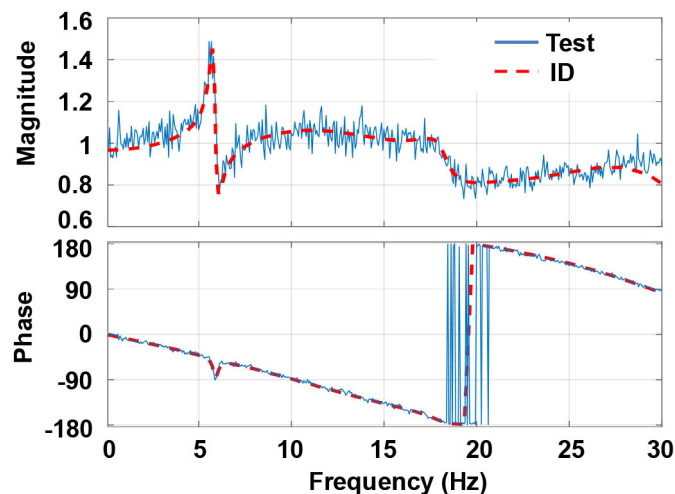


FIGURE 10 | System identification of the shake table with the experimental substructure of the simplified BMD system.

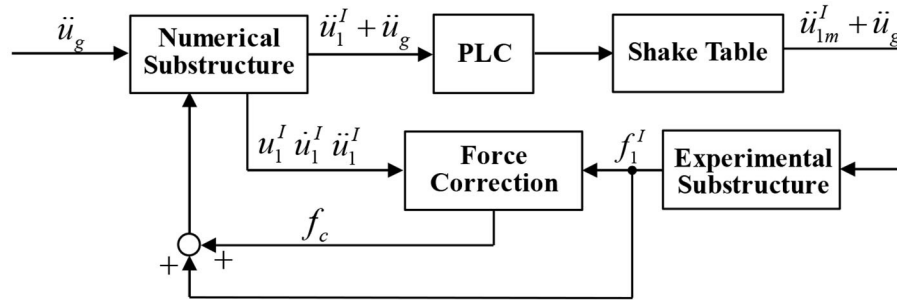


FIGURE 12 | Block diagram of the RTHS for the simplified BMD system.

TABLE 2 | RMSE of the substructure acceleration response with various compensation schemes.

Earthquakes	UC	FC	PLC	PLC + FC
Cape Mendocino	89.06	87.58	66.52	66.75
Chichi	93.43	90.30	72.12	66.94
Christchurch	Unstable	Unstable	61.13	59.81
Chuetsu-oki	82.01	79.41	67.86	63.52
Darfield	94.88	90.91	70.00	70.13
El Centro	95.39	90.98	76.65	69.90
Kobe	89.36	80.53	50.65	49.54
Kumamoto	94.78	92.61	69.50	65.72
Montenegro	95.83	85.91	58.48	56.77
Morgan hill	81.30	77.82	67.67	66.33
Northridge	89.57	75.88	50.71	48.56
Parkfield	82.72	76.89	48.11	47.08
Taipei	94.58	79.18	48.87	48.50

TABLE 3 | RMSE of the superstructure acceleration response with various compensation schemes.

Earthquakes	UC	FC	PLC	PLC + FC
Cape Mendocino	58.53	63.41	49.28	47.34
Chichi	57.43	54.51	53.30	51.33
Christchurch	Unstable	Unstable	50.67	48.49
Chuetsu-oki	65.98	59.20	50.29	48.08
Darfield	64.93	57.52	49.55	47.33
El Centro	62.30	49.61	53.91	53.34
Kobe	59.41	50.30	54.87	50.91
Kumamoto	53.64	42.93	43.56	42.94
Montenegro	69.55	57.34	58.74	58.19
Morgan hill	52.80	50.83	47.78	48.65
Northridge	56.61	49.08	49.37	50.47
Parkfield	53.71	49.49	48.71	48.84
Taipei	78.37	65.89	71.11	67.46

illustrates the block diagram of the RTHS of the simplified BMD system with both phase-lead compensation and force correction.

Experimental Results

A total of 13 earthquakes normalized to a peak ground acceleration of 1.0 m/s^2 were used as the excitation to the BMD system. A 3DOF numerical model with the same structural parameters was adopted as the benchmark for comparison purposes. The RTHS results were compared with the benchmark results by employing the root-mean-square error (RMSE) of the acceleration at each floor between the RTHS and the benchmark. The RMSE is defined as

$$RMSE(\%) = \sqrt{\frac{\sum_{k=1}^{N_s} (\ddot{u}[k] - \ddot{u}_{RTHS}[k])^2}{\sum_{k=1}^{N_s} \ddot{u}[k]^2}} \times 100\% \quad (12)$$

where $\ddot{u}[k]$ and $\ddot{u}_{RTHS}[k]$ are the absolute acceleration at each floor of the BMD system from the benchmark and RTHS at the k th step, respectively; and N_s is the total step number of the RTHS. Four compensation schemes were applied including uncompensated (UC), force correction (FC), PLC, and PLC

+ FC. Tables 2, 3 show the RMSE of the superstructure and substructure, respectively. It can be found that FC merely slightly improves the acceleration response at the substructure when it is compared with the uncompensated scheme. However, FC is not able to prevent RTHS from becoming unstable when the BMD system is subjected to the Christchurch ground acceleration because the frequency components of the Christchurch ground acceleration are higher than those of the other earthquakes. On the contrary, the implementation of PLC reduces the RMSE significantly compared with the uncompensated case and also achieves stable RTHS for the case with Christchurch ground excitation. Moreover, the RMSE is further reduced almost for all earthquake cases when the PLC is combined with FC, demonstrating that the PLC + FC is effective on achieving better RTHS results. Meanwhile, it seems that FC is more effective on reducing the RMSE of the acceleration response at the superstructure (experimental substructure) compared with that at the substructure (numerical substructure). It is also observed that even if the mass ratio of the experimental substructure to the entire BMD system is smaller than but close to the allowable mass ratio, RTHS could still become unstable considering the modeling error and system uncertainty. Therefore, compensation is essential to achieve more accurate and stable RTHS for BMD systems. In summary, PLC is more effective on reducing the

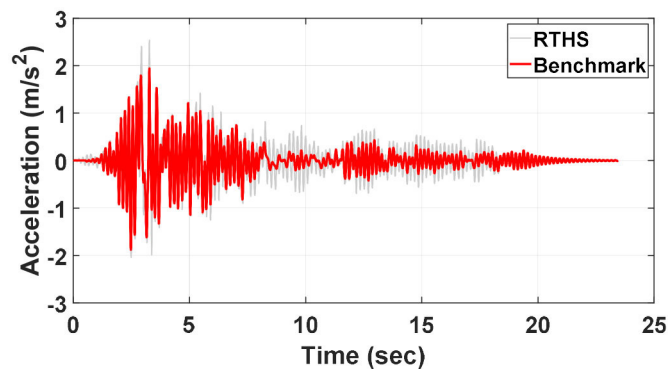


FIGURE 13 | Acceleration time histories of the superstructure from RTHS and benchmark.

RMSE of the acceleration response at the substructure than FC. However, PLC does not necessarily achieve more accurate response than FC does for the experimental substructure. It is suggested that both delay compensation and force correction are applied to RTHS of the BMD system for obtaining reasonable experimental results. **Figure 13** shows the acceleration response of the superstructure obtained from RTHS (PLC + FC) and the benchmark when the BMD system was subjected to the Parkfield excitation. It appears that the RTHS response was slightly larger than the benchmark response; however, the peak responses were considered fairly well. Future studies will be focused on the acceleration tracking control of shake table in order to further reduce the RMSE of RTHS.

CONCLUSIONS

A building mass damper (BMD) system which decomposes of a building into a substructure, a control layer and a superstructure, aiming to reduce the seismic response of the superstructure and substructure simultaneously by tuning structural parameters of the BMD system. Shake table testing provides an effective and straightforward approach to evaluate the seismic mitigation performance of a BMD system; however, repeated testing is not expectable when the experimental specimen of a BMD system behaves non-linearly under the earthquake excitation. For parametric studies of BMD systems, it could be costly to replace the specimens. As a result, real-time hybrid simulation (RTHS), which combines numerical simulation with structural testing could become an alternative approach to conduct parametric studies of BMD systems in a timely and cost-effective manner. In particular, RTHS using a seismic shake table is expected as the design of parameters for a BMD system merely considers the horizontal direction parallel to earthquake ground acceleration. Hence, a seismic shake table can be adopted as the interfacial degree of freedom between numerical and experimental substructures. In this study, stability analysis method for RTHS of a BMD system has been proposed and verified through conducting experiments in the laboratory.

In the stability analysis method, a BMD system can be simplified as a 3DOF structural model. Since the shear force from

the experimental substructure related to the mass is transmitted to the numerical substructure; therefore, the stability margin is represented as a mass ratio of the effective modal mass of the dominant mode of the experimental substructure to that of the numerical substructure and the experimental substructure. Stability analysis results indicate that it is challenging to conduct RTHS of a typical BMD system in which the mass of the superstructure is larger than that of the substructure even when delay compensation is applied. However, stable and successful RTHS can be achieved as long as the mass ratio is small and the first natural frequency of the substructure is low. In order to achieve more accurate RTHS, force correction method is proposed which is based on the unbalanced equation of motion of the numerical substructure. The force correction calculates the unbalanced force at the current time step and compensates the force at the next time step. Experimental results demonstrate that delay compensation is helpful to increasing the allowable mass ratio of a BMD system in RTHS; however, force correction is not. Meanwhile, delay compensation is more effective on reducing the root-mean-square error of the acceleration response at the numerical substructure than the force correction. However, it is not necessarily valid for the experimental substructure. Furthermore, force correction with delay compensation significantly reduces the root-mean-square error of the acceleration response at the numerical substructure. As a result, it is suggested that both delay compensation and force correction are required to RTHS of BMD systems not only for improving the experimental accuracy but also for increasing the allowable mass ratio for stable and successful RTHS.

DATA AVAILABILITY STATEMENT

The raw data supporting the conclusions of this article will be made available by the authors, without undue reservation.

AUTHOR CONTRIBUTIONS

Pe-CC: journal paper document, data analysis, and project supervision. M-WD: RTHS experiments and stability analysis.

Po-CC: data analysis. NN: project supervision. All authors contributed to the article and approved the submitted version.

FUNDING

This study was supported by the Collaboration Program between Tokushima University and National Taiwan University of Science and Technology (TU-NTUST-107-04). The APC was funded by the Taiwan Building Technology Center from The Featured

Areas Research Center Program within the framework of the Higher Education Sprout Project by the Ministry of Education in Taiwan.

ACKNOWLEDGMENTS

The experiments were conducted in the laboratory of National Center for Research on Earthquake Engineering (NCREE) in Taiwan. The authors would like to thank all the technical support from NCREE.

REFERENCES

- Anajafi, H., and Medina, R. A. (2018). Comparison of the seismic performance of a partial mass isolation technique with conventional TMD and base-isolation systems under broad-band and narrow-band excitations. *Eng. Struct.* 158, 110–123. doi: 10.1016/j.engstruct.2017.12.018
- Castaneda-Aguilar, N. E., Gao, X., and Dyke, S. J. (2012). RT-Frame2D: a computational platform for the real-time hybrid simulation of dynamically-excited steel frame structures. *J. Comput. Civil. Eng.* 29:04014049. doi: 10.1061/(ASCE)CP.1943-5487.0000341
- Chen, P. C., and Tsai, K. C. (2013). Dual-compensation strategy for real-time hybrid testing. *Earthq. Eng. Struct. Dyn.* 42, 1–23. doi: 10.1002/eqe.2189
- Chu, S. Y., Lu, L. Y., and Yeh, S. W. (2018). Real-time hybrid testing of a structure with a piezoelectric friction controllable mass damper by using a shake table. *Struct. Control Health Monitor.* 25:e2124. doi: 10.1002/stc.2124
- De Angelis, M., Perno, S., and Reggio, A. (2012). Dynamic response and optimal design of structures with large mass ratio TMD. *Earthq. Eng. Struct. Dyn.* 41, 41–60. doi: 10.1002/eqe.1117
- De Domenico, D., and Ricciardi, G. (2018a). An enhanced base isolation system equipped with optimal tuned mass damper inerter (TMDI). *Earthq. Eng. Struct. Dyn.* 47, 1169–1192. doi: 10.1002/eqe.3011
- De Domenico, D., and Ricciardi, G. (2018b). Earthquake-resilient design of base isolated buildings with TMD at basement: application to a case study. *Soil Dyn. Earthq. Eng.* 113, 503–521. doi: 10.1016/j.soildyn.2018.06.022
- Dyke, S. J., Spencer, B. F. Jr., Quast, P., and Sain, M. K. (1995). Role of control-structure interaction in protective system design. *J. Eng. Mech.* 121, 322–338. doi: 10.1061/(ASCE)0733-9399(1995)121:2(322)
- Matta, E., and De Stefano, A. (2009). Seismic performance of pendulum and translational roof-garden TMDs. *Mech. Syst. Signal Process.* 23, 908–921. doi: 10.1016/j.ymssp.2008.07.007
- Nakata, N., and Stehman, M. (2014). Compensation techniques for experimental errors in real-time hybrid simulation using shake tables. *Smart Struct. Syst.* 14, 1055–1079. doi: 10.12989/sss.2014.14.6.1055
- Schellenberg, A. H., Becker, T. C., and Mahin, S. A. (2017). Hybrid shake table testing method: theory, implementation and application to midlevel isolation. *Struct. Control Health Monitor.* 24:e1915. doi: 10.1002/stc.1822
- Wang, J. T., Gui, Y., Zhu, F., Jin, F., and Zhou, M. X. (2016). Real-time hybrid simulation of multi-story structures installed with tuned liquid damper. *Struct. Control Health Monitor.* 23, 1015–1031. doi: 10.1002/stc.1822
- Wang, S. J., Lee, B. H., Chuang, W. C., and Chang, K. C. (2018). Optimum dynamic characteristic control approach for building mass damper design. *Earthq. Eng. Struct. Dyn.* 47, 872–888. doi: 10.1002/eqe.2995
- Zhang, R., Lauenstein, P. V., and Phillips, B. M. (2016). Real-time hybrid simulation of a shear building with a uni-axial shake table. *Eng. Struct.* 119, 217–229. doi: 10.1016/j.engstruct.2016.04.022

Conflict of Interest: The authors declare that the research was conducted in the absence of any commercial or financial relationships that could be construed as a potential conflict of interest.

Copyright © 2020 Chen, Dong, Chen and Nakata. This is an open-access article distributed under the terms of the Creative Commons Attribution License (CC BY). The use, distribution or reproduction in other forums is permitted, provided the original author(s) and the copyright owner(s) are credited and that the original publication in this journal is cited, in accordance with accepted academic practice. No use, distribution or reproduction is permitted which does not comply with these terms.



Advances in Real-Time Hybrid Testing Technology for Shaking Table Substructure Testing

Yingpeng Tian¹, Xiaoyun Shao², Huimeng Zhou¹ and Tao Wang^{1*}

¹ Key Laboratory of Earthquake Engineering and Engineering Vibration, Institute of Engineering Mechanics, China Earthquake Administration, Harbin, China, ² Civil and Construction Engineering Department, Western Michigan University, Kalamazoo, MI, United States

OPEN ACCESS

Edited by:

Chia-Ming Chang,
National Taiwan University, Taiwan

Reviewed by:

Georgios A. Drosopoulos,
University of KwaZulu-Natal,
South Africa
Xueosng Cai,
Tongji University, China
Gaston A. Fermandois,
Federico Santa María Technical
University, Chile

*Correspondence:

Tao Wang
wangtao@iem.ac.cn

Specialty section:

This article was submitted to
Computational Methods in Structural
Engineering,
a section of the journal
Frontiers in Built Environment

Received: 24 April 2020

Accepted: 07 July 2020

Published: 07 August 2020

Citation:

Tian Y, Shao X, Zhou H and
Wang T (2020) Advances in Real-Time
Hybrid Testing Technology
for Shaking Table Substructure
Testing. *Front. Built Environ.* 6:123.
doi: 10.3389/fbuil.2020.00123

Shaking table substructure testing (STST) takes the substructure with complex behavior physically tested, with the behavior of the rest structural system being numerically simulated. This substructure testing allows the payload of a shaking table being fully utilized in testing of the most concerned part, thus significantly increases its loading capacity. The key to achieve a successful STST is to coordinate among the substructures, specifically, to satisfy compatibility, equilibrium, and synchronization at the boundary between numerical and experimental substructures. A number of studies have focused on the essential techniques of STST, and several applications have been carried out. Nonetheless, its progress is still in the preliminary stage, because of the limited applications using multi-directional shaking tables on large-scale specimens. This paper reviews a series of STSTs and their associated implementation aspects including hybrid testing frameworks, time integration algorithms, delay compensation methods, shaking table and actuator control schemes and boundary force measurement methods. The key techniques required for a successful test are also stressed, such as the force control of actuators to coordination among the substructures. Finally, challenges for future studies and applications are identified and presented.

Keywords: real-time hybrid test, shaking table substructure test, delay compensation, boundary coordination, numerical substructure

INTRODUCTION

Shaking table test is one of the most effective ways to reproduce earthquake excitations on engineering structures by imposing a predefined earthquake ground motion at the base of a structural model. However, the testing capacity of a shaking table is often restricted by the effective payload it can support. Localized damages within a structural system are difficult to be captured using small-scale specimens weighing tens to hundreds of tons. This is the reason why shaking tables are often used to examine the global performance of a structure, but rarely on the behavior of its components. To maximize the use of available shaking table testing capacity, several methods have been proposed and applied. Some applications employed rigid frames or foundations with larger space to extend the testing area of shaking tables (Xiong et al., 2008; Ba et al., 2017; Jia et al., 2017; He et al., 2018). Although the frames and foundations consume some effective payload, they are beneficial in testing relatively light and large space specimens, such as wooden buildings and

large space structures. The testing capacity can be significantly increased by constructing shaking table array (Soroushian et al., 2016; Xie et al., 2019), where several shaking tables can be flexibly configured to test long-span bridges or large space structures. Large size shaking tables, such as the largest shaking table of the world, E-Defense in Japan, and the largest outdoor shaking table in the US, are able to test large-scale to even full-scale specimens (Kim et al., 2012; Astroza et al., 2016). Although they are featured with thousands of tons of payload capacity, they are not necessarily adequate to test the entire engineering structure at acceptable scale ratio. Therefore, there is still a need to develop testing techniques for shaking tables. For example, a substructure test using the E-Defense shaking table was realized using an offline control scheme (Ji et al., 2009). To achieve large displacement and velocity responses at the top of a high-rise building, which exceeded the shaking table capacity, a rubber-mass system was designed and inserted between the table and the specimen to amplify the table input. This method, however, relies significantly on the dynamics of the target structure and characteristics of the amplifier mechanism.

Online hybrid test (Wu et al., 2007; Gao et al., 2013; Sarebanha et al., 2019) is able to test large-scale specimens, where the dynamics of the entire structural system are solved in the computer domain with restoring forces obtained from the physical specimen. When employing the substructure technique, its testing capacity can be further extended. It is promising to combine the substructure hybrid testing technique with the shaking table testing method, namely shaking table substructure test (STST), which will provide not only a larger testing capacity, but also the flexibility in dealing with various types of specimens. In an STST as shown in **Figure 1**, the most concerned part is physically tested, while the rest is numerically simulated, thus significantly increasing the loading capacity through the substructure testing and becoming a potential solution to address the scale challenge faced by traditional shaking table tests. STST (Horiuchi et al., 2000; Igarashi et al., 2000; Lee et al., 2007; Wang and Tian, 2009; Wang et al., 2010; Shao et al., 2011; Nakata and Stehman, 2012; Mosalam and Günay, 2014; Xu et al., 2014; Stefanaki and Sivaselvan, 2018) was proposed at the beginning of this century and has caught more attention recently because of the large number of shaking tables and shaking table arrays constructed in China. STST, although appealing to extend the testing capacity of shaking table, is not easy to be implemented due to the difficulties in maintaining the compatibility and equilibrium at the boundaries in the space domain, while ensuring the synchronization between substructures in the time domain. Since most shaking tables are designed to reproduce a predefined acceleration time history, it is challenging to realize the boundary condition between substructures using a shaking table, which is often solved step by step during a STST. The control strategy of shaking tables, such as the tri-variable control method, is quite different from the control method of a single actuator often used in real-time hybrid test, further hindering the development of STST. The knowledge accumulated from real-time hybrid test may not be directly applicable in STST. Despite all these difficulties, STST has been developed and advanced significantly in the past two decades. It is the intention of this

paper to review these progresses and identify potential challenges for future studies.

This paper firstly introduces the successful cases of STSTs applied in civil engineering, which can be categorized into two groups based on boundary implementation. The frameworks developed in these applications are reviewed next. Key techniques developed and adopted in STST are summarized, including time integration algorithms, delay compensation methods, and shaking table control schemes. The force control of actuators to coordinate substructures is specifically discussed together with boundary force measurement methods. Finally, challenges for future studies and applications are identified and presented.

STATE-OF-THE-ART AND STATE-OF-THE-PRACTICE OF STST

Shaking table substructure testing was first proposed in Japan and then studied extensively in the United States. Because of the construction upsurge of shaking tables in China, this technology has caught a lot of attention from both Chinese academia and engineers. This section introduces several STST frameworks developed in the past two decades. The configurations and applications are summarized first. Then the procedures are compared for two types of STST which are categorized based on substructure patterns. Finally, a typical hardware integration is described for researchers who may be interested in building their own STST system.

Current Studies and Applications of STST

Early Studies Around the Year 2000

Shaking table substructure testing was first proposed in Japan to examine soil-foundation interaction effects (Konagai et al., 1998). In the same period, Inoue proposed a STST system to test mechanical systems, which was later applied to test a secondary structural system attached to a primary structural system (Inoue et al., 1998; Horiuchi et al., 2000). In this application, a uniaxial shaking table was utilized to load the secondary system, while the primary structure was numerically simulated. The fundamental frequency of the target structure was 3.75 Hz. A linear acceleration method was employed to solve the equation of motion of the structural system subject to the ground motion based on the measured reaction force from the secondary system. Because of the inherent time difference between the numerical simulation and the physical testing, the shaking table command was predicted by extrapolating following an n -th order polynomial function. It was also found out that the stability of the STST was closely related to the order of the polynomial function. If a second order function is used, the mass ratio of the secondary system over the primary system shall be less than 1/7 to maintain the stability. The total delay of the shaking table and the numerical simulation was 5.5 ms, was successfully compensated using a second-order function in the STST. Nearly identical responses were observed between the pure numerical simulation and the STST test.

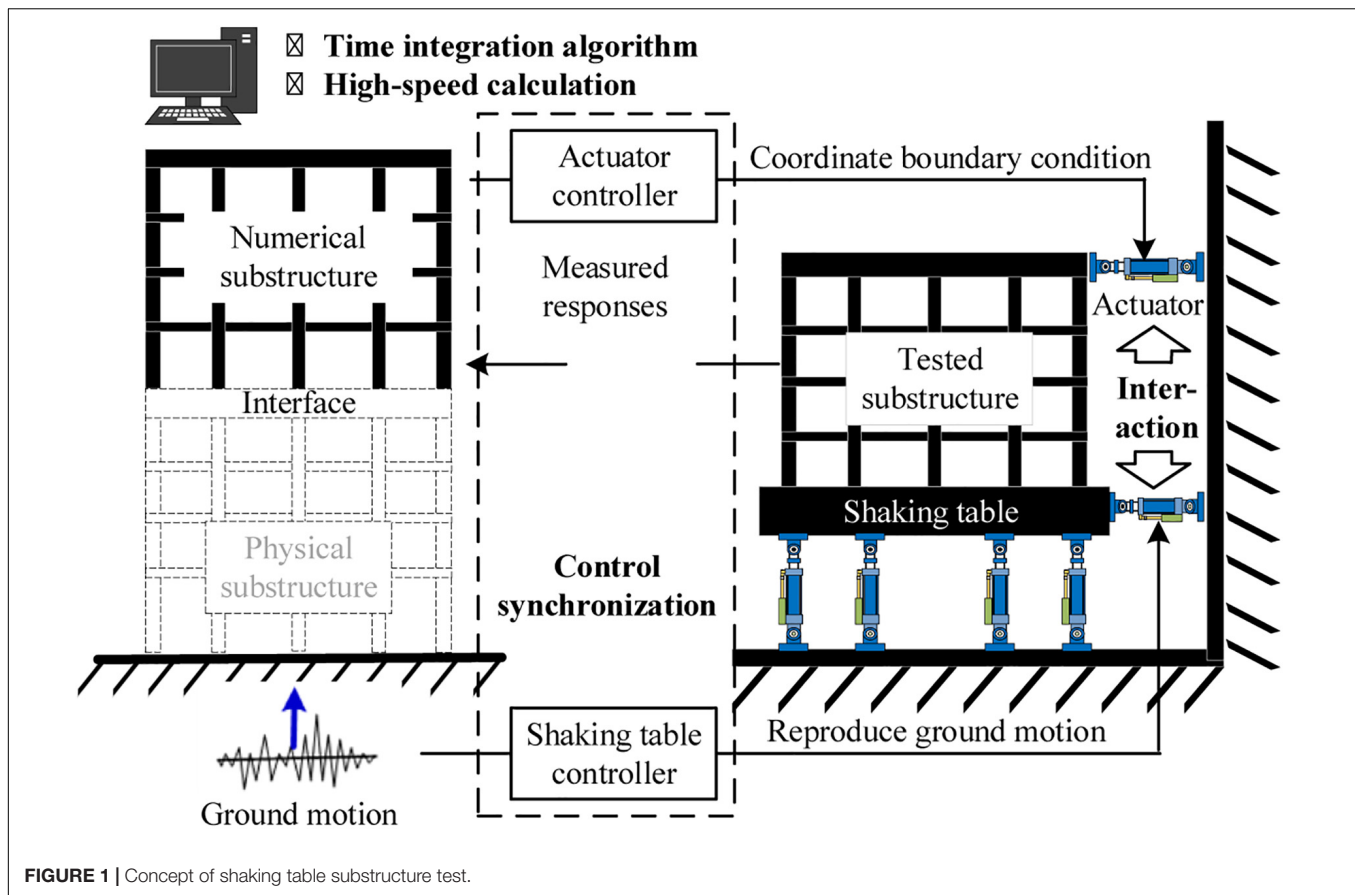


FIGURE 1 | Concept of shaking table substructure test.

Igarashi (Igarashi et al., 2000) reported a similar framework of STST. They derived the response of the entire system to the input as a transfer function considering the shaking table delay. It was found out that the mass ratio between the experimental substructure and the numerical substructure should be sufficiently small to achieve reliable testing result. For this reason, they believed that the STST system was ideal to test secondary systems in a building structure. For example, they conducted STST on the tuned mass damper (TMD) and the tuned liquid damper (TLD) which were at the top of the numerically simulated building structure (Igarashi et al., 2004). This numerical substructure was solved by the backward Euler method because of its computational efficacy. The measured base shear of the TMD or TLD was fed back and combined with the ground motion to formulate the input to the numerical simulation. The calculated roof displacement was used to drive the shaking table. To compensate the delay, a fourth-order finite-impulse-response (FIR) filter was employed to approximate the transfer function of the uniaxial shaking table, while the amplitude amplification introduced by this FIR phase-lead filter was mitigated using a third-order low-pass Butterworth infinite-impulse-response (IIR) filter as a preconditioner to the FIR filter. Testing was carried out on the TMD (natural frequency of 2.03 Hz) and the TLD (natural frequency of 1.14 Hz), respectively, demonstrating the feasibility of the proposed STST system.

In 2007, Lee (Lee et al., 2007) conducted a STST on a five-story building where the top two stories were selected as the experimental substructure while the rest was numerically simulated. The first five natural frequencies of the building structure ranged from 1.3 to 10.8 Hz, while the experimental substructure had two inherent frequencies of 2.5 and 8.6 Hz. The coordinated motion between the two substructures was implemented by a uniaxial shaking table with the input calculated from the numerical simulation based on the force feedback from the experimental substructure and the ground motion. To faithfully exert the absolute acceleration reference signal generated by the numerical simulation to the experimental substructure, an inverse transfer function of the measured acceleration with respect to the command signal was developed and adopted in the shaking table controller to overcome the distortion induced by the inherent dynamics of the shaking table. The test results agreed well with the numerical simulation. However, unexpected vibration of the experimental substructure was observed and passed onto the numerical simulation through force feedback. To overcome this distortion, a heavily damped experimental substructure was suggested by the authors.

Recent Studies From 2007

The above studies initiated further development of STST testing methods with more exemplary experiments. The stability of STST systems was also analyzed considering the delay due to numerical

simulations and shaking tables. These studies are deemed preliminary because the substructure scheme, the shaking table controller, and the boundary coordination are relatively simple. For example, the substructure scheme of these STST tests usually took the upper stories of or secondary systems above a building structure as the experimental substructure. However, most structures suffer more seismic damages at the bottom. To extend STST application scope, more studies were performed.

Reinhorn (Reinhorn et al., 2003, 2005) proposed a unified formulation for all real-time hybrid tests using a mass-splitting coefficient and a load-splitting coefficient. This unified formulation is capable of representing various testing methods, including the traditional hybrid testing, effective force testing, real-time hybrid testing and STST, by selecting different values of the splitting coefficients. The force-based feature of this unified formulation allows easy implementation of STST. However, this leads to the challenge of actuator force control due to specimens' resonant response and actuators' internal friction. To address this challenge, the authors proposed to convert the closed-loop force control into a closed-loop displacement control by adding a flexible spring compliance between the specimen and the actuator. With this idea, Shao (Shao, 2007; Shao et al., 2011) built up a modularized unified real-time hybrid testing framework, including data acquisition, real-time hybrid simulator, and testing controller, which is further described in section "A Typical Hardware Configuration of STST." A uniaxial shaking table and an actuator were employed as the loading devices in the framework to apply ground excitation and interface force at boundaries. Five testing cases of a three-story model with the natural frequencies from 1.55 to 4.87 Hz were defined based on the mass-splitting and load-splitting coefficients and examined. To compensate the time delay in the shaking table and the actuator as well as the time delay difference between the two loading devices, which ranged from 7 to 12 ms, the Smith's predictor was adopted. The test results well demonstrated the concept of the unified formulation of dynamic hybrid testing and the effectiveness of boundary control techniques.

A similar concept was adopted by Nakata (Nakata and Stehman, 2012) to develop a STST system. To formulate the boundary conditions between experimental and numerical substructures, the boundaries were categorized into three types: (1) the experimental acceleration compatibility provides ground motion at the bottom of the experimental substructure; (2) the computational acceleration compatibility specifies absolute acceleration measured at the top of the experimental substructure to the upper numerical substructure; and (3) the interface force compatibility exerts the reaction force obtained from the numerical substructure onto the top of the experimental substructure. The computational acceleration compatibility and the interface force compatibility guaranteed the equilibrium and compatibility of the boundary between the two substructures. To bypass the difficulty of actuator force control, the authors utilized a controlled mass to apply the interface force onto the experimental substructure. A numerical study was conducted to demonstrate the feasibility of the proposed STST system where a five-story building

was the prototype structure. The natural frequencies of the building ranged from 2 to 13.49 Hz. The bottom two stories were selected as the experimental substructure, while the rest was numerically simulated using the Newmark-family integration method. The results indicated a well reproduction of the target force history of the actuator through the controlled mass scheme.

Mosalam (Günay and Mosalam, 2014; Mosalam and Günay, 2014) proposed a STST system based on a uniaxial shaking table, which was employed to test electricity disconnect switches. The supporting frame of the disconnect switch was simulated numerically, while the disconnect switch on top of the supporting frame was experimentally tested on the shaking table. The natural frequencies of the numerical and the experimental substructures were about 3 and 5 Hz, respectively. The displacement at the interface between the two substructures became the input to the shaking table, while the force measured from the shaking table was fed back to the numerical substructure. To keep up the real-time loading required in the STST, the explicit Newmark integration method with a small time step of 1 ms was adopted. Meanwhile, to compensate the time delay, a feed-forward error compensation scheme was developed based on a predicted error function with respect to the actuator velocity. In this study, the uniaxial shaking table is displacement-controlled, similar to those actuators used in a typical real-time hybrid testing. To achieve more accurate shaking table control, the authors developed an advanced control method based on the three-variable control (TVC) scheme (Günay and Mosalam, 2015). This STST system was later applied to substation structure, where a three-dimensional numerical substructure was efficiently solved by the operator-splitting integration method formulated for the real-time hybrid testing.

Schellenberg (Schellenberg et al., 2017) carried out a series of STST tests to examine the seismic performance of buildings with midlevel seismic isolations. The isolated superstructure, consisting of a two-story steel moment frame supported by six triple friction pendulum bearings, were physically tested on the table while the portion below was numerically modeled. The natural frequencies of the isolated superstructure in the first and second sliding stages were about 0.76 and 0.53 Hz, respectively. The first two frequencies of the fixed-base superstructure were approximately 2.33 and 7.14 Hz. The maximum frequency of the entire building was nearly 16 Hz. A lumped mass shear type building model was used. Explicit time integration algorithms, such as the explicit Newmark method, the explicit generalized alpha method and the generalized alpha-OS method, were examined in the STST tests. OpenFresco served as the middleware to coordinate the numerical substructure with the experimental superstructure through the transfer system (i.e., the shaking table). The absolute displacement at the top of the numerical substructure was used as the input to the shaking table and the corresponding story shear force was fed back to the numerical substructure. Derivative feedforward (FF) and differential pressure controls included in an MTS-493 real-time controller were used to compensate the time delay of the transfer system and to

suppress the resonance around the oil column frequency. It was recommended that advanced delay compensation techniques and control strategies be adopted to improve tracking performance of the shaking table during STST, especially in the high-frequency range.

A similar study was conducted by Zhang (Zhang et al., 2017) on a 15-story midlevel isolated building. The lumped mass-spring model was used to represent the dynamics of the building structure. Frequencies of interest ranged from 0.24 to 5.49 Hz for the overall structure. In the STST test, the isolated upper six stories including the isolation layer were taken as the experimental substructure, among which the upper six stories was represented by an SDOF specimen with a natural frequency of 0.25 Hz. The lower nine stories were numerically simulated. Instead of the absolute displacement, the absolute acceleration response at the top of the numerical substructure was taken as the target command of the shaking table which served as the transfer system between the numerical and the experimental substructures. Based on a linearized model of the shake table system, a model-based control strategy was developed to accurately track the desired accelerations. The goals of this strategy were to cancel out the modeled dynamics of the shaking table through the feedforward control and to provide robustness against nonlinearities and uncertainties in the testing system through the Linear–Quadratic–Gaussian control.

Recently, Stefanaki (Stefanaki and Sivaselvan, 2018) proposed a new dynamic substructure strategy that can be used for STST. The novel aspect of this substructure strategy is to consider the numerical substructure as part of the boundary loading device so the tracking controller to reproduce the boundary compatibility (i.e., the control-structure interaction) is not required, nor the compensation of actuator delay or the time integration algorithm for the numerical substructure. Specifically, this strategy aims to replicate the behavior of the entire numerical substructure and to physically exert its influence onto the experimental substructure. To achieve this, a device conceptually similar to the one proposed by Nakata (Nakata and Stehman, 2012), called the active mass driver (AMD) was devised. This AMD adopted a simple feedforward approach and was completely decoupled from the experimental substructure. The AMD had two inputs (i.e., the control input and the feedback from the experimental substructure) and one output (i.e., the boundary condition to be imposed onto the experimental substructure). The authors derived transfer functions of the AMD system for both SDOF and two-DOF systems. They claimed that the derivation can be extended to MDOF systems. Note that a high-pass filter is needed if the damping of the system is not proportional to the stiffness. This strategy was experimentally investigated using a testing setup consisting of a shaking table and the AMD (Stefanaki and Sivaselvan, 2018). It was found out that the proposed dynamic substructure controller was effective in imitating numerical substructures with a wide range of frequencies from 5 to 40 Hz. When being applied on an experimental substructure, the interface force was generally reproduced well but with larger discrepancies at higher frequencies even with a 30 Hz low-pass filter. Nonetheless, the

ability of this new dynamic substructure scheme using shaking table and the AMD was demonstrated.

Studies and Applications of STST in China

The effectiveness of STST to advance shaking table testing capability also attracted Chinese scholars' attention. In 2009, Wang (Wang and Tian, 2009) presented the STST method and its application including the substructure coordinating procedure, the time integration method, and the boundary realization methods. In their STST system, the shaking table was used to impose the ground motion to the test specimen while simultaneously loaded by the actuator. The response measured from the specimen was sent to the numerical simulation together with the measured ground motion of the shaking table. The calculated interface force was then sent to the actuator be applied to the test specimen. The modified central difference integration was adopted and the feasibility of actuator force control was explored, but no effective solution was proposed. In the exemplary test, a three-story braced steel frame was first tested on the shaking table. Then the first story was tested as the experimental substructure loaded by the shaking table from the base and the actuator at the first floor. The force history measured from the three-story structure shaking table test was used as the input to the actuator. Although there was some time delay, the test result was relatively accurate. However, the authors claimed the delay should be eliminated in the real STST application.

In 2010, Wang (Wang et al., 2010) reported a real-time hybrid testing system using shaking table. The upper substructure was treated as the experimental substructure and the lower part was the numerical substructure. The shaking table was utilized to realize the boundary compatibility. Similar to the aforementioned STST systems, the boundary displacement or acceleration was the input to the shaking table which was numerically simulated. The measured reaction force from the experimental substructure corresponding to this boundary displacement or acceleration was fed back to the numerical substructure for the next step calculation. Wang et al. (2014) developed an explicit time integration algorithm based on the discrete control theory to efficiently solve the numerical substructure, where both displacement and velocity were explicitly formulated. When using the dual interval scheme, where the dynamics was solved using a larger time step and extrapolated using a smaller step as the command signal, the degrees of freedom of the numerical substructure model may exceed 1200 without jeopardizing the integration stability. The effect of shaking table time delay in STST was also analyzed by the root locus method using the Padé function to approximate the delay. It was found out that the stability of the system depended significantly on the mass ratio of the experimental and numerical substructures. Therefore, a third-order Lagrange polynomial function was suggested to predict the command and compensate the delay, comprehensively considering the stability and accuracy. The authors also suggested that a virtual shaking table (i.e., numerical model of the shaking table) is ideal to tune the control parameters without the risk of damaging physical specimens. Using the proposed STST framework, the authors examined several engineering problems including fluid-structure interaction (Chi

et al., 2010) and soil-structure interaction (Wang et al., 2014). In the latter application, the natural frequency of the specimen was about 4.4 Hz. The maximum error in the acceleration response were about 30%. This large error maybe to attributed to the third-order extrapolation function used to compensate the time delay, that resulted in high-frequency error, while the excitation frequency being close to the oil-column resonance frequency.

A similar STST system was developed by Zhou (Zhou and Wu, 2013) which took the upper part of a building model as the experimental substructure and the lower part as the numerical substructure. In this system, the numerical substructure was solved by the central difference method (CMD), and the shaking table was controlled in displacement. To overcome the adverse effect from the oil-column resonance, the pressure difference feedback control was developed to increase the hydraulic damping ratio, so that the noises introduced by the oil-column resonance were mitigated. The effectiveness of this control scheme was demonstrated in the STST test on an SDOF structure. The STST system was applied to a storage tank considering the soil-structure interaction (Xu et al., 2014). The water sloshing frequency was 0.67 Hz. A polynomial function was employed to predict the response and compensate the inherent system delay. Only numerical simulation was conducted, and the feasibility of the proposed STST was preliminarily demonstrated. Using this STST system, an TLD controlled structure with a natural frequency of 0.77 Hz was examined (Zhou et al., 2014). The shear force of the TLD was computed based on the measured acceleration at the based of the TLD. The comparison between the measured acceleration and the command acceleration indicated a noticeable error in the frequency range of 3–25 Hz.

Fu (Fu et al., 2019) conducted comparative STST tests to study vibration control effects of particle dampers (PD) and TLD on structures. The dampers on top of the structure were tested physically, and the structure was simulated numerically by a lumped-mass spring model. Three representative model-based integration algorithms (i.e., the generalized Chen and Ricles (GCR) algorithm, the Chang algorithm and the Kolay and Ricles KR- α algorithm) were adopted to solve the equation of motion, which are all unconditionally stable and have an explicit formulation. Three substructures with frequencies of 1.2, 2, and 3 Hz were simulated by the STST tests. The boundary displacement was taken as the input to the uniaxial shaking table, which was subject to the proportional-derivative (PD) control with an added velocity feedforward gain to improve the control performance.

The primary features of the developed STST systems presented in this section and their applications are summarized in **Table 1**.

Substructure Patterns in STST

The STST applications introduced above can be classified into two categories based on substructure patterns. It can be seen that early STST tests only tested one substructure using one shaking table as the boundary coordinator, during which the upper part of a structural system was tested while the lower part was numerically simulated, as shown in **Figure 2A**. Compared with those early studies, recent development adopted a more general substructure pattern through which the tested

substructure can be any part of a structural system. This is realized by synchronically using shaking table and actuator, as shown in **Figure 2B**. Although the unified formulation proposed by Reinhorn (Reinhorn et al., 2003, 2005) is able to describe both substructure patterns, this paper separately discusses these two substructure patterns so that the challenges in controlling shaking table and actuator can be explained separately.

In the first pattern, the upper structure is tested on a shaking table and the rest is numerically simulated. The response at the top of the numerical substructure, usually acceleration, is taken as the input of the shaking table to be imposed to the experimental substructure. The base shear of the experimental substructure is measured and sent to the numerical substructure as one input and earthquake ground motion is the other input. In this procedure, a closed-loop is formed from sending the acceleration response to the experimental substructure and the measured reaction force being fed back as the input. This closed-loop STST has to be conducted in real time. To achieve this, the response of the numerical substructure needs to be solved very efficiently, as is done in many real-time hybrid tests (Nakashima et al., 1992; Chen et al., 2012; Phillips and Spencer, 2013b; Ou et al., 2015). Therefore, techniques developed in these real-time hybrid tests can be directly applied herein, such as the polynomial-based prediction and the unconditionally stable explicit time integration algorithms. The difference between the STST using this substructure pattern and the real-time hybrid tests lies in the realization of the boundary condition using shaking table instead of actuator. However, the control scheme of the shaking table used in STST is significantly different from that used in the traditional shaking table tests. The input to the shaking table in STST is not pre-determined as the case in traditional tests. Thus, conventional methods to improve control accuracy, such as the offline iteration, cannot be applied in STST.

The second pattern is more complex, in which the upper part is the numerical substructure while the lower part is physically tested. The experimental substructure is excited by the shaking table from the bottom with a ground motion. The structural response, commonly the absolute acceleration measured at the top of the experimental substructure, is sent to the numerical simulation as the input for the time history analysis. The simulated reaction force of the numerical substructure is then sent to the actuator and applied to the top of the experimental substructure. Therefore, the experimental substructure is loaded by shaking table and actuator simultaneously. Because both loading devices are connected to the specimen, the controllers of the actuator and the shaking table are coupled, which shall be carefully designed typically through a de-coupling strategy to achieve a good control for both equipment. To do this, the feedbacks of both controllers would be sent to each other, as indicated by the red dashed line in **Figure 2B**. It shall be noted that the shaking table is usually used to reproduce a seismic acceleration history resulting in a distributed inertial force within the test specimen. Therefore, the actuator is better to be force controlled. This force-controlled dynamic STST is essentially different from the traditional real-time hybrid test methods. The ground acceleration history, usually measured from the shaking table, is used as the excitation input to the numerical

TABLE 1 | Features of existing STST systems and applications.

Primary features	Substructure pattern ¹	Structure frequency (Hz)	Time integration	Delay compensation (ms)	Shaking table	Control of shaking table	Input of shaking table	Input of actuator	Numerical substructure
Inoue et al., 1998	First	3.75	Linear acceleration	2nd order polynomial (5.5)	Uniaxial	–	Acceleration	–	Linear Mass-spring
Igarashi et al., 2004	First	1.14–2.03	Backward Euler	4th FIR-3rd IIR	Uniaxial	–	Displacement	–	Linear Mass-spring
Reinhorn et al., 2003	Second	1.55–4.87	–	Smith's predictor (7–12)	Uniaxial	–	Acceleration	Displacement, to force	Linear Mass-spring
Lee et al., 2007	First	1.3–10.8	–	–	Uniaxial	–	Acceleration	–	Linear Mass-spring
Wang and Tian, 2009	Second	–	Central difference method	–	–	–	Acceleration	Directly input	Linear Mass-spring
Nakata and Stehman, 2012	Second	2–13.49	Newmark method	–	–	–	Acceleration	Force by controlled	Linear Mass-spring
Zhou and Wu, 2013; Xu et al., 2014; Zhou et al., 2014	First	About 0.7	Central difference method	Polynomial function	Uniaxial	Pressure difference feedback	Displacement	–	Linear Mass-spring
Chi et al., 2010; Wang et al., 2010; Wang et al., 2014	First	About 4	Unconditionally stable explicit method	3rd order polynomial (11)	Uniaxial	–	Displacement	–	Linear 1200DOFs
Mosalam and Günay, 2014	First	3–5	OS method/Explicit Newmark	Feed forward compensation	Uniaxial	Three-variable control	Displacement	–	Linear Mass-spring
Schellenberg et al., 2017	First	2.33–7.14	Newmark method	Feed forward compensation	Uniaxial	Pressure difference feedback	Displacement	–	Linear Mass-spring
Zhang et al., 2017	First	0.24–5.49	–	Feed forward compensation	Uniaxial	LQG feedback control	Acceleration	–	Linear Mass-spring
Stefanaki et al., 2018	Second	5–40 Hz	–	–	–	–	–	Force by AMD	Linear
Fu et al., 2019	First	1.2–3	Model-based integration algorithms	–	Uniaxial	PD controller (velocity feedforward gain)	Displacement	–	Linear Mass-spring

¹Please refer to section “Substructure Patterns in STST.” ²Although it is classified in the second pattern, the readers shall be noted that this framework is different from other.

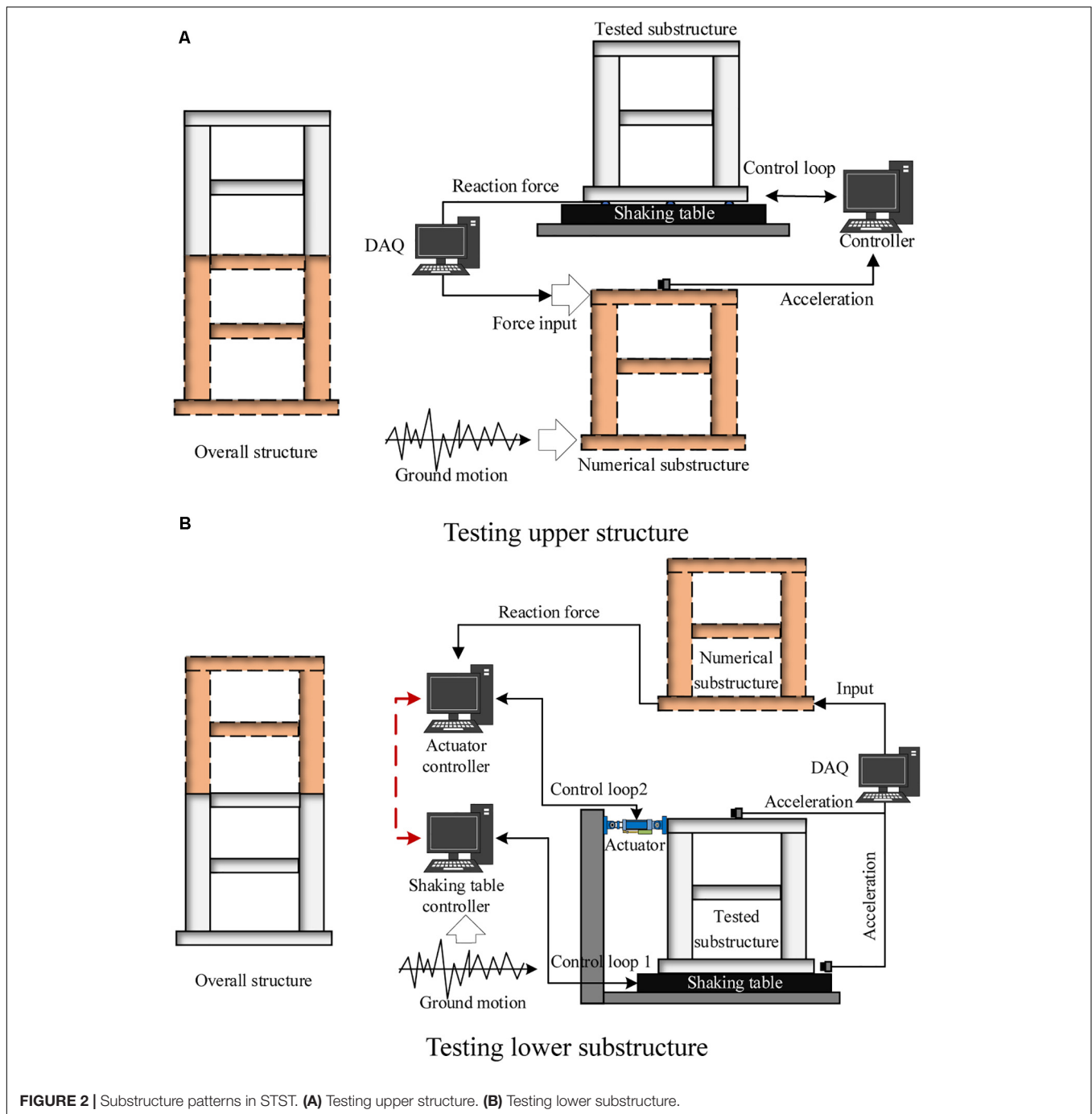


FIGURE 2 | Substructure patterns in STST. **(A)** Testing upper structure. **(B)** Testing lower substructure.

substructure, to avoid the discrepancy in the ground motion excitation to the experimental and the numerical substructures. Similar to the first pattern, the simulation of the numerical substructure shall catch up with the loading speed, which implies that synchronization among shaking table, actuator and numerical simulation shall be guaranteed. Therefore, in this substructure pattern, there are two closed-control loops. One closed-loop is used to control actuator, which strongly depends on simulation results of numerical substructure. The other is used to control shaking table, may or may not depend on

the numerical simulation results based on STST configuration. Please note that inherent control loop, also known as the inner controller provided by manufacturers of loading devices, is still required in both substructure patterns. This inner controller may be either incorporated into the entire control strategy or operated separately.

Another substructure pattern shall be noted is the substructure strategy proposed by Stefanaki (Stefanaki and Sivaselvan, 2018). Although similar to the second substructure pattern, this pattern indeed implements the numerical substructure as a part of the

boundary loading device. When designing the controller of the boundary loading device, the transfer function of numerical substructure is taken as a reference. The controlled boundary loading device shall generate the same reaction force when being given the same input. Therefore, the numerical substructure is incorporated into the inner control loop of the loading device. This way, on one hand, simplifies the entire STST system, and on the other hand, avoids the actuator-structure interaction. However, if the numerical substructure is expected to yield nonlinear response, the controller of the boundary loading device could be very complex.

Testing Procedures of STST

Testing procedures of STST with the first substructure pattern is much different from those of the second substructure pattern, as described in **Table 2** and illustrated in **Figure 3**. The first substructure pattern starts from the numerical simulation to determine the target acceleration of the shaking table step by step. Before exciting the experimental substructure, this target acceleration is fitted using polynomial functions to predict commands of the next several steps in case numerical simulation cannot catch up with real-time loading. In the shaking table inner controller, acceleration commands are usually integrated into displacement commands to drive the actuators. Therefore, the boundary loading is essentially controlled in displacement for the experimental substructure. After loading, the boundary shear force is measured either directly by load cells or indirectly by accelerometers attached to the substructure (see section “Force Measurement at the Boundary Between Substructures in STST” for details). In the real application, a low-pass filter is usually employed to eliminate the high-frequency noise in the measurement. The procedures of the second substructure pattern are more complex, as shown in **Figure 3B**. The STST starts from the experimental substructure. Two control loops are required for the shaking table and the actuator, respectively. The input to the shaking table is often pre-determined (i.e., ground acceleration history), while the command to the actuator is computed step by step through numerical simulation. Both shaking table and actuator are connected to the specimen. The strong coupling between these two loading devices, therefore, needs to be addressed when designing their respective control algorithms. Moreover, the shaking table and the actuator have to be synchronized during a STST. It shall be noted that, the specimen is actually loaded by the inertial force, although the shaking table is controlled by acceleration or displacement. Therefore, a force control is preferred for the actuator.

A Typical Hardware Configuration of STST

In a typical STST system, there are three dynamic subsystems, including numerical simulation, shaking table and actuator loading systems. The three dynamic subsystems are operated simultaneously and inter-dependently by exchanging data during the test. The entire system runs in real time and in a step-by-step manner, which means any time step difference

among the three dynamic subsystems shall be minimized as much as possible. To this end, devices running in real time mode shall be used and connected through high-speed data transfer cables. A typical hardware configuration of STST system consists of three modules: the data acquisition system (DAQ), the real-time hybrid simulator, and the testing controller (Shao et al., 2011). The DAQ module is composed of signal acquisition and signal conversion equipment. The collected data are transferred to the other two modules and used as inputs in algorithms running in the hybrid simulator or as reference signals in the loading devices' controllers. The real-time hybrid simulator includes one or several real-time targets (for example, Matlab/xPC target) to simulate response of the numerical substructures from which loading commands of shaking tables and actuators are determined. In this module, the control commands are usually compensated for the time delay in loading devices and synchronization among them is ensured. The testing controller module contains shaking table controllers and actuator controllers. The nonlinearity of specimens, the interaction between loading devices and specimens, and other factors affecting control stability and precision shall be considered in this module. To achieve data exchange in a real-time pattern, these modules are equipped with the shared common random-access memory network (SCRAMNET) cards which are connected by high-speed fiber optic cables, making it possible for instant memory writing/reading of the data being exchanged among different modules. It shall be noted that, this configuration is scalable and the hybrid simulator and the testing controller at different laboratories can be connected through Internet. By this way, multiple numerical substructures and experimental substructures are combined, so that a geographically distributed STST of a large and complex structure becomes possible when the internet delay is compensated properly.

KEY TECHNOLOGIES OF STST

Numerical simulation and physical experimentation combined in a STST test are implemented in a real time environment. There are two challenges in this process, i.e., the boundary coordinating between the numerical and the experimental substructures, and the control of loading devices that impose realistic dynamic loading to the experimental substructure. To achieve a real time coordination between the two substructures, the numerical simulation has to be carried out at the real-time rate, which requires efficient time integration algorithms. The synchronization between the two substructures is also important. Particularly, the delayed command from the numerical simulation will lead to undesired loading break on the experimental substructure. On the physical experimentation part, the interaction among shaking table, actuator and experimental substructure shall be considered to design the controller for each loading device. In particular, force control of actuator is very challenging because of oil-column resonance and its internal friction. Moreover, the inherent delay of

TABLE 2 | Test procedures of STST in different substructure pattern.

First substructure pattern	Second substructure pattern
Input ground motion (acceleration) to numerical substructure;	(1) Use ground motion (acceleration) to generate command signals for shaking table;
Measure reaction force from experimental substructure and feed it back to numerical simulation;	(2) Simulate reaction force of numerical substructure and send it to actuator controller;
Run time history analysis of numerical substructure with ground motion and reaction force inputs;	(3) Generate command signal for actuator, and predict next step target if needed;
Output absolute acceleration response at the top of numerical substructure to experimental substructure;	(4) Drive shaking table and actuator simultaneously following respective command;
Generate loading signals for shaking table, and predict for next step(s) to catch up numerical simulation if needed;	(5) Measure table motion and response at the top of experimental substructure, and send to numerical simulation;
Repeat steps 1–5, until the end of test.	(6) Run time history analysis of numerical substructure using measured responses as the input, and output reaction force to actuator controller;
	(7) Repeat steps 1–6, until the end of test.

loading devices shall be minimized to avoid instable STST. Therefore, key technologies for a successful STST system include efficient numerical simulation, delay compensation schemes, accurate control of shaking tables, force control of actuators and boundary force measurement, as discussed in detail in the following sections.

Efficient Numerical Simulation

In a STST, the numerical substructure shall be solved synchronously when the experimental substructure is being loaded, which implies that boundary response shall be determined and sent to the experimental substructure before it is needed. This is not easy for a large-scale numerical model with more than 1000 DOFs. The Jacobian solution used to solve equations of motion may take a good share of memory, and the communication between the memory and the hard disk also takes time. With the fast development of computer technology, the model scale that can be implemented in memory is significantly enlarged. However, the real-time application with more than 10,000 DOFs has not been reported yet. Most STST applications adopted simplified mass-spring model according to **Table 1**. The study by Wang (Wang et al., 2014) is the only one that employed a larger numerical model with more than 1000 DOFs. These models, however, were elastic. If the numerical models, which are very likely, involve nonlinearity, their response simulation in real-time would be more difficult, because the iteration required to solve the nonlinearity is uncertain at each step consuming very different amount of time. High-performance computer, even super computation clusters, cannot readily solve this difficulty yet.

One method to solve this difficulty is to adopt and/or develop explicit time integration algorithms to avoid the iteration procedure. Integration algorithms, such as the CMD and the explicit Newmark method, are most suitable in hybrid tests because only the responses from the previous steps are required to determine the target displacement of the current step (Pan et al., 2015). The explicit method was also adapted to real-time hybrid testing procedure (Wu et al., 2005) and has been applied in STST [CDM method by Wang and Tian (2009); CDM method by Zhou and Wu (2013); explicit Newmark

method by Mosalam and Günay (2014); explicit Runge-Kutta method by Li et al. (2011b)]. However, these explicit algorithms, although efficient, are conditionally stable, which highly depend on structural model stiffness. To overcome this difficulty, many researchers are engaged in developing unconditionally stable explicit integration algorithms. Chang (2007) developed an explicit method with unconditional stability, which is particularly suitable for online hybrid tests because of its better error propagation properties. Chen (Chen and Ricles, 2008; Chen et al., 2009) employed a discrete transfer function to study the stability of integration algorithms. By placing the poles of the discrete transfer function, a family of explicit algorithms was developed which are unconditionally stable. Similarly, Gui (Gui et al., 2014) developed a new family of explicit integration algorithms also based on discrete control theory, which are explicit for both displacement and velocity. It is worth noting that these algorithms require no factorization of damping matrix and stiffness matrix, so they are more efficient in real-time hybrid testing. Wang (Wang et al., 2018) proposed an explicit algorithm for hybrid tests based on the HHT- α algorithm. If the stiffness of a specimen is identified, the algorithm would be unconditionally stable even for specimen experiencing stiffness hardening. Different approach was adopted in the operator-splitting (OS) algorithm (Nakashima et al., 1990), during which explicit formulations are applied to the experimental substructure while implicit formulations are kept to solve the numerical substructure. This OS algorithm was later modified in a real-time hybrid test (Wu et al., 2006), and applied in a STST recently (Günay and Mosalam, 2015).

Some schemes were incorporated into time integration procedures to improve efficiency, such as the staggered integration scheme and the modal truncation scheme. The staggered integration scheme (Nakashima and Masaoka, 1999) adopted a larger time step to solve equations of motion, while using a smaller step to generate commands for actuators. An extrapolation is used to generate commands before the target value is available and it is immediately switched to an interpolation once the target value is computed. This scheme was later applied to a STST (Wang et al., 2014). The modal truncation scheme (Gutierrez and Lopez Cela, 1998) selects lower frequency vibration modes that most influence the responses

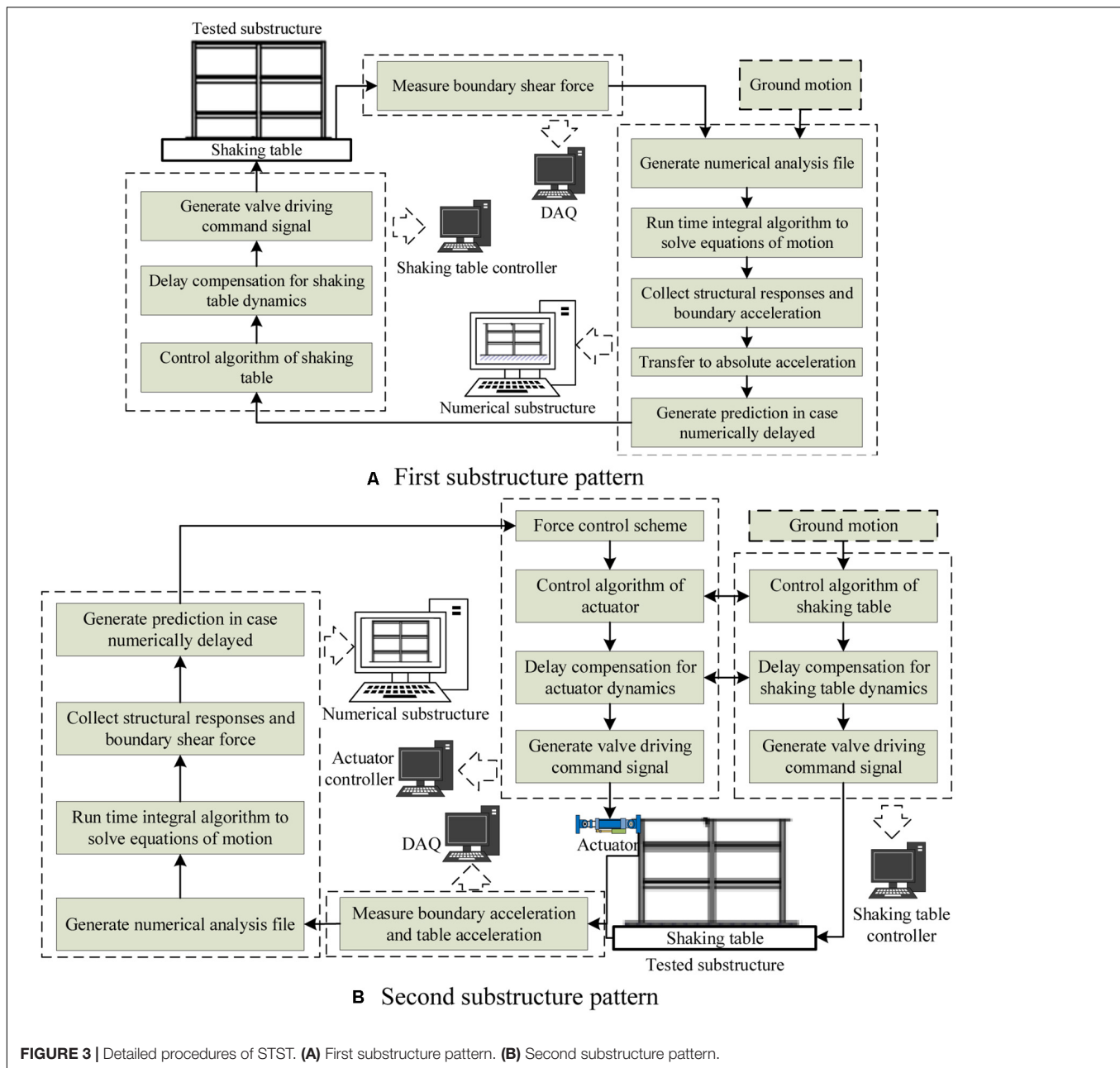


FIGURE 3 | Detailed procedures of STST. **(A)** First substructure pattern. **(B)** Second substructure pattern.

while attenuates the higher frequency modes, thus a larger step can be used to solve equations of motion.

Delay Compensation Schemes

As mentioned previously, the numerical simulation and the physical experimentation shall be synchronized in a STST test. Because loading devices require target values from the numerical simulation, whether the numerical simulation can provide such a target value in time becomes the key. This is also the reason why an efficient time integration algorithm is always desired in a real-time hybrid test. Although there are a lot of efficient time integration schemes available for STST tests, it is still possible that a numerical solution cannot find the committed

state in time, especially when solving nonlinear structural models. To overcome this possible delay, a polynomial function is often used to extrapolate the target value if the calculation is not completed. Once the target is obtained from numerical simulation, interpolation of the target is triggered to drive the specimen to the correct position. This delay compensation using polynomial function is easy to be implemented and widely adopted in real-time substructure hybrid tests (Nakashima et al., 1992; Wu et al., 2005; Zhang et al., 2005; Schellenberg et al., 2009; Zhu et al., 2014a).

Another source of delay comes from the inherent dynamics of loading devices. This delay shall be minimized first prior to STST because it introduces negative damping into the dynamic

system and leads to divergence. In the past decades, many delay compensation schemes have been developed and applied. They are generally classified into two groups, i.e., the polynomial function-based schemes and the model-based schemes. The former schemes are independent on dynamic systems, but rely on mathematic formulation. The latter schemes, on the contrary, are developed according to the system's dynamic model based on modern control theories.

Horiuchi (Horiuchi et al., 1999) proposed a polynomial extrapolation method to compensate the time delay which is widely used in real-time hybrid test. He also studied the negative damping effect of time delay on the accuracy and stability of substructure testing. Since the factors affecting the delay vary during a test (e.g., due to the nonlinear stiffness of a specimen, adaptive PID controllers, etc.), it is necessary to estimate the delay accurately during the test for compensation. Most STST tests discussed above adopted polynomial functions to compensate the time delay (see **Table 1**). The feed-forward method (Günay and Mosalam, 2015) that uses a feed-forward gain multiplied by the command velocity and added to the servo-valve command is another math-based method. Zhu (Zhu et al., 2014b, 2015) systematically studied the delay compensation method using a 3rd order polynomial function. The stability affected by the time delay in a STST system was analyzed by the discrete-time root locus technique. It was found out that the third order polynomial function can increase the stability limitation significantly.

The model-based scheme predicts the compensated commands of the system delay by using system transfer functions, which is usually identified before a hybrid test. Then, the inverse of the identified transfer function of the combined servo-hydraulic and test specimen system is developed. In one of the early studies, the fourth order FIR filter (Igarashi et al., 2004) that approximates the system transfer function was assigned with a phase lead to cancel the phase lag. The STST developed by Shao (Shao et al., 2011) adopted the Smith Predictor to compensate the time delay, during which the predictor was designed to approach the desired plant considering both the inherent delay and the modeling errors (Sivaselvan et al., 2008). Carrion (2007) used a model-based compensation method to predict actuator's response used as the input displacement. Later, Phillips and Spencer (2013a) developed a delay compensation method for real-time hybrid simulation based on the feedforward-feedback tracking control. Chen (Chen et al., 2009) developed a simple model for the servo-hydraulic system using a first-order discrete transfer function and applied the inverse of the model's transfer function to compensate the actuator delay. Hayati (Hayati and Song, 2016) designed a discrete-time compensator based on an Auto-Regressive with Exogenous model (ARX model). This method provides an optimal compensation allowing actuators to track inputs with higher frequency contents up to 30 Hz. Fernandois and Spencer (2017) proposed a model-based feedforward-feedback controller to improve the robustness and compensate the time delay of the 1/5th-scale Load and Boundary Condition Box (LBCB), and this method was verified in a six-DOF loading test.

Time delay is not a constant value, which indeed significantly depends on dynamic STST systems including servo-hydraulic

loading devices and test specimens. Darby (Darby et al., 2002) presented a method for estimating the delay during a test and verified this method in a twin-actuator system. Based on the fundamental concepts presented by Darby, Wallace (Wallace et al., 2005) proposed an adaptive compensation algorithm by a forward prediction to compensate the delay in the transfer system. Ahmadizadeh (Ahmadizadeh et al., 2008) used a learning gain to achieve online estimation of actuator delay. Chen (Chen and Ricles, 2010a,b; Chen et al., 2012) provided an adaptive inverse compensation procedure based on proportional and integral gains applied to a tracking indicator (TI) developed by Mercan (2007). The TI is an online indicator of phase lead or lag between actuator commands and measured displacements. To deal with inaccurate prediction and uncertain estimated delay, Wu (Wu et al., 2013) proposed a compensation scheme, in which the displacement was firstly overcompensated by an upper bound delay and the reaction force corresponding to the desired displacement was then selected by an optimal process. A robust integral actuator control method proposed by Ou (Ou et al., 2015) can be regarded as a combination of feedforward and feedback control, in which the feedback controller was based on the H_∞ method. Chen (Chen and Tsai, 2012) used a dual compensation method that included an adaptive second-order phase lead compensator and an online restoring force compensator. Chae (Chae et al., 2013) developed the adaptive time series (ATS) compensator using an online real-time linear regression analysis to continuously update the coefficients of ATS compensator. Based on the principles of ATS, Palacio-Betancur and Gutierrez Soto (2019) proposed a conditional adaptive time series (CATS) compensator for a benchmark problem in which a recursive least square (RLS) algorithm is adopted for the parameter estimation of the controller to reduce computational efforts. Zhou (Zhou et al., 2019) combined a linear-quadratic gaussian controller and a polynomial-based feedforward prediction algorithm to compensate the adverse effects of time delay and uncertainties on the RTHS testing system.

Considering the numerous compensation schemes proposed for real-time hybrid tests in the past two decades, this paper only introduces some of them that can be potentially applied in STST tests.

Accurate Control of Shaking Tables

Shaking table in STST tests is employed to realize the boundary compatibility between numerical and experimental substructures. Accurate loading is of critical importance to achieve a successful STST application. During a STST test, traditional control methods of shaking table, such as offline iterative method and adaptive inverse transfer function control, cannot be directly applied, due to the step-by-step manner and the closed-loop form of STST. Moreover, shaking table often carries a large payload, leading to the shaking table-specimen interaction. Therefore, shaking table controllers shall be carefully devised for STST tests.

In the STST applications listed in Table 1, the study on shaking table controller is very limited. The reason might be that shaking tables used in these applications were all uniaxial, and the specimen weight was relatively small compared with tables'

payload capacities. Hence, shaking tables worked essentially as a single actuator controlled in displacement or acceleration. Among these studies, Zhou (Zhou and Wu, 2013) adopted a pressure difference feedback control to overcome the adverse effect from the oil-column resonance. Günay (Günay and Mosalam, 2015) developed an advanced control method based on the TVC scheme to improve the displacement control accuracy of the shaking table. Different from the traditional TVC, a third differentiation was used to determine the jerk command to boost the frequencies above the oil-column frequency when the low-pass filter was not used to avoid distorting the displacement command. Similar control method (Li X. J. et al., 2018) was developed by incorporating jerk feedback and feed-forward signals into the control unit. The control of the frequencies higher than 50 Hz was improved. Neild (Neild et al., 2005) proposed two controllers for STST tests, i.e., a linear controller and an adaptive substructure method based on the minimal control synthesis algorithm. The adaptive controller does not require the dynamics of the shaking table and the experimental substructure, so that an accurate control of nonlinear specimens is possible.

Recent development on the control of shaking tables provides potential options for STST. Phillips (Phillips et al., 2014) proposed a model-based multi-metric control method for uniaxial shaking tables, during which the feedforward and feedback links was incorporated to accurately track an acceleration history. The robustness of this control method over the nonlinearities of the specimen and the servo-hydraulic system was demonstrated. To overcome uncertainties and nonlinearities in specimens and servo-hydraulic devices, Yang (Yang et al., 2015) proposed a hierarchical control strategy for uniaxial shaking tables. The sliding mode control technique was employed to provide robustness to compensate model nonlinearities and uncertainties experienced during tests. Experimental results demonstrated that a high control accuracy was achieved. Ryu (Ryu and Reinhorn, 2016) developed a nonlinear tracking control scheme based on the feedback linearization method to consider the nonlinear behavior of specimens. In this method, a real-time estimator using the extended Kalman filter was adopted to account for the changes and uncertainties in system models due to nonlinearities. Chen (Chen et al., 2017) proposed a control framework which incorporates a feedback controller into a weighted command shaping controller. The command shaping controller was model-based so that the control-structure interaction can be fully captured. The weights of the shaped displacement and acceleration were calculated by a linear interpolation algorithm. The robustness and accuracy of this framework was experimentally verified. Rajabi (Rajabi et al., 2018) developed a new trajectory tracking control for a ball-screw-driven shaking table. The controller was designed based on sliding mode approach with state online estimated by the extended Kalman filter or unscented Kalman filter (UKF), so it could achieve a high velocity and positioning accuracy regardless of the inherent noises, frictions, and uncertainties. In addition, other control algorithms, such as linear quadratic regulator (Kuehn et al., 1999), minimal controller synthesis algorithm (Stoten and Benschoubane, 1990; Shimizu et al., 2002), linear quadratic control with integral (Seto et al., 2002), fuzzy

neural network (Chen et al., 2007), and adaptive inverse control (Dertimanis et al., 2015), have been explored to solve the difficulties in controlling shaking tables with nonlinearities and uncertainties. This paper will not discuss them all in detail due to the page limitation.

In summary, most newly developed control algorithms employ an online updated model to achieve accurate control of shaking tables, which can be applied in STST without much effort of revising.

Force Control of Experimental Substructures

In the second substructure pattern, actuator is employed to realize the boundary compatibility between numerical and experimental substructures. Simultaneously, the experimental substructure is excited by a shaking table that induces inertial force. Therefore, the actuator attached to the experimental substructure is preferred to be controlled in force. However, dynamic force control of hydraulic actuators is difficult since it requires a low impedance system rather than a high impedance as in displacement control (Nachtigal and Martin, 1990). Force control accuracy is significantly affected by the dynamic characteristics of a test specimen, especially its nonlinear behavior, and actuator's nonlinearities, including mechanical friction, viscous damping, sealing of piston, and oil-column resonance.

Conrad and Jensen (1987) recognized that closed-loop dynamic force control was ineffective without velocity feedforward at the natural frequency of the structure due to the control-structure interaction. This finding was echoed by Dimig (Dimig et al., 1999) and Shield (Shield et al., 2001) when developing the effective force method, where an additional velocity feedback loop was incorporated to overcome the interaction. The oil column was expressed as a spring so that the force control can be achieved by displacement feedback. Inspired by the oil spring concept, Sivaselvan (Sivaselvan et al., 2008) introduced a compliance spring between actuator and structure to realize force control via a displacement-controlled actuator. The actuator has an inner closed-loop control using displacement feedback in the PID. Meanwhile, an outer control-loop takes the target force command and converts it into a displacement command of the actuator based on the Hooke's spring law. Similarly, Chae (Chae et al., 2017) implemented compliance springs and ATS compensator to achieve accurate force tracking control of actuators. This force-control method does not require structural modeling, thus especially suitable for nonlinear structures and its satisfactory force tracking performance was experimentally demonstrated. The proposed force-control method was later applied to a real-time hybrid simulation of an RC bridge pier, during which the springs were replaced by a flexible loading frame (FLF) and its optimal control performance was further manifested (Chae et al., 2018). A different methodology developed by Nakata (Nakata and Stehman, 2012) employed a controlled mass to reproduce the boundary force between numerical and experimental substructures. The boundary force was first

converted to the absolute acceleration of the controlled mass. Then the relative acceleration was obtained to calculate the relative displacement to drive the actuator. In this process, a high-pass filter was adopted to stabilize the relative displacement of the mass. The accuracy of the proposed control method was demonstrated through a numerical simulation. A similar scheme proposed by Verma (Verma et al., 2019) introduced an AMD whose impedance matches the numerical substructure so that uncertainties and nonlinearities in the dynamic system can be considered. An experiment was then conducted using an AMD at the top of the specimen during which the seismic response was well reproduced. Different from the above schemes, Nakata (Nakata et al., 2017) proposed a loop-shaping controller for the force-controlled actuator that can be applied in real-time hybrid tests. The loop-shaping controller was a model-based control method that requires a dynamic model relating the actuator valve to the force applied. The experimental results showed that the loop-shaping controller enabled accurate control of dynamic force on the specimen during the real-time hybrid simulation.

Force Measurement at the Boundary Between Substructures in STST

Accurate force control relies significantly on accurate measurement of forces. Generally, there are two methods to measure the force at the boundary between substructures in a STST: (1) the direct method that measures the force using load cells installed at the boundary and; (2) the indirect method that computes the force based on the acceleration responses of the experimental substructure measured by a network of accelerometers at the boundary (Li et al., 2011a; Li X. J. et al., 2018). The direct force measurement can be applied to both substructure patterns. In the first substructure pattern shown in **Figure 2A**, the shear force can be measured by a shear-type load cell (Zhou and Wu, 2013; Zhou et al., 2014), while for the second substructure pattern in **Figure 2B**, the dynamic force between the two substructures can be directly measured using the load cell of the actuator attached at the top of the specimen. When STST involving loading along multi-directions using a MDOF shaking table (Schellenberg et al., 2017), the direct force measurement is more complicated, and expensive triaxial loading sensors are often employed to measure the forces along multi-directions simultaneously. If the specimen is featured with concentrated masses, an indirect method could be utilized, by which the force is calculated based on the measured acceleration multiplied by the corresponding mass (Lee et al., 2007; Tian et al., 2020). It is worth noting that high-frequency noises exist in both load cells and accelerometers, which bring in challenges in direct-force control of actuators.

NEW DIRECTIONS

STST Test Using Shaking Table Array

Multiple shaking tables (i.e., table array) constructed in the same location can be combined to perform seismic simulation of large-scale engineering structures such as large-space structures and long-span bridges. If incorporated with the STST technique,

testing capacity of shaking table array can be further extended. Dorka (Dorka et al., 2006, 2007) conducted STST using distributed hydraulic shaking tables on a two-story steel frame with two TMDs on the top. Each TMD was placed on one uniaxial shaking table. The test results matched well with the shaking table test of the entire structure. Following the unified substructure scheme proposed by Reinhorn (Reinhorn et al., 2005) and the hardware framework by Shao (Shao and Reinhorn, 2012), multiple experimental substructures can be tested in one STST. The boundary coordination can be achieved in the same way as STST employing only one experimental substructure. However, physically achieving accurate boundary loading becomes more complex, and synchronizing loading devices is more critical. Several attempts have been made so far. For example, Zhu (Zhu et al., 2017) conducted a STST on two tuned liquid column dampers mounted on top of a building, during which each damper was loaded by one uniaxial shaking table, and the two shaking tables had the same input obtained from the numerical simulation. The same technique reported in a previous study (Zhu et al., 2014a) was adopted for this dual STST. Li (Li et al., 2011b) studied the effect of soil-structure interaction on a three-span bridge model installed on four shaking tables. The soil was simulated numerically and the response of each pier was input to the shaking table. The TVC controller combined with a linear controller was adopted to control the four shaking tables. Mosalam (Mosalam et al., 2016) conducted a STST test on interconnected electrical equipment using two shaking tables to quantify the influence of electrical cables on substation equipment. The supporting structure was the numerical substructure modeled by an SDOF system, and the two insulators connected by a conductor cable were tested on the two tables. These applications demonstrated the feasibility of STST using multiple shaking tables. However, there's only one boundary shared by the substructures in these tests (i.e., the building roof in Zhu's application, the soil-structure interface in Li's application and the substation electrical equipment in Mosalam's application), and the first substructure pattern was adopted for all three applications. The applications on more complex substructure pattern using multiple shaking tables and actuators have not been reported yet. It is still very challenging to realize such complex STST system.

Complete Boundary Coordination and Loading Device

The substructure patterns discussed above were generally based on multi-story building models, which means the boundaries between the substructures are either at the story level or the ground. The horizontal acceleration and the corresponding shear force can be easily imposed using shaking tables and actuators. The overturning moment and the vertical force, however, are difficult to be realized through this substructure pattern. A recent study by Stefanaki (Stefanaki and Sivaselvan, 2018; Stefanaki et al., 2018) proposed a multi-DOF loading device using multiple AMDs to realize the shear force and overturning moment from the upper numerical substructure. However, this technique is still regarded as a story-level solution. If there are multiple shear walls

in a frame structure, which are very likely in reality, the story overturning may not strong, but the overturning moment on each wall shall be considered. For this kind of complex boundary condition, it requires further study.

Loading devices are utilized in STST to replicate accurate boundary condition between the two substructures or the ground motion input. Servo-hydraulic actuators have peculiarities of larger loading and power than electromagnetic ones, so that almost all large-scale civil engineering laboratories are equipped with servo-hydraulic shaking tables while electromagnetic shaking tables are mainly used in small-scale facilities for education and proof-of-concept research. However, electromagnetic shaking tables with a high frequency bandwidth, low distortion, and linear behavior have been widely adopted in qualification tests of critical equipment in aerospace and automotive industries (Wang et al., 1990) and they have the potential to apply a MDOF force loading onto the experimental substructure. For example, Verma (Verma et al., 2019) employed an electromagnetic shaking table as an AMD to verify the impedance matching method. On the other hand, it is deemed that the dynamics of electromagnetic and hydraulic shakers are remarkably similar (Carl, 2008). For examples, the natural velocity feedback in hydraulic shaking table is akin to the back electromotive force (EMF) in electromagnetic shaking table; the linearized model of hydraulic shake table has three poles, which is the same case for electromagnetic shaking table.

Application to Other Engineering Problems

At present, STST has been applied to study soil-structure interaction and seismic performance of buildings including those equipped with TMDs, and these applications are considered as traditional civil engineering problems. However, the flexible configuration enabled by STST can be easily extended to address other engineering problems. In China, the high-speed train system has been developed significantly in the last ten years. Most railways were constructed on viaducts. The train-track-bridge interaction requires extensive study before a new train system is cast into market, which is a potential application of STST. Guo (Guo et al., in review) proposed a STST system during which a multi-span bridge was numerically simulated, while the track and the car were tested on a shaking table. The shaking table served as the transfer system to reproduce the vibration introduced by the deflection of bridge girders and the random vibration of high-frequency irregularity. In this STST application, the train was stationary while the bridge was moving relatively to the train. Similar STST system can be applied to analyze vehicle's safety on highways. The STST system is also capable of examining the fluid-structure interaction of wind turbines as explored by Tian (Tian et al., 2020), where the fluid field was numerically simulated. Underwater shaking table was recently proposed, which is deemed to be more suitable to examine fluid-structure interaction and could further expand STST application. Recent studies explored the feasibility of STST using underwater shaking table, including providing a practical similitude law (Li Z. et al., 2018) and applying to piers of a cross-sea bridge (Ding

et al., 2018). All these examples show the promise of STST being applied to other engineering systems.

SUMMARY

In a STST, the substructure with the most complex behavior is tested physically with the rest of the structure being numerically simulated. Boundary compatibility between numerical and experimental substructures is achieved by servo-hydraulic loading devices including shaking tables and actuators. This flexible testing configuration significantly extends testing capacity of shaking tables. This paper introduces frameworks and applications of existing STST and summarizes their primary features. The reported STST frameworks are classified into two categories according to their substructure patterns, i.e., testing the upper part or the lower part of a structure. A scalable hardware configuration is also introduced which can be extended for STST system involving multiple numerical and experimental substructures connected through the network. Then several key issues in developing a successful STST system are presented, including efficient algorithms of numerical simulations, delay compensation schemes, accurate control of shaking tables, force control of actuators and boundary force measurement. Finally, several future research directions identified are presented.

Shaking table substructure testing, as a new technique to examine seismic performance of engineering structures, is still in the preliminary stage. Most existing applications employed uniaxial shaking tables. The application on large multi-directional shaking table is still challenging because of the complex coupling of shaking table actuators. Therefore, accurate reproduction of boundary conditions is extremely difficult. Most delay compensation schemes were developed for a single actuator or uniaxial shaking table, without considering the coupling between them. Moreover, the experimental substructure in these applications were relatively soft, with frequencies associated with lower modes under 10 Hz. Whether these delay compensation methods are valid for high-frequency systems remains unknown. Therefore, there is a great potential to continue advancing STST technology.

The substructure patterns employed by existing STST systems are mostly at the story level of a building structure. This substructure pattern might be adequate to study structural global behavior, but cannot provide refined details to examine local behavior of a structural components because the exact boundary compatibility is not attained at the component level. Although several studies have addressed this challenge, a comprehensive study is needed to demonstrate the effectiveness of the developed techniques. One of the key issues to realize the boundary compatibility is the force control of actuators. Existing methods include adding spring compliance and employing AMD. The AMD is appealing as an integral approach to solve the force control in multiple directions. Finally, it shall be noted that one STST system might involve multiple dynamic systems, including shaking tables, actuators, and numerical simulations. It would be more complex if a shaking table array is employed. The interaction among these dynamic systems is very complex and

the stability of such a system shall be well examined before a real application.

In summary, STST is appealing to be applied to seismic performance evaluation of engineering structures. But more efforts are required for more sophisticated applications. STST is also a promising technique to solve other engineering problems, during which knowledge integration of multi-disciplines is needed.

AUTHOR CONTRIBUTIONS

All authors contributed to this review manuscript. YT wrote most part of the manuscript. XS reviewed the control of shaking tables as well as the force control of actuators. HZ gave a review on the

time delay compensation program. TW suggested the structure of the manuscript.

FUNDING

The study received financial support from the Scientific Research Fund of Institute of Engineering Mechanics, China Earthquake Administration (2017A02), the National Science Foundation of China (51678538 and 51878630), and the Heilongjiang Provincial Natural Science Fund for Distinguished Young Scholars (Grant No. JC2018018). Any opinions, findings, conclusions, or recommendations expressed in this article are those of the authors, and do not necessarily reflect the views of the sponsors.

REFERENCES

- Ahmadizadeh, M., Mosqueda, G., and Reinhorn, A. M. (2008). Compensation of actuator delay and dynamics for real-time hybrid structural simulation. *Earthq. Eng. Struct. Dyn.* 37, 21–42. doi: 10.1002/eqe.743
- Astroza, R., Ebrahimian, H., Conte, J. P., Restrepo, José, I., and Hutchinson, T. C. (2016). Influence of the construction process and nonstructural components on the modal properties of a five-story building. *Earthq. Eng. Struct. Dyn.* 45, 1063–1084. doi: 10.1002/eqe.2695
- Ba, P. F., Zhang, Y. G., Wu, J. Z., Zhang, Z. H., and Zheng, X. J. (2017). Whole process test and dynamic failure analysis for sing-layer spherical lattice shells. *J. Vibrat. Shock* 36, 31–37.
- Carl, J. (2008). *Improved Dynamic Testing by Impedance Control*. Ph.D. Thesis. Boulder, CO: University of Colorado.
- Carrion, J. E. (2007). *Model-Based Strategies for Real-Time Hybrid Testing*. Ph.D. dissertation. Illinois, IL: University of Illinois at Champaign.
- Chae, Y., Kazemibidokhti, K., and Ricles, J. M. (2013). Adaptive time series compensator for delay compensation of servo-hydraulic actuator systems for real-time hybrid simulation. *Earthq. Eng. Struct. Dyn.* 42, 1697–1715. doi: 10.1002/eqe.2294
- Chae, Y., Lee, J., and Park, M. (2018). Real-time hybrid simulation for an RC bridge pier subjected to both horizontal and vertical ground motions. *Earthq. Eng. Struct. Dyn.* 47, 1673–1679. doi: 10.1002/eqe.3042
- Chae, Y., Rabiee, R., Dursun, A., and Kim, C. Y. (2017). Real-time force control for servo-hydraulic actuator systems using adaptive time series compensator and compliance springs. *Earthq. Eng. Struct. Dyn.* 47, 854–871. doi: 10.1002/eqe.2994
- Chang, S. Y. (2007). Enhanced, unconditionally stable, explicit pseudodynamic algorithm. *J. Eng. Mech. ASCE* 133, 541–554. doi: 10.1061/(asce)0733-9399(2007)133:5(541)
- Chen, C., and Ricles, J. M. (2008). Development of direct integration algorithms for structural dynamics using discrete control theory. *J. Eng. Mech. ASCE* 134, 676–683. doi: 10.1061/(asce)0733-9399(2008)134:8(676)
- Chen, C., and Ricles, J. M. (2010a). Improving the inverse compensation method for real-time hybrid simulation through a dual compensation scheme. *Earthq. Eng. Struct. Dyn.* 39, 1237–1255. doi: 10.1002/eqe.904
- Chen, C., and Ricles, J. M. (2010b). Tracking error-based servohydraulic actuator adaptive compensation for real-time hybrid simulation. *J. Struct. Eng. ASCE* 136, 432–440. doi: 10.1061/(asce)st.1943-541x.0000124
- Chen, C., Ricles, J. M., and Guo, T. (2012). Improved adaptive inverse compensation technique for real-time hybrid simulation. *J. Eng. Mech. ASCE* 138, 1432–1446. doi: 10.1061/(asce)em.1943-7889.0000450
- Chen, C., Ricles, J. M., Marullo, T. M., and Mercan, O. (2009). Real-time hybrid testing using the unconditionally stable explicit CR integration algorithm. *Earthq. Eng. Struct. Dyn.* 38, 23–44. doi: 10.1002/eqe.838
- Chen, J. Q., Zhang, X. Z., Tan, P., and Zhou, F. L. (2007). Application study of ILC with fuzzy neural network in shaking table control system. *Int. Conf. Intell. Syst. Knowl. Eng.* 580–585.
- Chen, P. C., Lai, C. T., and Tsai, K. C. (2017). A control framework for uniaxial shaking tables considering tracking performance and system robustness. *Struct. Control Health Monitor.* 24:e2015. doi: 10.1002/stc.2015
- Chen, P. C., and Tsai, K. C. (2012). Dual compensation strategy for real-time hybrid testing. *Earthq. Eng. Struct. Dyn.* 42, 1–23. doi: 10.1002/eqe.2189
- Chi, F. D., Wang, J. T., Jin, F., and Wang, Q. (2010). Real-time dynamic hybrid testing for soil-structure-fluid interaction analysis. *Rock Soil Mech.* 31, 3765–3770.
- Conrad, F., and Jensen, C. J. D. (1987). Design of hydraulic force control systems with state estimate feedback. *IFAC Proc. Vol.* 20, 307–312. doi: 10.1016/s1474-6670(17)55388-4
- Darby, A. P., Williams, M. S., and Blakeborough, A. (2002). Stability and delay compensation for real-time substructure testing. *J. Eng. Mech. ASCE* 128, 1276–1284. doi: 10.1061/(asce)0733-9399(2002)128:12(1276)
- Dertimanis, V. K., Mouzakis, H. P., and Psycharis, I. N. (2015). On the acceleration-based adaptive inverse control of shaking tables. *Earthq. Eng. Struct. Dyn.* 44, 1329–1350. doi: 10.1002/eqe.2518
- Dimig, J., Shield, C., French, C., Bailey, F., and Clark, A. (1999). Effective force testing: a method of seismic simulation for structural testing. *J. Struct. Eng. ASCE* 125, 1028–1037. doi: 10.1061/(asce)0733-9445(1999)125:9(1028)
- Ding, Y., Ma, R., Shi, Y., and Li, Z. (2018). Underwater shaking table tests on bridge pier under combined earthquake and wave-current action. *Mar. Struct.* 58, 301–320. doi: 10.1016/j.marstruc.2017.12.004
- Dorka, U. E., Queval, J. C., Nguyen, V. T., and Maoult, A. L. (2006). “Real-time substructure testing on distributed shaking tables in CEA Saclay,” in *Proceedings of 4th World Conference on Structural Control and Monitoring*, San Diego, CA.
- Dorka, U. E., Queval, J. C., Nguyen, V. T., and Maoult, A. L. (2007). “Substructure testing on distributed shaking tables,” in *Proceeding of the 2nd International Conference on Advances in Experimental Structural Engineering (2AESE)*, Shanghai.
- Fernandois, C. G., and Spencer, B. F. (2017). Model-based framework for multi-axial real-time hybrid simulation testing. *Earthq. Eng. Eng. Vibrat.* 16, 671–691. doi: 10.1007/s11803-017-0407-8
- Fu, B., Jiang, H., and Wu, T. (2019). Comparative studies of vibration control effects between structures with particle dampers and tuned liquid dampers using substructure shake table testing methods. *Soil Dyn. Earthq. Eng.* 121, 421–435. doi: 10.1016/j.soildyn.2019.03.031
- Gao, X., Castaneda, N., and Dyke, S. J. (2013). Real time hybrid simulation: from dynamic system, motion control to experimental error. *Earthq. Eng. Struct. Dyn.* 42, 815–832. doi: 10.1002/eqe.2246
- Gui, Y., Wang, J. T., Jin, F., Chen, C., and Zhou, M. (2014). Development of a family of explicit algorithms for structural dynamics with unconditional stability. *Nonlinear Dyn.* 77, 1157–1170. doi: 10.1007/s11071-014-1368-3
- Günay, S., and Mosalam, K. M. (2014). Seismic performance evaluation of high voltage disconnect switches using real-time hybrid simulation: II. Parametric study. *Earthq. Eng. Struct. Dyn.* 43, 1223–1237. doi: 10.1002/eqe.2394
- Günay, S., and Mosalam, K. M. (2015). Enhancement of real-time hybrid simulation on a shaking table configuration with implementation of an

- advanced control method. *Earthq. Eng. Struct. Dyn.* 44, 657–675. doi: 10.1002/eqe.2477
- Gutierrez, E., and Lopez Cela, J. J. (1998). Improving explicit time integration by modal truncation techniques. *Earthq. Eng. Struct. Dyn.* 27, 1541–1557. doi: 10.1002/(sici)1096-9845(199812)27:12<1541::aid-eqe799>3.0.co;2-6
- Hayati, S., and Song, W. (2016). “Discrete-time compensation technique for real-time hybrid simulation,” in *Proceedings of the Conference on Society for Experimental Mechanics Series*, Cham, 351–358. doi: 10.1007/978-3-319-30084-9_33
- He, M. J., Luo, Q., Li, Z., Dong, H. L., and Li, M. H. (2018). Seismic performance evaluation of timber-steel hybrid structure through large-scale shaking table tests. *Eng. Struct.* 175, 483–500. doi: 10.1016/j.engstruct.2018.08.029
- Horiuchi, T., Inoue, M., and Konno, T. (2000). “Development of a real-time hybrid experimental system using a shaking table,” in *Proceedings of 12th World Conference on Earthquake Engineering*, Auckland.
- Horiuchi, T., Inoue, M., Konno, T., and Namita, Y. (1999). Real-time hybrid experimental system with actuator delay compensation and its application to a piping system with energy absorber. *Earthq. Eng. Struct. Dyn.* 28, 1121–1141. doi: 10.1002/(sici)1096-9845(199910)28:10<1121::aid-eqe858>3.0.co;2-o
- Igarashi, A., Iemura, H., and Suwa, T. (2000). “Development of substructured shaking table test method,” in *Proceedings of 12th World Conference on Earthquake Engineering*, Auckland.
- Igarashi, A., Iemura, H., Tanaka, H., and Tsuruta, D. (2004). “Experimental simulation of coupled response of structural systems using the substructure hybrid shake table test method,” in *Proceedings of 13th World Conference on Earthquake Engineering*, Vancouver, BC.
- Inoue, M., Horiuchi, T., and Momoi, Y. (1998). “Real-time hybrid experiment using a shaking table,” in *Proceedings of 10th Japan Earthquake Engineering Symposium*, Japanese.
- Ji, X. D., Kajiwar, K., Nagae, T., Enokida, R., and Nakashima, M. (2009). A substructure shaking table test for reproduction of earthquake responses of high-rise buildings. *Earthq. Eng. Struct. Dyn.* 38, 1381–1399. doi: 10.1002/eqe.907
- Jia, J. F., Zhao, J. Y., Guo, Y., and Ou, J. P. (2017). Shaking table tests on seismic simulation of three-dimensional isolated continuous girder bridges. *China J. Highway Transport.* 30, 290–298.
- Kim, Y., Kabeyasawa, T., Matsumori, T., and Kabeyasawa, T. (2012). Numerical study of a full-scale six-story reinforced concrete wall-frame structure tested at E-defense. *Earthq. Eng. Struct. Dyn.* 41, 1217–1239. doi: 10.1002/eqe.1179
- Konagai, K., Nogami, T., Katsukawa, T., Suzuki, T., and Mikami, A. (1998). Real time control of shaking table for soil-structure interaction simulation. *J. Struct. Mech. Earthq. Eng.* 598, 203–210. doi: 10.2208/jscej.1998.598_203
- Kuehn, J., Epp, D., and Patten, N. (1999). High-fidelity control of a seismic shake table. *Earthq. Eng. Struct. Dyn.* 28, 1235–1254. doi: 10.1002/(sici)1096-9845(199911)28:11<1235::aid-eqe864>3.0.co;2-h
- Lee, S. K., Park, E. C., Min, K. W., and Park, J. H. (2007). Real-time substructuring technique for the shaking table test of upper substructures. *Eng. Struct.* 29, 2219–2232. doi: 10.1016/j.engstruct.2006.11.013
- Li, X. J., Li, F. F., Ji, J. B., and Wang, J. K. (2018). A new control technology of shaking based on the jerk. *Adv. Eng. Sci.* 50, 64–72.
- Li, Z., Wu, K., Shi, Y., Li, N., and Ding, Y. (2018). Coordinative similitude law considering fluid-structure interaction for underwater shaking table tests. *Earthq. Eng. Struct. Dyn.* 47, 2315–2332. doi: 10.1002/eqe.3070
- Li, Z. B., Li, X. L., Tang, Z. Y., and Jiang, H. G. (2011a). Research on the methods of evaluating reaction force for dynamic sub-structure experiments using shaking table. *Earthq. Eng. Struct. Dyn.* 31, 65–70.
- Li, Z. B., Tang, Z. Y., Ji, J. B., Li, X. L., Zhou, D. X., and Yan, W. M. (2011b). Research on the dynamic sub-structuring testing method for SSI based on shaking table array. *Struct. Eng.* 27, 76–81.
- Mercan, O. (2007). *Analytical and Experimental Studies on Large Scale Real-Time Pseudodynamic Testing*. Ph. D. Dissertation. Bethlehem, PA: Lehigh University.
- Mosalam, K. M., and Günay, S. (2014). Seismic performance evaluation of high voltage disconnect switches using real-time hybrid simulation: I. System development and validation. *Earthq. Eng. Struct. Dyn.* 43, 1205–1222. doi: 10.1002/eqe.2395
- Mosalam, K. M., Günay, S., and Takhirov, S. (2016). Response evaluation of interconnected electrical substation equipment using real-time hybrid simulation on multiple shaking tables. *Earthq. Eng. Struct. Dyn.* 45, 2389–2404. doi: 10.1002/eqe.2767
- Nachtigal, C. L., and Martin, M. D. (1990). *Instrumentation and Control: Fundamentals and Applications*. Hoboken, NJ: John Wiley & Sons, Inc.
- Nakashima, M., Kaminosomo, T., Ishida, M., and Ando, K. (1990). “Integration techniques for substructuring pseudodynamic test,” in *Proceedings of the 4th U.S. National Conference on Earthquake Engineering*, Palm Springs, CA, 515–524.
- Nakashima, M., Kato, H., and Takao, E. (1992). Development of real-time pseudodynamic testing. *Earthq. Eng. Struct. Dyn.* 21, 79–92. doi: 10.1002/eqe.4290210106
- Nakashima, M., and Masaoka, N. (1999). Real-time on-line test for MDOF systems. *Earthq. Eng. Struct. Dyn.* 28, 393–420. doi: 10.1002/(sici)1096-9845(199904)28:4<393::aid-eqe823>3.0.co;2-c
- Nakata, N., Erb, R., and Stehman, M. (2017). Mixed force and displacement control for testing base-isolated bearings in real-time hybrid simulation. *J. Earthq. Eng.* 23, 155–171.
- Nakata, N., and Stehman, M. (2012). Substructure shake table test method using a controlled mass: formulation and numerical simulation. *Earthq. Eng. Struct. Dyn.* 41, 1977–1988. doi: 10.1002/eqe.2169
- Neild, S. A., Stoten, D. P., Drury, D., and Wagg, D. J. (2005). Control issues relating to real-time substructuring experiments using a shaking table. *Earthq. Eng. Struct. Dyn.* 34, 1171–1192. doi: 10.1002/eqe.473
- Ou, G., Ozdagli, A. I., Dyke, S. J., and Wu, B. (2015). Robust integrated actuator control: experimental verification and real-time hybrid-simulation implementation. *Earthq. Eng. Struct. Dyn.* 44, 441–460. doi: 10.1002/eqe.2479
- Palacio-Betancur, A., and Gutierrez Soto, M. (2019). Adaptive tracking control for real-time hybrid simulation of structures subjected to seismic loading. *Mech. Syst. Signal Process.* 134:106345. doi: 10.1016/j.ymssp.2019.106345
- Pan, P., Wang, T., and Nakashima, M. (2015). *Development of Online Hybrid Testing – Theory and Applications to Structural Engineering*. New York, NY: Elsevier.
- Phillips, B. M., and Spencer, B. F. (2013a). Model-based feedforward-feedback actuator control for real-time hybrid simulation. *J. Struct. Eng. ASCE* 139, 1205–1214. doi: 10.1061/(asce)st.1943-541x.0000606
- Phillips, B. M., and Spencer, B. F. (2013b). Model-based multiactuator control for real-time hybrid simulation. *J. Eng. Mech. ASCE* 139, 219–228. doi: 10.1061/(asce)em.1943-7889.0000493
- Phillips, B. M., Wierschem, N. E., and Spencer, B. F. (2014). Model-based multi-metric control of uniaxial shake tables. *Earthq. Eng. Struct. Dyn.* 43, 681–699. doi: 10.1002/eqe.2366
- Rajabi, N., Abolmasoumi, A. H., and Soleymani, M. (2018). Sliding mode trajectory tracking control of a ball-screw-driven shake table based on online state estimations using EKF/UKF. *Struct. Control Health Monitor.* 25, 1–13.
- Reinhorn, A. M., Bruneau, M., Chu, S. Y., Shao, X. Y., and Pitman, M. C. (2003). “Large scale real time dynamic hybrid testing technique-Shake tables substructure testing,” in *Proceedings of the 2003 Structures Congress & Exposition*, Seattle.
- Reinhorn, A. M., Sivaselvan, M. V., Liang, Z., Shao, X. Y., Pitman, M., and Weinreber, S. (2005). “Large scale real time dynamic hybrid testing technique-Shake tables substructure testing,” in *Proceedings of the 1st International Conference on Advances in Experimental Structural Engineering*, AESE, Nagoya.
- Ryu, K. P., and Reinhorn, A. M. (2016). Real-time control of shake tables for nonlinear hysteretic systems. *Struct. Control Health Monitor.* 24, 1–2015.
- Sarebanha, A., Schellenberg, A. H., Schoettler, M. J., Mosqueda, G., and Mahin, S. A. (2019). Real-time hybrid simulation of seismically isolated structures with full-scale bearings and large computational models. *Comp. Model. Eng. Sci.* 120, 693–717. doi: 10.32604/cmes.2019.04846
- Schellenberg, A. H., Becker, T. C., and Mahin, S. A. (2017). Hybrid shake table testing method: theory implementation and application to midlevel isolation. *Struct. Control Health Monitor.* 24:e1915. doi: 10.1002/stc.1915
- Schellenberg, A. H., Mahin, S. A., and Fenves, G. L. (2009). *Advanced Implementation of Hybrid Simulation*. Report No: PEER 2009/104. Berkeley: University of California.
- Seto, K., Fuji, D., Hiramathu, H., et al. (2002). “Motion and vibration control of three dimensional flexible shaking table using LQI control approach,” in

- Proceedings of the 2002 American Control Conference*, Anchorage, AK, 3040–3045.
- Shao, X., and Reinhorn, A. M. (2012). Development of a controller platform for force-based real-time hybrid simulation. *J. Earthq. Eng.* 16, 274–295. doi: 10.1080/13632469.2011.597487
- Shao, X. Y. (2007). *Unified Control Platform for Real Time Dynamic Hybrid Simulation*. Ph.D. dissertation. Buffalo, NY: State University of New York.
- Shao, X. Y., Reinhorn, A. M., and Sivaselvan, M. V. (2011). Real-time hybrid simulation using shake tables and dynamic actuators. *J. Struct. Eng. ASCE* 137, 748–760. doi: 10.1061/(asce)st.1943-541x.0000314
- Shield, C. K., French, C. W., and Timm, J. (2001). Development and implementation of the effective force testing method for seismic simulation of large-scale structures. *Philos. Trans. R. Soc. A Math. Phys. Eng. Sci.* 359, 1911–1929. doi: 10.1098/rsta.2001.0879
- Shimizu, N., Shinohara, Y., and Sato, E. (2002). New development of control method of shaking table with bi-linear structures. *Press. Vessels Piping Conf.* 445, 75–82.
- Sivaselvan, M., Reinhorn, A. M., Shao, X. Y., and Weinreber, S. (2008). Dynamic force control with hydraulic actuators using added compliance and displacement compensation. *Earthq. Eng. Struct. Dyn.* 37, 1785–1800. doi: 10.1002/eqe.837
- Sororoushian, S., Mragakis, M., Zaghi, A., Rahmanishamsi, E., Itani, A., and Pekcan, G. (2016). Response of a 2-story test-bed structure for the seismic evaluation of nonstructural systems. *Earthq. Eng. Eng. Vibrat.* 15, 19–29. doi: 10.1007/s11803-016-0302-8
- Stefanaki, A., and Sivaselvan, M. V. (2018). A simple strategy for dynamic substructuring: I. Concept and development. *Earthq. Eng. Struct. Dyn.* 47, 1801–1822. doi: 10.1002/eqe.3039
- Stefanaki, A., Sivaselvan, M. V., Weinreber, S., and Pitman, M. (2018). A simple strategy for dynamic substructuring: II. Experimental evaluation. *Earthq. Eng. Struct. Dyn.* 47, 1823–1843. doi: 10.1002/eqe.3041
- Stoten, D. P., and Benchoubane, H. (1990). Robustness of a minimal controller synthesis algorithm. *Int. J. Control* 51, 851–861. doi: 10.1080/00207179008934101
- Tian, Y. P., Wang, T., and Zhou, H. M. (2020). Reproduction of wind and earthquake coupling effect on wind turbine tower by shaking table substructure test. *Int. J. Lifecycle Perform. Eng.* (in press).
- Verma, M., Sivaselvan, M. V., and Rajasankar, J. (2019). Impedance matching for dynamic substructuring. *Struct. Control Health Monitor.* 26:e2402.
- Wallace, M. I., Wagg, D. J., and Neild, S. A. (2005). An adaptive polynomial based forward prediction algorithm for multi-actuator real-time dynamic substructuring. *Proc. R. Soc. A Math. Phys. Eng. Sci.* 461, 3807–3826. doi: 10.1098/rspa.2005.1532
- Wang, J. T., Jin, F., Xu, Y. J., and Zhang, C. H. (2014). Theory and practice of real-time dynamic hybrid testing. *Eng. Mech.* 31, 1–14.
- Wang, J. T., Wang, Q., Chi, F. D., and Jin, F. (2010). Solutions to system construction of real-time dynamic hybrid testing based on shaking-table. *J. Earthq. Eng. Eng. Vibrat.* 30, 16–23.
- Wang, M. L., Shah, S. P., and Baker, J. P. (1990). An electromagnetic closed-loop materials testing station. *Exp. Tech.* 14, 52–55. doi: 10.1111/j.1747-1567.1990.tb01116.x
- Wang, T., Zhou, H. M., Zhang, X. P., and Ran, T. R. (2018). Stability of an explicit time-integration algorithm for hybrid tests, considering stiffness hardening behavior. *Earthq. Eng. Eng. Vibrat.* 17, 595–606. doi: 10.1007/s11803-018-0465-6
- Wang, X. Y., and Tian, S. Z. (2009). Principle and implementation of the hybrid testing method based on substructure techniques by using shaking table. *J. Earthq. Eng. Eng. Vibrat.* 29, 46–52.
- Wu, B., Bao, H., Ou, J., and Tian, S. Z. (2005). Stability and accuracy analysis of the central difference method for real-time substructure testing. *Earthq. Eng. Struct. Dyn.* 34, 705–718. doi: 10.1002/eqe.451
- Wu, B., Wang, Q., Shing, P. B., and Ou, J. (2007). Equivalent force control method for generalized real-time substructure testing with implicit integration. *Earthq. Eng. Struct. Dyn.* 36, 1127–1149. doi: 10.1002/eqe.674
- Wu, B., Wang, Z., and Bursi, O. S. (2013). Actuator dynamics compensation based on upper bound delay for real-time hybrid simulation. *Earthq. Eng. Struct. Dyn.* 42, 1749–1765. doi: 10.1002/eqe.2296
- Wu, B., Xu, G. S., Wang, Q. Y., and Williams, S. M. (2006). Operator-splitting method for real-time substructure testing. *Earthq. Eng. Struct. Dyn.* 35, 293–314. doi: 10.1002/eqe.519
- Xie, W., Sun, L. M., and Lou, M. L. (2019). Shaking table test on a pile-soil-cable-stayed bridge full model under multi-support excitations. *China Civil Eng. J.* 52, 79–89.
- Xiong, H. B., Xu, S., and Lu, W. S. (2008). Test study of fundamental periods of wood-frame houses. *J. Tongji Univ.* 36, 449–453.
- Xu, G. S., Xu, J. F., Wang, Z., Zhou, H. M., Wu, B., Zhou, L. J., et al. (2014). Substructure testing method and numerical simulation of storage tank considering interaction between soil and structure. *J. Disaster Prevent. Mitigat. Eng.* 34, 347–352.
- Yang, T. Y., Li, K., Lin, J. Y., Li, Y. J., and Tung, D. P. (2015). Development of high-performance shake tables using the hierarchical control strategy and nonlinear control techniques. *Earthq. Eng. Struct. Dyn.* 44, 1717–1728. doi: 10.1002/eqe.2551
- Zhang, R. Y., Phillips, B. M., Taniguchi, S., Ikenaga, M., and Ikago, K. (2017). Shake table real-time hybrid simulation techniques for the performance evaluation of buildings with inter-story isolation. *Struct. Control Health Monitor.* 24:e1971. doi: 10.1002/stc.1971
- Zhang, Y., Sause, R., Ricles, J. M., and Naito, C. J. (2005). Modified predictor-corrector numerical scheme for real-time pseudo dynamic tests using state-space formulation. *Earthq. Eng. Struct. Dyn.* 34, 271–288. doi: 10.1002/eqe.425
- Zhou, H. M., and Wu, B. (2013). Validation study of shaking table hybrid test platform. *J. Vibrat. Eng.* 26, 500–505.
- Zhou, H. M., Wu, B., Tan, X. J., and Dai, J. W. (2014). Shaking table substructure test of tuned liquid damper. *China Civil Eng. J.* 47, 70–75.
- Zhou, H. M., Xu, D., Shao, X. Y., Ning, X. Z., and Wang, T. (2019). A robust linear-quadratic-gaussian controller for the real-time hybrid simulation on a benchmark problem. *Mechan. Eng. Signal Process.* 133:106260. doi: 10.1016/j.ymssp.2019.106260
- Zhu, F., Wang, J. T., Jin, F., Chi, F. D., and Gui, Y. (2015). Stability analysis of MDOF real-time dynamic hybrid testing systems using the discrete-time root locus technique. *Earthq. Eng. Struct. Dyn.* 44, 221–241. doi: 10.1002/eqe.2467
- Zhu, F., Wang, J. T., Jin, F., and Lu, L. Q. (2017). Real-time hybrid simulation of full-scale tuned liquid column dampers to control multi-order modal responses of structures. *Eng. Struct.* 138, 74–90. doi: 10.1016/j.engstruct.2017.02.004
- Zhu, F., Wang, J. T., Jin, F., Gui, Y., and Zhou, M. X. (2014a). Analysis of delay compensation in real-time dynamic hybrid testing with large integration time-step. *Smart Struct. Syst.* 14, 1269–1289. doi: 10.12989/sss.2014.14.6.1269
- Zhu, F., Wang, J. T., Jin, F., Zhou, M. X., and Gui, Y. (2014b). Simulation of large-scale numerical substructure in real-time dynamic hybrid testing. *Earthq. Eng. Eng. Vibrat.* 13, 599–609. doi: 10.1007/s11803-014-0266-5

Conflict of Interest: The authors declare that the research was conducted in the absence of any commercial or financial relationships that could be construed as a potential conflict of interest.

Copyright © 2020 Tian, Shao, Zhou and Wang. This is an open-access article distributed under the terms of the Creative Commons Attribution License (CC BY). The use, distribution or reproduction in other forums is permitted, provided the original author(s) and the copyright owner(s) are credited and that the original publication in this journal is cited, in accordance with accepted academic practice. No use, distribution or reproduction is permitted which does not comply with these terms.



Robust Model Predictive Control for Dynamics Compensation in Real-Time Hybrid Simulation

Nikolaos Tsokanas^{1*}, David Wagg² and Božidar Stojadinović¹

¹ Institute of Structural Engineering, Department of Civil, Environmental and Geomatic Engineering, ETH, Zurich, Switzerland,

² Department of Mechanical Engineering, University of Sheffield, Sheffield, United Kingdom

OPEN ACCESS

Edited by:

Wei Song,
University of Alabama, United States

Reviewed by:

Richard Christenson,
University of Connecticut,
United States
Ehsan Noroozinejad Farsangi,
Graduate University of Advanced
Technology, Iran
Tao Wang,
China Earthquake Administration,
China

*Correspondence:

Nikolaos Tsokanas
tsokanas@ibk.baug.ethz.ch

Specialty section:

This article was submitted to
Computational Methods in Structural
Engineering,
a section of the journal
Frontiers in Built Environment

Received: 30 April 2020

Accepted: 13 July 2020

Published: 14 August 2020

Citation:

Tsokanas N, Wagg D and
Stojadinović B (2020) Robust Model
Predictive Control for Dynamics
Compensation in Real-Time Hybrid
Simulation. *Front. Built Environ.* 6:127.
doi: 10.3389/fbuil.2020.00127

Hybrid simulation is an efficient method to obtain the response of an emulated system subjected to dynamic excitation by combining loading-rate-sensitive numerical and physical substructures. In such simulations, the interfaces between physical and numerical substructures are usually implemented using transfer systems, i.e., an arrangement of actuators. To guarantee high fidelity of the simulation outcome, conducting hybrid simulation in hard real-time is required. Albeit attractive, real-time hybrid simulation comes with numerous challenges, such as the inherent dynamics of the transfer system used, along with communication interrupts between numerical and physical substructures, that introduce time delays to the overall hybrid model altering the dynamic response of the system under consideration. Hence, implementation of adequate control techniques to compensate for such delays is necessary. In this study, a novel control strategy is proposed for time delay compensation of actuator dynamics in hard real-time hybrid simulation applications. The method is based on designing a transfer system controller consisting of a robust model predictive controller along with a polynomial extrapolation algorithm and a Kalman filter. This paper presents a proposed tracking controller first, followed by two virtual real-time hybrid simulation parametric case studies, which serve to validate the performance and robustness of the novel control strategy. Real-time hybrid simulation using the proposed control scheme is demonstrated to be effective for structural performance assessment.

Keywords: real-time hybrid simulation, model predictive control, actuator dynamics, dynamic response, polynomial extrapolation, Kalman filter, uncertainty propagation

1. INTRODUCTION

Hybrid simulation (HS), also known as hardware-in-the-loop (HIL), online computer-controlled testing technique or model-based simulation, is a dynamic response simulation method. It is based on a step-by-step numerical solution of the governing equations of motions for a model that consolidates both numerical and physical substructures (Schellenberg et al., 2009). It is an efficient technique, since it merges the advantages of numerical simulations with the verisimilitude of experimental testing to form a high-fidelity tool for studying the dynamic response of systems whose size and complexity exceed the capacity of typical testing laboratories. Furthermore, substructures that are complex to model numerically can be tested physically, allowing for real measurements of the output quantities of interest (QoI). Moreover, substructures whose dynamic response is sensitive to the rate of loading can be tested in real-time,

in the so-called real-time hybrid simulation (RTHS). In this way, many assumptions and model distortions made in the process of modeling complicated systems are avoided, increasing the fidelity of and trust in simulation outcomes.

In every HS time step, the numerical substructure generates a command that needs to be followed by the physical substructure to maintain continuity of forces and displacements at the interface. In control engineering, this is known as reference tracking, since the output of the system under control (control plant hereafter) should follow the reference signal (the command). In HS the commanded signal is then transferred to the physical substructure through a transfer system. In most cases, this is an arrangement of linear hydraulic or linear electric actuators. During the test, the dynamic response of the physical substructure is measured and fed back to the numerical substructure, completing the unknown terms of the governing equations of motion of the hybrid model needed to compute the following command for the next time step of the simulation. This feedback loop continues until the end of the HS process. If the command signal is displacement or force, then HS is conducted under displacement or force control, respectively. In structural RTHS applications, displacement and/or force command signals are usually used. However, velocity or acceleration control can also be employed, depending on the application needs.

HS is often conducted on a distorted time scale, with the rate of physical substructure testing slowed down to accommodate the power of the transfer system. Such HSs are the so-called pseudodynamic test (Thewalt and Mahin, 1987). Real-time hybrid simulation (RTHS) is an extension of HS, in which the dynamic boundary conditions at the interfaces between numerical and physical substructures are being synchronized in real-time (Nakashima et al., 1992). Albeit attractive, RTHS comes with numerous challenges. The inherent dynamics of the transfer system used, along with interruptions to the communication between numerical and physical substructures, introduce time delays into the hybrid model, altering the dynamic response of the tested system (Gao and You, 2019). As a result, implementation of adequate control techniques to compensate for such time delays is necessary.

Recently, several control approaches have been proposed to compensate for time delays in RTHS. A selection of these approaches is highlighted below. Horiuchi developed a compensation technique using a polynomial extrapolation methodology to overcome time delays (Horiuchi, 1996), which was later modified into an adaptive scheme (Wallace M. et al., 2005; Wallace M. I. et al., 2005). Phase-lead compensators were also proposed by several authors. These work by compensating for the phase shift of the transfer system (Zhao et al., 2003; Gawthrop et al., 2007; Jung et al., 2007). Another popular compensation method was inverse compensation, in which an inverse model of the transfer function is used as a feedforward compensator—see, for example, Chen and Ricles (2009) and references therein. Following the initial work of Wagg and Stoten (2001) and Neild et al. (2005), adaptive compensation strategies were employed to improve the robustness of RTHS by online estimation of controller parameters (Chae et al., 2013; Chen et al., 2015). Many authors adapted general control methods to RTHS.

For example, Carrion and Spencer developed a method using model-based and LQG algorithms (Carrion and Spencer, 2007). Phillips and Spencer further enhanced this method by adding feedforward and feedback terms, accounting for multi-actuator schemes as well (Phillips and Spencer, 2013a,b). H_∞ loop shaping controller designs were also proposed as an additional technique to improve the performance and robustness of RTHS under the presence of uncertainties in the experimental procedure (Gao et al., 2013; Ou et al., 2015; Ning et al., 2019). Lately, a self-tuning nonlinear controller based on a combined robust-adaptive scheme was proposed, aiming at capturing nonlinearities of the dynamic interaction between transfer systems and physical substructures (Maghareh et al., 2020). Recently, Condori et al. (2020) proposed a robust control approach with a nonlinear Bayesian estimator to address uncertain nonlinear systems.

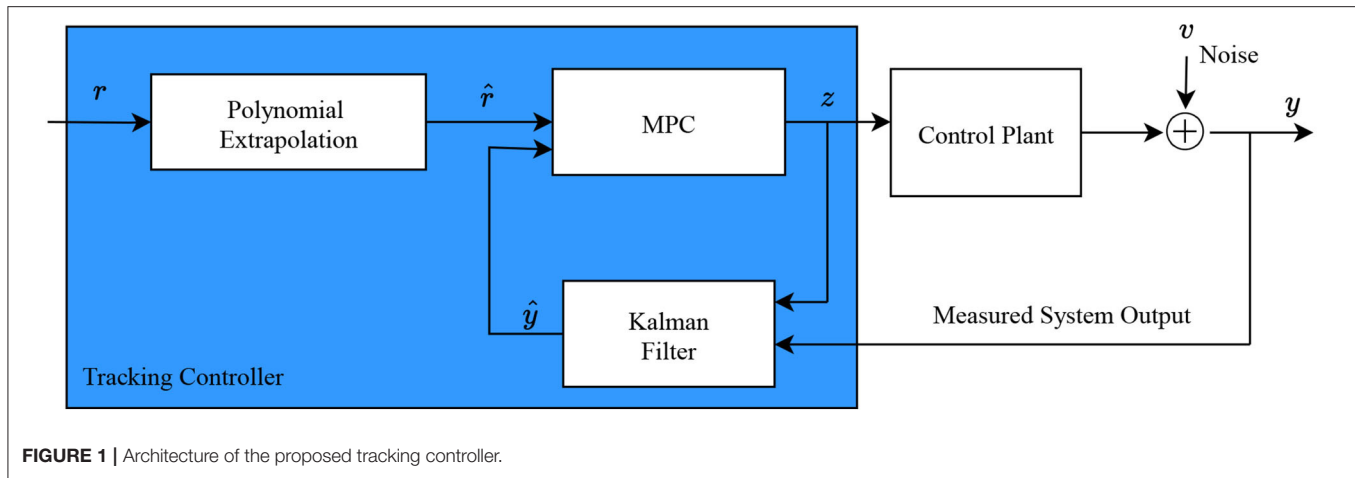
In this study, a novel control method is proposed, in which the tracking controller consists of a robust model predictive controller (MPC) along with a polynomial extrapolation algorithm and a Kalman filter. One important advantage of MPC is its capability to adapt the control law online, compensating for time delays and uncertainties for a set of specific simulation time steps. This is of significant importance for RTHS, since experimental errors and actuator dynamics introduce arbitrarily delays in the system, which need to be compensated for online. Another significant advantage of MPC is the fact that it can perform online optimization, handling at the same time constraints of the system under consideration. Following the design formulation of the proposed tracking controller, two virtual RTHS (vRTHS) parametric case studies are examined in order to validate the performance and robustness of the proposed control scheme. Variations in the parameters of the hybrid model will prove the robustness of the proposed controller to uncertainties introduced throughout the RTHS procedure. RTHS using the proposed control scheme is demonstrated to be effective for structural seismic performance assessment.

2. THE TRACKING CONTROLLER

In this section, the architecture of the proposed tracking controller is explained. The controller consists of a robust MPC along with a polynomial extrapolation algorithm and a Kalman filter. In **Figure 1**, the tracking controller's block diagram is shown. In the following sections, the main parts of the controller are described in detail. The control plant corresponds to the system under consideration, namely the actuator in series with the physical substructure used within the RTHS framework. The subsequent vRTHS case studies will give more insight into the control plant dynamics and architecture.

2.1. Model Predictive Control

Model Predictive Control (MPC) is a control strategy in which the ongoing control law is adapted by computing, at every control interval, a finite horizon optimization problem, applying the ongoing state of the control plant as the initial state. The optimization generates an optimal control sequence consisting of a series of individual control laws, out of which the first one is applied to the control plant for the current control



interval (Mayne et al., 2000). The control interval is defined as a sampling instant or, in other words, as a set of continuous time steps of the simulation, serving as an internal time step for the MPC in order to gather sufficient feedback measurements to accurately predict future control plant outputs and to advance the optimization to the next control sequence. In MPC, a standard finite horizon optimal control problem is being solved similar to H_∞ and LQR control approaches. In H_∞ and LQR control, the optimal problem could be of infinite horizon as well, while that's not the case for MPC. What differs, nonetheless, is the fact that in MPC new control laws are computed in each control interval, whilst in classical control theory a single control law, which is computed offline prior to the simulation, is used for the whole duration of the simulation. This is the fundamental difference between MPC and classical control theory. Online control law derivation is also a feature of adaptive control theory. However, in the latter, conducting system identification needed for the adaptive controller can cause numerical delays, whilst in MPC the model used in the controller remains the same and therefore no identification is needed. Changing online the parameters of the model used in MPC would result in the so-called adaptive MPC, but this is not part of this study.

Every application imposes mandatory (hard) constraints. For example: (i) actuators are of limited stroke/capacity meaning that the produced displacement/force is limited; and/or (ii) safety limits are applied in almost every experimental setup. The problem of meeting hard constraints in control applications is well established in the literature. MPC has proven to be one of the few adequate control methodologies to suitably satisfy constraints on the inputs, states and/or outputs of the system under consideration, maintaining concurrently the desired performance (Zafriou, 1990).

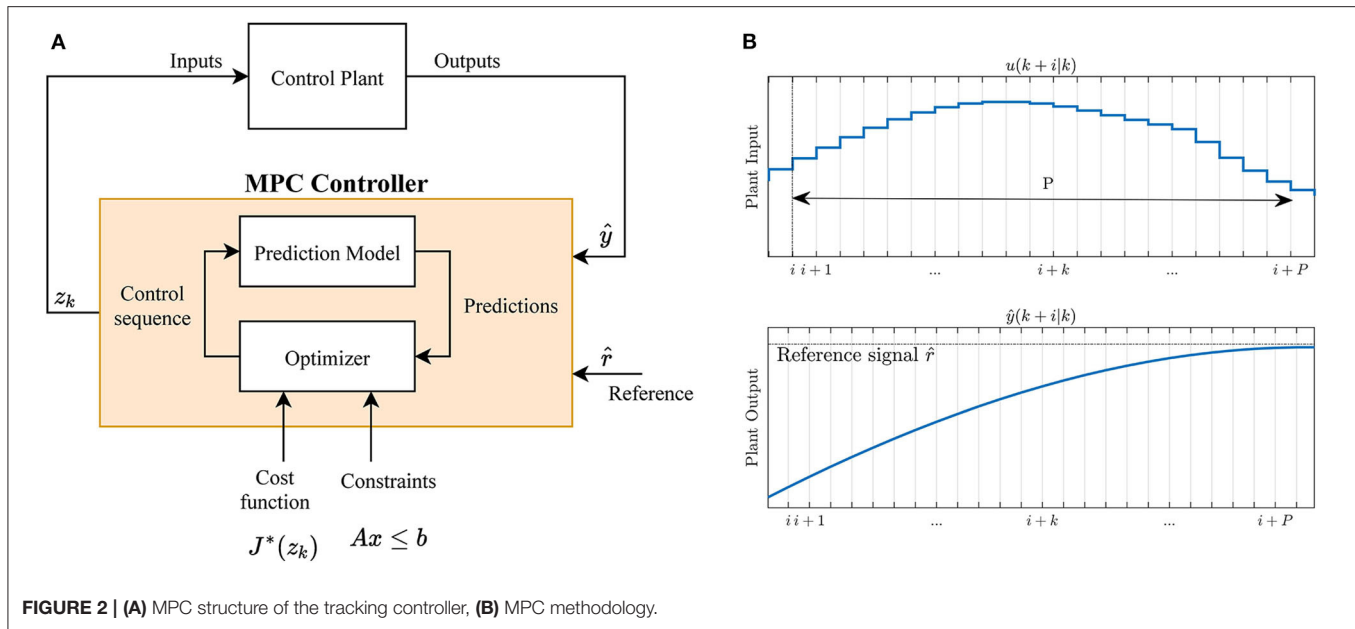
The proposed tracking MPC controller consists of four elements; (a) the prediction model, (b) the performance index or cost function, (c) the constraints, and (d) a solver to derive the control laws. The prediction model serves as the core of MPC since it is responsible for the future predictions of the control plant outputs, taking into account the past and present values of the computed optimal control laws. The prediction model should

be as accurate as possible in order to be able to sufficiently capture the control plant dynamics and its behavior. Therefore, a detailed prediction model could improve MPC performance. However, there is a trade-off between the complexity of the prediction model and the computational power needed to compute it at every control interval. Care must be taken in order not to introduce delays due to numerical calculations, especially in real-time applications, as RTHS, in which timing is crucial.

The MPC methodology used in this study is described below and illustrated in **Figure 2B**. In **Figure 2A**, the structure of the MPC controller is shown. At each control interval k , MPC optimizes the control plant outputs y_j . Namely, the future outputs $\hat{y}_j(k+i|k)$, for $k = 0, \dots, P$ of a predefined prediction horizon P are predicted at each control interval k using the prediction model. The i -th prediction horizon step is a time instant of the current control interval k . The latter depends on the known values up to this k and on the future control laws $u(k+i|k)$, for $k = 0, \dots, P-1$. The control sequence $z_k^T = [u(k|k)^T \dots u(k+i|k)^T \dots u(k+P-1|k)^T]$ consists of a sequence of control laws $u(k+i|k)$. It is calculated by optimizing a quadratic cost function at each k . The cost function embodies the tracking error, i.e., the error between the reference trajectory and the predicted output values of the control plant, and is expressed as follows:

$$J^*(\hat{r}_k, \hat{y}_k, z_k) = \sum_{j=1}^{n_y} \sum_{i=1}^P \{w^{y_j} [\hat{r}_j(k+i|k) - \hat{y}_j(k+i|k)]\}^2 + \sum_{j=1}^{n_u} \sum_{i=0}^{P-1} \{w^{u_j} [u_j(k+i|k) - u_j(k+i-1|k)]\}^2 \quad (1)$$

where n_y correspond to the number of control plant outputs, n_u the number of control plant inputs, $\hat{r}_j(k+i|k)$ the reference value to be tracked at the i -th prediction horizon step from the j -th control plant output, $\hat{y}_j(k+i|k)$ the predicted value of the j -th control plant output at the i -th prediction horizon step, $u_j(k+i|k)$ the j -th control plant input at the i -th prediction horizon step, w^{y_j} the tuning weight of the j -th control plant output and w^{u_j} the



tuning weight of the j -th control plant input. $(i|k)$ represents the current step i of the prediction horizon P at the control interval k .

Additionally, in the proposed tracking controller an output disturbance model w is used as described in Equation (2). The input of the model u_w , is assumed to be white noise and the disturbance w is additive to the control plant outputs. The disturbance model is used to include potential unmeasured noise that could occur during RTHS, e.g., experimental measurement errors. In the proposed design, the disturbance model follows:

$$\begin{aligned} x_w(k+1) &= A_w x_w(k) + B_w u_w(k) \\ w(k) &= C_w x_w(k) + D_w u_w(k) \end{aligned} \quad (2)$$

where A_w , B_w , C_w , and D_w are matrices associated with the disturbance w .

The k , P , w^{y_j} , and w^{u_j} parameters from Equation (1) remain constant for the entire RTHS. MPC constantly receives reference trajectories, $\hat{r}_j(k+i|k)$, for the whole prediction horizon P , which in RTHS corresponds to the outputs of the numerical substructure and uses the prediction model along with the Kalman filter (see section 2.2) to predict the control plant outputs, $\hat{y}_j(k+i|k)$, which depend on the control sequence z_k , the disturbance $w(k)$ and the Kalman filter's estimates. The control sequence z_k is computed in the optimizer (see Figure 2A), which takes into account the cost function (and in essence the tracking error, as it's embedded in the cost) and the constraints. The quadratic cost function of Equation (1) can be transformed into a Quadratic Programming (QP) problem (Delbos and Gilbert, 2003; Tøndel et al., 2003) and this is what is essentially being solved in the optimizer. The QP problem is formulated as follows:

$$\min_x \left(\frac{1}{2} x^T H x + f^T x \right) \quad (3)$$

$$\text{subject to } Ax \leq b \quad (4)$$

where the $Ax \leq b$ inequality corresponds to the constraints applied, x is the solution vector, H the Hessian matrix, A is a matrix of linear constraints coefficients, b is a vector relevant with the constraints, and f is a vector obtained by:

$$f = Kx^T x_{kf}(k|k) + Kr(k|k)^T r(k|k) + Ku(k|k-1)^T u(k|k-1) \quad (5)$$

where $x_{kf}^T = [x_p^T \ x_w^T]$ is the vector corresponding to the states of the Kalman filter (see section 2.2) and consists of the control plant states x_p and of the disturbance w states x_w , $r(k|k)$ is the reference signal at the current control interval, $u(k|k-1)$ is the control law applied to the control plant in the previous control interval and K a weighting factor.

In the proposed tracking controller, an active-set solver applying the KWIK algorithm (Schmid and Biegler, 1994) is used for solving the QP problem. This is a built-in QP solver from the Model Predictive Toolbox of MATLAB, used in this study to derive the control law sequence.

The MPC algorithm used in the proposed tracking controller can be summarized as follows:

1. Assuming the output disturbance model from Equation (2), consider a discrete-time multiple-input-multiple-output (MIMO), linear time invariant (LTI) system, representing a linearized model of the control plant:

$$\begin{aligned} x_p(k+1) &= A_p x_p(k) + B_p u(k) \\ y(k) &= C_p x_p(k) + D_p u(k) + D_{pw} w(k) \end{aligned} \quad (6)$$

where A_p , B_p , C_p , D_p , and D_{pw} are matrices corresponding to the control plant. This is the prediction model used along with estimates from the Kalman filter (see section 2.2) to provide MPC with predictions of future control plant outputs.

2. MPC performs the optimization at every control interval $k = 0, 1, \dots$:

$$\min_{z_k} \mathbf{J}^*(\hat{r}_k, \hat{y}_k, z_k) \quad (7)$$

$$\text{subject to } u_{j_{\min}} \leq u_j \leq u_{j_{\max}} \quad \text{and} \quad (8)$$

$$\dot{u}_{j_{\min}} \leq \dot{u}_j \leq \dot{u}_{j_{\max}} \quad (9)$$

where the above constraints correspond to the physical limitations of the actuator regarding displacement and velocity capacity and $\mathbf{J}^*(\hat{r}_k, \hat{y}_k, z_k)$ to the cost of Equation (1). The above limitations/capacities of the actuator are implemented as internal hard constraints of MPC. As a result, MPC guarantees, for the case studies addressed in section 3, that the performance of the controller is not affected by how close the actuator is to its limits.

3. The control sequence $z_k^T = [u(k|k)^T \dots u(k+i|k)^T \dots u(k+P-1|k)^T]$ is obtained for every control interval k :

$$z_k := \arg \min \mathbf{J}^*(\hat{r}_k, \hat{y}_k, z_k) \quad (10)$$

from the QP solver and it's applied to the control plant.

4. Steps 1–3 are repeated until the end of the RTHS.

In RTHS, the uncertainties and experimental errors are neither constant nor predictable. MPC enables computing a new control law for every control interval within the simulation time, making it possible to compensate specifically for the incurred time delays, uncertainties and/or experimental errors that are introduced in RTHS at each specific control interval. In contrast, classical control techniques utilize a single pre-computed control law that is robust enough to compensate for all the delays coming into play in the entire simulation process. In addition, RTHS always involves experimental equipment, which has physical boundaries, e.g., limited actuator force capacity. Hence, the command signals must be limited to satisfy these boundaries. MPC can solve optimization problems and concurrently satisfy hard constraints, which in the RTHS case, can be laboratory limitations. The aforementioned points make MPC desirable and suitable for RTHS applications. In the case studies presented in the following sections, the selection of the control interval k , the prediction horizon P , and the weights w^{y_j} and w^{u_j} is made through trial and error as there exists a trade-off between optimal controller performance and computational effort. Selection of the above MPC parameters is case study dependent. However, for control interval k and prediction horizon P , the following rules may be applied as a first trial (Bemporad et al., 2020):

- obtain each k at a sampling rate T_s , between 10 and 25% of the minimum desired closed-loop response time. A radical decrease of T_s will result in computational effort increase. T_s cannot be smaller than the sampling rate of RTHS.
- set P such that the desired closed-loop response time T , is approximately equal to PT_s , and the controller is internally stable.
- further optimization of the controller should be done through tuning of the weight coefficients w , but not through tuning of P .

MPC theory is quite extensive, covering various subjects (e.g., convex optimization, optimal control theory, computational solvers) that are taken into account during the design and implementation process of MPC and are not described in full detail in this paper. For a more comprehensive literature in MPC, the reader is encouraged to consult (Bitsoris, 1988; Rossiter, 2003; Boyd and Vandenberghe, 2004; Camacho and Bordons, 2007; Rawlings et al., 2017).

2.2. Kalman Filter

As mentioned above, good accuracy of the predicted control plant outputs is significant as it affects the performance of MPC. In order to improve the predictions' accuracy, a Kalman filter is implemented to estimate the future control plant output values. The purpose of the Kalman filter is to estimate how the current control law will alter the future control plant outputs and use these estimations to optimize the control sequence. The Kalman filter state-space formulation used in MPC follows:

$$x_{kf}(k+1) = A_{kf}x_{kf}(k) + B_{kf}u_{kf}(k) \quad (11)$$

$$\hat{y}(k) = C_{kf}x_{kf}(k) + D_{kf}u_{kf}(k)$$

where

$$A_{kf} = \begin{bmatrix} A_p & 0 \\ 0 & A_w \end{bmatrix}, \quad B_{kf} = \begin{bmatrix} B_p & 0 \\ 0 & B_w \end{bmatrix} \quad (12)$$

$$C_{kf} = [C_p \ C_w], \quad D_{kf} = [0 \ D_w] \quad \text{and}$$

$$u_{kf}^T = [z_k^T \ u_w(k)^T]$$

The weighting coefficients for the Kalman filter are derived from the following expectations:

$$Q = \mathbb{E}[B_{kf}u_{kf}u_{kf}^TB_{kf}^T], \quad R = \mathbb{E}[D_{kf}u_{kf}u_{kf}^TD_{kf}^T], \\ N = \mathbb{E}[B_{kf}u_{kf}u_{kf}^TD_{kf}^T] \quad (13)$$

In **Figure 1** is illustrated how the Kalman filter is integrated within the proposed tracking controller. More specifically, in the beginning of each control interval k , the state of the Kalman filter, $x_{kf}^T = [x_p^T \ x_w^T]$, is estimated for the next interval as follows:

- $x_{kf}(k|k)$ is updated based on the latest measurements:

$$x_{kf}(k|k) = x_{kf}(k|k-1) + M[y(k) - C_{kf}x_{kf}(k|k-1)] \quad (14)$$

- The state for the next, $k+1$, control interval is estimated as:

$$x_{kf}(k+1|k) = A_{kf}x_{kf}(k|k-1) + B_{kf}u(k) \\ + L[y(k) - C_{kf}x_{kf}(k|k-1)] \quad (15)$$

where L, M are the Kalman filter gain matrices and $u(k)$ the optimal control law assumed to be used from the control interval $(k-1)$ until k . $y(k)$ is the measured control plant output at the control interval k .

Once the state for the $k + 1$ interval is estimated, the values of the control plant output at this interval can be predicted as follows:

- For any successive step, $i = 1 : P$, within the ongoing control interval k , the next state is estimated as:

$$x_{kf}(k + i|k) = A_{kf}x_{kf}(k + i - 1|k) + B_p u(k + i - 1|k) \quad (16)$$

- Hence, the predicted control plant output value is calculated as:

$$\hat{y}(k + i|k) = C_{kf}x_{kf}(k + i|k), \quad \text{for } i = 1, \dots, P \quad (17)$$

where i corresponds to the prediction horizon step.

2.3. Polynomial Extrapolation

MPC can guarantee adequate tracking performance and robustness under uncertainties and disturbances. However, since in RTHS even small tracking errors can significantly alter the simulation outcome, a fourth-order polynomial extrapolation (Horiuchi, 1996; Wallace M. et al., 2005; Wallace M. I. et al., 2005; Ning et al., 2019) is integrated in the tracking controller as illustrated in **Figure 1**, in order to further compensate for time delays and additionally improve the MPC performance. Its formulation follows:

$$\hat{r}_k = a_0 r_{(0,k)} - a_1 r_{(1,k)} + a_2 r_{(2,k)} - a_3 r_{(3,k)} + a_4 r_{(4,k)} \quad (18)$$

where $r_{(i,k)} = r(t_k - iT_d)$ is the discrete reference signal by adding shifts of a pure time delay T_d by integer values of i . The polynomial coefficients $a_0 - a_4$ are obtained using the Lagrange basis function by trial and error.

3. CASE STUDIES

The following two virtual RTHS parametric case studies (CS) serve as validation for the performance and robustness of the proposed tracking controller. The case studies are virtual in that both the physical substructures of the hybrid models are implemented numerically in software, not physically as specimens in a laboratory. This was done to facilitate the development and testing of the proposed MPC. For each case study, the dynamics of the tested system are explained, then the tracking controller design properties are addressed and finally, results are presented. Since the goal of each case study is to examine the behavior of the tracking controller, the outputs of the hybrid models are exclusively related to the controller's performance. The outputs will be:

1. Tracking time-delay, defined as:

$$J_1 = \left(\arg \max_k (\text{Corr}(r(i), y(i - k))) \right) f_{RTHS} \quad [\text{msec}] \quad (19)$$

where f_{RTHS} is the sampling frequency of RTHS.

2. Normalized Root Mean Square (NRMS) of the tracking error, defined as:

$$J_2 = \sqrt{\frac{\sum_{i=1}^N [y(i) - r(i)]^2}{\sum_{i=1}^N [r(i)]^2}} \times 100 \quad [\%] \quad (20)$$

3. Peak Tracking Error (PTE), defined as:

$$J_3 = \frac{\max |y(i) - r(i)|}{\max |r(i)|} \times 100 \quad [\%] \quad (21)$$

J_1 is established as the maximum cross-correlation between the reference and the measured signal, multiplied by the sampling frequency of RTHS. It is a metric of how different in time these two signals are. The cross-correlation describes how many time steps the measured signal should be shifted in order to match the reference. When $J_1 > 0$ the measured signal is delayed with respect to the reference (tracking delay), whilst when $J_1 < 0$, the measured signal is leading the reference (overcompensation). The desire is to have zero time tracking delay, meaning the value of J_1 to be as close to zero as possible, without overcompensating. J_2 represents how quantitatively different the reference and measured signals are accounting for the whole simulation period, whilst J_3 accounts only for the maximum value of the tracking error. The performance of the tracking controller is assessed by how close to zero J_1 , J_2 , and J_3 are (Silva et al., 2020).

3.1. CS1: vRTHS of a Structure With an Attached Pendulum

3.1.1. Problem Formulation

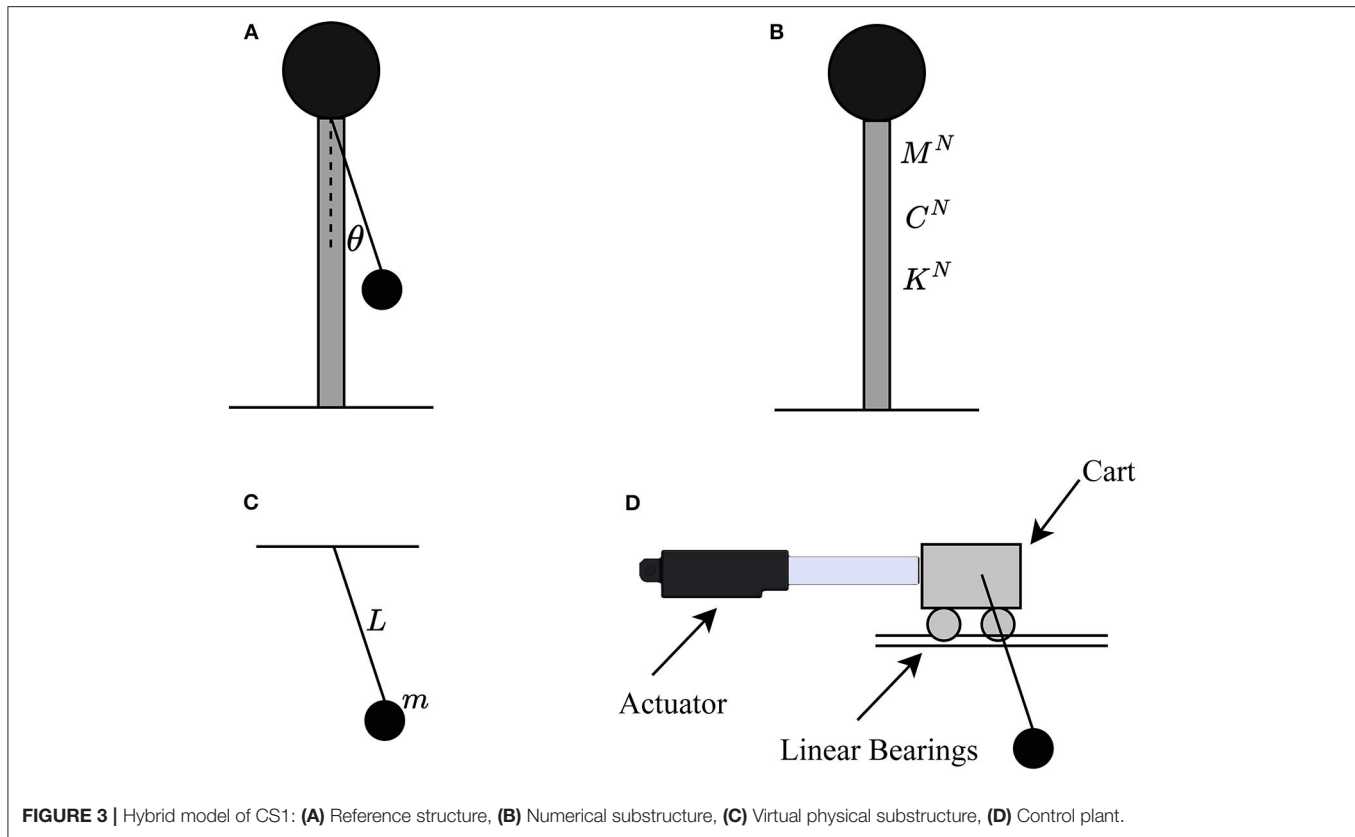
The reference system under consideration for CS1 corresponds to a vertical cantilever beam with mass concentrated at its top, and a pendulum attached to the center of gravity of the cantilever mass, as shown in **Figure 3A**. The numerical substructure is the cantilever beam (**Figure 3B**), described by Equation (22), while the virtual physical substructure is the pendulum (**Figure 3C**).

The Equation of Motion (EoM) for the reference structure follows:

$$M^N \ddot{x} + C^N \dot{x} + K^N x = -M^N \ddot{x}_g + f^P \quad (22)$$

where \ddot{x} , \dot{x} , and x correspond to acceleration, velocity and displacement of the numerical substructure relative to the ground, $M^N = 100$ [Kg], $C^N = 100$ [$\frac{Ns}{m}$], and $K^N = 10e4$ [$\frac{N}{m}$] are mass, damping and stiffness of the numerical substructure respectively, \ddot{x}_g is the ground motion applied to the hybrid model and f^P the force measured from the virtual physical substructure.

The virtual physical substructure corresponds only to the pendulum. However, to move the pendulum pivot point horizontally in a lab, an actuator could be attached to a cart mounted on a horizontal rail. Thus, the cart and the actuator would be the transfer system. As a result, the cart dynamics and its interaction with the pendulum are taking into account for solving the equations for the virtual physical substructure. The virtual physical substructure is described by the Equations (23) and (24). Moreover, in order to reduce as much as possible the



friction due to the cart movement μ , low friction linear bearings are assumed to be implemented. The friction at the pendulum pivot, b , is assumed to be small.

The EoM for the cart with the pendulum follows:

$$\ddot{x} = \frac{mL^2\dot{\theta}^2 \sin(\theta) + mLg \sin(\theta) \cos(\theta) + \dot{\theta}b \cos(\theta) - \mu L\dot{x} + f^P L}{L(m \sin^2(\theta) + M)} \quad (23)$$

$$\ddot{\theta} = \frac{-mL^2\dot{\theta}^2 \sin(\theta) \cos(\theta) - \dot{\theta}b(1 + \frac{M}{m}) - gL(M + m) \sin(\theta) + \dot{x}L\mu \cos(\theta) + f^P L \cos(\theta)}{L^2(m \sin^2(\theta) + M)} \quad (24)$$

where the parameters from Equations (23) and (24) correspond to:

- Pendulum angle, angular velocity, angular acceleration $\rightarrow \theta, \dot{\theta}, \ddot{\theta}$, respectively
- Cart position, velocity, acceleration $\rightarrow x, \dot{x}, \ddot{x}$, respectively
- Force generated from the pendulum $\rightarrow f^P$
- Pendulum mass $\rightarrow m = 0.15$ [Kg]
- Cart mass $\rightarrow M = 2$ [Kg]
- Rod length $\rightarrow L = 0.7$ [m]
- Cart friction coefficient $\rightarrow \mu = 0.001$ [-]
- Pendulum friction coefficient $\rightarrow b = 0.0001$ [-]
- Acceleration of gravity $\rightarrow g = 9.81$ [$\frac{m}{s^2}$].

Since this is a virtual simulation, an actuator model needs to be implemented representing the dynamics of the real actuator.

For CS1, a linear hydraulic actuator was chosen. Its model consists of three transfer functions; (i) G_{sv} represents the servo-valve dynamics as in Equation (25), (ii) G_a the actual actuator dynamics as in Equation (26), and (iii) G_{CSI} the control-structure-interaction (CSI) (Dyke et al., 1995) as in Equation (27). The way these transfer functions are interconnected is shown using a block diagram of the actuator model in Figure 4. Taking the above into consideration, the control plant for CS1, corresponds to the actuator model along with the cart and the pendulum. A graphical representation of the control plant is illustrated in Figure 3D and its block diagram in Figure 4. The control plant is a single-input-multiple-output (SIMO) model with input the displacement of the actuator z and four outputs; x, \dot{x}, θ , and $\dot{\theta}$. In the tracking controller, only the first output, the cart position x is used, described by a single-input-single-output (SISO) transfer system as in Equation (28).

$$G_{sv} = \frac{2.128e13}{s^2 + 425s + 99976} \quad (25)$$

$$G_a = \frac{1}{s + 3.3} \quad (26)$$

$$G_{CSI} = 7.26e5s \quad (27)$$

$$G_{cp} = \frac{0.5s^2 + 0.0007823s + 8.058}{s^4 + 0.001963s^3 + 15.07s^2 + 0.007s} \quad (28)$$

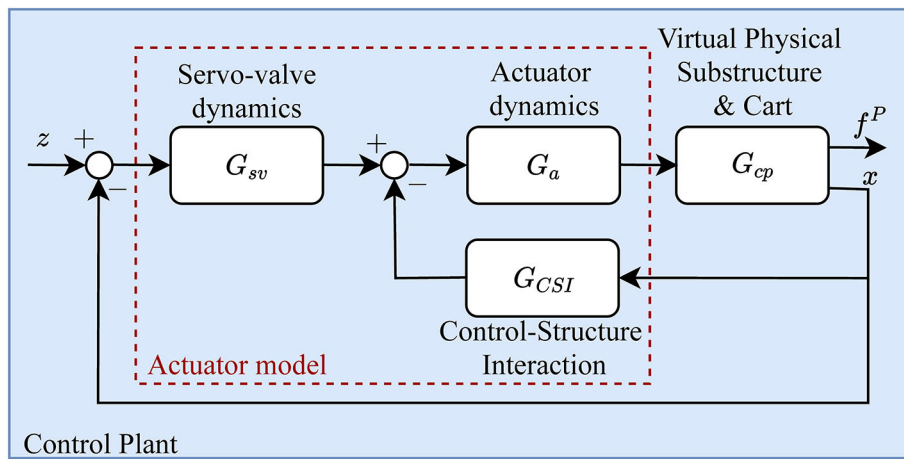


FIGURE 4 | Block diagram of the control plant in CS1.

The block diagram of the overall hybrid model is presented in **Figure 5A**. It consists of the numerical and virtual physical substructures, the proposed tracking controller and the control plant. The RTHS is conducted in displacement control; in every time step the measured displacement of the cart (same as the horizontal displacement of the pendulum), x , is fed back in the tracking controller, while the measured force generated from the movement of the pendulum, f^P is fed back to the numerical substructure to compute the next displacement command r . The coupling of the two substructures is achieved through force f^P . Furthermore, apart from the disturbance described in Equation (2), in order to capture even more realistic results, additional white noise v is added in the calculated displacement x and force f^P , representing measurement noise from the displacement and force sensors, respectively. The displacement and force sensor noise is modeled with two correlated standard Gaussian distributions, generated at the same frequency as the sampling of RTHS and amplified each by $1.5e-7$ m and $6e-5$ N, respectively, which approximately equals to 0.01% of the respective full spans. The sampling frequency of RTHS was set to $f_{RTHS} = 4,096$ Hz. For the numerical integration scheme, the RK4 (fourth-order Runge–Kutta) method is used with a fixed time step of $1/4,096$ s. The reference ground motion of the hybrid model \ddot{x}_g is a historical acceleration record from the El Centro 1940 earthquake downsampled by 0.4, as shown in **Figure 6A**. In **Figure 6B**, the power spectral density of the respective record is illustrated.

3.1.2. Tracking Controller Design Properties

The prediction model used in MPC for CS1 is a linearized model of the control plant. Since MPC functions in discrete time, the linearized model of the control plant is discretized with the sampling frequency of RTHS, f_{RTHS} . Essentially it's a discrete LTI SISO model described using the state-space formulation as follows:

$$\begin{aligned} x(k+1) &= A_p x(k) + B_p u(k) \\ y(k) &= C_p x(k) + D_p u(k) + D_{pw} w(k) \end{aligned} \quad (29)$$

where A_p , B_p , C_p , D_p , and $D_{pw} = 1$ are the prediction model matrices, equal to:

$$\begin{aligned} A_p &= \begin{bmatrix} 0.4762 & -0.3993 & -0.2475 & -0.2307 & -0.2279 & -0.0009 & -0.0143 \\ 0.7532 & 0.7912 & -0.1315 & -0.1222 & -0.1272 & -0.0005 & -0.008 \\ 0.2103 & 0.4645 & 0.9775 & -0.0209 & -0.0223 & 0 & -0.0014 \\ 0.0184 & 0.0603 & 0.2486 & 0.9987 & -0.0014 & 0 & 0 \\ 0.0012 & 0.0051 & 0.0312 & 0.2499 & 1 & 0 & 0 \\ 0 & 0 & 0.0002 & 0.002 & 0.0156 & 1 & 0 \\ 0 & 0 & 0 & 0 & 0.0001 & 0.0156 & 1 \end{bmatrix}, \\ B_p &= \begin{bmatrix} 0.0118 \\ 0.0066 \\ 0.0012 \\ 0 \\ 0 \\ 0 \\ 0 \end{bmatrix}, \\ C_p &= [0 \ 0 \ 0 \ 0 \ 19.86 \ 0.002 \ 1.25], D_p = [0] \end{aligned} \quad (30)$$

The disturbance model used, expressed by Equation (2), is added to the control plant output and its model follows:

$$\begin{aligned} x_w(k+1) &= A_w x_w(k) + B_w u_w(k) \\ w(k) &= x_w(k) \end{aligned} \quad (31)$$

with $A_w = 1$, $B_w = 0.0009766$, $C_w = 1$, and $D_w = 0$. The Kalman filter gain matrices follow:

$$\begin{aligned} L &= [0.0096 \ -0.0062 \ -0.0269 \ 0.0021 \ 0.0148 \ 0.0004 \ -0.0003 \ 0.0008]^T \\ M &= [0.0071 \ -0.0147 \ -0.0215 \ 0.0082 \ 0.0135 \ 0.0002 \ -0.0003 \ 0.0008]^T \end{aligned} \quad (32)$$

Starting with Equations (30), (31), and (32) the derivation of the Kalman filter formulation in Equation (11) is straightforward. The MPC weight coefficients used in Equation (1) are selected

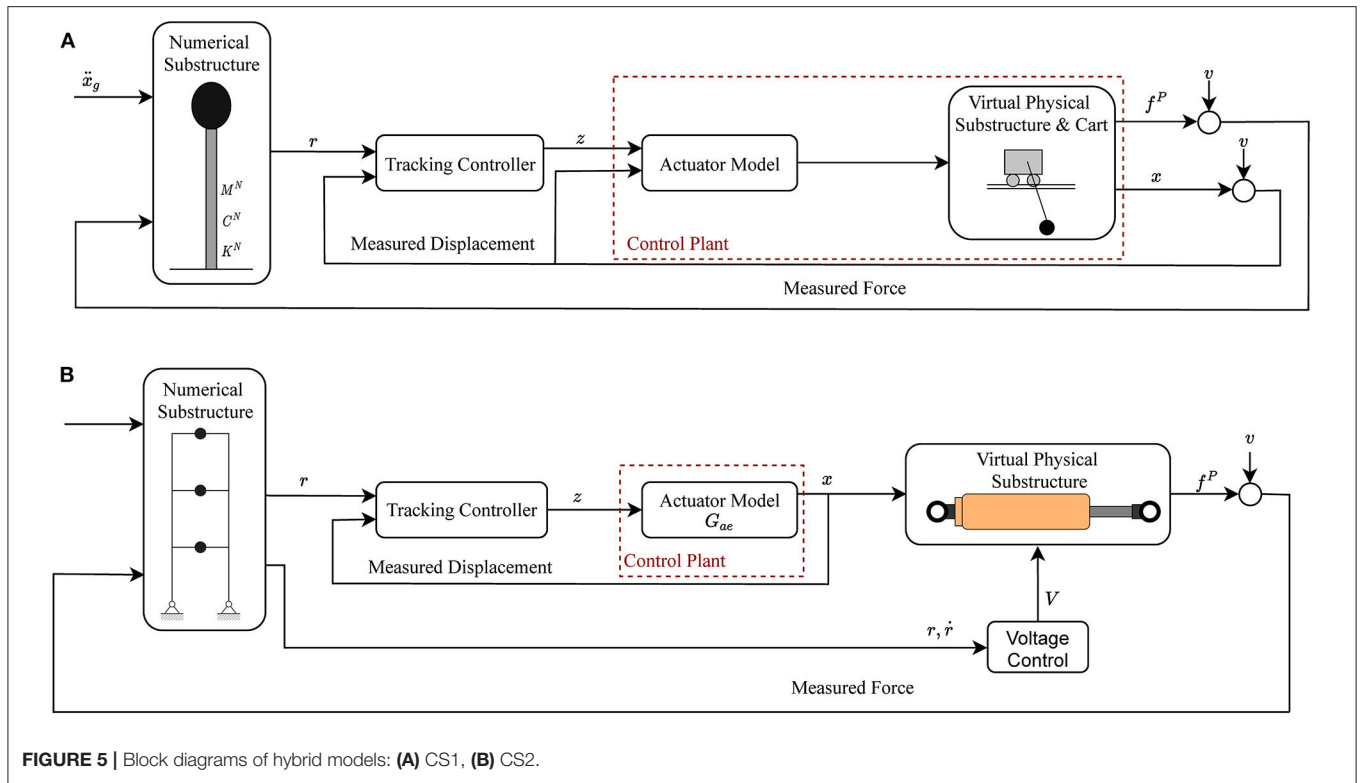


FIGURE 5 | Block diagrams of hybrid models: (A) CS1, (B) CS2.

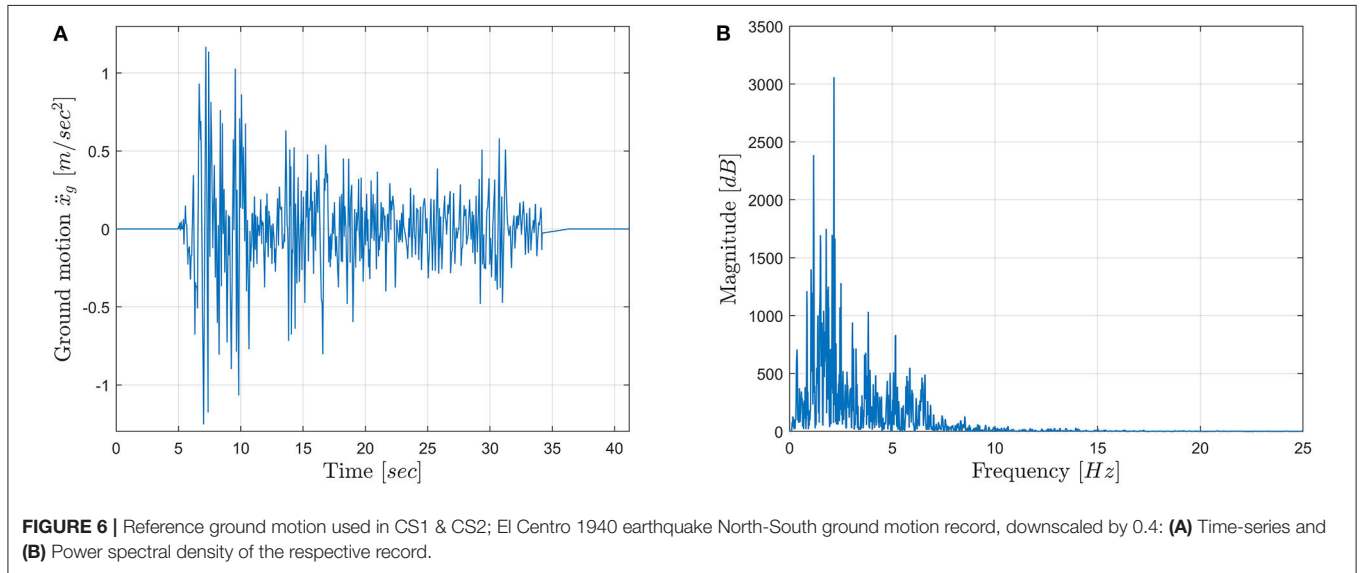


FIGURE 6 | Reference ground motion used in CS1 & CS2; El Centro 1940 earthquake North-South ground motion record, downscaled by 0.4: (A) Time-series and (B) Power spectral density of the respective record.

to be $w^y = 15.26$ and $w^u = 0.63$. The number of control plant outputs n_y is 1 and the number of control plant inputs n_u , is also 1. The prediction horizon was set to $P = 8$ and each control interval k was obtained at a sampling frequency of 1,024 Hz, one fourth of the RTHS sampling rate. The constraints applied represent the physical limitations of the actuator to provide bounded displacements and velocity. It's assumed that the virtual actuator has a maximum stroke of ± 250 [mm] and maximum velocity of ± 100 [$\frac{mm}{sec}$]. So the

constraints follow:

$$\begin{aligned} -250 \leq \hat{z}(k+i|k) &\leq 250, & \left[\frac{mm}{sec} \right] & \text{ for } i = 1, \dots, P \\ -100 \leq \dot{\hat{z}}(k+i|k) &\leq 100, & \left[\frac{mm}{sec} \right] & \text{ for } i = 1, \dots, P \end{aligned} \quad (33)$$

The polynomial extrapolation coefficients used in CS1 for the proposed tracking controller follow:

$$\hat{r}_k = 5r_{(0,k)} - 10r_{(1,k)} + 10r_{(2,k)} - 5r_{(3,k)} + r_{(4,k)} \quad (34)$$

TABLE 1 | CS1: Variation of the random parameters in the hybrid model.

Input variable	Probability distribution	Mean value (μ)	Stand. dev. (σ)	Coeff. of variat. (CV) (%)	Parameter description	Units
M	Lognormal	2	0.4	20	Cart mass	Kg
m	Lognormal	0.15	0.03	20	Pendulum mass	Kg
L	Lognormal	0.7	0.21	30	Rod length	m
M^N	Lognormal	100	20	20	Cantilever beam mass	Kg
C^N	Lognormal	100	30	30	Cantilever beam damping	Ns/m
K^N	Lognormal	10e4	3e4	30	Cantilever beam stiffness	N/m

3.1.3. CS1 Results

In order to test the robustness of the proposed tracking controller, six dominant parameters of the hybrid model were chosen to vary. The first three parameters originate from the control plant and correspond to its M , m , and L , while the remaining three originate from the numerical substructure and correspond to its M^N , C^N , and K^N . These parameters are treated as random with known probability distributions. Their distribution characteristics are described in **Table 1**.

Using the Latin Hypercube Sampling (LHS) methodology, 200 samples were generated from all six parameters and 200 runs of the vRTHS were conducted using combinations of all parameters in each iteration. The tracking controller was kept the same for each one of the 200 runs. The simulation of the 200 vRTHS runs is referred as stochastic vRTHS hereafter. The resulting J_1 , J_2 , and J_3 outputs of the nominal and the stochastic vRTHS are shown in **Table 2** for both CS1 and CS2 for brevity. The nominal values correspond to the parameters used in Equations (22), (23), and (24). The normalized histograms of the J_1 , J_2 , and J_3 out of the 200 vRTHS are shown in **Figure 7**. The aforementioned histograms are a more comprehensive, graphical representation of the values presented in **Table 2**, illustrating the mean values as well as the deviations from them. It is also a metric of robustness; more robust tracking controllers would result in lower deviations in the histograms.

Analysis of the results using uncertainty quantification techniques indicated that 200 runs were sufficient to unveil how the tracking controller performance is affected by parameter variations. Specifically, surrogate models were developed to replicate the response of the CS as the number of runs (in the surrogate training data set) was increasing. With a training data set of 200 samples, validation errors of the surrogate models were <5%. No new runs were added to the data set as this error was deemed to be sufficiently small.

To check if the proposed tracking controller remains stable as the hybrid model parameters vary, vRTHS simulations using the minimum and the maximum values of the random variables were conducted first. No instabilities were observed. Furthermore, none of the conducted 200 simulations was unstable. The same holds for CS2.

The reference, command and measured signals of the hybrid model in the nominal vRTHS are illustrated in **Figure 8**. The reference signal corresponds to the displacement response of the reference model (one with integrated physical and

TABLE 2 | Tracking controller performance and robustness results for CS1 and CS2.

	CS1			CS2		
	Nominal	Stochastic		Nominal	Stochastic	
		Mean values	Stand. dev.		Mean values	Stand. dev.
J_1 [msec]	0.24	0.21	0.21	0	0	0
J_2 [%]	1.88	2.04	0.67	1.89	2.95	0.65
J_3 [%]	1.86	2.01	0.57	2.29	3.04	0.63

CS2 is addressed in the next section 3.2. CS2 results are presented here for brevity and for simpler comparison with results from CS1.

numerical substructures). The command signal corresponds to the displacement response r computed from the numerical substructure at each given time step of vRTHS and is the one that should be followed from the control plant. Finally, the measured signal corresponds to the measured displacement response x of the virtual physical substructure. An ideal tracking controller should be able to compensate the hybrid model in such a way that the command r and measured x to be identical. As it's shown from **Figure 8**, those two signals are, indeed, very close. The comparison with the reference signal is provided in order to validate the fidelity of the hybrid model with respect to the reference structure.

In **Figure 9**, the performance index of the MPC versus time for the nominal case is displayed. This graph illustrates how well MPC managed to minimize the given objective cost function of Equation (1) in every time step of the simulation. A zero value would mean that the cost function was minimized as desired and the “best” optimal control sequence was computed for the given time step. From **Figure 9**, we can observe that the performance index is almost zero during the entire vRTHS, while it is not zero in the time steps in which the highest peaks of the reference signal are attained. This is expected, as the peaks of the command signal are approached, the controller is challenged more and more and has to adapt.

Since the performance of the tracking controller is assessed by how close to zero J_1 , J_2 , and J_3 are, it's clear from **Table 2** and **Figures 7–9** that the proposed tracking controller can provide the desired performance under the presence of any combination of all six random parameters of the hybrid model

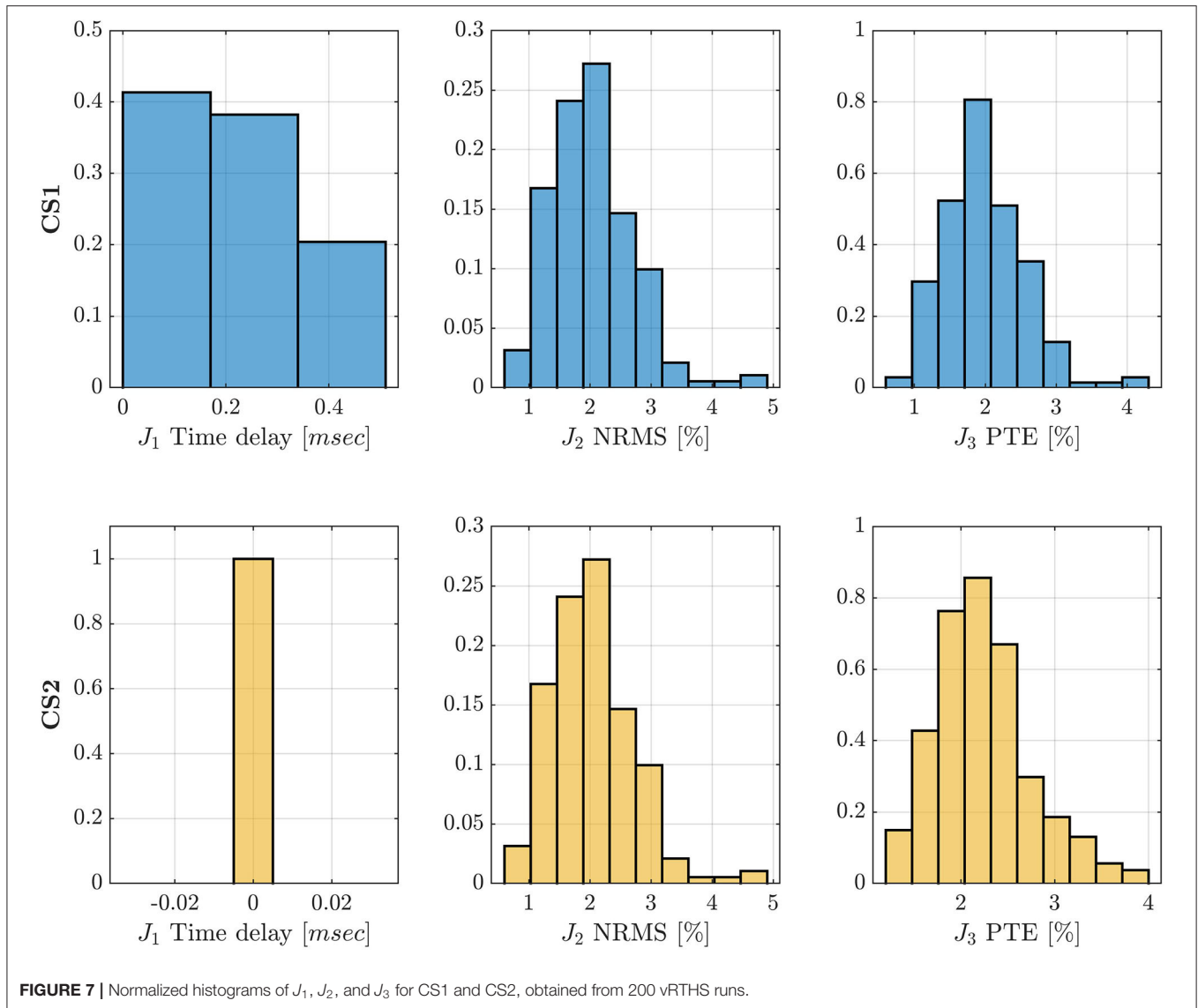


FIGURE 7 | Normalized histograms of J_1 , J_2 , and J_3 for CS1 and CS2, obtained from 200 vRTHS runs.

chosen here, which also demonstrates its robustness. The effects of these stochastic parameters could represent the effect of potential uncertainties (aleatory and/or epistemic) that could be introduced during RTHS. On top of that, it should be pointed out that the controller maintains its performance even in the presence of the additional noise ν and disturbance w that were added in the hybrid model.

3.2. CS2: vRTHS of a Magnetorheological Damper Attached to a 3-Story Structure

3.2.1. Problem Formulation

The reference structure in CS2 corresponds to a 3-story structure equipped with a magnetorheological damper (MRD), installed between the ground and first floor (Dyke et al., 1998) as shown in **Figure 10A**. The numerical substructure corresponds to the 3-story structure (**Figure 10B**), while the virtual physical to the MRD (**Figure 10C**).

The EoM of the reference model reads:

$$\mathbf{M}^N \ddot{\mathbf{x}} + \mathbf{C}^N \dot{\mathbf{x}} + \mathbf{K}^N \mathbf{x} = -\mathbf{M} \Lambda \ddot{x}_g + \mathbf{F} f^p \quad (35)$$

where $\mathbf{x} = [x_1, x_2, x_3]^T$, $\dot{\mathbf{x}} = [\dot{x}_1, \dot{x}_2, \dot{x}_3]^T$, and $\ddot{\mathbf{x}} = [\ddot{x}_1, \ddot{x}_2, \ddot{x}_3]^T$ correspond to the displacement, velocity, and acceleration relative to the ground, \ddot{x}_g is the ground motion and f^p corresponds to the force generated from the MRD. The \mathbf{M}^N , \mathbf{C}^N , \mathbf{K}^N matrices represent the mass, damping and stiffness of the 3-story structure, respectively, as follows:

$$\mathbf{M}^N = \begin{bmatrix} 1,000 & 0 & 0 \\ 0 & 1,000 & 0 \\ 0 & 0 & 1,000 \end{bmatrix} [\text{Kg}], \quad (36)$$

$$\mathbf{C}^N = 1e4 * \begin{bmatrix} 1.408 & -0.787 & 0.044 \\ -0.787 & 1.494 & -0.635 \\ 0.044 & -0.635 & 0.722 \end{bmatrix} \left[\frac{Ns}{m} \right],$$

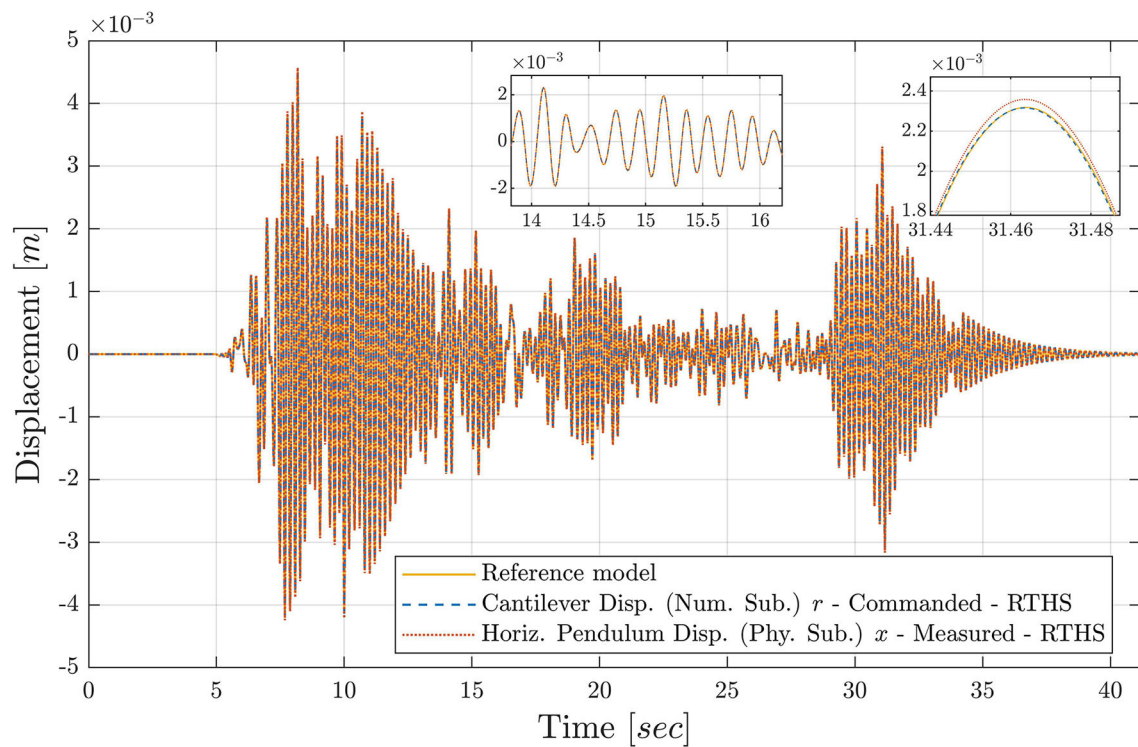


FIGURE 8 | Displacement responses of the reference model and of the numerical and physical vRTHS substructures in CS1.

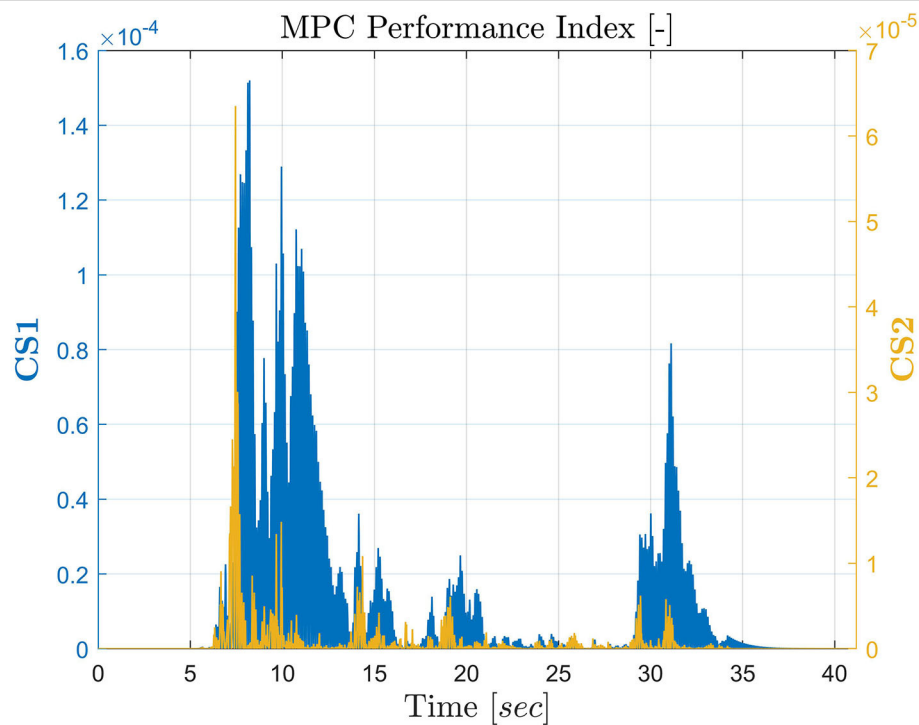


FIGURE 9 | MPC optimization performance index for CS1 and CS2.

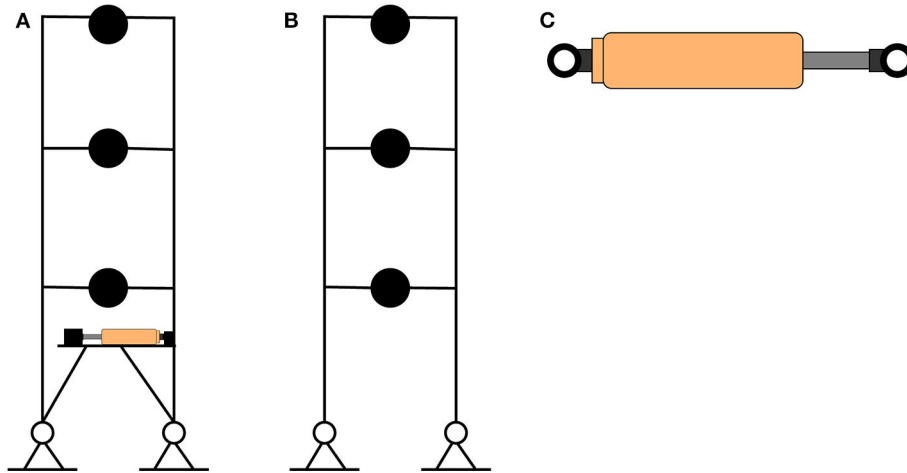


FIGURE 10 | Hybrid model of CS2: **(A)** Reference structure, **(B)** Numerical substructure, **(C)** Virtual physical substructure.

$$\mathbf{K}^N = 1e7 * \begin{bmatrix} 2.605 & -2.313 & 0.594 \\ -2.313 & 3.256 & -1.442 \\ 0.594 & -1.442 & 0.927 \end{bmatrix} \begin{bmatrix} N \\ - \\ m \end{bmatrix}$$

Vector $\mathbf{\Lambda} = [1 \ 1 \ 1]^T$ is the ground motion influence vector, while vector $\mathbf{\Gamma} = [1 \ 0 \ 0]^T$ represents the effect of the MRD on the structure. In RTHS, a state-space representation of the Equation (35) is used, which follows:

$$\begin{aligned} \dot{\mathbf{x}} &= \mathbf{A}\mathbf{x} + \mathbf{B}\mathbf{u} \\ \mathbf{y} &= \mathbf{C}\mathbf{x} + \mathbf{D}\mathbf{u} \end{aligned} \quad (37)$$

where $\mathbf{x} = [x_1, x_2, x_3, \dot{x}_1, \dot{x}_2, \dot{x}_3]^T$, $\mathbf{u} = [\ddot{x}_g, f^P]^T$, $\mathbf{y} = [x_1, x_2, x_3, \dot{x}_1, \dot{x}_2, \dot{x}_3, \ddot{x}_1, \ddot{x}_2, \ddot{x}_3]^T$, and

$$\begin{aligned} \mathbf{A} &= \begin{bmatrix} \mathbf{0} & \mathbf{I} \\ -\mathbf{M}^{N-1}\mathbf{K}^N & -\mathbf{M}^{N-1}\mathbf{C}^N \end{bmatrix}, \quad \mathbf{B} = \begin{bmatrix} \mathbf{0} & \mathbf{0} \\ -\mathbf{\Lambda} & -\mathbf{M}^{N-1}\mathbf{\Gamma} \end{bmatrix} \\ \mathbf{C} &= \begin{bmatrix} \mathbf{I} & \mathbf{0} \\ \mathbf{0} & \mathbf{I} \\ -\mathbf{M}^{N-1}\mathbf{K}^N & -\mathbf{M}^{N-1}\mathbf{C}^N \end{bmatrix}, \quad \mathbf{D} = \begin{bmatrix} \mathbf{0} & \mathbf{0} \\ \mathbf{0} & \mathbf{0} \\ -\mathbf{\Lambda} & -\mathbf{M}^{N-1}\mathbf{\Gamma} \end{bmatrix} \end{aligned} \quad (38)$$

The block diagram of the hybrid model of CS2 is shown in **Figure 5B**. The reference signal r , in **Figure 5B**, corresponds to the displacement of the first story x_1 . Respectively, $\dot{r} = \dot{x}_1$. RTHS is conducted in displacement control, as in CS1. The ground motion applied to the hybrid model is the same as in CS1, a historical acceleration record from the El Centro 1940 earthquake downsampled by 0.4. As in CS1, apart from the additive disturbance described in Equation (2), additional white noise v is added in the calculated force from MRD f^P , which represents measurement noise from the load cell. The load cell measurement noise is modeled with a standard Gaussian distribution, generated at the same frequency as the sampling of RTHS and amplified by 0.15 N, which approximately equals to 0.01% of the load cell full span. The sampling frequency of RTHS was set to $f_{RTHS} = 4,096$ Hz.

For the numerical integration scheme, the RK4 method is used with a fixed time step of $1/4,096$ s.

To model the virtual physical substructure, the MRD in CS2, the Viscous + Dahl model (Ikhoulane and Dyke, 2007) was employed. Its dynamics are described as follows:

$$\begin{aligned} f^P(t) &= [k_{x_a} + k_{x_b} V(t)]\dot{x}(t) + [k_{w_a} + k_{w_b} V(t)]W(t) \\ \dot{W}(t) &= \rho(\dot{x}(t) - |\dot{x}|W(t)) \\ W(0) &= \frac{f^P(0) - [k_{x_a} + k_{x_b} V(0)]\dot{x}(0)}{k_{w_a} + k_{w_b} V(0)} \end{aligned} \quad (39)$$

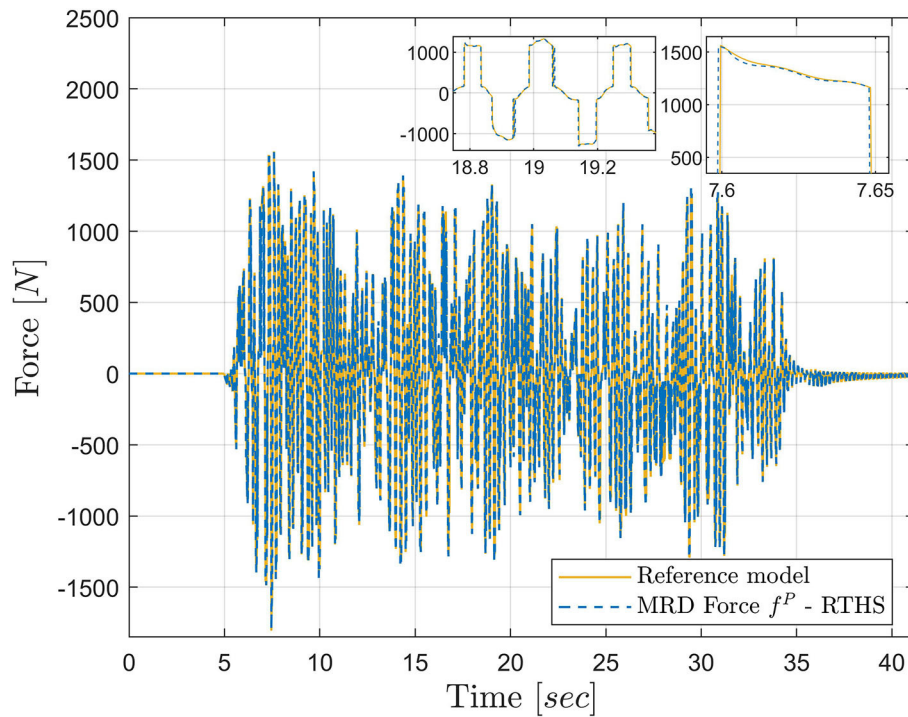
where $\dot{x}(t)$ denotes the MRD piston velocity, $V(t)$ the voltage input command, $f^P(t)$ the damping force, W the damper's nonlinear behavior, k_{x_a} and k_{x_b} the viscous friction coefficient, k_{w_a} and k_{w_b} the dry friction coefficient and t refers to the simulation time. The parameter ρ is calculated as in Tsouroukdissian et al. (2008) and selected to be $\rho = 4,795$ (m^{-1}). The friction parameters are calculated from linear regression as $k_{x_a} = 978$ (Nsm^{-1}), $k_{x_b} = 4,075$ ($Nsm^{-1}V^{-1}$), $k_{w_a} = 160.11$ (N), and $k_{w_b} = 500.78$ (NV^{-1}). The inputs of the MRD model are the displacement $x(t)$ and the voltage $V(t)$, while the output is the force f^P . The latter is the variable that couples the two substructures.

In a MRD, a relatively small electric current applied to the MR valve can change the behavior from very high to very low resistance to motion over a very short time period. In order to ensure optimal response, a bang-bang voltage controller is designed and implemented as illustrated in **Figure 5B**. More specific, when $\text{sgn}(r(t)) = \text{sgn}(\dot{r}(t))$ then the controller provides the MRD with the maximum input voltage, resulting in maximum MRD force f^P . Otherwise, the MRD force is minimum. This bang-bang controller is part of the MRD and it's exclusively responsible for the internal behavior of the MRD.

In CS2, a different approach of the control plant is investigated compared to CS1, since in this case the control plant corresponds

TABLE 3 | CS2: Variation of the random parameters in the hybrid model.

Input variable	Probability distribution	Mean value (μ)	Stand. dev. (σ)	Coeff. of variat. (CV) (%)	Parameter description	Units
L_b	Lognormal	0.762	0.1524	20	Beam length	m
L_c	Lognormal	0.635	0.127	20	Column length	m
M^N	Lognormal	1,000	200	20	Floor mass	kg
Z	Lognormal	0.05	0.01	20	Damping ratio	–
K_{x_a}	Lognormal	978	195.6	20	Viscous friction coef. of MR	Ns/m
K_{w_a}	Lognormal	160.11	32.022	20	Dry friction coef. of MR	N

**FIGURE 11** | MRD generated force in the reference model and in vRTHS in CS2.

only to the actuator model. In contrast with the control plant represented the actuator model in series with the virtual physical substructure in CS1. Results presented later on prove that the compensation of time delays is sufficient and the performance of RTHS is as desired, when this approach is followed. Moreover, in this way, the dynamics of the control plant are much simpler. Hence, the complexity of the tracking controller is reduced significantly as well. This can be observed by comparing the prediction models used in the two case studies (Equations 30, 40). Therefore, in CS2 the control plant is a SISO model described by Equation (40) with input the desired displacement of the actuator z and output x , the achieved displacement of the actuator. So, in the J_1 , J_2 , and J_3 criteria the measured signal $y(i)$ of Equations (19), (20), and (21) corresponds to the actuator achieved displacement x . Furthermore, in order to try the proposed tracking controller under different actuator scenarios, the actuator model used in CS2 corresponds to an

electric actuator, represented by a second-order transfer function, G_{ae} , described by the dynamics of Equation (40).

$$G_{ae} = \frac{3060}{s^2 + 267s + 3060} \quad (40)$$

3.2.2. Tracking Controller Design Properties

As in CS1, the prediction model used in MPC is the control plant, discretized by the sampling frequency of RTHS. The state-space formulation of the discretized model follows (Equation 29) with:

$$A_p = \begin{bmatrix} 0.7693 & -0.0411 \\ 0.055 & 1 \end{bmatrix}, B_p = \begin{bmatrix} 0.0069 \\ 0.0002 \end{bmatrix}, C_p = [0 \ 5.98], D_p = 0 \quad (41)$$

The disturbance model is the same as in Equation (31). The Kalman filter gain matrices in this case are:

$$L = [-0.001 \ 0.723 \ 0.974]^T * 1e(-3) \quad (42)$$

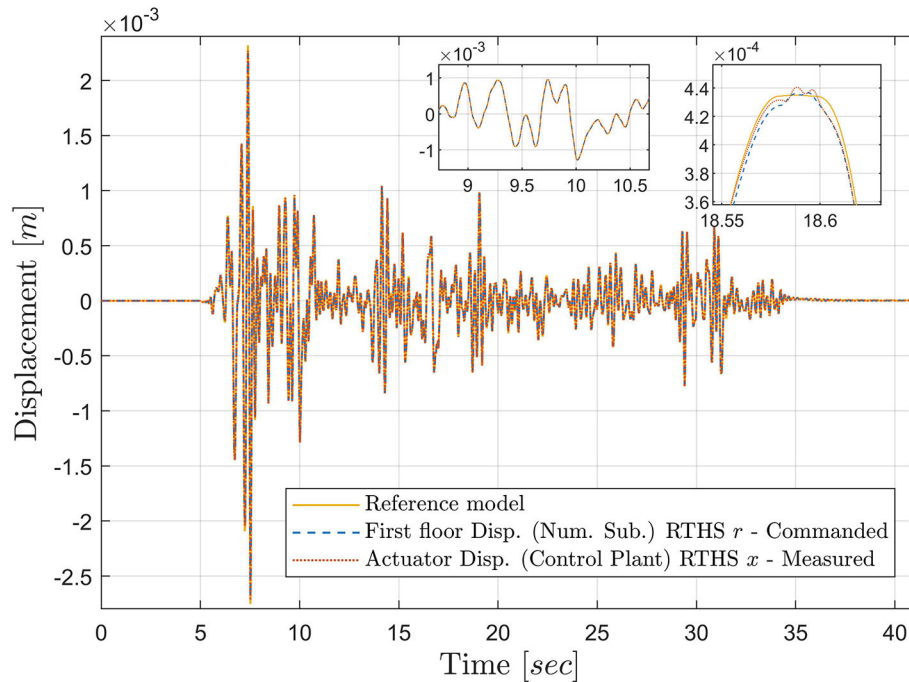


FIGURE 12 | Displacement responses of the reference model, the numerical substructure, and control plant in CS2.

$$M = [0.037 \ 0.721 \ 0.974]^T * 1e(-3)$$

In CS2, the MPC parameters are selected as follows:

- $n^y = 1$ and $n^u = 1$
- $w^y = 64.073$ and $w^u = 0.002$
- $P = 10$
- Each control interval k is obtained on a sampling frequency of 1,024 Hz
- The constraints remain the same with Equation (33).

The polynomial extrapolation coefficients are the same as in Equation (34).

3.2.3. CS2 Results

As in CS1, in order to test the robustness of the tracking controller, six dominant parameters are selected to be random variables with known probability distributions. The first four originate from the numerical substructure:

- Beam length $\rightarrow L_b$
- Column length $\rightarrow L_c$
- Floor mass $\rightarrow M^N$
- Damping ratio $\rightarrow Z$.

The remaining two parameters correspond to the virtual physical substructure and more specific to K_{x_a} and K_{w_a} . These parameters are of particular importance for the MRD model since they are responsible for its nonlinear behavior. All six parameters along with their distribution characteristics are displayed in **Table 3**. As in the previous case study, 200 samples are generated with the LHS method from

the six parameters, and 200 vRTHS runs are conducted accounting for the variability of all parameters in each run. Again the tracking controller was kept the same in all vRTHSs. The nominal case for CS2 are the parameter values from Equations (37) and (39). The arithmetic results for J_1 , J_2 , and J_3 can be found in **Table 2**. Their corresponding normalized histograms for the stochastic vRTHS are illustrated in **Figure 7**.

In **Figure 11**, the force generated by the MRD in the reference model is compared against the one obtained from the vRTHS framework. We can observe that the forces are almost identical. This serves as a demonstration that, although the virtual physical substructure was not included in the control plant, since the latter consists only of the actuator model, its response is compensated sufficiently from time delays and tracking errors. In **Figure 12**, a comparison between three displacement responses is shown; the displacement response of the reference model, the displacement response of the first floor of the numerical substructure r (this is the command signal to the control plant), and the displacement response x , measured from the control plant [this should track r]. The latter two signals prove that the performance of the tracking controller is as desired, as **Figure 12** serves as a graphical illustration of the nominal results shown in **Table 2**. We can observe that due to the proposed controller, x follows the commanded r with minimum delay and tracking error. Finally, in **Figure 9**, the performance index of MPC for CS2 is illustrated.

As in the previous case study, from the **Table 2**, **Figures 7, 12**, it's shown that the controller performance does not get affected by the presence of the introduced random variables, and it provides the requested performance in all considered cases.

4. CONCLUSIONS

In this study, a novel control method to develop a time delay and experimental error compensation strategy in RTHS is presented. The proposed tracking controller aims to conduct RTHS in hard-real time while compensating for potential time delays and tracking errors, under the uncertainties that may arise during RTHS. The tracking controller consists of a robust MPC along with a polynomial extrapolation algorithm and a Kalman filter. The fact that MPC can solve optimization problems online, adapt the new control laws during RTHS using the same model of the system, and simultaneously handle constraints for the system under consideration, indicates that the proposed novel control method is promising for RTHS applications. Polynomial extrapolation was employed to further assist MPC performance, as even small tracking errors can alter the hybrid model's dynamic response. A Kalman filter was used so as to provide MPC with future estimations of the system, in order to derive optimal control laws.

In this paper, the proposed tracking controller formulation was addressed first, followed by two virtual RTHS parametric case studies to assess the performance and robustness of the tracking controller. Dominant parameters of the hybrid model in both case studies were selected and given random perturbations via prescribed probability distributions, varied with at least a 20% coefficient of variation. In each case study, 200 samples were generated from the random parameters and 200 RTHS runs were conducted in order to verify if the proposed tracking controller was robust enough to maintain the desired performance under the introduced uncertainties. Such parameter variations represent potential uncertainties that could be present in real RTHSs. Furthermore, a random disturbance was added in the hybrid model loop along with additional white noise additive to the measured signals. The added disturbance and noise represent systematic or random errors occurring in a real experiment. Since the two case studies were virtual, actuator

models had to be developed in order to simulate actuator dynamics. Two different actuators models were employed in order to assess the tracking controller performance in a wider range of potential experimental equipment. Results from the two case studies illustrate that the proposed tracking controller can guarantee very small time delays and tracking errors under uncertainties that may be introduced in RTHS. Notably, the delays and errors were very close to zero in both case study reference models. Therefore, RTHS using the proposed tracking controller scheme is demonstrated to be effective for structural performance assessment. Ongoing work is focused on implementing the presented case studies in a laboratory and conducting real RTHS using the proposed tracking controller.

DATA AVAILABILITY STATEMENT

The datasets presented in this study can be found in online repositories. The names of the repository/repositories and accession number(s) can be found below: ETH Research Collection, <https://www.research-collection.ethz.ch/handle/20.500.11850/424317>, <https://doi.org/10.3929/ethz-b-000424317>.

AUTHOR CONTRIBUTIONS

NT: conceptualization, methodology, writing. DW and BS: supervision, funding acquisition, and writing. All authors contributed to the article and approved the submitted version.

FUNDING

This project has received funding from the European Union's Horizon 2020 research and innovation programme under the Marie Skłodowska-Curie grant agreement No. 764547. The sole responsibility of this publication lies with the author(s). The European Union is not responsible for any use that may be made of the information contained herein.

REFERENCES

- Bemporad, A., Ricker, N. L., and Morari, M. (2020). *Model Predictive Control Toolbox: Getting Started Guide*. The Math Works.
- Bitsoris, G. (1988). Positively invariant polyhedral sets of discrete-time linear systems. *Int. J. Control* 47, 1713–1726. doi: 10.1080/00207178808906131
- Boyd, S. P., and Vandenberghe, L. (2004). *Convex Optimization*. Cambridge; New York, NY: Cambridge University Press. doi: 10.1017/CBO9780511804441
- Camacho, E. F., and Bordons, C. (2007). "Model predictive control," in *Advanced Textbooks in Control and Signal Processing*, eds M. J. Grimble and M. A. Johnson (London: Springer London), 405. doi: 10.1007/978-0-85729-398-5
- Carroll, J. E., and Spencer, B. F. (2007). *Model-Based Strategies for Real-Time Hybrid Testing*. Technical Report NSEL-006, Newmark Structural Engineering Laboratory. University of Illinois at Urbana-Champaign.
- Chae, Y., Kazemibidokhti, K., and Ricles, J. M. (2013). Adaptive time series compensator for delay compensation of servo-hydraulic actuator systems for real-time hybrid simulation. *Earthq. Eng. Struct. Dyn.* 42, 1697–1715. doi: 10.1002/eqe.2294
- Chen, C., and Ricles, J. M. (2009). Analysis of actuator delay compensation methods for real-time testing. *Eng. Struct.* 31, 2643–2655. doi: 10.1016/j.engstruct.2009.06.012
- Chen, P.-C., Chang, C.-M., Spencer, B. F., and Tsai, K.-C. (2015). Adaptive model-based tracking control for real-time hybrid simulation. *Bull. Earthq. Eng.* 13, 1633–1653. doi: 10.1007/s10518-014-9681-2
- Condori, J., Maghareh, A., Orr, J., Li, H.-W., Montoya, H., Dyke, S., et al. (2020). Exploiting parallel computing to control uncertain nonlinear systems in real-time. *Exp. Techn.* doi: 10.1007/s40799-020-00373-w
- Delbos, F., and Gilbert, J. C. (2003). *Global Linear Convergence of an Augmented Lagrangian Algorithm for Solving Convex Quadratic Optimization Problems*. Technical Report 00071556, INRIA.
- Dyke, S. J., Spencer, B. F., Quast, P., and Sain, M. K. (1995). Role of control-structure interaction in protective system design. *J. Eng. Mech.* 121, 322–338. doi: 10.1061/(ASCE)0733-9399(1995)121:2(322)
- Dyke, S. J., Spencer, B. F., Sain, M. K., and Carlson, J. D. (1998). An experimental study of MR dampers for seismic protection. *Smart Mater. Struct.* 7, 693–703. doi: 10.1088/0964-1726/7/5/012
- Gao, X., Castaneda, N., and Dyke, S. J. (2013). Real time hybrid simulation: from dynamic system, motion control to experimental error. *Earthq. Eng. Struct. Dyn.* 42, 815–832. doi: 10.1002/eqe.2246
- Gao, X. S., and You, S. (2019). Dynamical stability analysis of MDOF real-time hybrid system. *Mech. Syst. Signal Process.* 133:106261. doi: 10.1016/j.ymssp.2019.106261

- Gawthrop, P. J., Wallace, M. I., Neild, S. A., and Wagg, D. J. (2007). Robust real-time substructuring techniques for under-damped systems. *Struct. Control Health Monit.* 14, 591–608. doi: 10.1002/stc.174
- Horiuchi, T. (1996). “Development of a realtime hybrid experimental system with actuator delay compensation,” in *Proc. 11th World Conference on Earthquake Engineering* (Acapulco).
- Ikhoulane, F., and Dyke, S. J. (2007). Modeling and identification of a shear mode magnetorheological damper. *Smart Mater. Struct.* 16, 605–616. doi: 10.1088/0964-1726/16/3/007
- Jung, R.-Y., Benson Shing, P., Stauffer, E., and Thoen, B. (2007). Performance of a real-time pseudodynamic test system considering nonlinear structural response. *Earthq. Eng. Struct. Dyn.* 36, 1785–1809. doi: 10.1002/eqe.722
- Maghareh, A., Dyke, S. J., and Silva, C. E. (2020). A Self-tuning Robust Control System for nonlinear real-time hybrid simulation. *Earthq. Eng. Struct. Dyn.* 49, 695–715. doi: 10.1002/eqe.3260
- Mayne, D. Q., Rawlings, J. B., Rao, C. V., and Scokaert, P. O. M. (2000). Constrained model predictive control: stability and optimality. *Automatica* 36, 789–814. doi: 10.1016/S0005-1098(99)00214-9
- Nakashima, M., Kato, H., and Takaoka, E. (1992). Development of real-time pseudo dynamic testing. *Earthq. Eng. Struct. Dyn.* 21, 79–92. doi: 10.1002/eqe.4290210106
- Neild, S. A., Stoten, D. P., Drury, D., and Wagg, D. J. (2005). Control issues relating to real-time substructuring experiments using a shaking table. *Earthq. Eng. Struct. Dyn.* 34, 1171–1192. doi: 10.1002/eqe.473
- Ning, X., Wang, Z., Zhou, H., Wu, B., Ding, Y., and Xu, B. (2019). Robust actuator dynamics compensation method for real-time hybrid simulation. *Mech. Syst. Signal Process.* 131, 49–70. doi: 10.1016/j.ymssp.2019.05.038
- Ou, G., Ozdagli, A. I., Dyke, S. J., and Wu, B. (2015). Robust integrated actuator control: experimental verification and real-time hybrid-simulation implementation. *Earthq. Eng. Struct. Dyn.* 44, 441–460. doi: 10.1002/eqe.2479
- Phillips, B., and Spencer, B. (2013a). Model-based feedforward-feedback actuator control for real-time hybrid simulation. *J. Struct. Eng.* 139, 1205–1214. doi: 10.1061/(ASCE)ST.1943-541X.0000606
- Phillips, B., and Spencer, B. Jr. (2013b). Model-based multiactuator control for real-time hybrid simulation. *J. Eng. Mech.* 139, 219–228. doi: 10.1061/(ASCE)EM.1943-7889.0000493
- Rawlings, J. B., Mayne, D. Q., and Diehl, M. M. (2017). *Model Predictive Control: Theory, Computation, and Design*, 2nd Edn. Madison, WI: Nob Hill Publishing.
- Rossiter, J. A. (2003). *Model-Based Predictive Control: A Practical Approach*. Control series. Boca Raton, FL: CRC Press.
- Schellenberg, A. H., Mahin, S. A., and Fenves, G. L. (2009). *Advanced Implementation of Hybrid Simulation*. Technical Report PEER 2009/104, Pacific Earthquake Engineering Research Center, University of California, Berkeley, CA.
- Schmid, C., and Biegler, L. T. (1994). Quadratic programming methods for reduced hessian SQP. *Comput. Chem. Eng.* 18, 817–832. doi: 10.1016/0098-1354(94)E0001-4
- Silva, C. E., Gomez, D., Maghareh, A., Dyke, S. J., and Spencer, B. F. (2020). Benchmark control problem for real-time hybrid simulation. *Mech. Syst. Signal Process.* 135:106381. doi: 10.1016/j.ymssp.2019.106381
- Thewalt, C. R., and Mahin, S. A. (1987). *Hybrid Solution Techniques for Generalized Pseudodynamic Testing*. Technical Report UCB/EERC-87/09, Earthquake Engineering Research Center.
- Tøndel, P., Johansen, T. A., and Bemporad, A. (2003). An algorithm for multi-parametric quadratic programming and explicit MPC solutions. *Automatica* 39, 489–497. doi: 10.1016/S0005-1098(02)00250-9
- Tsouroukdissian, A. R., Ikhoulane, F., Rodellar, J., and Luo, N. (2008). Modeling and identification of a small-scale magnetorheological damper. *J. Intell. Mater. Syst. Struct.* 20, 825–835. doi: 10.1177/1045389X08098440
- Wagg, D. J., and Stoten, D. P. (2001). Substructuring of dynamical systems via the adaptive minimal control synthesis algorithm. *Earthq. Eng. Struct. Dyn.* 30, 865–877. doi: 10.1002/eqe.44
- Wallace, M., Wagg, D., and Neild, S. (2005). An adaptive polynomial based forward prediction algorithm for multi-actuator real-time dynamic substructuring. *Proc. R. Soc. A* 461, 3807–3826. doi: 10.1098/rspa.2005.1532
- Wallace, M. I., Sieber, J., Neild, S. A., Wagg, D. J., and Krauskopf, B. (2005). Stability analysis of real-time dynamic substructuring using delay differential equation models. *Earthq. Eng. Struct. Dyn.* 34, 1817–1832. doi: 10.1002/eqe.513
- Zafiriou, E. (1990). Robust model predictive control of processes with hard constraints. *Comput. Chem. Eng.* 14, 359–371. doi: 10.1016/0098-1354(90)87012-E
- Zhao, J., French, C., Shield, C., and Posbergh, T. (2003). Considerations for the development of real-time dynamic testing using servo-hydraulic actuation. *Earthq. Eng. Struct. Dyn.* 32, 1773–1794. doi: 10.1002/eqe.301

Conflict of Interest: The authors declare that the research was conducted in the absence of any commercial or financial relationships that could be construed as a potential conflict of interest.

Copyright © 2020 Tsokanas, Wagg and Stojadinović. This is an open-access article distributed under the terms of the Creative Commons Attribution License (CC BY). The use, distribution or reproduction in other forums is permitted, provided the original author(s) and the copyright owner(s) are credited and that the original publication in this journal is cited, in accordance with accepted academic practice. No use, distribution or reproduction is permitted which does not comply with these terms.



Online Stability Analysis for Real-Time Hybrid Simulation Testing

Cristóbal Gálmez and Gastón Fernandois*

Departamento de Obras Civiles, Universidad Técnica Federico Santa María, Santiago, Chile

OPEN ACCESS

Edited by:

Wei Song,
University of Alabama, United States

Reviewed by:

Amin Maghareh,
Purdue University, United States
Cheng Chen,
San Francisco State University,
United States

*Correspondence:

Gastón Fernandois
gaston.fernandois@usm.cl

Specialty section:

This article was submitted to
Earthquake Engineering,
a section of the journal
Frontiers in Built Environment

Received: 29 April 2020

Accepted: 22 July 2020

Published: 25 August 2020

Citation:

Gálmez C and Fernandois G (2020)
Online Stability Analysis for Real-Time
Hybrid Simulation Testing.
Front. Built Environ. 6:134.
doi: 10.3389/fbuil.2020.00134

Real-time hybrid simulation (RTHS) is an experimental technique where a critical element of a structural system is tested in the laboratory while the rest is represented through numerical simulations. A challenging aspect of this technique is the correct application of boundary conditions on the experimental substructure using actuators and sensors. The inherent dynamics of an actuator and its interaction with the physical specimen causes a time delay between commanded and measured displacements. It has been shown that delay in RTHS affects the accuracy of an experiment and even can cause instability. Therefore, to avoid stability problems, a proper partitioning choice and an appropriate compensation method for actuator dynamics should be considered. However, there will always be uncertainty in the experimental structure's behavior, so it is essential to check the system's stability during the test execution. In this paper, a stability analysis using energy methods is performed to develop an online stability indicator for the RTHS test. This indicator's goal is to detect stability problems before it can cause excessive displacements in the system, thus avoiding damage in the physical specimen or the laboratory equipment. The effectiveness of the proposed online stability indicator is demonstrated through numerical simulations taking into account the virtual RTHS benchmark problem with different compensation strategies. The proposed indicator is an excellent tool to monitor the RTHS test, improving the reliability of the experimental test while maintaining the safety of the laboratory resources.

Keywords: real-time hybrid simulation, stability analysis, energy methods, delay, negative damping

1. INTRODUCTION

Laboratory tests are essential to study structural systems' behavior, calibrate mathematical models, and develop robust design methods to achieve economic and safe structures. In the case of seismic tests, the most realistic experimental technique is the shake table test. However, these experiments are very challenging for full-scale systems, not only for the laboratory requirements in terms of equipment and capacity but also for the manufacturing costs and time required to build each specimen to be tested. Alternatively, another technique called real-time hybrid simulation (RTHS) has proven to be a cost-effective and reliable approach to conducting seismic performance assessment.

Real-time hybrid simulation (RTHS) is an experimental technique for structural testing. A critical component is studied in the laboratory, while a numerical model represents the rest of the structural system (Nakashima et al., 1992). Representing the numerical part of the structure reduces the costs of each experiment considerably. The technique involves solving the equation of motion

(EOM) of the numerical substructure with an integration algorithm, then imposing the calculated displacements over the experimental substructure using a transfer system (i.e., actuators). The experimental restoring forces are measured and incorporated into the equation of motion to calculate the displacement at the following time step (McCrum and Williams, 2016).

The synchronization in the boundary between numerical and experimental substructures is one of the biggest challenges of RTHS. The dynamic properties of the transfer system produce amplitude and delay errors between commanded and measured displacements. This effect not only depends on actuator properties but also on the interaction with the physical specimen (Dyke et al., 1995). The delay errors are the most harmful for RTHS because it has been proved that delay is equivalent to introducing negative damping to the hybrid system (Horiuchi et al., 1999), which affects the accuracy of the experiment and even can cause instability in the experimental setup. Several authors have studied the effect of delay in RTHS. Wallace et al. (2005a) performed a stability analysis with analytical delay differential equations. Mercan and Ricles (2008) considered pseudo-delay techniques for determining the size of delay to initiate instability. Maghareh et al. (2017) established a predictive stability indicator, demonstrating that some partitioning choices are more sensitive to delay than others. Gao and You (2019) proposed generalized EOM for the hybrid system to predict the RTHS stability limit. All of these methodologies are useful to evaluate different partitioning choices, avoiding cases susceptible to instability. However, three significant limitations are identified: (i) methodologies above were developed for linear systems; (ii) they require knowledge of the dynamic properties of experimental substructure to determine critical delay values; and (iii) these tools are used to assess the stability of the test offline before a simulation, so they cannot be implemented to check the stability online during the RTHS testing.

On the other hand, to minimize the synchronization errors and improve the accuracy of the test, several compensation methods have been proposed in the literature; for example, polynomial extrapolation (Horiuchi et al., 1999) or model-based compensation (Carrion and Spencer, 2007; Gao et al., 2013). More sophisticated techniques are known as adaptive compensation (Wallace et al., 2005b; Bonnet et al., 2007), where the control parameters are adjusted during the RTHS to improve synchronization. Meanwhile, methods such as Tao and Mercan (2019) or Xu W. et al. (2019) are based on a frequency domain analysis to adjust parameters of a first-order transfer function. Other methods like Chae et al. (2013) or Palacio-Betancur and Gutierrez Soto (2019) estimate the plant through Taylor series expansion and adjust the parameters in the time domain. Different approaches consider polynomial extrapolation, such as Wang et al. (2019) or Xu D. et al. (2019). Adaptive model-based compensation (Chen et al., 2015) found in this paper consists of an estimate of the plant in frequency-domain; then, compensation is implemented in time-domain using numeric derivatives of the commanded signal and adaptation based on gradient.

Even with an appropriate compensation method, it is possible to observe synchronization errors due to uncertainty or non-linear behavior in the experimental substructure; therefore, it is necessary to monitor the performance of an RTHS test for safety purposes in a quantitative manner. Additionally, it is worth mentioning that a response of the reference structure is not always available in RTHS, so it is not trivial to evaluate the experimental response's reliability during the test.

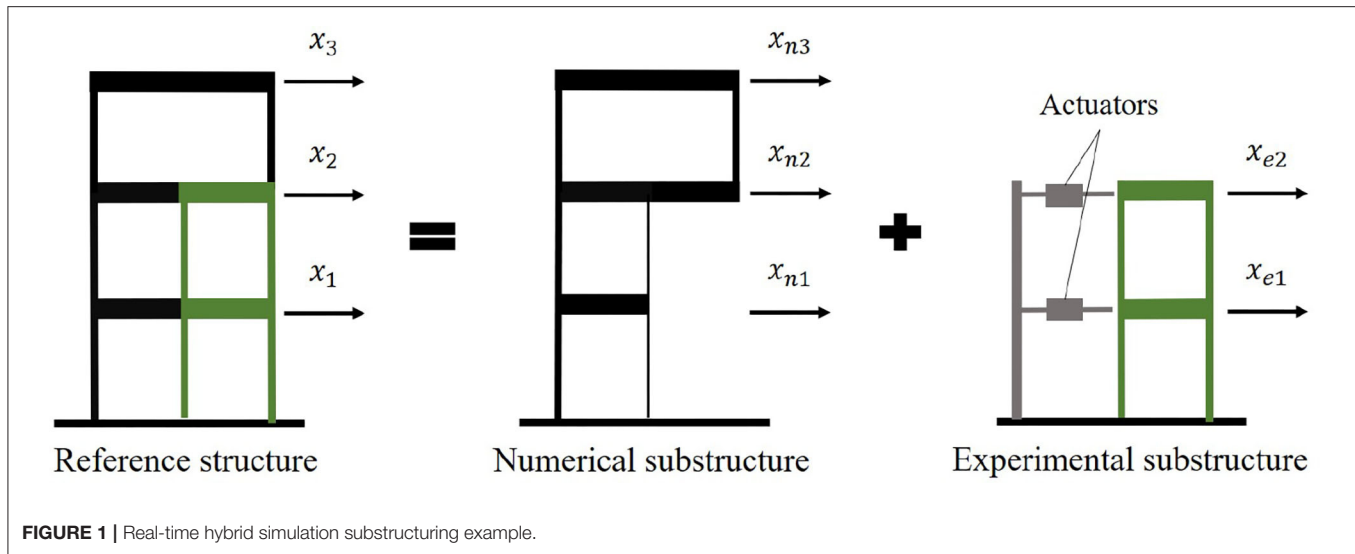
Some studies are available in the literature where online indicators are proposed for hybrid simulation tests. Guo et al. (2014) proposed the *Frequency Evaluation Index* (FEI) to evaluate the tracking performance of an actuator in the frequency domain. Besides, FEI can be implemented online using a moving window Fast Fourier Transform (FFT) (Xu W. et al., 2019). Although FEI could be used to measure synchronization errors quantitatively, it does not measure the effect of this delay on the hybrid system's stability. Meanwhile, Ahmadizadeh and Mosqueda (2009) proposed the *Energy Error Indicator* (EEI), which can be implemented online to measure the accumulated errors in RTHS. Although experimental errors can trigger instability in a hybrid system, there is no way to determine which level of EEI is associated with instability. Thus, the EEI is not efficient if the goal is to detect instability rather than errors.

This study presents a hybrid system stability analysis using energy methods to develop a stability indicator that can be evaluated online during the RTHS test. The proposed indicator aims to detect instability before it can cause excessive displacements in the system that can damage the physical specimen or the laboratory equipment. The structure of this study is the following: Section 2 presents the methodology of the proposed indicator. Section 3 describes the virtual RTHS benchmark problem (Silva et al., 2020), which is a well-recognized and representative testbed to simulate realistic RTHS experiments by the hybrid simulation community (Dyke et al., 2020). This benchmark problem was considered as an example of the implementation and validation of the proposed stability indicator. Adaptive model-based compensation (Chen et al., 2015), with some modifications (Ferandois et al., 2020), is employed with different control parameters to show the effectiveness of the proposed indicator in unfavorable scenarios. Section 4 provides the results of different simulations, demonstrating the capacity of the proposed indicator to detect instability early. Finally, section 5 discusses the principal findings and final remarks of this study.

2. METHODOLOGY

2.1. Substructuring in RTHS

Consider a reference structure subjected to a ground acceleration as shown in **Figure 1**. The reference structure is separated into a numerical substructure and a experimental substructure. The boundary conditions of the common degrees of freedom at the interface between substructures are imposed by actuators over the experimental substructure. In terms of equations, the substructuring is described as follow. The equation of motion (EOM) of the reference structure (subscript r) is expressed as:



$$M_r \ddot{x}(t) + C_r \dot{x}(t) + K_r x(t) = -M_r \Gamma \ddot{u}_g(t) \quad (1)$$

where M_r , K_r , and C_r are the mass, stiffness, and damping matrices, respectively. $x(t)$, $\dot{x}(t)$, and $\ddot{x}(t)$ are the displacement, velocity, and accelerations vectors, respectively, all measured relative to the ground motion. $\ddot{u}_g(t)$ is the ground acceleration, and Γ is the seismic influence vector.

The reference structure is separated into a numerical (subscript n) and a experimental (subscript e) substructures, as shown in Equation (2):

$$(M_n + M_e) \ddot{x}(t) + (C_n + C_e) \dot{x}(t) + (K_n + K_e) x(t) = -(M_n + M_e) \Gamma \ddot{u}_g(t) \quad (2)$$

Then, the EOM of the numerical substructure can be rewritten as shown in Equation (3), including the earthquake equivalent forces of the experimental substructure:

$$M_n \ddot{x}_n(t) + C_n \dot{x}_n(t) + K_n x_n(t) = -(M_n + M_e) \Gamma \ddot{u}_g(t) - F_e(t) \quad (3)$$

where $x_n(t)$, $\dot{x}_n(t)$, and $\ddot{x}_n(t)$ corresponds to the displacement, velocity, and acceleration of the numerical substructure, all relative to the ground motion. Meanwhile, F_e corresponds to the feedback forces from the experimental substructure described in Equation (4):

$$F_e(t) = M_e \ddot{x}_e(t) + C_e \dot{x}_e(t) + K_e x_e(t) \quad (4)$$

where $x_e(t)$, $\dot{x}_e(t)$, and $\ddot{x}_e(t)$ corresponds to the experimental displacement, velocity, and acceleration of the experimental substructure, and in the ideal case, the actuators imposes $x_e = x_n$. However, in an RTHS test, the experimental displacements are not necessarily equal to the numerical displacements due to synchronization errors introduced by the transfer system and interaction with the experimental substructure (Dyke et al., 1995).

2.2. Energy Balance

Consider that the numerical substructure is an isolated system subjected to two external forces: (i) earthquake equivalent forces; and (ii) experimental feedback forces. Assuming that an appropriate numerical integration method is implemented, so that the calculated numerical substructure response is numerically stable (Chen et al., 2009; Bas and Moustafa, 2020), the equation of motion of the numerical substructure can be expressed as an energy balance, allowing to focus the stability analysis on the interaction between hybrid substructures due to experimental errors. If numerical substructure matrices M_n , C_n , K_n are symmetric; the energy balance can be obtained by taking the inner product with an infinitesimal numerical displacement trajectory, dx_n , and then integrating both sides of Equation (3) over the displacement trajectory:

$$\int \ddot{x}_n^T M_n dx_n + \int \dot{x}_n^T C_n dx_n + \int x_n^T K_n dx_n = \int -\ddot{u}_g \Gamma^T M_r dx_n + \int -F_e^T dx_n \quad (5)$$

Equation (3) can be later expressed as a scalar equation as shown in Equation (6):

$$E_k + E_d + E_s = W_I + W_F \quad (6)$$

where E_k , E_d , and E_s are the kinetic, dissipated and strain energy of numerical substructure, respectively, as described in Equation (7):

$$E_k = \int \ddot{x}_n^T M_n dx_n; \quad E_d = \int \dot{x}_n^T C_n dx_n; \quad E_s = \int x_n^T K_n dx_n \quad (7)$$

meanwhile, W_I is the work done by the earthquake forces (namely as input work), and W_F is the work done by the experimental forces (namely as feedback work):

$$W_I = \int -\ddot{u}_g \Gamma^T M_r dx_n; \quad W_F = \int -F_e^T dx_n \quad (8)$$

It is worth mentioning that the energy balance from Equation (6) must be fulfilled during a test even if the experimental force is delayed, and the hybrid system is unstable. In this sense, the feedback force is just another external excitation supplied over the numerical substructure.

2.3. Proposed Stability Indicator

When a hybrid system becomes unstable, the mechanical energy of both substructures will grow exponentially even if the earthquake signal goes zero. This issue could happen if the experimental substructure introduces additional energy to the numerical substructure. Horiuchi et al. (1999) demonstrated that delay causes negative damping in the hybrid system, which is equivalent to adding external energy to the hybrid system. It is desirable to detect this problem before the mechanical energy grows up at levels that can damage the experimental equipment.

During an RTHS test, it is expected that the mechanical energy of the numerical substructure increases, because the earthquake forces introduces energy to the system, but the mechanical energy should not be greater than the input work. Reordering Equation (6) and grouping E_k and E_s in mechanical energy E_{mec} , Equation (9) is obtained:

$$W_I - E_{mec} = E_d - W_F \quad (9)$$

If the feedback work, W_F , gets bigger than the dissipated energy E_d , the right side of Equation (9) becomes negative. Due to the energy balance, the left side becomes negative and indicates that mechanical energy gets bigger than the input energy. Thus, when the hybrid system's inherent dissipated energy is insufficient to counteract the added energy from the feedback force, the system will become unstable.

Therefore, the proposed analysis consists in comparing the feedback work with the dissipated energy through an indicator described in Equation (10):

$$SW = \frac{W_F}{E_d + C_{SW}} H(W_F) \cdot 100\% \quad (10)$$

where SW is called the *Stability Warning Indicator*, and $H(\cdot)$ is the Heaviside function used to compute SW only when W_F is positive. Notice that the dissipated energy is always strictly positive (i.e., $E_d > 0$); hence, $E_d - W_F$ could be negative only if W_F is positive. Meanwhile, C_{SW} is a constant chosen to prevent large values of SW when the test starts (i.e., when E_d is close to zero). Notice that $E_d = 0$ at $t = 0$ (i.e., before the earthquake starts), so C_{SW} should be a constant selected that is bigger enough to make the denominator to be non-zero in the SW and to prevent large values of SW if W_F is dominated by noise in the force measurements. Moreover, C_{SW} should be small enough, so the SW denominator would be dominated by the E_d term during and after the earthquake. As a recommendation, both conditions could be satisfied if C_{SW} is selected as two magnitude orders below the maximum input work over the structural system. It is worth mentioning that this input work can not be calculated before the test since the complete hybrid system's response is unknown. However, an offline estimation of the input work magnitude order is enough to select a proper C_{SW} .

The explanation of the SW values is provided herein. When $SW = 0\%$, due to negative values of W_F , there is no risk of instability because the experimental substructure is removing energy from the numerical substructure. Next, if $0\% < SW < 100\%$, the experimental substructure is adding energy; but, the damping of the numerical substructure is enough to counter this effect. Finally, if $SW \geq 100\%$, then the numerical substructure's mechanical energy overcomes the input work, causing instability.

The main difference between EEI and SW indicators is that the former evaluates simulation accuracy when affected by synchronization errors, and the latter is focused on assessing the stability of the hybrid system. For example, if a hybrid system presents a significant delay in the transfer system, the experimental errors will cause the experimental substructure to add energy to the numerical substructure. Nevertheless, if the numerical substructure has enough damping to maintain the system stable, the SW will be $< 100\%$; meanwhile, EEI will show large values due to the synchronization errors produced by the delay.

3. NUMERICAL APPLICATION

3.1. Benchmark Problem

The virtual RTHS benchmark problem from Silva et al. (2020) is considered as a practical example to prove the capacity of the proposed indicator to detect instability. This problem consists of a three-story moment frame with three lateral degrees of freedom as the reference structure (see **Figure 2**). This structure is separated into a 3DOF numerical substructure and an SDOF experimental substructure.

The reference structure properties are: mass per floor $m = 1,000$ kg; natural frequencies $f = [3.61, 16.00, 38.09]$ Hz; and modal damping $\zeta = 3\%$ for each mode. These properties corresponds to Case IV from Silva et al. (2020). The reference structure is partitioned as described in Equation (11):

$$M_r = M_n + M_e; \quad C_r = C_n + C_e; \quad K_r = K_n + K_e \quad (11)$$

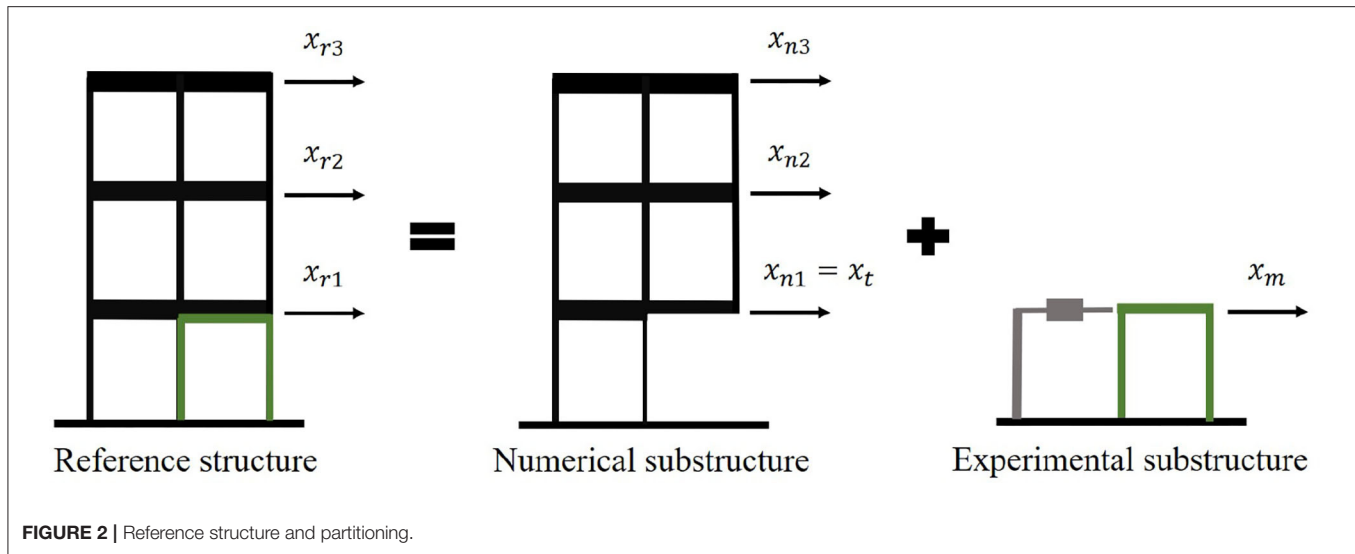
where $M_e = \text{diag}(m_e, 0, 0)$; $C_e = \text{diag}(c_e, 0, 0)$; and $K_e = \text{diag}(k_e, 0, 0)$. The structural properties of the experimental substructure are $m_e = 29.1$ kg; $c_e = 114.6$ Nsec/m; and $k_e = 1.19 \times 10^6$ N/m.

The reference structure and the numerical substructure are implemented in the state-space form using Simulink for direct integration. The solver utilized is a 4th Order Runge-Kutta with a fixed time step of $\Delta t = 1/4,096$ s. The reference structure model is presented in Equations (12) and (13) with ground acceleration as input and reference displacements as output.

$$\begin{Bmatrix} \dot{x}_r \\ \ddot{x}_r \end{Bmatrix} = \begin{bmatrix} 0 & I \\ -M_r^{-1}K_r & -M_r^{-1}C_r \end{bmatrix} \begin{Bmatrix} x_r \\ \dot{x}_r \end{Bmatrix} + \begin{bmatrix} 0 \\ -I \end{bmatrix} \ddot{u}_g \quad (12)$$

$$\begin{Bmatrix} x_r \\ \dot{x}_r \end{Bmatrix} = [I \ 0] \begin{Bmatrix} x_r \\ \dot{x}_r \end{Bmatrix} + [0] \ddot{u}_g \quad (13)$$

The numerical substructure model is presented in Equations (14) and (15) with ground acceleration and experimental force as



inputs and numerical displacements, velocities, and accelerations as outputs.

$$\begin{Bmatrix} \dot{x}_n \\ \ddot{x}_n \end{Bmatrix} = \begin{bmatrix} 0 & I \\ -M_n^{-1}K_n & -M_n^{-1}C_n \end{bmatrix} \begin{Bmatrix} x_n \\ \dot{x}_n \end{Bmatrix} + \begin{bmatrix} 0 & 0 \\ -M_n^{-1}M_r\Gamma & -M_n^{-1}\gamma \end{bmatrix} \begin{Bmatrix} \ddot{u}_g \\ f_e \end{Bmatrix} \quad (14)$$

$$\begin{Bmatrix} x_n \\ \dot{x}_n \\ \ddot{x}_n \end{Bmatrix} = \begin{bmatrix} I & 0 \\ 0 & I \\ -M_n^{-1}K_n & -M_n^{-1}C_n \end{bmatrix} \begin{Bmatrix} x_n \\ \dot{x}_n \end{Bmatrix} + \begin{bmatrix} 0 & 0 \\ 0 & 0 \\ -M_n^{-1}M_r\Gamma & -M_n^{-1}\gamma \end{bmatrix} \begin{Bmatrix} \ddot{u}_g \\ f_e \end{Bmatrix} \quad (15)$$

where $\gamma = [1; 0; 0]^T$ and f_e is experimental force calculated as shown in Equation (16):

$$f_e = k_e x_m + c_e \dot{x}_m + m_e \ddot{x}_m \quad (16)$$

and x_m , \dot{x}_m , and \ddot{x}_m are the measured displacement, velocity and acceleration imposed on the experimental substructure.

To compute the Stability Warning Indicator (SW) it is necessary to evaluate different energy terms using numerical integration. To calculate the accumulated energy $E[j]$ of a force $P[i]$ over a displacement increment $\Delta x[i]$, $\forall i \in [1, j]$, a trapezoidal rule is formulated in Equation (17):

$$E[j] = \sum_{i=1}^j \frac{1}{2} (P[i] + P[i-1]) (x[i] - x[i-1]) \quad (17)$$

This integration method is implemented in Simulink, as shown in the block diagram of **Figure 3**, where Discrete Finite Impulse Response (FIR) Filters and Product blocks are employed to obtain the area of each trapezoid, and a Discrete-time Integrator block is required to obtain the accumulation over time. In the case of W_F the input force is $P = f_e$ and the input displacement is $x = x_n^{(1)}$

(scalar signals); meanwhile, to evaluate E_d , the input forces are $P = C_n \dot{x}_n$ and the displacements are $x = x_n$ (vector signals).

Additionally, to compare the proposed stability indicator, the EEI (Ahmadizadeh and Mosqueda, 2009) is calculated for each simulation. The EEI can be obtained as follow:

$$EEI = \frac{W_I - (E_k^* + E_d^* + E_s - W_{exp})}{W_I + E_E^{max}} \quad (18)$$

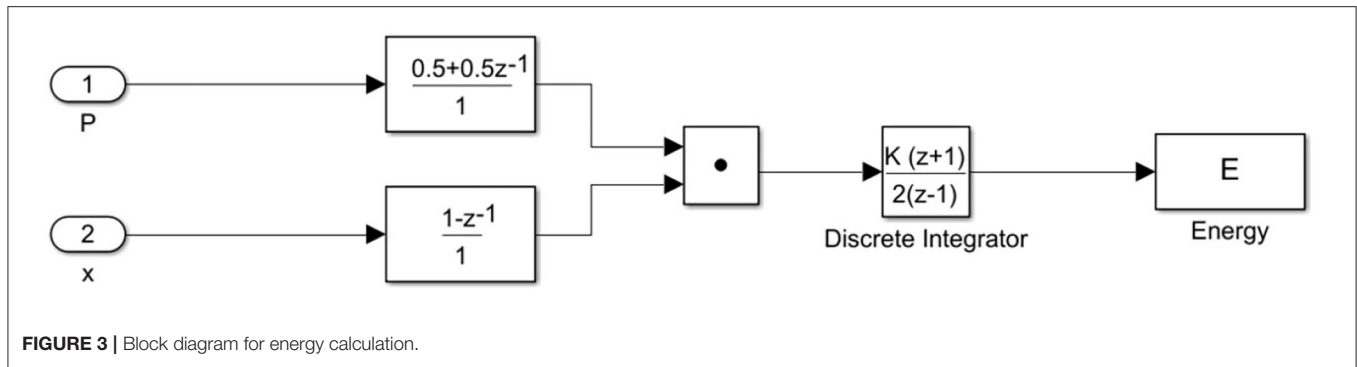
where E_k^* , E_d^* are the kinetic and dissipated energy calculated with the first derivative of displacement instead of velocity of numerical substructure. E_E^{max} is a nonzero elastic energy term utilized to normalize EEI when W_I is close to zero at the beginning of the test. It is important to declare that non-compensated delay implies added energy to the system, resulting in negative values of EEI . W_{exp} is the work done by experimental force over the measured displacement as shown in Equation (19):

$$W_{exp} = \int -f_e^T dx_m \quad (19)$$

In this study, the reference structure is subjected to the Kobe earthquake with a peak ground acceleration (PGA) scaled to 40%, and the maximum input work from the earthquake is around 100 Joules. This value can be computed from the integration of the reference structure. In a real RTHS experiment, the magnitude order of the input energy can be estimated from the ground motion and global properties of the structure, such as total mass and approximated damping and stiffness. Therefore, the denominator constants are selected considerably smaller, such as 1% of the maximum input work:

$$E_E^{max} = C_{SW} = 1 \text{ Joule} \quad (20)$$

This value is bigger enough to prevent large values for each indicator at the beginning of the earthquake. Also, these constants will have a negligible effect on each indicator during and after the earthquake, since C_{SW} will be relatively small



compared with E_d in the denominator of Equation (10), just like E_E^{max} will be smaller than W_I in the denominator of Equation (18).

3.2. Critical Delay Estimation

Before conducting the RTHS simulations with different delay values, an estimation of the critical delay is obtained with the method proposed by Gao and You (2019). This method consists in constructing the EOM of the hybrid system with some assumptions synchronization errors (delay and amplitude errors). The EOM of the hybrid system has the following equivalent mass, damping, and stiffness:

$$M_{eq} = M_n \Phi \Phi^{-1} + M_e \Phi \Delta \Phi^{-1} - C_e \Phi \Delta \delta \Phi^{-1} \quad (21)$$

$$C_{eq} = C_n \Phi \Phi^{-1} + M_e \Phi \Delta \omega^2 \delta \Phi^{-1} + C_e \Phi \Delta \Phi^{-1} - K_e \Phi \Delta \delta \Phi^{-1} \quad (22)$$

$$K_{eq} = K_n \Phi \Phi^{-1} + K_e \Phi \Delta \Phi^{-1} \quad (23)$$

where Φ is the modal matrix of the reference system, ω is a diagonal matrix with the natural frequencies of the reference system, δ is a diagonal matrix with the delay for each mode, and Δ is a diagonal matrix with the amplitude error for each mode. With the equivalent properties of the hybrid system, the state matrix A_{eq} is constructed as shown in Equation (24):

$$A_{eq} = \begin{bmatrix} 0 & I \\ -M_{eq}^{-1}K_{eq} & -M_{eq}^{-1}C_{eq} \end{bmatrix} \quad (24)$$

The hybrid system is stable if the matrix A_{eq} has eigenvalues with negative real part; thus, the critical delay can be obtained by searching the minimum constant delay that produces eigenvalues with positive real part. For the partitioning of this problem, assuming $\Delta = I$ and $\delta = \text{diag}(\tau_{cr}; \tau_{cr}; \tau_{cr})$, the critical delay is:

$$\tau_{cr} = 8.5 \text{ msec} \quad (25)$$

This critical delay serves as a reference for the simulations with constant delay. It is expected that simulations with delays smaller than this critical value would remain stable while running the simulations. In contrast, the opposite will result in an unstable response.

4. RESULTS

4.1. RTHS With Constant Delay

The Simulink block diagram for the simulations with constant delay is presented in **Figure 4**, where the output of the numerical substructure, denoted as “target vector,” is defined as $x_t = [x_n^{(1)}; \dot{x}_n^{(1)}; \ddot{x}_n^{(1)}]^T$ (displacement, velocity and acceleration of first degree of freedom). Then, the Delay block generates a discrete delay of the input signal x_t by a specified number of samples d , so the time delay τ is a multiple of the simulation time step. Then, the delayed boundary conditions are:

$$x_d = [x_n^{(1)}(t - \tau); \dot{x}_n^{(1)}(t - \tau); \ddot{x}_n^{(1)}(t - \tau)]^T \quad (26)$$

Finally, the outputs of experimental substructure are described in Equations (27) and (28):

$$x_m = x_n^{(1)}(t - \tau) \quad (27)$$

$$f_e = [k_e; c_e; m_e] x_d \quad (28)$$

Four simulations are performed with different delay values from 0 to 9 ms. The structure is subjected to the Kobe earthquake with a peak ground acceleration (PGA) scaled to 40%. The measured displacement of experimental substructure x_m is compared with the first degree of freedom displacement x_{r1} from the reference structure, as shown in **Figure 5**. Measured displacements are very close to reference displacements for lower values of delay ($\tau = 0$ ms and $\tau = 0.98$ ms). Then, for higher delay $\tau = 7.1$ ms, a notorious synchronization error in displacements appear, but at least the measured displacement decays at the end of the simulation. This does not happen with $\tau = 9$ msec $> \tau_{cr}$, where the measured displacement grows exponentially after the earthquake reaches zero.

In **Figure 6**, the error of displacement x_m respect to x_{r1} for each delay is presented, including the normalized root mean square error (NRMSE) for each case. Clearly, for $\tau = 0$ ms and $\tau = 0.98$ ms, the system is stable; while, for $\tau = 9$ ms is unstable (i.e., error grows exponentially). However, for $\tau = 7.1$ ms, the error is considerable, with $NRSME = 144\%$, but the system is still stable. It is easy to classify the case with $\tau = 9$ ms as unstable after

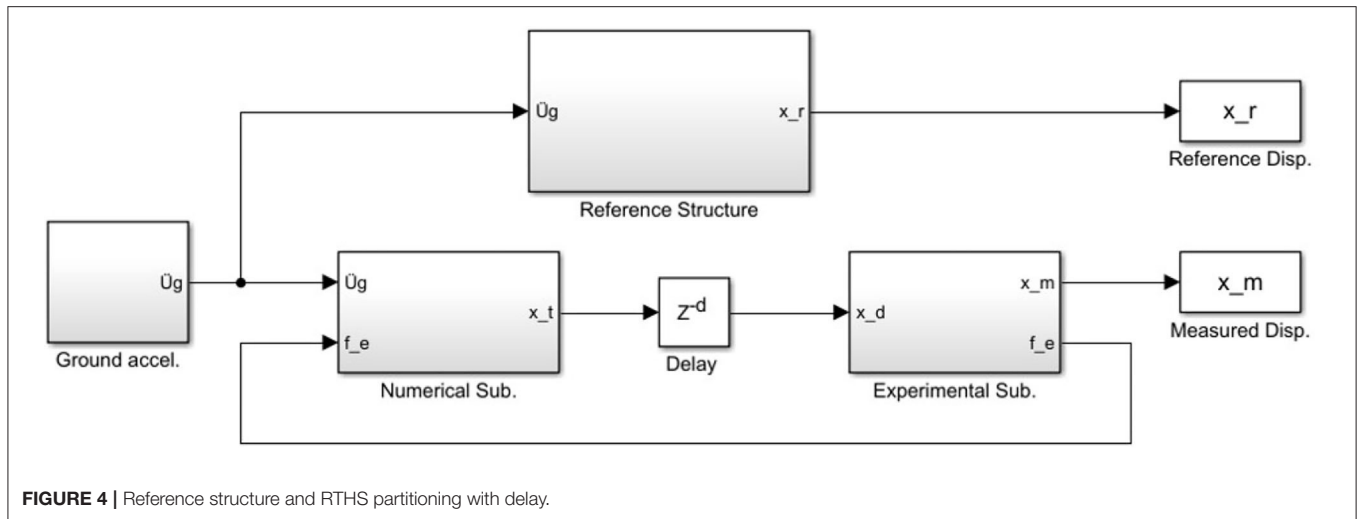


FIGURE 4 | Reference structure and RTHS partitioning with delay.

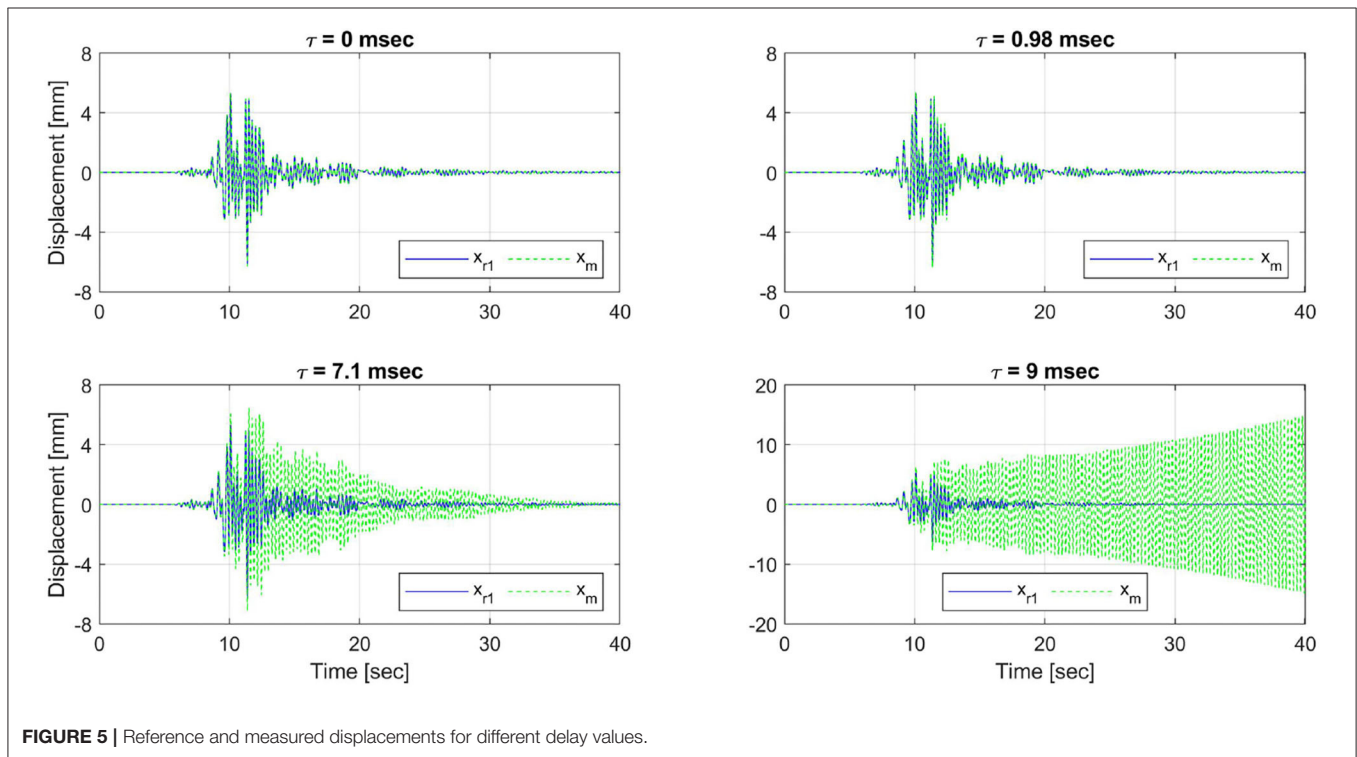


FIGURE 5 | Reference and measured displacements for different delay values.

the test. Still, it would be beneficial to detect unstable behavior before the system reaches a large response.

In Figure 7, the SW indicator is calculated for each model scenario. For $\tau = 0$ ms, $\tau = 0.98$ ms, and $\tau = 7.1$ ms, the indicator stays under 100% during the entire test, showing the stable behavior of each simulation. In contrast, for the unstable case with $\tau = 9$ ms, the indicator exceeds 100% near 10 s of simulation, much earlier than the instant when the system reaches the large displacements presented in Figure 5. Thus, the SW indicator could help stop the simulation in time, avoiding any dangerous behavior in the RTHS test.

For the sake of comparison, Figure 8 shows the absolute value of EEI for each case scenario. The EEI grows up with higher values of delay but is not evident in which case is stable and in which it is not. For $\tau = 0$ ms, the EEI values are relatively small. Moreover, for $\tau = 0.98$ ms, the EEI stays under 15% during the test; both cases are indeed stable. However, for $\tau = 7.1$ ms, the behavior of EEI is similar to $\tau = 9$ ms before 15 s of simulation, so it is not possible to detect instability until the earthquake signal dies out. If the EEI is utilized to stop unstable testing, it is quite challenging to define a threshold that relates EEI with instability. For example, for a threshold of $EEI = 100\%$, the simulations

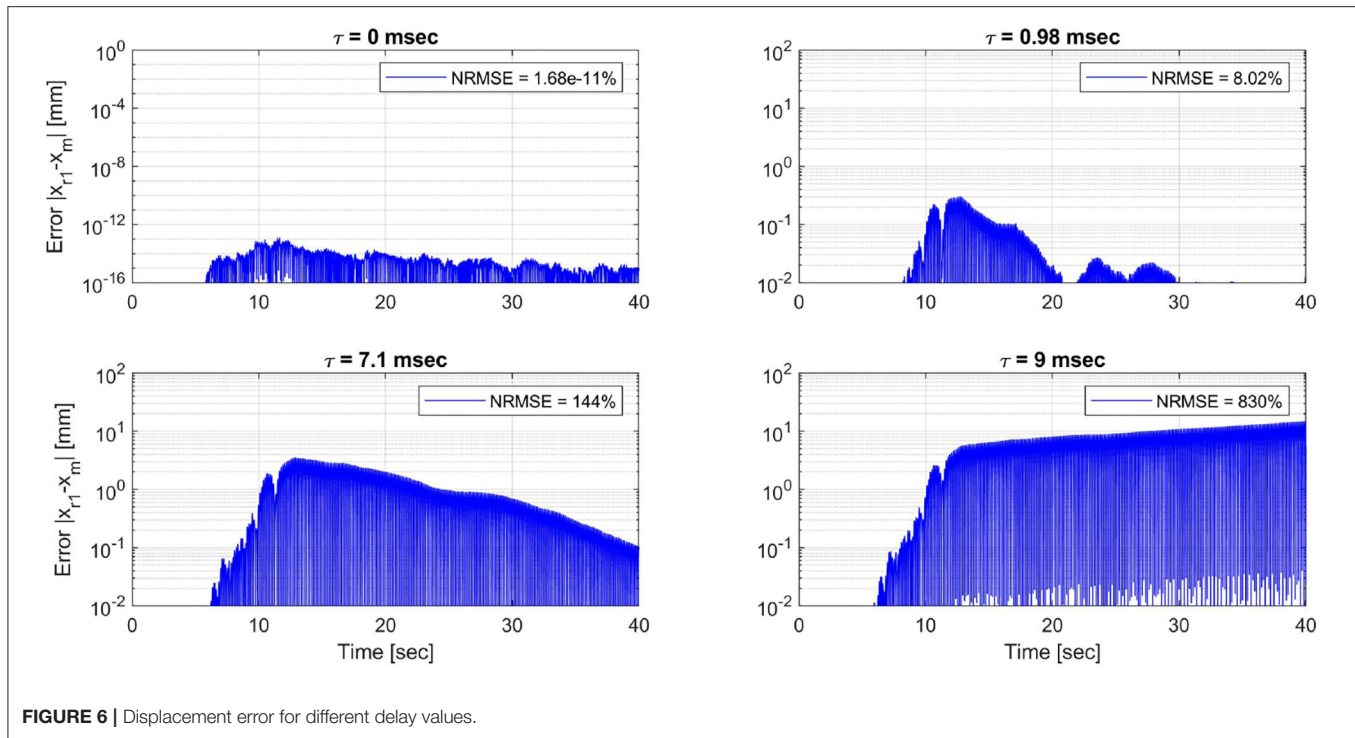


FIGURE 6 | Displacement error for different delay values.

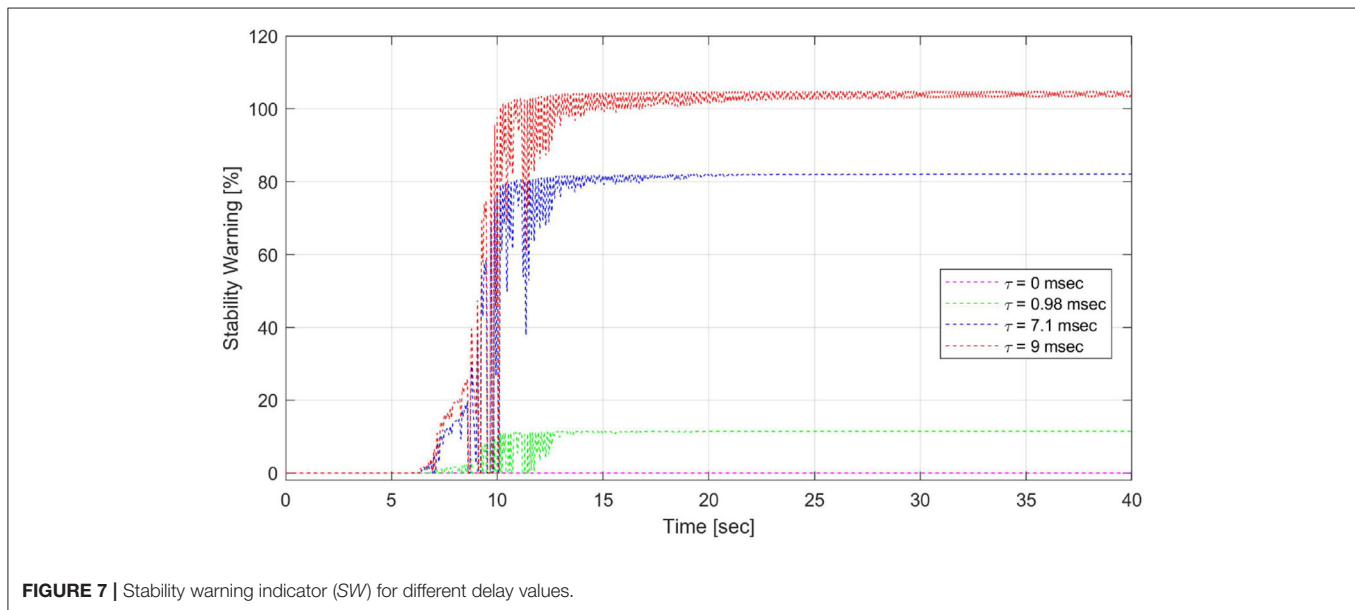


FIGURE 7 | Stability warning indicator (SW) for different delay values.

with $\tau = 7.1$ ms and $\tau = 9$ ms should be stopped before 10 sec, even when the simulation with $\tau = 7.1$ ms is stable and does not present any risk of large displacements. Nevertheless, it must be recognized that *EEI* is an excellent tool to assess the accuracy of the results from an RTHS test through a post-processing analysis.

4.2. RTHS With Actuator Model and Dynamic Compensation

In this subsection, the same partitioning as in the previous subsection is utilized, but in this case a transfer system is

modeled as presented in Silva et al. (2020), and adaptive compensation with different design parameters is implemented to minimize the errors produced by the transfer system. The block diagram utilized to model this problem in Simulink is presented in Figure 9, where the output of the numerical substructure is the target displacement $x_t = x_n^{(1)}$ (displacement of first degree of freedom). Then, the target displacement is sent to the adaptive controller to determine the commanded displacement for the actuator. The plant (i.e., actuator connected to the experimental substructure)

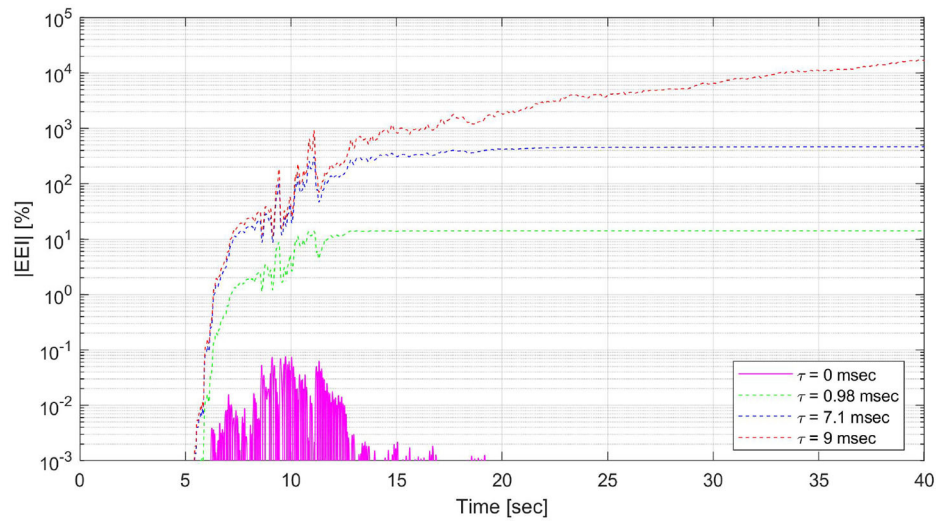


FIGURE 8 | Energy error indicator (EE) for different delay values.

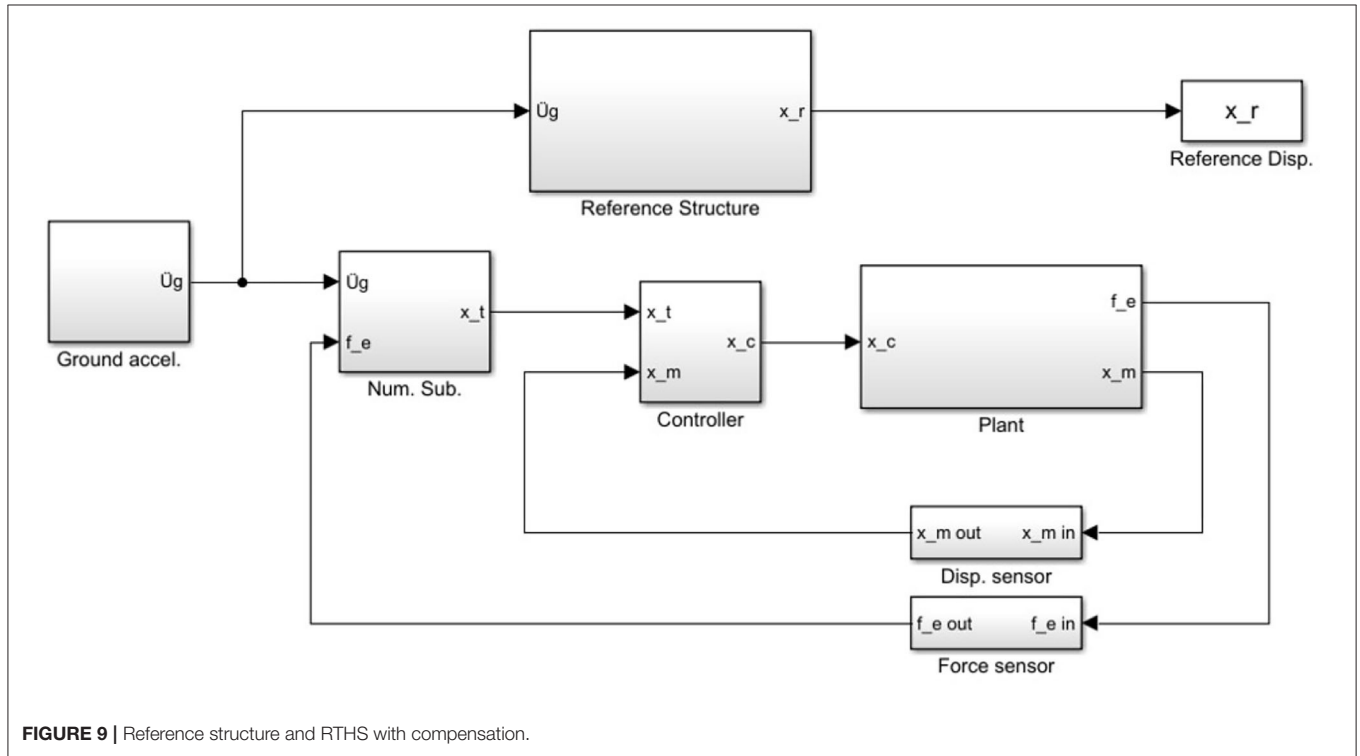


FIGURE 9 | Reference structure and RTHS with compensation.

is modeled with the transfer function presented in Equation (29), which includes actuators parameters and interaction with the experimental substructure, and relates the commanded displacement x_c with the measured displacement x_m :

$$x_m = \frac{2.19 \times 10^{13}}{(29.1)s^5 + (1.26 \times 10^4)s^4 + (8.42 \times 10^6)s^3 + (2.33 \times 10^9)s^2 + (5.44 \times 10^{11})s + (2.17 \times 10^{13})} x_c \quad (29)$$

where $s = i\omega$, is the Laplace variable, i is the complex number and ω is the circular frequency. This transfer function has a frequency-dependent phase. The phase is another way to state that the measured and commanded displacements are

delayed. Thus, the delay is frequency-dependent for stable and underdamped linear systems.

The interaction forces are obtained with Equation (30):

$$f_e = (m_e s^2 + c_e s + k_e) x_m \quad (30)$$

Besides, sensor noise has been added to the measured displacement x_m and the experimental force f_e using band-limited white noise (BLWN) blocks to model the physical sensors. Then, the signal x_m is sent to the controller for the adaptation process. Consequently, the signal f_e is fed back to the numerical substructure to be considered in the integration of the numerical EOM. Notice that force measurement noise could impact the experimental force power, but it has a small effect on the work done by this force due to the numerical integration process to calculate work. However, measurement noises can affect the hybrid loop, depending on the structural properties, transfer system, and dynamic compensation.

The adaptive compensation implemented in the controller consist in adaptive model-based compensation (Chen et al., 2015)

with the modifications presented in Fernandois et al. (2020). A first-order adaptive feedforward determines the commanded displacement as shown in Equation (31):

$$x_c = a_0 x_t + a_1 \dot{x}_t \quad (31)$$

where a_0 and a_1 are the adaptive control parameters, and \dot{x}_t is approximated using the backwards difference method. The adaptation laws of a_0 and a_1 are described in Equation (32):

$$\begin{Bmatrix} \dot{a}_0 \\ \dot{a}_1 \end{Bmatrix} = \Gamma e \begin{Bmatrix} x_m \\ \dot{x}_m \end{Bmatrix} \quad (32)$$

where $\Gamma = \text{diag}(\Gamma_0, \Gamma_1)$ is the adaptive gain matrix associated with the adaptation rate of parameters a_0 and a_1 , respectively, and e is an estimation error of the adaptive parameters described in Equation (33):

$$e = \frac{x_c - (a_0 x_m + a_1 \dot{x}_m)}{1 + (x_m^2 + \dot{x}_m^2)} \quad (33)$$

Both signals x_c and x_m are filtered with a fourth-order Butterworth low-pass filter with a cutoff frequency of 20 Hz, and \dot{x}_m is obtained with the backward difference method.

This subsection aims to demonstrate the performance of the SW stability indicator for different compensation scenarios. Notice that the goal of the SW indicator is to detect instability during a test with a predefined compensation design, and not to tune the compensation/adaptation parameters. In these simulations, the initial adaptive parameters are selected as $a_0(t = 0) = 1$ and $a_1(t = 0) = 10/1,000$ s. With these parameters,

TABLE 1 | Adaptive gains for each case.

Case	Γ_0	Γ_1
Γ_a	0	0
Γ_b	10	5
Γ_c	1×10^5	1×10^4
Γ_d	2.4×10^6	1.1×10^5

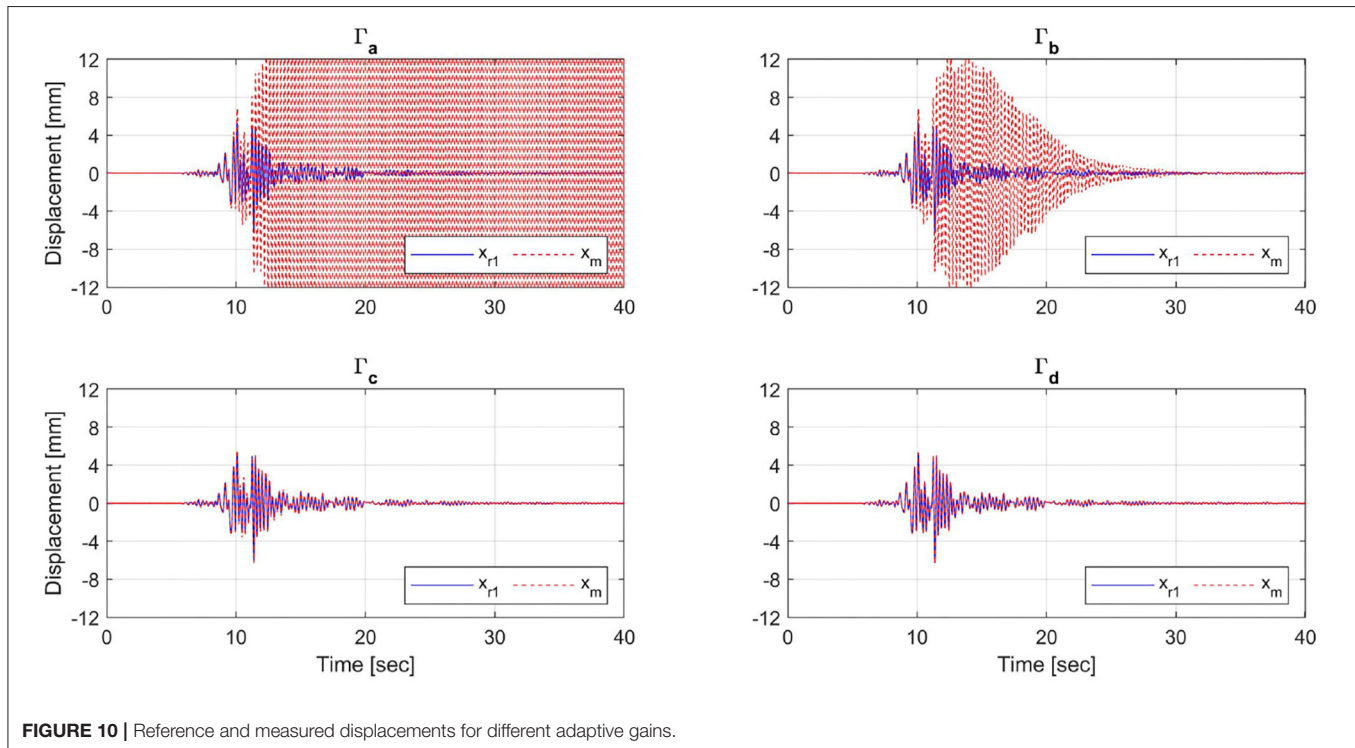


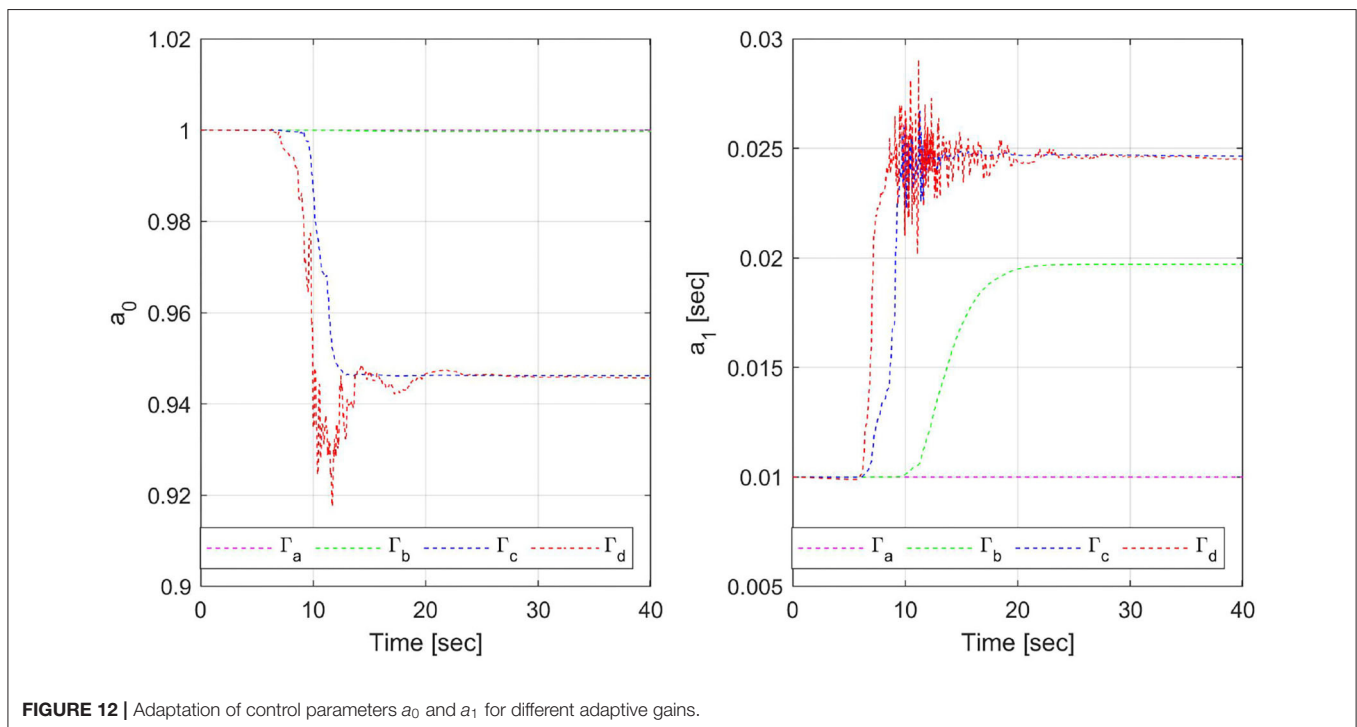
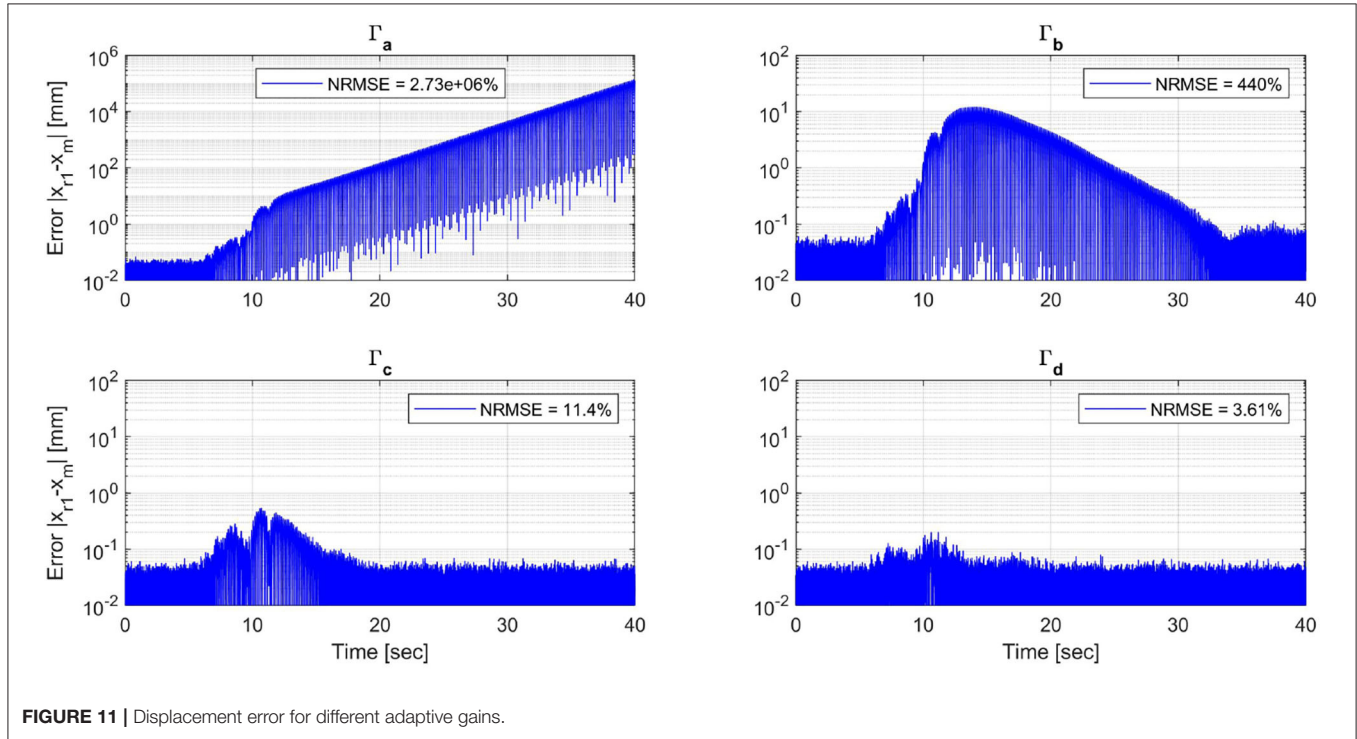
FIGURE 10 | Reference and measured displacements for different adaptive gains.

the controller cannot compensate for the control plant delay successfully; therefore, parameter adaptation is necessary.

Four simulations are performed with different adaptive gains presented in **Table 1**, where Γ_a corresponds to a non-adaptive case, Γ_d to an optimally calibrated case (Fernandois et al., 2020),

and Γ_b and Γ_c are intermediate cases of adaptation. The structure is subjected to the Kobe earthquake scaled to 40% PGA.

The measured displacement of experimental substructure x_m is compared with the first degree of freedom displacement x_{r1} from the reference structure in **Figure 10**, where the case



with Γ_a is unstable, while the case with Γ_b presents large measured displacements, but that decreases after the earthquake. Considering that in true RTHS tests, the reference displacement is not available, it would be difficult to distinguish if the measured displacements are correct or are associated with an unstable response. On the other hand, for Γ_c and Γ_d simulations are stable.

In **Figure 11**, the error of displacement x_m respect to x_{r1} for each adaptive gains is presented, including the normalized root mean square error (NRMSE) for each case. The cases with Γ_a present unacceptable errors, while for Γ_b , the errors are substantial, but at least decrease after the earthquake. For the cases with Γ_c and Γ_d , the errors are relatively small.

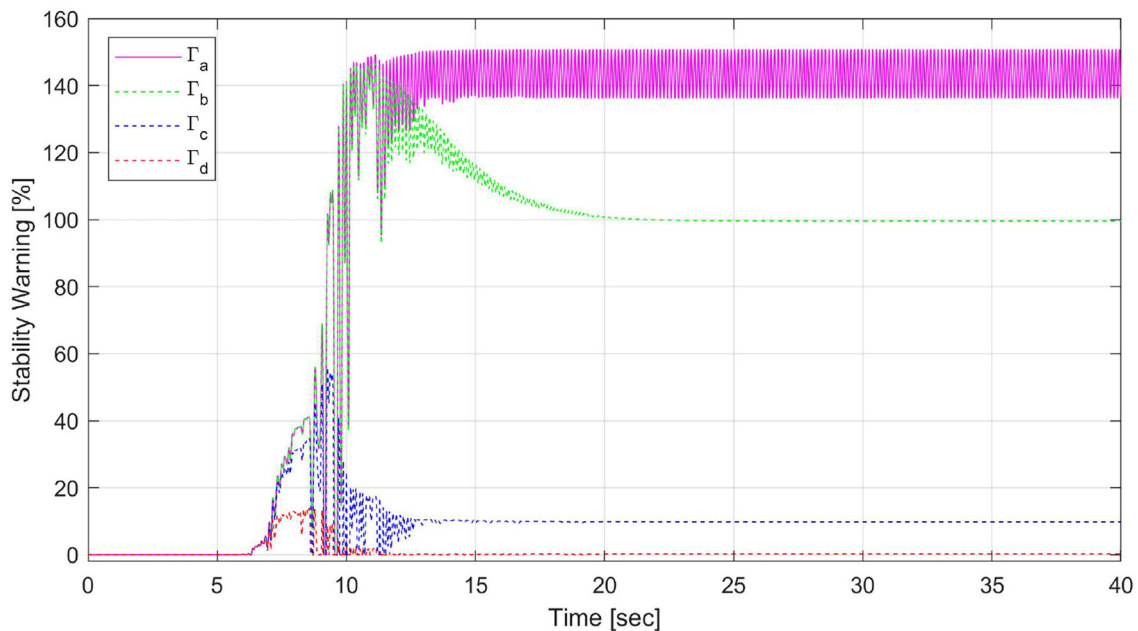


FIGURE 13 | Stability warning indicator (SW) for different adaptive gains.

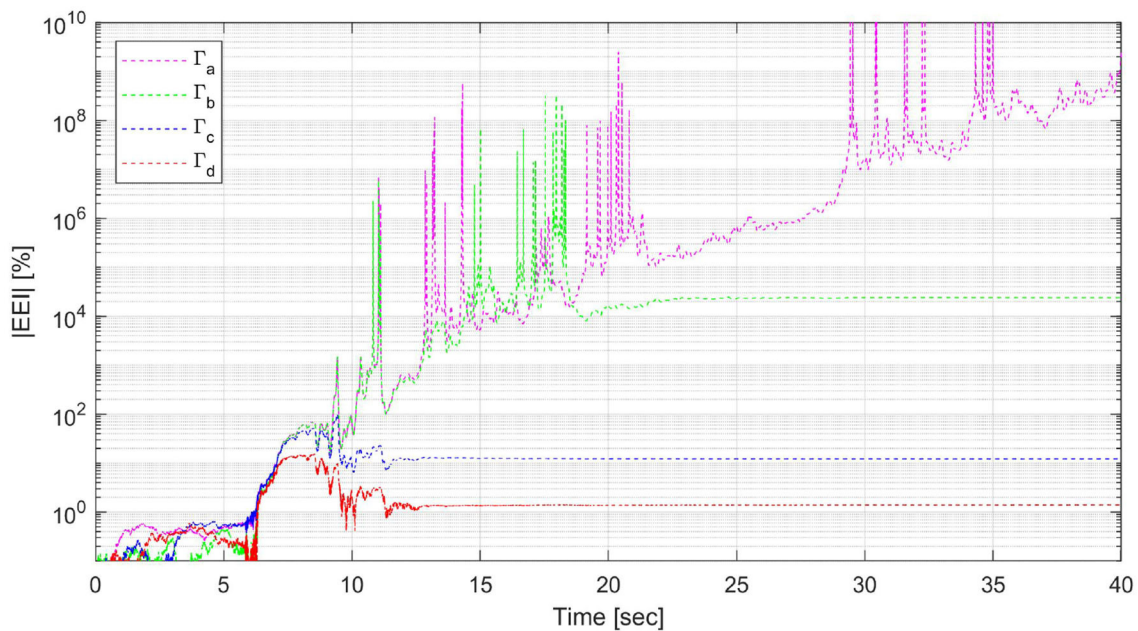


FIGURE 14 | Energy error indicator (EEI) for different adaptive gains.

The difference between each case is explained by the adaptation process presented in **Figure 12**, where there is no adaptation for Γ_a , slow adaptation for Γ_b , and the same convergence for Γ_c and Γ_d but with different rates. The parameter a_1 is directly related to the delay compensation, so it is expected that for Γ_a and Γ_b , the non-compensated delay produces large errors in the simulations. However, the adaptation for Γ_b is apparently enough to stabilize the system during the test.

In **Figure 13**, the SW indicator for each case is presented. For Γ_c and Γ_d , the indicator is growing at the beginning of the earthquake. Then, the SW indicator decays due to the adaptation and good compensation, and stays under 100% during the entire simulation, confirming the stability of these simulations. For Γ_a and Γ_b , the indicator reaches 100% near 10 s of simulation, so much before each simulation presents large displacements. So, the stability warning indicator could help stop the simulation in time before any damage occurs in the test setup. In the particular case with Γ_b , the stability warning indicator exceeds 100% between 10 and 20 s, consistent with the large response of the system in that interval. After 20 s of simulation, when the controller has reached enough adaptation to compensate for the delay, the SW indicator decays below 100%. This result is consistent with the stable behavior of this case at the end of the simulation. However, this simulation could be stopped when the indicator reaches 100% to avoid the behavior shown between 10 and 20 s.

Moreover, notice that for Γ_b and Γ_c cases, the SW does not decay to zero at the end of the simulation. This situation occurs because of uncompensated delay during the earthquake, which causes a surplus of energy inserted into the numerical substructure. Later, when the delay is compensated, displacements and forces are too small, so the work done by the experimental forces remains constant. This effect does not happen for Γ_d , where the delay is compensated early when the earthquake strikes. The experimental substructure dissipates energy during the rest of the earthquake, leading W_F to zero and consequently, SW to zero as well.

Furthermore, the control plant in the benchmark problem is modeled as a linear time-invariant system, but in these simulations, the adaptive controller produces time-varying compensation. Therefore, the delay between target and measured displacements is a time-varying property. This scenario is a complicated situation to predict the stability of a system before the test. However, with the online analysis of the SW it is possible to detect which case results in stable behavior and which are not.

For comparison, **Figure 14** shows the absolute value of EEI for each adaptive case scenario. For Γ_a and Γ_b , the EEI presents large values, while for Γ_d , the EEI keeps low during the test. So, the EEI could allow lab technicians to stop the simulations with Γ_a and Γ_b , and accept the simulation with Γ_d . However, for Γ_c case, the EEI reaches 100% before 10 s where the displacements are small, and the controller is adapting, and the test still has good chance to give acceptable results without the risk of instability. Thus, the EEI is an excellent tool to analyze the errors after the RTHS test, but it is not reliable for detecting instability online.

Additionally, in these simulations, displacement and force measurement noises do not have a notorious impact on the

hybrid system response. The numerical substructure acts like a low-pass filter for the force measurement, and the adaptive compensator is not affected by the displacement noise.

5. CONCLUSIONS

Energy analysis for real-time hybrid simulation tests is conducted to establish a stability indicator for online evaluation. The features of the proposed indicator to detect instability is demonstrated through numerical simulations with constant delay, including an actuator model with adaptive compensation for different design scenarios. The stability warning indicator (SW) allows the detection of unstable behavior before the system reaches large displacements that can damage the experimental substructure or laboratory equipment. The proposed indicator only requires the measured force from the experimental substructure and information from the numerical substructure. Hence, it is independent of the compensation method and does not require a model of the experimental substructure or the transfer system (i.e., actuation system). This indicator can be implemented to stop an RTHS test that is rendered unstable automatically. The test should be stopped if the SW reaches 100% (i.e., it is unnecessary to stop a test with a $SW < 100$). So, this indicator is an excellent complement to any compensation method. It provides further safety guarantees to the test, especially for adaptive compensation if there is considerable uncertainty in the plant or the controller's adaptation capacity. It is worth mentioning that the proposed indicator provides safety for the test, but it does not ensure accuracy compared to the reference structure's true response. However, priority should always be given to conducting a safe experiment. Then, the reliability of the results could be studied in detail after the test has ended.

Finally, the effectiveness of the SW indicator is demonstrated for linear systems. Future work will consider non-linear systems and the corresponding experimental validation of the proposed indicator, together with the implementation of existing compensation techniques in RTHS testing and its synergism.

DATA AVAILABILITY STATEMENT

All datasets generated for this study are included in the article/supplementary material.

AUTHOR CONTRIBUTIONS

CG and GF conceived the presented idea for this study. CG developed the methodology and performed the numerical simulations. GF supervised the findings of this work. CG wrote the manuscript with support from GF. All authors discussed the results and contributed to the final manuscript.

ACKNOWLEDGMENTS

The authors gratefully acknowledge the financial support from the Universidad Técnica Federico Santa María (Chile) through

the research grant *Proyecto Interno de Línea de Investigación No. PI_L_18_07*, and from the Chilean National Commission for Scientific and Technological Research (CONICYT), FONDECYT

Iniciación Research Project, Grant No. 11190774. The authors' opinions, findings, conclusions, or recommendations are those of the authors and do not necessarily reflect those of the sponsors.

REFERENCES

- Ahmadzadeh, M., and Mosqueda, G. (2009). Online energy-based error indicator for the assessment of numerical and experimental errors in a hybrid simulation. *Eng. Struct.* 31, 1987–1996. doi: 10.1016/j.engstruct.2009.03.002
- Bas, E. E., and Moustafa, M. A. (2020). Performance and limitations of real-time hybrid simulation with nonlinear computational substructures. *Exp. Tech.* doi: 10.1007/s40799-020-00385-6
- Bonnet, P. A., Lim, C. N., Williams, M. S., Blakeborough, A., Neild, S. A., Stoten, D. P., et al. (2007). Real-time hybrid experiments with Newmark integration, MCSmd outer-loop control and multi-tasking strategies. *Earthq. Eng. Struct. Dyn.* 36, 119–141. doi: 10.1002/eqe.628
- Carrion, J. E., and Spencer, B. F. (2007). *Model-Based Strategies for Real-Time Hybrid Testing*. Technical Report NSEL-006, Department of Civil and Environmental Engineering, University of Illinois at Urbana-Champaign, Urbana, IL.
- Chae, Y., Kazemibidokhti, K., and Ricles, J. M. (2013). Adaptive time series compensator for delay compensation of servo-hydraulic actuator systems for real-time hybrid simulation. *Earthq. Eng. Struct. Dyn.* 42, 1697–1715. doi: 10.1002/eqe.2294
- Chen, C., Ricles, J. M., Marullo, T. M., and Mercan, O. (2009). Real-time hybrid testing using the unconditionally stable explicit CR integration algorithm. *Earthq. Eng. Struct. Dyn.* 38, 23–44. doi: 10.1002/eqe.838
- Chen, P.-C., Chang, C.-M., Spencer, B. F. Jr., and Tsai, K.-C. (2015). Adaptive model-based tracking control for real-time hybrid simulation. *Bull. Earthq. Eng.* 13, 1633–1653. doi: 10.1007/s10518-014-9681-2
- Dyke, S. J., Gomez, D., and Spencer, B. F. (2020). Editorial: Special issue on the real-time hybrid simulation benchmark problem. *Mech. Syst. Signal Process.* 142:106804. doi: 10.1016/j.ymssp.2020.106804
- Dyke, S. J., Spencer, B. F. Jr., Quast, P., and Sain, M. (1995). Role of control-structure interaction in protective system design. *J. Eng. Mech.* 121, 322–338. doi: 10.1061/(ASCE)0733-9399(1995)121:2(322)
- Fermandois, G., Gálmez, C., and Valdebenito, M. (2020). “Optimal gain calibration of adaptive model-based compensation for real-time hybrid simulation testing,” in *17th World Conference on Earthquake Engineering (17WCEE)* (Sendai).
- Gao, X., Castaneda, N., and Dyke, S. J. (2013). Real time hybrid simulation: from dynamic system, motion control to experimental error. *Earthq. Eng. Struct. Dyn.* 42, 815–832. doi: 10.1002/eqe.2246
- Gao, X. S., and You, S. (2019). Dynamical stability analysis of MDOF real-time hybrid system. *Mech. Syst. Signal Process.* 133:106261. doi: 10.1016/j.ymssp.2019.106261
- Guo, T., Chen, C., Xu, W., and Sanchez, F. (2014). A frequency response analysis approach for quantitative assessment of actuator tracking for real-time hybrid simulation. *Smart Mater. Struct.* 23:045042. doi: 10.1088/0964-1726/23/4/045042
- Horiuchi, T., Inoue, M., Konno, T., and Namita, Y. (1999). Real-time hybrid experimental system with actuator delay compensation and its application to a piping system with energy absorber. *Earthq. Eng. Struct. Dyn.* 28, 1121–1141. doi: 10.1002/(SICI)1096-9845(199910)28:10<1121::AID-EQE858>3.0.CO;2-O
- Maghareh, A., Dyke, S., Rabieniaharatbar, S., and Prakash, A. (2017). Predictive stability indicator: a novel approach to configuring a real-time hybrid simulation. *Earthq. Eng. Struct. Dyn.* 46, 95–116. doi: 10.1002/eqe.2775
- McCrum, D., and Williams, M. (2016). An overview of seismic hybrid testing of engineering structures. *Eng. Struct.* 118, 240–261. doi: 10.1016/j.engstruct.2016.03.039
- Mercan, O., and Ricles, J. M. (2008). Stability analysis for real-time pseudodynamic and hybrid pseudodynamic testing with multiple sources of delay. *Earthq. Eng. Struct. Dyn.* 37, 1269–1293. doi: 10.1002/eqe.814
- Nakashima, M., Kato, H., and Takaoka, E. (1992). Development of real-time pseudo dynamic testing. *Earthq. Eng. Struct. Dyn.* 21, 79–92. doi: 10.1002/eqe.4290210106
- Palacio-Betancur, A., and Gutierrez Soto, M. (2019). Adaptive tracking control for real-time hybrid simulation of structures subjected to seismic loading. *Mech. Syst. Signal Process.* 134:106345. doi: 10.1016/j.ymssp.2019.106345
- Silva, C. E., Gomez, D., Maghareh, A., Dyke, S. J., and Spencer, B. F. (2020). Benchmark control problem for real-time hybrid simulation. *Mech. Syst. Signal Process.* 135:106381. doi: 10.1016/j.ymssp.2019.106381
- Tao, J., and Mercan, O. (2019). A study on a benchmark control problem for real-time hybrid simulation with a tracking error-based adaptive compensator combined with a supplementary proportional-integral-derivative controller. *Mech. Syst. Signal Process.* 134:106346. doi: 10.1016/j.ymssp.2019.106346
- Wallace, M., Sieber, J., Neild, S. A., Wagg, D. J., and Krauskopf, B. (2005a). Stability analysis of real-time dynamic substructuring using delay differential equation models. *Earthq. Eng. Struct. Dyn.* 34, 1817–1832. doi: 10.1002/eqe.513
- Wallace, M., Wagg, D., and Neild, S. (2005b). An adaptive polynomial based forward prediction algorithm for multi-actuator real-time dynamic substructuring. *Proc. R. Soc. A Math. Phys. Eng. Sci.* 461, 3807–3826. doi: 10.1098/rspa.2005.1532
- Wang, Z., Ning, X., Xu, G., Zhou, H., and Wu, B. (2019). High performance compensation using an adaptive strategy for real-time hybrid simulation. *Mech. Syst. Signal Process.* 133:106262. doi: 10.1016/j.ymssp.2019.106262
- Xu, D., Zhou, H., Shao, X., and Wang, T. (2019a). Performance study of sliding mode controller with improved adaptive polynomial-based forward prediction. *Mech. Syst. Signal Process.* 33:106263. doi: 10.1016/j.ymssp.2019.106263
- Xu, W., Chen, C., Guo, T., and Chen, M. (2019b). Evaluation of frequency evaluation index based compensation for benchmark study in real-time hybrid simulation. *Mech. Syst. Signal Process.* 130, 649–663. doi: 10.1016/j.ymssp.2019.05.039

Conflict of Interest: The authors declare that the research was conducted in the absence of any commercial or financial relationships that could be construed as a potential conflict of interest.

Copyright © 2020 Gálmez and Fermandois. This is an open-access article distributed under the terms of the Creative Commons Attribution License (CC BY). The use, distribution or reproduction in other forums is permitted, provided the original author(s) and the copyright owner(s) are credited and that the original publication in this journal is cited, in accordance with accepted academic practice. No use, distribution or reproduction is permitted which does not comply with these terms.



Conceptual Study of a Real-Time Hybrid Simulation Framework for Monopile Offshore Wind Turbines Under Wind and Wave Loads

Wei Song^{1*}, Chao Sun², Yanhui Zuo^{1,3}, Vahid Jahangiri², Yan Lu³ and Qinghua Han³

¹ Department of Civil, Construction and Environmental Engineering, University of Alabama, Tuscaloosa, AL, United States,

² Department of Civil and Environmental Engineering, Louisiana State University, Baton Rouge, LA, United States, ³ School of Civil Engineering, Tianjin University, Tianjin, China

OPEN ACCESS

Edited by:

Eleni N. Chatzi,
ETH Zürich, Switzerland

Reviewed by:

Giuseppe Abbiati,
Aarhus University, Denmark
Francesco Tornabene,
University of Salento, Italy
Imad Abdallah,
ETH Zürich, Switzerland

*Correspondence:

Wei Song
wsong@eng.ua.edu

Specialty section:

This article was submitted to
Computational Methods in Structural
Engineering,
a section of the journal
Frontiers in Built Environment

Received: 02 June 2020

Accepted: 15 July 2020

Published: 26 August 2020

Citation:

Song W, Sun C, Zuo Y, Jahangiri V,
Lu Y and Han Q (2020) Conceptual
Study of a Real-Time Hybrid
Simulation Framework for Monopile
Offshore Wind Turbines Under Wind
and Wave Loads.
Front. Built Environ. 6:129.
doi: 10.3389/fbuil.2020.00129

As an attractive renewable energy source, offshore wind plants are becoming increasingly popular for energy production. However, the performance assessment of offshore wind turbine (OWT) structure is a challenging task due to the combined wind-wave loading and difficulties in reproducing such loading conditions in laboratory. Real-time hybrid simulation (RTHS), combining physical testing and numerical simulation in real-time, offers a new venue to study the structural behavior of OWTs. It overcomes the scaling incompatibilities in OWT scaled model testing by replacing the rotor components with an actuation system, driven by an aerodynamic simulation tool running in real-time. In this study, a RTHS framework for monopile OWTs is proposed. A set of sensitivity analyses is carried out to evaluate the feasibility of this RTHS framework and determine possible tolerances on its design. By simulating different scaling laws and possible error contributors (delays and noises) in the proposed framework, the sensitivity of the OWT responses to these parameters are quantified. An example using a National Renewable Energy Lab (NREL) 5-MW reference OWT system at 1:25 scale is simulated in this study to demonstrate the proposed RTHS framework and sensitivity analyses. Three different scaling laws are considered. The sensitivity results show that the delays in the RTHS framework significantly impact the performance on the response evaluation, higher than the impact of noises. The proposed framework and sensitivity analyses presented in this study provides important information for future implementation and further development of the RTHS technology for similar marine structures.

Keywords: monopile, offshore wind turbine, real-time hybrid simulation, wind load, wave load, froude scale, cauchy scale

INTRODUCTION

As an emerging field of wind power generation, offshore wind power is growing rapidly in recent years due to its vast potential in energy production capacity (Esteban et al., 2011; Musial et al., 2016; Keivanpour et al., 2017). With the development of offshore wind energy technology, the turbine capacity and the hub height are constantly climbing, and at the same time, these offshore wind turbines (OWTs) are facing a more complicated and extreme marine environment as their regions of deployment going to deeper ocean (Perveen et al., 2014; Anaya-Lara et al., 2018).

To ensure the structural integrity and operation safety of these energy harnessing systems during their foreseen lifetime (20–25 years) (Dnvgl, 2016; Anaya-Lara et al., 2018), it is imperative to enhance our understanding on OWTs' structural behavior in the complex marine environment.

Due to their working environment at exposed sites, OWTs are subjected to combined actions of multiple loads during their normal operations. These loads include wind, wave, and underwater current. These different forms of environmental loads combined with turbine operation condition, soil-structure interaction and flexible member dynamics make it difficult to accurately quantify the complicated dynamics and predict the system behavior of OWT (Dnvgl, 2016; Aasen et al., 2017; Bhattacharya, 2019). Wind and wave-current loads are the main external loads applied on operational OWTs, which may lead to a great overturning moment and shear force at its foundation and supporting structure (Alagan Chella et al., 2012; Stansby et al., 2013; Morató et al., 2017). Because of its special structural configuration (slender high-rising structural system with a concentrated mass at its top), an OWT's fundamental frequency often lies between the dominant frequency ranges of offshore lateral loads (Arany et al., 2017; Bhattacharya, 2019), which implies that its response is sensitive to those lateral forces such as wind and wave-current excitations. In addition, the misalignment between wind and wave plays an important role in predicting the extreme and fatigue loads in OWT systems. In a sensitivity study carried out in Barj et al. (2014), it is shown that considering only aligned wind and waves leads to an underestimation of the tower base side-side bending moment by approximately 50% and an overestimation of the tower-base fore-aft bending moment by about 5%. To accurately characterize and capture the structural behavior of OWTs, it is of great importance to consider the combined wind and wave-current actions.

Numerical tools are available to calculate wind and wave-current loads acting on OWT. The blade element momentum theory (BEM) (Hansen, 2015) is the most widely used method to estimate the aerodynamic loads on rotor blades. In the BEM theory, time series of aerodynamic loading are computed based on the momentum theory, the blade characteristics and the operational conditions. To characterize hydrodynamic loads caused by wave and current, wave climate first needs to be defined, usually in the form of a variance density spectrum, called wave spectrum. Two often used standard wave spectra are the Pierson—Moskowitz wave spectrum (Pierson and Moskowitz, 1964) and the Joint North Sea Wave Project (JONSWAP) wave spectrum (Hasselmann et al., 1973). Characterizing current load is a more challenging task, because current velocities vary in space and time as wind velocities, but with much larger variations in both length and time scales than those of wind. Although the well-established linear wave theory has been applied in modeling ocean wave dispersions (Lamb, 1945; Newman, 1977), complex physical phenomena, such as wave-current interaction effects, viscous loads, or extreme wave loads, are still not fully understood, nor confidently modeled (Sauder et al., 2016). Despite the development of increasingly sophisticated numerical models and tools, physical hydrodynamic model testing in wave tank facilities is still required for calibrating parameters in

numerical models, assessing performance of current designs, and verifying new designs of OWTs.

Model testing in wave tank facilities usually adopts Froude scaling law, i.e., the scaling between experimental model and full-scale prototype maintains constant Froude number. By preserving the ratio of gravitational and inertial forces, Froude scaling ensures the similitude of free surface hydrodynamics, but it cannot maintain the same viscous effect due to the reduced Reynolds number (Campagnolo, 2013; Canet et al., 2018). While the Reynolds number dependence of the hydrodynamic load is often neglected in marine structure tests, the associated change of aerodynamic Reynolds number poses a challenge for OWT tests, because wind turbine aerodynamics are very sensitive to the viscous forces which are dominating at small scales (Martin, 2011; Robertson et al., 2013). One solution to address the incompatibility between the Froude and Reynolds scaling laws is to modify the design of the rotor blades. By adjusting the chord length and twist angle of blades, low-Reynolds number airfoil designs are developed to achieve similar thrust coefficients as full-scale blade in Froude scaled wind (De Ridder et al., 2014; Kimball et al., 2014; Du et al., 2016). Although this approach can mitigate the Froude-Reynold scaling conflict, the distortion in geometry leads to limitations such as mismatch in aerodynamic torque, generator torque, and roll-forcing (Bredmose et al., 2012).

A promising alternative to address the above scaling incompatibility is real-time hybrid simulation (RTHS). RTHS is a powerful dynamic testing technique for large or complex structural systems, in particular of those systems with multiple components and complex interactions (Carrion and Spencer, 2007; Phillips and Spencer, 2012). It originates in the field of earthquake engineering (Nakashima et al., 1992). In RTHS, part of the structural system is simulated using numerical models with good accuracy and confidence, and the rest of the system requires physical testing under realistic operational conditions. By interfacing physical testing with numerical simulation in real-time via actuators and sensors, RTHS not only provides insights into detailed dynamic behavior of the physical subsystem, but also offers a better understanding of the entire complex structural system. Due to its closed-loop nature, a successful RTHS framework needs to control the delays and noises in the interfacing actuator and sensor systems, as they tend to bring destabilizing effect into RTHS, causing large experimental error or even failure (Christenson et al., 2014; Maghareh et al., 2014; Hayati and Song, 2017). Research studies have also been conducted to quantify uncertainties in RTHS due to experimental errors (Sauder et al., 2019) and modeling choices (Abbiati et al., 2021).

RTHS has been applied in scaled wave tank tests for floating wind turbines (FWTs) to resolve the Froude-Reynold scaling conflict. Chabaud et al. (2013) proposed a RTHS set up for a conceptual FWT, simplified as a single degree-of-freedom (DOF) mass-spring system, and conducted a case study to identify potential challenges and corresponding solutions. Hall et al. (2014) used a set of wind turbine simulations to determine the performance specifications for a RTHS system. Later, Hall et al. (2018) applied a similar approach to study RTHS strategies with two different coupling locations. Sauder et al. (2016)

presented a RTHS testing method (ReaTHM) of a FWT and discussed possible error sources and their quantification. The same RTHS method later was applied in testing a 10-MW FWT (Thys et al., 2018). In these wave basin RTHS tests, the numerical component is the aerodynamic portion of the FWT simulated by a computer model, and the physical component is the Froude scaled floating structure including the tower. An interfacing system including both sensors and actuators provides the coupling between the two components. Because the scaling can be set arbitrarily in a simulation, the Froude-Reynold scaling conflict is therefore eliminated. In addition, by simulating the aerodynamic loading numerically, the RTHS testing method offers a convenient way to consider different rotor blade designs with fine controlled wind field and avoids geometry distortion in blade and the demand of wind production during tests. The above developments demonstrated the great potential of RTHS in studying structural behavior of OWT under combined actions of wind and wave, especially took a solid step toward the RTHS implementation. However, they were mostly studied only in one scale (either reduced scale for RTHS or full-scale for prototype) to examine the performance of interfacing system or conducted in an open loop setting without fully exploring the coupled dynamics between numerical and physical components. None of them have provided a systematic investigation on the errors between the scaled RTHS and the matching full-scale prototype or discussed how the delays and noises in RTHS and different scaling laws will impact these errors. In addition, these above studies are mostly focused on FWTs, and have not covered the OWTs with fixed foundation, such as monopile OWTs.

In this study, a RTHS framework for monopile OWTs is proposed. A series of sensitivity analyses are conducted by comparing the responses of the proposed RTHS framework in reduced scale and those of the matching full-scale prototype under the influence of a variety of factors, including scaling laws, delays, noises, and wind-wave loading characteristics. Among these factors, the experimental errors (e.g., noise and delay) can provide information on RTHS compensation designs, and the modeling choices (e.g., scaling laws, wave heights, and misalignment angles) can guide specimen designs. Both the RTHS and the prototype are simulated numerically under controlled condition to isolate the influencing factors. The obtained results can help to better understand if the proposed RTHS framework can achieve desired accuracy and robustness in capturing the behavior of a full-scale OWT design. They also offer insights to guide the future RTHS implementation by identifying possible contributors that may impact the RTHS performance and quantifying the associated specification tolerance.

PRELIMINARIES

To facilitate the numerical simulation, a fully coupled three-dimensional (3D) dynamic model for monopile OWT is established using Euler-Lagrange equation and finite element (FE) method. The modeling details are described in Section Preliminaries.

Description of OWT Model

A typical monopile OWT subjected to the combined action of wind and wave is shown in **Figure 1A**. A cartesian coordinate system originating at the intersection of the tower center line and the mean sea level (MSL) is defined in the same graph. The wind-wave misalignment angle is denoted as β . The turbine blades are modeled by considering the major bending modes in the edgewise and flapwise directions of the blade, with the corresponding mode shapes denoted as ϕ_{1e} and ϕ_{1f} , respectively. The DOFs of the blades are illustrated in **Figure 2**: $u_1 \sim u_3$ denotes the modal coordinates in edgewise direction, $u_4 \sim u_6$ denotes the modal coordinates in flapwise direction, and u_7 and u_8 denotes the movements of the nacelle (and the hub) in the fore-aft (x) and side-side (y) directions at the top of the tower, respectively. The blades rotating speed is denoted as Ω (rad/sec) and the azimuthal angle $\psi_j(t)$ of the j th blade can be expressed as:

$$\psi_j(t) = \Omega t + \frac{2\pi}{3}(j-1), \quad j = 1, 2, 3 \quad (1)$$

Simplified foundation models are shown in **Figure 3**. Soil effects are considered by translational springs with coefficients k_x and k_y and rotational springs with coefficients $k_{x\phi}$ and $k_{y\phi}$. Similarly, the damping properties of the soil are considered by introducing translational and rotational dashpots with coefficients c_x , c_y , $c_{x\phi}$, and $c_{y\phi}$. In Section FE Model for Tower Including Foundation, these stiffness and damping parameters are included in the FE model of the tower.

In this study, the modeling of the aerodynamic and hydrodynamic components of OWT follows the procedure described in Sun and Jahangiri (2018); Sun (2018a); Sun (2018b). The tower, however, is modeled by FE method with physical movements as the DOFs instead of modal coordinates—the major bending modes in x and y directions adopted in Sun and Jahangiri (2018); Sun (2018a); Sun (2018b). The equations of motion of the OWT are established accordingly. The derivation details are shown in the Sections FE Model for Tower Including Foundation, Kinetic Energy, Potential Energy, Loads on OWT.

FE Model for Tower Including Foundation

In actual RTHS implementation, usually the tower structure of the OWT is built in wave tank facility in reduced scale. In this concept study, all the components of the RTHS, including the experimental component (tower structure), are simulated numerically. As shown in **Figure 1B**, the entire tower of the OWT, including the tower structure above the MSL and below until seabed (also called the wet section), is modeled together as one tower model using two-node 3D elastic beam elements. Each node contains four DOFs: two translations (u_x, u_y) and two rotations (θ_x, θ_y) with respect to the x and y axis. The torsional behavior and axial deformation of the tower are ignored in this study. Assuming modal damping, the formulation of the mass \mathbf{M}_{tow} , stiffness \mathbf{K}_{tow} , and damping \mathbf{C}_{tow} matrices can be found in standard texts (Przemieniecki, 1968; Craig and Kurdila, 2006) and hence are not repeated here. The pile is modeled as part of the tower structure extended to the seabed. Once the global mass, stiffness, and damping matrices of the tower are

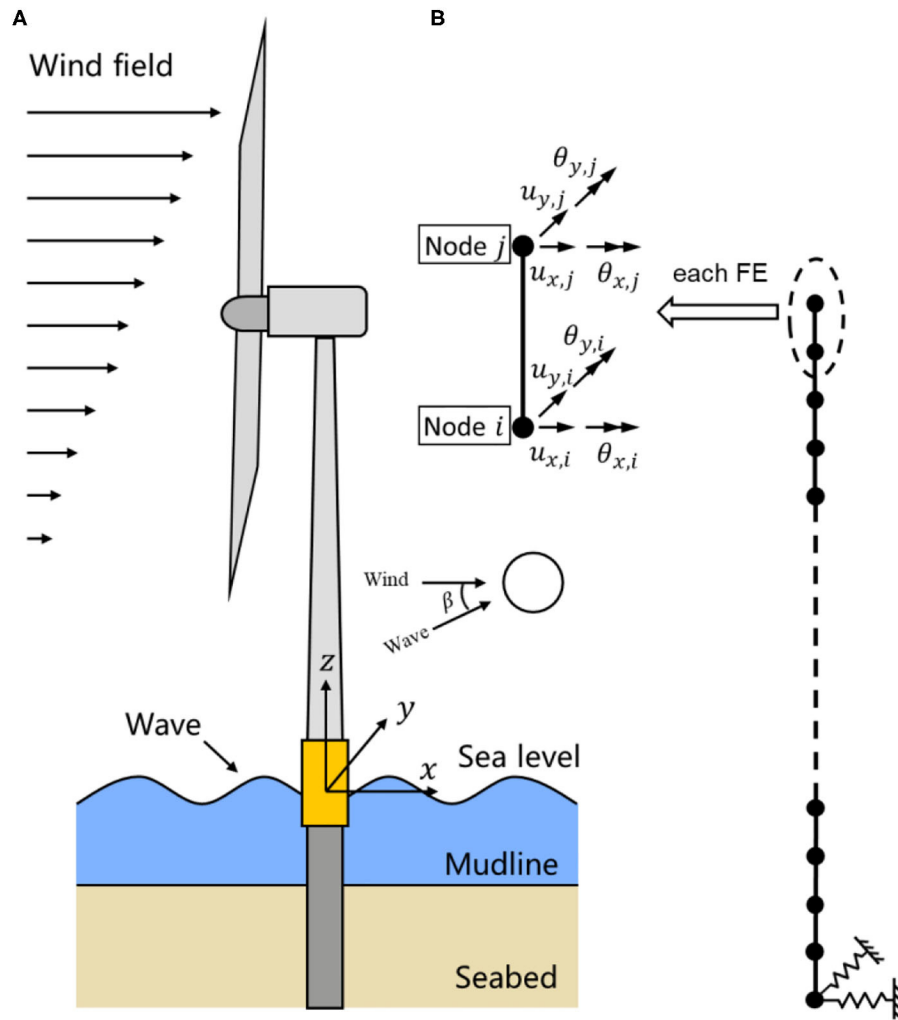


FIGURE 1 | Monopile offshore wind turbine and its FE model. **(A)** Overview of the monopile offshore wind turbine. **(B)** FE model of the tower.

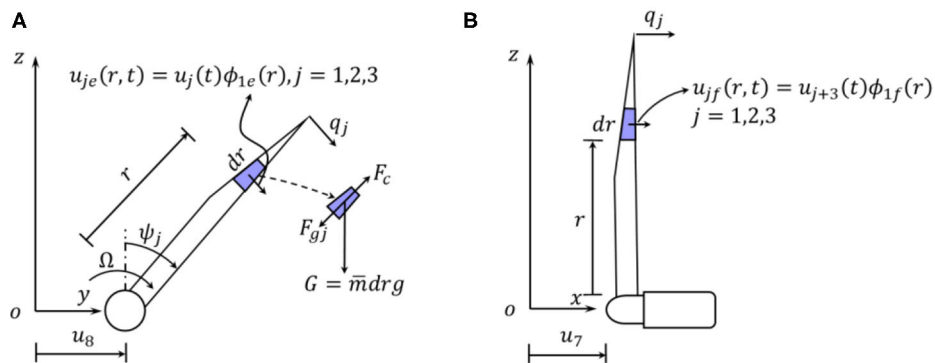


FIGURE 2 | Degrees-of-freedom of the rotor blades. **(A)** Blade in-plane movement. **(B)** Blade out-of-plane movement.

assembled, they are further modified by adding the stiffness (k_x , k_y , $k_{x\phi}$, and $k_{y\phi}$) and damping (c_x , c_y , $c_{x\phi}$, and $c_{y\phi}$) terms from the foundation model shown in **Figure 3** to the corresponding

DOFs. With the FE model of the tower established, the kinetic energy T_{tow} and potential energy V_{tow} of the tower can be expressed as

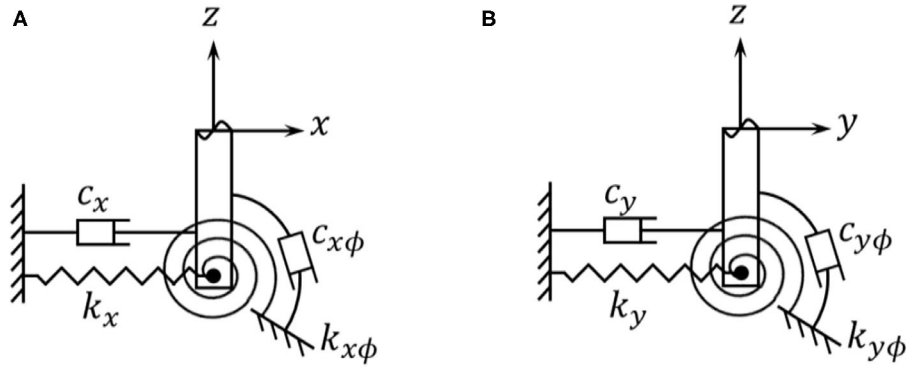


FIGURE 3 | Simplified foundation model of the offshore wind turbine. **(A)** Foundation model in xz plane. **(B)** Foundation model in yz plane.

$$T_{tow} = \frac{1}{2} \mathbf{v}_{tow}^T \mathbf{M}_{tow} \mathbf{v}_{tow} \quad (2)$$

and

$$V_{tow} = \frac{1}{2} \mathbf{u}_{tow}^T \mathbf{K}_{tow} \mathbf{u}_{tow} \quad (3)$$

where \mathbf{M}_{tow} and \mathbf{K}_{tow} are the mass matrix and stiffness matrix; \mathbf{u}_{tow} and \mathbf{v}_{tow} are the displacement and velocity response vectors of the DOFs of the tower; Superscript “T” indicates transpose operation. It is noted that u_7 and u_8 are included in the vector \mathbf{u}_{tow} too.

Kinetic Energy

Based on **Figures 1, 2**, the absolute velocity of the nacelle (and the hub) v_{nac} is expressed as

$$v_{nac}(r, t) = \sqrt{\dot{u}_7^2 + \dot{u}_8^2} \quad (4)$$

Consider an infinitesimal unit dr of the j th blade in **Figure 2**, its movements $(x_{r,j}, y_{r,j}, z_{r,j})$ in the xyz coordinate system can be expressed as ($j = 1, 2, 3$)

$$x_{r,j} = u_7 + u_{jf} = u_7 + u_{j+3}\phi_{1f} \quad (5)$$

$$y_{r,j} = u_8 + r \sin \psi_j + u_{je} \cos \psi_j = u_8 + r \sin \psi_j + u_j \phi_{1e} \cos \psi_j \quad (6)$$

$$z_{r,j} = r \cos \psi_j - u_{je} \sin \psi_j = r \cos \psi_j - u_j \phi_{1e} \sin \psi_j \quad (7)$$

Taking the derivative with respect to time, the magnitude of the absolute velocity of the unit dr of the j th blade $v_{b,j}$ in **Figure 2** is

$$v_{b,j}(r, t) = \sqrt{(\dot{x}_{r,j})^2 + (\dot{y}_{r,j})^2 + (\dot{z}_{r,j})^2} \quad (8)$$

Therefore, the total kinetic energy T of the OWT is given as

$$T = \frac{1}{2} \sum_{j=1}^3 \int_0^R \bar{m} v_{b,j}^2(r, t) dr + \frac{1}{2} (M_{nac} + M_{hub}) v_{nac}^2 + T_{tow}$$

$$= \frac{1}{2} \sum_{j=1}^3 \int_0^R \bar{m} v_{b,j}^2(r, t) dr + \frac{1}{2} \begin{bmatrix} \dot{u}_7 \\ \dot{u}_8 \end{bmatrix}^T \begin{bmatrix} M_{nac} + M_{hub} & 0 \\ 0 & M_{nac} + M_{hub} \end{bmatrix} \begin{bmatrix} \dot{u}_7 \\ \dot{u}_8 \end{bmatrix} + \frac{1}{2} \mathbf{v}_{tow}^T \mathbf{M}_{tow} \mathbf{v}_{tow} \quad (9)$$

where R denotes the length of the blade; M_{nac} and M_{hub} are the mass for the nacelle and hub, respectively; \bar{m} is the mass density per length of the blade.

Potential Energy

The total potential energy of the blades V_b is calculated considering the strain energy due to bending and the stiffening effects due to centrifugal force and gravity. It is expressed as Sun and Jahangiri (2018).

$$V_b = \frac{1}{2} \sum_{j=1}^3 \left[(k_{eg} + k_{ge,eg} - k_{gr,eg} \cos \psi_j) u_j^2 + (k_{fp} + k_{ge,fp} - k_{gr,fp} \cos \psi_j) u_{j+3}^2 \right] \quad (10)$$

where the bending stiffness in edge and flap direction, k_{eg} and k_{fp} , are expressed as,

$$k_{eg} = \int_0^R EI_{eg}(r) (\phi_{1e}'')^2 dr$$

$$k_{fp} = \int_0^R EI_{fp}(r) (\phi_{1f}'')^2 dr$$

the tension stiffening geometric stiffness in edge and flap direction due to centrifugal force, $k_{ge,eg}$ and $k_{ge,fp}$, are expressed as,

$$k_{ge,eg} = \Omega^2 \int_0^R \int_r^R [\bar{m}(\xi) \xi d\xi] (\phi_{1e}')^2 dr$$

$$k_{ge,fp} = \Omega^2 \int_0^R \int_r^R [\bar{m}(\xi) \xi d\xi] (\phi_{1f}')^2 dr$$

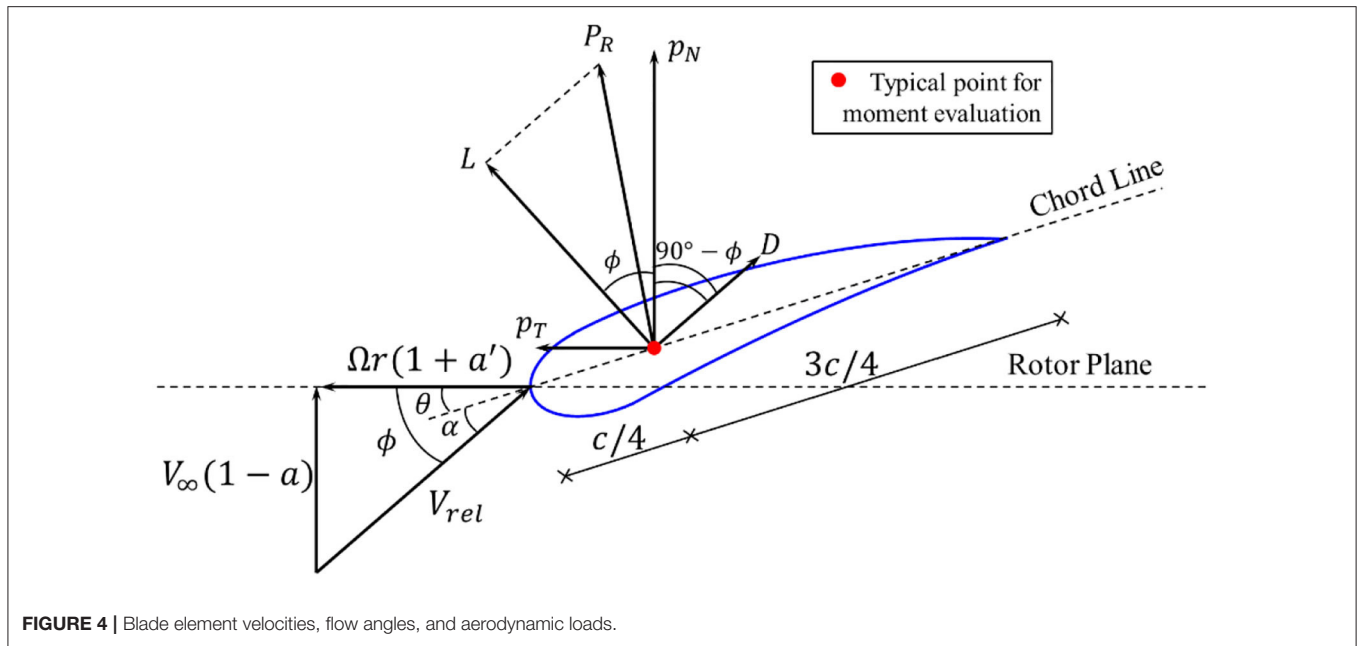


FIGURE 4 | Blade element velocities, flow angles, and aerodynamic loads.

the tension stiffening geometric stiffness in edge and flap direction due to gravity, $k_{gr,eg}$ and $k_{gr,fp}$, are expressed as,

$$k_{gr,eg} = g \int_0^R \int_r^R [\bar{m}(\xi) d\xi] (\phi_{1e}')^2 dr$$

$$k_{gr,fp} = g \int_0^R \int_r^R [\bar{m}(\xi) d\xi] (\phi_{1f}')^2 dr$$

where I_{eg} and I_{fp} are the moment of inertia in the edgewise and flapwise direction, g is the gravitational acceleration; the superscripts “ $'$ ” and “ $''$ ” denote the first and second order derivatives with respect to the blade length R . Therefore, the total potential energy V of the OWT is.

$$V = V_b + V_{tow} = V_b + \frac{1}{2} \mathbf{u}_{tow}^T \mathbf{K}_{tow} \mathbf{u}_{tow} \quad (11)$$

Loads on OWT

This section presents the derivation of wind, wave, and damping forces based on the principle of virtual work and FE method.

Wind Loading

The generation of the wind field follows IEC 61400-1 standard (Iec, 2005) using the Kaimal spectral model, with the length of roughness is set equal to 0.03. The associated coherence function is defined as,

$$\text{Coh}(i, j; f) = \exp \left(-a \sqrt{\left(\frac{fL}{\bar{V}_{hub}} \right)^2 + \left(\frac{0.12L}{L_c} \right)^2} \right) \quad (12)$$

where $a = 12$, $L_c = 340.2 \text{ m}$ are adopted in this study. During implementation, a three dimensional wind field profile covering the domain of the rotor disk is generated using the TurbSim

program (Jonkman and Kilcher, 2012). A MATLAB code is developed to map the generated wind field onto each spanwise elements of the rotating blades to apply the BEM theory.

In this study, the BEM theory (Hansen, 2015) is applied to calculate the aerodynamic loads on the rotor blades. **Figure 4** shows a blade element with the velocities and angles that determine the aerodynamic loads on the element. The angle of attack is denoted as α ; c is the local chord length; θ is the sum of the local pitch angle and the twist of the blade element, which are determined by the blade profile; the relative velocity V_{rel} is a combination of the axial velocity $V_\infty(1-a)$ and the tangential velocity $\Omega r(1+a')$ at the rotor plane, where V_∞ is the flow velocity; r is the radial distance from the blade element to the rotor center; a and a' are the axial and tangential induction factors, respectively. The lift and drag forces are projected to the directions normal to and tangential to the rotor plane to obtain the aerodynamic forces (per length) normal to the rotor plane p_N and tangential to the rotor plane p_T , as shown in the Equation (13),

$$p_N = L \cos \phi + D \sin \phi = \frac{1}{2} \rho_A V_{rel}^2 c (C_l \cos \phi + C_d \sin \phi)$$

$$p_T = L \sin \phi - D \cos \phi = \frac{1}{2} \rho_A V_{rel}^2 c (C_l \sin \phi - C_d \cos \phi) \quad (13)$$

where ρ_A is the air density; the lift and drag coefficients C_l and C_d can be determined from a given blade profile.

In practice, because the induction factors a and a' are not known, an iterative procedure is required to implement the BEM theory. In this study, a MATLAB code is developed to calculate the time series of p_N and p_T based on an algorithm proposed in Sun (2018a). Prandtl's model and Glauert correction are considered in the MATLAB code to account for tip- and hub-loss.

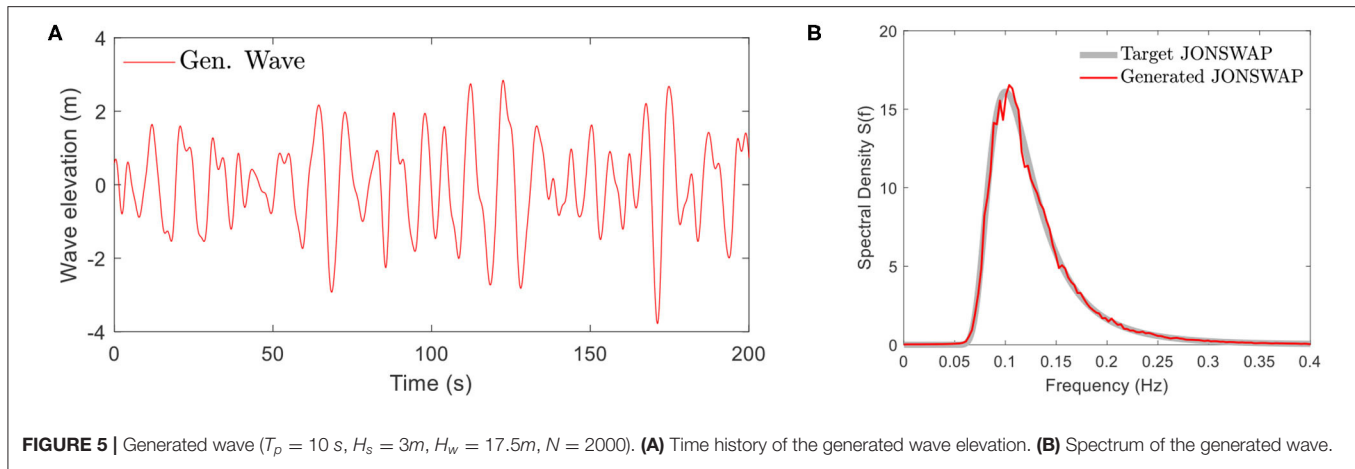


FIGURE 5 | Generated wave ($T_p = 10$ s, $H_s = 3$ m, $H_w = 17.5$ m, $N = 2000$). **(A)** Time history of the generated wave elevation. **(B)** Spectrum of the generated wave.

After the aerodynamic forces are determined, the principle of virtual work is applied to calculate the generalized aerodynamic loads on the OWT model.

Under p_N and p_T , the virtual work δW_{wind} done by external wind load is expressed as,

$$\delta W_{wind} = \sum_{j=1}^3 \left[\int_0^R p_{Tj}(r, t) (\phi_{1e} \delta u_j + \delta u_8 \cos \psi_j) dr + \int_0^R p_{Nj}(r, t) (\phi_{1f} \delta u_{j+3} + \delta u_7) dr \right] \quad (14)$$

where p_{Nj} and p_{Tj} denote the normal and tangential aerodynamic forces (per length) p_N and p_T acting on the j th blade. It is noted that the work done by the aerodynamic load acting on the DOFs of the tower is shown to be zero, except at the tip of the tower where the nacelle (and the hub) is located, i.e., u_7 and u_8 .

Wave and Current Loading

In this study, the JONSWAP wave spectrum is adopted to characterize wave climate. Based on the spectral representation method and linear wave theory, the random wave surface elevation η_w , current velocity \dot{u}_w , and acceleration \ddot{u}_w can be generated as,

$$\eta_w(x, t) = \sum_{j=1}^N A_j \cos(2\pi f_j t - k_j x + \phi_j) \quad (15)$$

$$\dot{u}_w(x, z, t) = \sum_{j=1}^N (2\pi f_j) A_j \frac{\cosh[k_j(z + H_w)]}{\sinh(k_j H_w)} \cos(2\pi f_j t - k_j x + \phi_j) \quad (16)$$

$$\ddot{u}_w(x, z, t) = - \sum_{j=1}^N (2\pi f_j)^2 A_j \frac{\cosh[k_j(z + H_w)]}{\sinh(k_j H_w)} \sin(2\pi f_j t - k_j x + \phi_j) \quad (17)$$

where $\Delta f = f_{cut}/N$ denotes the resolution of the frequency domain; N , usually a large number, indicates the number of

segments that the frequency domain is divided into; and f_{cut} is the upper cut-off frequency for wave spectrum S ; $A_j = 2\sqrt{S(f_j) \Delta f}$ and $f_j = j \cdot \Delta f$, $j = 1, \dots, N$; S is the JONSWAP wave spectrum (Dnvgl, 2010); ϕ_j is the generated random phase angle uniformly distributed from 0 to 2π ; H_w denotes water depth; k_j represents wave number, which is related to f_j by the dispersion equation (Faltinsen, 1990)

$$(2\pi f_j)^2 = g k_j \tanh(k_j H_w) \quad (18)$$

In **Figure 5**, the time history (for 200 s) and the spectrum of a generated random wave with the setting of wave peak period $T_p = 10$ s, significant wave height $H_s = 3$ m, water depth $H_w = 17.5$ m, number of segments $N = 2,000$ are generated and compared with the target JONSWAP spectrum. The close match indicates the generated wave achieves the desired wave climate and can be used for load evaluation.

With the current velocity \dot{u}_w and acceleration \ddot{u}_w obtained from Equations (16) and (17), the hydrodynamic forces exerted on a unit length of a pile can be evaluated using Morison's equation (Morison et al., 1950).

$$F = F_d + F_a = \frac{1}{2} \rho_w D C_d \dot{u}_w |\dot{u}_w| + \frac{1}{4} \rho_w \pi D^2 C_m \ddot{u}_w \quad (19)$$

Where $F_d = \frac{1}{2} \rho_w D C_d \dot{u}_w |\dot{u}_w|$ denotes the drag orce (per length) and $F_a = \frac{1}{4} \rho_w \pi D^2 C_m \ddot{u}_w$ denotes the inertia force (per length); ρ_w is the density of the fluid ($\rho_w = 1,025$ kg/m³ is adopted in this study); D is the diameter of the pile section; C_d and C_m are the drag and inertial coefficients ($C_d = 1.2$, $C_m = 2.0$ are adopted in this study). The virtual work δW_{wave} done by the hydrodynamic forces along the tower including the monopile under MSL can be expressed as,

$$\begin{aligned} \delta W_{wave} &= \int_{-H_w}^0 F [(\cos \beta \delta u_x + \sin \beta \delta u_y)] \\ &\approx \sum_{i=1}^{N_w} \delta \mathbf{u}_{tow,i}^T \mathbf{F}_{wave,i} \end{aligned} \quad (20)$$

where δu_x and δu_y indicate the virtual displacement along x and y directions, respectively. The last approximation in Equation (20) is based on work-equivalent nodal force using the FE model established in Section FE Model for Tower Including Foundation. N_w indicates the total number of elements that are below MSL; $\mathbf{F}_{wave,i}$ and $\delta \mathbf{u}_{tow,i}$ are the work-equivalent nodal force vector and virtual displacement vector of the i th element of the tower FE model, respectively. It is noted that δW_{wave} does not involve the DOFs above the MSL.

Damping Load

Modal damping is assumed for both the blades and the tower. The virtual work done by the damping force is given as,

$$\begin{aligned} \delta W_{damping} &= \delta W_{damping,bl} + \delta W_{damping,tow} \\ &= - \sum_{j=1}^3 (c_{bj,eg} \dot{u}_j \delta u_j + c_{bj,fp} \dot{u}_{j+3} \delta u_{j+3}) \\ &\quad - \begin{bmatrix} \delta u_7 \\ \delta u_8 \end{bmatrix}^T \begin{bmatrix} c_{aero,x} & 0 \\ 0 & c_{aero,y} \end{bmatrix} \begin{bmatrix} \dot{u}_7 \\ \dot{u}_8 \end{bmatrix} - (\delta \mathbf{u}_{tow})^T \mathbf{C}_{tow} \mathbf{v}_{tow} \end{aligned} \quad (21)$$

where $c_{bj,eg}$ and $c_{bj,fp}$ are the edgewise and flapwise modal damping coefficients of the j th blade; $c_{aero,x}$ and $c_{aero,y}$ are the aerodynamic damping coefficients of the nacelle in x and y directions, respectively; \mathbf{C}_{tow} is the modal damping matrix of the FE model of the tower.

Equations of Motion of OWT

With the kinetic energy, potential energy, and the forces obtained, the equations of motion of the monopile OWT can be obtained using the Euler-Lagrange equation as follows,

$$\frac{d}{dt} \frac{\partial T}{\partial \dot{u}_i} - \frac{\partial T}{\partial u_i} + \frac{\partial V}{\partial u_i} = F_i \quad (22)$$

where the kinetic energy T and potential energy V can be obtained from Equation (9) and Equation (11), respectively; u_i indicates each DOF of the FE model of the tower; the corresponding forcing term F_i can be obtained by,

$$F_i = \frac{\partial (\delta W)}{\partial (\delta u_i)} = \frac{\partial (\delta W_{wind} + \delta W_{wave} + \delta W_{damping})}{\partial (\delta u_i)} \quad (23)$$

with δW_{wind} , δW_{wave} , and $\delta W_{damping}$ obtained from Equations (14), (20), and (21).

After collecting the terms in Equation (22), the following equations of motion can be obtained,

$$\mathbf{M}\ddot{\mathbf{u}} + \mathbf{C}\dot{\mathbf{u}} + \mathbf{K}\mathbf{u} = \mathbf{F} \quad (24)$$

where $\mathbf{u} = [u_1 \ u_2 \ u_3 \ u_4 \ u_5 \ u_6 \ \mathbf{u}_{tow}^T]^T$; the corresponding mass matrix \mathbf{M} , damping matrix \mathbf{C} , stiffness matrix \mathbf{K} , and force vector \mathbf{F} are listed in the **Appendix**.

PROPOSED REAL-TIME HYBRID SIMULATION FRAMEWORK

A RTHS framework is proposed in this section to study the structural behavior of the monopile OWT shown in **Figure 1A**.

Its details, including the framework descript, possible scaling laws applied, and error contributors are explained in Section. Proposed Real-Time Hybrid Simulation Framework.

Framework Description

The proposed RTHS platform is shown in **Figure 6**. In this RTHS platform, the numerical component contains the rotor blades and aerodynamic loads; the experimental component contains the tower structure (including the nacelle, hub, and foundation) along with the hydrodynamic loading effects provided by wave tank and necessary hardware (actuators and sensors). It is noted that, the numerical component is simulated under full-scale, and the experimental component is tested in reduced scale. The two components are interfaced through the displacement DOFs (u_7 and u_8) at the top of the tower. This RTHS framework directly resolves the Froude-Reynold scaling conflict by applying full-scale aerodynamic simulation in the numerical component, and meanwhile it can preserve the complex hydrodynamic behaviors in the wave tank facility at a reduced scale, including soil-structure interaction and wave-current interaction. In this concept study, to assess the feasibility of the proposed RTHS framework and identify possible contributors that may impact the RTHS performance, a “virtual” RTHS is established through numerical simulation of both the numerical and experimental components.

To explain, the displacement vector of the entire OWT, \mathbf{u} , defined in Equation (24) is partitioned based on the proposed RTHS framework as,

$$\mathbf{u} = [u_1 \ u_2 \ u_3 \ u_4 \ u_5 \ u_6 \ \mathbf{u}_{tow}^T]^T = [\mathbf{u}_N^T \ \mathbf{u}_I^T \ \mathbf{u}_E^T]^T \quad (25)$$

where $\mathbf{u}_N = [u_1 \ u_2 \ u_3 \ u_4 \ u_5 \ u_6]^T$, $\mathbf{u}_I = [u_7 \ u_8]^T$, and \mathbf{u}_E is the tower displacement vector \mathbf{u}_{tow} excluding the DOFs of \mathbf{u}_I . The subscripts “I”, “N”, and “E” indicate the DOFs are related to the interfacing system, numerical component, and experimental component of the proposed RTHS framework, respectively. Based on the partition shown in Equation (25), the equations of motion, Equation (24), can be written into the partitioned formulation as,

$$\begin{aligned} &\begin{bmatrix} \mathbf{M}_{NN} & \mathbf{M}_{NI} & \mathbf{0} \\ \mathbf{M}_{IN} & \mathbf{M}_{II}^N + \mathbf{M}_{II}^E & \mathbf{M}_{IE} \\ \mathbf{0} & \mathbf{M}_{EI} & \mathbf{M}_{EE} \end{bmatrix} \begin{bmatrix} \ddot{\mathbf{u}}_N \\ \ddot{\mathbf{u}}_I \\ \ddot{\mathbf{u}}_E \end{bmatrix} \\ &+ \begin{bmatrix} \mathbf{C}_{NN} & \mathbf{C}_{NI} & \mathbf{0} \\ \mathbf{C}_{IN} & \mathbf{C}_{II}^N + \mathbf{C}_{II}^E & \mathbf{C}_{IE} \\ \mathbf{0} & \mathbf{C}_{EI} & \mathbf{C}_{EE} \end{bmatrix} \begin{bmatrix} \dot{\mathbf{u}}_N \\ \dot{\mathbf{u}}_I \\ \dot{\mathbf{u}}_E \end{bmatrix} \\ &+ \begin{bmatrix} \mathbf{K}_{NN} & \mathbf{K}_{NI} & \mathbf{0} \\ \mathbf{K}_{IN} & \mathbf{K}_{II}^N + \mathbf{K}_{II}^E & \mathbf{K}_{IE} \\ \mathbf{0} & \mathbf{K}_{EI} & \mathbf{K}_{EE} \end{bmatrix} \begin{bmatrix} \mathbf{u}_N \\ \mathbf{u}_I \\ \mathbf{u}_E \end{bmatrix} = \begin{bmatrix} \mathbf{F}_N \\ \mathbf{F}_I^N + \mathbf{F}_I^E \\ \mathbf{F}_E \end{bmatrix} \end{aligned} \quad (26)$$

The subscripts are defined in the same manner as in Equation (25). The superscripts “E” and “N” indicate the term originates from the experimental component or from the numerical component. The detailed expressions for each term are listed in the **Appendix**.

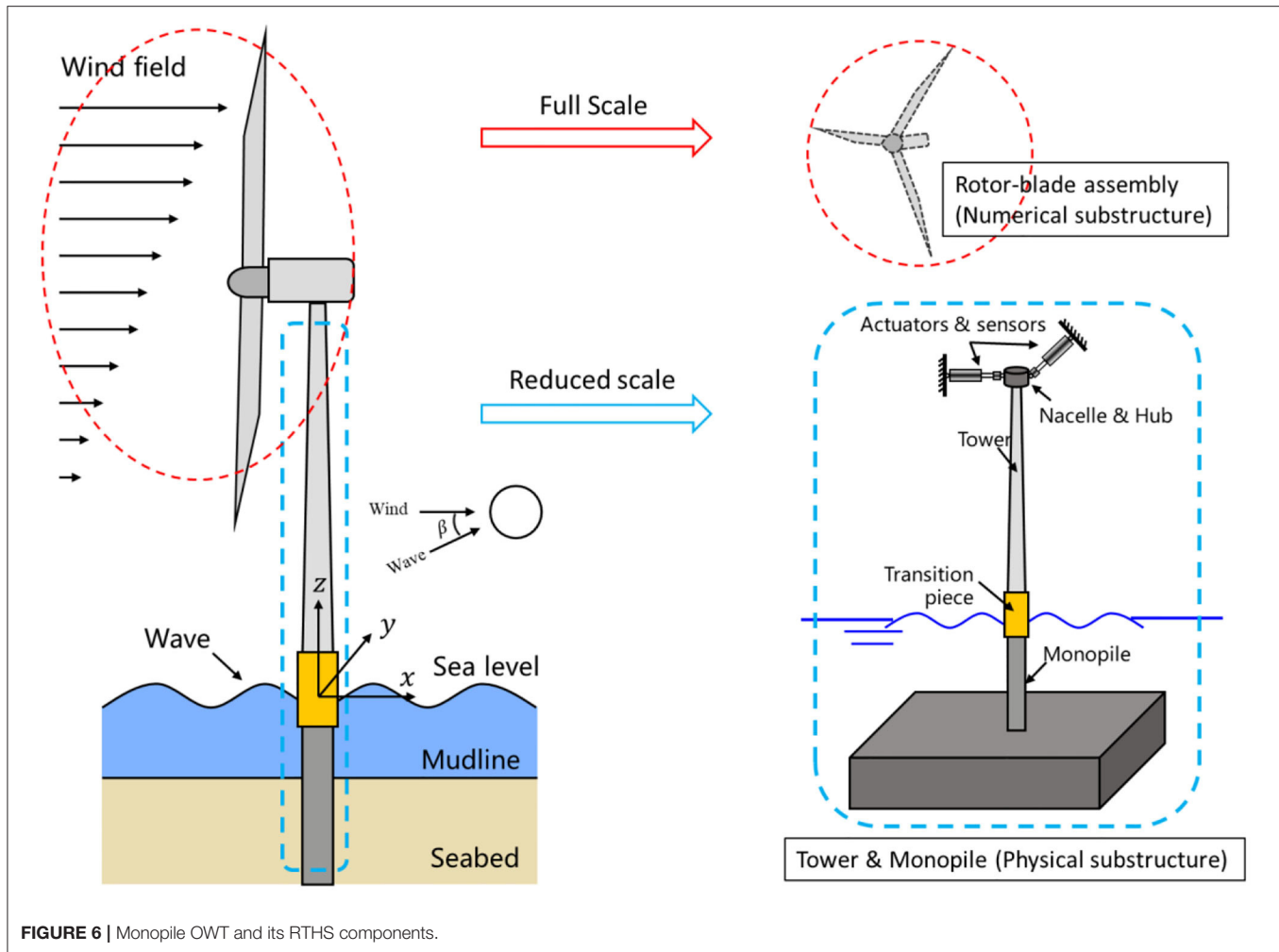


FIGURE 6 | Monopile OWT and its RTHS components.

Based on Equation (26), the equation of motion for the numerical component [1st block row in Equation (26)] of the RTHS framework can be determined as

$$\mathbf{M}_{NN}\ddot{\mathbf{u}}_N + \mathbf{C}_{NN}\dot{\mathbf{u}}_N + \mathbf{K}_{NN}\mathbf{u}_N = \mathbf{F}_N - \mathbf{f}_I^N \quad (27)$$

where \mathbf{f}_I^N indicates the interface force acting on the numerical component. It can be computed as

$$\mathbf{f}_I^N = \mathbf{M}_{NI}\ddot{\mathbf{u}}_I + \mathbf{C}_{NI}\dot{\mathbf{u}}_I + \mathbf{K}_{NI}\mathbf{u}_I = \mathbf{M}_{NI}\ddot{\mathbf{u}}_I \quad (28)$$

The last equality in Equation (28) holds because $\mathbf{C}_{NI} = \mathbf{0}$ and $\mathbf{K}_{NI} = \mathbf{0}$ (see **Appendix**).

Similarly, the equation of motion for the experimental component [2nd and 3rd block rows in Equation (26)] of the RTHS framework can be determined as

$$\begin{bmatrix} \mathbf{M}_{II}^E & \mathbf{M}_{IE} \\ \mathbf{M}_{EI} & \mathbf{M}_{EE} \end{bmatrix} \begin{bmatrix} \ddot{\mathbf{u}}_I \\ \ddot{\mathbf{u}}_E \end{bmatrix} + \begin{bmatrix} \mathbf{C}_{II}^E & \mathbf{C}_{IE} \\ \mathbf{C}_{EI} & \mathbf{C}_{EE} \end{bmatrix} \begin{bmatrix} \dot{\mathbf{u}}_I \\ \dot{\mathbf{u}}_E \end{bmatrix} + \begin{bmatrix} \mathbf{K}_{II}^E & \mathbf{K}_{IE} \\ \mathbf{K}_{EI} & \mathbf{K}_{EE} \end{bmatrix} \begin{bmatrix} \mathbf{u}_I \\ \mathbf{u}_E \end{bmatrix} = \begin{bmatrix} \mathbf{F}_I^E \\ \mathbf{F}_E \end{bmatrix} + \begin{bmatrix} \mathbf{F}_I^N - \mathbf{f}_I^E \\ \mathbf{0} \end{bmatrix} \quad (29)$$

where \mathbf{f}_I^E indicates the interface force acting on the experimental component. It can be computed as

$$\begin{aligned} \mathbf{f}_I^E &= \mathbf{M}_{IN}\ddot{\mathbf{u}}_N + \mathbf{C}_{IN}\dot{\mathbf{u}}_N + \mathbf{K}_{IN}\mathbf{u}_N + \mathbf{M}_{II}^N\ddot{\mathbf{u}}_I + \mathbf{C}_{II}^N\dot{\mathbf{u}}_I + \mathbf{K}_{II}^N\mathbf{u}_I \\ &= \mathbf{M}_{IN}\ddot{\mathbf{u}}_N + \mathbf{C}_{IN}\dot{\mathbf{u}}_N + \mathbf{K}_{IN}\mathbf{u}_N + \mathbf{M}_{II}^N\ddot{\mathbf{u}}_I + \mathbf{C}_{II}^N\dot{\mathbf{u}}_I \end{aligned} \quad (30)$$

The last equality in Equation (30) holds because $\mathbf{K}_{II}^N = \mathbf{0}$ (see **Appendix**). In addition, if sufficient amount of mass can be added to the experimental component to include the mass effect from the nacelle and rotor systems, i.e., \mathbf{M}_{II}^N , then $\mathbf{M}_{II}^N\ddot{\mathbf{u}}_I$ can be removed from Equation (30) as it will be naturally considered during the testing of experimental component.

Based on the numerical and experimental components defined in **Figure 6**, the procedure for RTHS using wave tank facility can be extracted from Equations (27)~(30). To summarize, the numerical component takes the measurement of $\ddot{\mathbf{u}}_I$ during the test to compute \mathbf{f}_I^N [Equation (28)]. The response of numerical component, \mathbf{u}_N , under the combined action of aerodynamic load \mathbf{F}_N and \mathbf{f}_I^N , is determined through numerical integration by solving Equation (27). The solved responses (\mathbf{u}_N , $\dot{\mathbf{u}}_N$, and $\ddot{\mathbf{u}}_N$) are used to compute \mathbf{f}_I^E (Equation 30). In wave tank facility, \mathbf{f}_I^E combined with the aerodynamic force \mathbf{F}_I^N are

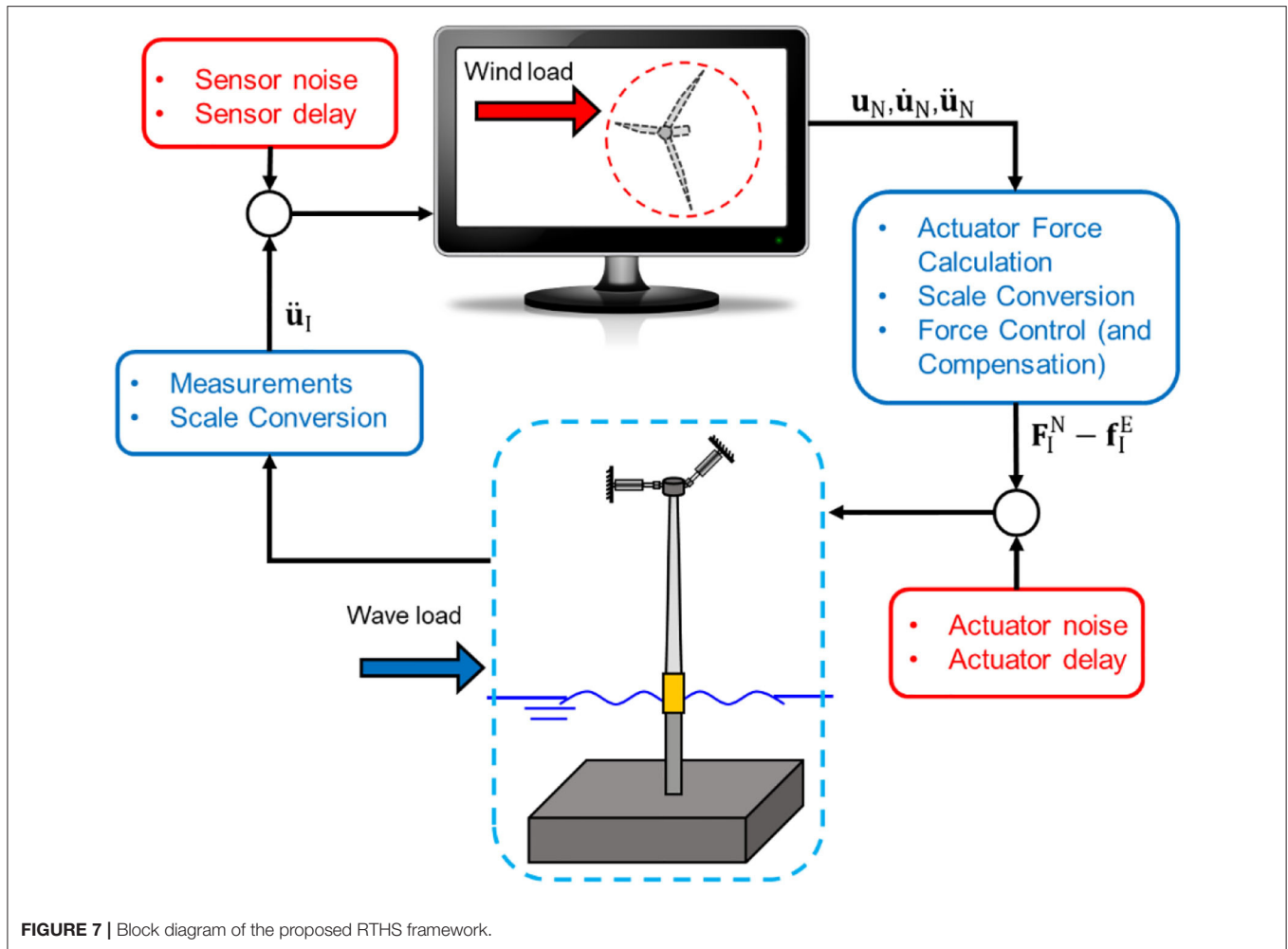


FIGURE 7 | Block diagram of the proposed RTHS framework.

applied to the OWT specimen via actuators, while the force vector $[(F_I^E)^T (F_E)^T]^T$ is generated via wavemaker. Then, the induced response ($\ddot{\mathbf{u}}_I$) is measured through sensors and fed to the numerical component to close the loop. A block diagram describing this process is provided in Figure 7.

Scaling Laws

In the proposed RTHS framework (Figure 6), the scaling conflict is avoided because the aerodynamic effects are simulated in full-scale, which is separated from the hydrodynamic effects produced in wave tank facility in reduced scale. So far, most of the existing scaled wave tank tests adopt Froude scaling, because the Froude number, Fr , defined in Equation (31) below, characterizes the gravitational effect which is dominating in problems with free surface waves.

$$Fr = V/\sqrt{gL} \quad (31)$$

where V is the wave celerity or propagation speed, g is the gravitational acceleration, and L is the characteristic length. However, hydrodynamic effects due to water waves are not the only dynamic effects need to be considered in the RTHS tests.

The elastic effect due to slender specimen deformation also needs to be considered. Following the Froude scaling, it can be shown that the consistent scaling to preserve the similitude in structural modal information (natural frequencies and mode shapes) is (Martin, 2011; Bredmose et al., 2012)

$$\lambda_{EI} = \lambda_\rho \lambda_L^5 \quad (32)$$

where λ_{EI} , λ_ρ , and λ_L are the scaling factor of bending stiffness (EI), density (ρ), and length (L), between the model and the prototype. It is noted that (Equation 32) implies that if the density of the material stays unchanged ($\lambda_\rho = 1$), the elastic modulus E needs to be modified. This requirement is usually difficult to achieve directly. Often for the OWT tower, it is sufficient that the bending stiffness EI scales correctly, which provides some freedom in the model design. Therefore, the combination of material density, stiffness, and geometry are usually tuned together to achieve the scaling goal. This method, although challenging, has been applied in OWT wave tank studies (Martin, 2011; Martin et al., 2014).

In this study, several alternatives have been considered in addition to the above Froude scaling law. In earthquake

engineering, Cauchy scaling combined with Froude scaling are often considered in designing scaled models for dynamic testing. Cauchy scaling preserves the Cauchy number, Ca , defined in Equation (33), which is important in characterizing the deformation of the specimen.

$$Ca = \rho V^2 / E \quad (33)$$

With the condition $\lambda_E = \lambda_\rho \lambda_L$, Froude and Cauchy similitudes are simultaneous. It implies that if the same material is used for both prototype and model with $\lambda_E = 1$, the density of the specimen needs to be increased. Usually added artificial masses are distributed to the model specimen to achieve that and minimize the change in mass distribution. However, when applying this simultaneous Fr-Ca scaling law, the hydrodynamic effects are distorted, because water usually is the only liquid considered in wave tank facilities. Under the Fr-Ca similitude, the proper scaling factor for force acting on the OWT $\lambda_{tf} = \lambda_L^2$. But with water used as the testing fluid, the scaling factor for hydrodynamic force induced by wave and current is, $\lambda_{hf} = \lambda_L^3 \neq \lambda_{tf}$, which causes distortion in hydrodynamic force scaling. To consider the impacts of possible scaling laws on the proposed RTHS, a total of three scaling laws are considered in this study:

- Froude scaling with $\lambda_\rho = 1$. In this case, all terms are properly scaled but it poses a challenge to the model construction in preserving the similitude in bending stiffness;
- Conventional Fr-Ca scaling, which induces distorted hydrodynamic force induced from the wave tank;
- Fr-Ca scaling with increased wave amplitude. By increasing the amplitude of the generated wave by a factor of $\sqrt{1/\lambda_L}$, the drag force F_d in Equation (19) can be properly scaled with a factor of λ_L^2 , matching the requirement from the OWT. However, the inertia force F_a is still distorted under this scaling law.

The last two of the scaling laws both are derived from Fr-Ca scaling. A systematic way of model construction is the advantage in them, comparing to the Froude scaling. The trade-off is they both suffer from distorted hydrodynamic effects. One of the goals in this study is to examine how these scaling laws impact the error in the proposed RTHS framework. Other options have also been considered in the early stage of this study:

- Fr-Ca scaling with increased depth by a factor of $1/\lambda_L$. In this case, the wet section of the tower ($z \in [-H_w, 0]$) is effectively unscaled, then the similitude of hydrodynamic forces generated on the specimen are preserved. But it is infeasible for wave tank facility to offer such a depth to study OWT. In addition, the design of the unscaled section needs to be adjusted to preserve the similitude in bending stiffness and mass.
- Fr-Ca scaling with increased wave amplitude by a factor of $1/\lambda_L$. In this case, the amplitude of the generated wave is effectively unscaled. The inertia force F_a is properly scaled with a factor of λ_L^2 , but the drag force F_d is distorted. This option is infeasible due to its high demand in the wavemaker.
- Froude scaling with $\lambda_\rho = 1$ and no further adjustment for the tower geometry, i.e., no added mass nor a matching bending

stiffness EI . In this case, the hydrodynamic effects from the wave tank are properly scaled, but the modal properties of the OWT is distorted which causes significant response error.

These three options all have been rejected due to issues in their feasibility or accuracy.

Error Contributors

In RTHS, experimental errors accumulate in real-time closed loop through the numerical integration scheme due to control and measurement discrepancies. It is known that delays and noises in the interfacing actuator and sensor systems are the main contributors to the above errors, as they tend to bring destabilizing effect into RTHS, causing large experimental error or even failure (Christenson et al., 2014; Maghareh et al., 2014; Hayati and Song, 2017). Such destabilizing effect is more pronounced in reduced scaled model testing than in full-scale, because the frequency of interest is amplified according to scaling process (Hayati and Song, 2018; Wu and Song, 2019). In addition, the impact of modeling choices (e.g., scaling laws, wave heights, and misalignment angles) on errors are also studied to guide future specimen designs.

In this study, to evaluate the feasibility and assess the performance of the proposed RTHS framework, noises, and delays are considered as the primary error contributors and modeled into the RTHS. As a concept study, the hardware implementation issues of sensors and actuators are out of the current scope. In **Figure 7**, a block diagram is provided to illustrate the general RTHS process described in Section. Framework Description. The noises and delays considered are the actuator noise, actuator delay, sensor noise, and sensor delay, which are also shown in **Figure 7**. The details of how the delays and noises are generated can be found in Section. Case I: Delay and Section. Case II: Noise, respectively. In addition, the other possible error contributors considered in this study are the scaling laws, misalignment angle β and the significant wave height H_s .

NUMERICAL STUDY

A concept study is carried out to assess the feasibility and identify the impact of the selected contributors on the performance of the proposed RTHS. The details and results for the study are described in Section. Numerical Study.

System Parameters

The National Renewable Energy Lab (NREL) 5-MW reference wind turbine (Jonkman et al., 2009) is used in this study. Details of the modeling parameters are presented in **Table 1**.

As indicated in **Figure 3**, soil effects are considered using linear springs and dashpots. According to Carswell et al. (2015); Sun and Jahangiri (2018), the values for the spring stiffness are chosen as $k_x = k_y = 3.89 \times 10^9 \text{ N/m}$ and $k_{x\phi} = k_{y\phi} = 1.14 \times 10^{11} \text{ Nm/rad}$ to represent clay soil condition. Soil damping coefficients c_x , c_y , $c_{x\phi}$, and $c_{y\phi}$ are selected such that the corresponding damping ratios are $\zeta_x = \zeta_y = \zeta_{x\phi} = \zeta_{y\phi} = 0.6\%$. Based on the FE model, the natural frequencies

TABLE 1 | Modeling parameters of the NREL 5-MW reference wind turbine.

Rotor	Rating	5 MW
	Rotor diameter	126 m
	Rated wind speed	12 m/s
	Rated rotor speed	12.1 rpm
Blade	Length	61.5 m
	Mass	17,740 kg
	Natural frequency of 1st edgewise bending mode	1.08 Hz
	Natural frequency of 1st flapwise bending mode	0.68 Hz
Nacelle and Hub	Damping ratios (edgewise and flapwise) of 1st mode	0.48%
	Nacelle mass	240,000 kg
	Hub mass	56,780 kg
	Hub diameter	3 m
OWT	Hub height	90 m
	Height above the seabed	87.6 m
	Overall (integrated) mass	347,460 kg
	Natural frequency of 1st fore-aft bending mode	0.324 Hz
	Natural frequency of 1st side-side bending mode	0.312 Hz
	Damping ratios of all modes	1%

of the major bending mode with and without soil effects are 0.315 Hz and 0.335 Hz, respectively. Comparing to the natural frequency listed in **Table 1**, both values are close to the original natural frequency of 0.324 Hz, although the soil effects reduce the fundamental frequency by $\sim 6\%$. The natural frequencies of the blade are obtained as 1.09 Hz (edgewise) and 0.68 Hz (flapwise), also match the values listed in **Table 1**.

Simulated Loads

According to the procedure in Section. Wind Loading and the parameters in **Table 1**, the aerodynamic loading corresponding to a rotor speed of $V_r = 12.1 \text{ rpm}$, an average wind speed of $V_\infty = 12 \frac{\text{m}}{\text{s}}$ at the hub height 90m, and a turbulence intensity of $TI = 10\%$, is generated. According to the procedure in Section. Wave and Current Loading, a random wave corresponding to with the setting of $T_p = 10 \text{ s}$, $H_s = 3\text{m}$, $H_w = 17.5\text{m}$ (same as shown in **Figure 5**), is generated. Then, the nodal forces and moments, \mathbf{F}_{wave} , at a misalignment angle $\beta = 30^\circ$ are computed accordingly. It is noted that the selected parameters in Section. System parameters and in generating these structural loads constitute a representative case of typical OWT behavior to investigate the proposed RTHS framework. Complex OWT behavior under specific site conditions will be investigated in future study.

Numerical Models

In this study, the prototype and the RTHS models are simulated using MATLAB (MathWorks, 2020). The prototype is modeled using the parameters provided in Section. System parameters and the loads generated in Section. Simulated loads. The RTHS models are modeled in a similar way. The scaling laws described in Section. Error contributors are applied in creating experimental component in the corresponding RTHS models. Therefore, three RTHS models are created with one for each

TABLE 2 | Scaling relations for the RTHS models.

Quantities	RTHS Models		
	Froude scaling (Fr)	Froude-Cauchy scaling (Fr-Ca)	Froude-Cauchy scaling with drag force correction (Fr-Ca-dg)
Length/displacement	λ_L	λ_L	λ_L
Elastic modulus	λ_L	1	1
Moment of inertia	λ_L^4	λ_L^4	λ_L^4
Density	1	$1/\lambda_L$	$1/\lambda_L$
Mass	λ_L^3	λ_L^2	λ_L^2
Velocity	$\sqrt{\lambda_L}$	$\sqrt{\lambda_L}$	$\sqrt{\lambda_L}$
Acceleration	1	1	1
Force	λ_L^3	λ_L^2	λ_L^2
Time	$\sqrt{\lambda_L}$	$\sqrt{\lambda_L}$	$\sqrt{\lambda_L}$
Frequency	$\sqrt{1/\lambda_L}$	$\sqrt{1/\lambda_L}$	$\sqrt{1/\lambda_L}$
Wave spectrum	$\lambda_L^{5/2}$	$\lambda_L^{5/2}$	$\lambda_L^{3/2}$
Wave force	λ_L^3	λ_L^3	N/A

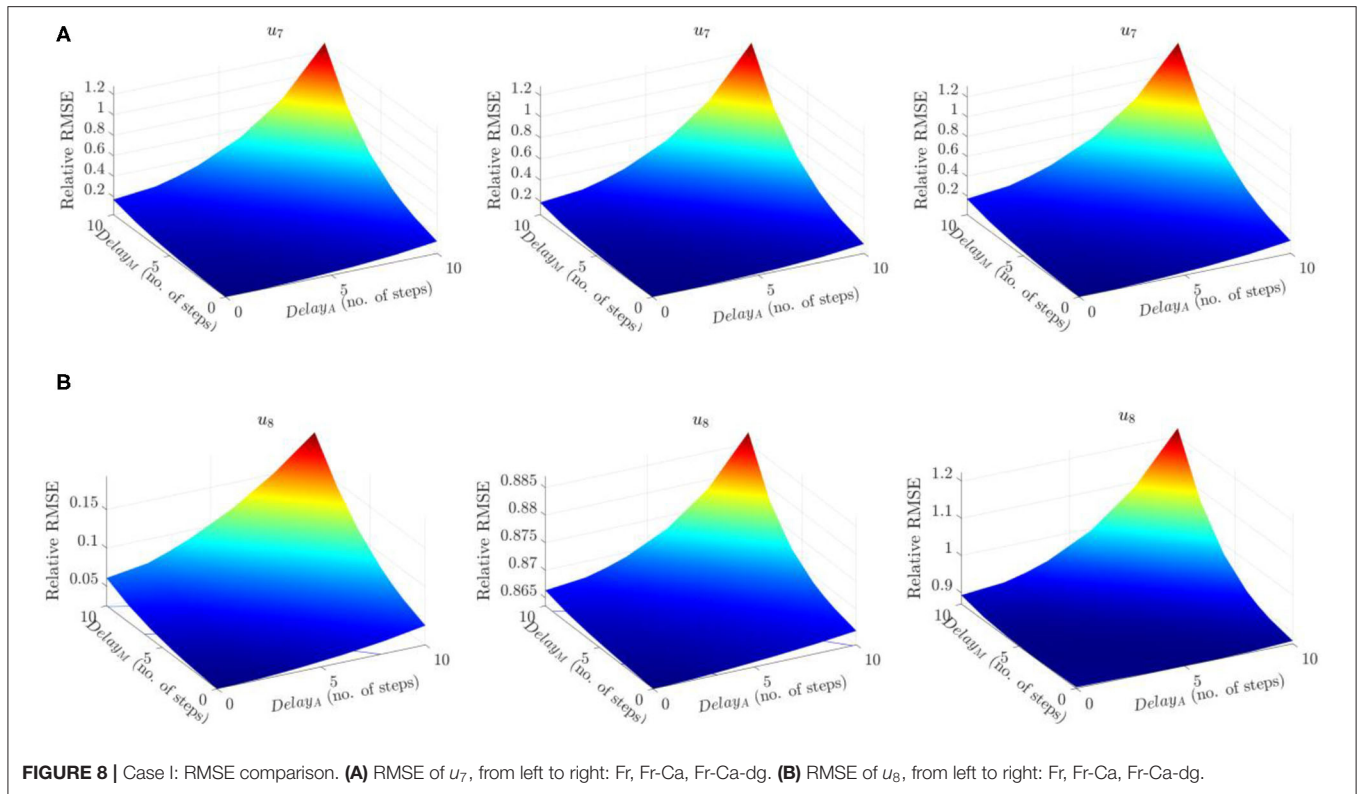
scaling law. The details about the scaling relations are shown in **Table 2**.

In all RTHS models, a length scale $\lambda_L = 1/25$ is used for the experimental component (the tower structure) and the water is considered as the fluid for the wave tank (hence $\lambda_{\rho_w} = 1$). Based on **Table 2**, it is noted that

- The only scaling law completely preserves the similitude is the “Fr” model. The wave force generated in “Fr-Ca” and “Fr-Ca-dg” models does not match the force similitude of the tower structure. But it is noted that the specimen design is more challenging for the “Fr” model than the other two models as described in Section. Error contributors.
- The difference between “Fr-Ca” and “Fr-Ca-dg” models is that the wave spectrum is adjusted by a factor of $1/\lambda_L$, or wave amplitude by a factor of $\sqrt{1/\lambda_L}$. As pointed out in Section. Error contributors, although such an adjustment preserves the similitude of drag force F_d , but the overall wave force scale is still distorted.

Study Cases

A total of five cases are considered in this study to evaluate the feasibility and identify error contributors of the proposed RTHS framework. In each case, sensitivity analysis is performed to determine the influence of the error contributors and their tolerances for a feasible RTHS design. The relative root-mean-square error (RMSE) between the responses obtained from RTHS and the prototype model is used to measure the performance. Prior to the RMSE calculation, the responses obtained from the RTHS models are scaled back to full-scale using the corresponding scale factors listed in **Table 2**. Each numerical simulation runs with a time step of $1/1,024 \text{ s}$ and a duration of 120 s.



Case I: Delay

In this case, both the actuator delay and the sensor delay shown in **Figure 7** are considered in the RTHS simulations. Seven different delayed time steps are considered, which are 0, 2, 3, 4, 6, 8, and 10, for both delays. Therefore, a total of 49 simulations are performed for each RTHS model. To focus on the impact from delay, noises are set as zero in all the simulations.

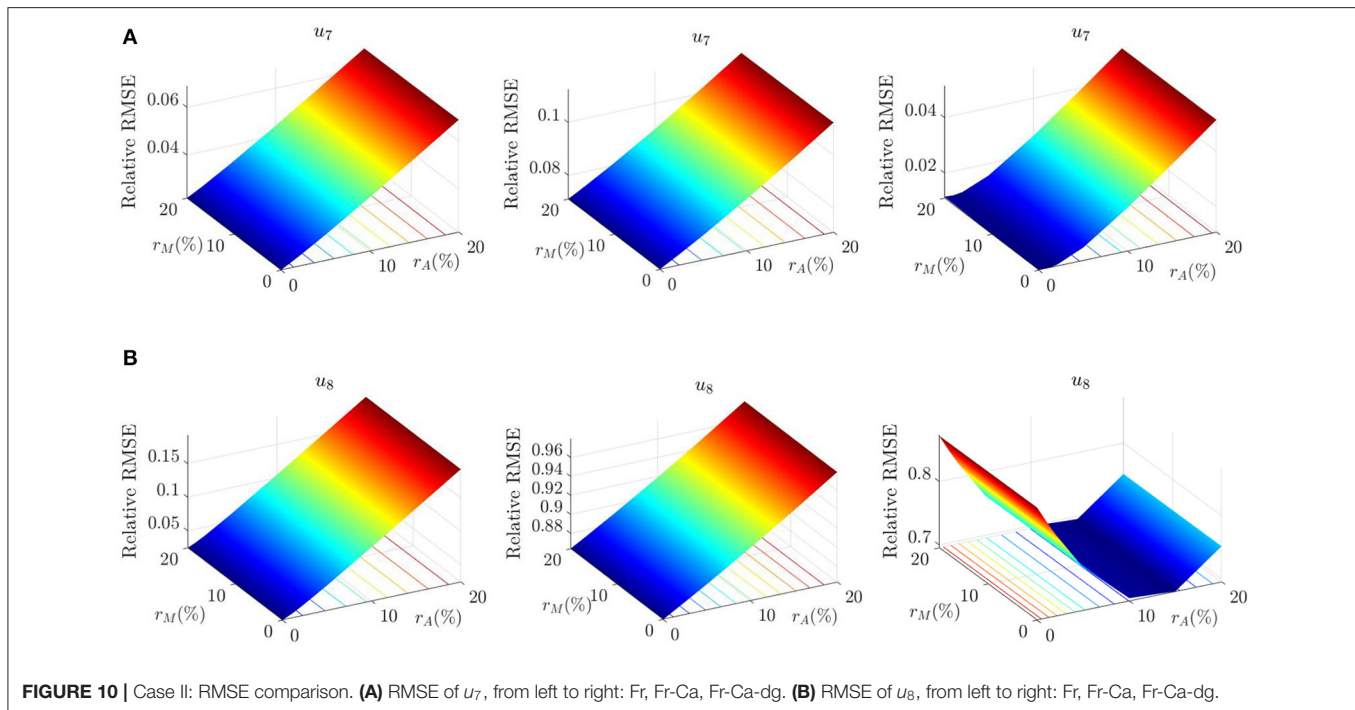
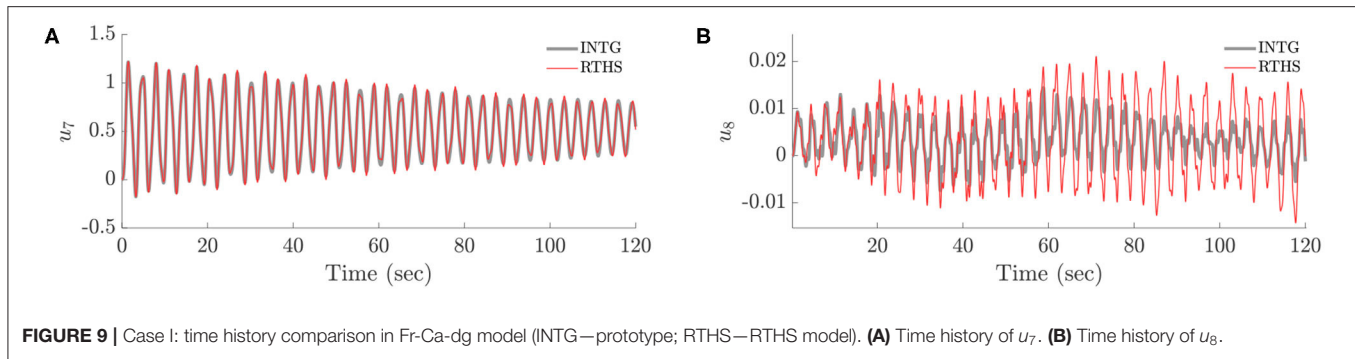
The RMSE for the responses u_7 and u_8 are summarized in **Figure 8**. The responses of these two DOFs are chosen because they are the interfacing DOFs whose accuracy directly impacts the accuracy of both numerical and experimental components, and hence the overall performance. Abbreviations “Fr,” “Fr-Ca,” and “Fr-Ca-dg” indicate RTHS models obtained using Froude scaling, Froude-Cauchy scaling, and Froude-Cauchy scaling with drag force correction, respectively. The axes “ $delay_A$ ” and “ $delay_M$ ” indicate the number of delayed time steps in actuator and sensor (measurement) systems, respectively.

From **Figure 8**, the RMSE error quickly increases as the delays increase. For the response in u_7 the performance of the three RTHS models are similar. But, for the response in u_8 , the error in Fr model is much smaller than the other two, indicating a better performance due to its preserved similitude. The contrast between u_7 and u_8 is because most of the response in u_7 is induced by wind load, and most of the response in u_8 is induced by the hydrodynamic forces. The error in u_8 serves as a better indicator for scaling distortion in hydrodynamic force. For the RTHS models “Fr-Ca” and “Fr-Ca-dg,” where the hydrodynamic forces are distorted, their u_8 responses are expected with higher errors than the “Fr” model.

To determine the tolerance on delays, a closer view on the RMSE results indicates, when both delays are 3 steps, the RMSEs for the Fr, Fr-Ca, Fr-Ca-dg are 5.5, 9.3, 5.3% for u_7 , and 3.4, 86.5, 87.0% for u_8 . These results indicate that the drag force correction improves the accuracy of u_7 in the Fr-Ca-dg model comparing to the Fr-Ca model. But clearly, Fr model is the one that can provide accurate response estimation for both u_7 and u_8 . When inspecting **Figure 9**, the time histories in the Fr-Ca-dg model indicates that, although the comparison between the “INTG” (prototype) and the “RTHS” in u_8 show obvious discrepancies, the amplitude of u_8 is much smaller (almost negligible) than u_7 . Actually, the root-mean-square (RMS) value of u_8 is only 5% of that of u_7 . Therefore, if only the significant fore-aft response is of concern, the Fr-Ca-dg RTHS model can also be considered as a viable alternative when both delays are 3 steps. For the Fr-Ca model, even when both delays are zero, the RMSE is still around 7%, which is the worst among all three RTHS models.

Case II: Noise

To determine the influence of noise on the performance of the proposed RTHS framework, both the actuator noise and the sensor noise shown in **Figure 7** are considered in the RTHS simulations. The noises are generated as normally distributed random numbers with a zero mean and a standard deviation equal to a ratio of the standard deviation of the corresponding signal. r_A and r_M denote such ratios for the actuator noise and the sensor noise, respectively. Seven values for both ratios are chosen as 0, 1, 2, 5, 10, 15, and 20%. Therefore, a total of 49 simulations



are performed for each RTHS model. To focus on the impact from noise, delays are set as zero in all the simulations.

From **Figure 10**, it is shown that, for u_7 , both the Fr and the Fr-Ca-dg models produce smaller errors than the Fr-Ca model; for u_8 , the Fr model yields the smallest error, and both the Fr-Ca and the Fr-Ca-dg models produce similar levels of error, due to their distorted hydrodynamic effects. The contour lines in parallel to r_M axis in all the graphs indicate that the RMSEs are more sensitive to the noise levels in the actuator system than in the sensor system. The reason is that the numerical component simulated in full-scale has lower natural frequencies than the experimental component. The sensor noises fed into the numerical system is effectively “filtered” by the numerical system and impose little influence on the system responses. While most of the RMSE results demonstrate an increasing trend with respect to the noise level, the RMSE of u_8 in the Fr-Ca-dg model shows a decreasing phase before the increasing trend. The exact reason to this observation is unknown, but it may be related to the drag force correction. The RMSEs of the blade responses ($u_1 \sim u_6$)

are also examined, but only small changes are shown with the considered noise range, and therefore are not shown in this study.

Because the RMSEs show weak sensitivity with respect to the sensor noises, **Table 3** is prepared by averaging all the RMSEs with the same actuator noise levels but different sensor noises.

Based on **Table 3**, it can be seen that the Fr-Ca-dg model yields the smallest error on u_7 , and the next is the Fr model. Both of them yield around 4 – 5% error under 15% level of noise. The Fr-Ca model, however, produces more than 10% RMSE at 15% level of noise. For u_8 , similar as Case I, only the Fr model can produce accurate tracking up to 5% level of noise. Again, if u_8 is not of concern, then both the Fr and the Fr-Ca-dg models can be adopted for RTHS development.

Case III: Delay Combined With Noise

To examine the performance under combined effects of delay and noise, the actuator delay and the sensor delay are set to be equal to each other with the seven predetermined values, i.e., $delay_A = delay_M = delay = 0, 2, 3, 4, 6, 8$, and 10; and the

noises are also set in a similar manner with $r_A = r_M = r = 0, 1, 2, 5, 10, 15$, and 20% . A total of 49 simulations are performed for each RTHS model.

In **Figure 11**, three RMSE plots are presented for the Fr model. The blade response u_1 is selected to represent the blade edgewise responses, $u_1 \sim u_3$, and u_4 to represent the flapwise responses, $u_4 \sim u_6$. All three plots indicate an increasing trend with response to the delays, and the contour lines show that RMSEs are more sensitive to the delays than to the noise levels. It is also noted that the blade flapwise response u_4 has a much higher RMSE value than the others, which is inspected further when discussing the tolerance. It is observed that the RMSEs of u_1 , u_4 , and u_7 in the Fr-Ca and Fr-Ca-dg models are similar as those in **Figure 11**, and therefore are not repeated here.

The RMSEs for u_8 of the three RTHS models are compared in **Figure 12**. They all show sensitivities to both delay and noise

levels to some extent. The Fr-Ca model shows higher sensitivity to noises than to delays, while the Fr model shows similar levels of sensitivities to both. The Fr-Ca-dg model provides a non-monotonic relation against noise, which matches the observation made in Case II. The RMSEs in the Fr-Ca and Fr-Ca-dg models are much higher than the Fr model, similar as observed from Cases I and II.

Because the RMSEs of u_1 , u_4 , and u_7 show weak sensitivity to noise levels, **Table 4** is prepared to demonstrate the delay impacts on error tolerance by averaging all the RMSEs with the same delays but different noise levels. Note that the delays applied in this section carry a doubled-effect because both actuator and sensor are specified with the same amount of delay. Based on the results in **Table 4**, all three models show similar performance for u_1 and u_4 . For u_7 , both the Fr and Fr-Ca-dg models provide superior performance to the Fr-Ca model, and

TABLE 3 | Averaged RMSE (%) for Case II: actuator noise impact.

Noise ratio (r_A) %	Fr model		Fr-Ca model		Fr-Ca-dg model	
	u_7	u_8	u_7	u_8	u_7	u_8
0	2.2	2.4	7.1	86.4	1.1	87.2
1	2.4	3.0	7.3	86.9	1.1	84.7
2	2.6	3.8	7.5	87.4	1.1	82.4
5	3.3	6.2	8.0	89.1	1.6	76.3
10	4.4	10.5	9.0	91.9	2.6	69.9
15	5.6	14.8	10.1	94.9	3.9	69.5
20	6.9	19.2	11.2	97.9	5.1	75.1

TABLE 4 | Averaged RMSE (%) for Case III: delay impact.

Delay (# of steps)	Fr model			Fr-Ca model			Fr-Ca-dg model		
	u_1	u_4	u_7	u_1	u_4	u_7	u_1	u_4	u_7
0	1.5	4.3	3.9	1.7	4.3	8.6	1.5	4.3	2.4
2	5.9	15.7	5.3	6.0	15.8	9.5	5.9	15.7	4.1
3	9.8	27.6	7.1	9.8	27.8	10.7	9.8	27.7	6.1
4	14.8	45.4	9.9	14.9	45.6	12.9	14.9	45.6	9.3
6	30.5	114.6	22.0	30.6	115.1	23.6	30.6	115.0	22.0
8	58.4	283.5	52.6	58.6	284.6	53.5	58.6	284.6	53.6
10	105.7	696.6	128.3	105.9	699.3	129.1	105.9	699.2	131.1

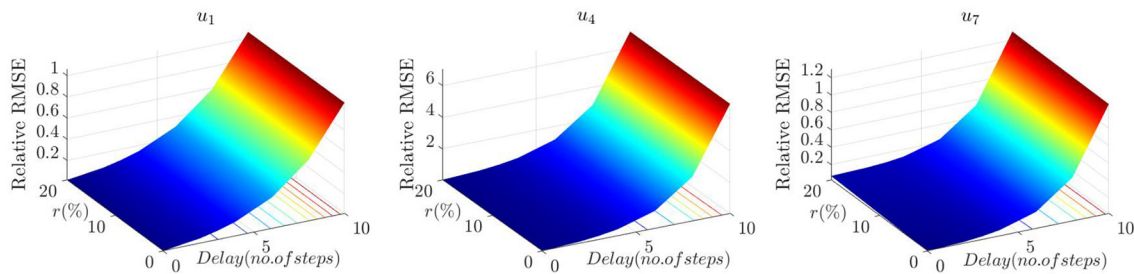


FIGURE 11 | Case III: RMSE comparison for u_1 , u_4 , and u_7 in Fr model.

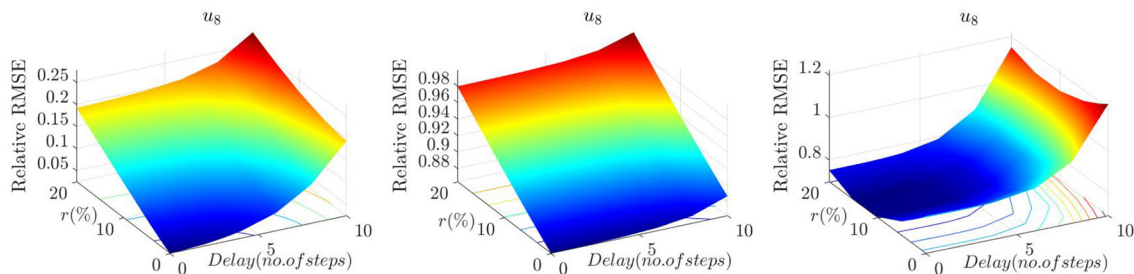


FIGURE 12 | Case III: RMSE comparison for u_8 (from left to right: Fr, Fr-Ca, Fr-Ca-dg).

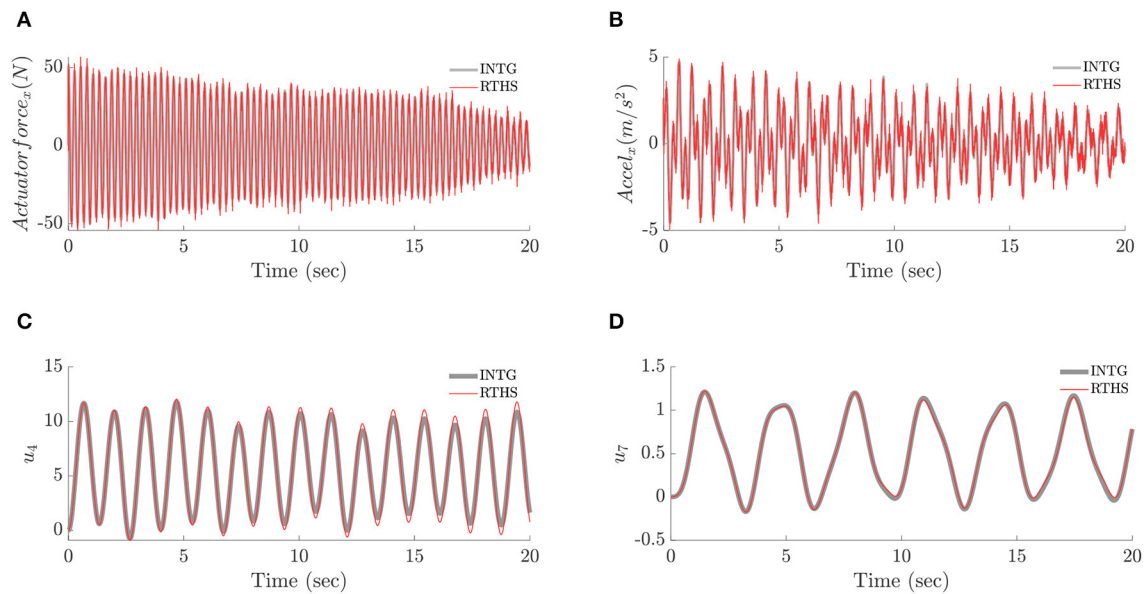


FIGURE 13 | Case III: time history comparison in Fr model for $\text{delay} = 2$ and $r = 20\%$ (INTG—prototype; RTHS—RTHS model). **(A)** Time history of actuator force. **(B)** Time history of sensor measurement. **(C)** Time history of u_4 . **(D)** Time history of u_7 .

Fr-Ca-dg model is slightly better than the Fr model. It is noted that, even with very low delays, the RMSE for u_4 is around 4% and increases rapidly as the delay increases. However, such a level of RMSEs in the blade responses do not induce a large error in the tower response, u_7 , because tower is evaluated under a reduced scale and the errors in the full-scale blade responses are reduced accordingly before sending to the experimental component. Therefore, if the blade responses are of interest, the RTHS implementation needs to guarantee a well-compensated RTHS to address the delay issues. To further understand the behavior of the scaled RTHS model, 20 s of time histories of the actuator force (in x direction), $F_1^N - F_1^E$, the sensor measurement (in x direction), \ddot{u}_1 , and the responses, u_4 and u_7 , are shown in **Figure 13** for the Fr model with $\text{delay} = 2$ and $r = 20\%$. In the plots, the “INTG” curve indicates the prototype behavior without delay and noise, and the “RTHS” curve indicates the behavior from the Fr model. It can be seen that although the actuator force and sensor measurement are contaminated by noises, the responses show fairly smooth behavior and follow the natural frequencies of the blade and the tower. The reason is the broadband noises are effectively filtered by the blade and tower which has low fundamental frequencies (see **Table 1**) even after the scaling.

Case IV: Misalignment Angle

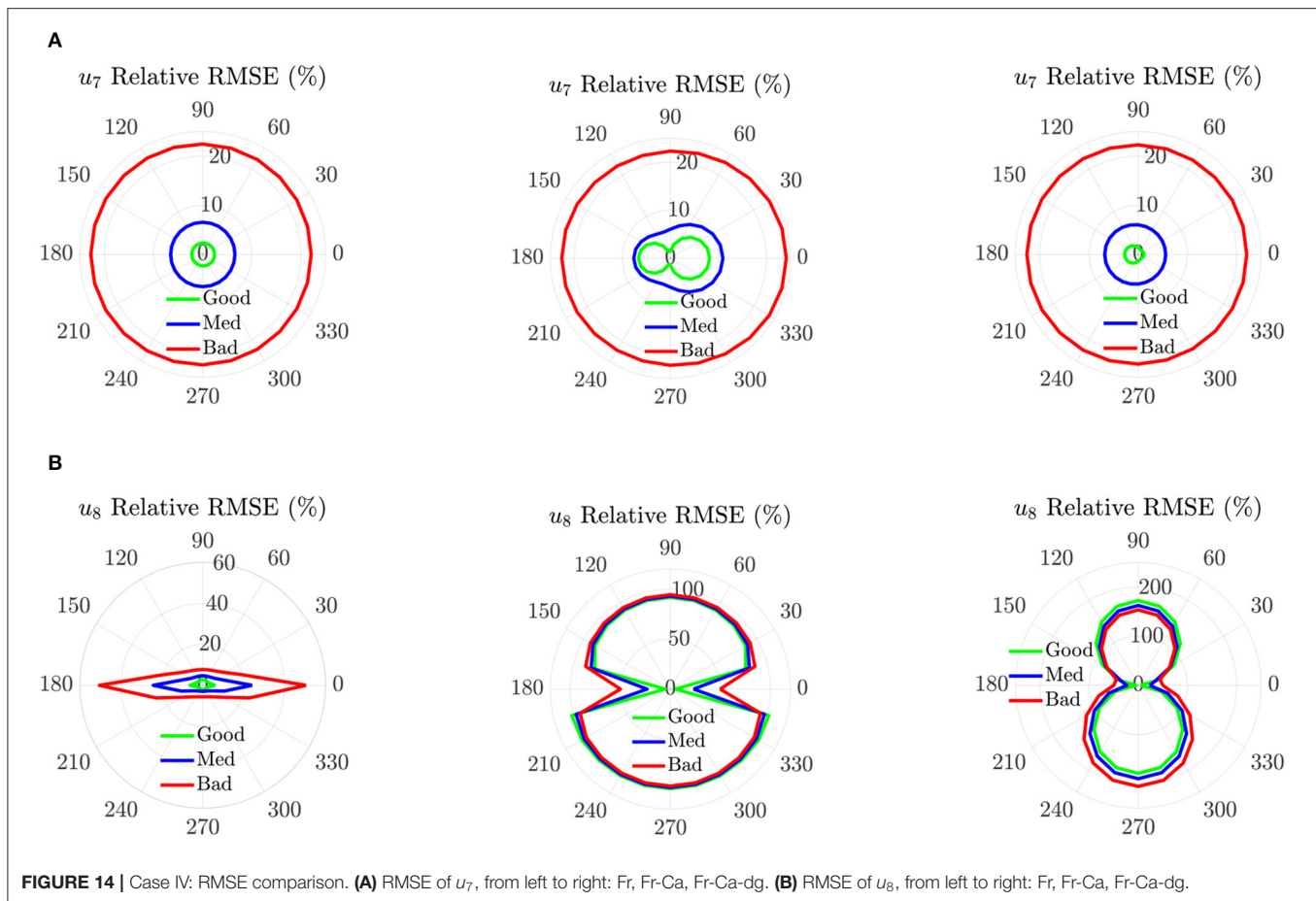
The misalignment angle $\beta = 30^\circ$ is applied in Cases I, II, and III. Based on their results, the errors generated in RTHS models are closely related to the delays and noise levels. For the Fr-Ca and Fr-Ca-dg models, the errors are also attributed to the distorted hydrodynamic effects. Therefore, the hydrodynamic load generation is further examined. In this case, the impact of misalignment angle β on the RTHS performance is studied.

For each RTHS model, three nominal delay-noise combinations are considered:

- Good condition: $\text{delay}_A = \text{delay}_M = \text{delay} = 1$, $r_A = r_M = r = 1\%$;
- Medium condition: $\text{delay}_A = \text{delay}_M = \text{delay} = 3$, $r_A = r_M = r = 5\%$;
- Bad condition: $\text{delay}_A = \text{delay}_M = \text{delay} = 6$, $r_A = r_M = r = 10\%$.

These conditions correspond to the quality of the actuator compensation design and fidelity of the sensor signals. For each condition, the misalignment angles ranging from 0° to 360° are considered with an increment of 15° .

The RMSE results for u_7 and u_8 are shown in **Figure 14**. For u_7 , the performances of the Fr and the Fr-Ca-dg model are similar and show no particular dependence on β . The Fr-Ca model, however, shows that the errors near $\beta = 90^\circ$ or 270° are lower than the other β values. For u_8 , only the Fr model demonstrates RMSE values lower than 5% in all β values under the good condition. The Fr model also shows that higher RMSEs are expected when β is near 0° or 180° in all conditions. In contrast, for the Fr-Ca and the Fr-Ca-dg models, the RMSE is lower (around 5%) when β is near 0° or 180° (alongwind) under the good condition. This observation is expected because the distorted hydrodynamic effects only influence the fore-aft responses in this case and causes a lower impact in the side-side responses comparing to the wind load. High RMSEs are expected in other β values. Therefore, they can be considered for RTHS implementation for the alongwind cases. The RMSEs of the blade responses ($u_1 \sim u_6$) for all three RTHS models are also examined. They show no particular dependence on β , and therefore, are not repeated here.



Case V: Wave Height

Another parameter related to the hydrodynamic load generation is the significant wave height H_s . In all previous cases, a significant wave height $H_s = 3m$ is used. To study the impact of different wave heights on the RTHS performance, H_s values equal to 0.5, 1.5, 3, and 4.5 m, are considered. For each H_s value, the misalignment angles ranging from 0° to 360° are considered with an increment of 15° . In all simulations, only the “good condition” delay-noise combination is applied, i.e., $delay_A = delay_M = delay = 1$, $r_A = r_M = r = 1\%$.

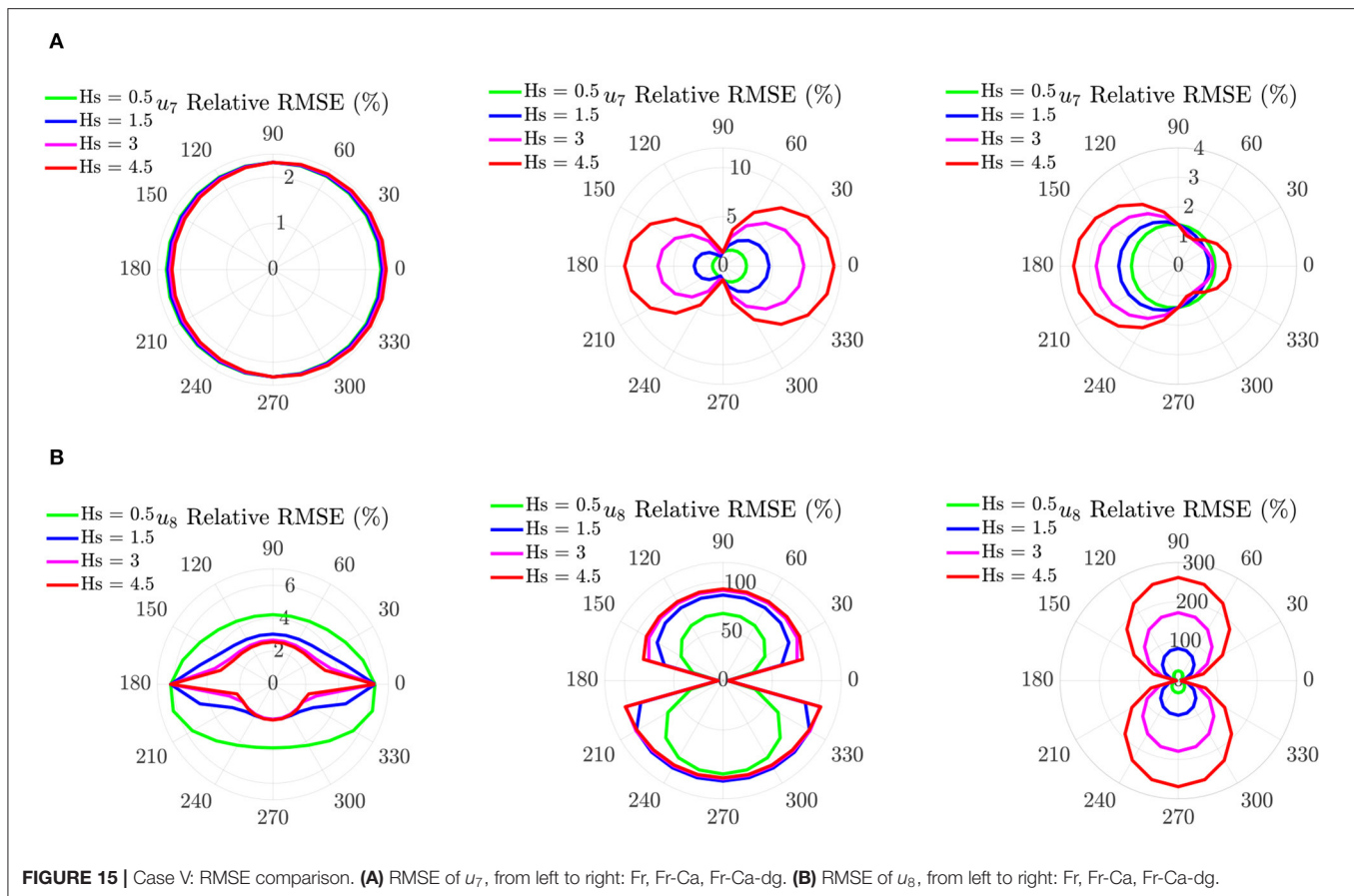
The RMSE results for u_7 and u_8 are shown in **Figure 15**. For u_7 , the Fr model shows no particular dependence on H_s . The Fr-Ca-dg model provides similar RMSEs as the Fr model, except near the region $\beta = 120^\circ \sim 240^\circ$, where the error increases as H_s increases. The RMSEs in Fr-Ca-dg model increase as H_s increases, except near $\beta = 90^\circ$ or 270° , where the errors are lower and insensitive to the change in H_s . For u_8 , only the Fr model provides RMSE values lower than 5% in all β values. The RMSE in the Fr model demonstrates a decreasing trend as H_s increases and reaches the highest values when β is near 0° or 180° . Both the Fr-Ca and the Fr-Ca-dg models show an RMSE increasing trend as H_s increases. In contrast to the Fr model, their RMSEs reaches the lowest values (around 5%) when β is near 0° or 180° (alongwind), and the highest when β is near 90° or 270° (crosswind). This

observation is consistent with Case IV. The RMSEs of the blade responses ($u_1 \sim u_6$) for all three RTHS models are also examined. They show no particular dependence on H_s , and therefore are not repeated here.

CONCLUSIONS

In this study, a RTHS framework for monopile OWT is proposed. Three RTHS models, representing three different scaling laws, are modeled and simulated. By comparing their responses with those of the prototype in a set of sensitivity analyses, the performance and the possible error contributors of the proposed RTHS are evaluated. The findings provide important insights for future RTHS implementations. These findings include:

- RTHS using Froude scaling (the Fr RTHS) can provide the best overall performance in capturing the responses in both the numerical (blades) and the experiment (tower) components. It can achieve $<5\%$ RMSE for all responses with all misalignment angles and wave heights under the “good condition,” i.e., $delay_A = delay_M = delay = 1$, $r_A = r_M = r = 1\%$. Its specimen design and construction are more challenging than the other two scaling laws considered. But if the difficulty in specimen design can be overcome,



the Froude scaling RTHS is the preferred method for RTHS implementation.

- RTHS using Froude-Cauchy scaling with drag force correction (the Fr-Ca-dg RTHS) is a viable alternative to the one with Froude scaling. It offers similar performance as the Fr model in almost all responses, except the ones in side-side direction (u_8), due to the distorted hydrodynamic effects. However, if the responses in side-side direction is not of concern or when they are in much lower amplitude than the wind-induced responses, for example, when the wave is aligned with the wind direction (β is near 0° and 180°), the Fr-Ca-dg RTHS can also be considered for RTHS implementation. Its advantage over the Froude scaling is in the specimen design—it provides a systematic way to construct the scaled specimen (using added artificial mass).
- RTHS using the conventional Froude-Cauchy scaling (the Fr-Ca RTHS) is the least attractive one in this study. It offers the same advantage in specimen design and construction like the Fr-Ca-dg model, and it has the same issue on capturing the side-side responses. But even for the fore-aft response (e.g., u_7), it demonstrates lower robustness against noise and delay comparing to the Fr-Ca-dg RTHS (see **Tables 3, 4**). It does have an advantage over the Fr-Ca-dg RTHS in that it is less demanding in the wave generation, as it does not require the drag force correction.

- Even with the Froude scaling, it is observed that, the proposed RTHS framework is more sensitive to the delays than to the noises, and it is more sensitive to the actuator noises than to the sensor noises.
- To accurately capture the responses in blades, a small (around 1~2 steps) delay needs to be specified. If only the responses in tower is of concern, the delay requirement can be relaxed to 4~6 steps (see **Table 4**).

As a concept study, only numerical simulations are considered herein, and the modeling parameters are selected to represent typical OWT behavior to investigate the proposed RTHS framework. Experimental implementations of the proposed RTHS framework will be carried out in the future. In addition, torsional DOFs of the tower are not considered at the current stage. As the study further develops, more complex modeling techniques, and loading cases will be considered in implementing the proposed RTHS framework with specific OWT designs and site conditions.

DATA AVAILABILITY STATEMENT

The datasets generated for this study are available on request to the corresponding author.

AUTHOR CONTRIBUTIONS

WS completed the main writing task of the paper and the main coding. Oversee the development of the study presented in the paper. CS completed part of the coding (on wave load generation) used in the analysis. YZ completed part of the literature review and the writing of the paper. VJ completed part of the coding (on wind load generation) used in the analysis. YL contribute to the review, editing, and assist the development of the study presented

in the paper. QH contribute to the review, editing, and assist the development of the study presented in the paper. All authors contributed to the article and approved the submitted version.

SUPPLEMENTARY MATERIAL

The Supplementary Material for this article can be found online at: <https://www.frontiersin.org/articles/10.3389/fbuil.2020.00129/full#supplementary-material>

REFERENCES

- Aasen, S., Page, A., Skau, K., and Nygaard, T. (2017). Effect of foundation modelling on the fatigue lifetime of a monopile-based offshore wind turbine. *Wind Energy Sci.* 2, 361–376. doi: 10.5194/wes-2-361-2017
- Abbiati, G., Marelli, S., Tsokanas, N., Sudret, B., and Stojadinović, B. (2021). A global sensitivity analysis framework for hybrid simulation. *Mech. Syst. Signal Process.* 146:106997. doi: 10.1016/j.ymssp.2020.106997
- Alagan Chella, M., Tørum, A., and Myrhaug, D. (2012). An overview of wave impact forces on offshore wind turbine substructures. *Energy Procedia* 20, 217–226. doi: 10.1016/j.egypro.2012.03.022
- Anaya-Lara, O., Tande, J. O., Uhlen, K., and Merz, K. (2018). *Offshore Wind Energy Technology*. Hoboken, NJ: Wiley Online Library.
- Arany, L., Bhattacharya, S., Macdonald, J., and Hogan, S. J. (2017). Design of monopiles for offshore wind turbines in 10 steps. *Soil Dyn. Earthq. Eng.* 92, 126–152. doi: 10.1016/j.soildyn.2016.09.024
- Barj, L., Jonkman, J. M., Robertson, A., Stewart, G. M., Lackner, M. A., Haid, L., et al. (2014). “Wind/wave misalignment in the loads analysis of a floating offshore wind turbine,” in *32nd ASME Wind Energy Symposium* (National Harbor, MD: American Institute of Aeronautics and Astronautics).
- Bhattacharya, S. (2019). *Design of Foundations for Offshore Wind Turbines*. Hoboken, NJ: Wiley Online Library.
- Bredmose, H., Larsen, S., Matha, D., Rettenmeier, A., Marino, E., and Sætran, L. (2012). *Marine Renewables Infrastructure Network (MARINET) Report*. Collation of offshore wind wave dynamics.
- Campagnolo, F. (2013). *Wind Tunnel Testing of Scaled Wind Turbine Models: Aerodynamics and Beyond*. Milan: Politecnico di Milano.
- Canet, H., Bortolotti, P., and Bottasso, C. L. (2018). Gravo-aeroelastic scaling of very large wind turbines to wind tunnel size. *J. Phys. Conf. Ser.* 1037:042006. doi: 10.1088/1742-6596/1037/4/042006
- Carrion, J. E., and Spencer, B. F. Jr. (2007). Model-based Strategies for Real-time Hybrid Testing. *Newmark Structural Engineering Laboratory Report Series 006*, Urbana, IL: University of Illinois at Urbana-Champaign.
- Carswell, W., Johansson, J., Løvholt, F., Arwade, S. R., Madhus, C., Degroot, D. J., et al. (2015). Foundation damping and the dynamics of offshore wind turbine monopiles. *Renew. Energy* 80, 724–736. doi: 10.1016/j.renene.2015.02.058
- Chabaud, V., Steen, S., and Skjetne, R. (2013). “Real-time hybrid testing for marine structures: challenges and strategies,” in *2013 32nd International Conference on Ocean, Offshore and Arctic Engineering* (Nantes: ASME).
- Christenson, R., Dyke, S. J., Zhang, J., Mosqueda, G., Chen, C., Nakata, N., et al. (2014). “Hybrid simulation: a discussion of current assessment measures,” in *Hybrid Simulation Task Force Meeting sponsored by US National Science Foundation (NSF)* (West Lafayette, IN).
- Craig, R. R., and Kurdila, A. J. (2006). *Fundamentals of Structural Dynamics*, 2nd Ed. John Wiley & Sons.
- De Ridder, E.-J., Otto, W., Zondervan, G.-J., Huijs, F., and Vaz, G. (2014). “Development of a scaled-down floating wind turbine for offshore basin testing,” in *2014 33rd International Conference on Ocean, Offshore and Arctic Engineering* (San Francisco, CA: American Society of Mechanical Engineers Digital Collection).
- Dnvgl. (2010). *DNVGL-RP-C205 Environmental Conditions and Environmental Loads*. DNVGL.
- Dnvgl. (2016). *DNVGL-ST-0126 Support Structures for Wind Turbines*. Oslo: DNV GL.
- Du, W., Zhao, Y., He, Y., and Liu, Y. (2016). Design, analysis and test of a model turbine blade for a wave basin test of floating wind turbines. *Renew. Energy* 97, 414–421. doi: 10.1016/j.renene.2016.06.008
- Esteban, M. D., Diez, J. J., López, J. S., and Negro, V. (2011). Why offshore wind energy? *Renew. Energy* 36, 444–450. doi: 10.1016/j.renene.2010.07.009
- Faltinsen, O. (1990). *Sea Loads on Ships and Offshore Structures*. Cambridge, UK: Cambridge University Press.
- Hall, M., Goupee, A., and Jonkman, J. (2018). Development of performance specifications for hybrid modeling of floating wind turbines in wave basin tests. *J. Ocean Eng. Mar. Energy* 4, 1–23. doi: 10.1007/s40722-017-0089-3
- Hall, M., Moreno, J., and Thiagarajan, K. (2014). “Performance specifications for real-time hybrid testing of 1:50-scale floating wind turbine models,” in *International Conference on Offshore Mechanics and Arctic Engineering* (San Francisco, CA: American Society of Mechanical Engineers).
- Hansen, M. O. (2015). *Aerodynamics of Wind Turbines 3rd Ed.* London; New York, NY: Routledge.
- Hasselmann, K., Barnett, T., Bouws, E., Carlson, H., Cartwright, D., Enke, K., et al. (1973). Measurements of wind-wave growth and swell decay during the Joint North Sea wave project (JONSWAP). *Deut. Hydrogr. Z* 8, 1–95.
- Hayati, S., and Song, W. (2017). An optimal discrete-time feedforward compensator for real-time hybrid simulation. *Smart Struct. Syst.* 20, 483–498. doi: 10.1007/978-3-319-54777-0_27
- Hayati, S., and Song, W. (2018). Design and Performance Evaluation of an Optimal Discrete-Time Feedforward Controller for Servo-Hydraulic Compensation. *J. Eng. Mech.* 144:04017163. doi: 10.1061/(ASCE)EM.1943-7889.0001399
- Iec. (2005). *IEC 61400-1 Wind Turbines Part 1: Design Requirements*. International Electrotechnical Commission.
- Jonkman, B. J., and Kilcher, L. (2012). *Turbsim User's Guide: Version 1.06.00*. Golden, CO: National Renewable Energy Lab (NREL), 87.
- Jonkman, J., Butterfield, S., Musial, W., and Scott, G. (2009). *Definition of a 5-MW Reference Wind Turbine for Offshore System Development*. Golden, CO: National Renewable Energy Laboratory.
- Keivanpour, S., Ramudhin, A., and Ait Kadi, D. (2017). The sustainable worldwide offshore wind energy potential: a systematic review. *J. Renew. Sustain. Energy* 9:065902. doi: 10.1063/1.5009948
- Kimball, R., Goupee, A. J., Fowler, M. J., De Ridder, E.-J., and Helder, J. (2014). “Wind/wave basin verification of a performance-matched scale-model wind turbine on a floating offshore wind turbine platform,” in *International Conference on Offshore Mechanics and Arctic Engineering* (San Francisco, CA: American Society of Mechanical Engineers).
- Lamb, H. (1945). *Hydrodynamics*, 6th Revised Ed. New York, NY: Dover Publications.
- Maghareh, A., Dyke, S. J., Prakash, A., and Bunting, G. B. (2014). Establishing a predictive performance indicator for real-time hybrid simulation. *Earthq. Eng. Struct. Dyn.* 43, 2299–2318. doi: 10.1002/eqe.2448
- Martin, H. R. (2011). *Development of a Scale Model Wind Turbine for Testing of Offshore Floating Wind Turbine Systems*. MS Thesis, Orono, ME: The University of Maine.
- Martin, H. R., Kimball, R. W., Viselli, A. M., and Goupee, A. J. (2014). Methodology for wind/wave basin testing of floating offshore wind turbines. *J. Offshore Mech. Arctic Eng.* 136:020905. doi: 10.1115/1.4025030
- MathWorks (2020). *MATLAB R2020a*. Natick, MA.
- Morató, A., Sriramula, S., Krishnan, N., and Nichols, J. (2017). Ultimate loads and response analysis of a monopile supported offshore wind

- turbine using fully coupled simulation. *Renew. Energy* 101, 126–143. doi: 10.1016/j.renene.2016.08.056
- Morison, J., O'Brien, M., Johnson, J., and Schaaf, S. (1950). The force exerted by surface waves on piles. *Petroleum Trans.* 189, 149–154. doi: 10.2118/950149-G
- Musial, W., Heimiller, D., Beiter, P., Scott, G., and Draxl, C. (2016). *2016 Offshore Wind Energy Resource Assessment for the United States*. Golden, MO: National Renewable Energy Lab (NREL).
- Nakashima, M., Kato, H., and Takaoka, E. (1992). Development of real-time pseudo dynamic testing. *Earthq. Eng. Struct. Dyn.* 21, 79–92. doi: 10.1002/eqe.4290210106
- Newman, J. N. (1977). *Marine Hydrodynamics*. Cambridge, MA: The MIT Press.
- Perveen, R., Kishor, N., and Mohanty, S. R. (2014). Off-shore wind farm development: present status and challenges. *Renew. Sustain. Energy Rev.* 29, 780–792. doi: 10.1016/j.rser.2013.08.108
- Phillips, B. M., and Spencer, B. F. Jr. (2012). Model-Based Framework for Real-Time Dynamic Structural Performance Evaluation. *Newmark Structural Engineering Laboratory Report Series 031*, Urbana, IL: University of Illinois at Urbana-Champaign.
- Pierson, W. J. Jr., and Moskowitz, L. (1964). A proposed spectral form for fully developed wind seas based on the similarity theory of S. A. Kitaigorodskii. *J. Geophys. Res.* 69, 5181–5190. doi: 10.1029/JZ069i024p05181
- Przemieniecki, J. S. (1968). *Theory of Matrix Structural Analysis*. New York, NY: McGraw-Hill.
- Robertson, A., Jonkman, J., Goupee, A., Coulling, A., Prowell, I., Browning, J., et al. (2013). “Summary of conclusions and recommendations drawn from the deepwind scaled floating offshore wind system test campaign,” in *International Conference on Offshore Mechanics and Arctic Engineering* (Nante: sAmerican Society of Mechanical Engineers).
- Sauder, T., Chabaud, V., Thys, M., Bachynski, E. E., and Sæther, L. O. (2016). “Real-time hybrid model testing of a braceless semi-submersible wind turbine: part I—the hybrid approach,” in *2016 35th International Conference on Ocean, Offshore and Arctic Engineering* (Busan: ASME).
- Sauder, T., Marelli, S., and Sørensen, A. J. (2019). Probabilistic robust design of control systems for high-fidelity cyber-physical testing. *Automatica* 101, 111–119. doi: 10.1016/j.automatica.2018.11.040
- Stansby, P. K., Devaney, L., and Stallard, T. (2013). Breaking wave loads on monopiles for offshore wind turbines and estimation of extreme overturning moment. *Renew. Power Gener.* 7, 514–520. doi: 10.1049/iet-rpg.2012.0205
- Sun, C. (2018a). Mitigation of offshore wind turbine responses under wind and wave loading: Considering soil effects and damage. *Struct. Control. Health Monit.* 25:e2117. doi: 10.1002/stc.2117
- Sun, C. (2018b). Semi-active control of monopile offshore wind turbines under multi-hazards. *Mech. Syst. Signal Process.* 99, 285–305. doi: 10.1016/j.ymssp.2017.06.016
- Sun, C., and Jahangiri, V. (2018). Bi-directional vibration control of offshore wind turbines using a 3D pendulum tuned mass damper. *Mech. Syst. Signal Process.* 105, 338–360. doi: 10.1016/j.ymssp.2017.12.011
- Thys, M., Chabaud, V., Sauder, T., Eliassen, L., Sæther, L. O., and Magnussen, Ø. B. (2018). “Real-time hybrid model testing of a semi-submersible 10MW floating wind turbine and advances in the test method,” in *2018 1st International Offshore Wind Technical Conference* (San Francisco, CA: ASME).
- Wu, T., and Song, W. (2019). Real-time aerodynamics hybrid simulation: wind-induced effects on a reduced-scale building equipped with full-scale dampers. *J. Wind Eng. Ind. Aerod.* 190, 1–9. doi: 10.1016/j.jweia.2019.04.005

Conflict of Interest: The authors declare that the research was conducted in the absence of any commercial or financial relationships that could be construed as a potential conflict of interest.

Copyright © 2020 Song, Sun, Zuo, Jahangiri, Lu and Han. This is an open-access article distributed under the terms of the Creative Commons Attribution License (CC BY). The use, distribution or reproduction in other forums is permitted, provided the original author(s) and the copyright owner(s) are credited and that the original publication in this journal is cited, in accordance with accepted academic practice. No use, distribution or reproduction is permitted which does not comply with these terms.



Investigation of Hybrid Simulation With Model Updating Compared to an Experimental Shake Table Test

Ge Ou^{1*}, Ge Yang², Shirley Dyke^{3,4} and Bin Wu²

¹ Department Civil and Environmental Engineering, University of Utah, Salt Lake City, UT, United States, ² School of Civil Engineering and Architecture, Wuhan University of Technology, Hubei, China, ³ School of Mechanical Engineering, Purdue University, West Lafayette, IN, United States, ⁴ Lyles School of Civil Engineering, Purdue University, West Lafayette, IN, United States

In hybrid simulation, response time history measured from an experimental substructure can be utilized to identify the model associated with the tested specimen in real time. To improve the modeling accuracy, the updated model parameters can substitute the initial parameters of similar components (as the tested specimen) that reside in the numerical substructure. In this study, a detailed investigation into the fidelity improvement using model updating in hybrid simulation has been carried out. This study has focused on both local and global assessment of hybrid simulation with model updating (HSMU) by comparing HSMU with conventional simulation and shake table testing. In the local assessment, the updating efficiency with different nonlinear models (one phenomenological model and one FEM model) have been illustrated; in the global assessment, the HSMU response time histories have been compared to experimental shake table testing. Observations and comments on model selection, parameter convergence, and time and frequency domain performance of HSMU have been provided.

Keywords: hybrid simulation, model updating, finite element method (FEM) model, Bouc-Wen model, steel structure, shake table testing

OPEN ACCESS

Edited by:

Vasilis K. Dertimanis,
ETH Zürich, Switzerland

Reviewed by:

Michele Betti,
University of Florence, Italy
Dimitrios Giagopoulos,
University of Western Macedonia,
Greece

*Correspondence:

Ge Ou
ge.ou@utah.edu

Specialty section:

This article was submitted to
Computational Methods in Structural
Engineering,
a section of the journal
Frontiers in Built Environment

Received: 10 February 2020

Accepted: 04 June 2020

Published: 10 September 2020

Citation:

Ou G, Yang G, Dyke S and Wu B
(2020) Investigation of Hybrid
Simulation With Model Updating
Compared to an Experimental Shake
Table Test. *Front. Built Environ.* 6:103.
doi: 10.3389/fbuil.2020.00103

1. INTRODUCTION

Hybrid simulation was initially introduced by Hakuno et al. (1969) and Mahin and Shing (1985) and is typically viewed as a cost-effective method for dynamic analysis of infrastructures. In a hybrid simulation, structural components are (1) expected to experience significant nonlinearity or (2) difficult to model accurately and are thus tested physically and are known as the experimental substructure. The rest of the structure is included in a numerical model, denoted by the numerical substructure. The experimental and numerical substructures are coupled at each of the boundaries through loading devices. These loading devices, such as hydraulic actuators, electric motors, and shake tables, etc., apply the calculated responses (normally a displacement) at the boundary to the physical specimen. The responses of the physical specimens are then measured accordingly and sent back to the numerical model, as in Phillips and Spencer (2012) and Ou et al. (2015). The responses of the entire structure, including story drifts, displacements, and accelerations, can be monitored during the test. Therefore, this testing method can evaluate global structural performance. For the experimental substructure to be tested physically, its local behaviors, including crack initialization, material, and geometric nonlinearity evolution under loading, and even failure modes, can also be investigated during testing (Gomez et al., 2014). Therefore, hybrid simulation is known to preserve both global and local observations for structural performance assessment.

In the previous applications, hybrid simulation has shown great advantages in studying local and global performance of structural vibration control devices (Christenson et al., 2008; Karavasilis et al., 2011; Lin et al., 2012; Gao et al., 2013). Due to the isolated and critical role of these devices and components, it was intuitive to select them as the experimental substructure. New advances have taken place in the infrastructural system and component design, such as shear walls and rocking frames, distributed structural fuses, etc., and their behaviors are also to be studied. These components, with their appearance patterns repetitively and spatially distributed among the entire structure design, do not have a substantially different role between one component to the other (Elnashai et al., 2008). To investigate their performance in a hybrid simulation setup, a couple of challenges need to be addressed. Due to the more equally weighted contribution of these components to the structure level performance, it is difficult to select the experimental substructure among their multiple use. Meanwhile, the facility capacity (number of actuators and lab space), available budget, and the number of the experimental substructure are limited. As a result, for hybrid simulation to be applied in these cases, a larger portion of the target components must still reside in the numerical substructure. Therefore, the hybrid simulation fidelity is affected by modeling accuracy of numerical components rather than the response of their physical counterparts. Two questions were posed in Kwon and Kammula (2013): (1) Out of many similar structural elements, which elements should be experimentally represented? (2) How much increase in accuracy can be achieved by physically modeling only a few elements?

To address such challenges, a new branch of hybrid simulation has been established recently, known as hybrid simulation with model updating (HSMU). In HSMU, hybrid simulation is integrated with on-line system identification methods. Here, the input and response histories measured from the physical specimen are used in an online identification module to estimate model parameters that best represent the physical specimen. The identified model is then used to update the portions of the numerical model that are associated with the counterparts to that physical specimen. Several researchers have concluded that using model updating in a hybrid simulation yields large improvements in the results (for instance Hashemi et al., 2014; Wu and Wang, 2015; Elanwar and Elnashai, 2016; Shao et al., 2016; Ou et al., 2017). The fidelity of HSMU is commonly assessed to be evaluating the model identification accuracy and the convergence of model parameters which can be only a local optimal criterion. Ou and Dyke (2016) further demonstrated the improvement of fidelity assessment with additional verification tests after an HSMU. In the validation stage, a new specimen representing one numerical counterpart in the HSMU was loaded with its displacement trajectory and experienced numerically in the HSMU. Later, the measured force response was compared to the calculated response (force) in the HSMU with the model parameter updated in real time.

In the state-of-the-art study, the HSMU used the following assumptions: the model updating method is adaptive to the ground motion and can identify a converged set of numerical parameters of the model; and the local performance assessment

can indicate the fidelity of the HSMU. In this paper, we present the investigation of the two assumptions and studied the improvements in model fidelity while using HSMU with two models. The experimental HSMU responses of a five-story frame with identical floors are examined; the frame is expected to develop distributed nonlinearity across several floors. Time response analysis is performed using (1) conventional simulation, (2) HSMU, and (3) shake table testing. The first story is selected as the experimental substructure while the upper stories are included in the computational substructure. The parameters of the model of the experimental substructure are identified during testing and used to update the numerical substructure. In case I, each frame (each floor) is modeled with a concentrated nonlinear Bouc-Wen model in a lumped mass system. In case II, a fiber model with material nonlinearity is used as the nonlinear model to be identified, and the material properties are identified using measured responses. The improvements in the accuracy of the results are investigated at both the local and global level. Local assessment of HSMU performance focuses on the accuracy and efficiency of the model updating, and the parameters' adaptiveness using ground motions with different magnitude. Global performance is assessed through a direct comparison of the responses with pure simulation and shake table results. Conclusions will be addressed from the point of view of both the time and frequency domain analyses.

2. HSMU FORMULATION AND IMPLEMENTATION

In a conventional simulation, the dynamic response of the whole structure is represented by the equation of motion:

$$M\ddot{x} + C\dot{x} + F(x, \dot{x}) + R(x, \dot{x}, \theta_R) = -M\Gamma\ddot{x}_g \quad (1)$$

where, \ddot{x}_g is the ground motion; M , C , and K are the mass, damping, and stiffness matrices of the master structure, respectively; R is the nonlinear restoring force; and θ_R is the parameter set governs the nonlinear behavior of the structure.

In a hybrid simulation, the structure is partitioned, and the associated equations of motion then take the form

$$M^N\ddot{x}^N + C^N\dot{x}^N + F^E(x^E, \dot{x}^E) + R^N(x^N, \dot{x}^N, \theta_R) = -M\Gamma\ddot{x}_g \quad (2)$$

$$M^E\ddot{x}^E + C^E\dot{x}^E + R^E(x^E, \dot{x}^E) = F^E(x^E, \dot{x}^E) \quad (3)$$

where, the superscripts $()^N$ and $()^E$ denote the portions of the structure that reside in the numerical substructure and experimental substructures. Here, $M = M^E + M^N$, $C = C^E + C^N$, $K = K^E + K^N$, and F^E is the force measured from the experimental substructure. When the physical specimen is selected to be a structural component that is used repeatedly in multiple instances within the master structure, a limited number of substructures are selected for physical experimentation. Thus, a significant portion of their counterparts reside in the numerical substructure ($R^N \gg R^E$) and have similar behavior. When the numerical model is unknown, and thus potentially inaccurate

(either the type of model or model parameters), modeling errors present in R^N may dominate the source of errors of the hybrid simulation.

To reduce the modeling errors in the numerical substructure, hybrid simulation is enhanced by incorporating model updating. Thus, the equations of motion become:

$$M^N \ddot{x}^N + C^N \dot{x}^N + K^N x^N + F^E(x^E, \dot{x}^E) + R^N(x^N, \dot{x}^N, \tilde{\theta}_R) = -M\Gamma \ddot{x}_g \quad (4)$$

$$M^E \ddot{x}^E + C^E \dot{x}^E + K^E x^E + R^E(x^E, \dot{x}^E) = F^E(x^E, \dot{x}^E) \quad (5)$$

$$\tilde{\theta}_R = \Psi(R^E, x^E, \dot{x}^E, \theta_\Psi) \quad (6)$$

where Ψ is the model-updating module used in the HSMU, which is executed in real time, and $\tilde{\theta}_R$ is the recursively identified nonlinear model parameters that minimize an associated cost function. Therefore, with the nonlinear restoring parameter set $\tilde{\theta}_R$ updated according to the numerical substructure response in Equation (4), the numerical restoring force $R^N(x^N, \dot{x}^N, \tilde{\theta}_R)$ is assumed to have been updated to the experimental nonlinear behavior.

The constrained unscented Kalman filter (CUKF) was developed based on the unscented Kalman Filter and is selected as the model updating algorithm in this study. For structural analysis, it is common for the model parameters to have physical meanings, and many of these parameters fall within a certain range. CUKF allows a constrained projection on the state estimation for the unscented Kalman Filter, as presented by Kandepe et al. (2008).

The execution of CUKF in hybrid simulation is formulated as shown in **Figure 1**. The input space of the model is the displacement measured in the experimental substructure, and the output space is the experimental nonlinear restoring force. Ψ_{ICUT} indicates the interval constrained unscented transformation, γ_j is a coefficient set with γ_j associated with the j th transformed sigma points χ (total number of sigma points is $2L + 1$), where L is the number of parameters to be updated. d and e are the lower and upper bounds for the model parameters. $h()$ is the model function which takes each sigma point and projects it to the output space. P^{XX} , P^{XY} , and P^{YY} are the variance and co-variance matrices during state estimation. A detailed derivation of the formulation can be found in Ou et al. (2017).

3. EXPERIMENTAL SETUP AND SUBSTRUCTURING FOR HYBRID SIMULATION

In this study, nonlinear seismic responses of a five-story steel frame is investigated. Each story in the frame is identical, and the drawing of a typical story is shown in **Figure 2A**. Based on previous research and experiments (Song and Dyke, 2013), this structure behaves like a shear frame, and the use of this frame as the target structure enables a comparison of the results of hybrid simulation to shake table tests.

For the shake table testing, the entire structure is mounted on a 6 DOFs shake table in the Intelligent Infrastructure System Lab (<https://engineering.purdue.edu/IISL/>) at Purdue University.

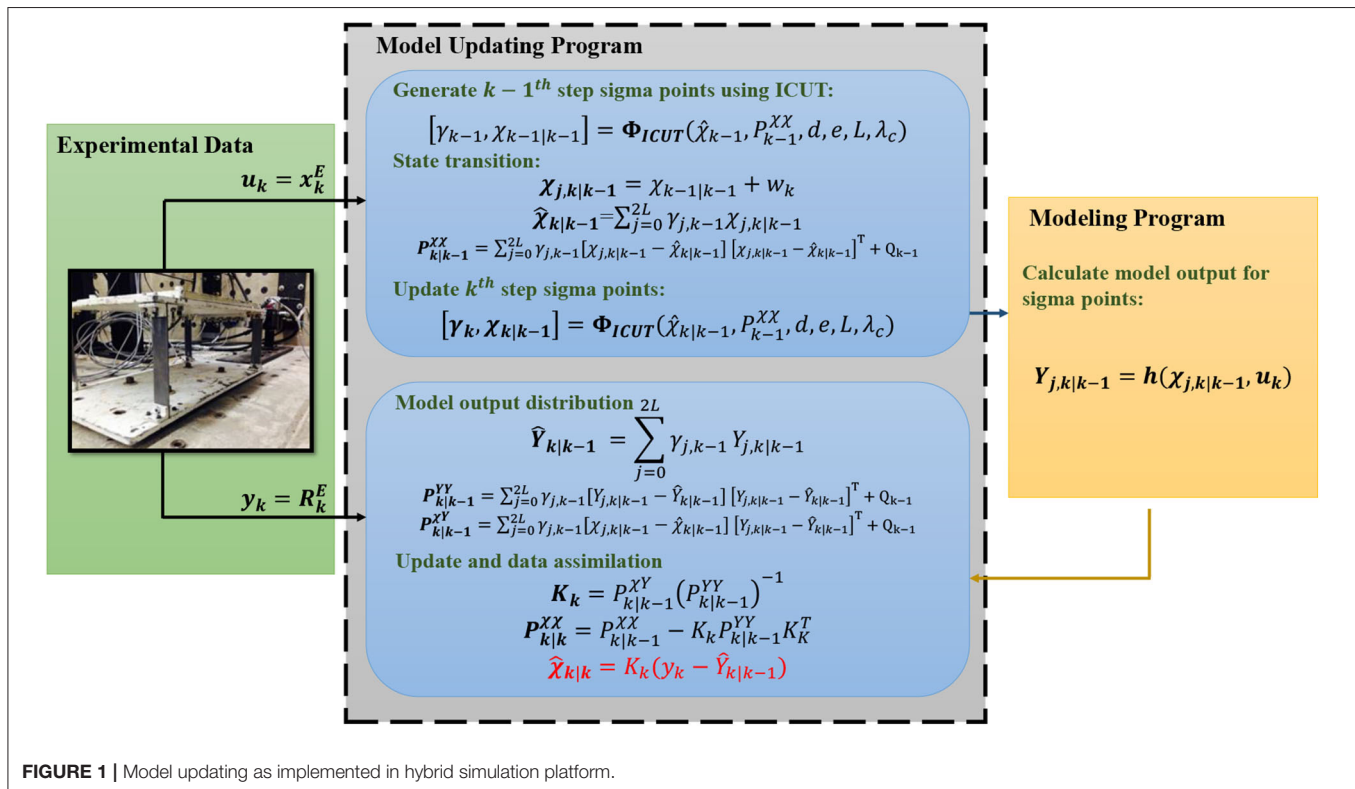
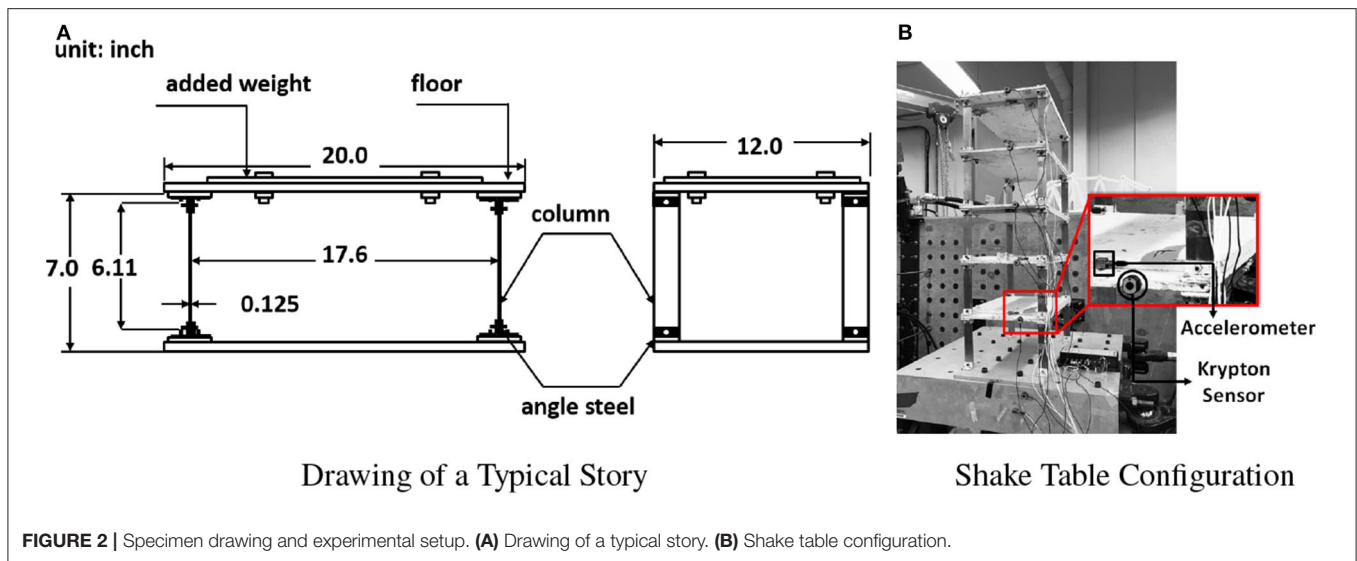


FIGURE 1 | Model updating as implemented in hybrid simulation platform.



The shake table is driven by six hydraulic actuators: two in the x-axis, one in the y-axis, and three in the z-axis. All actuators are controlled in the integrated SW6000 controller made by Shore Western. In this study, the ground motion is imposed only in the y axis. During the shake table tests, absolute acceleration and displacement responses of the frame are measured using accelerometers and optical sensors, as indicated in **Figure 2B**. VibPilot, a high resolution DAQ system, is used to record the structural acceleration response with a sampling frequency of 2,048 Hz, embedded anti-aliasing filters are applied during data acquisition. A 6D Krypton optical tracking system is used to measure the position of LED sensors placed on each floor which captures the 6D position and dynamic movement of each LED. The sampling rate of the Krypton system is set at 60 Hz.

The El Centro earthquake record is used as the ground motion for the structure. The earthquake is imposed twice sequentially, with an increasing magnitude to generate different level of nonlinearity. The ground motion is also condensed in time (using a reduction factor of 2) to develop nonlinear behavior in the structure while compensate the limitation of the maximum stroke to be applied to the shake table actuator. The entire excitation lasts 40 s. In the first 20 s (section 1, denoted as S1), the peak acceleration is 6.98 m/s^2 , and in the later 20 s (section 2, denoted as S2), the acceleration reaches a peak of 18.3 m/s^2 . The desired ground motion is shown in **Figure 3A**, and the measured shake table acceleration (as discussed later in **Figure 6**) is used as the excitation input in HSMUs and numerical simulations.

For HSMU, the frame is partitioned into an experimental substructure (the first floor) and a numerical substructure (the remaining upper floors). The experimental substructure is attached to a Shore Western 1 kip hydraulic actuator as in **Figure 3B**. The SW6000 provides a PID loop for stabilization and inner loop control of the hydraulic actuator. Communication between the numerical substructure and experimental substructure is achieved using National Instruments (NI) hardware and LabVIEW software. During each computational

time interval, the LabVIEW program receives the displacement command from the numerical solver and converts it into an analog signal to send to the SW6000 input. Note that, after each test, either in the case of a hybrid simulation or a shake table test, all columns with any evidence of yielding are replaced with new ones. All columns used in this study were cut from the same batch of steel to provide behavior that is quite similar. Therefore, the difference in the initial condition of the structure for each test is assumed to be negligible.

Two cases of HSMUs are conducted in this study. In case I, specimen nonlinearity is modeled with a Bouc-Wen-Baber-Noori model proposed by Baber and Wen (1981) and Baber and Noori (1985). In case II, the specimen nonlinearity in the numerical substructure is modeled with the constitutive steel model in OpenSees. Detailed explanations of each case are described in sections 3.1 and 3.2, respectively.

3.1. HSMU Case I: Bouc-Wen Model

In case I, the nonlinear behavior of the single-story frame is modeled with the phenomenological Bouc-Wen-Baber-Noori model. This model can capture the pinching and degradation effects in a structural component, represented by Equations (7)–(16).

$$R(x^E, z) = \alpha k x^E + (1 - \alpha) k z \quad (7)$$

$$\dot{z} = h(z) \left\{ \frac{\dot{x}^E - v(\varepsilon)(\beta |\dot{x}^E| |z|^{n-1} z + \gamma \dot{x}^E |z|^n)}{\eta(\varepsilon)} \right\} \quad (8)$$

where k is the stiffness coefficient, and $0 \leq \alpha \leq 1$ determines the level of nonlinearity. $\alpha = 1$ indicates the system is purely linear and $\alpha = 0$ indicates the system is purely hysteretic. The energy dissipation is represented by $E(t)$:

$$E(t) = \int (1 - \alpha) k z \dot{x}^E dt \quad (9)$$

$$\varepsilon(t) = \int z \dot{x}^E dt \quad (10)$$

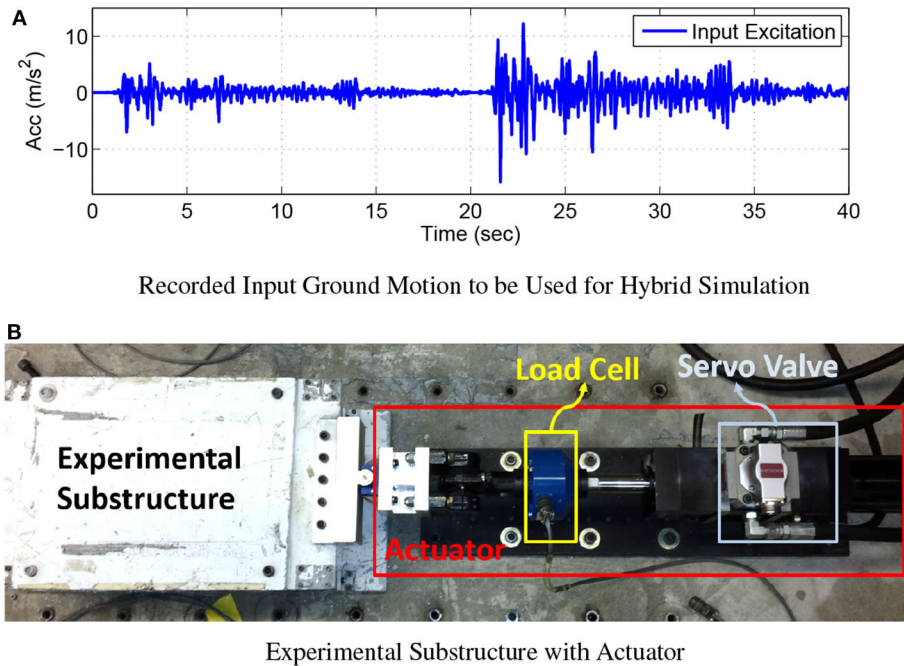


FIGURE 3 | Testing ground motion and experimental substructure setup. **(A)** Recorded input ground motion to be used for hybrid simulation. **(B)** Experimental substructure with actuator.

$v(\varepsilon)$ and $\eta(\varepsilon)$ are degradation shape functions, and δ_v , δ_η are degradation parameters.

$$v(\varepsilon) = 1 + \delta_v \varepsilon \quad (11)$$

$$\eta(\varepsilon) = 1 + \delta_\eta \varepsilon \quad (12)$$

A function $h(z)$ describes the pinching effect is given by:

$$h(z) = 1 - \zeta_1 e^{-[z \cdot \text{sgn}(\dot{x}^E) - qz\dot{x}^E]^2 / \zeta_2^2} \quad (13)$$

$$\zeta_1(\varepsilon) = \zeta_s(1 - e^{-p\varepsilon}) \quad (14)$$

$$\zeta_2(\varepsilon) = (\Psi + \delta_\Psi \varepsilon)(\lambda + \zeta_1) \quad (15)$$

$$z_{x^E} = \left[\frac{1}{v(\varepsilon)(\beta + \gamma)} \right]^{\frac{1}{n}} \quad (16)$$

The parameters λ , ζ_s , p , q , Ψ , and δ_Ψ are involved in describing the pinching effect. p quantifies the initial drop in the slope, ζ_s relates to the total slip, Ψ is a parameter that contributes to the amount of pinching. δ_Ψ specifies the desired rate of pinching. The parameter set to be updated is defined: $\theta_R(k) = [\alpha, k, \beta, n, \delta_\eta, \delta_v, q, \gamma, \zeta_s, p, \Psi, \delta_\Psi, \lambda, \varepsilon z]^T$, and $u(k) = [x^E(k) \dot{x}^E(k)]$.

Similar to conventional hybrid simulation, information exchange in HSMU requires communication and synchronization between physical components, numerical components, and also model updating components using a coordination program. The coordination program used here is the HyTest platform by Yang et al. (2015, 2017). Both the model updating algorithm and the numerical substructure model are executed in Matlab, and the external loading to the experimental substructure is implemented through Labview. In the Matlab

program, the estimated parameter of the Bouc-Wen is first identified through CUKF using a numerical model of the single story of the shear frame (experimental substructure) subjective to the measured response R^E and measured displacement x^E . Next, the numerical substructure restoring force is calculated using the parameter $\tilde{\theta}_R$ by solving the associated equation of the motion, and the numerical response X^N is computed. The displacement at the boundary between the numerical and physical substructures is imposed to the hydraulic actuator driving the physical specimen with LabVIEW ($x^E = x^N$ at the boundaries, ideally).

3.2. HSMU Case II (Bilinear FEM Model)

In HSMU case II, a constitutive bilinear model is used to describe steel hysteretic behavior at a material level. This model can be implemented in different commercial or open source software or can be implemented by a user-programmed finite element code. In this study, the Open System for Earthquake Engineering Simulation (OpenSees) is selected as the software framework for modeling the numerical substructure as well as the experimental substructure which parameters are adaptive to changes from model updating. Here, this numerical model of the experimental substructure is denoted as a function $\text{OpenSees}(\theta_R, u)$, where θ_R is the parameter to be identified in CUKF, and u is the input to the OpenSees model, which is the measured displacement of the physical specimen x^E .

If only considers the isotropic hardening, the simplified bilinear material relationship can be described:

$$E^p = b_s \cdot E \quad (17)$$

The parameters that describe the hysteretic behavior of the steel material are initial young's modulus E , stiffness hardening factor b_s , and yield stress σ_y .

Similarly, the coordination program in case II is the HyTest platform. In case II, the numerical substructure, model updating components (in Matlab), and the numerical model of the physical specimen (in OpenSees) are implemented in the same software. The model updating component contains (1) an OpenSees model $OpenSees(\theta_R, u)$, used to estimate the experimental substructure response with different parameter sets $\theta_R = \tilde{\theta}_R$, and (2) a model-updating algorithm modeled in Matlab, used to implement the CUKF optimization. Because $2 \times L + 1$ sigma points are required for the one CUKF optimization iteration, there are $2 \times L + 1$ sets of $\tilde{\theta}_R$, sent to $OpenSees(\theta_R, u)$ to calculate the corresponding R_{est}^E for each iteration time step. To enable the sub-steps information exchange, lower level communication between two different software is implemented through TCP/IP protocol with holding the upper-level communication between experimental-numerical substructure. Further details of HyTest in HSMU with finite element model updating can be found in Yang et al. (2017).

4. HSMU PERFORMANCE ASSESSMENT

The performance of the HSMU is assessed through local and global performance. In local performance assessment, the hysteresis response is normally constructed by measured displacement-force from the experimental substructure. For HSMU, the fidelity of testing depends on the reduction of the modeling error in the numerical substructure, which is governed by the success of the model updating module. Since a shake table test is performed as a reference response, the global level performance of HSMUs can be directly compared to shake table testing results. Therefore, in this section, displacement and acceleration responses from two HSMUs are compared to the measured responses from shake table testing.

4.1. HSMU Local Performance Assessment

Two criterion are used to assess the local performance of the HSMU, the parameter convergence and also the model updating RMS, which is defined as

$$RMS_E = \sqrt{\frac{\sum_{i=1}^n (R_{est}(i) - R_m(i))^2}{n}} / \sqrt{\frac{\sum_{i=1}^n (R_m(i) - \text{mean}(R_m))^2}{n}} \quad (18)$$

where R_{est} is either the estimated force from model updating for HSMU, or the force calculated with a numerical model with an initial model, and R_m is the measured force from experiment.

To implement CUKF in the model-updating module, an initial parameter set for the associated model is required. One major drawback of using the Bouc-Wen model is that not all model parameters have physical meanings, which makes it very difficult to estimate a reasonable initial parameter set. Also, knowledge of previous component testing (cyclic or

hybrid simulation experimental substructure) results cannot be transmitted to a new specimen if any geometrical parameter changes. Therefore, a quasi-static cyclic test is conducted to identify the initial parameters of the phenomenological model. The loading protocol and structural responses of the cyclic tests. Several parameter sets satisfied the optimization criterion in the offline identification. Each parameter is spread across a range as listed in **Table 1**. Thus, the parameter set describes the physical specimen hysteretic behaviors is not unique. Before the CUKF can be implemented, one initial parameter set is chosen, also the upper and lower bound for each parameter are determined based on the results of the offline identification. Due to each parameter's clear physical meaning, the upper and lower bound for the bilinear fiber model are less arbitrary, and these are listed in **Table 2**.

In HSMU case I, the numerical model to be updated is the Bouc-Wen model, and the state vector contains 13 parameters and two states. During model updating, noise and estimation tolerance R is determined at 100 N, disturbance matrix $Q = \text{diag}[10^{-6}, 10^{-4}, 10^{-4}, 10^{-5}, 10^{-4.5}, 10^{-4}, 10^{-4}, 10^{-5}, 10^{-6}, 10^{-6}, 10^{-6}, 10^{-6}, 10^{-5}, 10^{-12}, 10^{-12}]$, and an initial variance matrix of $P_0 = 10 \times I_{15}$. These model-updating-related parameters (Q , R , P_0) are still determined on a case-by-case basis. The selection of R and Q and their effect to model updating performance are discussed in Ou et al. (2017).

The online updating results are illustrated in **Figure 4**. For the first 20 s (S1), the results confirm that most of the Bouc-Wen model parameters can converge 3 s after the testing starts and where the first peak response occurs. A total of 20 s (S2) later,

TABLE 1 | Model parameters of Bouc-Wen model.

Parameter	Offline ID range	CUKF range	HSMU initial parameter
δ_v	[1.02 2.56]	[0 20]	2.31
β	[55 168]	[0 200]	92.185
γ	[0.155 0.39]	[0 10]	0.94
δ_η	[1.17 4.3]	[0 20]	3.1142
α	[0.07 0.17]	[0 1]	0.156
n	[1 1.8]	[1 3]	1.1833
K	[1.4e+5 1.8e+5]	[1.0e+5 2.0e+5]	1.55e+5
δ_ψ	[0.03 0.07]	[0 0.1]	0.05
s_s	[0.56 1.41]	[0 5]	0.92
Ψ	[0.6 1.5]	[0 2]	0.94
ρ	[0.015 0.0375]	[0 0.05]	0.025
q	[0.022 0.07]	[0 0.1]	0.045
λ	[0.13 0.8]	[0 1]	0.476

TABLE 2 | Model parameters of bilinear steel material.

Parameter	Offline ID range	CUKF range	HSMU initial parameter
F_y	[3.0e+8 5.2e+8]	[1.0e+8 8.0e+8]	4.8e+8
E	[2.0e+11 2.0e+11]	[1.5e+11 3.0e+11]	2.0e+11
b_s	[0.04 0.15]	[0.01 0.8]	0.045

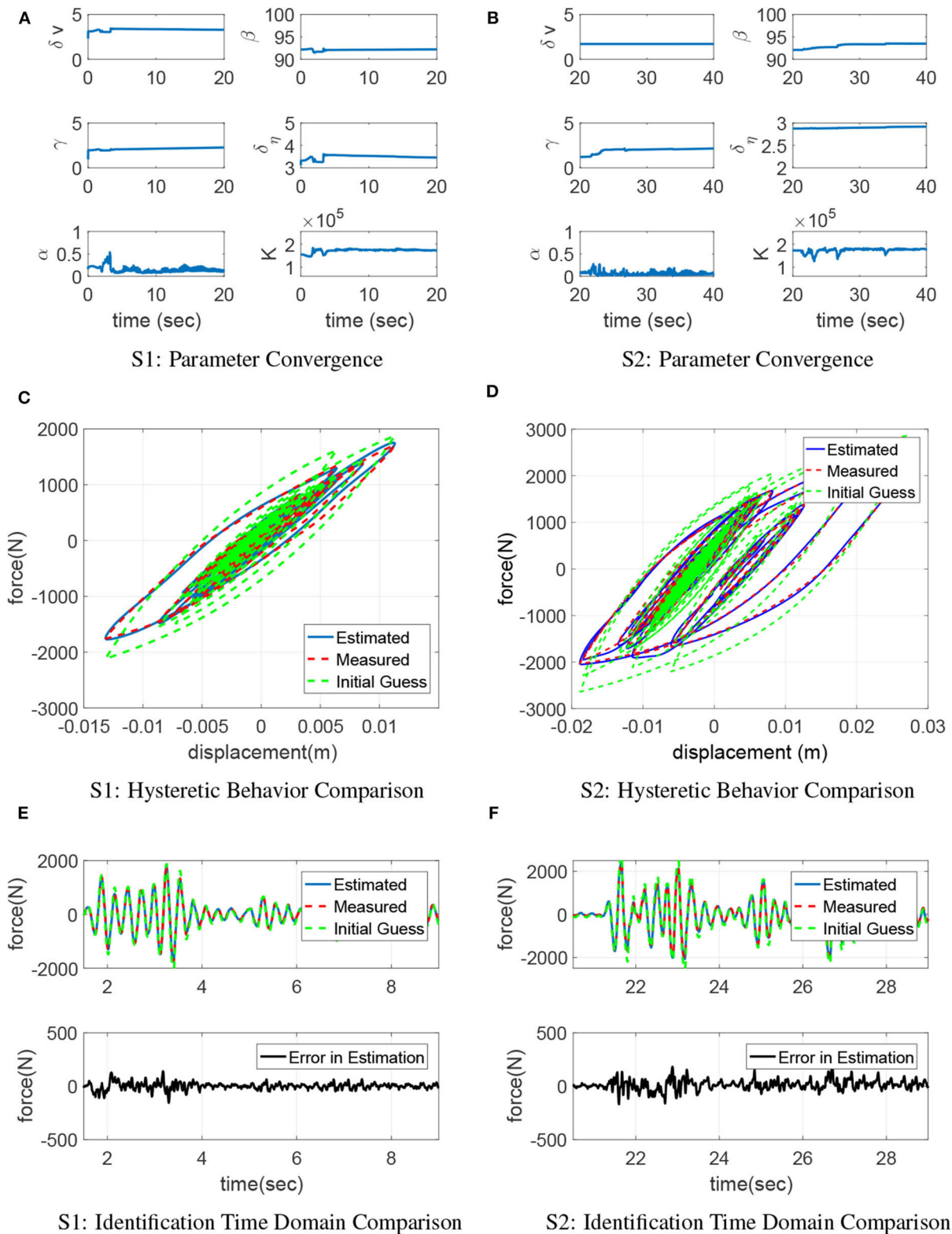


FIGURE 4 | Model updating performance using Bouc-Wen model. **(A)** S1: parameter convergence, **(B)** S2: parameter convergence, **(C)** S1: hysteretic behavior comparison, **(D)** S2: hysteretic behavior comparison, **(E)** S1: identification time domain comparison, **(F)** S2: identification time domain comparison.

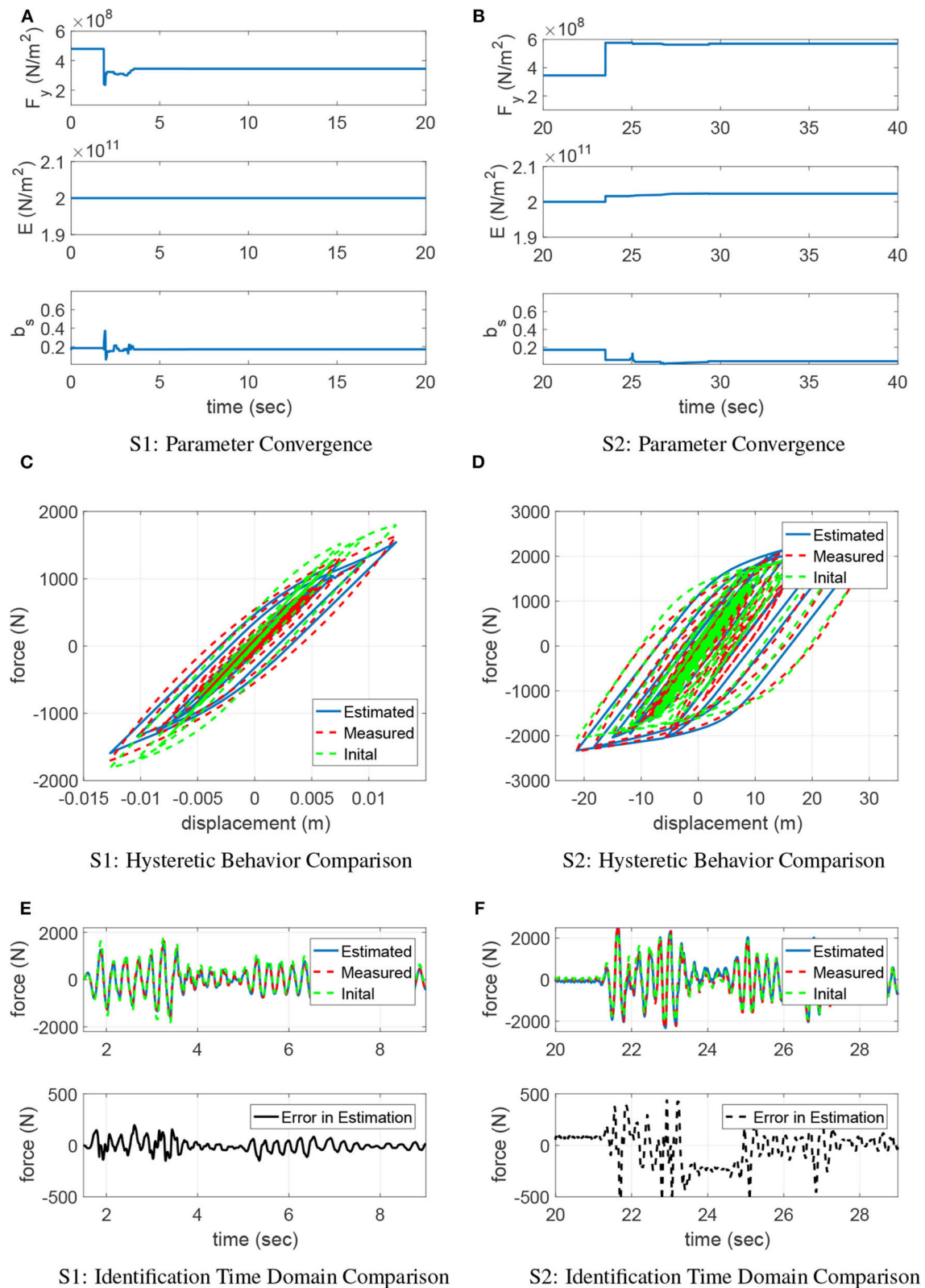


FIGURE 5 | Model updating performance case II. **(A)** S1: parameter convergence, **(B)** S2: parameter convergence, **(C)** S1: hysteretic behavior comparison, **(D)** S2: hysteretic behavior comparison, **(E)** S1: identification time domain comparison, **(F)** S2: identification time domain comparison.

the structural response reaches a larger peak due to the increased ground excitation. Most of the parameters vary and settle to another optimal state. It may be concluded that the parameters have only converged to a local optimum in S1. When the peak response evolves in S2, the converged parameters in S1 can no longer represent the specimen behavior. Therefore, the model updating algorithm continues to adjust the model parameters and brings them to a new converged set.

Along the entire time history, the Bouc-Wen model can well represent the steel frame nonlinearity. The error between model estimation and measured response is negligible with RMS error of 3.04, 3.59, and 3.34% for S1, S2, and the entire time history, compared to the RMS error in the initial model which is 21.39, 25.32, and 22.78%, respectively. CUKF is effective in updating the phenomenological parameters.

In HSMU case II, only three parameters are identified in the bilinear model. During model updating, noise and estimation tolerance R is also determined to be 100 N, $Q = \text{diag}[10^{-5}, 10^{-5}, 10^{-7}]$, $P_0 = 10 \times I_3$, $L = 3$, and $\lambda_L = -1$. Lower-bound d_k and upper-bound e_k of constrained parameters are listed in **Table 2**. According to the persistence excitation requirement Astrom and Wittenmark (2013), parameters converge faster after the earthquake starts, as in **Figures 5A,B**. In S1, the estimated yield stress F_y is reduced from the initial parameter 480 N/m^2 to 380 N/m^2 , Young's modulus E and the hardening factor b_s did not change. In S2, when a larger peak response occurs, this convergence is clearly affected, and eventually converged to $F_y = 560 \text{ N/m}^2$ and $b_s = 0.04$. Later in S2, the level of nonlinearity evolves where the deformation of structural component increases, the material settles at the second curve where the yield stress is 480 N/m^2 and the reduction factor is around 0.05. The final estimation performs better than the initial guess in S2. From the sequential ground motion, it can be concluded a bilinear curve is not sufficient to describe the steel property since a trilinear behavior is revealed.

Figure 5C illustrates that initial model underestimates the energy dissipated by the physical component in S1. Later in S2 as shown in **Figure 5D**, both initial model and updated model have similar behavior. **Figures 5E,F** show the time history comparison between the measured force R^E , the estimated output R_{est} , and the difference (error) between the two. In S1, frame hysteresis behavior is improved in HSMU with an RMS error of 8.39% where the initial model yields an RMS error of 26.41%. In S2, the parameters converge at a new optimal, the estimation RMS error in HSMU is 15.11%, which does not improve significantly as the RMS error is 19.85% using the initial guess parameters.

In addition, the results illustrate that the model-updating performance is associated with the choice of the model. Comparing the model-updating accuracy of case I and II, the RMS error for the entire time history is 3.34% for case I and 13.21% for case II because the Bouc-Wen model can better capture the steel frame hysteresis than the bilinear model. The model-updating performance further affects the fidelity of hybrid simulation results. The RMS errors between two model updating cases are summarized in **Table 3**.

TABLE 3 | RMS error in two model updating cases.

Error case	Phenomenon model (%)	Constitutive model (%)
S1: ID error	3.04	8.39
S1: Error with initial guess	21.39	26.41
S2: ID error	3.59	15.11
S2: Error with initial guess	25.23	19.85
Entire time history: ID error	3.34	13.21
Entire time history: Error with initial guess	22.78	24.51

4.2. Global Response Comparison Between HSMU and Shake Table Testing

Displacement and acceleration responses from two HSMUs (labeled as HSMU-BW and HSMU-BL) are compared to the measured responses of an experimental shake table testing. In addition, two numerical simulations are conducted, using the initial values of the phenomenon and constitutive model, respectively.

Besides the RMS error index, two additional indicators are introduced to quantify the peak responses error between each HSMU or simulation result and shake table test result, and several critical response peaks are indicated in **Figure 6**, labeled from A to I.

$$J_{1,j} = \sum_{i=1}^5 \frac{x_j(i) - x_{s,j}(i)}{\sum_{i=1}^5 x_{s,j}(i)} \quad (19)$$

$$J_{2,j} = \sum_{i=1}^5 \frac{\ddot{x}_j(i) - \ddot{x}_{s,j}(i)}{\sum_{i=1}^5 \ddot{x}_{s,j}(i)} \quad (20)$$

where J_1 is the peak displacement error, J_2 is the peak acceleration error, x_s indicates measured displacement from shake table test, \ddot{x}_s indicates measured acceleration from shake table test, and j is the profile number (A to I).

In S1 (0–20 s), the entire structure is excited with the first set of El-Centro ground motion. **Figure 7** illustrates the time domain displacement and the acceleration responses from two HSMUs and the shake table test on the top floor. It shows consistent matching between HSMU-BW and the shake table response, with only slightly undershoot after 14 s. This undershoot of HSMU-BW may be introduced by the overestimation of the energy dissipation of the Bouc-Wen model when interstory displacement is small. For HSMU-BL, overshoots in both displacement and acceleration are observed. This observation aligned with conclusions from the local assessment that the bilinear constitutive model cannot well captured the Bauschinger effect of the steel frame, and therefore underestimates the energy dissipation. Later in S2 (20–40 s), the entire steel frame is excited by a larger magnitude El-Centro earthquake with peak ground acceleration reaches $18.3 \text{ m}^2/\text{s}$. The first story

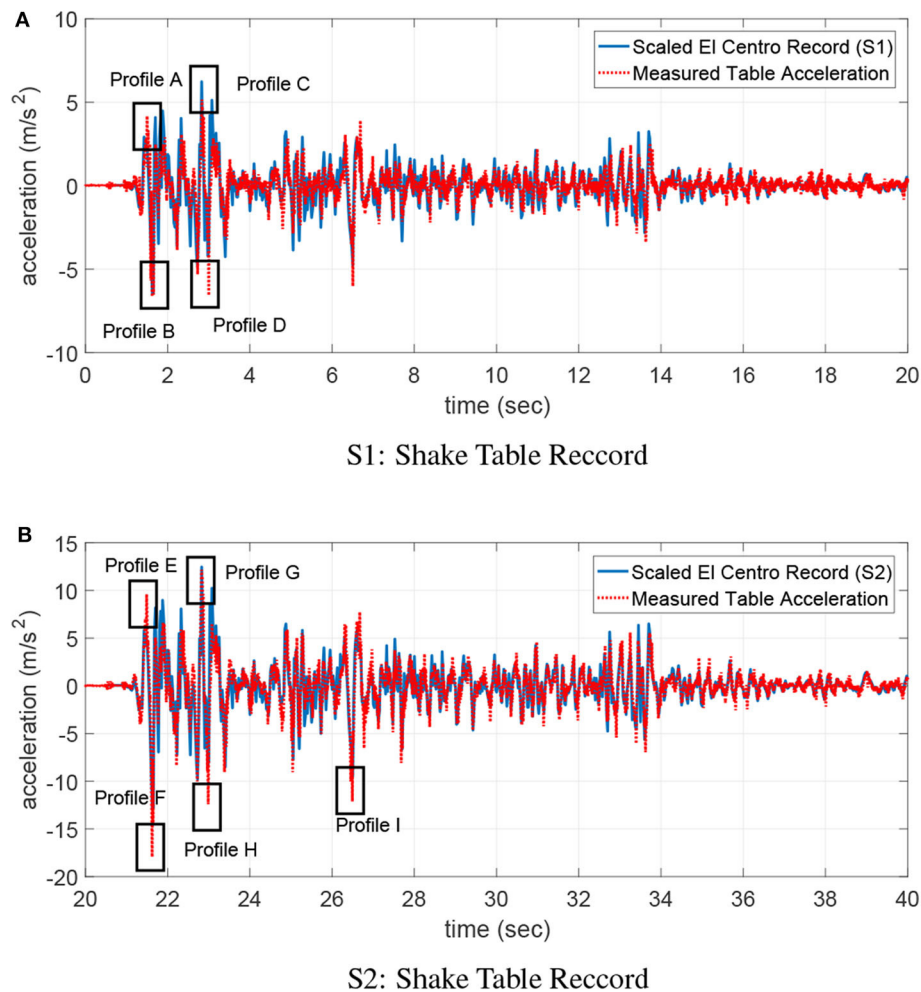


FIGURE 6 | Shake table ground motion records. **(A)** S1: shake table record, **(B)** S2: shake table record.

frame experiences a peak drift at 21.5 s, labeled as location E. Later after E, a residual drift is observed as shown in **Figure 8** for top floor displacement. However, residual drifts are quite difficult to capture with high accuracy, both HSMU-BW and HSMU-BL cases fail to match measured displacements in shake table exactly. Some possible explanations can be (1) deficiency in the connection manufacturing; (2) a fixed-end simplification of the connection is not sufficient; and (3) the inertia effect is numerically applied. Further studies to improve the residual drift prediction using simulation model are needed.

HSMU and shake table test data are analyzed in the frequency domain as well, and results are shown in **Figure 9**. Some observations are made: (1) the first and second modes are off for Sim-BW and Sim-BL after updating cases (HSMU-BW and HSMU-BL) have improved their accuracy; (2) the Bouc-Wen model overestimated the damping of the structure, even after the model updating, and, in contrast, the bilinear model always underestimated this damping/energy dissipation; (3) results indicate the model updating is effective for both models. However, the selection of the model can be more

dominant after the parameters of the selected model is correctly calibrated.

Displacement profiles are further compared and demonstrated in **Figures 10A,B**. A simulation using initial Bouc-Wen model parameters (SIM-BW) underestimates the maximum displacement in profile B, C, and D, which is similar to what was discussed in the frequency analysis. The quantified displacement errors are listed in **Table 4**. In the first section, HSMU-BW has the least error for profile A, C, and D, and SIM-BW has the largest error for all peaks. The improvement is significant after model updating, and total error reduces from 1.526 to 0.1681. Error in the displacement is only slightly reduced from 0.4492 to 0.4021 as comparing the HSMU-BL with the SIM-BL. One explanation is that the model-updating efficiency is taken over by the inherent modeling error (the selected model is not sufficient to represent a certain behavior) in the bilinear model case. In the second section, J_1 index reaches its maximum at peak location F for all cases, which is the first response peak (in the reverse direction) after the residual drift occurred at E. This can also be visualized in **Figure 10B**. In displacement profile G-I, due to the existence of the residual drifts on each story, the error

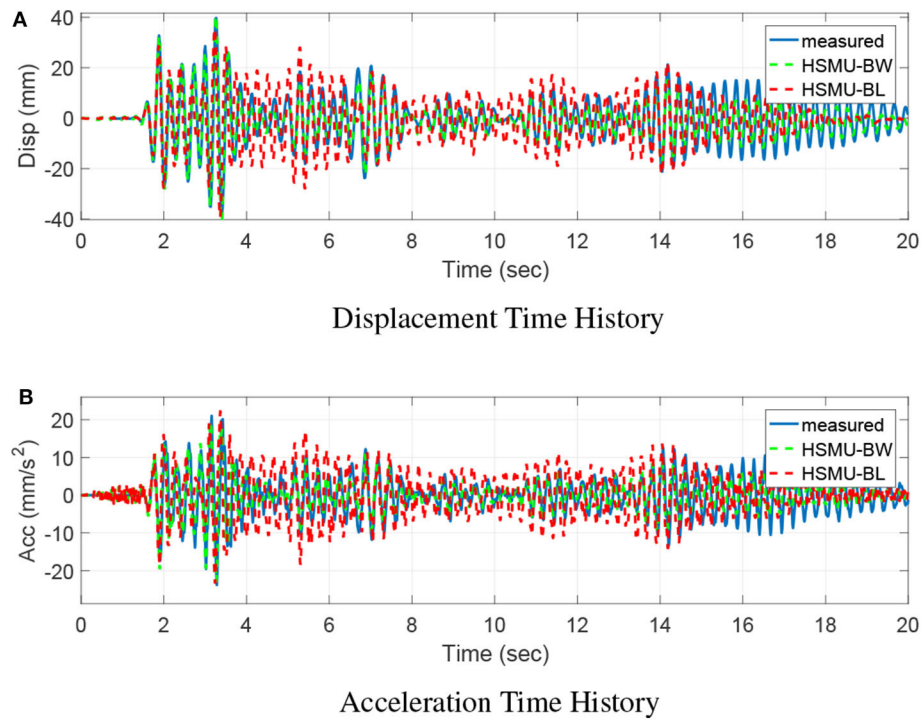


FIGURE 7 | S1: Top floor time history responses. **(A)** Displacement time history, **(B)** Acceleration time history.

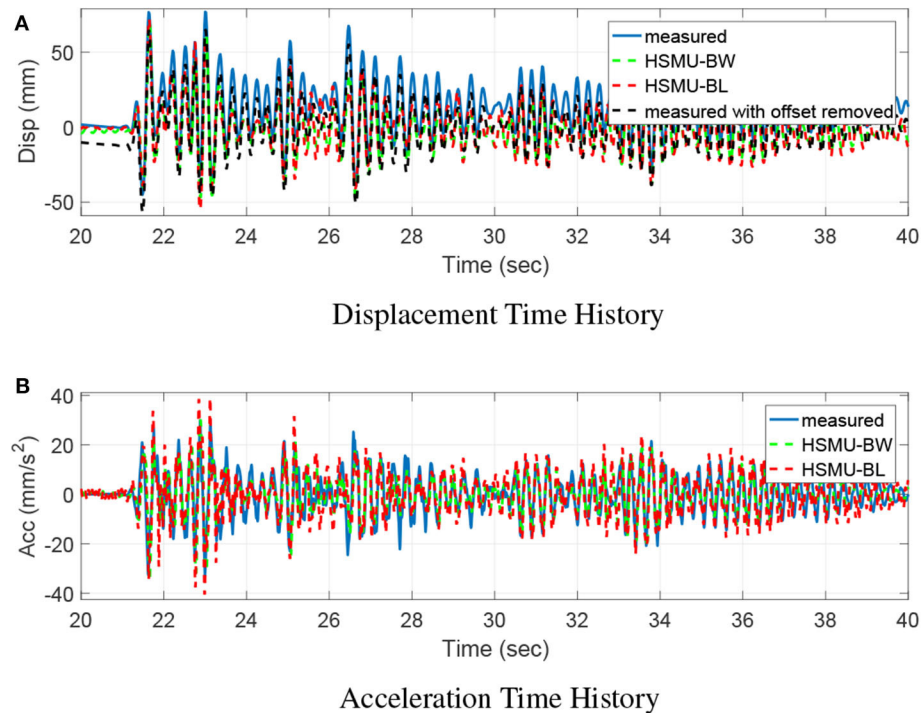


FIGURE 8 | S2: Top floor time history responses. **(A)** Displacement time history, **(B)** Acceleration time history.

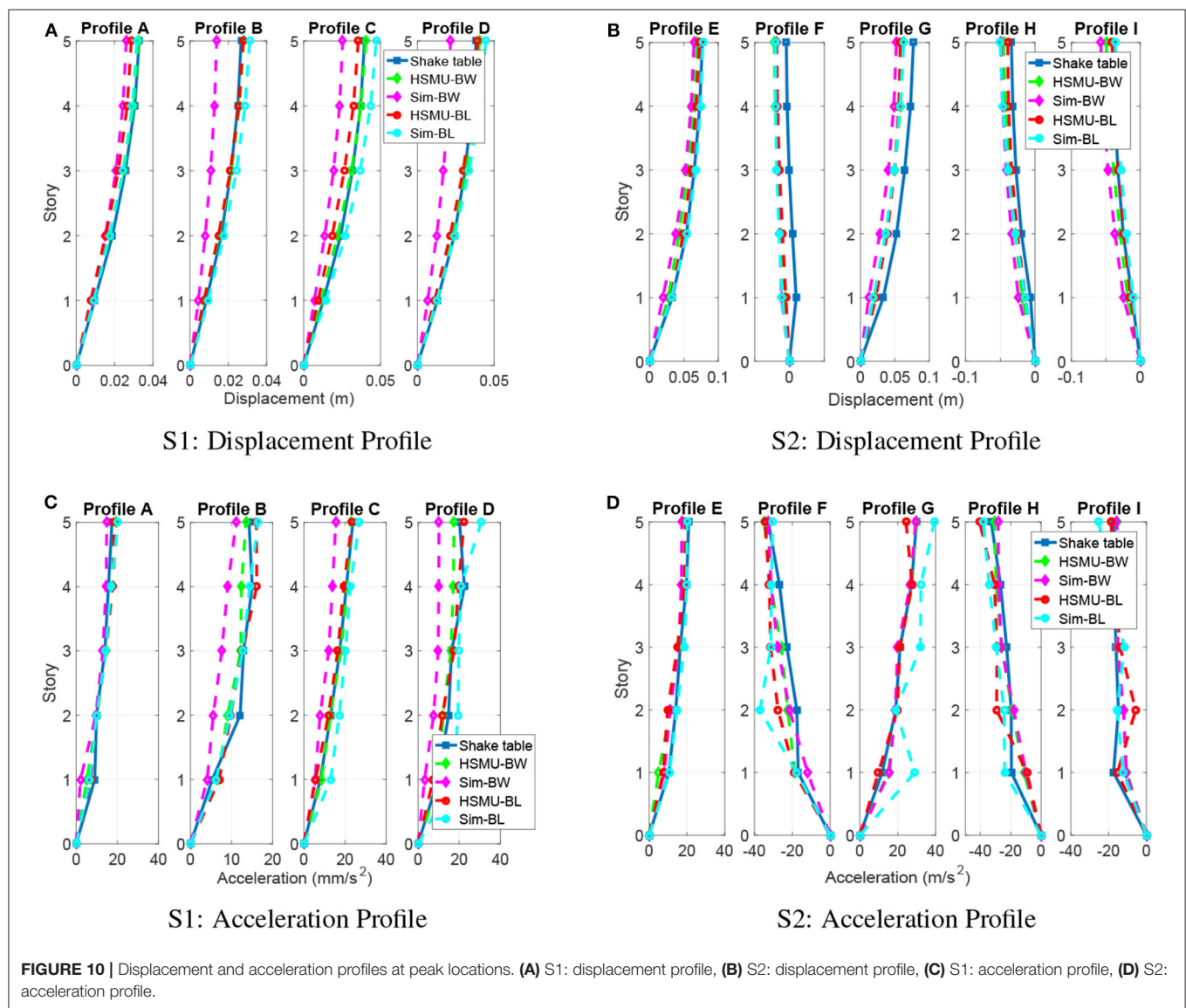
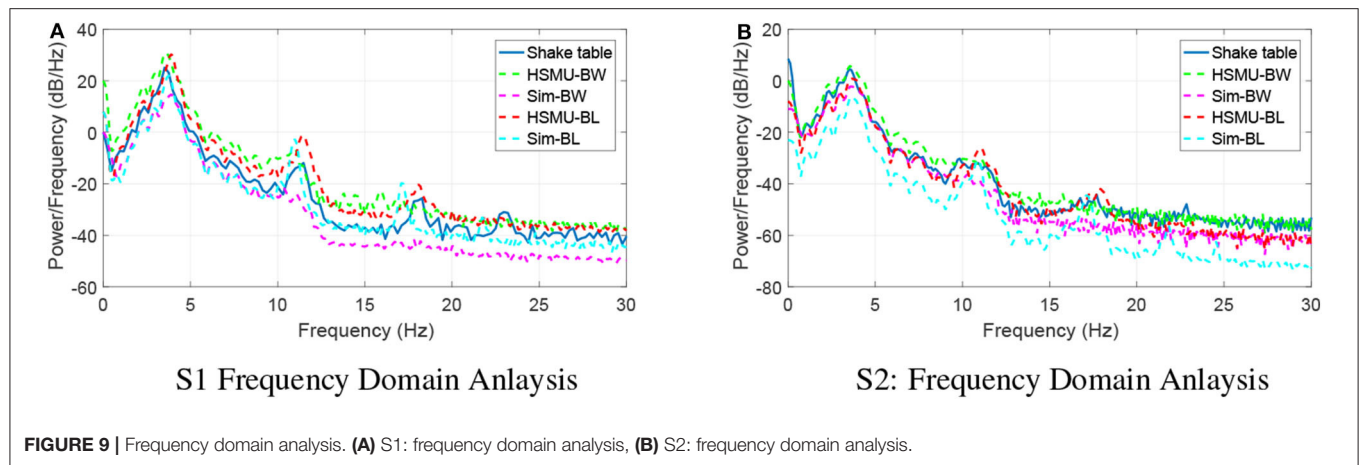


TABLE 4 | J_1 Peak displacement error.

Case	HSMU-BL	HSMU-BW	SIM-BL	SIM-BW
Profile A	0.1466	0.0381	0.0473	0.1552
Profile B	0.0475	0.0479	0.1360	0.3435
Profile C	0.1583	0.0373	0.1630	0.2959
Profile D	0.0397	0.0447	0.1028	0.3579
Profile E	0.069	0.1375	0.0217	0.2215
Profile F	2.3316	2.8261	2.7960	2.5020
Profile G	0.2513	0.2390	0.2498	0.3941
Profile H	0.2579	0.4308	0.4872	0.6282
Profile I	0.0409	0.2472	0.1164	0.5058

TABLE 5 | J_2 Peak acceleration error.

Case	HSMU-BL	SIM-BL	HSMU-BW	SIM-BW
Profile A	0.0826	0.1360	0.1066	0.1192
Profile B	0.1212	0.1400	0.1074	0.3142
Profile C	0.0738	0.0314	0.2040	0.1543
Profile D	0.1381	0.1439	0.3333	0.3068
Profile E	0.1397	0.1795	0.0470	0.4612
Profile F	0.2363	0.1386	0.3016	0.1437
Profile G	0.0807	0.0424	0.5294	0.2180
Profile H	0.3121	0.1395	0.2999	0.2955
Profile I	0.1849	0.1642	0.2480	0.4784

indicators do not represent the performance well. Results are more informative in the acceleration responses.

Figures 10C,D illustrates the acceleration profiles, and Table 5 listed J_2 errors, for all cases. In S1, the same observations as in the displacement profiles are observed at peak A to D. In S2, HSMU-BW yields the smallest error in J_2 , which indicates the responses are more accurate. This error is reduced from 1.5968 from the SIM-BW, the largest error among all the cases. For the bilinear case, by comparison with S1, the acceleration response improvement is more significant, as J_2 decreases from 1.43, as in SIM-BL, to 0.95, as in HSMU-BL. It may be concluded that (1) the model-updating process is very effective for the phenomenological model and is adaptive to different excitation amplitudes, and (2) the main reason for such improvement in HSMU fidelity is due to the first floor response measured from the experimental substructure. Even the bilinear model cannot capture the Bauschinger effect well for upper stories, and the critical first floor response is the true response from the specimen.

5. CONCLUSION

Model updating is introduced into hybrid simulation to improve the fidelity of the testing when components similar to the physical specimen are also present in the numerical substructure. To understand how model updating in hybrid simulation improves the experimental fidelity, this paper compared HSMU results to shake table results. Both the phenomenological Bouc-Wen model and bilinear steel constitutive finite element model were used in

the numerical substructure and have been updated. The main conclusions of this study are as follows:

- Overall, the HSMU approach can be successfully implemented to concentrated Bouc-Wen and distributed material nonlinear models. The parameters for each model can converge adaptively under different excitation intensities.
- From the local assessment, the Bouc-Wen model better captured the hysteresis behavior of the experimental substructure, which is also more responsive to model updating. However, the initial parameter selection for Bouc-Wen model is not intuitive. In contrast, the bilinear model cannot well capture the Bauschinger effect of the steel frame, the model error introduced by the model selection overruled the parameter updating improvement. Despite this, the determination of its initial parameters is less arbitrary.
- From the global assessment, frequency domain analysis is carried out for all HSMUs and simulations, and results indicated that significant improvement is observed in both HSMU cases. The first modes of the structure after model updating are much more accurate compared to the first modes resulted from the initial models.
- In the time domain analysis, results indicate the Bouc-Wen model may overestimate the energy dissipation or damping of the components, and the HSMU-BW case shows undershoots of peak responses. In the bilinear finite element model, energy dissipation is always underestimated, which resulted in overshoots at response peaks. This observation matched the local assessment observations as well.
- The steel frame developed large residual drift on the first floor after the peak strike of the larger ground motion (S2). Neither HSMU-BW nor HSMU-BL case can exact estimate this residual drift, which still is a challenging topic for seismic analysis in general.
- The main reason for such improvement in HSMU fidelity is due to the first floor response measured from the experimental substructure. Even the bilinear model cannot capture the Bauschinger effect well for upper stories, and the critical first floor response is the true response from the specimen.

After all, in HSMU, it should be the users to decide the tradeoff between the modeling accuracy based on model selection and its complexity. Other constitutive models such as Menegotto-Pinto model can be a desired alternative. Different model updating algorithms that are robust with larger experimental and numerical uncertainties and that are adaptive to model selection instead of parameter identification should be developed in the later studies.

DATA AVAILABILITY STATEMENT

The datasets generated for this study are available on request to the corresponding author.

AUTHOR CONTRIBUTIONS

All authors listed have made a substantial, direct and intellectual contribution to the work, and approved it for publication.

FUNDING

This material was based upon work supported by the National Science Foundation under Grant CNS 1136075

REFERENCES

- Astrom, K. J., and Wittenmark, B. (2013). *Adaptive Control*. Courier Corporation.
- Baber, T., and Noori, M. N. (1985). Random vibration of degrading, pinching systems. *J. Engrg. Mech.* 111, 1010–1026. doi: 10.1061/(ASCE)0733-9399(1985)111:8(1010)
- Baber, T., and Wen, Y. K. (1981). Random vibration of hysteretic degrading systems. *J. Engrg. Mech.* 107, 1069–1089.
- Christenson, R., Lin, Y. Z., Emmons, A., and Bass, B. (2008). Large-scale experimental verification of semiactive control through real-time hybrid simulation I. *J. Struct. Eng.* 134, 522–534. doi: 10.1061/(ASCE)0733-9445(2008)134:4(522)
- Elanwar, H. H., and Elnashai, A. S. (2016). Framework for online model updating in earthquake hybrid simulations. *J. Earthquake Eng.* 20, 80–100. doi: 10.1080/13632469.2015.1051637
- Elnashai A. S., Spencer, B. F., Kim, S. J., Holub, C. J., and Kwon, O. S. (2008). Hybrid distributed simulation of a bridge-foundation-soil interacting system,” in *The 4th International Conference on Bridge Maintenance, Safety, and Management* (Seoul).
- Gao, X., Castaneda, N., and Dyke, S. J. (2013). Real time hybrid simulation: from dynamic system, motion control to experimental error. *Earthq. Eng. Struct. Dyn.* 42, 815–832. doi: 10.1002/eqe.2246
- Gomez, D., Dyke, S. J., and Maghareh, A. (2014). Enabling role of hybrid simulation across NEES in advancing earthquake engineering. *Smart Struct. Syst.* 15, 913–929. doi: 10.12989/sss.2015.15.3.913
- Hakuno, M., Shidawara, M., and Hara, T. (1969). Dynamic destructive test of a cantilever beam, controlled by an analog-computer. *Trans. Jpn. Soc. Civil Eng.* 171:a1. doi: 10.2208/jscej1969.1969.171_1
- Hashemi, M. J., Masroor, A., and Mosqueda, G., (2014). Implementation of online model updating in hybrid simulation. *Earthq. Eng. Struct. Dyn.* 134, 395–412. doi: 10.1002/eqe.2350
- Kandepu, R., Imsland, L., and Foss, B. A. (2008). “Constrained state estimation using the unscented Kalman filter,” in *Proceedings of the 16th Mediterranean Conference on Control and Automation* (New York, NY: Institute of Electrical and Electronics Engineers), 1453–1458.
- Karavasilis, T. L., Ricles, J. M., Sause, R., and Chen, C. (2011). Experimental evaluation of the seismic performance of steel MRFs with compressed elastomer dampers using large-scale real-time hybrid simulation. *Eng. Struct.* 33, 1859–1869. doi: 10.1016/j.engstruct.2011.01.032
- Kwon, O. S., and Kammula, V. (2013). Model updating method for substructure pseudo-dynamic hybrid simulation. *Earthq. Eng. Struct. Dyn.* 42, 1971–1984. doi: 10.1002/eqe.2307
- Lin, P. C., Tsai, K. C., Wang, K. J., Yu, Y. J., Wei, C. Y., Wu, A. C., et al. (2012). Seismic design and hybrid tests of a full-scale three-story buckling-restrained braced frame using welded end connections and thin profile. *Earthq. Eng. Struct. Dyn.* 41, 1001–1020. doi: 10.1002/eqe.1171
- Mahin, S. A., and Shing, P. S. (1985). Pseudodynamic method for seismic testing. *J. Struct. Eng.* 111, 1482–1503. doi: 10.1061/(ASCE)0733-9445(1985)111:7(1482)
- Ou, G., and Dyke, S. J. (2016). “Real time hybrid simulation with online model updating on highly nonlinear device,” in *Rotating Machinery, Hybrid Test Methods, Vibro-Acoustics & Laser Vibrometry*, Vol. 8 (Cham: Springer), 343–350.
- Ou, G., Dyke, S. J., and Prakash, A. (2017). Real time hybrid simulation with online model updating: an analysis of accuracy. *Mech. Syst. Signal Process.* 84, 223–240. doi: 10.1016/j.ymssp.2016.06.015
- Ou, G., Ozdagli, A. I., Dyke, S. J., and Wu, B. (2015). Robust integrated actuator control: experimental verification and real-time hybrid-simulation implementation. *Earthq. Eng. Struct. Dyn.* 44, 441–460. doi: 10.1002/eqe.2479
- Phillips, B. M., and Spencer, B. F. Jr. (2012). Model-based feedforward-feedback actuator control for real-time hybrid simulation. *J. Struct. Eng.* 139, 1205–1214. doi: 10.1061/(ASCE)ST.1943-541X.0000606
- Shao, X., Mueller, A., and Mohammed, B. A. (2016). Real-time hybrid simulation with online model updating: methodology and implementation. *J. Eng. Mech.* 142:04015074. doi: 10.1061/(ASCE)EM.1943-7889.0000987
- Song, W., and Dyke, S. (2013). Real-time dynamic model updating of a hysteretic structural system. *J. Struct. Eng.* 140:04013082. doi: 10.1061/(ASCE)ST.1943-541X.0000857
- Wu, B., and Wang, T. (2015). Model updating with constrained unscented Kalman filter for hybrid testing. *Smart Struct. Syst.* 14, 1105–1129. doi: 10.12989/sss.2014.14.6.1105
- Yang, G., Wang, Z., Wu, B., Yang, J., Xu, G., and Chen, Y. (2015). Development of hyTest for structural hybrid simulation. *J. Build. Struct.* 36, 149–156. doi: 10.14006/j.jzjgxb.2015.11.019
- Yang, G., Wu, B., Ou, G., Wang, Z., and Dyke, S. (2017). HyTest: Platform for structural hybrid simulations with finite element model updating. *Adv. Eng. Softw.* 112, 200–210. doi: 10.1016/j.advengsoft.2017.05.007

and National Natural Science Foundation of China, Joint Research Grant 91315301-9. The author would like to also acknowledge Purdue University Bilsland Fellowship for the financial support.

Conflict of Interest: The authors declare that the research was conducted in the absence of any commercial or financial relationships that could be construed as a potential conflict of interest.

Copyright © 2020 Ou, Yang, Dyke and Wu. This is an open-access article distributed under the terms of the Creative Commons Attribution License (CC BY). The use, distribution or reproduction in other forums is permitted, provided the original author(s) and the copyright owner(s) are credited and that the original publication in this journal is cited, in accordance with accepted academic practice. No use, distribution or reproduction is permitted which does not comply with these terms.



Communication Development and Verification for Python-Based Machine Learning Models for Real-Time Hybrid Simulation

*Elif Ecem Bas and Mohamed A. Moustafa**

Department of Civil and Environmental Engineering, University of Nevada, Reno, Reno, NV, United States

OPEN ACCESS

Edited by:

Wei Song,
The University of Alabama,
United States

Reviewed by:

Gaston A. Fermandois,
Federico Santa María Technical
University, Chile
Liang Cao,
Lehigh University, United States
Pei-Ching Chen,
National Taiwan University of Science
and Technology, Taiwan

*Correspondence:

Mohamed A. Moustafa
mmoustafa@unr.edu

Specialty section:

This article was submitted to
Earthquake Engineering,
a section of the journal
Frontiers in Built Environment

Received: 22 June 2020

Accepted: 12 August 2020

Published: 11 September 2020

Citation:

Bas EE and Moustafa MA (2020)
Communication Development
and Verification for Python-Based
Machine Learning Models
for Real-Time Hybrid Simulation.
Front. Built Environ. 6:574965.
doi: 10.3389/fbuil.2020.574965

Hybrid simulation (HS) combines analytical modeling with experimental testing to provide a better understanding of both structural elements and entire systems while keeping cost-effective solutions. However, extending real-time HS (RTHS) to bigger problems becomes challenging when the analytical models get more complex. On the other hand, using machine learning (ML) techniques in solving engineering problems across different disciplines keeps evolving and likewise is a promising resource for structural engineering. The main goal of this study is to explore the validity of ML models for conducting RTHS and specifically introduce and validate the necessary communication schemes to achieve this goal. A preliminary study with a simplified linear regression ML model that can be readily implemented in Simulink is presented first to introduce the idea of using metamodels as analytical substructures. However, for ML, commonly used platforms for RTHS such as Simulink and MATLAB have limited capacity when compared to Python for instance. Thus, the main focus of this study was to introduce Python-based advanced ML models for RTHS analytical substructures. Deep long short-term memory networks in Python were considered for advanced metamodeling for RTHS tests. The performance of Python can be enhanced by running the models using high-performance computers, which was also considered in this study. Several RTHS tests were successfully conducted at the University of Nevada, Reno, with Python-based ML algorithms that were run from both local PC and a cluster. The tests were validated through comparisons with the pure analytical solutions obtained from finite element models. The study also explored the idea of embedding the delay compensators within the ML model for RTHS.

Keywords: real-time hybrid simulation, machine learning, data transfer, linear regression, long-short term memory, deep neural networks, seismic response prediction

INTRODUCTION

Hybrid simulation (HS) is a widely used dynamic testing method that simultaneously benefits from the advantages of numerical modeling and experimental testing. In an HS setup, experimental components are integrated with numerical models, and this provides accurate, realistic, cost-effective, and reliable investigations for both physical substructure and overall system behavior.

The first HS test was conducted by Takanashi et al. (1975), where a discrete spring-mass model is used, and the non-linear differential equation was solved by updating the structural stiffness at each time step from the structural experiment. From the early 70s until today, a broad range of studies has been conducted to improve the HS capabilities and widen the feasibility of this technique for several dynamic applications.

The dynamic analysis for the coupled experimental-computational model in slow HS or real-time HS (RTHS) is usually solved using direct numerical integration algorithms, where the computational system is modeled using the finite element method (FEM). Many of the direct integration methods were developed for pure analytical solutions and not necessarily suitable for HS tests (Schellenberg et al., 2009b). Because of this need, one of the main focuses of HS/RTHS research has been to develop numerical integration algorithms that are specialized to solve the substructured equation of motion in HS to have accurate and reliable test results (e.g., Chang, 2002; Bonelli and Bursi, 2005; Chen et al., 2009; Kolay and Ricles, 2014). However, the developed HS-specific methods have still some challenges and limitations, particularly for complex and large analytical substructures with many degrees of freedoms and/or large non-linearities. Del Carpio et al. (2017) examined the performance of two commonly used integration methods for HS, where complex structural systems were considered. According to that study, a careful numerical sensitivity analysis was found to be necessary to provide stable and accurate simulations for large and complex structures. That is because numerical errors could accumulate with the noise of the experimental feedback. Recently, Bas and Moustafa (2020) conducted a comprehensive study to assess currently available direct integration algorithms for RTHS and understand the performance and limitations of existing methods when computational models involve complex non-linear behavior. The study identified the current integration algorithms limitations for RTHS for some types of non-linear behaviors and showed that testing becomes more sensitive to hardware capabilities and experimental errors when such non-linear models are considered.

Another critical aspect of conducting HS/RTHS is accurate actuator control. Typically, in every time step, the integration algorithm calculates the displacement response and that is applied to the experimental substructure where the force of the experimental specimen is measured and fed back to the numerical substructure. The combined dynamics of the experimental substructure and the servo-hydraulic actuator can lead to a delay in response and amplitude error to the commanded displacement. These cause inaccurate results, especially in RTHS (Chae et al., 2013). Various compensation methods were proposed to compensate by considering both constant delay compensation (e.g., Zhao et al., 2003; Carrion and Spencer, 2007; Phillips and Spencer, 2013) and adaptive delay compensation (e.g., Darby et al., 2002; Wallace et al., 2005; Ahmadizadeh et al., 2008; Chen and Ricles, 2010). Moreover, an adaptive time series (ATS) compensator has been introduced and commonly used nowadays to compensate for the delay (Chae et al., 2013). The ATS compensator uses online real-time linear regression (LR) analysis to continuously update the

system's coefficients at each time step without the need for user-defined parameters.

As the challenges to conducting the RTHS tests continue, recent advancements in various disciplines and research fields can be used to address such challenges. In structural dynamic analysis and specifically RTHS testing, using FEM for non-linear time history analysis could be computationally demanding even with the current technology we have today. There has been a large number of studies that suggest alternative approaches for FEM to obtain structural responses using input/output relations based on system identification methods, and some of them have been applied to RTHS as well (e.g., Mai et al., 2016; Abbiati et al., 2019; Miraglia et al., 2020). Machine learning (ML) is one of the disciplines that have the potential to improve the capabilities and extend the possible range of applications of RTHS. Shortly, ML is the science of programming computers so that they can learn from the data (Géron, 2017). ML has been used for many earthquake engineering applications, including seismic hazard analysis, system identification, damage detection, seismic fragility assessment, and structural control for earthquake mitigation (Xie et al., 2020). ML models can be grouped in many different forms such as grouping based on the tasks ML models are designed to solve, i.e., classification, regression, and clustering. This study aims to set the stage for a new paradigm of RTHS testing that would use ML to replace finite element (FE) models to predict the analytical model response.

Because ML models are designed to predict the continuous response, the task here is regression. During the past decade, artificial neural networks (ANNs) have been used in predicting non-linear behavior of static and dynamic responses of structures (e.g., Wang et al., 2009; Lagaros and Manolis, 2012). Moreover, Mucha (2019) used ANNs to replace FEM of the HS to reduce the computational cost of RTHS for a bicycle frame under time-varying excitation force. The study did not focus on structural or earthquake engineering applications, which have been the classical venue for HS/RTHS. Moreover, the capacity of ANNs is limited, and there are some studies that use more advanced deep learning algorithms such as convolutional neural networks (CNNs) and recurrent neural networks (RNNs), which are more suitable for long-range time-varying structural response predictions. For example, Zhang et al. (2019b) used deep long short-term memory (LSTM) networks to model non-linear seismic response of structures. Other examples include physics-guided CNNs that have been recently proposed for data-driven seismic response modeling (Zhang et al., 2019a).

The main goal of this article is to develop and validate communication schemes and overall RTHS test performance when advanced ML models, also referred to as metamodels, are included in the RTHS loop to represent the analytical substructure. The article first introduces the ML-based RTHS system components and capabilities with a simplified ML model, i.e., an LR algorithm, to model a linear-elastic one-story, one-bay braced frame model. This simple exercise is conducted to assess the overall system performance and explore another new benefit of using ML models. This new benefit is concerned with potentially eliminating the time delay between actuator input and feedback within the metamodel instead of using a time-delay

compensator, which is investigated further throughout the article. Next, modeling and training assumptions for more complex and representative ML models are explained in detail. The advanced models are generated using LSTM networks, which are modeled in Python. A large number of ML research studies prefer Python as one of the most popular high-level programming languages that include many frameworks and large ML libraries. To our best knowledge, this article presents the first attempt that combines an advanced ML model within the RTHS loop. The article then focuses on the communication development and validations when Python-based ML models are introduced in the RTHS loop. Two scenarios for calling the Python models from local computer as well as a cluster of high-performance computing are presented. Finally, results from online RTHS tests without test specimens, but with LSTM networks that represent non-linear analytical substructures, are discussed, and key findings are summarized.

SIMPLIFIED MACHINE LEARNING MODEL FOR RTHS

This section first introduces the HS setup and verification with a simplified ML model. An LR model is selected, and the training and model assumptions are explained in detail. In this section, the ML model is built and compiled into Simulink, which is a common RTHS test setup.

HS System Components

The compact HS setup recently developed and assembled by the authors at the Large-Scale Structures Laboratory at the University of Nevada, Reno (UNR), is used for this study (Bas et al., 2020b). This small-scale setup has been developed for investigating computational challenges in substructuring (e.g., Bas and Moustafa, 2020; Bas et al., 2020a), educational demonstrations, developing new substructuring concepts in HS/RTHS, and developing innovative approaches for computational substructures as discussed in this article. **Figure 1** shows the components of the HS setup, which consists of the following: (1) a small-scale load frame with a dynamic actuator that is run by an isolated hydraulic pump; (2) MTS STS controller (MTS 493) with 2048 Hz clock speed; (3) real-time high-performance Simulink machine (Speedgoat xPC target); (4) Windows machine (host PC) for analytical substructures (such as MATLAB, OpenSees, or Python) and the HS middleware OpenFresco; (5) SCRAMNetGT ring that provides shared memory locations for real-time communication.

The small-scale load frame is used for the experimental substructure in this setup with an actuator with 31.14 kN (7 kips) maximum load capacity and ± 25.4 mm (± 1 in) stroke. The actuator's peak velocity at no load is 338.84 mm/s (13.34 in/s). The isolated hydraulic power supply system includes a pumping capacity of 8.71 lt/min (2.3 gpm), and the reservoir capacity of oil volume is 56.78 lt (15 gallons).

The FEM of the analytical substructures can be modeled in either OpenSees or Simulink. The setup is capable of running both real-time and slow (pseudodynamic) HS experiments. The slow HS case can be conducted using a predictor–corrector

algorithm to control different time ranges that is defined in OpenFresco middleware (Schellenberg et al., 2009a,b). The host PC and xPC target machine have a TCP/IP connection to initialize and map the SCRAMNetGT memory locations. The xPC target machine is an environment that connects Simulink and Stateflow models to the physical components. The xPC solves Simulink-based analytical models. For the models other than Simulink, the analytical substructures are run from the host PC. For the applications where OpenSees/OpenFresco architecture is used, the xPC target is used as a middleware that transfers data between the analytical and experimental substructure. The calculated analytical substructure response is sent to the controller through the xPC target machine.

The STS controller has four channels that can control up to four actuators simultaneously, but using the current setup in **Figure 1**, only one channel is used to control one actuator. Displacement control is preferred for the actuator where computed displacement input controls the actuator, and the force feedback is measured and fed back to the physical substructure. It is important to mention that all HS components have SCRAMNetGT card, which uses shared memory locations with fiber optic communications to transfer data in real time. More details about the HS system development and verification where FEM is used can be found in Bas et al. (2020b).

In this research, this setup is used first with a simplified ML model, which is straightforward enough to model directly in Simulink. Therefore, no additional communication other than what is explained above is necessary. When a more complex ML model is introduced, some modifications and/or developments were sought on the communication side as explained later in *Communication Development and Verification*.

Modeling Assumptions and Training Dataset

A one-story, one-bay steel concentrically braced frame (CBF) with diagonal brace configuration was selected for the verifications and evaluations in this study. CBFs are convenient for the substructuring where the columns and beams of CBFs can be modeled with high accuracy, i.e., form the analytical substructure. Meanwhile, braces are better tested physically to accurately capture complex behavior such as buckling, and in turn, braces make the experimental substructure. A single small-scale brace can be tested as the experimental substructure in the used HS setup and can be combined with a prototype steel frame at full scale for the analytical substructure. For the sake of this study, a linear analytical model is first used, and then a heavily non-linear analytical substructure is considered for the advanced ML modeling. In both cases, no physical braces were used, and instead, a multiplier of the actuator's actual achieved displacement is fed back to the RTHS loop to represent a hypothetical linear elastic test specimen as explained later. In other words, a non-linear experimental behavior was not considered in this study to make it simpler for verification purposes.

Figure 2 shows the CBF substructuring for HS testing. The analytical substructure involves two columns ($W14 \times 311$),

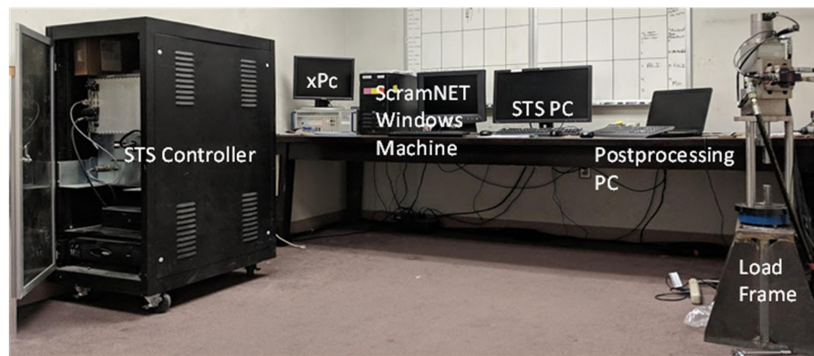


FIGURE 1 | Compact HS/RTHS test setup at UNR.

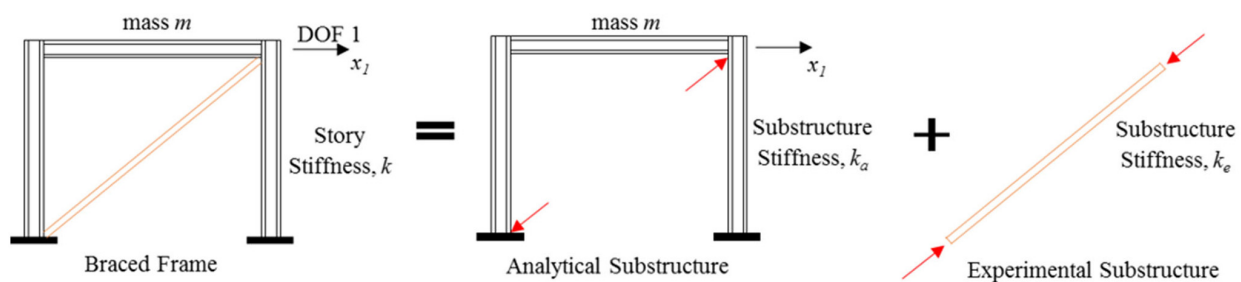


FIGURE 2 | Model and substructuring of diagonal CBF for HS testing.

which are fixed at the base and a beam ($W36 \times 150$) that has moment connections to the columns. The brace, on the other hand, has a pinned connection at both ends, where it works as an axial element. The bay width and the height of the frame are about 3.7 m. For this section, both columns and the beam are considered to be linear elastic. The mass and the damping are also considered to be a part of the analytical substructure. For simplicity in the validation and modeling purposes, the CBF is simplified as a single degree of freedom model. The mass of the system is selected to be 1.75 kN-s²/mm. The frame stiffness (analytical substructure stiffness) is calculated to be 176.75 kN/mm, where the axial brace stiffness is 1,224.1 kN/mm. The natural period of the system is calculated to be 0.294 s. A 2% Rayleigh damping is assumed to be the inherent damping of the structure. The pure analytical model of the overall system is developed in Simulink. The explicit integration algorithm provided by Chang (2009) is used to solve the equation of motion with 1/2,048-s time step. This explicit algorithm is unconditionally stable for linear systems and any instantaneous stiffness softening systems and conditionally stable for instantaneous stiffness hardening systems. Here, the time step of the controller and the integration algorithm are selected to be the same to synchronize the data transfer. The 1940 El-Centro ground motion acceleration (**Figure 3A**) was selected to be used for both training and HS testing purposes in this study.

As mentioned earlier, an LR method is used as a simplified metamodel for the first part of this study, which was trained by using a pure analytical solution of the CBF. An LR is one of the

simplest ML algorithms that perform a task to make predictions based on the weighted sum of the input values and a bias term as a constant (Géron, 2017). The general equation is shown in Eq. 1, where \hat{y} is the predicted value, n is the number of the features, x_i is the i^{th} feature, and θ_j is the j^{th} model parameter (θ_0 is the bias term, where $\theta_1, \theta_2, \dots, \theta_n$ are the feature weights).

$$\hat{y} = \theta_0 + \theta_1 x_1 + \theta_2 x_2 + \dots + \theta_n x_n \quad (1)$$

The training dataset was obtained from a pure analytical dynamic analysis of the overall system. The brace displacement and force time histories were obtained in local coordinates and used as training datasets in addition to the ground motion acceleration (see **Figure 3** for these training components). Because the dataset is provided offline, the model is considered as batch learning. In total, five input features were selected to train the model to predict the output, which would be the command displacement of the experimental substructure of the HS system. The training features were selected to be (i) ground motion acceleration, (ii) displacement feedback value of the brace (from experimental substructure), (iii) force feedback value of the brace (from experimental substructure), (iv) one previous step of the predicted displacement, and (v) two previous steps of the predicted displacement. Because the pure analytical solution is used for the training dataset, an estimated 28-time-steps delay has also been considered to better represent the feedback that should come from the experimental substructure. However, to obtain a

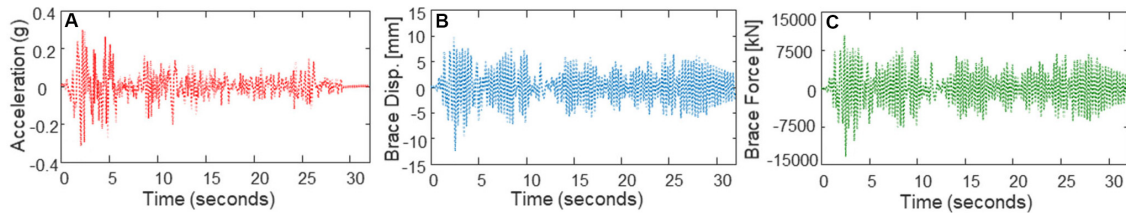


FIGURE 3 | Datasets used for LR model training: **(A)** El-Centro ground motion acceleration, **(B)** brace displacement history, and **(C)** force history, both in local brace coordinates as obtained from the pure analysis.

more accurate delay estimation better than the assumed 28-time steps, the trained model was run in the HS setup first without including the actuator's feedback, which were obtained to be used in the next training phase. Then, a more refined model was generated by using these "real" displacement and force feedback data with the other three features.

A brief overview of how the LR training was conducted is as follows. In this study, the "Regression Learner" app in MATLAB, which is under the ML group, was used to train the LR algorithm. First, the predictors and response were defined, and then a validation method was selected. The cross-validation with five folds was selected to protect the model against overfitting by partitioning the datasets into folds and estimating the accuracy of each fold. A session was started next for training, and an LR model was selected. Afterward, the model training was done, and the model root mean square error (RMSE) values were checked. Once the model was trained, the model was exported to the workspace to obtain the LR parameters to make new predictions. After getting the parameters, a Simulink model was generated to represent the HS case where at every step the predicted displacement is calculated, and the determined force feedback is fed back to the system to make new predictions.

RTHS Test Results

Once the model is trained for the features explained above, a Simulink model with MATLAB function was prepared to represent the LR model but was first assessed against the pure analytical FEM solution. The developed LR model formulation is shown in Eq. 2, where x is represented as displacement of the brace, F is the force of the brace, and \ddot{x}_g is the ground motion acceleration. **Table 1** shows the model parameters that belong to the trained model.

$$\begin{aligned}
 x_{\text{prediction},i+1} &= f(\ddot{x}_g, x_{\text{feedback},i}, F_{\text{feedback},i}, x_{\text{prediction},i}, \\
 &\quad x_{\text{prediction},i-1}) \\
 &= \theta_1 \ddot{x}_g + \theta_2 x_{\text{feedback},i} + \theta_3 F_{\text{feedback},i} \\
 &\quad + \theta_4 x_{\text{prediction},i} + \theta_5 x_{\text{prediction},i-1}
 \end{aligned} \quad (2)$$

TABLE 1 | LR model parameters.

θ_1	θ_2	θ_3	θ_4	θ_5
-6.51e-05	0	3.46e-11	-0.998	1.997

The brace displacement response of the FE model and the prediction from the LR metamodel were compared as the two alternative pure analytical solutions. The FE model response was considered to be the exact solution, and in turn, a normalized RMSE (NRMSE) was calculated to evaluate the comparison. It should be noted that for the pure analytical response, because there is no feedback from the actuator included yet, the displacement feedbacks are generated using 28-time-steps delay as discussed earlier. **Figure 4** shows the comparison between the pure analytical brace displacement response of the FE model and the LR model. The NRMSE value was calculated as 0.15%, which confirms that the LR prediction can be used further.

Moreover, for complete evaluation of using the LR model, RTHS validation tests were conducted using the LR model and compared to the pure analytical FE solution. The validation tests were considered for a hypothetical linear elastic experimental specimen where the displacement command was multiplied with the constant stiffness value of the specimen to represent a force feedback value. The verified MATLAB-based LR metamodel explained above was then compiled in the xPC Target machine. Two types of RTHS tests were conducted, namely, offline and online RTHS tests. The offline test is where the feedback from the experimental model is taken from the command of the system's controller, i.e., without actually moving the actuator. For the offline RTHS test, again, instead of using the actual actuator's feedback, the command displacement value was used with a 28-time step delay from the predicted displacement value. **Figure 5A** shows the brace displacement time history comparison for the pure analytical model and from offline RTHS with the LR metamodel. The NRMSE value was calculated as 0.15%, which is very reasonable given the simplicity of the problem and test.

Next, an online test was considered where the hydraulic system is turned on and the actuator was moved, and the actual feedback was fed into the analytical model. This is to test the capability of the metamodel to derive the actuator in the closed loop RTHS setting. The displacement value was obtained from the actual actuator displacement, and again the force feedback was obtained from a constant stiffness to mimic a linear elastic specimen. For such tests, the ATS compensator mentioned above (Chae et al., 2013) was used to compensate for the actuator delay. **Figure 5B** shows the online RTHS results for brace displacement comparison with the pure analytical model. The NRMSE value was calculated to be 0.07%, which verifies the acceptable performance of the metamodel-driven system. It is noted that the conducted test

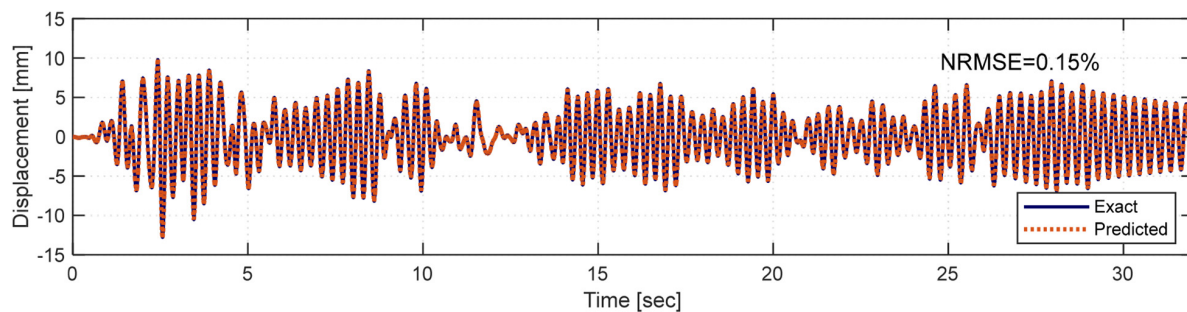


FIGURE 4 | Comparison of the brace displacement time histories from FE model and LR metamodel.

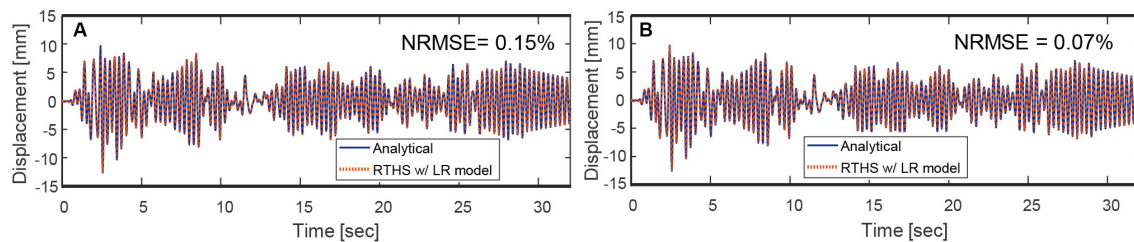


FIGURE 5 | Results from (A) offline and (B) online RTHS with the LR metamodel and validation against pure analytical solution.

considered linear elastic analytical and hypothetical experimental substructures. Thus, the dynamic response was accurately obtained from pure analytical solutions and in turn accurately trained the LR metamodel. So, the low error is not meant to assess the quality of LR metamodel predictions, but rather confirm the performance of the overall RTHS hardware and communication system.

Such simple linear elastic case was possible to easily model with the LR algorithm, which was also simple enough to code using MATLAB and Simulink functions and directly compile it into the RTHS hardware. However, the modeling capacity of LR models is rather limited and cannot be used for complex non-linear systems. Thus, more complicated ML algorithms are likely to be used to push the boundaries of future RTHS testing, which motivated the next part of the study. More complex ML algorithms such as deep learning were considered, which required integrating Python into the RTHS loop. Developing the ML models for the next phase of validation is the focus of the next section, which is then followed by the communication schemes development and verification for RTHS with Python-based complex ML models.

ADVANCED ML TECHNIQUES FOR RTHS

This section provides first a brief overview of more complex ML models, which includes the LSTM model used in this study. The section also provides more details on LSTM model features, training sets used for this study, and sensitivity analysis to understand the performance of the model as it pertains to the structural modeling problem in hand.

One of the subgroups of ML methods is deep learning, which uses neural networks with many layers. Deep learning studies deep neural networks, which is a form of stacking several layers of ANNs. The most straightforward architecture of ANN is the perceptron, which takes the weighted sum of the inputs and then multiplies this sum with an activation function and outputs the result. The perceptrons are not capable of learning complex patterns; thus, multilayer perceptron (MLP), which is a stacked version of multiple perceptrons, is suggested to improve some of the limitations. This type of ANNs contains one input layer, one or more hidden layers, and an output layer. For these models, the input-to-output flow is only one way, which represents a feedforward neural network. An ANN has simple architecture and is used for both classification and regression problems. However, more advanced models developed recently, such as CNN and RNN, offer more opportunities while modeling non-linear structural responses due to their impressive feature extraction (Zhang et al., 2019b).

Convolutional neural networks are a family of deep learning, which is mostly used for image classification. However, they are also capable of handling long sequence data for regression analysis (LeCun and Yoshua, 1995). The architecture of CNN is inspired by the brain's visual cortex, which uses the function of pattern connectivity function that the brain has. CNN has two different layers than the regular ANN, which are convolutional layers and pooling layers. The most critical difference in CNN is the convolutional layer, where the previous layer's inputs are only connected to their receptive fields, which defines the neurons' weight. By using this feature, the network hierarchically splits the input features, and each neuron analyzes the small region of the image. On the other hand, the pooling layer aims to

subsample the image, which also reduces the computational load and the possible overfitting. These advances separate CNN from other deep neural networks because it is beneficial on large inputs by reducing the connections and correspondingly the training parameters.

The other crucial neural network is RNN, which has connections to the previous input points. The difference of the RNN from previously defined neural networks is these backward connections where the previous ones are feedforward neural networks. The architecture of the RNNs includes a recurrent neuron which receives the output from the previous time step with the input. This allows this type of network to be capable of time-series forecasting. Although it is successful in sequence datasets, the method has two main disadvantages for longer sequences: (i) unstable gradients and (ii) utilizing a very limited short-time memory (Bengio et al., 1994). To overcome these problems, the LSTM cell was proposed, which can detect long-term dependencies, rapidly converge, and perform better (Hochreiter and Jürgen, 1997).

In this study, the LSTM networks were selected and used for the purpose of modeling and dynamic response prediction of the analytical substructures needed for the sought communication schemes development and RTHS demonstration. The modeling assumptions, training, and model tuning are explained in detail in the following sections.

LSTM Networks

The LSTM networks were developed, especially to answer the need in long sequence datasets. **Figure 6A** shows a typical deep LSTM network, with input, hidden, and output layers. The architecture of an LSTM cell is shown in **Figure 6B**. In particular, an LSTM cell includes $\mathbf{h}_{(t)}$ and $\mathbf{c}_{(t)}$ apart from inputs ($\mathbf{x}_{(t)}$) and outputs ($\mathbf{y}_{(t)}$), which are representing short- and long-term states, respectively.

In each time step, the LSTM cell receives two input vectors that are the current time step input vector $\mathbf{x}_{(t)}$ and previous time step output vector $\mathbf{h}_{(t-1)}$ (which is also $\mathbf{y}_{(t-1)}$) and fed into four different fully connected layers. The output of $\mathbf{g}_{(t)}$ analyzes these two inputs, which is the weighted sum of the inputs followed with an activation function (tanh function). A regular RNN cell only has this feature, which directly gives the output. However, in the LSTM cell, three other layers, which are the gate controllers, help control the memory information. These three gates use logistic function, $\sigma(\cdot)$, as an activation function where the output changes from 0 to 1. The forget gate (output of $\mathbf{f}_{(t)}$), is where the unnecessary parts of the long-term state are erased. On the other hand, the input gate (output of $\mathbf{i}_{(t)}$), controls the parts of $\mathbf{g}_{(t)}$ to be added in the long-term state. Lastly, the output gate manages the parts of the long-term state that should be read and output to both $\mathbf{h}_{(t)}$ and $\mathbf{y}_{(t)}$. The LSTM computations are briefly outlined and given in Eqs 3 through 8. In these equations, the input vector of the current state $\mathbf{x}_{(t)}$ in each layer is connected with the weight matrices of each layer \mathbf{W}_{xi} , \mathbf{W}_{xf} , \mathbf{W}_{xg} , and \mathbf{W}_{xo} , where the previous short-term state vector $\mathbf{h}_{(t-1)}$ is connected to their layers with the weight matrices of \mathbf{W}_{hi} , \mathbf{W}_{hf} , \mathbf{W}_{hg} , and \mathbf{W}_{ho} . In each layer, \mathbf{b}_i , \mathbf{b}_f , \mathbf{b}_o , and \mathbf{b}_g are the bias terms. Lastly, \otimes is the element-wise multiplication. It should also be noted that, as

suggested by Jozefowicz et al. (2015), the bias term of the forget gate (\mathbf{b}_f) is initialized as “1”s to prevent forgetting everything at the beginning of the training.

$$\mathbf{i}_{(t)} = \sigma \left(\mathbf{W}_{xi}^T \mathbf{x}_{(t)} + \mathbf{W}_{hi}^T \mathbf{h}_{(t-1)} + \mathbf{b}_i \right) \quad (3)$$

$$\mathbf{f}_{(t)} = \sigma \left(\mathbf{W}_{xf}^T \mathbf{x}_{(t)} + \mathbf{W}_{hf}^T \mathbf{h}_{(t-1)} + \mathbf{b}_f \right) \quad (4)$$

$$\mathbf{o}_{(t)} = \sigma \left(\mathbf{W}_{xo}^T \mathbf{x}_{(t)} + \mathbf{W}_{ho}^T \mathbf{h}_{(t-1)} + \mathbf{b}_o \right) \quad (5)$$

$$\mathbf{g}_{(t)} = \tanh \left(\mathbf{W}_{xg}^T \mathbf{x}_{(t)} + \mathbf{W}_{hg}^T \mathbf{h}_{(t-1)} + \mathbf{b}_g \right) \quad (6)$$

$$\mathbf{c}_{(t)} = \mathbf{f}_{(t)} \otimes \mathbf{c}_{(t-1)} + \mathbf{i}_{(t)} \otimes \mathbf{g}_{(t)} \quad (7)$$

$$\mathbf{y}_{(t)} = \mathbf{h}_{(t)} = \mathbf{o}_{(t)} \otimes \tanh(\mathbf{c}_{(t)}) \quad (8)$$

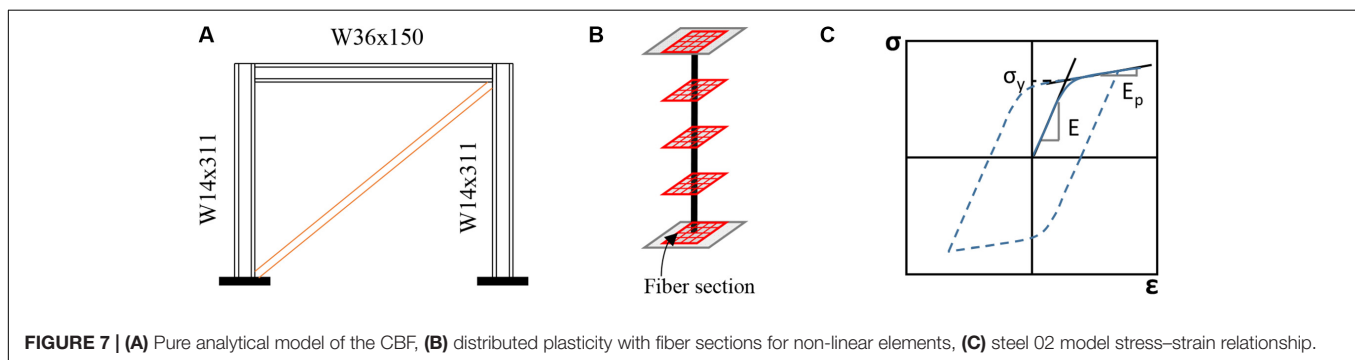
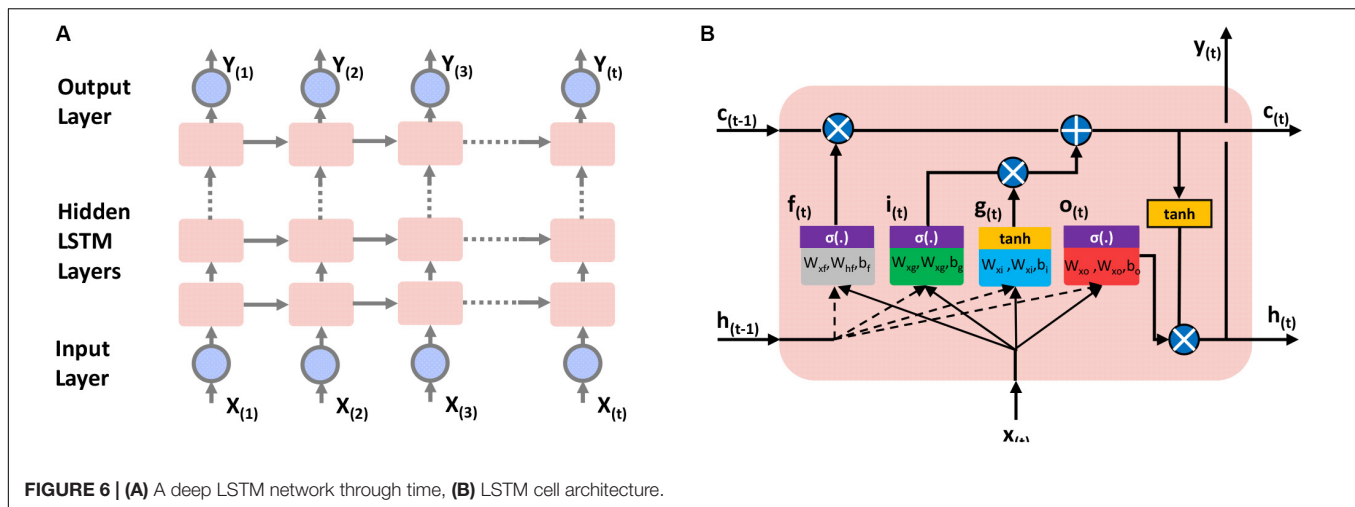
Briefly, an LSTM cell can observe the input importance, remember the long history of time series while storing them in the long-term state, and store longer information as long as it is needed and remove whenever it is unnecessary. Therefore, even if the problem is highly non-linear, the LSTM is capable of capturing long-term patterns in the time series (Zhang et al., 2019b).

Training Datasets

A similar one-story, one-bay steel braced frame as discussed in *Simplified Machine Learning Model for RTHS*, but with some modifications, was selected for this part of the study for generating training datasets. The analytical substructure was designed to be non-linear for the RTHS tests where this non-linear analytical substructure is to be represented with an advanced ML model. Again, the main goal of this fundamental study is to explore validity of using ML modeling for RTHS and develop/verify the needed communication schemes. Hence, the experimental element was selected to be linear elastic so that it can be still combined with the non-linear analytical substructure to obtain pure analytical solutions for validating the RTHS tests.

The pure analytical model of the overall system was modeled in OpenSees (McKenna et al., 2000), which offers a wide range of material models, elements, and solution algorithms. The columns ($W36 \times 150$) and beam ($W14 \times 311$) elements were defined using fiber sections with non-linear material behavior as illustrated in **Figure 7**. The non-linear material behavior was defined with Steel02 material in OpenSees (**Figure 7C**), which is uniaxial Giuffre–Menegotto–Pinto steel material with isotropic strain hardening (Filippou et al., 1983). The implicit Newmark method was used for all the conducted analysis to obtain the training dataset, and the parameters were set as $\gamma = 0.50$ and $\beta = 0.25$.

The yield stress of the material was selected to be 345 MPa with modulus of elasticity of 200 GPa. On the other hand, the brace, which is the experimental substructure in the RTHS tests, was modeled to be linear elastic with axial stiffness of 278 kN/mm. The choice of the brace stiffness allowed the CBF to experience larger displacements and higher non-linearities to provide a wider range of behavior for training the ML model. The mass of the system was selected to be 1.75 kN-s²/mm. The



natural period of this CBF system was calculated to be 0.47 s. A 2% Rayleigh damping was assumed for modeling the inherent damping of the structure.

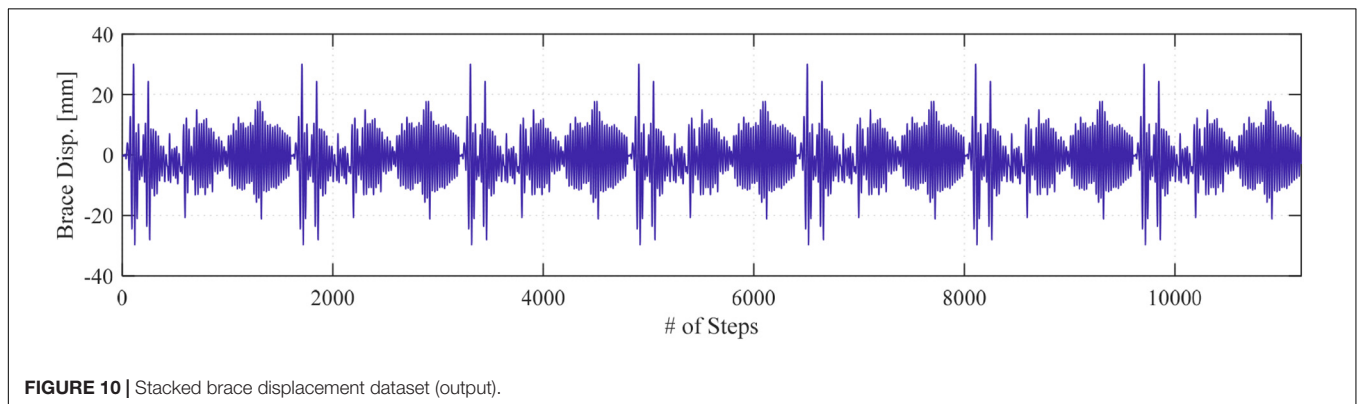
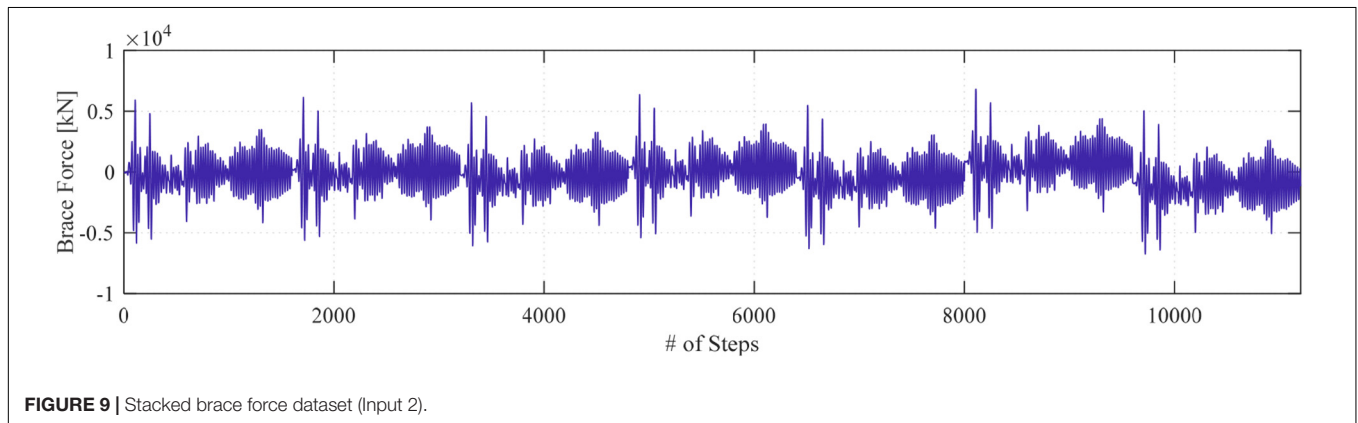
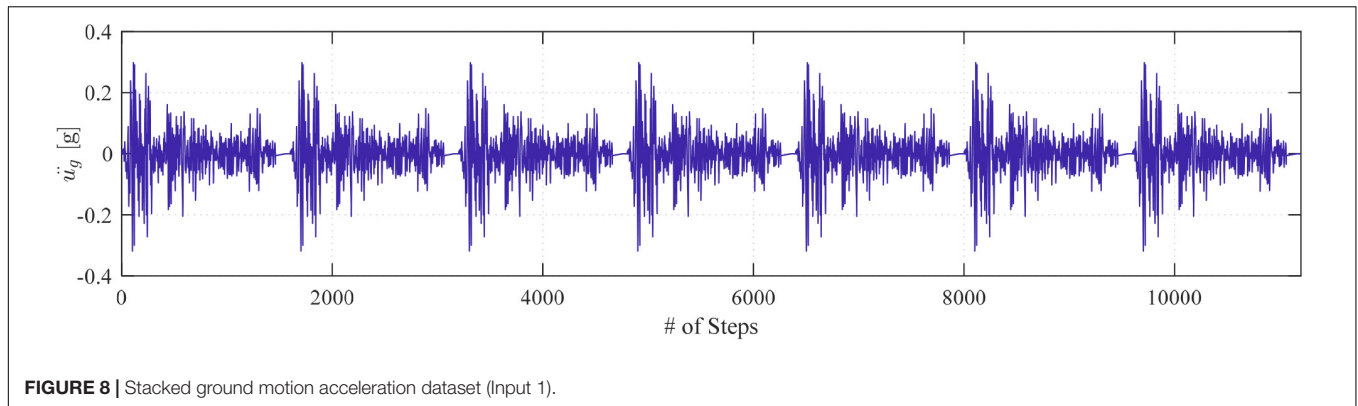
The non-linear time history analysis of the pure analytical model of the overall system was obtained using the implicit Newmark method (average acceleration), which is considered the “correct” solution for the further investigation and validation in this study. A proper convergence study was carried out, and the time step for the integration was selected to be 0.02 s, which is also equal to the ground motion time step. The 1940 El-Centro earthquake was selected again for this part. While the duration of the earthquake record is 31.2 s, the analyses were carried out for full 32 s, which generated 1,600 data points for each response.

The training dataset for the deep LSTM model of the non-linear analytical substructure was selected to be the ground motion acceleration and brace force time histories. The brace axial displacement in local coordinates, i.e., the scaled actuator command in the used substructured test setup shown in **Figure 2**, was selected to be the output for the model training purposes. This is to be later sought as the ML model output or prediction when in the RTHS loop. Thus, the ML model used two inputs to give the brace displacement command prediction to the experimental substructure. It should be noted that, during an online RTHS test, the system is a closed-loop one, and the brace force is dependent on the predicted brace displacement. This dependence between the input and output brings a high level of

uncertainty, and the model can become unstable even in the pure analytical examination of the model.

Moreover, the experimental setup can also bring addition sources of errors and uncertainties due to the nature of the servo hydraulic system. Therefore, a systematic error, which is referred to as bias here for simplicity, was introduced to expand the training environment. This bias is added only to the brace force time history and is meant to account for unforeseen experimental errors and metamodel non-linearity due to input output correlation. For instance, the ML model is trained to predict, for example, a 25-mm displacement output value for 25-kN force feedback input and 0.25-g ground motion excitation. However, the actual force feedback looped back to the ML model during the RTHS test and needed to make the next prediction for the 0.25-g ground motion acceleration could be 26 kN instead of 25 kN because of the experimental errors. Thus, for the ML model to still predict the intended 25-mm displacement, it needs to have been trained that at 0.25-g ground motion input, the force could be 25 or 26 kN or something else. For this purpose, additional force histories were generated using ± 5 , ± 10 , $\pm 15\%$ of the brace force and were added to create the biased dataset.

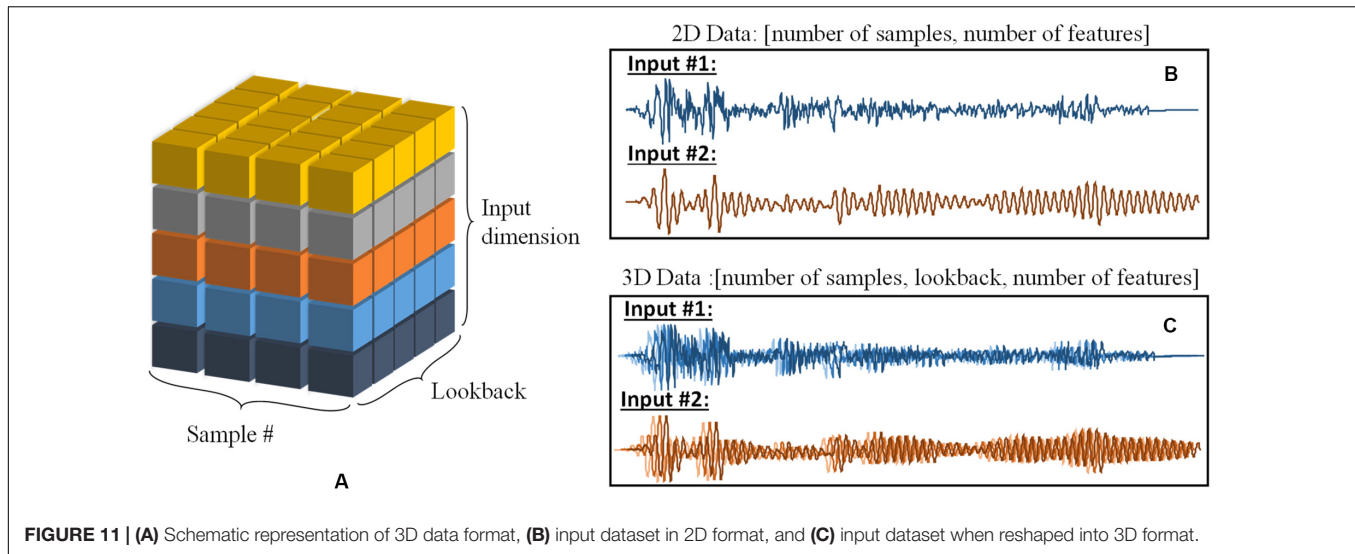
The original dataset along with the six conceived datasets with the added bias were stacked together for the overall training dataset. This required the same ground motion to be repeated seven times to go with the seven cases of force input to prepare the ML model that, for a given ground motion input, the force could



have one of seven possible values based on the devised bias. This training scheme resulted in a total of 11,200 data points for the force input and the seven-times repeated ground motion input. The stacked ground motion acceleration, i.e., Input 1, and the stacked force time history of the brace, i.e., Input 2, are shown in **Figures 8, 9**, respectively. The stacked brace displacement dataset obtained from the OpenSees analysis and used to represent the output of the training is shown in **Figure 10**.

Once the training dataset is generated, it should be modified and reshaped to be able to train the LSTM model. The input sequences of LSTM networks are formatted to be three-dimensional (3D) arrays, as in other time-series prediction models (Géron, 2017) and as illustrated in **Figure 11**. The first

dimension is the batch size or the number of samples of the dataset. The second dimension is the lookback, which defines how many past time steps that the model should get. Finally, the third dimension is the size of the input dimension or number of features. The lookback parameter is one of the key parameters that should be tuned carefully as it makes LSTMs more reliable because it allows the algorithm to look back in the past time steps to make better future predictions. Although it extends the used information, it might increase the memory requirements. On the other hand, the output shape can be either 2D or 3D arrays, which depends on the return sequences. Generally, in between the layers of the deep LSTM network, the return sequence is set to be true except for the last layer, which means the final output contains



a single output value per time step. For this study, the 2D data format was considered for the output shape of the model.

Figure 11A shows a schematic representation of the 3D data format, where each color represents different input feature (input dimension). In this study, the number of features is two, i.e., Input 1 and Input 2, as mentioned earlier. In **Figure 11B**, these two inputs are represented in 2D data shape, and **Figure 11C** presents the reshaped version of the data. For simplicity, only one ground motion and corresponding brace force time history are shown in the figure instead of a full stack of the input datasets.

Implementation Methodology and Sensitivity Analysis for LSTM Model

The deep LSTM model used in this study was trained and generated in the Python environment using Tensorflow 2.0 framework, which is a high-performance computing library introduced by Google (Abadi et al., 2015). Tensorflow offers many packages and features, and one of the most popular ones it supports is Keras (Chollet, 2015). Keras is a high-level Application Program Interface that is highly attractive for building and training deep learning models. Generating workflows in Keras is simple because there are several standalone modules, such as neural layers, optimizers, cost functions, and user-defined modules. Thus, one can easily connect and stack these modules to generate an ML model. The inputs and output training datasets were fed into the deep LSTM models to tune the hyperparameters, i.e., size of the hidden layer, number of layers, number of neurons, batch size, lookback size, number of epochs, learning rate, etc. To train a large deep neural network, a faster optimizer should be used because the training time can take longer. The Adam (Adaptive Moment Estimator) optimizer was selected to train for the models used in this study, with a learning rate of 0.001, because it is computationally efficient and well-suited for problems with large datasets (Kingma and Ba, 2015). The number of epochs was set to be 10^3 . Moreover, the model was trained to minimize the cost function defined in Eq. 9, which is mean square error (MSE) between the

given displacement values (x_n) and the predicted displacement values (\hat{x}_n).

$$J(\theta) = \text{MSE} = \frac{1}{N} \sum_{n=1}^N (x_n - \hat{x}_n)^2 \quad (9)$$

In this study, several layer numbers with different sizes of hidden layers were evaluated. The models had an input layer, four LSTM layers with 30 units in each layer, and one dense layer, which is a fully connected layer that outputs the prediction. For these models, different lookback values, i.e., 1, 5, 10, 15, and 20, were selected to select and fine-tune the most accurate model to be used as computational substructure in the RTHS loop. Moreover, 70% of the dataset was set to be the “training” part of the dataset, and the rest was used as the “test” dataset. The brace displacement response prediction values from the LSTM models with different lookback values were compared against the pure analytical model response. The performance of the model prediction was evaluated using the NRMSE, normalized energy error (NEE), and maximum amplitude error (MAE) given in Eqs 10 to 12. The NRMSE is an adequate way of evaluating the overall model performance, whereas the NEE and MAE are more focused on amplitude errors between the datasets.

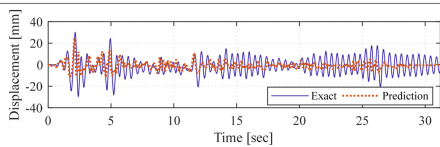
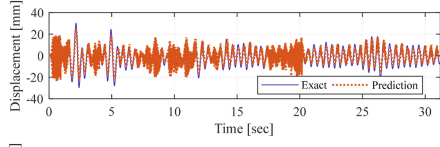
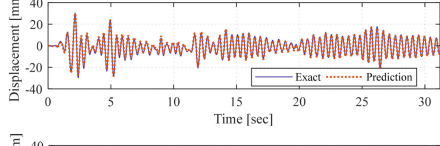
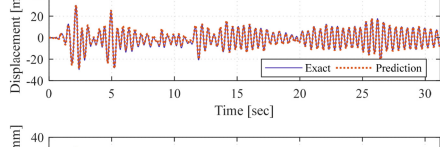
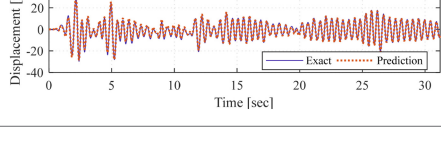
$$\text{NRMSE} = \frac{\sqrt{\frac{1}{N} \sum_{n=1}^N (x_n - \hat{x}_n)^2}}{\max(\hat{x}) - \min(\hat{x})} \quad (10)$$

$$\text{NEE} = \left| \frac{\sum_{n=1}^N (x_n)^2 - \sum_{n=1}^N (\hat{x}_n)^2}{\sum_{n=1}^N (\hat{x}_n)^2} \right| \quad (11)$$

$$\text{MAE} = \left| \frac{\max(|x|) - \max(|\hat{x}|)}{\max(|\hat{x}|)} \right| \quad (12)$$

For the pure analytical assessment of the metamodel response, there was no real feedback from the actuator. That is because

TABLE 2 | Deep LSTM model comparison for different lookback values.

Lookbacks	Comparison plots for exact and predicted displacement time histories	Errors (%)
1		NRMSE = 21.55 NEE = 395.81 MAE = 18.54
5		NRMSE = 14.34 NEE = 4.6 MAE = 18.14
10		NRMSE = 1.57 NEE = 3.25 MAE = 0.3
15		NRMSE = 1.60 NEE = 0.078 MAE = 0.7
20		NRMSE = 1.63 NEE = 3.57 MAE = 0.19

the brace force used as input for the model at a given time step was obtained from multiplying the predicted displacement response from previous step by the axial stiffness of the brace. **Table 2** summarizes the performance evaluation of the deep LSTM models with different lookback values. It can be seen from the error calculations and the plots that the model trained with only one lookback data has the worst performance compared with the others. When this value was increased to five, the model performed slightly better in terms of amplitude; however, the prediction resulted in a very noisy signal. The models trained and evaluated with 10, 15, and 20 performed relatively close to each other. However, the model with 15 lookbacks stood out for best performance. The LSTM models with 15 and 20 lookbacks, referred to as Model 1 and Model 2, respectively, were selected and used for the validation and demonstration RTHS tests.

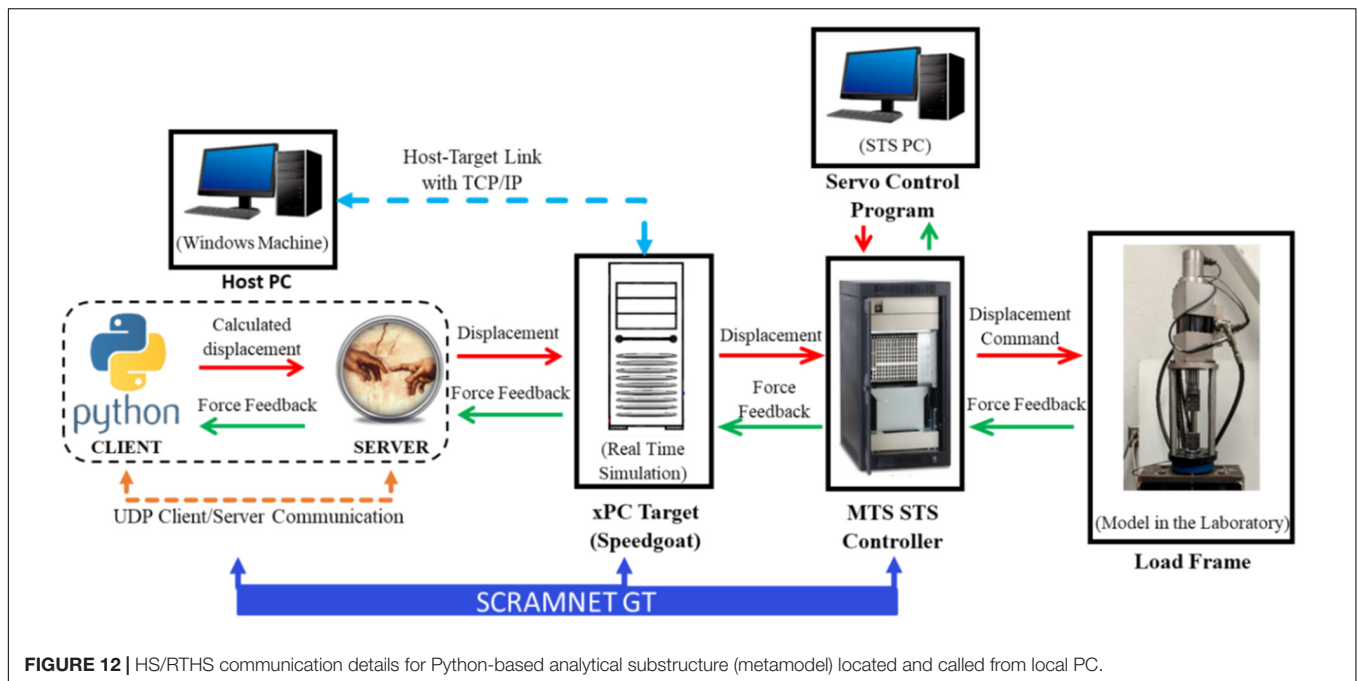
COMMUNICATION DEVELOPMENT AND VERIFICATION

One of the critical aspects of HS/RTHS is the proper data communication between the analytical substructure and experimental substructure. The UNR setup components and configuration information are given above in *HS System Components*. As mentioned earlier, the analytical substructure of the HS/RTHS tests can be modeled in either Simulink directly or in an FE software such as OpenSees along with a middleware such as OpenFresco (Schellenberg et al., 2009a). OpenFresco is a software that connects FE models to the controllers and

data acquisition systems in laboratories to enable HS. It allows interfacing different computational drivers. In this study, a novel communication scheme was developed to connect the Python-based models to the HS/RTHS loop via OpenFresco as a middleware. The authors have previous experience in developing and verifying new HS communication schemes that also used OpenFresco (Moustafa and Mosalam, 2015a,b).

To assess the online performance of the LSTM models in providing a prediction and in anticipation of future models that could be more complex and larger in size, two scenarios for calling the LSTM models were considered and tested. The first case used a local PC that was physically part of the RTHS, and the second considered a high-performance computing cluster. The communication details for Python-based metamodel substructures when located in local PC (host PC) are presented first.

Figure 12 shows the hardware components and the communication details schematically. In this configuration, Python is located at the host PC, where the xPC connection and the SCRAMNetGT initializations are made. Python can be run either from the command prompt (i.e., python.exe) or Anaconda prompt or Jupyter notebook. The OpenFresco architecture for Python connection is the “client&middle-tier server,” where OpenFresco serves as a middle-tier server, and Python is the client. At the OpenFresco side, the server is started by opening a UDP/TCP channel, and the simulation application site is set. On the other hand, Python has a “socket” module to set the connection and send and receive data with either TCP or UDP protocols. In this study, the data communication between Python



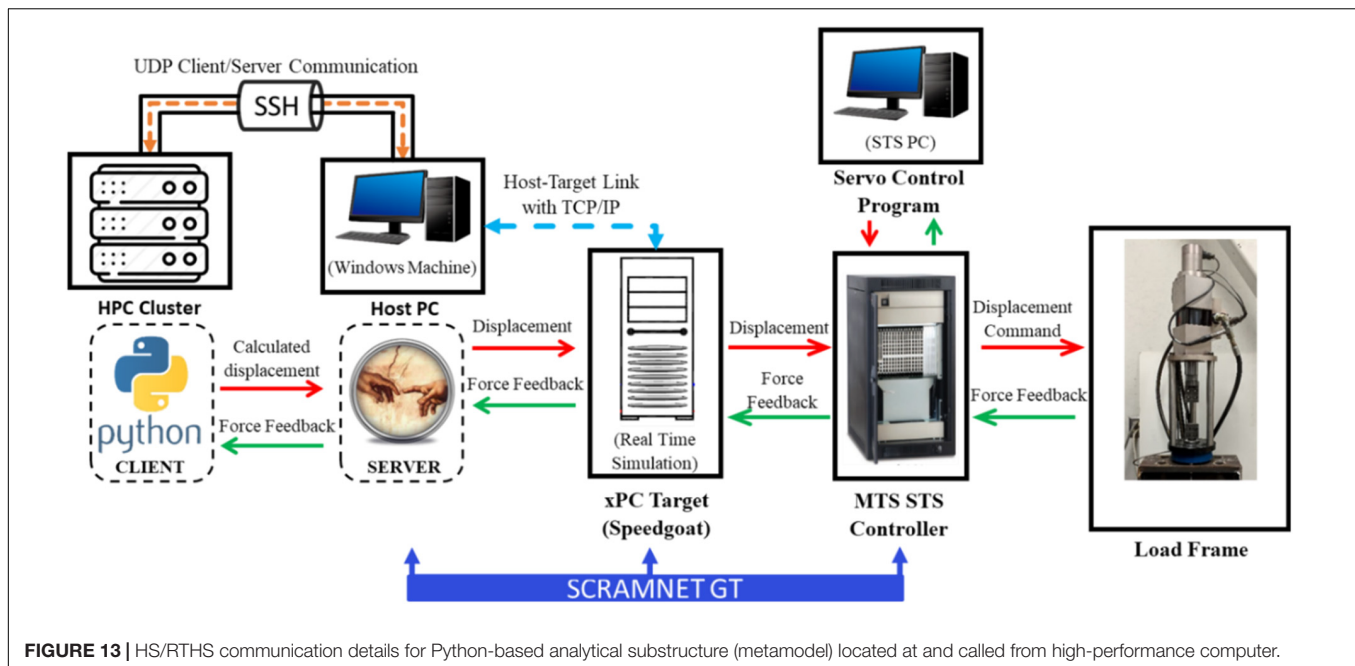
and OpenFresco is provided with the UDP communication protocol. The experimental site is also connected with this middle-tier server, which is a local experimental site in this study. Moreover, the experimental control, which is the interface with the laboratory hardware system, should be defined. This is where the data to/from the controller through the xPC target are transferred. The connection between the host PC and the xPC Target can be set up with either TCP/IP or SCRAMNetGT connection. The SCRAMNetGT connection was considered here because it provides more stable and faster data transfer.

The communication details when a high-performance computer cluster is considered are provided next. The cluster that has been used in this study belongs to UNR's Department of Computer Science and Engineering and used for teaching and simple research studies. Python packages and modules can be run from a cluster, especially when complicated calculations are needed to be done at high speeds. For this communication, Python models were run in the cluster, while OpenFresco is in the host PC. The cluster and the host PC were connected through the Secure Shell (SSH) network protocol. The data transfer was performed with UDP tunneling through the SSH connection. The schematic communication details of this configuration are shown in **Figure 13**. Other than this, the data transfer procedure is the same as it is explained for local PC.

The overall concept of the data transfer in this RTHS setting is as follows. The trained deep LSTM network model (metamodel), which is the analytical substructure of the RTHS test, runs from Python. Python can be run from either the local PC or the cluster. At each time step, this metamodel calculates the input displacement and sends it as displacement command to the experimental substructure. Then, the experimental substructure sends the measured force from the specimen and feeds it back to the metamodel. OpenFresco has a predictor–corrector algorithm,

which is programmed in Simulink and Stateflow, and runs in the xPC target machine to manage the real-time environment, which synchronizes the integration time step, the simulation time step, and the controller time step (Schellenberg et al., 2009b). The predictor–corrector algorithm generates smooth command signals at the same rate as the control system base clock frequency, and this allows generating displacement targets from the non-deterministic rate numerical models (Serebanha et al., 2019). For real-time tests, the simulation time step should be equal to the integration time step. During the RTHS, the numerical model solves the new target displacement, and the predictor–corrector algorithm generates command displacements based on polynomial forward prediction. The new target displacement should be calculated and sent within 60% of the simulation time step to allow the remaining time frame for data transfer for RTHS. If this is not satisfied at a single point, then the predictor–corrector provides a solution with slowing down the command displacement until the new target is received (Serebanha et al., 2019). In the proposed system with metamodels, i.e., no integration for the equation of motion is needed, the integration time becomes the prediction time step. The prediction time step was set to be 0.02 s, which was the same as the training time step.

The validation for the aforementioned communication scheme is first tested between the computer and controller and checked against the pure analytical case. For this validation scenario, offline RTHS tests were conducted while the hydraulic system was off. Because no actual actuator feedback was available yet, the force feedback was obtained from the command of the system, where the stiffness multiplier was applied to the displacement command, as opposed to the actual actuator feedback in online tests. It is noted again that for all tests considered in this study, a linear elastic experimental



substructure was considered through the stiffness multiplier to make it possible to compare with pure analytical cases for verification. The offline RTHS test results are presented in **Figures 14A,B** for the deep LSTM network model with 15 and 20 lookbacks, i.e., Model 1 and Model 2, respectively, located at the local PC. Moreover, **Figure 15** shows the same comparisons for the RTHS tests that were conducted from the cluster. The RTHS test results, i.e., brace displacement, were compared with the pure analytical response to estimate NRMSE, NEE, and MAE. All error values from for both experiments are provided in the figures. The figures show that Model 2 with 20 lookbacks had overall less NRMSE and MAE values than Model 1. However, for all cases, the RTHS results were very comparable to the pure analytical solutions, which verifies the real-time communications for both host PC and the cluster.

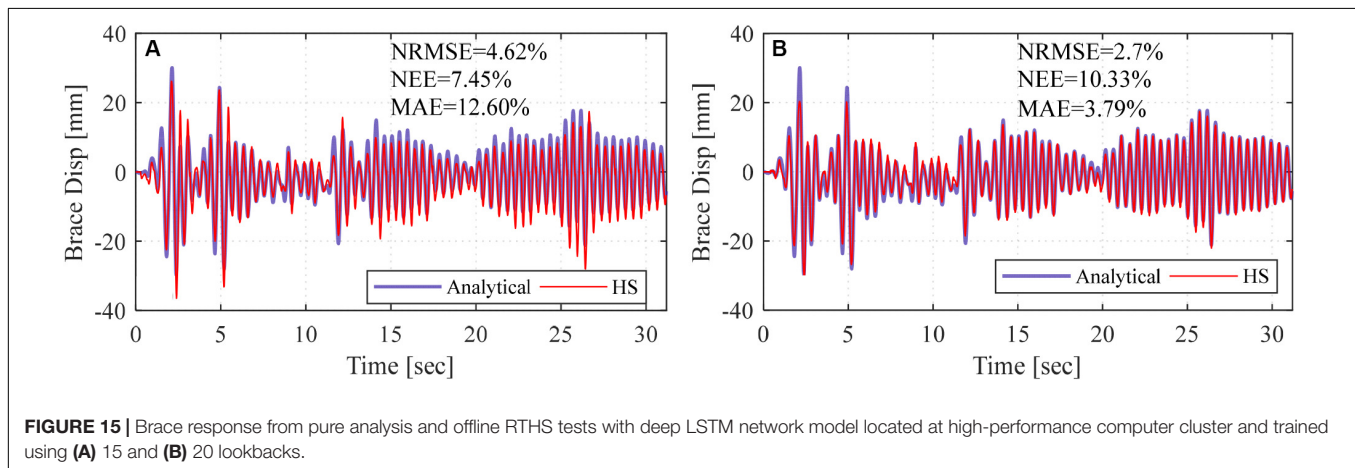
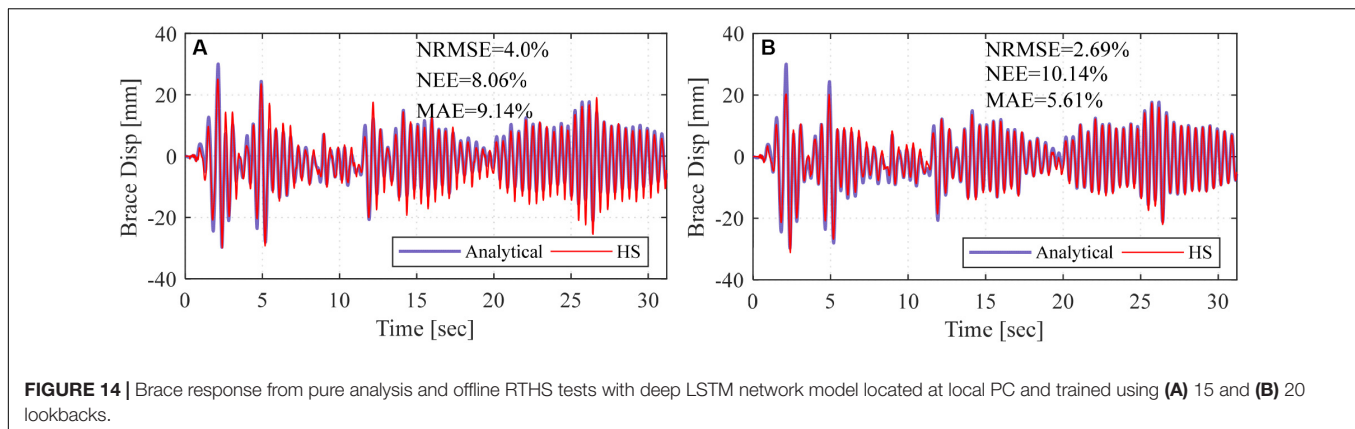
ONLINE RTHS TESTS

In this section, the deep LSTM network models with lookbacks 15 and 20 are further used to evaluate the ML-based RTHS approach and communication among different components using full online tests. Thus, for all the RTHS tests that are presented and discussed in this section, the hydraulic system was on with the actuator free to move, and in turn, actual feedback from the actuator was obtained and fed into the analytical substructure. At each time step, the actual achieved actuator's displacement was modified using the constant brace stiffness multiplier to feedback an equivalent, yet representative, force feedback of a linear elastic experimental substructure. Different geometric scales (S_L) were considered for the mock experimental specimen to test the RTHS system and ML-driven actuator at wide range of displacements and velocities for better assessment. The relevant considered scale factors were S_L for length and S_L^2 for the force values,

and these scale factors are controlled through Simulink blocks that are compiled in xPC Target. Several tests were conducted, and the respective discussion is presented in three subsections to make proper comparisons. First, results from online RTHS with conventional non-linear FE models are presented to serve as reference for ML-based tests verification. Next, computational time is evaluated and compared for RTHS test results with the ML model located at local PC and cluster to explore whether there are benefits in using cluster as opposed to local PC. Finally, the RTHS tests that used local PC are discussed further through comparisons against both RTHS tests with FE models and the pure analytical solution. A total of 40 different online RTHS were conducted with different geometric scales, varying LSTM models, and with or without using a dedicated time delay compensator. Selected results are shown, but all error calculations (NRMSE, NEE, and MAE) for the 40 tests are summarized and discussed in the last subsection.

Online RTHS With FE Model

Conducting RTHS with large or heavily non-linear analytical substructure models could be challenging and has limitations that could be mostly associated with insufficient computational time within the RTHS loop. For example, when both stiffness and strength degradation are considered, direct integration methods were found to have some limitations, only for RTHS (Bas and Moustafa, 2020). The idea of using an ML approach or metamodels could eliminate such limitations, which is the motivation behind this study. Thus, the system capabilities and online RTHS tests are first evaluated with the FE model. For these tests, OpenSees was used to model the analytical substructure. The model properties and modeling assumptions were the same as given in *Training Datasets*. For the experimental substructure, several length scale factors were considered at 5, 10, 15, 20,



and 25. All tests were conducted in real time where both the integration and simulation time steps were set to 0.02 s. The integration algorithm was selected to be the explicit KR- α (Kolay et al., 2015). Two sets of tests were conducted with and without using the ATS compensator to correct for the actuator delay. The KR- α integration and ATS compensator initial parameters that were used in the RTHS tests are listed in **Table 3**. A side convergence study was conducted to obtain the best input value for one of the integration parameters, i.e., ρ_∞ , as illustrated in **Figure 16**. The brace displacement time histories were obtained for different ρ_∞ values, and the NRMS errors were calculated for assessment. Although there were no significant differences between 0.75 and 1.0, the ρ_∞ was assigned to be 1.0 because this was the case that corresponded to the least error. All tests were compared against the pure analytical solution of non-linear CBF, which used implicit integration methods and considered to be the “correct” solution when only the brace is considered linear elastic as explained before.

Figure 17 shows the test results from the online RTHS with FE model and without using ATS compensator. Five tests with different geometric scales are shown and compared against the pure analytical solution. Same tests were conducted but with using the ATC actuator delay compensator, and results are shown in **Figure 18**. For all tests, the obtained brace displacements are shown at the prototype scale so that the different scale tests could

be compared. From the figures, it shown that the geometric scale of the experimental substructure, i.e., different range of actuator displacements and velocities, did not affect the test results, which demonstrates the capability of the hydraulic system and actuator. However, it can be clearly seen that the delay of the actuator affected the response in terms of phase difference and amplitude. The ATS is shown to significantly improve the test performance and critically needed for RTHS, which might not be the case when ML models are used in lieu of FE models as discussed in the last section.

To demonstrate whether the prototype CBF goes non-linear under the 100% scale El Centro ground motion used throughout this study, the force–displacement relationship of the full frame is shown in **Figure 19**. The figure compares the pure analytical case and one of the online RTHS tests with FE model (with ATS and $S_L = 15$) as an example. It is shown that even when ATS is

TABLE 3 | Initial parameters for defining KR- α integration and ATS compensator for RTHS tests.

KR- α integration parameters			ATS parameters		
ρ_∞	K_{eq}^e	C_{eq}^e	a_{0k}	a_{1k}	a_{2k}
1.00	278 kN/mm	0	1.20	0.014	9.8E-05

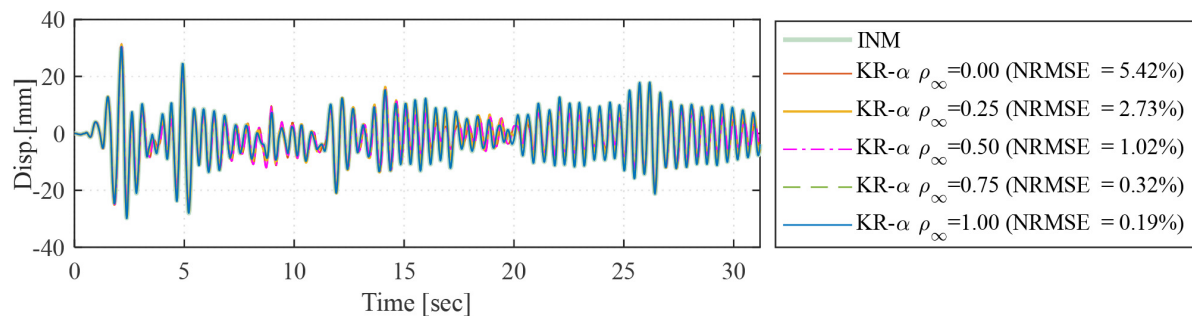


FIGURE 16 | Brace displacement response time histories for different ρ_{∞} parameter values along with NRMSE errors with respect to the implicit Newmark method.

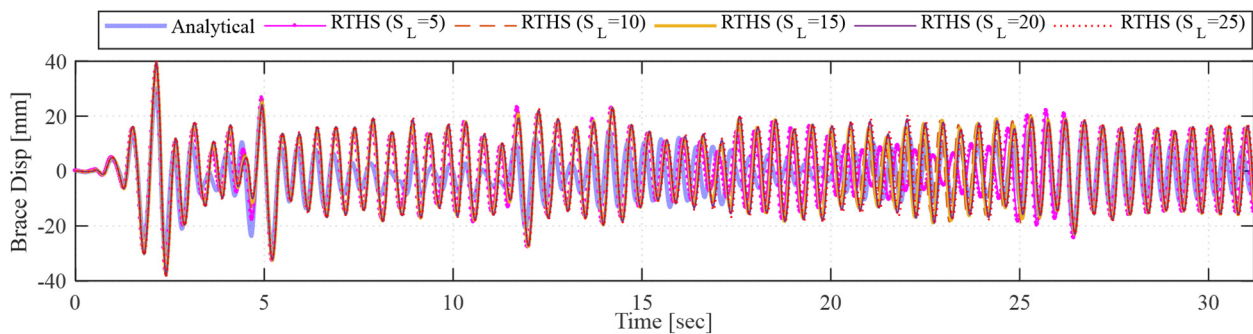


FIGURE 17 | Comparison of brace displacements from online RTHS tests without using ATS compensator (for different geometric scales) against pure analytical solution.

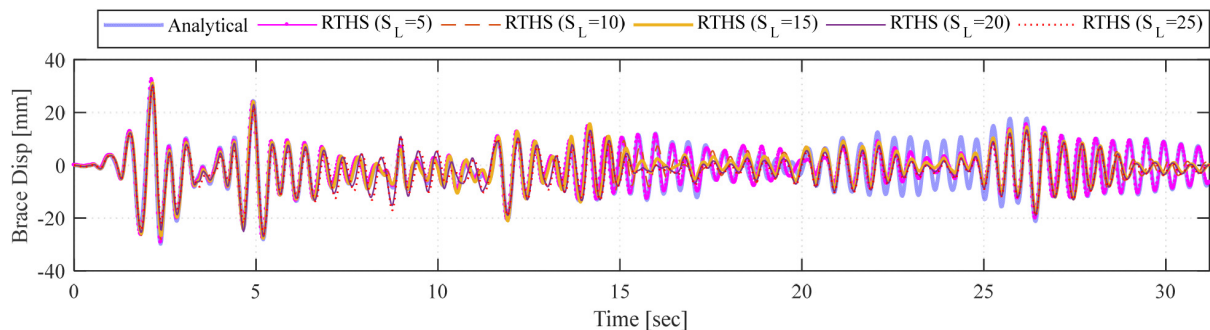


FIGURE 18 | Comparison of brace displacements from online RTHS tests with using ATS compensator (for different geometric scales) against pure analytical solution.

used the FE solution for the non-linear model becomes erroneous during online RTHS tests. This error might be attributed to improper estimation of the equivalent initial elastic stiffness or damping matrix for instance. However, such results confirm the need of proper parameters estimation and careful investigation to conduct reliable RTHS tests, which is discussed in detail in Bas and Moustafa (2020). Moreover, to further quantify the performance when non-linear FE model is used for RTHS and to establish a reference case for further ML validations, the NRMSE, NEE, and MAE values were calculated and listed in **Table 4**. The error values from the cases with and without ATS confirm the importance of using an error compensator for RTHS with FE

analytical substructure. The table also confirms that even with ATS, there is still considerable error with respect to the pure analytical solution. Lastly, the error values suggest that system becomes relatively more erroneous at larger geometric scales leading to much smaller actuator displacements.

RTHS Testing With ML Models From Local PC and Cluster

As previously mentioned, two ways of running the LSTM ML models have been considered. The data communication is possible when the Python model is run from a high-performance

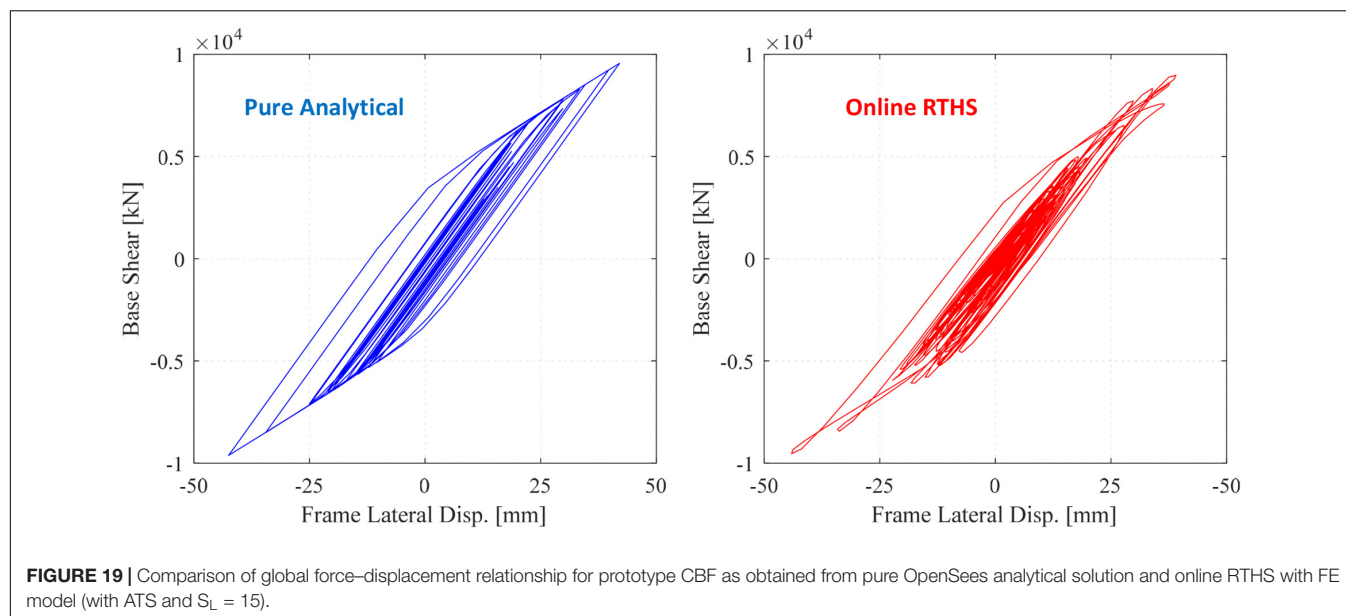


FIGURE 19 | Comparison of global force–displacement relationship for prototype CBF as obtained from pure OpenSees analytical solution and online RTHS with FE model (with ATS and $S_L = 15$).

TABLE 4 | Errors (%) in brace displacement response from online RTHS with FE model as compared to the pure analytical solution.

Error metrics	$S_L = 05$		$S_L = 10$		$S_L = 15$		$S_L = 20$		$S_L = 25$	
	With ATS	Without ATS	With ATS	Without ATS	With ATS	Without ATS	With ATS	Without ATS	With ATS	Without ATS
NRMSE (%)	3.7	12.4	7.1	13.3	8.0	13.6	9.0	13.9	9.6	14.1
NEE (%)	14.5	45.3	27.8	51.7	32.5	54.2	30.6	55.4	35.7	56.4
MAE (%)	8.2	22.1	6.5	28.2	3.7	30.7	1.3	32.2	0.9	33.4

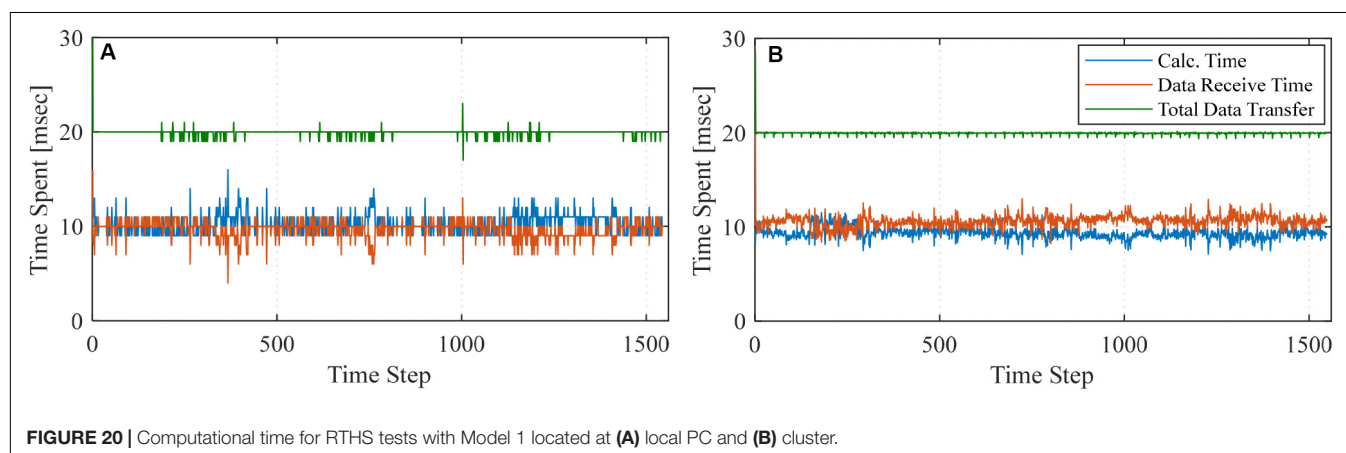


FIGURE 20 | Computational time for RTHS tests with Model 1 located at (A) local PC and (B) cluster.

computer or the local computer (i.e., host PC in the UNR setup). In this section, the computational time at each analysis step is presented for both ways of conducting the ML-based RTHS tests. The considered time steps included the time spent for the ML model to evaluate the prediction, i.e., calculation time, the time spent to receive the data from the experimental substructure, and the total data transfer time. It should be noted that the prediction time step and the simulation time step were set to be 0.02 s.

The computational time spent for the online RTHS where Model 1 (with 15 lookbacks) was used as the computational

substructure is shown in **Figure 20A** for the local computer and **Figure 20B** for the cluster. The average time spent for the ML prediction is estimated to be 10.2 ms for the local PC and 9.4 ms for the cluster. Moreover, the figure shows the overall data transfer time for each analysis step, which is desired to be 20 ms to satisfy the real-time testing through proper OpenFresco handling. It can be seen from **Figure 20A** that some of the time steps showed minor spikes that took slightly longer than the simulation time step when the tests were conducted from the host PC. However, the total data transfer time remained less than

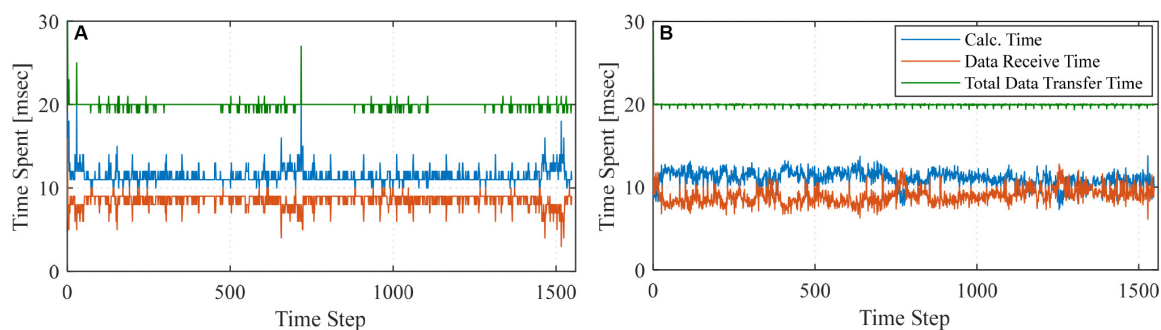


FIGURE 21 | Computational time for RTHS tests with Model 2 located at (A) local PC and (B) cluster.

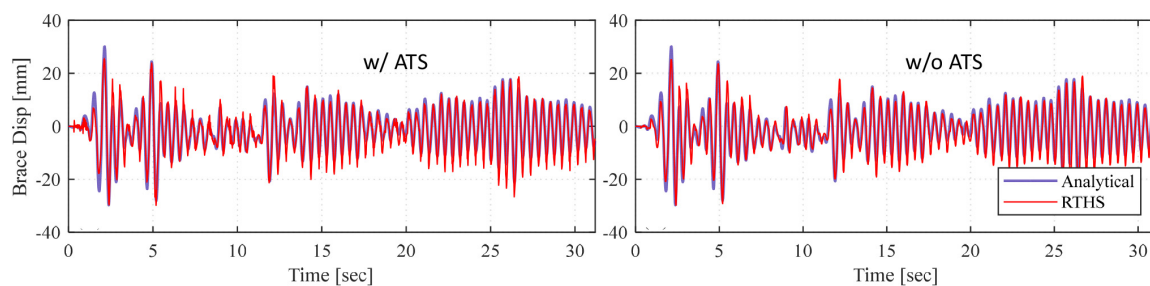


FIGURE 22 | RTHS response comparison with analytical solution for Model 1 ($S_L = 15$) with and without using ATS when the first row of the force input was selected to be updated.

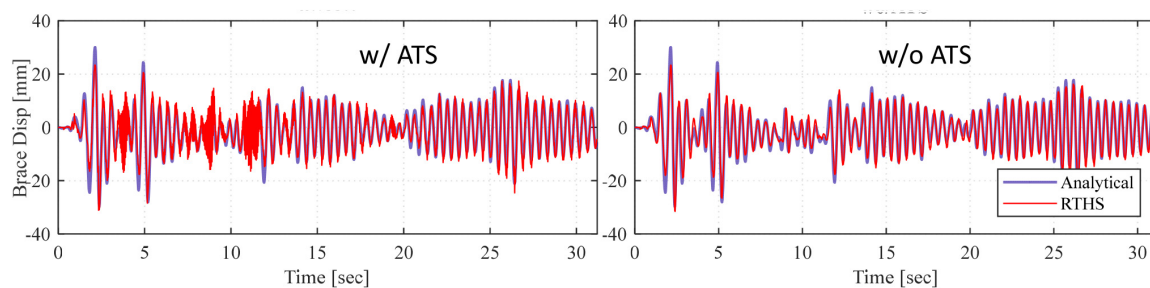


FIGURE 23 | RTHS response comparison with analytical solution for Model 1 ($S_L = 15$) with and without using ATS when the last row of the force input was selected to be updated.

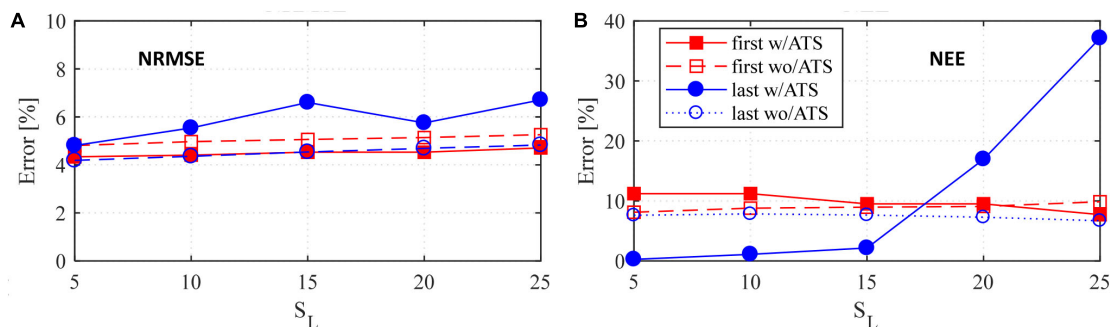


FIGURE 24 | RTHS (A) NRMSE and (B) NEE calculation for Model 1 (all geometric scales).

or equal to 20 ms when cluster communication was provided through the SSH network protocol. **Figure 21** shows the same comparison when Model 2 with 20 lookbacks was used. The average calculation time for Model 2 was estimated as 11.8 ms for local PC and 10.7 ms for the cluster. It should be noted that Model 2 has a larger dataset dimension (lookback), which slightly increases the prediction time when Models 1 and 2 are compared. Overall, the observations show that the prediction takes slightly less time for cluster than the local computer for both models. For both configurations, the data transmission is done through the UDP channel. However, the UDP channel is provided through SSH network protocol for the cluster, which provides highly stable communication and ensures the desired simulation time step is achieved.

Validation of RTHS Tests With ML Models and Effect of Delay Compensator

A series of 40 RTHS tests were conducted, which included different ML models and scale factor. The same two advanced LSTM models as before, i.e., Models 1 and 2, were used when located at the local PC, and tests were conducted also at same geometrical scale factors as before, i.e., 5, 10, 15, 20, and 25. Models 1 and 2 were also handled differently to create two more subgroups of models as discussed in the next paragraphs. Additional tests were also conducted using the cluster. However, there was no significant difference in test results when using the local PC and cluster. Therefore, this section only presents the RTHS tests where advanced ML models located and ran from the local PC.

The data shapes of the inputs for Models 1 and 2 are in three dimensions as explained before in *Advanced ML Techniques for RTHS*. For the RTHS testing, the single value of the force feedback that is obtained from the experimental substructure at each time step is fed into the LSTM model. However, such online value can be used to overwrite, or simply update, one or more of the dimensions of the LSTM lookbacks, i.e., 15 predefined brace force input values, for instance. In this study, two different submodels for both Models 1 and 2 were investigated, which considered two arbitrary dimensions for the update. For first case, the overwritten/updated value was the first row of the 15 or 20 force input lookbacks, which was updated with the online force feedback. The other case considered using the force feedback to update the last row of the lookbacks instead. The two cases are referred to as FIRST and LAST for the remainder of the discussion. For brevity, only few plots from selected RTHS tests are presented, which were obtained for Model 1 with $S_L = 15$. However, a summary of results from all tests is still provided in terms of error estimation with respect to the pure analytical FE model response.

Figure 22 presents the brace displacement response as adopted from the actuator for RTHS with ML model and with and without using ATS. The figure also compares the RTHS response against the pure analytical solution. The results shown are from a “FIRST”-type case where only the first term on the force input’s lookback dimension was updated with the force feedback obtained from the experimental substructure. The first main and

TABLE 5 | Error estimation (%) for all conducted online RTHS tests with different ML models with respect to the pure analytical solution.

			Model 1			Model 2		
			NRMSE	NEE	MAE	NRMSE	NEE	MAE
$S_L = 5$	FIRST	With ATS	4.3	11.2	1.0	3.1	7.1	6.4
		Without ATS	4.8	8.1	0.7	3.3	9.1	5.3
	LAST	With ATS	4.8	0.3	7.4	6.9	1.3	4.0
		Without ATS	4.2	7.6	5.1	5.3	10.8	2.1
	$S_L = 10$ FIRST	With ATS	4.4	11.2	0.2	3.2	8.7	5.5
		Without ATS	5.0	8.8	1.0	3.4	8.7	4.9
$S_L = 15$	LAST	With ATS	5.5	1.1	5.6	10.8	25.0	17.7
		Without ATS	4.4	7.8	4.8	7.5	20.3	3.9
	FIRST	With ATS	4.5	9.5	0.7	3.3	13.7	7.5
		Without ATS	5.1	9.0	0.9	3.6	8.2	4.5
	LAST	With ATS	6.6	2.2	3.5	14.1	48.9	28.5
		Without ATS	4.5	7.7	5.0	4.7	7.7	1.2
$S_L = 20$	FIRST	With ATS	4.5	9.5	0.7	3.8	25.5	2.9
		Without ATS	5.1	9.1	1.0	3.7	7.6	4.7
	LAST	With ATS	5.8	17.0	0.3	15.4	64.5	40.7
		Without ATS	4.7	7.3	5.0	4.4	5.7	0.1
	$S_L = 25$ FIRST	With ATS	4.7	7.7	4.2	4.3	39.7	1.7
		Without ATS	5.3	9.9	0.9	3.8	7.1	4.3
$S_L = 25$	LAST	With ATS	6.7	37.1	1.9	20.1	69.8	33.9
		Without ATS	4.8	6.7	5.0	4.6	5.6	1.1

big observation is that RTHS testing with advanced ML model used for non-linear analytical substructure is demonstrated to be a valid approach with very comparable results when compared to analytical solution. The displacement command was predicted well-enough, based on the online received feedback, to conduct the RTHS tests successfully. Results from another test that used the same model but considered the last row of the force input for updating are shown in **Figure 23**. When the cases with and without ATS are compared in both **Figures 22, 23**, there is no significant effect on the response. In fact, the feedback that was

obtained from the case with ATS was worse and noisier in some cases as in the sample shown in **Figure 23**, i.e., the actuator became more sensitive to the updated force value when the last term in the lookbacks is overwritten. Nonetheless, even with the added noise in some ML model cases, the response of the actuator remained stable, and the RTHS tests were successfully completed.

To comprehensively assess all conducted tests, the NRMSE and NEE values were obtained and summarized in **Figure 24** and **Table 5**. **Figure 24** shows the error values for Model 1 for all the RTHS tests with different geometric scales. It can be observed that the effect of the ATS compensator is more pronounced when the last row of the force input is updated with the feedback value from the actuator and at larger-scale factors where smaller actuator displacements were expected. However, this effect of using ATS is even an adverse effect. For instance, using ATS for the case with $S_L = 25$ led to dramatic increase in error value. Regardless of the ATS effect, it is shown that ML models do not need to be used with actuator delay compensation because of the nature of the model training that indirectly accommodates actuator delays. This preliminary observation is worth further investigation where ML models could be considered to improve actuator control in cases of non-linear dynamic systems.

Table 5 presents all the error metrics for 40 different RTHS tests with ML models located at host PC. Detailed evaluations for Models 1 and 2 are reported in terms of NRMSE, NEE, and MAE. All RTHS tests were successfully completed for each model and geometric scale factor. In most cases, the RMSE is less than 5%, which is reasonably accurate to confidently validate the proposed concept of using ML models to replace FE models within the RTHS loop. Moreover, Models 1 and 2 do not show any significant differences for most of the considered tests. It is observed that the most problematic cases were observed when the last row of the force input was updated, and larger geometric scales were used with the ATS compensator. However, even for these cases, the tests remained stable, and none of the tests were stopped unlike what was previously reported for using non-linear FE models (Bas and Moustafa, 2020). The results are encouraging in terms of eliminating the need for any delay compensator when ML models are used for RTHS. In summary, this study sets the stage for a new way of conducting RTHS testing in the future. However, the results also show that the hardware, geometric scale, and type of ML model could have significant effect on accuracy of RTHS testing and justify the call for further research studies to identify best ML practices and modeling procedures for future RTHS testing.

SUMMARY AND CONCLUSION

In this article, the idea of using complex ML models to replace FE models for RTHS was validated, and foundational work was provided for RTHS communication development and verification for Python-based deep learning ML metamodels. This study was motivated by the potential for ML-based computational substructures to advance RTHS testing and help explore new research areas in the future. The article touches on ML models sensitivity and performance for time-series

prediction, as well as using high-performance computers for running online ML models. The need for commonly used practices in RTHS testing, e.g., actuator delay compensation, was also assessed when ML metamodels are used for the computational substructures. For all ML models and system evaluations, a one-bay, one-story steel braced frame was selected. The columns and beam defined the analytical substructure, whereas the brace defined the experimental substructure for RTHS testing. The key aspects of the study along with the main findings can be summarized as follows.

- A simplified ML model was first generated with LR algorithms for a linear elastic system. The LR model was coded using MATLAB/Simulink and compiled on the xPC machine as part of the RTHS loop. No specific communication scheme was needed, and the simple tests showed that using metamodels to derive the actuator in an RTHS setting is possible.
- For accurate modeling of dynamic response of non-linear braced frames, LR models could not be used, and more advanced ML algorithms were needed. Deep LSTM networks were selected because of their capability of capturing long-term patterns in time series. Python was used to generate the LSTM models using training datasets obtained from analytical OpenSees models. A linear elastic brace was considered along with the non-linear frame, and several ML models were evaluated against the pure analytical FE model response to tune the hyperparameters of the model. Two LSTM metamodels were demonstrated to accurately predict non-linear response and in turn, selected to be used further in the RTHS tests.
- The training domain is crucial and should be devised carefully for a robust ML model. In this study, in order to consider the uncertainties due to force–displacement dependencies and hardware errors (e.g., initial load frame feedback, noise from actuator, etc.), the training domain was expanded using seven episodes of the force input to the LSTM model with introduced bias. Although this approach helped, there is need to devise other different training approaches in future studies to account for wide range of uncertainties.
- In order to use Python as a computational driver for ML-based RTHS tests, a communication scheme that uses OpenFresco was proposed and successfully verified. OpenFresco serves a middle-tier server, and Python is the client in this form of architecture. The data transfer is made through UDP socket between Python and OpenFresco. Data communication from both local PC and high-performance computer cluster was verified. The cluster communication is achieved through UDP socket but under the secure shell portal.
- When comparing the use of local PC versus cluster for running online RTHS Python LSTM models, no significant improvement in computational time is observed for the considered CBF structure. However, it is reported that using the cluster through the secure shell network protocol provides more stable communication than local PC where

no data transfer time spikes were observed. The data transfer time for each analysis step was always guaranteed to be equal to or less than the defined simulation time step when the cluster was used.

- Several RTHSs were successfully conducted, and their results were used to assess the performance of the developed communication, as well as the python-based deep LSTM model validity. Several RTHS tests were conducted using non-linear FE to better assess the benefits of the ML modeling approach. It was shown that FE models, in case of non-linearity, could result in relatively more errors and is much more dependent on actuator delay compensators when compared to ML models.
- The preliminary results presented in this study suggest that a dedicated actuator delay compensator might not be needed. Instead, such compensation can be embedded within the ML model, which works with recurrent data, and considered *a priori* as part of the training. While sufficient evidence and verification are still needed, this observation is worth further investigation to explore the use of ML models to improve actuator control in cases of non-linear dynamic systems.
- Overall, the communication developments for RTHS tests with advanced Python-based ML models are successfully validated for the first time. The goal of the article was not necessarily to present most the accurate or exact ML

models for a given non-linear analytical substructure, but rather to demonstrate the concept of using ML algorithms within the HS loop. The study shows the applicability of using robust clusters and calls for future research to consider supercomputers, clusters with GPU, etc., for running ML models for RTHS. One main limitation in this study is not using realistic or non-linear experimental substructures. Thus, future work is recommended to consider new ML methods that can be trained for non-linear specimen response.

DATA AVAILABILITY STATEMENT

The raw data supporting the conclusions of this article will be made available by the authors, without undue reservation.

AUTHOR CONTRIBUTIONS

EB: system development, testing, data collection and analysis, data and results interpretation, and writing original manuscript. MM: conceptualization, data and results interpretation, reviewing and editing manuscript, and project supervising. Both authors contributed to the article and approved the submitted version.

REFERENCES

- Abadi, M., Ashish, A., Paul, B., Eugene, B., Zhifeng, C., Craig, C., et al. (2015). *TensorFlow: Large-Scale Machine Learning on Heterogeneous Distributed Systems*. Available online at: <http://arxiv.org/abs/1603.04467> (accessed June 3, 2020).
- Abbiati, G., Lanese, I., Cazzador, E., Bursi, O. S., and Pavese, A. (2019). A computational framework for fast-time hybrid simulation based on partitioned time integration and state-space modeling. *Struct. Contr. Health Monit.* 26, 1–28. doi: 10.1002/stc.2419
- Ahmadizadeh, M., Gilberto, M., and Andrei, M. R. (2008). Compensation of actuator delay and dynamics for real-time hybrid structural simulation. *Earthquake Engin. Struct. Dynam.* 37, 21–42. doi: 10.1002/eqe.743
- Bas, E. E., and Moustafa, A. M. (2020). Performance and limitations of real-time hybrid simulation with nonlinear computational substructures. *Exper. Techniq.* 2020, 121. doi: 10.1007/s40799-020-00385-6
- Bas, E. E., Moustafa, M. A., Feil-Seifer, D., and Blankenburg, J. (2020a). Using machine learning approach for computational substructure in real-time hybrid simulation. *arXiv* 2004.02037.
- Bas, E. E., Mohamed, A. M., and Gokhan, P. (2020b). Compact hybrid simulation system: validation and applications for braced frames seismic testing. *J. Earthqu. Engin.* 2020, 1–30. doi: 10.1080/13632469.2020.1733138
- Bengio, Y., Patrice, S., and Paolo, F. (1994). Learning long-term dependencies with gradient descent is difficult. *IEEE Transac. Neur. Net.* 5, 157–166. doi: 10.1109/72.279181
- Bonelli, A., and Bursi, S. O. (2005). Predictor-corrector procedures for pseudo-dynamic tests. *Engin. Comput.* 22, 783–834. doi: 10.1108/02644400510619530
- Carrion, J. E., and Spencer, B. F. (2007). *Model-Based Strategies for Real-Time Hybrid Testing*. NSEL Report No. NSEL-006 India: Indian Institute Of Technology.
- Chae, Y., Karim, K., and James, M. R. (2013). Adaptive time series compensator for delay compensation of servo-hydraulic actuator systems for real-time hybrid simulation. *Earthquake Engin. Struct. Dynam.* 42, 1697–1715. doi: 10.1002/eqe.2294
- Chang, S.-Y. (2002). Explicit pseudodynamic algorithm with unconditional stability. *J. Engin. Mechan.* 128, 935–947. doi: 10.1061/(ASCE)0733-9399(2002)128:9(935)
- Chang, S.-Y. (2009). An explicit method with improved stability property. *Int. J. Num. Method. Engin.* 77, 1100–1120. doi: 10.1002/nme.2452
- Chen, C., and Ricles, J. M. (2010). Tracking error-based servohydraulic actuator adaptive compensation for real-time hybrid simulation. *J. Struct. Engin.* 136, 432–440. doi: 10.1061/(ASCE)ST.1943-541X.0000124
- Chen, C., Ricles, J. M., Marullo, T. M., and Mercan, O. (2009). Real-time hybrid testing using the unconditionally stable explicit CR integration algorithm. *Earthquake Engin. Struct. Dynam.* 38, 23–44. doi: 10.1002/eqe.838
- Chollet, F. (2015). *Keras: Deep Learning Library for Theano and Tensorflow*. Available online at: <https://keras.io/k> (accessed June 3, 2020).
- Darby, A. P., Williams, M. S., and Blakeborough, A. (2002). Stability and delay compensation for real-time substructure testing. *J. Engin. Mechan.* 128, 1276–1284. doi: 10.1061/(ASCE)0733-93992002128:121276
- Del Carpio, M., Hashemi, M. J., and Mosqueda, G. (2017). Evaluation of integration methods for hybrid simulation of complex structural systems through collapse. *Earthquake Engin. Vibr.* 16, 745–759. doi: 10.1007/s11803-017-0411-z
- Filippou, F. C., Popov, E. P., and Bertero, V. V. (1983). *Effects of Bond Deterioration on Hysteretic Behavior of Reinforced Concrete Joints*. Report No. UCB/EERC-83/19 California, CA: UCB.
- Géron, A. (2017). *Hands-on Machine Learning with Scikit-Learn and TensorFlow*. Massachusetts: O'Reilly Media, Inc.
- Hochreiter, S., and Jürgen, S. (1997). Long short-term memory. *Neur. Comput.* 9, 1735–1780. doi: 10.1162/neco.1997.9.8.1735
- Jozefowicz, R., Wojciech, Z., and Ilya, S. (2015). “An empirical exploration of recurrent network architectures,” in *Proceedings of the 32nd International Conference on Machine Learning* (France: ICML).
- Kingma, D. P., and Ba, L. J. (2015). “Adam: a method for stochastic optimization,” in *3rd International Conference on Learning Representations, ICLR 2015 - Conference Track Proceedings* (France: ICML), 1–15.

- Kolay, C., James, M. R., Marullo, T. M., Mashvashmohammadi, A., and Sause, R. (2015). Implementation and application of the unconditionally stable explicit parametrically dissipative KR-Alpha method for real-time hybrid simulation. *Earthquake Engin. Struct. Dynam.* 44, 735–755. doi: 10.1002/eqe.2484
- Kolay, C., and Ricles, M. J. (2014). Development of a family of unconditionally stable explicit direct integration algorithms with controllable numerical energy dissipation. *Earthquake Engin. Struct. Dynam.* 43, 1361–1380. doi: 10.1002/eqe
- Lagaros, N. D., and Manolis, P. (2012). Neural network based prediction schemes of the non-linear seismic response of 3D buildings. *Adv. Engin. Soft.* 44, 92–115. doi: 10.1016/j.advengsoft.2011.05.033
- LeCun, Y., and Yoshua, B. (1995). “Convolutional networks for images, speech, and time-series,” in *The Handbook of Brain Theory and Neural Networks*, ed. M. A. Arbib (Cambridge: MIT Press), 255–258.
- Mai, C. V., Spiridonakos, M. D., Chatzi, E. N., and Sudret, B. (2016). Surrogate modelling for stochastic dynamical systems by combining NARX models and polynomial chaos expansions. *arXiv* 1604.07627.
- McKenna, F., Fenves, G. L., and Scott, M. H. (2000). *Open System for Earthquake Engineering Simulation Pacific Earthquake Engineering Research Center*. Belgium: PEER.
- Miraglia, G., Petrovic, M., Abbiati, G., Mojsilovic, N., and Stojadinovic, B. (2020). A model-order reduction framework for hybrid simulation based on component-mode synthesis. *Earthquake Engin. Struct. Dynam.* 49, 737–753. doi: 10.1002/eqe.3262
- Moustafa, M. A., and Mosalam, K. M. (2015a). “Development of hybrid simulation system for multi-degree-of-freedom large-scale testing,” in *6th International Conference on Advances in Experimental Structural Engineering* (Urbana: University of Illinois).
- Moustafa, M. A., and Mosalam, K. M. (2015b). *Structural Behavior of Column-Bent Cap Beam-Box Girder Systems in Reinforced Concrete Bridges Subjected to Gravity and Seismic Loads Part II: Hybrid Simulation and Post-Test Analysis*. California: University of California, Berkeley.
- Mucha, W. (2019). Application of artificial neural networks in hybrid simulation. *Appl. Sci.* 9:4495. doi: 10.3390/app9214495
- Phillips, B. M., and Spencer, B. F. (2013). Model-based feedforward-feedback actuator control for real-time hybrid simulation. *J. Struct. Engin.* 139, 1205–1214. doi: 10.1061/(ASCE)ST.1943-541X.0000606
- Schellenberg, A. H., Kim, H. K., and Mahin, S. A. (2009a). *OpenFresco*. California: University of California, Berkeley.
- Schellenberg, A. H., Mahin, S. A., and Fenves, G. L. (2009b). *Advanced Implementation of Hybrid Simulation*. Report No. PEER 2009/104 California: Berkeley.
- Schellenberg, A., Kim, H. K., Fenves, G. L., and Mahin, S. A. (2009c). *OpenFresco Framework for Hybrid Simulation: Simulation Finite Element Adapter Experimental Control Example. Engineering Simulation*. California: Berkeley.
- Schellenberg, A., Kim, H. K., Takahashi, Y., Fenves, G. L., and Mahin, S. A. (2009d). *OpenFresco Command Language Manual*. California: Berkeley.
- Serebanha, A., Schellenberg, A. H., Schoettler, M. J., Mosqueda, G., and Mahin, S. A. (2019). Real-time hybrid simulation of seismically isolated structures with full-scale bearings and large computational models. *CMES* 120, 693–717. doi: 10.32604/cmes.2019.04846
- Takanashi, K., Udagawa, K., Seki, M., Okada, T., and Tanaka, H. (1975). Non-linear earthquake response analysis of structures by a computer-actuator on-line system. *Transac. Arch. Instit. J.* 229, 77–83. doi: 10.3130/aijsaxx.229.0_77
- Wallace, M. I., Wagg, D. J., and Neild, S. A. (2005). An adaptive polynomial based forward prediction algorithm for multi-actuator real-time dynamic substructuring. *Proc. Roy. Soc. A Math., Phys. Engin. Sci.* 461, 3807–3826. doi: 10.1098/rspa.2005.1532
- Wang, Y., Chong, W., Hui, L., and Zhao, R. (2009). “Artificial neural network prediction for seismic response of bridge structure,” in *2009 International Conference on Artificial Intelligence and Computational Intelligence AICI 2009*, Vol. 2 (Berlin: Springer), 503–506.
- Xie, Y., Sichani, M. E., Padgett, J. E., and DesRoches, R. (2020). The promise of implementing machine learning in earthquake engineering: a state-of-the-art review. *Earthquake Spectra* 2020, 1–33. doi: 10.1177/8755293020919419
- Zhang, R., Liu, Y., and Sun, H. (2019a). Physics-guided convolutional neural network (PhyCNN) for data-driven seismic response modeling. *arXiv* 216:110604.
- Zhang, R., Zhao, C., Chen, S., Zheng, J., Büyüköztürk, O., and Sun, H. (2019b). Deep long short-term memory networks for nonlinear structural seismic response prediction. *Comput. Struct.* 220, 55–68. doi: 10.1016/j.compstruc.2019.05.006
- Zhao, J., French, C., Shield, C., and Posbergh, T. (2003). Considerations for the development of real-time dynamic testing using servo-hydraulic actuation. *Earthquake Engin. Struct. Dynam.* 32, 1773–1794. doi: 10.1002/eqe.301

Conflict of Interest: The authors declare that the research was conducted in the absence of any commercial or financial relationships that could be construed as a potential conflict of interest.

Copyright © 2020 Bas and Moustafa. This is an open-access article distributed under the terms of the Creative Commons Attribution License (CC BY). The use, distribution or reproduction in other forums is permitted, provided the original author(s) and the copyright owner(s) are credited and that the original publication in this journal is cited, in accordance with accepted academic practice. No use, distribution or reproduction is permitted which does not comply with these terms.



Real-Time Aeroelastic Hybrid Simulation of a Base-Pivoting Building Model in a Wind Tunnel

Moniruzzaman Moni¹, Youchan Hwang², Oh-Sung Kwon^{1*}, Ho-Kyung Kim² and Un Yong Jeong³

¹ Civil and Mineral Engineering, University of Toronto, Toronto, ON, Canada, ² Department of Civil and Environmental Engineering, Seoul National University, Seoul, South Korea, ³ Gradient Wind Engineering Inc., Ottawa, ON, Canada

OPEN ACCESS

Edited by:

Vasilis K. Dertimanis,
ETH Zürich, Switzerland

Reviewed by:

Xiaoyun Shao,
Western Michigan University,
United States
Brian M. Phillips,
University of Florida, United States

*Correspondence:

Oh-Sung Kwon
os.kwon@utoronto.ca

Specialty section:

This article was submitted to
Computational Methods in Structural
Engineering,
a section of the journal
Frontiers in Built Environment

Received: 09 May 2020

Accepted: 18 August 2020

Published: 22 September 2020

Citation:

Moni M, Hwang Y, Kwon O-S,
Kim H-K and Jeong UY (2020)
Real-Time Aeroelastic Hybrid
Simulation of a Base-Pivoting Building
Model in a Wind Tunnel.
Front. Built Environ. 6:560672.
doi: 10.3389/fbuil.2020.560672

The wind tunnel test is one of the most reliable methods for evaluating the dynamic response of high-rise buildings considering wind-structure interaction. In conventional aeroelastic wind tunnel tests, the calibration of stiffnesses, masses and the damping properties of a scaled specimen is required. This takes extensive time and effort, especially when the tests need to be repeated with various geometric designs during design iterations. This study introduces a new testing method that combines a numerical simulation and the conventional aeroelastic wind tunnel test through the real-time hybrid simulation method. The stiffness, damping and partial mass of a scaled building model are represented numerically, while the rest of the mass, the wind-induced pressure around the model and the wind-structure interaction are represented physically in a wind tunnel. The building model in the wind tunnel rests on a base-pivoting system, which is controlled with a linear motor. The base moment induced by wind pressure and the inertial force from the mass of the physical specimen is measured; those measurements are then fed back into a numerical integration scheme. A delay-compensation scheme is implemented to minimize the effects of actuator delay on the dynamic response of the system. Several tests are carried out to validate and calibrate the developed test apparatus and control scheme including (1) tests for the identification of actuator delay, (2) free vibration tests for characterization of the dynamic properties of the hardware and the control system, and (3) wind tunnel tests for system validation through aeroelastic real-time hybrid simulation. This paper presents the overall design of the experimental apparatus, the adopted delay compensation and numerical integration schemes, and a summary of the test results. Test results confirmed that the developed experimental technique can replace the conventional aeroelastic wind tunnel tests of a building model, thus improving the efficiency of the aeroelastic wind tunnel testing.

Keywords: real-time aeroelastic hybrid simulation, RTAHS, base pivoting model, wind tunnel test, high-rise building

INTRODUCTION

The number of new high-rise building construction has rapidly increased due to advancements in construction technology and to house the increasing populations in urban areas. For the design of these structures, proper estimation of lateral loads, such as earthquake and wind, is essential. Advancements in the seismic design of high-rise buildings have decreased their weight

significantly to reduce the effect of earthquake forces on the buildings. If the weight of a high-rise structure decreases, the damping of the structure tends also to decrease, which in turn increases the vibration-induced acceleration of a structure subjected to wind load (Kanda et al., 2003). It is imperative to properly evaluate the dynamic response of high-rise buildings subjected to wind load at the design phase.

Both static and dynamic analysis methods have been used to evaluate the response of high-rise structures under wind loads. In the static analysis method, it is assumed that the dynamic interaction between a building and the wind load is negligible. In practice, static analysis is usually recommended for buildings up to 50 meters in height. This method cannot be applied to buildings that are tall, have a high slenderness ratio, or are susceptible to vibration under wind loads. For buildings with an aspect ratio (height to width ratio) of more than five and having the first natural period larger than 1 s, a dynamic analysis is required (Mendis et al., 2007). The dynamic effect of wind loads on tall buildings can be evaluated by performing computational fluid dynamics (CFD) analysis or boundary layer wind tunnel (BLWT) tests. Elshaer et al. (2015) used the CFD models, or surrogate models such as neural networks (NN), to evaluate the vibration of a tall building under wind load. The CFD analysis can accurately predict structural responses only for idealized boundary conditions at the expense of large computational time. However, CFD analysis cannot reliably simulate the wind fluctuation characteristics of natural winds and requires many assumptions and approximations. In such situations, the response of high-rise buildings subjected to wind can be more accurately evaluated with BLWT tests.

There are two test methods with a BLWT: the aerodynamic test method and the aeroelastic test method (Duthinh and Simiu, 2011). In the aerodynamic test method, a rigid model is used. Either the high-frequency base balance (HFBB) method or the high-frequency pressure integration (HFPI) method is used to measure the bending and torsional moments and base shear forces in the wind tunnel (Aly, 2013). Dragoiescu et al. (2006) performed wind tunnel tests of the CAARC (Commonwealth Advisory Aeronautical Council) standard tall building model using both HFBB and HFPI methods. The study concluded that each method has advantages and disadvantages. The main advantage of the HFBB is that the model can be constructed quickly, typically within 2–3 weeks. However, the method relies on the assumption of nearly linear mode shapes. The HFBB cannot provide any information to assess the pedestrian level wind. The HFBB method is not suitable for a building that has non-linear mode shapes nor is it suitable when the natural frequencies for higher modes are in the range where significant wind energy is available. The main advantage of HFBB method is not only the low cost of running the test, but also its technical simplicity, easy operation, and small time requirement (Zou et al., 2017). In tall buildings that have a linear translational mode shape, the measured base moment from the HFBB method is distributed as equivalent lateral force along with the height of the building, based on the mode shape and the mass distribution.

In comparison, the main advantage of using HFPI is its inclusion of the correlation and coherence of the force

components. The variation of wind loads along the height of the structure is available in detail from pressure transducers. The construction of a model for the HFPI method is more time-consuming than the construction of a model for the HFBB method. For models with very complex geometry, many pressure taps are required. Besides, the model needs an ample interior space to run pressure tubes. For a complex building, the HFPI method requires simplification of the geometry to distribute the pressure taps. The main challenge in both aerodynamic methods (HFBB and HFPI methods) is the inability to consider the vibration of a structure and the corresponding wind-structure interaction effect that governs the serviceability of flexible high-rise buildings.

The aeroelastic test is required for slender tall buildings. Depending on the dynamic properties of a building, aerodynamic damping can reduce the wind-induced force, acceleration, and displacement for buildings. However, under aeroelastic instability conditions, the aerodynamic damping becomes negative, which can increase the displacement and acceleration of a tall building (Kareem et al., 1999; Amin and Ahuja, 2010; Kim et al., 2016). Thus, for a tall building that has a high slenderness ratio, an aeroelastic test is necessary (Sullivan, 1977; Xu and Kwok, 1993; Pozzuoli, 2012; Zhou et al., 2002; Zhao et al., 2011) to accurately evaluate the effect of aerodynamic damping on dynamic responses. The aeroelastic test method can simulate the wind-structure interaction effect by modeling the deformation of a building due to wind load.

Multi-degree of freedom (MDOF) or single degree of freedom (SDOF) models are used for aeroelastic tests. The MDOF model is recommended when a building has significant higher mode contributions and coupling in mode shapes. If the building has an approximately linear mode shape and does not exhibit a coupled mode of vibration, an SDOF model can be used to evaluate the aeroelastic effect. Many tall buildings' center of mass does not coincide with the center of stiffness, which results in coupling of translational and torsional motion. These coupled vibration modes cannot be represented with the SDOF aeroelastic test (Thepmongkorn et al., 1999). The SDOF aeroelastic test, however, is more efficient than the multi-degree of freedom aeroelastic test in terms of design, fabrication, calibration and measurement (Zhou and Kareem, 2003).

In the SDOF aeroelastic test, it is essential to match the frequency of the scaled specimen with that of the prototype building after applying a scaling factor. In addition, the first mode generalized mass (MGM) or mass moment of inertia (MMI) of a scaled model needs to be matched with that of the prototype building after imposing a scaling factor (Zhou and Kareem, 2003). The development of a test specimen satisfying the above conditions require significant time and effort. For this reason, the aeroelastic test is not commonly used in compared with the aerodynamic test.

The hybrid simulation is rapidly gaining acceptance in the field of structural engineering since it is cost-effective and can address the challenges that exist in conventional tests. Pseudo-dynamic (PsD) hybrid simulation is typically carried out for rate-independent structural elements. Various frameworks have been developed to facilitate PsD hybrid simulations such as

UT-SIM Framework (Mortazavi et al., 2017; Huang and Kwon, 2018) or OpenFresco (Schellenberg et al., 2009), and there have been many applications in research projects (Kammula et al., 2014; Mojiri et al., 2019; among many others). Real-time hybrid simulation (RTHS), in which the simulation is carried out in real-time to model the behavior of rate-dependent structural elements, is an extension of the conventional PsD hybrid simulation method. RTHS has been performed widely in the field of earthquake engineering (Ahmadizadeh, 2007; Christenson et al., 2008; Mercan and Ricles, 2009; Chen et al., 2012; Botelho and Christenson, 2017; Guo et al., 2017; Solum, 2017; among many others) and fire engineering (Wang et al., 2019).

There have been applications of real-time hybrid simulation in wind engineering, which is termed as real-time aeroelastic hybrid simulation (RTAHS). The RTAHS method is beneficial over conventional aeroelastic tests as a user can easily define the dynamic parameters numerically. Also, RTAHS provides additional benefits. For example, the main program can be extended by implementing tuned mass damper, tuned liquid damper, or any other supplemental damper models in the control system, which allows rapid prototyping of appropriate damping system to control the vibration of a building subjected to wind load. However, The RTAHS method has some shortcomings as well. For example, a wind testing facility needs to invest in hardware, which is certainly more expensive than springs or masses for conventional tests. To operate the equipment properly, a technician needs a certain level of training. Also, the user interface needs to be developed for the user-friendly and fail-proof operation of the equipment.

The early studies on the development and applications of the RTAHS method are Kanda et al. (2003, 2006), Nishi and Kanda (2010), and Kato and Kanda (2014). Kanda et al. (2003) proposed a RTAHS method to estimate the performance of a high-rise building for across and along wind directions considering the wind-structure interaction. For the RTAHS, the dynamic properties of the model building were defined in a numerical model, and the aerodynamic force was measured from a specimen in a wind tunnel. In that study, two rotary servomotors were used to excite the model building, and load cells were used to measure the forces. In each time step, external forces were measured with the load cells based on which the displacements of the specimen were calculated using a time integration scheme. Then, the calculated displacements were imposed to the model. This process continued in real-time up to the end of the experiment. Kanda et al. (2006) presented details about the numerical integration scheme for the aeroelastic hybrid simulation considering the multi-degree of freedom model. Using load cells in a RTAHS has a downside; the load cells cannot separate the inertia forces from the wind forces. Thus, Nishi and Kanda (2010) proposed a RTAHS method using the HFPI technique. Later, Kato and Kanda (2014) used the HFPI method to simulate the aerodynamic vibrations of a tall building in a wind tunnel. In that study, the authors also explored the application of the RTAHS method to a building with a base isolation system, which was modeled numerically. Recently, Wu and Song (2019) numerically investigated the feasibility of RTAHS of a building equipped with dampers. Wu et al. (2019) proposed a RTAHS

method of a bridge deck section model subjected to wind loads. Kwon et al. (2019) proposed a conceptual design of experimental setup for RTAHS of base-pivoting building model and bridge deck section model. Al-subaihawi et al. (2020) performed a real-time hybrid simulation in which the wind load was modeled numerically to evaluate wind-induced vibration in a tall building with damped outriggers.

The main objective of this paper is to propose a new design of an experimental apparatus using electric linear motor that can perform a real-time aeroelastic hybrid simulation for a single degree of freedom base-pivoting building model. An experimental apparatus and control scheme are developed, which can impose pivoting motion by controlling the linear motor. The delay of the actuator is partially compensated for by using the inverse compensation technique. Section “Framework for Real-Time Aeroelastic Hybrid Simulation (RTAHS)” of this paper presents the overall framework and experimental apparatus, followed by experimental verification tests in section “Preliminary Tests for Characterization of Dynamic Properties” and wind tunnel tests in section “Real-Time Aeroelastic Hybrid Simulation (RTAHS).” Section “Conclusion” summarizes the main developments and findings from this study.

FRAMEWORK FOR REAL-TIME AEROELASTIC HYBRID SIMULATION (RTAHS)

In this study, a real-time aeroelastic hybrid simulation system for a base-pivoting high-rise model building is proposed. The equation of motion for a base-pivoting model subjected to wind loads can be expressed as below:

$$I\ddot{\theta}(t) + c\dot{\theta}(t) + k\theta(t) = M(\theta, \dot{\theta}, s(t)) \quad (1)$$

where I , c , and k are the rotational inertia, damping coefficient for rotational velocity and rotational spring coefficient. For the sake of simplicity, these terms will be referred to as mass, damping and stiffness coefficients hereafter. θ is rotation angle, and dots denote derivatives of the rotation angle. Since buildings are designed to behave in the elastic range when subjected to wind load, these properties remain constant throughout the test. The right side of the equation represents moment induced by wind load, which is a function of three factors: $s(t)$ is a time-varying component of the wind velocity, and θ and $\dot{\theta}$ are displacement and velocity of the structure, respectively.

The substructuring for the RTAHS is different from the substructuring for typical RTHS for a structure subjected to seismic load. In the latter, a structural system is substructured into numerical and physical elements. In the former, however, the right-hand side of the Eq. (1) is modeled physically. In addition, the mass of the model, I , is split into physical and numerical components because it is nearly impossible to develop a physical model without having mass. Thus, for the real-time aeroelastic hybrid simulation, Eq. (1) can be modified as below:

$$(I_E + I_N)\ddot{\theta}(t) + c\dot{\theta}(t) + k\theta(t) = M(\theta, \dot{\theta}, s(t)) \quad (2)$$

where I_E and I_N represent the mass of the specimen and the numerically represented mass, respectively. In the proposed RTAHS, the measured force (i.e., a base moment) includes the inertial force and the wind-induced force. Thus, Eq. (2) can be written as Eq. (3) where the right-hand side is experimentally measured:

$$I_N \ddot{\theta}(t) + c \dot{\theta}(t) + k \theta(t) = M(\theta, \dot{\theta}, s(t)) - I_E \ddot{\theta}(t) \quad (3)$$

Consequently, in the numerical integration scheme only the numerical rotational mass, I_N , needs to be defined. The Eqs. (1, 3) are mathematically identical. In RTAHS, however, there is a delay in the actuator's response, which impacts the dynamic characteristics of the system. This will be further elaborated in section "Delay Compensation."

The overall configuration of the proposed RTAHS is illustrated in **Figure 1**. The proposed RTAHS platform mainly consists of a linear motor with a magnetic encoder, a load cell, a motor controller, a motor driver and a real-time data acquisition and control (NI cDAQ-9133) system. The control loop mainly consists of a numerical integration scheme, a delay compensation scheme and a PID control loop, as shown in **Figure 1**. In this figure, r is the distance from the pivoting point to the point where the load transfer element is mounted (see **Figure 2**), u_p is the linear predicted displacement, u_m is the measured linear displacement, θ_t is the target displacement calculated by solving the equation of motion and F_m is the measured force. A is the electric current output from the motor driver, which energizes the magnetic field of the linear motor.

The following sections present the main components of the proposed RTAHS apparatus.

Experimental Setup

An experimental apparatus is developed to perform the RTAHS for a base-pivoting building model for a crosswind direction. **Figure 2A** shows the schematic of the developed experimental setup for this study. **Figure 2B** shows the plan view of the developed system without the model, and **Figure 2C** shows the developed system in the wind tunnel facility. The main components for the experimental apparatus are as below.

Supporting Frame

A rigid frame is designed to support the linear motor and the base-pivoting system. The frame elements are selected such that they do not develop resonance during the RTAHS. The dimension of the frame is 490 mm in height and 560 mm in width, which is determined based on the geometry of the opening in the wind tunnel. The top of the frame is flush with the wind tunnel floor. The linear motor is mounted to the supporting frame. The specimen mount (crosshead in **Figure 2E**) is supported on the frame.

Actuation

A linear motor was chosen as an actuator. A rotary motor with a precision gear was also considered as a potential actuator. However, after consulting an equipment manufacturer, it was concluded that a rotary motor was not suitable due to

the potential control issue associated with backlash in gear. The direct-drive rotary motor is also possible, but precisely controlling maximum 0.02 rad of rotation angle at maximum 8 Hz would be challenging due to the resolution of the rotary encoder. In addition, implementing a bi-directional pivoting motion in the future upgrade would be challenging when two rotatory motors are used. A load transfer mechanism is designed to transfer the linear motion to a base-pivoting motion, as shown in **Figure 2D**. The linear motor has a total stroke of 60 mm, peak force of 790 N, continuous force of 176 N, and peak velocity of 2.5 m/s, all of which are far higher than the requirements for the RTAHS. The peak linear velocity corresponds to the angular velocity of 33 rad/s, considering the dimension of the crosshead in **Figure 2A**.

Sensors

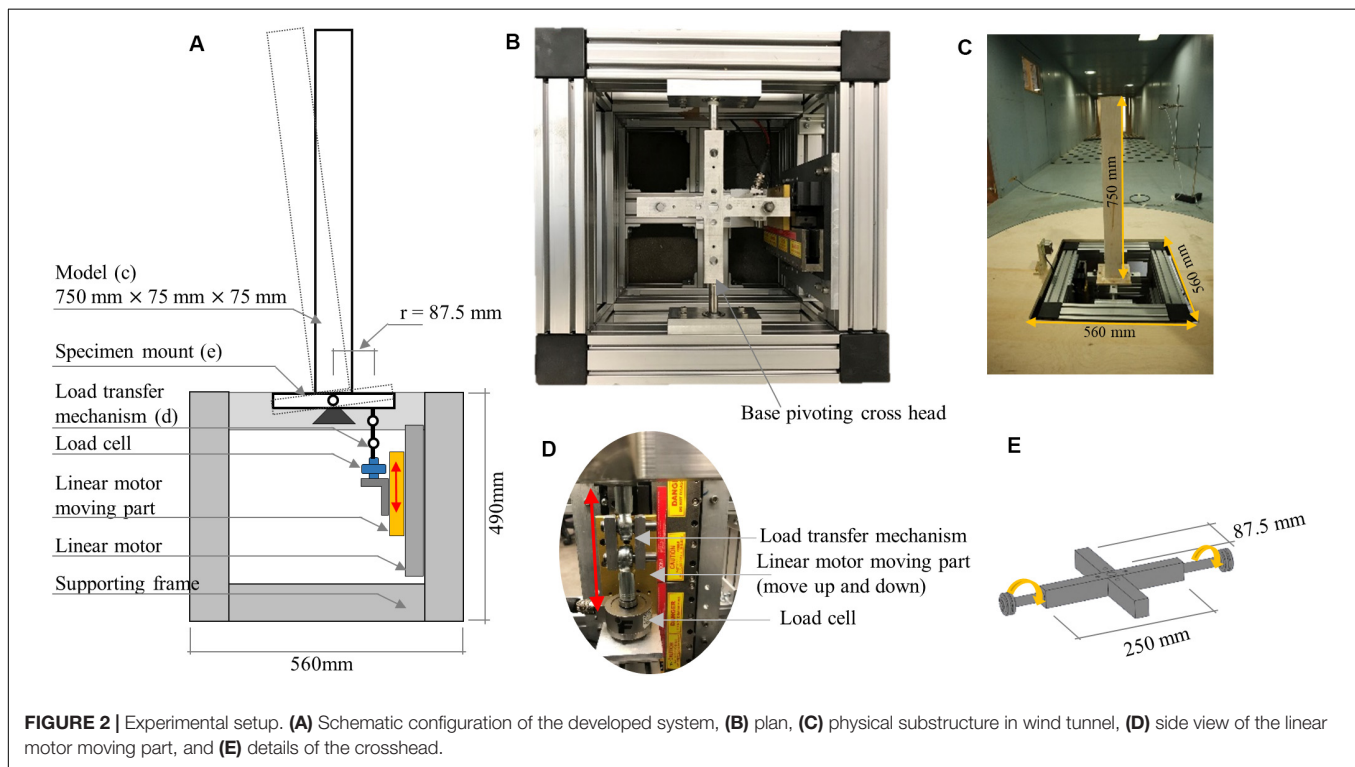
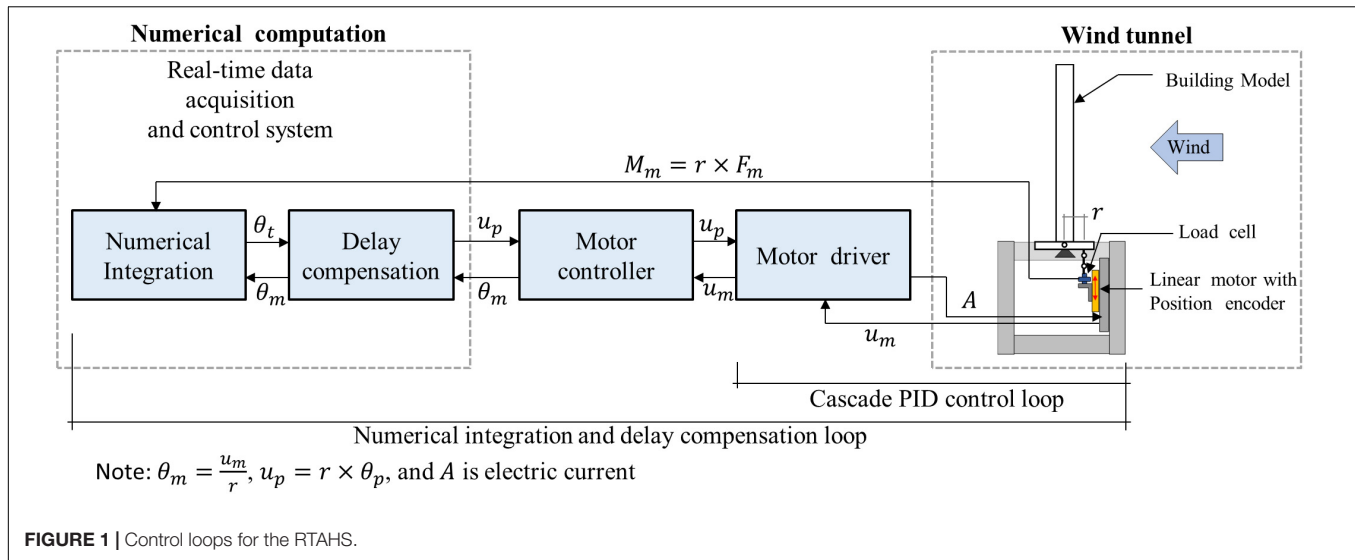
The position of the electric motor is measured with a magnetic encoder with a resolution of 0.001 mm. The base rotation angle is calculated based on the distance from the pivoting point to the point where the load transfer element is mounted (r in **Figure 2A**). The HFBB method is used to measure wind-induced force in this study. While the HFBB method has its own challenge, as discussed in section "Introduction," it was advantages as well. For example, the load cell can transfer data at a faster rate than pressure transducers, and the model development is relatively easier than using pressure tabs for an HFPI model. The HFPI model in hybrid simulation also requires the integration of the measured pressures from the pressure taps to calculate the force or moment approximately. This can result in inaccuracies if the geometry of a specimen is complicated. In the proposed design of the experimental setup, the force is measured with a uniaxial tension-compression load cell with a capacity of 445 N. One end of the load cell is connected to the moving part of the linear motor, and the other end is connected to the crosshead through the load transfer element.

Building Model

The building model is constructed with balsa wood. The building model has a height of 750 mm and planner dimensions of 75 mm \times 75 mm, which represent a prototype building of 300 m in height and 30 m in width and depth.

Numerical Integration Scheme

This study adopted the central difference method (CDM) to perform numerical integration. There are various numerical integration algorithms developed for hybrid simulations to improve stability and accuracy. The stability resulting from the CDM is not an issue in this study because the smallest period of the base-pivoting single degree of freedom (SDOF) system is sufficiently larger than the integration time step. The stability of CDM depends on the time step and the shortest natural period of the structure. If the shortest period of the structure is τ_{\min} and the time step of the integration scheme is Δt , the numerical



integration is stable when the following equation is satisfied:

$$\Delta t < \frac{\tau_{\min}}{\pi} \quad (4)$$

In the current study, the period of the single degree of freedom system is considered 125 ms (i.e., $f = 8$ Hz), and the time step of the integration scheme considering the processing speed of the real-time controller is 5 ms, which satisfies the above stability criteria.

In the RTAHS, the equation of motion needs to be modified as shown in Eq. (3) because the measured moment includes the

moment from the dynamic wind pressure, $M(\theta, \dot{\theta}, s(t))$, and the moment resulting from the acceleration of the specimen and other load transfer elements, $-I_E \ddot{\theta}(t)$. The measured moment is denoted as $M_m(t)$ in Eq. (5)

$$M_m(t) = M(\theta, \dot{\theta}, s(t)) - I_E \ddot{\theta}(t) \quad (5)$$

Then, Eq. (3) can be written in discrete form for step i at time $t_i = i \Delta t$.

$$I_N \ddot{\theta}_i + c \dot{\theta}_i + k \theta_i = M_{m,i} \quad (6)$$

Eq. (6) needs to be solved to predict the displacement in each step. In the CDM, the velocity and acceleration at step i are calculated based on Eqs. (7, 8)

$$\dot{\theta}_i = \frac{\theta_{i+1} - \theta_{i-1}}{2 \Delta t} \quad (7)$$

$$\ddot{\theta}_i = \frac{\theta_{i+1} - 2\theta_i + \theta_{i-1}}{\Delta t^2} \quad (8)$$

After substituting Eqs. (7, 8) into Eq. (6), the displacement at step $i + 1$, θ_{i+1} , can be calculated from the measured moment, $M_{m,i}$; numerical mass, I_N ; damping coefficient, c ; structural stiffness coefficient, k ; time step, Δt ; the previous steps' displacements θ_i and θ_{i-1} as shown in Eq. (9)

$$\theta_{i+1} = \frac{2\Delta t^2}{2I_N + c\Delta t} \left(\left(\frac{2I_N}{\Delta t^2} - k \right) \theta_i + \left(\frac{c}{2\Delta t} - \frac{I_N}{\Delta t^2} \right) \theta_{i-1} + M_{m,i} \right) \quad (9)$$

The displacement predicted with Eq. (9), which is denoted as target displacement, θ_t , in **Figure 1**, is modified for delay compensation, which is then transferred to the motor driver. The motor controller in **Figure 1** does not have any role in the hybrid simulation other than relaying commands and measurements. The motor controller is required to enable communication from the real-time data acquisition and control system (NI-cDAQ) and the motor driver. A host PC is used between the NI-cDAQ and the motor controller. The data is transferred in real-time from the NI-cDAQ to the motor controller through the host PC.

Delay Compensation

In a real-time hybrid simulation (RTHS), it is essential to impose motion without significant delay. The delay may result in unintended negative damping and a corresponding stability issue, or unintended positive damping. Depending on the dynamic characteristics of the specimen and the actuation system, the delay may be frequency dependent. Besides, if a structural system behaves in the inelastic range (i.e., there are changes in stiffness during a simulation), the initially tuned gain parameters may not work properly. Advanced adaptive delay compensation methods, such as Chae et al. (2013), have been proposed to consider the frequency-dependency or non-linearity in the system.

In the configuration of the testing apparatus proposed for an RTAHS, the selected linear motor has a large continuous force capacity (176 N) in comparison with the actual force required to run the test. The maximum measured peak force was less than 50 N in this research; thus, the specimen-actuator interaction is negligible. In addition, while there is some non-linearity resulting from wind-structure interaction, the overall mass and stiffness of the system can be considered constant. Time delay is observed in preliminary tests of the control scheme, but the delay was constant in the frequency range of interests. Thus, in this study, the inverse time delay compensation method developed by Chen (2007) is adopted, which assumes a constant delay. The method is briefly summarized below, and the method is illustrated in **Figure 3B**.

In the presence of delay, the measured displacement $\theta_{m,i+1}$ at time step $i + 1$ can be expressed as

$$\theta_{m,i+1} = \theta_{m,i} + \frac{1}{\alpha} (\theta_{t,i+1} - \theta_{m,i}) \quad (10)$$

where α is the ratio between the time to reach the target displacement ($\alpha \Delta t$ in **Figure 3A**) and the time step Δt , assuming a constant delay. Eq. (10) can be rearranged in terms of the target displacement, $\theta_{t,i+1}$.

$$\theta_{t,i+1} = \alpha \theta_{m,i+1} - (\alpha - 1) \theta_{m,i} \quad (11)$$

By applying the first-order discrete Z-transform, the relationship between the target displacement and the measured response can be obtained, as shown in the transfer function in Eq. (12).

$$G_d(z) = \frac{X_{m,\theta}(z)}{X_{t,\theta}(z)} = \frac{1}{\alpha - (\alpha - 1)z^{-1}} = \frac{z}{\alpha z - (\alpha - 1)} \quad (12)$$

where $X_{m,\theta}(z)$ and $X_{t,\theta}(z)$ are the discrete Z-transform of $\theta_{m,i+1}$ and $\theta_{t,i+1}$, respectively. Note that when there is no delay (i.e., $\alpha = 1$), the value of the transfer function becomes one. To compensate for the delay, the predicted displacement, $\theta_{p,i+1}$, can be imposed on the controller instead of the target displacement, $\theta_{t,i+1}$, where the predicted displacement is calculated as:

$$\theta_{p,i+1} = \alpha \theta_{t,i+1} - (\alpha - 1) \theta_{t,i} \quad (13)$$

In a conventional RTHS of structures where the restoring force is a function of the deformation of a specimen, the delay in the actuator's response leads to negative damping, which can lead to a stability issue. In the case of RTAHS, however, the measured force includes the inertial force term $I_E \ddot{\theta}(t)$ as shown in Eq. (5), which is proportional to acceleration. For an oscillating system, the phase of the acceleration is 180 deg apart (i.e., opposite sign) from the phase of the displacement. Thus, the delay in the actuator's response leads to the delay in the acceleration response, which in turn leads to a positive damping effect rather than a negative one.

To further elaborate, let us consider an SDOF system with an angular frequency of ω_o subjected to steady-state harmonic displacement with an amplitude of θ_o as defined in Eq. (14). This displacement profile is imposed on a control system; thus, the displacement is denoted as target displacement, θ_t :

$$\theta_t = \theta_o \sin(\omega_o t) \quad (14)$$

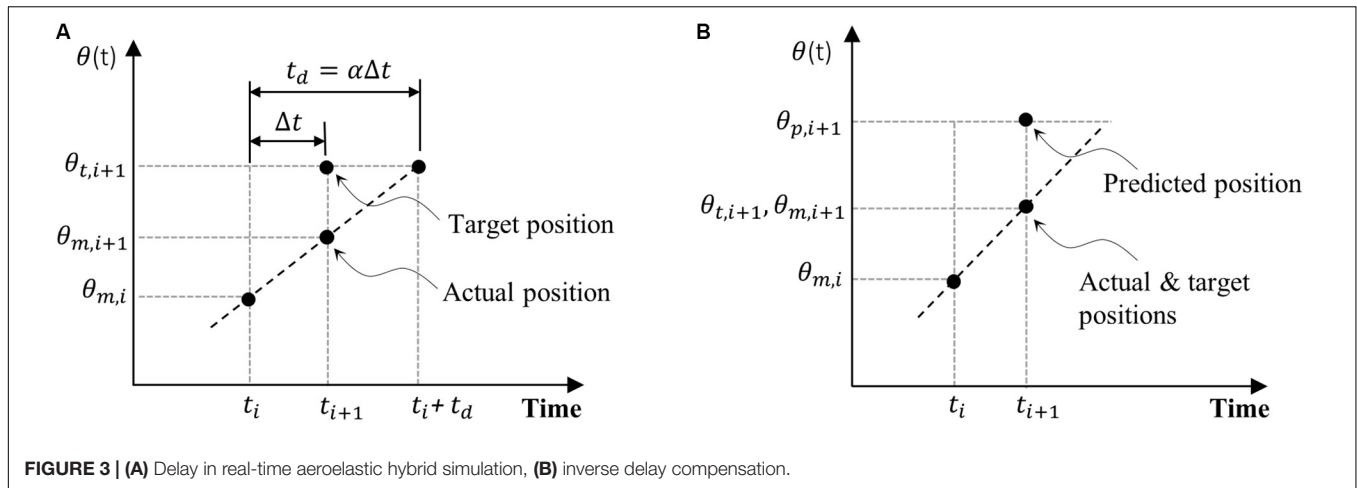
If there is a constant delay of, δt , the measured displacement and acceleration are:

$$\theta_m = \theta_o \sin(\omega_o(t - \delta t)) \quad (15)$$

$$\ddot{\theta}_m = -\theta_o \omega_o^2 \sin(\omega_o(t - \delta t)) \quad (16)$$

The inertial moment due to the physical mass of the system, $M_I = I_E \ddot{\theta}_m$, depends on the measured acceleration in Eq. (16). Then, the apparent energy increment per each cycle of motion (i.e., duration of $T = 2\pi/\omega_o$) due to the inertial moment, M_I , is,

$$\begin{aligned} \delta E &= \int_0^T M_I \frac{d\theta_t}{dt} dt = \int_0^T I_E \ddot{\theta}_m \frac{d\theta_t}{dt} dt = \pi I_E \theta_o^2 \omega_o^3 \delta t \\ &= \pi \theta_o^2 \omega_o M_R k \delta t \end{aligned} \quad (17)$$



where M_R is the ratio between the experimental inertia mass, I_E , and the total inertia mass, I , as defined in Eq. (18) and k is the stiffness of the system as defined in Eq. (1).

$$M_R = \frac{I_E}{I} = \frac{I_E}{I_E + I_N} \quad (18)$$

As shown in Eq. (17) the delays in the actuator's response leads to positive damping, i.e., energy dissipation, not negative damping. It is worth noting that a similar expression for a displacement-dependent force (e.g., linear spring) leads to negative damping.

The energy dissipation in Eq. (17) can be expressed as equivalent viscous damping, C_{eq} . The energy dissipated per cycle by a viscous damping force in a SDOF system oscillating with an amplitude of θ_o and frequency of ω_o can be derived as,

$$\delta E = \pi \theta_o^2 \omega_o C_{eq} \quad (19)$$

By equating Eqs. (17, 19), one can find an equivalent damping coefficient and corresponding damping ratio, as shown in Eqs. (20, 21), respectively,

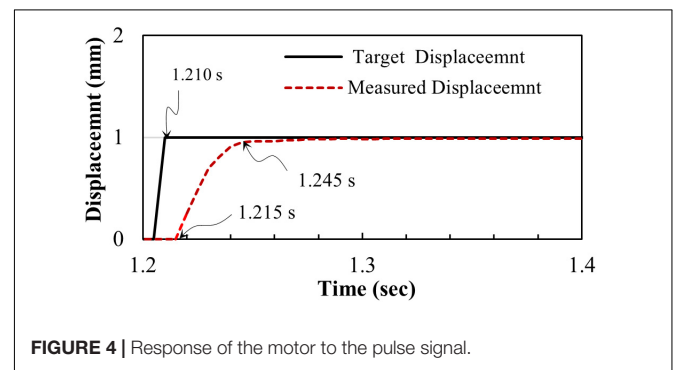
$$C_{eq} = M_R k \delta t \quad (20)$$

$$\zeta_{eq} = \frac{C_{eq}}{2\sqrt{Ik}} = \frac{M_R k \delta t}{2\sqrt{Ik}} = \frac{M_R \delta t}{2} \sqrt{\frac{k}{I}} = \frac{M_R \delta t}{2} \omega_o = \pi M_R f_0 \delta t \quad (21)$$

Thus, the equivalent damping ratio, ζ_{eq} , can be expressed as a function of mass ratio, M_R , frequency of the structure, f_o , and constant delay, δt , of the actuator-control system. The observed delay from the experiment and the corresponding damping ratio is further discussed in section "Free Vibration Test."

Cascade PID Control of Linear Motor

The predicted displacement in Eq. (13), $\theta_{p, i+1}$, is imposed on the motor driver in **Figure 1** after converting the rotary motion to linear motion, i.e., $u_{p, i+1} = \theta_{p, i+1} \times r$. The motor driver controls the linear motor using a cascade PID control. It is the default control structure implemented in the motor drive, and the



user can optimize the gain parameters. The cascade PID control includes three different control loops: the position loop, velocity loop and current loop. The current loop acts as the inner loop for the velocity loop, and the velocity loop act as an inner loop of the position loop.

For optimal performance, the control gains need to be tuned. In this study, the gains were calibrated after attaching all physical components, including the model building. After calibration, the system response was observed, as shown in **Figure 4**. From this figure, it can be observed that the response does not overshoot and monotonically approach the target command. There are 5 ms of delay before the system starts moving. This delay is due to the 5 ms of loop time used in the controller. It took 30 ms to reach the target displacement. After running all tests, the authors learned that the gain parameters could have been further tuned to reduce the 30 ms of delay before the delay compensation was applied.

PRELIMINARY TESTS FOR CHARACTERIZATION OF DYNAMIC PROPERTIES

Dynamic characteristics of the experimental apparatus and the control system are identified by imposing a white noise displacement profile, cyclic tests, and free vibration tests.

A white noise displacement profile is used to identify the delay characteristics. The cyclic tests are used to measure the actual inertia mass of the specimen and the moving parts in the pivoting system. Free vibration tests are performed to evaluate the relationship between the input and output values of frequency and damping.

White Noise Test and Cyclic Test

The white noise signal, which was filtered through a low-pass filter, is used to measure the delay characteristics of the actuator. The input signal is a predefined displacement history, which has a magnitude of 1 mm and a frequency range of 0.1–10 Hz. Note that the numerical integration scheme is not used in these tests because the displacement histories are predefined.

The input displacement histories and the response of the linear motor are used to obtain a transfer function in the form of the Bode plot. The Bode plot of the white noise signal with and without delay compensation technique is presented in **Figure 5**. The delay for the system without delay compensation (i.e., $\alpha = 1$) is observed to be 29 ms, which is consistent with the observation from the step response shown in **Figure 4**. Chen et al. (2009) defined α as the ratio of the actuator delay to the servo controller sampling time (i.e., time step). The actuator delay is defined as the time difference between the time when the compensated command ($\theta_p = u_p/r$ in **Figure 1**) is issued and the time when the measured displacement (θ_m) becomes similar to the compensated command. When the time delay compensation is not applied ($\alpha = 1$), the target command (θ_t) is identical to the compensated command as shown in Eq. (13). From the white noise test with $\alpha = 1$, it was found that the actuator delay was 29 ms. Because the sampling time of the servo controller was 5 ms, the proper value of α is approximately 6.

After the first test with $\alpha = 1$, the inverse delay compensation scheme discussed in section “Delay Compensation” was used with α values ranging from 2 to 6 to observe the performance of the delay compensation scheme. It was observed from the tests that the delay decreases as the value of α increases. However, as the value of α increases, the amplitude error was increasing as a function of frequency. With the α value of 6, the amplitude increases to 146% at the frequency of 8 Hz as shown in **Figure 5B**. In addition, the delay of 16 ms was still observed with the α value of 6. Thus, with the inverse delay compensation scheme, the maximum value of α is deemed to be 3, as it did not introduce amplitude error that was observed in **Figure 5B**. At this value of α , the observed delay was 23 ms as shown in **Figure 5A**, which was not a significant improvement from 29 ms. The delay of 23 ms leads to additional damping, as discussed in section “Apparent Damping,” which was compensated by tuning the numerical damping parameter.

The authors also carried out additional tests with an independent experimental setup. We observed that the inverse delay compensation scheme does not fully reduce the delay and tends to amplify the vibration as the value of α increases. Therefore, it is suggested to adopt a more advanced delay compensation scheme in future tests.

After the installation of the specimen, cyclic tests were also performed to measure the physical mass, I_E in Eq. (3).

A displacement amplitude of 0.4375 mm was imposed at each frequency, which is equivalent to 1/200 radian of rotation. After the completion of the cyclic tests, the relationship between the RMS value of measured force, F_{rms} , and the RMS value of angular acceleration, $\ddot{\theta}_{rms}$ was found. The physical mass, I_E of the moving part was obtained by using Eq. (22). In this equation, r is the distance in mm of the pivoting point from the load cell, as shown in **Figure 2A**:

$$I_E = \frac{F_{rms} r}{\ddot{\theta}_{rms}} \quad (22)$$

The considered frequency range is 4–8 Hz. The mass moment of inertia from this test is found to be $I_E = 35,900 \text{ kg}\cdot\text{mm}^2$. This value is used to perform the free vibration test and the RTAHS.

Free Vibration Tests

Free vibration tests were performed considering a mass ratio, M_R , of 0.5 to 20%; the mass ratio is the ratio of physical mass to the total mass as presented in Eq. (18). The frequency ranges from 4 to 8 Hz, and the damping ratio of -1.5 to 0% was considered to run the free vibration tests. Note that negative damping was imposed because of the additional damping introduced by the approximately 23 ms of delay discussed in section “White Noise Test and Cyclic Test.” The free vibration test was performed by applying an initial displacement of 0.875 mm, which is equivalent to 1/100 radian of rotation. The measured force, which includes the inertial component, $-I_E\ddot{\theta}(t)$ in Eq. (5), but not wind-induced force, is fed back to the equation of motion.

Figures 6A,B presents the target command predicted by Eq. (9), which is labeled as “Target” in the figure, the predicted command after delay compensation in Eq. (13) which is labeled as “Compensated,” and the measured response for the case with a mass ratio of 5% ($M_R=7$ in **Table 1**), damping ratio of 0% and a frequency of 6 Hz. It can be observed that even with 0% of the damping ratio, the system shows logarithmic decay due to the additional damping from the delay. In this case, the observed delay of 23 ms is consistent with the delay when $\alpha = 3$ in **Figure 5**. From a series of parametric tests summarized in **Table 1**, however, we found that the delay varies from 14 to 23 ms, and the average delay is 19 ms depending on the test parameters of specified frequency, mass ratio, or damping ratio. The difference between the average delay (19 ms) from free vibration tests and the delay observed from white noise tests with α of 3 (23 ms) is about 5 ms. Further investigation is required to find out the cause of this delay difference. A more robust delay compensation method needs to be implemented in future test.

In order to evaluate the dynamic characteristics of the proposed testing apparatus in the presence of the delay, a series of free vibration tests are carried out by using mass ratio, damping ratio and natural frequency as control parameters. In **Table 1**, the physical mass, I_E , is fixed for all tests. The mass density is the average mass density of a high-rise building structure. The typical range of mass density for high-rise buildings varies from 200 to 450 kg/m³. In this study, however, much higher values of mass density are also used to investigate the impact of the mass ratio on the additional damping (i.e., Eq. 21). The total mass in **Table 1** is the rotational mass of the scaled model, considering

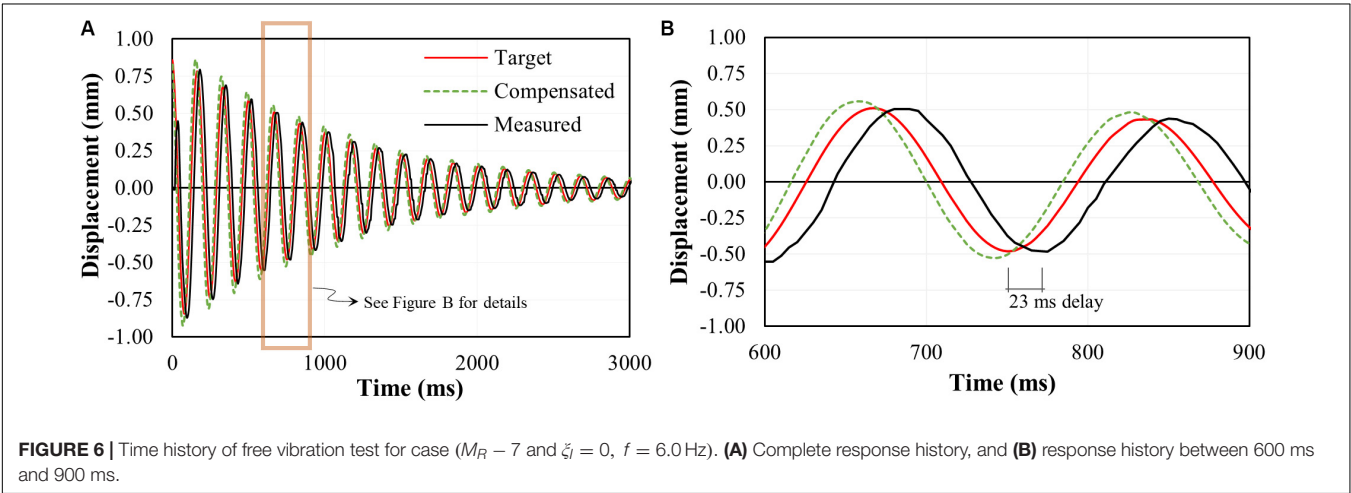
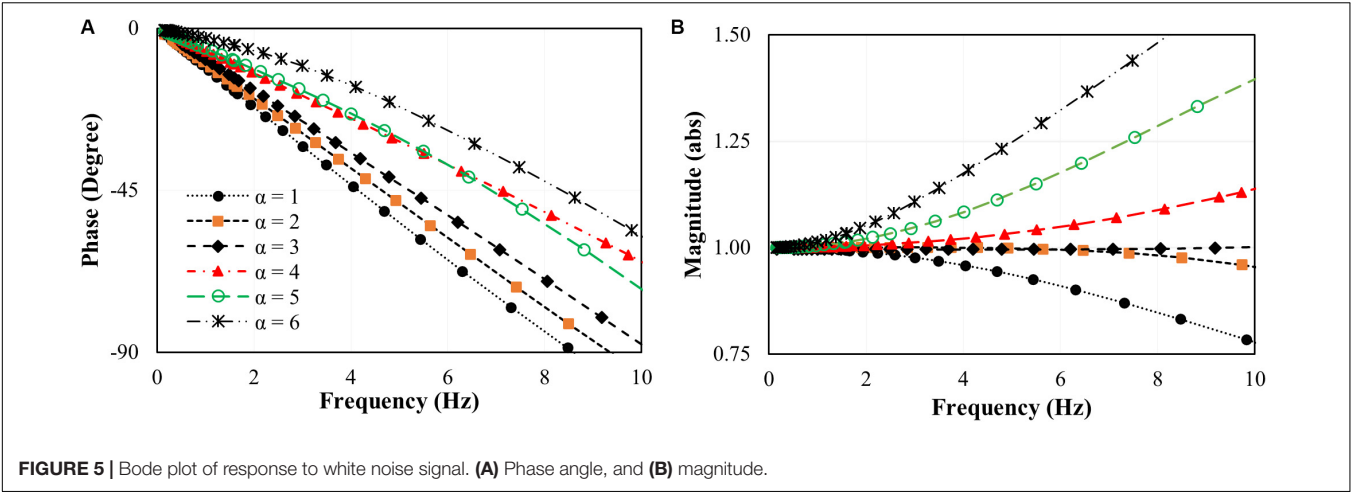


TABLE 1 | Control parameters of free vibration test.

Test no.	Mass density, ρ_s (kg/m ³)	Total mass, I (kg-mm ²)	Physical mass, I_E (kg-mm ²)	Numerical mass, I_N (kg-mm ²)	Mass ratio, M_R (%)	Input damping, ξ_i (%)	Input frequency, f_i (Hz)
M_R -1	225	178,400	35,900	142,500	20.1	-1.5 to 0	4 to 8
M_R -2	300	237,800		201,900	15.1	-1.5 to 0	4 to 8
M_R -3	350	277,500		241,600	12.9	-1.5 to 0	4 to 8
M_R -4	400	317,100		281,200	11.3	-1.5 to 0	4 to 8
M_R -5	475	376,600		340,700	9.5	-1.5 to 0	4 to 8
M_R -6	675	535,200		499,300	6.7	-1.5 to 0	4 to 8
M_R -7	900	713,600		677,700	5.0	-1.5 to 0	4 to 8
M_R -8	1,125	892,100		856,200	4.0	0	4 to 8
M_R -9	1,500	1,189,400		1,153,500	3.0	0	4 to 8
M_R -10	2,300	1,823,800		1,787,900	2.0	0	4 to 8
M_R -11	4,500	3,568,400		3,532,500	1.0	0	4 to 8
M_R -12	9,000	7,136,900		7,101,000	0.5	0	4 to 8

the dynamic similitude law. Then, the numerical mass is defined as the difference between the total mass and the physical mass. After the parametric experiments, the observed apparent frequency and damping ratio of the system are presented in the following subsections.

Apparent Frequency

After completing the free vibration tests, the frequency of the system is evaluated from the measured displacement response. In Table 2, the input frequency, f_i , is the frequency defined as the property of the system in Eq. (1). The observed apparent

TABLE 2 | Free vibration result.

Mass ratio		M_{R-1}		M_{R-2}		M_{R-3}		M_{R-4}		M_{R-5}		M_{R-6}		M_{R-7}		M_{R-8}		M_{R-9}		M_{R-10}		M_{R-11}		M_{R-12}	
		20.1%		15.1%		12.9%		11.3%		9.5%		6.7%		5.0%		4.0%		3.0%		2.0%		1.0%		0.5%	
f_I (Hz)	ξ_I (%)	f_M (Hz)	ξ_M (%)	f_M (Hz)	ξ_M (%)	f_M (Hz)	ξ_M (%)	f_M (Hz)	ξ_M (%)	f_M (Hz)	ξ_M (%)	f_M (Hz)	ξ_M (%)	f_M (Hz)	ξ_M (%)	f_M (Hz)	ξ_M (%)	f_M (Hz)	ξ_M (%)	f_M (Hz)	ξ_M (%)	f_M (Hz)	ξ_M (%)	f_M (Hz)	ξ_M (%)
4	0.0	3.7	6.8	3.7	5.5	4.0	4.5	4.0	4.0	4.0	3.7	4.0	2.3	4.0	1.8	4.0	1.6	4.0	1.1	4.0	0.8	4.0	0.4	4.0	0.2
	0.5	3.7	6.3	3.7	5.4	4.0	4.4	4.0	3.9	4.0	3.8	4.0	2.1	4.0	1.6					Not tested.					
	−1.0	3.7	5.9	3.7	5.2	4.0	4.2	4.0	3.6	4.0	3.7	4.0	1.9	4.0	1.0										
	−1.5	3.7	5.6	3.7	4.4	4.0	3.3	4.0	2.6	4.0	2.4	4.0	0.9	4.0	0.6										
5	0.0	4.7	9.6	4.7	7.3	5.0	5.3	5.0	5.0	5.0	4.4	5.0	3.2	5.0	2.3	4.9	1.7	5.0	1.2	5.0	0.8	5.0	0.4	5.0	0.2
	−0.5	4.7	7.6	5.0	6.8	5.0	5.1	5.0	4.8	5.0	3.7	5.0	2.7	5.0	1.8					Not tested.					
	−1.0	5.0	7.5	4.7	5.6	5.0	4.4	5.0	3.8	5.0	3.0	5.0	2.0	5.0	1.0										
	−1.5	4.7	6.2	4.7	5.2	5.0	3.7	5.0	3.0	5.0	3.1	5.0	1.7	5.0	0.6										
6	0.0	6.0	9.8	6.0	7.9	6.0	5.8	6.0	5.4	6.0	4.6	6.0	3.5	6.0	2.4	6.0	1.7	6.0	1.4	6.0	0.9	6.0	0.5	6.0	0.2
	−0.5	5.6	8.86	6.0	7.2	6.0	5.1	6.0	4.9	6.0	4.1	6.0	2.7	6.0	1.8					Not tested.					
	−1.0	5.6	7.43	6.0	6.3	6.0	4.7	6.0	4.3	6.0	3.9	6.0	2.1	6.0	1.8										
	−1.5	5.6	7.0	6.0	5.7	6.0	4.6	6.0	4.0	6.0	2.9	6.0	1.5	6.0	0.8										
7	0.0	7.0	10.5	7.0	8.2	7.0	6.8	7.0	5.7	7.0	4.8	7.0	3.8	7.0	2.5	6.9	2.1	7.0	1.4	7.0	0.9	7.0	0.5	7.0	0.2
	−0.5	7.0	9.8	7.0	7.4	7.0	6.2	7.0	5.1	7.0	4.5	7.0	3.4	7.0	2.2					Not tested.					
	−1.0	7.0	8.9	7.0	7.3	7.0	5.8	7.0	4.9	7.0	4.1	7.0	2.4	7.0	1.6										
	−1.5	6.5	8.2	7.0	6.1	7.0	4.9	7.0	4.1	7.0	3.5	7.0	2.1	7.0	1.1										
8	0.0	8.0	12.4	8.0	8.5	8.0	7.1	8.0	6.5	8.0	5.2	8.0	4.1	8.0	2.7	8.0	2.1	8.0	1.6	8.0	1.0	8.0	0.5	8.0	0.3
	−0.5	8.0	11.4	8.0	8.0	8.0	6.7	8.0	5.7	8.0	4.6	8.0	3.4	8.0	2.2					Not tested.					
	−1.0	8.0	10.5	8.0	7.3	8.0	5.1	8.0	5.1	8.0	4.2	8.0	2.5	8.0	1.8										
	−1.5	8.0	9.1	8.0	6.9	8.0	4.6	8.0	4.6	8.0	3.6	8.0	2.2	8.0	1.2										

f_I , Input Frequency; ξ_I , Input Damping; f_M , Measured Frequency; ξ_M , Measured Damping.

frequencies are listed in the columns with the label f_M which is evaluated based on the Fast Fourier Transform (FFT) of the measured response. From this table, it can be observed that with the increase of the mass ratio, the difference of input and output frequency increases. The largest difference between the input and measured frequencies was 6.8%, which was observed from the test cases M_R -1 when the input frequency was 6 Hz. For test cases from M_R -3 to M_R -12 (i.e., mass ratio less than 12.9%), the maximum frequency error is 0.3%. From this observation, it can be concluded that the mass ratio influences the frequency error. If the mass ratio is below a certain threshold (e.g., 12.9% in this study), the frequency error is negligible.

Apparent Damping

The observed apparent damping ratio is evaluated from the measured displacement signal by assuming logarithmic decay. Table 2 shows the apparent damping ratio for different frequencies, numerically defined damping ratios and mass ratios. Figure 7A shows the relationship between the mass ratio and measured damping ratios. The input damping for this figure is zero, and the input frequencies are 4.0, 6.0, and 8.0 Hz. The predicted damping ratio from Eq. (21), which is calculated based on the time delay of 23 ms observed in the white noise test (as discussed in section “White Noise Test and Cyclic Test”) and the input frequency, is also presented in solid lines. Figure 7A shows that the trend is similar in the measured damping ratio and the predicted damping ratio and that the damping ratio increases as the mass ratio increases. The discrepancy between the measured damping ratio and the predicted damping ratio would have resulted from one or more of the following: the frequency

error, an inconsistent delay in each test, energy dissipation from swivel joint, or the numerical evaluation of the damping ratio from the measured time-series data. When the damping ratio is large, the response decays quickly. Thus, using only a few data points to fit the logarithmic decay curve would result in an error estimating the damping ratio.

Figure 7B compares the predicted damping ratio using Eq. (21) added to the input damping ratio, ξ_I , in Table 2, against the measured damping ratios from all tests. It can be observed from the figure that the predicted and measured damping ratios are well-correlated with an average slope of 0.93. The discrepancy between the predicted and measured damping ratios deserves further investigation, especially after reducing the delay in the actuator’s response and reducing the mass of the moving parts in the experimental apparatus.

REAL-TIME AEROELASTIC HYBRID SIMULATION (RTAHS)

RTAHS is performed with the building model introduced in section “Experimental Setup.” The building model is a 1:400 scale model of a prototype structure with a height of 300 m. A total of 45 RTAHS tests were conducted by controlling several parameters, as summarized in Table 3. Two mass ratios, 6.7 and 5% were chosen for this study, which corresponds to effective mass density ratios of 551 and 735. These mass density ratios are greater than mass density ratios of typical high-rise buildings. Because the objective of the tests is to validate the hybrid simulation method, rather than evaluating the wind response

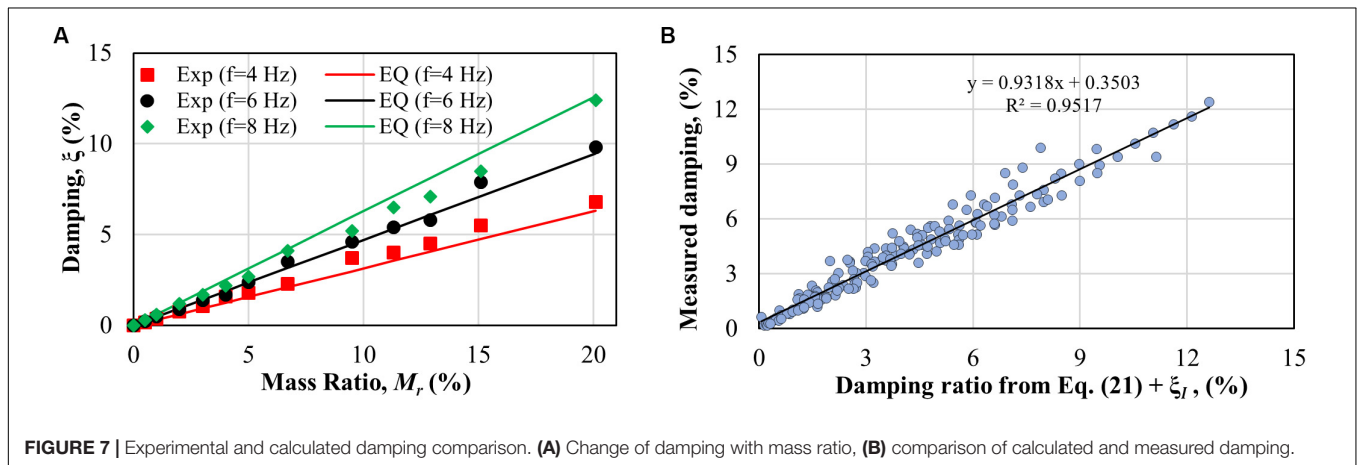


FIGURE 7 | Experimental and calculated damping comparison. (A) Change of damping with mass ratio, (B) comparison of calculated and measured damping.

TABLE 3 | Parameters for real-time and conventional aeroelastic hybrid simulation.

Test ID	Height, h (mm)	Width, B (mm)	Length, L (mm)	Effective mass density ratio, $\frac{\rho_s}{\rho_a}$	Experimental mass, I_E (kg-mm ²)	Numerical mass, I_N (kg-mm ²)	Input Frequency, f_I (Hz)	Target damping ratio, ξ_T (%)	Mass ratio, M_R (%)	Target mass damping parameter, $\delta = \frac{\rho_s \xi_T}{\rho_a}$	Wind velocity (m/s)
R-1	750	75	75	551	35,900	447,800	4.2, 6.0, and 8.0	1.5	6.7	8.27	4, 5, 6, 7, 8, and 9
R-2				551		447,800		1.25	6.7	6.88	4, 5, 6, 7, 8, and 9
R-3				735		626,000		0.8	5.0	5.88	5, 6, and 7
C				191	185,614		6.18	1.1	N/A	2.10	4, 5, 6, 7, 8, and 9

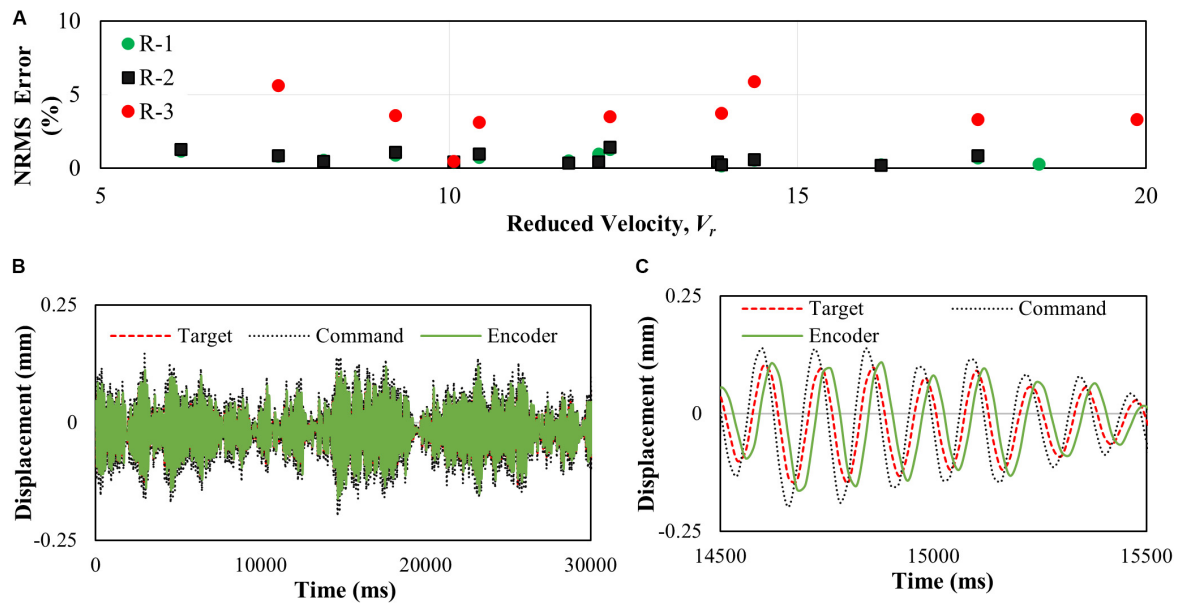


FIGURE 8 | Accuracy of the developed system. **(A)** Amplitude error, **(B)** time history for real-time hybrid simulation, **(C)** zoom-in view of time history for a real-time hybrid simulation.

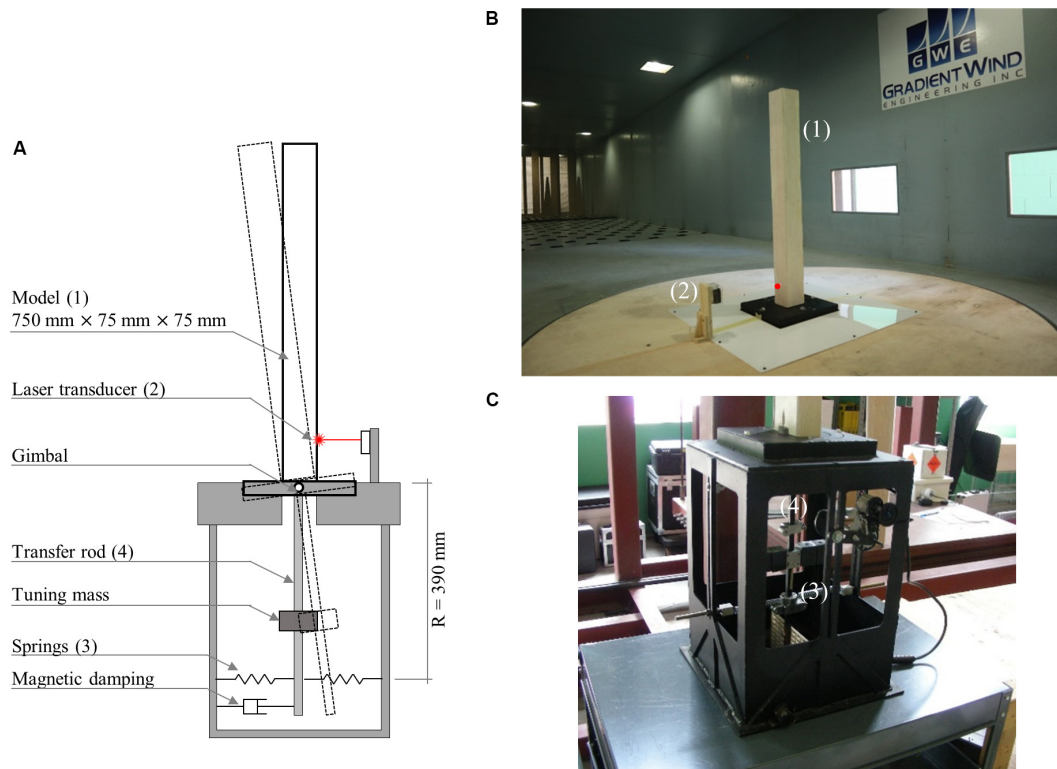


FIGURE 9 | Conventional aeroelastic test for buildings. **(A)** Schematic configuration, **(B)** base-pivoting model in wind tunnel, and **(C)** aeroelastic test rig (the lower part with spring, mass and damper).

of a specific building, the effective mass density ratios were deemed appropriate. Because of the presence of the damping introduced in the delay, the damping coefficient in Eq. (1) is

adjusted to achieve a target damping ratio. The target damping ratio $\xi_T(\%)$ for the RTAHS cases R-1, R-2, and R-3 are 1.5, 1.25, and 0.8%, respectively. Three different frequencies, 4.2, 6.0, and

8.0 Hz, are used to perform the RTAHS. The mean wind velocity measurements at the top of the building model are 4, 5, 6, 7, 8, and 9 m/s for cases R-1 and R-2, and 5, 6, and 7 m/s for the R-3 case. The RTAHS is performed by considering open terrain for the considered building.

The normalized root means square (NRMS) error of the measured displacement is calculated to confirm that the linear motor is achieving the target displacement accurately. In the current RTAHS, most tests have an NRMS error of less than 5%, as shown in **Figure 8A**. In most cases, the NRMS error is less than 2%, which confirms that the linear motor follows the command without significant error. The displacement history record for an RTAHS case (R-1 with a frequency of 8 Hz and wind velocity 9 m/s) is shown in **Figures 8B,C**. These figures also confirm that the linear motor follows the target command properly with a certain level of delay.

Validation of the Test Result

In order to validate the RTAHS method, the test results are compared against conventional aeroelastic tests with the same building model, and also against the available test results in Kato and Kanda (2014). The properties of the conventional aeroelastic test specimen are summarized in **Table 3**. The conventional aeroelastic test was performed by considering an effective mass density, $\frac{\rho_s}{\rho_a}$, of 191 where ρ_a is the density of the air, structural damping ratio, ζ , of 1.1%, and frequency of 6.18 Hz. In the conventional aeroelastic test, two linear springs with stiffness of 0.92 N/mm are fixed to the supporting frame, as shown in **Figure 9A**. A mass is attached to the rod, which can move vertically to tune the frequency of the model. A magnetic damper based on eddy current damping is attached at the base, which can be adjusted to tune the damping coefficient. The illustration for the overall configuration and experimental setup is shown in **Figure 9**.

The response of a building model under wind load depends on the mass-damping parameter, δ , and the reduced (or normalized) wind velocity. The mass-damping parameter is defined as below:

$$\delta = \frac{\rho_s}{\rho_a} \zeta \quad (23)$$

where ρ_s is the mass density of the building, ρ_a is the air density and ζ the structural damping ratio. As shown in Eq. (23), higher damping and higher structural mass lead to a higher mass-damping parameter. Thus, a smaller structural response is expected with a higher mass-damping parameter. The mass-damping parameters, δ , for the conventional aeroelastic test, and R-1 and R-3 of RTAHS are 2.1, 5.88, and 8.27, respectively, whereas the mass-damping parameter of the test results in Kato and Kanda (2014) is 2.0.

The reduced velocity (V_r) is a dimensionless parameter, which is defined as the ratio of the mean wind speed (u) to the frequency (f) and width (b) of the building:

$$V_r = \frac{u}{fb} \quad (24)$$

The wind velocity for the conventional aeroelastic tests varies from approximately 4–9 m/s, which corresponds to the reduced

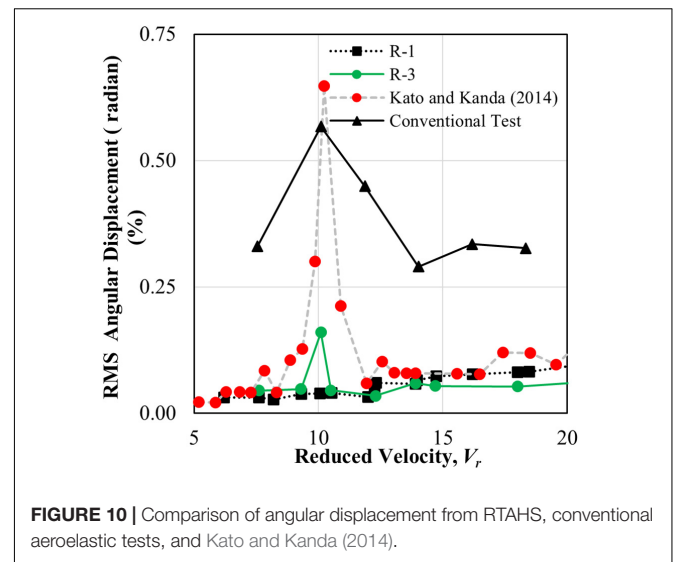


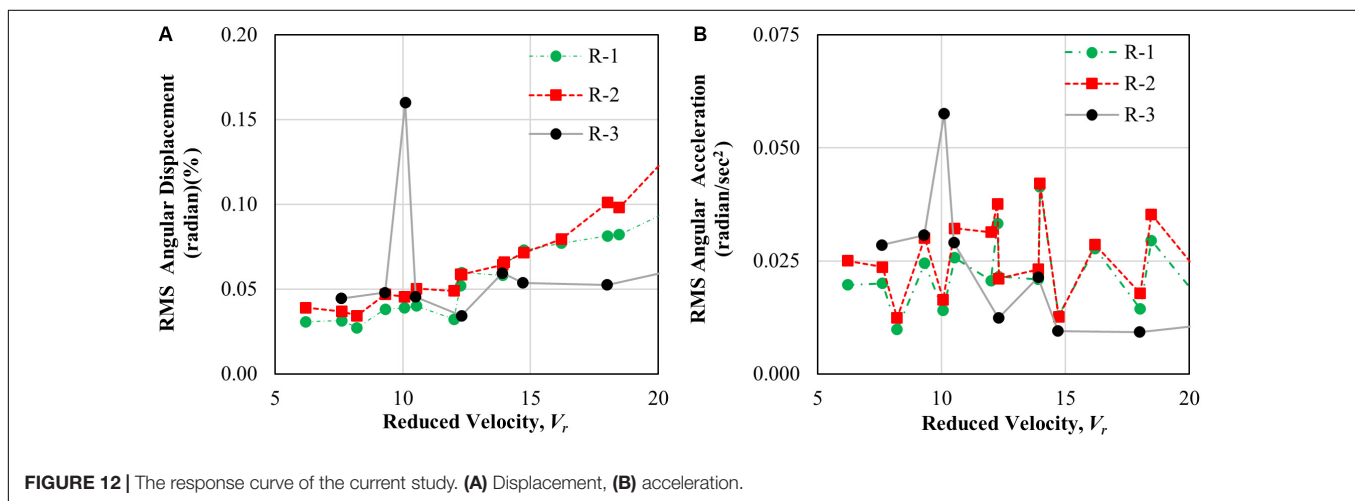
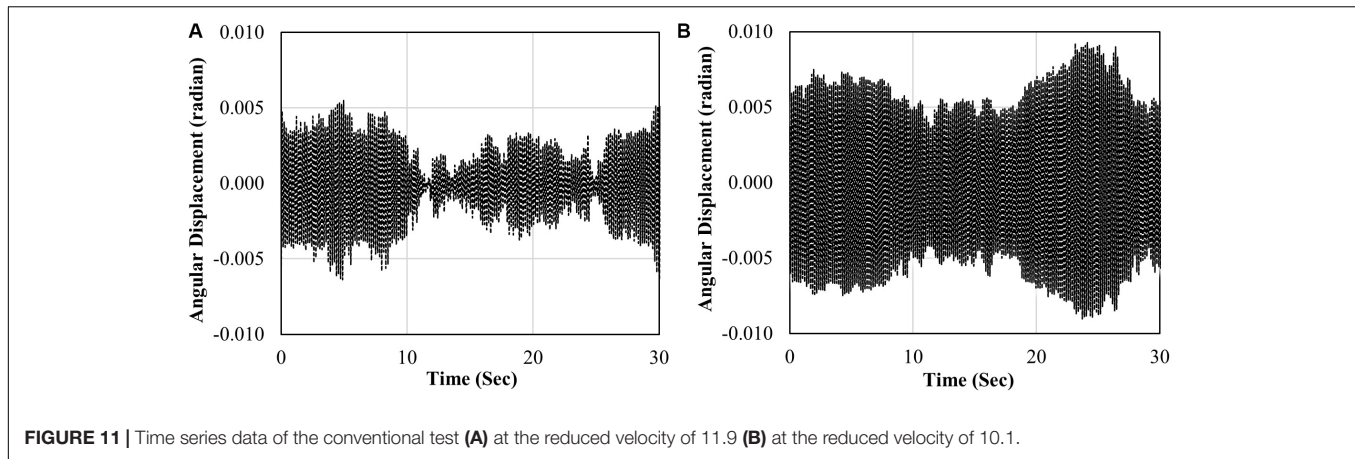
FIGURE 10 | Comparison of angular displacement from RTAHS, conventional aeroelastic tests, and Kato and Kanda (2014).

velocity, V_r , from 8.61 to 19.41. The vibration amplitude of the model is measured with two laser displacement transducers.

Figure 10 compares the RMS angular response of the specimen from four different test cases. Because the test cases have different characteristic mass-damping parameters, it is difficult to directly compare the absolute values of response from the RTAHS, the conventional test and the results reported in Kato and Kanda (2014). Nevertheless, the tendency of the responses as a function of reduced velocity and as a function of the mass-damping parameter can be qualitatively compared. Because the RTAHS R-1 has a higher mass-damping parameter, it shows little angular vibration amplitude compared to the other three cases.

In the case of conventional tests, the vortex-induced vibration phenomenon is not clearly visible, unlike the results from Kato and Kanda (2014), which have similar mass-damping parameters. In addition, the vibration amplitude of conventional tests is relatively large, not only in the vortex-induced vibration region but also in other wind velocity regions. In order to analyze the conventional test results in detail, the vibration results at the reduced velocity of 10.1 and 11.9 are plotted in **Figure 11**. **Figure 11A** shows the measured rotation angle history from the conventional aeroelastic test at a reduced velocity of 11.9. The peak-factor of the vibration at that velocity is 3.2, which is within the range of 3–4 observed in the buffeting response. Thus, it is speculated that the relatively large response of the conventional tests is due to the buffeting response of the specimen. The result at the reduced velocity of 10.1 in **Figure 11B** shows that the vibration is in an almost steady-state. Because the peak-factor value for this case is 2.5, it seems that the vortex-induced vibration was not fully generated for the conventional aeroelastic test.

The cases R-1 and R-3 show little response in most regions in comparison with the conventional aeroelastic test due to the high-mass damping parameters. Case R-3 showed a larger response at the reduced velocity of around 10, which coincides with the reduced velocity when the conventional test and the results from Kato and Kanda (2014) showed peak response.



This reduced velocity is due to vortex shedding. The reason why vortex-induced vibration did not occur in the R-1 case can be explained by the mass-damping parameter, which is consistent with Cheng et al. (2002), where it was found that the vortex-shedding effect is not manifested when the mass-damping parameters are equal to or greater than 6.28.

The Response Curve for Angular Displacement and Acceleration

Figures 12A,B present the RMS angular displacements and RMS angular acceleration as functions of the reduced velocity, respectively. For the RTAHS test case, as well as R-1 and R-2, the effective mass density ratio of the building is 551. The considered damping ratios for R-1 and R-2 are 1.5 and 1.25%, respectively, as summarized in Table 3. The mass-damping parameter for the R-1 and R-2 is 8.27 and 6.88, respectively. For the case of R-3, the vortex shedding happened at a reduced velocity of 10.1, with the magnitude of the angular displacement being 0.16%. The vortex shedding effect for R-1 and R-2 is not observed in this study since the cases have a higher mass-damping parameter. In buildings with a mass-damping parameter greater than or equal to 6.28, the vortex shedding effect does not occur (Cheng et al., 2002). The maximum angular acceleration observed at the vortex shedding

condition is 0.058 rad/sec^2 for test case R-3, and at reduced wind speed, it was observed to be 10.1. The RMS angular acceleration is obtained from the RMS angular displacement, using Eq. (25). In this equation, T is the fundamental period of the structure.

$$\ddot{\theta}_{rms} = \frac{\theta_{rms}}{T^2} \quad (25)$$

CONCLUSION

This study presents a new design of an experimental apparatus for real-time aeroelastic hybrid simulation of a base-pivoting building model. The experimental apparatus mainly consists of a linear motor, a motor driver, a real-time controller, and transducers. The inverse delay compensation scheme is adopted to reduce the actuator time delay. A series of preliminary tests and RTAHS tests are carried out. The following are the main findings from the tests:

- From white noise tests, the delay in the linear motor was about 29 ms when delay compensation was not used. It is speculated that the constant delay could have been reduced if PID gains were further optimized.

- With the presence of 29 ms of constant delay, the inverse delay compensation scheme was used. The delay was reduced to 23 ms when $\alpha = 3$, without having an amplitude error. It was expected that when the value of α was 6, the phase and amplitude error should be small. However, the experimental results showed an increase in the amplitude error when the value of α was larger than 3. This observation requires further investigation.
- An expression is derived to relate apparent damping, which results from the delay in the motor's response, the physical mass of the specimen and the specified natural frequency of the specimen. Unlike conventional substructuring tests of displacement-dependent elements, the result of the delay is an increase in damping ratio. The free vibration tests confirmed that the measured damping ratios are consistent with the derived equation.
- Based on a series of free vibration tests, it was observed that the delay does not impact the frequency of the system when there is a mass ratio of less than 15%.
- RTAHS tests were conducted to validate the developed system. A relatively large mass-damping ratio was used in the tests. There was only one case (R-3) in which the vortex-induced vibration was observed at the reduced velocity of approximately 10, a result consistent with those from the literature. In other cases (R-1 and R-2), the vortex-induced vibrations were not observed due to a higher mass-damping ratio, which is also consistent with the existing literature.

The main contributions of this study are the noble design of the experimental apparatus, as well as the verification and validation of the implemented control schemes. The RTAHS is beneficial over conventional aeroelastic tests as a user can rapidly define the dynamic characteristic of the system. In addition, RTAHS provides additional benefits. For example, the main program can be further extended by implementing tuned mass damper, tuned liquid damper, or any other supplemental damper models, which will allow rapid prototyping of appropriate damping system to control the vibration of a building subjected to wind load. There are a few topics that remain to be investigated in future studies. Some of the following are currently in progress:

- The gains of the controllers need further calibration to make the system more responsive.
- The observed issue in the inverse delay compensation and the variation of delay at different testing parameters needs to be addressed by implementing an advanced delay compensation method.
- Further systematic RTAHS experiments need to be carried out at low mass-damping ratios.

REFERENCES

- Ahmazadeh, M. (2007). *Real-Time Seismic Hybrid Simulation Procedures for Reliable Structural Performance Testing*. Ph.D. thesis, State University of New York, Buffalo, NY.
- Al-subaihawi, S., Kolay, C., Marullo, T., Ricles, J. M., and Quiel, S. E. (2020). Assessment of wind-induced vibration mitigation in a tall building with

- The configuration shown in **Figure 1** includes a redundant motor controller. Research is in progress to simplify the configuration beyond the design presented in this paper.
- It is necessary to expand the experimental setup to model both along-wind and across-wind vibration by using two linear motors.
- While the impact of delay can be compensated by adjusting numerical damping, the impact of delay can be further reduced by optimizing the design of the moving part of the experimental setup to reduce the mass ratio.

DATA AVAILABILITY STATEMENT

All datasets generated for this study are included in the article/supplementary material.

AUTHOR CONTRIBUTIONS

MM designed the testing apparatus, conducted the tests, and drafted the manuscript. YH contributed to the implementation of the control scheme and configuration of the RTAHS. O-SK and H-KK supervised the research. UJ provided practical advice on aeroelastic tests, proposed a range of testing parameters, and provided supports in fabrication and testing in the wind tunnel facility. All authors contributed to the article and approved the submitted version.

FUNDING

The equipment for the research was funded by the Natural Sciences and Engineering Research Council of Canada (NSERC) Research Tools and Instruments grant (RTI-2017-00471). The students and the tests at the wind tunnel facility were funded through the Ontario Centres of Excellence (OCE) VIP I Grant (#30735) and NSERC Engage Grant (EGP 530176-18). MM was partially funded by the NSERC Alexander Graham Bell Canada Graduate Scholarship-Doctoral (CGS D).

ACKNOWLEDGMENTS

We are grateful to Mr. Marco Aulla Villacres and Mr. Junyan Xiao, Ph.D. students at the University of Toronto, for providing supports during the testing at the GWE wind tunnel facility. We would like to acknowledge the technical staff at the Gradient Wind Engineering for their assistance during the RTAHS tests.

damped outriggers using real-time hybrid simulations. *Eng. Struct.* 205:10044. doi: 10.1016/j.engstruct.2019.110044

Aly, A. M. (2013). Pressure integration technique for predicting wind-induced response in high-rise buildings. *Alexandria Eng. J.* 52, 717–731. doi: 10.1016/j.aej.2013.08.006

Amin, J. A., and Ahuja, A. K. (2010). Aerodynamic modifications to the shape of the buildings: a review of the state-of-the-art. *Asian J. Civ. Eng.* 11, 433–450.

- Botelho, R. M., and Christenson, R. E. (2017). "Dynamics of coupled structures," in *Proceedings of the 35th IMAC, A Conference and Exposition on Structural Dynamics*, eds M. S. Allen, R. L. Mayes, and D. J. Rixen (Cham: Springer International Publishing), 4. doi: 10.1007/978-3-319-54930-9
- Chae, Y., Kazemibidokhti, K., and Ricles, J. M. (2013). Adaptive time series compensator for delay compensation of servo-hydraulic actuator systems for real-time hybrid simulation. *Earthq. Eng. Struct. Dyn.* 42, 1697–1715. doi: 10.1002/eqe.2294
- Chen, C. (2007). *Development and Numerical Simulation of Hybrid Effective Force Testing Method*. Ph.D. thesis, Lehigh University, Bethlehem, PA.
- Chen, C., Ricles, J., Marullo, T., and Mercan, O. (2009). Real-time hybrid testing using the unconditionally stable explicit CR integration algorithm. *Earthq. Eng. Struct. Dyn.* 38, 23–44. doi: 10.1002/eqe.838
- Chen, C., Ricles, J. M., Karavasilis, T. L., Chae, Y., and Sause, R. (2012). Evaluation of a real-time hybrid simulation system for performance evaluation of structures with rate dependent devices subjected to seismic loading. *Eng. Struct.* 35, 71–82. doi: 10.1016/j.engstruct.2011.10.006
- Cheng, C. M., Lu, P. C., and Tsai, M. S. (2002). Acrosswind aerodynamic damping of isolated square-shaped buildings. *J. Wind Eng. Ind. Aerodyn.* 90, 1743–1756. doi: 10.1016/S0167-6105(02)00284-2
- Christenson, R., Lin, Y., Emmons, A., and Bass, B. (2008). Large-scale experimental verification of semiactive control through real-time hybrid simulation. *J. Struct. Eng.* 134, 522–534. doi: 10.1061/(ASCE)0733-94452008134:4(522)
- Dragoiescu, C., Garber, J., and Kumar, K. S. (2006). A comparison of force balance and pressure integration techniques for predicting wind-induced responses of tall buildings. *Struct. Congr.* 2006, 1–10. doi: 10.1061/40889(201)14
- Duthinh, D., and Simiu, E. (2011). The use of wind tunnel measurements in building design. *Wind Tunnels and Experimental Fluid Dynamics Research*. 281–300. doi: 10.5772/18670
- Elshaer, A., Bitsuamlak, G., and El Damatty, A. (2015). "Vibration control of tall buildings using aerodynamic optimization," in *Canadian Congress of Applied Mechanics*, At London, ON, doi: 10.13140/RG.2.1.1703.3120
- Guo, J. W. W., Ashasi-Sorkhabi, A., Mercan, O., and Christopoulos, C. (2017). Real-time hybrid simulation of structures equipped with viscoelastic-plastic dampers using a user-programmable computational platform. *Earthq. Eng. Eng. Vib.* 16, 693–711. doi: 10.1007/s11803-017-0408-7
- Huang, X., and Kwon, O.-S. (2018). A generalized numerical/experimental distributed simulation framework. *J. Earthq. Eng.* 24, 682–703. doi: 10.1080/13632469.2018.1423585
- Kammula, V., Erochko, J., Kwon, O., and Christopoulos, C. (2014). Application of hybrid-simulation to fragility assessment of the telescoping self-centering energy dissipative bracing system. *Earthq. Eng. Struct. Dyn.* 43, 811–830. doi: 10.1002/eqe.2374
- Kanda, M., Kawaguchi, A., Koizumi, T., and Maruta, E. (2003). A new approach for simulating aerodynamic vibrations of structures in a wind tunnel—development of an experimental system by means of hybrid vibration technique. *J. Wind Eng. Ind. Aerodyn.* 91, 1419–1440. doi: 10.1016/j.jweia.2003.07.002
- Kanda, M., Koizumi, T., and Maruta, E. (2006). Numerical integration scheme for hybrid vibration technique. *J. Wind Eng.* 31, 1–14. doi: 10.5359/jwe.31.1
- Kareem, A., Kijewski, T., and Tamura, Y. (1999). Mitigation of motions of tall buildings with specific examples of recent applications. *Wind Struct. An Int. J.* 2, 201–251. doi: 10.12989/was.1999.2.3.201
- Kato, Y., and Kanda, M. (2014). Development of a modified hybrid aerodynamic vibration technique for simulating aerodynamic vibration of structures in a wind tunnel. *J. Wind Eng. Ind. Aerodyn.* 135, 10–21. doi: 10.1016/j.jweia.2014.09.005
- Kim, W., Yi, J., Tamura, Y., and Ohtake, K. (2016). *Aerodynamic Damping of Helical Shaped Super Tall Building*. Jeju Island: Advance in Civil, Environmental, and Material Research (ACEM 16).
- Kwon, O.-S., Kim, H.-K., Jeong, U. Y., Hwang, Y.-C., and Moni, M. (2019). "Design of experimental apparatus for real-time wind-tunnel hybrid simulation of bridge decks and buildings," in *Proceedings of ASCE Structures Congress* (Orlando, FL), 235–245. doi: 10.1061/9780784482247.022
- Mendis, P., Ngo, T., Haritos, N., Hira, A., Samali, B., and Cheung, J. (2007). Wind loading on tall buildings. *EJSE Spec. Issue Load. Struct.* 3, 41–54.
- Mercan, O., and Ricles, J. M. (2009). Experimental studies on real-time testing of structures with elastomeric dampers. *J. Struct. Eng.* 135:1124. doi: 10.1061/(ASCE)0733-94452009135:91124
- Mojiri, S., Kwon, O., and Christopoulos, C. (2019). Development of a ten-element hybrid simulation platform and an adjustable yielding brace for performance evaluation of multi-story braced frames subjected to earthquakes. *Earthq. Eng. Struct. Dyn.* 48, 749–771. doi: 10.1002/eqe.3155
- Mortazavi, P., Huang, X., Kwon, O., and Christopoulos, C. (2017). *Example Manual for University of Toronto Simulation (UT-SIM) Framework. An open-source framework for Integrated Multi-Platform Simulations for Structural Resilience*, 2nd Edn. Toronto, ON: University of Toronto.
- Nishi, M., and Kanda, M. (2010). "Application of hybrid experimental technique for simulating aerodynamic vibration of structures in a wind tunnel," in *The Fifth International Symposium on Computational Wind Engineering*, Chapel Hill, NC.
- Pozzuoli, C. (2012). *Aeroelastic Effects on Tall Buildings: Performance-Based Comfort Analysis*. Ph.D. Thesis, University of Braunschweig, Braunschweig.
- Schellenberg, A. H., Mahin, S. A., and Fenves, G. L. (2009). "Advanced implementation of hybrid simulation," in *Pacific Earthquake Engineering Research Center*, (Berkeley, CA: University of California).
- Solum, V. R. (2017). *Real-Time Hybrid Model Testing*. Trondheim: Norwegian University of Science and Technology.
- Sullivan, P. P. (1977). *Aeroelastic Galloping of Tall Structures in Simulated Winds*. Vancouver, BC: University of British Columbia.
- Thepmongkorn, S., Kwok, K. C. S., and Lakshmanan, N. (1999). A two-degree-of-freedom base hinged aeroelastic (BHA) model for response predictions. *J. Wind Eng. Ind. Aerodyn.* 83, 171–181. doi: 10.1016/s0167-6105(99)00070-7
- Wang, X., Kim, R. E., Kwon, O., Yeo, I., and Ahn, J. (2019). Continuous real-time hybrid simulation method for structures subject to Fire. *J. Struct. Eng.* 145:04019152. doi: 10.1061/(ASCE)ST.1943-541X.0002436
- Wu, T., Li, S., and Sivaselvan, M. (2019). Real-time aerodynamics hybrid simulation: a novel wind-tunnel model for flexible bridges. *J. Eng. Mech.* 145, 1–11. doi: 10.1061/(ASCE)EM.1943-7889.0001649
- Wu, T., and Song, W. (2019). Real-time aerodynamics hybrid simulation: wind-induced effects on a reduced-scale building equipped with full-scale dampers. *J. Wind Eng. Ind. Aerodyn.* 190, 1–9. doi: 10.1016/j.jweia.2019.04.005
- Xu, Y. L., and Kwok, K. C. S. (1993). Mode shape corrections for wind tunnel tests of tall buildings. *Eng. Struct.* 15, 387–392. doi: 10.1016/0141-0296(93)90042-3
- Zhao, X., Ding, J. M., and Sun, H. H. (2011). "Structural design of Shanghai tower for wind loads," in *The Twelfth East Asia-Pacific Conference on Structural Engineering and Construction*, *Procedia Eng.* 14, 1759–1767. doi: 10.1016/j.proeng.2011.07.221
- Zhou, Y., Kareem, A., and Gu, M. (2002). Mode shape corrections for wind load effects. *J. Eng. Mech.* 128, 15–23. doi: 10.1061/(asce)0733-9399(2002)128:1(15)
- Zhou, Y., and Kareem, A. (2003). Aeroelastic balance. *J. Eng. Mech.* 129, 283–292. doi: 10.1061/(ASCE)0733-9399(2003)129:3(283)
- Zou, L., Shi, T., Song, J., and Cai, C. S. (2017). Application of the high-frequency base balance technique to tall slender structures considering the effects of higher modes. *Eng. Struct.* 151, 1–10. doi: 10.1016/j.engstruct.2017.08.005

Conflict of Interest: UJ was employed by the company Gradient Wind Engineering Inc.

The remaining authors declare that the research was conducted in the absence of any commercial or financial relationships that could be construed as a potential conflict of interest.

Copyright © 2020 Moni, Hwang, Kwon, Kim and Jeong. This is an open-access article distributed under the terms of the Creative Commons Attribution License (CC BY). The use, distribution or reproduction in other forums is permitted, provided the original author(s) and the copyright owner(s) are credited and that the original publication in this journal is cited, in accordance with accepted academic practice. No use, distribution or reproduction is permitted which does not comply with these terms.



A Reflective Framework for Performance Management (REFORM) of Real-Time Hybrid Simulation

Amin Maghareh^{1*}, Yuguang Fu¹, Herta Montoya², Johnny Condori², Zixin Wang², Shirley J. Dyke^{1,2} and Arturo Montoya³

¹ School of Mechanical Engineering, Purdue University, West Lafayette, IN, United States, ² Lyles School of Civil Engineering, Purdue University, West Lafayette, IN, United States, ³ Department of Civil and Environmental Engineering, The University of Texas at San Antonio, San Antonio, TX, United States

OPEN ACCESS

Edited by:

Chia-Ming Chang,
National Taiwan University, Taiwan

Reviewed by:

Takehiko Asai,
University of Tsukuba, Japan
Richard Christenson,
University of Connecticut,
United States

*Correspondence:

Amin Maghareh
amaghare@purdue.edu

Specialty section:

This article was submitted to
Computational Methods in Structural
Engineering,
a section of the journal
Frontiers in Built Environment

Received: 02 June 2020

Accepted: 18 August 2020

Published: 25 September 2020

Citation:

Maghareh A, Fu Y, Montoya H,
Condori J, Wang Z, Dyke SJ and
Montoya A (2020) A Reflective
Framework for Performance
Management (REFORM) of Real-Time
Hybrid Simulation.
Front. Built Environ. 6:568742.
doi: 10.3389/fbuil.2020.568742

Currently, the lack of (1) a sufficiently integrated, adaptive, and reflective framework to ensure the safety, integrity, and coordinated evolution of a real-time hybrid simulation (RTHS) as it runs, and (2) the ability to articulate and gauge suitable measures of the performance and integrity of an experiment, both as it runs and *post-hoc*, have prevented researchers from tackling a wide range of complex research problems of vital national interest. To address these limitations of the current state-of-the-art, we propose a framework named Reflective Framework for Performance Management (REFORM) of real-time hybrid simulation. REFORM will support the execution of more complex RTHS experiments than can be conducted today, and will allow them to be configured rapidly, performed safely, and analyzed thoroughly. This study provides a description of the building blocks associated with the first phase of this development (REFORM-I). REFORM-I is verified and demonstrated through application to an expanded version of the benchmark control problem for real-time hybrid simulation.

Keywords: real-time hybrid simulation, run-time sensitivity indicator, self-tuning robust control, run-time stability threshold, RTHS, REFORM, real-time control, RTHS framework

INTRODUCTION

Engineers in the coming decades will need to push the boundaries in infrastructure design. New materials, additive construction methods, smart materials and dampers, bio-inspired designs, etc. are being developed to support this vision for an incredible infrastructure of tomorrow. However, realizing the implementation of these novel materials and structure first requires that we provide evidence that they can perform at levels that go well beyond present-day expectations. They must be able to withstand extreme loads under uncertain conditions; they must be proven to sustain the severe loads that earthquakes, hurricanes, tsunamis, and tornadoes frequently impose on our structures (Gardoni and LaFave, 2016). The experiments of today enable the infrastructure of tomorrow. As these transformational concepts are developed for infrastructure systems, the research community demands new testing platforms for dynamic experimentation that are realistic and cost-effective. Experimentation with and validation of such systems within the complex scenarios in which they will operate require a new generation of experimental platforms that are flexible, adaptive, predictive, and safe. As the range of scenarios involving dynamic experimentation

necessarily becomes more complex, it is clear that the experimental platforms required to conduct sufficiently deep investigations of these engineering systems do not yet exist (Condori et al., 2020).

Real-time hybrid simulation (RTHS, hereafter) is a powerful cyber-physical technique for dynamic experimentation that allows researchers to study the complex dynamical behaviors of infrastructure systems in realistic scenarios (Karavasilis et al., 2011; Gao et al., 2013). RTHS couples physical specimens and computational models in a single experiment to simulate a complete structural system. Transfer systems (e.g., hydraulic actuators and shake tables) are used to enforce interface conditions, numerical models are used to simulate the virtual components, and measurements are collected to feed into the numerical model. Control schemes are needed in this closed-loop system to compensate for transfer system dynamics and interactions with physical specimens, ensuring that the entire simulation is conducted safely and in the most realistic manner possible. The entire simulation is executed in real-time (i.e., the test duration is the duration of the extreme event) requiring strict timing guarantees.

Due to deep uncertainties in the physical substructure and transfer system, and the need for aggressive control to maintain stability and safety, advanced non-linear control, uncertainty quantification, estimation and prediction must be employed. Several of these issues have been examined in isolation and thus, RTHS has been a subject for continuous development over the past two decades. For instance, researchers have improved the accuracy and stability of interface condition enforcement, see (Gao et al., 2013; Ou et al., 2015; Palacio-Betancur and Gutierrez Soto, 2019; Tao and Mercan, 2019; Wang et al., 2019; Xu D. et al., 2019). Further, Chae et al. (2013), Chen et al. (2015), Maghareh et al. (2020), and Condori et al. (2020) developed adaptive actuator compensation schemes to achieve improved control of servo-hydraulic systems with non-linearities. Fermandois and Spencer (2017) developed a multi-input, multi-output control design approach with accurate reference tracking and noise rejection. Wallace et al. (2005), Mercan and Ricles (2008), Maghareh et al. (2014), Maghareh et al. (2017), Gao and You (2019), and Xu W. et al. (2019) have also established and validated stability and accuracy metrics to enhance credibility and to encourage much broader applications of RTHS than have been possible to date, for example real-time aerodynamics hybrid simulation by Wu and Song (2019) and Su and Song (2019), experimental testing of spacecraft parachute deployment using RTHS by Harris and Christenson (2019). Nonetheless, despite the potential for using RTHS to conduct low-cost, high-efficiency experiments, the lack of a modular framework that can systematically integrate these existing capabilities, and do so while establishing clear requirements for the safety, integrity, and coordinated evolution of an RTHS experiment, has prevented researchers from tackling a broader range of complex problems.

This study presents the first phase of development and numerical validation of *Reflective Framework for Performance Management* (hereinafter referred to as REFORM) of real-time hybrid simulation. The main objective of this phase of development (REFORM-I) is to define the building blocks and

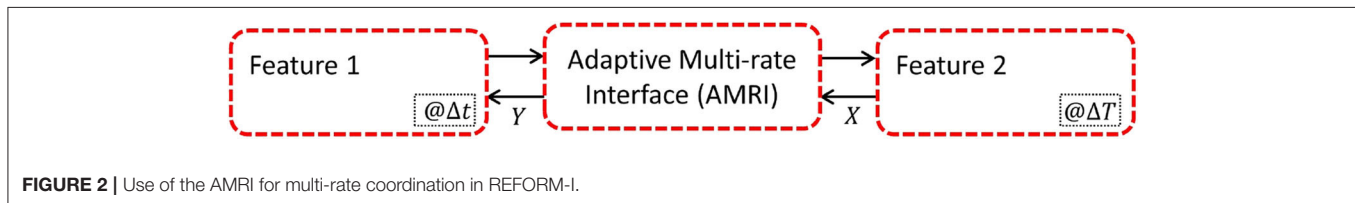
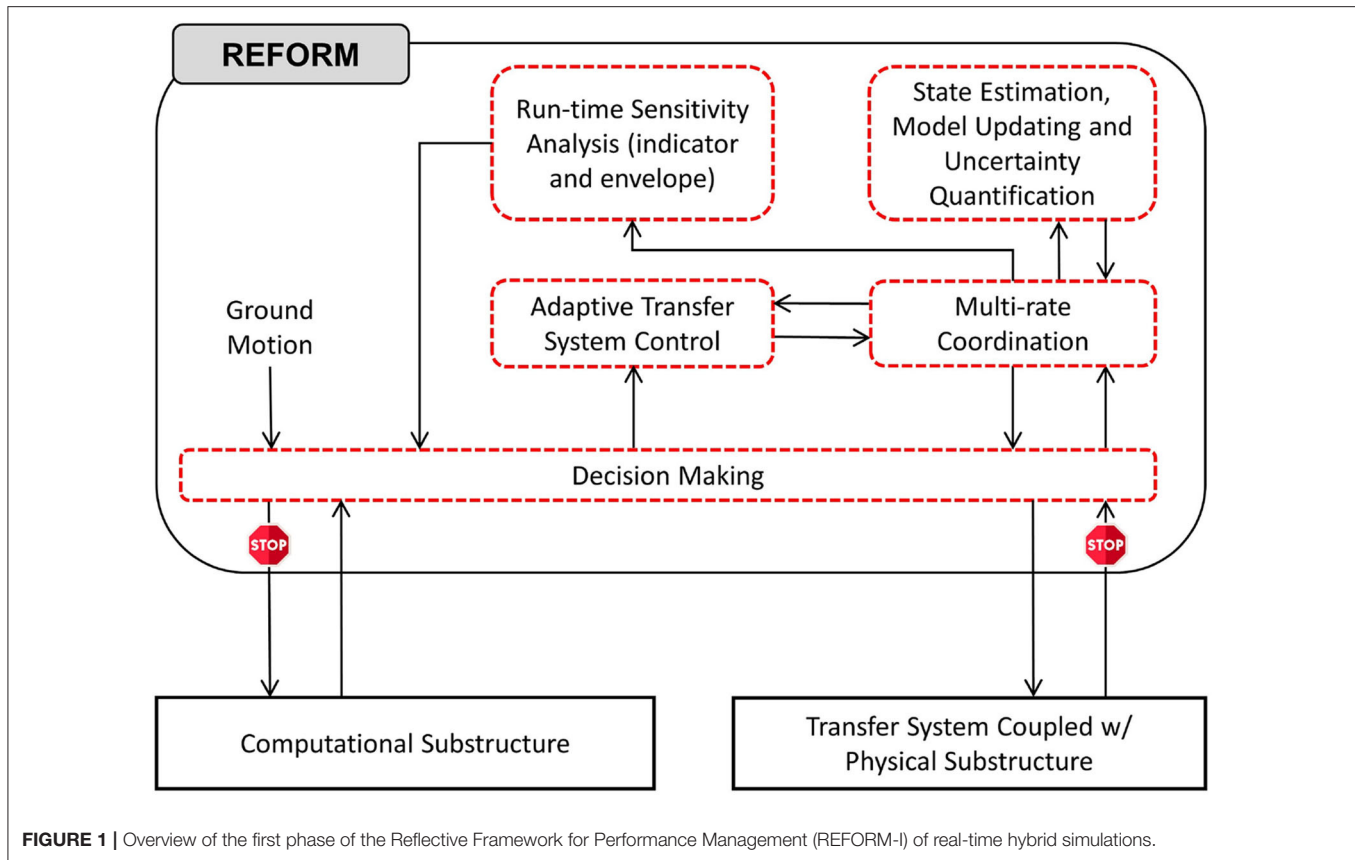
develop a modular architecture that will enable conducting black-box and reference-free experiments safely and with high confidence. A key aspect of this is having the ability to appropriately allocate dedicated resources to control and prediction tasks. In future phases of REFORM development, we will develop and share a highly modular framework capable of (1) exploiting existing prediction, control and model-updating techniques developed by different researchers in the RTHS research community, (2) adapting computational and control workloads and simulation rates, and (3) enabling more challenging and realistic experiments safely and with high confidence. We will make this available through an NSF-funded Research Coordination Network on this topic, known as the Multi-hazard Engineering Collaboratory on Hybrid Simulation (MECHS, <https://mechs.designsafe-ci.org/>).

FRAMEWORK DESCRIPTION

RTHS is intended to minimize the need for full-scale dynamic testing (e.g., shake table testing), and as such, these experiments must be performed without a full physical reference experiment. Thus, simulations are characterized by deep uncertainties in the physical substructure, significant coupling/interaction between the physical and computational substructures, and deep uncertainty in the emergent system behavior. When knowledge of the physical specimen, and therefore the reference structure, is limited, such *black-box* and *reference-free* testing necessitates the use of the latest developments in adaptive and robust control systems, prediction and estimation. REFORM-I is, therefore, broken down into five generic building blocks: (1) multi-rate coordination; (2) transfer system control; (3) state estimation and model updating; (4) run-time indicators; and (5) decision making. **Figure 1** shows an overview of REFORM-I representation and coordination between these building blocks.

Multi-Rate Coordination

In REFORM-I, a multi-rate coordination technique is required to enable users to coordinate the necessary multi-rate functionalities of the various building blocks. This multi-rate coordination block facilitates the use of complex and high-fidelity features. The Adaptive Multi-rate Interface (Maghareh et al., 2016) is utilized to meet this objective. The adaptive multi-rate interface (AMRI, hereafter) was initially developed as a mechanism to facilitate greater fidelity in the computational substructure by running the numerical model at a larger time-interval than what is used for the control system, thereby providing supporting use of a computationally demanding model. In REFORM-I, however, AMRI serves more generally as the multi-rate coordination technique that enable effective communications between feature blocks with different sampling rates, see **Figure 2**. In this method, after selecting a set of orthonormal bases (e.g., polynomial or exponential) sampling frequency ratio between the feature blocks. Then, a synchronized signal is generated by AMRI at the rate of Δt where X is the input signal at coarse time interval ΔT , Y is the output signal at sub-interval Δt , SFR is the sampling frequency ratio ($\Delta T/\Delta t$), k is the number of orthogonal bases used for interpolation, r is the number of points used for



interpolation, p is the compensation coefficient, and $p\Delta T$ is the time to be compensated.

Chebyshev polynomials of the first kind are used as the set of orthonormal bases for interpolation and rate transitioning from ΔT to Δt . The polynomials are defined by the following recurrence relation.

$$\begin{cases} T_1(s) = 1 \\ T_2(s) = s \\ T_{i+1}(s) = 2sT_i(s) - T_{i-1}(s) \end{cases} \quad (1)$$

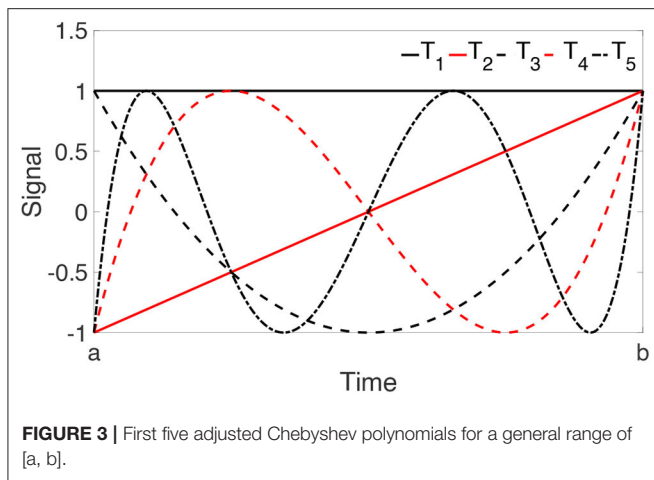
These polynomials are adjusted to be within a general range of $[a, b]$, where, $a = (p + r - 1)\Delta T$ and $b = p\Delta T$. For this adjustment, $s = \frac{2x - (a+b)}{b-a}$ 100 where x corresponds to a dummy variable in the range of $[-1, 1]$, see **Figure 3**. Next, the following linear equation

is solved to obtain $\{\beta_1, \beta_2 \dots \beta_K\}$.

$$\begin{pmatrix} (T_1[(p+1-r)\Delta T] \dots T_k[(p+1-r)\Delta T]) \\ \vdots \\ T_1[(p)\Delta T] \dots T_k[(p)\Delta T] \end{pmatrix}_{r \times k} \times \begin{pmatrix} \beta_1 \\ \beta_2 \\ \vdots \\ \beta_k \end{pmatrix} = \begin{pmatrix} X_{n-r+p+1} \\ \vdots \\ X_n \\ \vdots \\ X_{n+p} \end{pmatrix} \quad (2)$$

Using the β coefficients, the output signal at the coarse time interval Δt can be reconstructed as follows:

$$Y(h) = \beta_1 T_1(h) + \beta_2 T_2(h) + \dots + \beta_k T_k(h) \quad (3)$$



where

$$h \in \{(n + p - 1)\Delta T, (n + p - 1)\Delta T + \Delta t, (n + p - 1)\Delta T + 2\Delta t \dots (n + p)\Delta T\}.$$

Adaptive Transfer System Control

This building block is broken down into two main tasks: (1) developing a physics-based, control-oriented non-linear dynamical model of a multi-actuator transfer system coupled with a non-linear physical specimen; and (2) designing a high-precision self-tuning robust controller to accommodate extensive variations in a non-linear control plant, such as non-stationary behavior or component failure.

In RTHS, controllability is a significant property of the transfer system. The key to modeling the control plant is making realistic assumptions within the operating range of an experiment, maintaining the essential dynamics, and discarding the insignificant ones. A fundamental step before developing a control strategy and designing a control law is realizing existing constraints and making realistic assumptions, for instance, the dynamic interactions between physical substructure and transfer system (a.k.a., control-structure interaction, Dyke et al., 1995) and extensive performance variations and uncertainties associated with the control plant (Maghareh et al., 2018a,b; Condori et al., 2020).

In REFORM-I, we have developed deterministic and stochastic physics-based non-linear dynamical models of a servo-hydraulic transfer system coupled with a non-linear physical specimen. These models have been developed for single- and multi-actuator systems and experimentally validated for a single actuator system coupled with a non-linear physical specimen (Maghareh et al., 2018a,b). Transforming the plant model into a controllable canonical dynamical model makes it appealing for developing more advanced non-linear control systems. Adopting these models becomes especially important in two cases: (1) when control-structure interaction dominates the dynamics of the coupled systems; and (2) when the

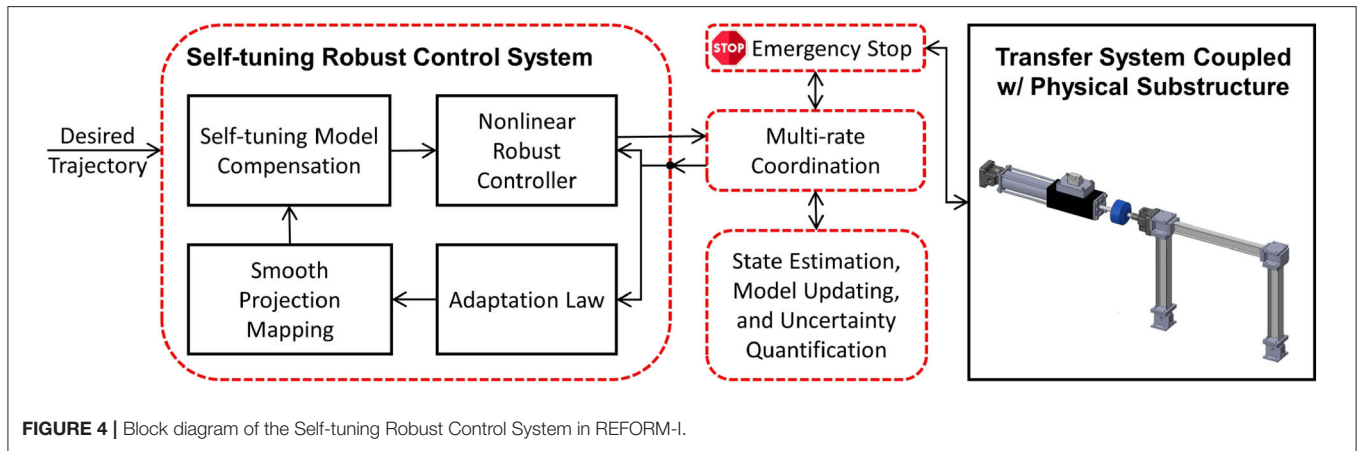
hydraulic system is coupled with a physical specimen with high uncertainty.

The physics-based, non-linear dynamical models of a servo-hydraulic transfer system coupled with a non-linear physical specimen serve as the basis for developing an effective control strategy which accommodate highly uncertain dynamics of the control plant and *control-structure interaction* (Maghareh et al., 2018a,b; Montoya et al., under review). To illustrate the capabilities required in this building block, we use a model-based, multi-layer nonlinear control system (*Self-tuning Robust Multi-directional Control System*, hereinafter referred to as SRCSys) developed by Maghareh et al. (2020) as the adaptive transfer system control strategy, see **Figure 4**. This control strategy has been developed, validated and incorporated in REFORM-I to accommodate extensive performance variations and uncertainties in the physical substructure. Our initial experiments with the Self-tuning Robust Multi-directional Control System also suggest that it has significant promise for complex multi-directional scenarios. SRCSys consists of two layers, robustness and adaptation. The robustness layer synthesizes a non-linear control law such that the closed-loop dynamics perform as intended under a broad range of parametric and non-parametric uncertainties. Then the adaptation layer reduces those uncertainties at run-time through slow and controlled learning of the control plant. SRCSys is developed for single- and multi-actuator transfer systems and experimentally validated for single-actuator RTHS experiments (Maghareh et al., 2020).

Here, the layer of adaption is designed to reduce estimation error, while the stability of the layer of robustness remains intact. In an RTHS experiment, there are parametric and non-parametric uncertainties associated with the control plant. Under certain conditions, the layer of robustness filters out the high frequency unmodeled dynamics in the transfer system (Maghareh et al., 2020). However, unless the parametric uncertainties are gradually reduced at run-time by a self-tuning mechanism, they may cause tracking performance degradation. Thus, the layer of adaptation is to suppress the parametric uncertainties, or the parametric variations—e.g., yielding or internal resonance in the physical substructure—or both, while tracking performance is consistently improving. The control and adaptation laws associated with SRCSys are provided in (Slotine and Li, 1991; Maghareh et al., 2020).

State Estimation, Model Updating, and Uncertainty Quantification

To facilitate run-time model updating and uncertainty quantification, and to eventually develop run-time performance indicators, strategies to improve computational efficiency are essential. RTHS experiments are frequently performed to study unexpected behavior or a part of the physical substructure may experience a failure, drastically changing its dynamics. Such a change will impact the safety and integrity of the experiment. Therefore, the run-time model updating and uncertainty quantification methods adopted must be able to handle such large variations in behavior. The remainder of this section



presents the choices of the particle filter for model updating and uncertainty quantification in REFORM-I.

Various strategies are available for run-time model updating and uncertainty quantification. One conventional approach is to apply an optimization strategy to identify the parameters that minimize the difference between the predicted and measured model properties (e.g., residual-based model updating by Li et al., 2018). However, most of these model updating methods are deterministic, and do not consider uncertainties in the measurements or in the model adopted. In contrast, methods grounded in Bayesian inference determine the distribution of each of the uncertain model parameters based on observations (Zarate et al., 2012). Thus, they not only offer the ability to estimate the model parameters, but they directly facilitate rigorous uncertainty quantification for those parameters and/or states. However, due to high computational cost of such methods, and the lack of efficient sampling schemes using Monte Carlo simulation, they are quite limited for use during run-time in most RTHS experiments (Yang and Lam, 2018). Alternatively, various Bayesian filtering techniques have the potential to support both model updating and uncertainty quantification at run-time (Sarkka, 2013). Typical examples of such techniques include the extended Kalman filter, unscented Kalman filter, and particle filter. After initialization, this class of algorithms support predictive capabilities to estimate the distribution of model parameters or responses at each time step, and update the posterior distribution based on observed data.

The particle filter is a non-parametric, recursive Bayesian state estimator. It represents the posterior probability density function of the states as samples, or particles, with associated weights (Aru, 2007). In this building block, the particle filter is used for parameter estimation, uncertainty quantification, and response prediction, facilitating run-time model updating. The workflow of the particle filter block is illustrated in Figure 5. The particle filter is first initialized by assigning the number of particles and initial conditions (state and covariance). The particles are then sampled from a Gaussian distribution representing the prior density function. Afterwards, particles predict the next state based on an appropriate state transition function. For an illustrative example of the use of the particle filter for parameter

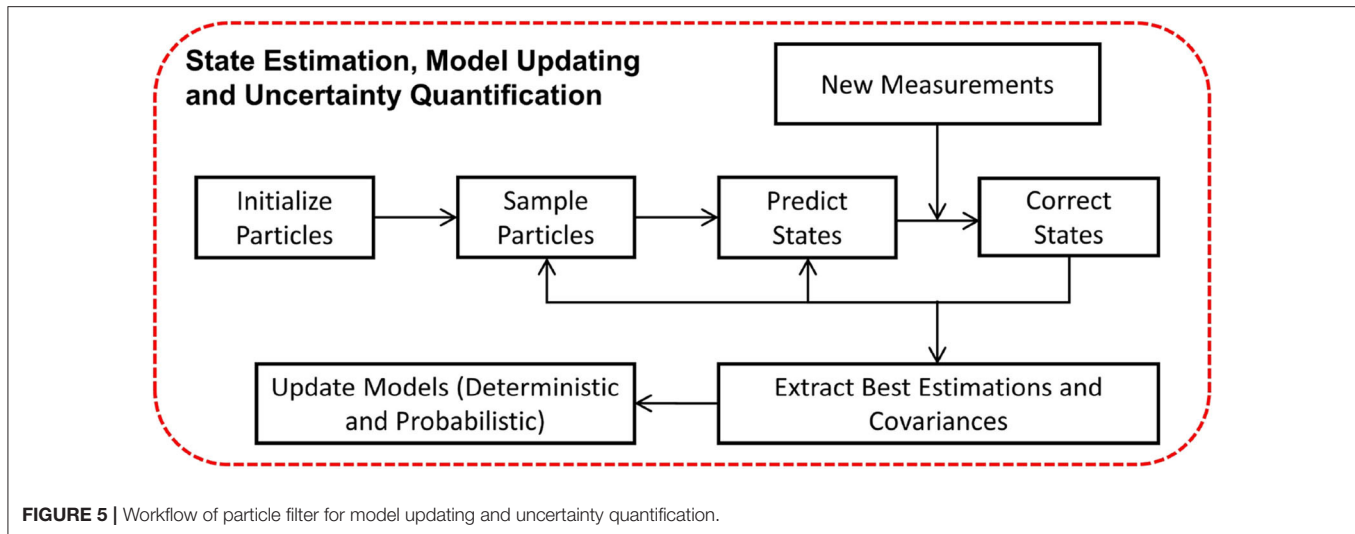
identification in highly non-linear systems (see Condori-Urbe et al., 2019).

To enable black-box RTHS and accommodate extensive variations in the physical specimen, such as non-stationary behavior or component failure, non-linear estimators (e.g., unscented Kalman filters, particle filters) are needed. Run-time execution of such filters enables: (1) estimation of the states and updating of the parameters of the physical specimen model for SRCsSys implementation; and (2) monitoring, in real time, of the overall performance of the dynamic simulation. In REFORM-I, real-time non-linear estimators are developed by adopting a particle filter algorithm that takes advantage of measured displacement and force signals. The particle filter algorithm developed for this building block can serve multiple purposes including: parameter estimation (a.k.a. model updating), uncertainty quantification, and state estimation.

This approach is shown to significantly improve the performance of the real-time control system and accommodates extensive variations in the behavior of the physical specimen (Condori-Urbe et al., 2019). In addition, it enables run-time estimation and associated uncertainties of the model parameters, thus serving as the basis for *run-time sensitivity indicators* and *run-time sensitivity envelope*. However, including computationally-intensive estimation techniques does necessitate the use of the multi-rate coordination block for run-time execution. Further details on the state estimation building block for non-linear systems using the particle filter are provided in Condori-Urbe et al. (2019).

Run-Time Sensitivity Indicator and Stability Threshold

An essential building block in REFORM-I is the run-time thresholds and indicators to facilitate safe and accurate experiments. Stability and accuracy of a particular RTHS configuration are mainly functions of four factor: (1) overall dynamics of the reference structure; (2) fidelity of the computational substructure (related to computational workload and simulation rate); (3) partitioning configuration; and (4) capability to implement interface conditions (related to control workload and simulation rate) (Maghareh et al., 2017).



In this building block, we have established run-time sensitivity indicator, run-time sensitivity envelope, and run-time stability threshold based on the first, third, and fourth factors. To compute the sensitivity indicator, envelope, and the stability threshold on-the-fly, we (1) use updated parameters and associated uncertainties of the physical substructure (from the non-linear estimator in the preceding section); (2) evaluate tracking performance at the interface; and (3) compute critical time delay.

In REFORM-I, we developed the run-time sensitivity indicator based on the knowledge gained in developing predictive (before any testing) stability and performance indicators intended to support the design of challenging RTHS experiments (Maghareh et al., 2014, 2017). For these predictive indicators, the sensitivity in partitioning of any linear or piecewise linear partitioned system to interface desynchronization is computed before the testing. The run-time sensitivity indicator (and run-time sensitivity envelope), however, are computed based on the sensitivity of the potential partitioning associated with the computational substructure and the estimated model (and associated uncertainties) of the physical substructure in real-time. To compute these in real-time, we: (1) characterize the potential critical time delay (i.e., the delay associated with the first occurrence of stability switch in **Figure 6**) associated with a wide and specific range for parametric variations ($\alpha_1, \alpha_2, \dots, \alpha_n$, see **Figure 7**) in the potential physical substructure model using the method developed in Maghareh et al. (2017); (2) update the physical substructure model in real-time using a particle filter; (3) update the uncertainties associated with these parameters; (4) compute, on the fly, the critical time delays (τ_{cr}) associated with virtual frameworks shown in **Figure 6**; and, (5) compute the run-time sensitivity indicator (RSI) and run-time envelope as follows:

$$RSI = -\log_{10}[\tau_{cr}(\text{msec})] \quad (4)$$

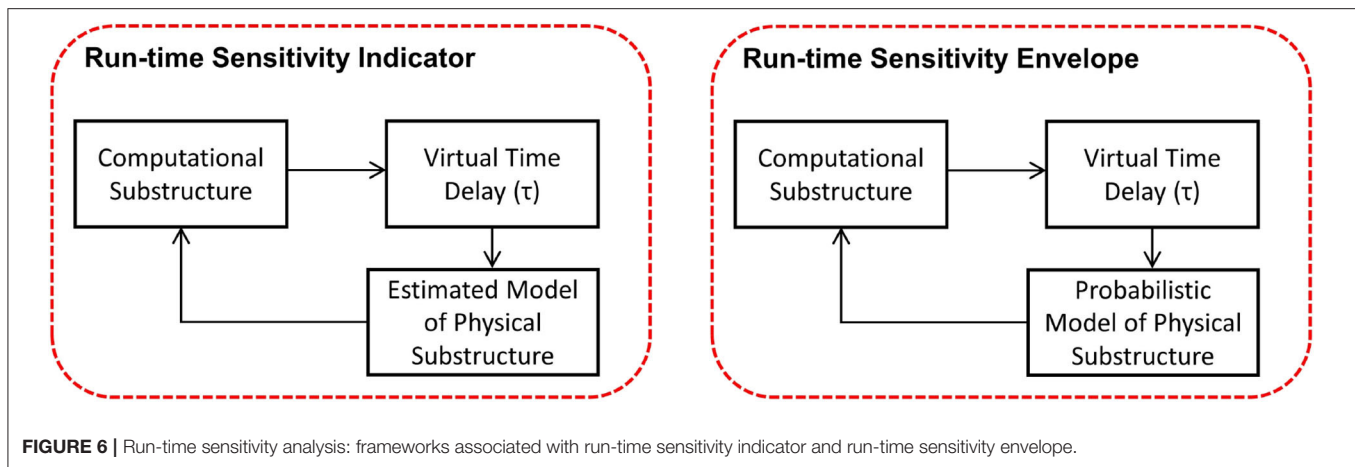
Equation (4) maps $\tau_{cr} \in (0, \infty)$ to the $RSI \in (-\infty, \infty)$. To calculate the run-time sensitivity envelope, however, a vector

of run-time sensitivity indicators (associated with the updated range of parametric variations in **Figure 6** obtained from the particle filter) are computed using Equation (4) and the envelope is constructed based on the maximum and minimum values at each time step.

The run-time stability threshold, however, evaluates tracking performance, in real-time, at the interface between the physical and computational substructures. This threshold is based on two factors: (1) the control strategy, and (2) the actual and instant sensitivity of the experiment. The latter is estimated using the RSI. The remainder of this section discusses the adopted strategy to monitor the run-time stability of the experiment using SRCSys.

In SRCSys, we have broken down the tasks associated with the non-linear tracking problem into two parts (Slotine and Li, 1991; Maghareh et al., 2020): (1) the control law is designed based on defining a compact tracking error. The compact tracking error creates a time-varying hyperplane called boundary layer. As a part of developing the control law, the time-varying boundary layer is designed to be an invariant set; (2) once the time-varying boundary layer is reached, the tracking error is determined, bounded and stability is guaranteed based on Barbalat's lemma (Slotine and Li, 1991).

The control law in the SRCSys is based on the assumption that the uncertainties associated with the dynamics of the plant are bounded. This assumption is aligned with our goal of determining the specific ranges of parametric variations in developing the RSI. In other words, the design of the SRCSys control law also specifies the ranges of parametric variations associated with the physical specimen. During an RTHS experiment, the boundary layer thickness and the compact tracking error over time convey a significant amount of information about whether the specific ranges of parametric variations are suitably chosen or not. A violation of this threshold, i.e., when the compact tracking error breaches the boundary layer, indicates that the stability of the control loop (and therefore the entire simulation) may be compromised. Thus, in REFORM-I the run-time stability threshold is a time-varying metric which is monitored in real-time and computed



as the minimum distance between the compact tracking error and the boundary layer. **Figure 8** demonstrates the real-time computation and visualization of the run-time stability threshold.

REFORM-I is designed to provide a robust control framework without compromising the stability and safety of an RTHS experiment. Together, the run-time stability threshold, the run-time sensitivity indicator and envelope serve as the foundation for evaluating the integrity and safety of an RTHS experiment. During an RTHS experiment using REFORM-I, should the run-time stability threshold become negative, the emergency stop function would be activated and will decouple the computational and physical substructures through switching off the ground excitation signal and the feedback force from the physical substructure to the computational substructure. Thus, the entire simulation will become a simple tracking control problem which tracks a smooth decay signal which is associated with the unforced response of the computational substructure. The purpose of the emergency stop function is to ensure a stable experiment, suppressing any situation in which large actuators could potentially generate dangerous physical instabilities in the lab environment. During an experiment, run-time indicators are used to predict such behavior and trigger the emergency stop function. Upon the activation of the emergency stop, the computational substructure will be decoupled from the transfer system. At the same time, the command signal(s) to the hydraulic actuator(s) will follow a smooth decay signal(s) to a safe state.

NUMERICAL VALIDATION

The RTHS benchmark control problem (Silva et al., 2020) is employed for illustration and numerical validation of the building blocks that comprise REFORM-I. This section is structured as follows. First, we provide a brief overview of the benchmark problem. Next, we describe the three numerical studies considered in this section, and their corresponding virtual-RTHS (vRTHS, hereafter) results.

The Benchmark Control Problem for RTHS

The benchmark control problem considers a laboratory model of a typical frame structure. The model has three stories and two

bays, has pinned connections at the base, and moment-resisting connections with strong-column weak-beam design. A two-dimensional finite element (FE) model is developed using linear elastic models. Simplifying assumptions are made to reduce the order of the FE model from 30 DOF to 3 DOF, lowering the computational complexity of the model. The equation of motion for the reduced order model is referred to as the reference model,

$$M_r \ddot{x} + C_r \dot{x} + K_r x = -M_r \ddot{x}_g \quad (5)$$

where M_r , C_r , and K_r are mass, stiffness, and damping matrices of the reference model, respectively. \ddot{x}_g denotes ground acceleration and x , \dot{x} and \ddot{x} are displacement, velocity, and acceleration vectors, respectively. The reference model is then partitioned into numerical and experimental substructures as shown in **Figure 9**. The red solid lines represent the experimental substructure. Accordingly, the partitioned equation of motion can be expressed as

$$M_n \ddot{x} + C_n \dot{x} + K_n x = -M_r \ddot{x}_g - \underbrace{(M_e \ddot{x} + C_e \dot{x} + K_e x)}_{fe} \quad (6)$$

where the $(\cdot)_n$ and $(\cdot)_e$ subscripts refer to the computational and physical substructures, respectively. System identification is performed using the experimental data to obtain the experimental structural mass ($m_e = 29.1$ kg), lateral stiffness ($k_e = 1.19 \times 10^6$ N/m), and damping coefficient ($c_e = 114.6$ N·s/m). Since the experimental substructure is fixed, several partitioning cases are defined by varying the structural parameters of the reference structure, as shown in **Table 1**. Variations are considered in both the modal damping and the mass of each floor of the reference structure, thus yielding different stability and performance scenarios. Using the predictive stability indicator and the proposed sensitivity classifications (Maghareh et al., 2017), the partitioning configurations associated with Cases 1–3 fall within the slightly sensitive class, while Case 4 falls within the moderately sensitive class. Thus, Cases 1–3 are less sensitive to desynchronization at the interface as compared to Case 4. Further, the predictive indicators reveal that when using the same transfer system control strategy, a researcher should expect somewhat less accuracy in the

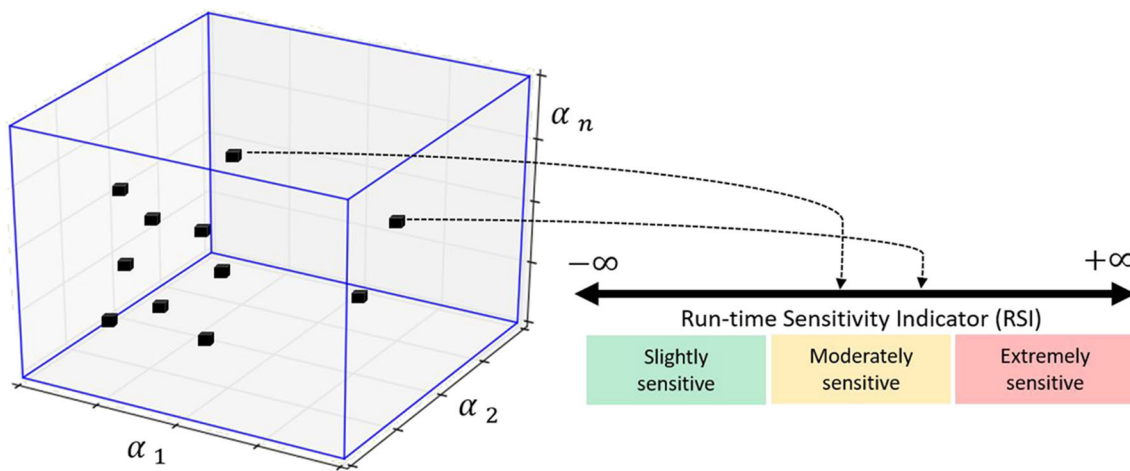


FIGURE 7 | Geometric representation of mapping from an n-dimensional hyperplane associated with varying parameters of the physical substructure model to the RSI. Prior to conducting an experiment, the range of possible values of the RSI is classified, on the basis of system instability as extremely sensitive (red), moderately sensitive (yellow), and slightly sensitive (green) (Maghareh et al., 2017; Silva et al., 2020).

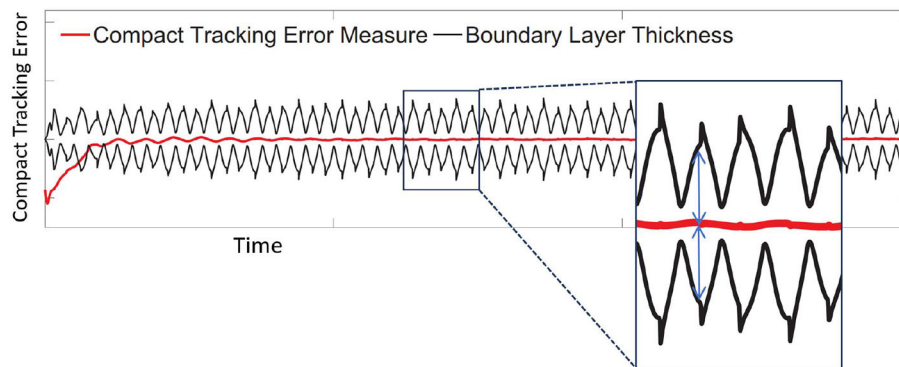


FIGURE 8 | Real-time computation and visualization of the run-time stability threshold.

results associated with Case 4 compared to the results from Cases 1–3. It should be noted that this paper only studies the extreme ones, Case 1 (i.e., the least sensitive case to desynchronization) and Case 4 (i.e., the most sensitive case to desynchronization).

Figure 10 shows the implementation of RTHS using a sample control strategy [i.e., a phase-lead compensator and a proportional-integral (PI) controller] provided by Silva et al. (2020) to demonstrate the problem. The ground input (\ddot{x}_g) and the feedback force vector (f_e) are the inputs of the numerical substructure whose 296 output (y_n) is fed into the tracking controller. The controller generates a command signal to the transfer system. The force at the first floor is measured and fed back to the numerical substructure to construct the force feedback loop (see Equation 6). The displacement output of the experimental substructure is used to form the tracking feedback loop.

Virtual RTHS Studies and Results

This section presents the numerical validation of the building blocks provided in REFORM-I. Because this phase is focused on developing a *modular framework* to enable conducting experiments *safely and with high confidence* by dedicating the appropriate resources to perform the control and prediction tasks, we perform three vRTHS studies using REFORM-I. Study 1 focuses on Cases 1 and 4 in the benchmark problem, as defined previously and in the original problem statement. Then in Studies 2 and 3 we consider a sudden component failure during a vRTHS of Cases 1 and 4. In Study 2 and Study 3, we artificially define a story drift threshold (4.4 mm) at which a failure of one of the experimental columns in the benchmark structure occurs (i.e., k_e drops by 50%). In Studies 1 and 2, we implement the sample linear control strategy provided in the benchmark problem. However, in Study 3, the building blocks provided in REFORM-I are activated to enhance the safety and integrity of the simulation. To quantitatively evaluate the performance of each study, we

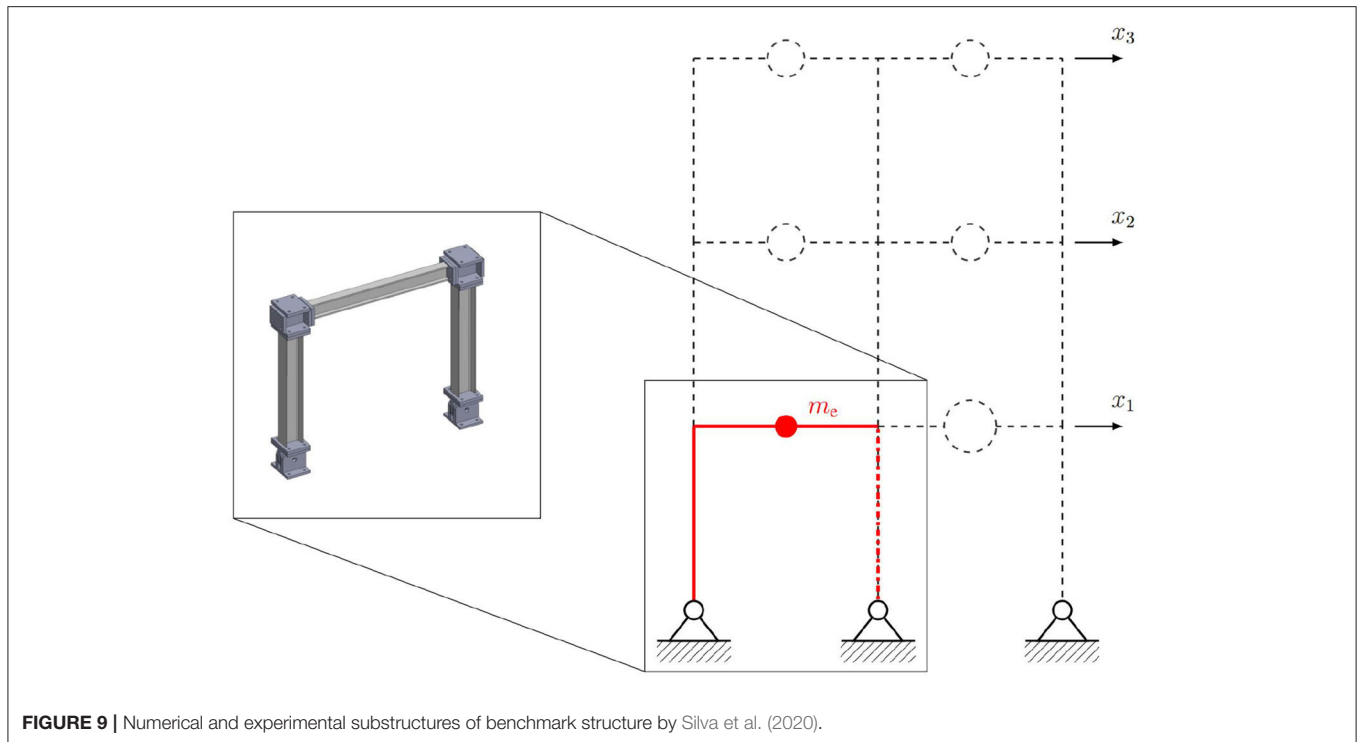


FIGURE 9 | Numerical and experimental substructures of benchmark structure by Silva et al. (2020).

utilize a cumulative normalized error indicator which is a global simulation performance indicator. The cumulative normalized error is defined as follows:

$$\text{CNE}_1(w) = \frac{1}{\max(|x_1^{\text{ref}}|)} \sum_{i=1}^w (|x_1^{\text{vRTHS}}(i) - x_1^{\text{ref}}(i)| \times \Delta t) \quad (7)$$

where CNE_1 , x_1^{vRTHS} , x_1^{ref} , and Δt refer to cumulative normalized error associated with the first floor, virtual-RTHS displacement at the first floor, reference displacement at the first floor, and sub-interval time step which is associated with displacement measurement. Note the cumulative normalized error is extremely sensitive to time desynchronization between the two signals which makes it a suitable error indicator for stability analysis of different systems and configurations.

Figures 11, 12 show the reference model responses, the vRTHS responses and cumulative normalized errors associated with Study 1 (Case 1) and Study 1 (Case 4), respectively. These results match those provided in the RTHS benchmark control problem by Silva et al. (2020). As noted earlier, the results show that the predictive stability indicator (PSI) associated with Case 1 ($\text{PSI} = 1.17$) is greater than that associated with Case 4 ($\text{PSI} = 0.94$), confirming that using the same transfer system control strategy leads to greater global accuracy in Case 1 as compared to Cases 4.

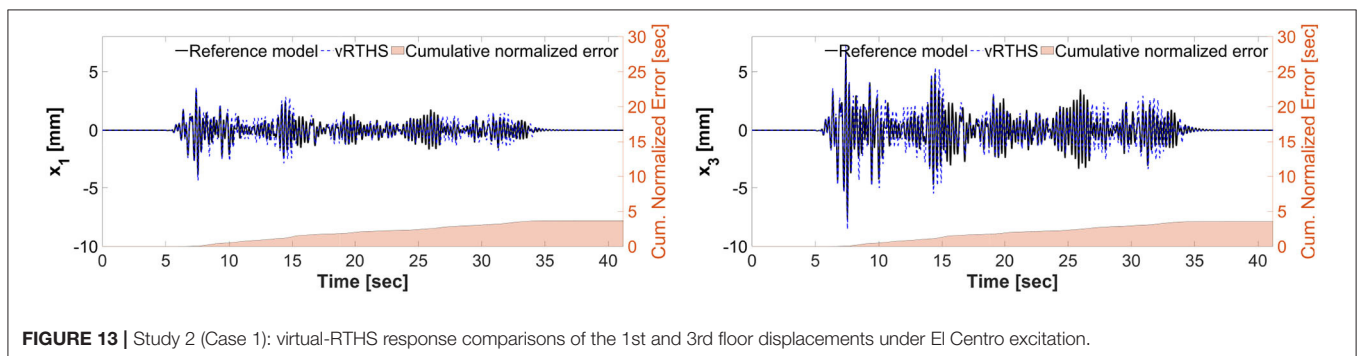
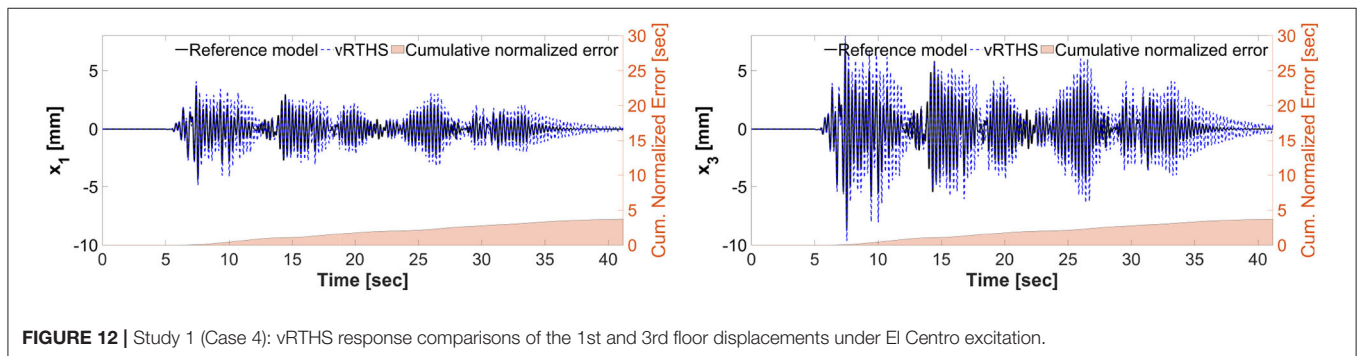
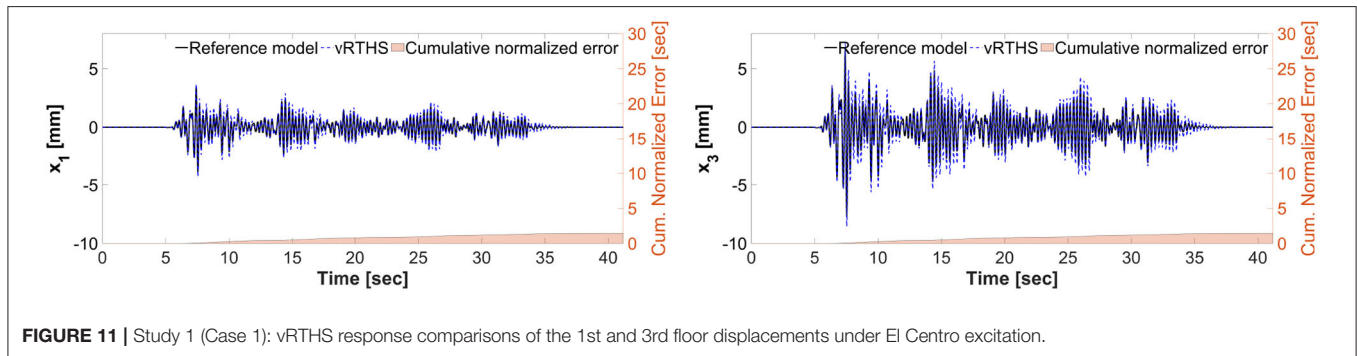
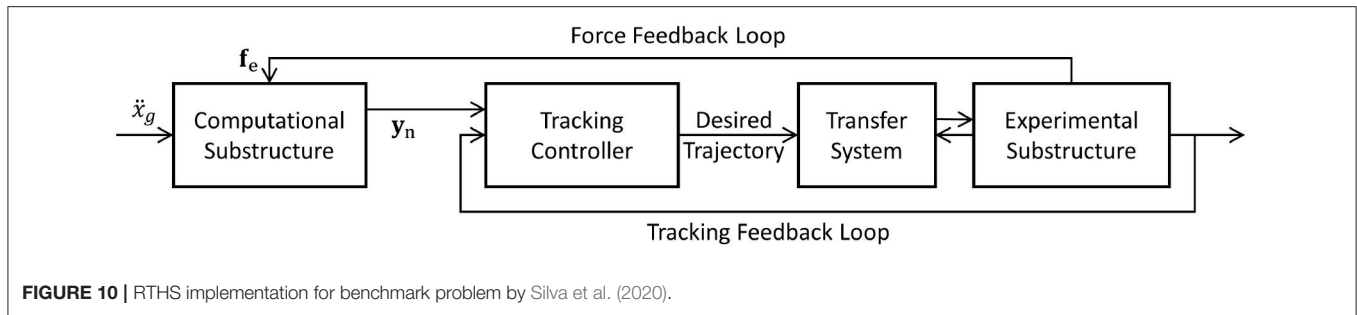
Figures 13, 14 show the reference model responses, the vRTHS responses and cumulative normalized errors associated with Study 2 (Case 1) and Study 2 (Case 4), respectively. In these simulations the lateral stiffness associated with the experimental substructure drops by 50% at 7.53 and 7.48 s,

TABLE 1 | Virtual-RTHS partitioning cases proposed by Silva et al. (2020).

Partitioning configuration	Reference floor mass (kg)	Reference modal damping (%)
Case 1	1,000	5
Case 2	1,100	4
Case 3	1,300	3
Case 4	1,000	3

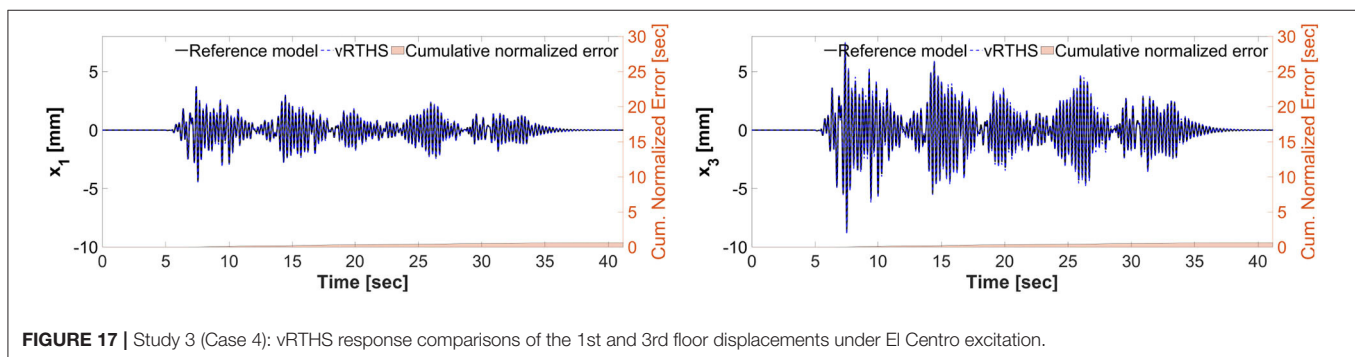
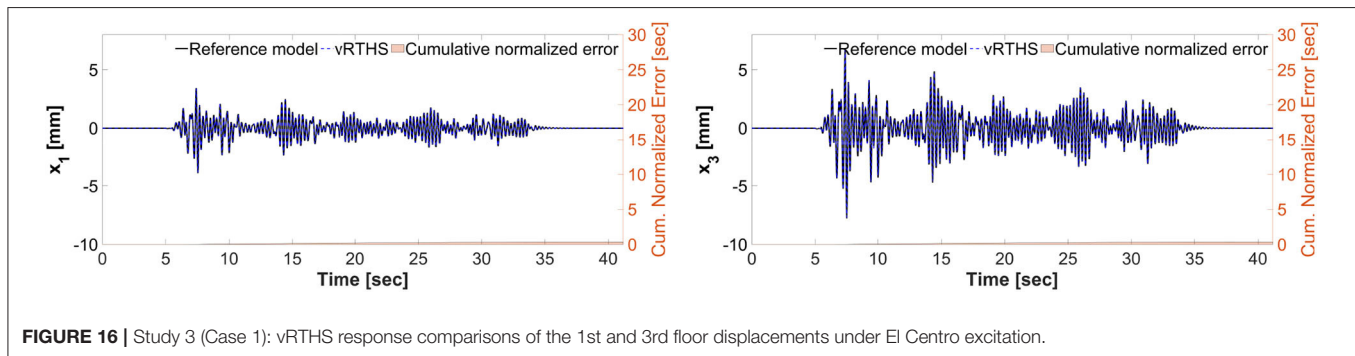
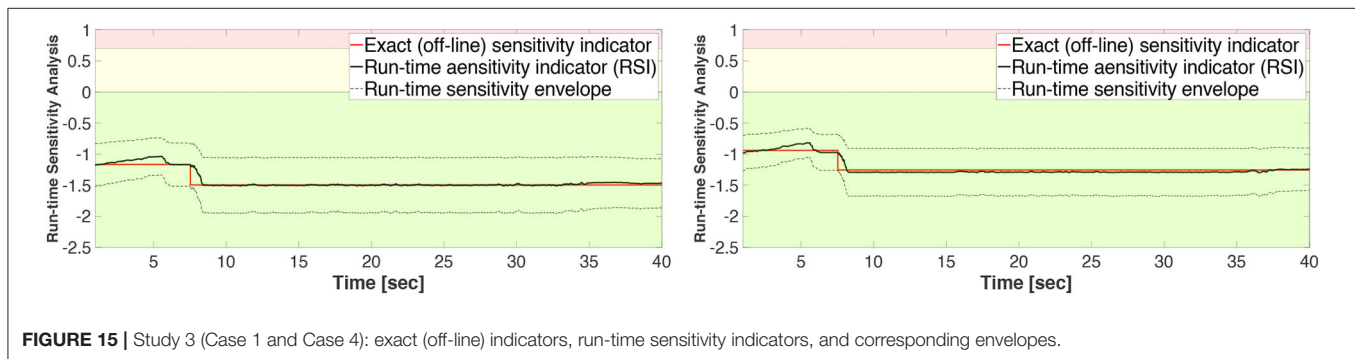
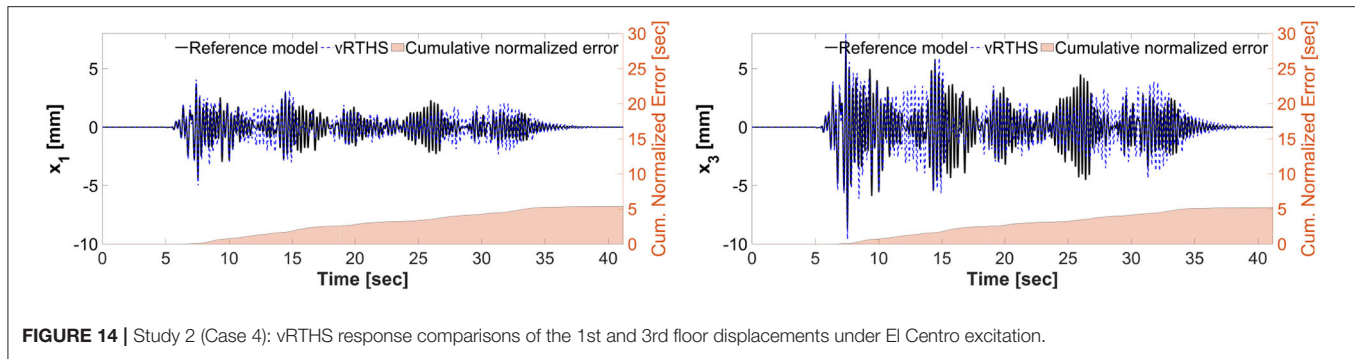
respectively. The results confirm that Case 1 [PSI (before damage) = 1.17, PSI (after damage) = 1.50] is less sensitive to desynchronization at the interface as compared to Case 4 [PSI (before damage) = 0.94, PSI (after damage) = 1.25]. In addition, a comparison of the results between Study 1 and Study 2 shows that although the damage creates less sensitive configurations [compare PSI (before damage) and PSI (after damage)], the global performance of Study 1 is slightly more accurate than that of Study 2. This observation can be attributed to the fact that the sample linear controller provided in the RTHS benchmark problem definition lacks the level of robustness and adaptation required to accommodate extensive variations during a real-time hybrid simulation.

Figures 15–17 show the results of Study 3 (Case 1 and Case 4). In these simulations the lateral stiffness associated with the experimental substructures drops by 50% at 7.61 and 7.72 s, respectively. **Figure 15** shows the exact (off-line) sensitivity indicators, run-time sensitivity indicators, and run-time sensitivity envelopes associated with Cases 1 and 4. Prior



to conducting the simulations, the range of possible values of the RSI is classified, on the basis of system instability as extremely sensitive (red, $RSI > 0.7$), moderately sensitive (yellow, $0 \leq RSI \leq 0.7$), and slightly sensitive (green, $RSI < 0$), see **Figures 6, 15**.

These results also demonstrate that Case 1 is less sensitive to desynchronization at the interface both before and after the damage event. The exact sensitivity indicators are computed off-line using (1) the exact time of damage occurrence, and (2) full knowledge of the physical substructure parameters both



before and after the damage occurrence. However, in an RTHS experiment neither will be available before the test begins. Therefore, we use (a) the model updating building block to estimate, on-the-fly, the parameters of the physical substructure

and (2) compute and monitor, in real-time, the sensitivities of the simulations before and after the occurrence of the damage. Aligned with our observation in Study 2, **Figure 17** also confirms that the failure of the column makes the simulation less sensitive

to desynchronization at the interface. However, unlike the poor global performance results associated with Study 2, the results of Study 3 provided in **Figures 16, 17** show significant improvements due to the built-in adaptation and robustness capabilities within REFORM-I.

Figure 15 shows that the exact sensitivity indicator falls within the run-time sensitivity envelope. This outcome is a critical requirement in case any extensive variations occur within the physical substructure (e.g., component failure, bifurcation, non-stationary dynamics, and dynamical switching), leading to more sensitivity to desynchronization at the interface. Whether or not the envelope can capture the exact sensitivity of the simulation will depend on the robustness of the run-time model updating and estimation building block.

CONCLUSIONS

Despite the potential for using RTHS to conduct cost-effective experiments at scale, the hazards engineering community has not been able to fully exploit this realistic testing method. The lack of systematic procedures and stringent requirements for the safety, integrity, and coordinated evolution of an RTHS test (during the experiment) and measures for the accuracy of experimental results (both during and after the experiment) have prevented researchers from tackling many problems that are of great interest to the hazards community. For instance, RTHS of systems with component damage or failure require advanced methods that can assess the system and adapt to changing parameters, necessitating run-time estimation of the new parameters and the associated uncertainty. In response to this technical hurdle, REFORM is developed to provide a modular framework that will enable conducting more challenging and realistic experiments safely and with high confidence. REFORM-I (this first phase of REFORM development and numerical validation) serves as a foundation for extending RTHS

application to black-box RTHS experiments: a general physical substructure with unanticipated dynamical behaviors. Herein we describe and demonstrate the building blocks and the numerical validation considered within REFORM-I. These building blocks (i.e., run-time sensitivity indicator, run-time stability threshold, run-time state-estimation and model updating technique, multi-rate coordination, and self-tuning robust control system) which are grounded in non-linear control and estimation theories, provide both mechanisms to support adaptation and robustness and the knowledge to use them effectively for conducting RTHS experiments. The methods are demonstrated and validated using a well-known benchmark problem in RTHS.

DATA AVAILABILITY STATEMENT

The raw data supporting the conclusions of this article will be made available by the authors, without undue reservation.

AUTHOR CONTRIBUTIONS

AMa developed the self-tuning control system. YF and ZW developed the run-time model updating. JC developed the run-time state estimation. AMo and SD developed the validation problem. HM developed the run-time indicator.

FUNDING

This work was supported in part by a Space Technology Research Institutes grant (number 80NSSC19K1076) from NASA's Space Technology Research Grants Program, the Resilient Extraterrestrial Habitats project, funded by the Purdue University Office of the Provost (New Horizons program), the Research Coordination Network in Hybrid Simulation for Multi-hazard Engineering through NSF-CMMI 1661621, and the Purdue University Systems Collaboratory Fellows Program.

REFERENCES

- Aru, Y. (2007). A tutorial on particle filters for online nonlinear/nongaussian bayesian tracking. *Bayesian Bounds Parameter Estimat. Nonlinear Filter. Track.* 50, 723–737. doi: 10.1109/9780470544198
- Chae, Y., Kazemibidokhti, K., and Ricles, J. M. (2013). Adaptive time series compensator for delay compensation of servo-hydraulic actuator systems for real-time hybrid simulation. *Earthquake Eng. Struct. Dyn.* 42, 1697–1715. doi: 10.1002/eqe.2294
- Chen, P.-C., Chang, C.-M., Spencer, B. F., and Tsai, K.-C. (2015). Adaptive model-based tracking control for real-time hybrid simulation. *Bull. Earthquake Eng.* 13, 1633–1653. doi: 10.1007/s10518-014-9681-2
- Condori, J., Maghareh, A., Orr, J., Li, H.-W., Montoya, H., Dyke, S., et al. (2020). Exploiting parallel computing to control uncertain nonlinear systems in real-time. *Exp. Techn.* doi: 10.1007/s40799-020-00373-w
- Condori-Urbe, J., Maghareh, A., and Dyke, S. J. (2019). Estimating states for nonlinear systems using the particle filter. *arXiv [Preprint]. arXiv:1911.03263*.
- Dyke, S. J., Spencer, B. F., Quast, P., and Sain, M. K. (1995). Role of control-structure interaction in protective system design. *J. Eng. Mech.* 121, 322–338. doi: 10.1061/(ASCE)0733-9399(1995)121:2(322)
- Fernandois, G. A., and Spencer, B. F. (2017). Model-based framework for multi-axial real-time hybrid simulation testing. *Earthquake Eng. Eng. Vibrat.* 16, 671–691. doi: 10.1007/s11803-017-0407-8
- Gao, X., Castaneda, N., and Dyke, S. J. (2013). Real time hybrid simulation: from dynamic system, motion control to experimental error. *Earthquake Eng. Struct. Dyn.* 42, 815–832. doi: 10.1002/eqe.2246
- Gao, X. S., and You, S. (2019). Dynamical stability analysis of MDOF real-time hybrid system. *Mech. Syst. Signal Process.* 133:106261. doi: 10.1016/j.ymssp.2019.106261
- Gardoni, P., and LaFave, J. M. (2016). “Multi -hazard approaches to civil infrastructure engineering: mitigating risks and promoting resilience,” in *Multi-hazard Approaches to Civil Infrastructure Engineering*, eds P. Gardoni and J. M. LaFave (Cham: Springer International Publishing), 3–12. doi: 10.1007/978-3-319-29713-2_1
- Harris, M. J., and Christenson, R. E. (2019). “Experimental test of spacecraft parachute deployment using real-time hybrid substructuring,” in *Sensors and Instrumentation, Aircraft/Aerospace and Energy Harvesting*, eds E. Wee Sit, C. Walber, P. Walter, A. Wicks, and S. Seidlitz (Cham: Springer), 67–70. doi: 10.1007/978-3-319-74642-5_8
- Karavasilis, T. L., Ricles, J. M., Sause, R., and Chen, C. (2011). Experimental evaluation of the seismic performance of steel MRFs

- with compressed elastomer dampers using large-scale real-time hybrid simulation. *Eng. Struct.* 33, 1859–1869. doi: 10.1016/j.engstruct.2011.01.032
- Li, D., Dong, X., and Wang, Y. (2018). Model updating using sum of squares (SOS) optimization to minimize modal dynamic residuals. *Struct. Control Health Monitor.* 25, 1–16. doi: 10.1002/417.stc.2263
- Maghareh, A., Dyke, S., Rabieniaharatbar, S., and Prakash, A. (2017). Predictive stability indicator: a novel approach to configuring a real-time hybrid simulation. *Earthquake Eng. Struct. Dyn.* 46, 95–116. doi: 10.1002/eqe.2775
- Maghareh, A., Dyke, S. J., Prakash, A., and Bunting, G. B. (2014). Establishing a predictive performance indicator for real-time hybrid simulation. *Earthquake Eng. Struct. Dyn.* 43, 2299–2318. doi: 10.1002/eqe.2448
- Maghareh, A., Dyke, S. J., and Silva, C. E. (2020). A self-tuning robust control system for nonlinear real-time hybrid simulation. *Earthquake Eng. Struct. Dyn.* 49, 695–715. doi: 10.1002/eqe.3260
- Maghareh, A., Silva, C. E., and Dyke, S. J. (2018a). Parametric model of servo-hydraulic actuator coupled with a nonlinear system: experimental validation. *Mech. Syst. Signal Process.* 104, 663–672. doi: 10.1016/j.ymssp.2017.11.009
- Maghareh, A., Silva, C. E., and Dyke, S. J. (2018b). Servo-hydraulic actuator in controllable canonical form: Identification and experimental validation. *Mech. Syst. Signal Process.* 100, 398–414. doi: 10.1016/j.ymssp.2017.07.022
- Maghareh, A., Waldbjorn, J. P., Dyke, S. J., Prakash, A., and Ozdagli, A. I. (2016). Adaptive multi-rate interface: development and experimental verification for real-time hybrid simulation. *Earthquake Eng. Struct. Dyn.* 45, 1411–1425. doi: 10.1002/eqe.2713
- Mercan, O., and Ricles, J. M. (2008). Stability analysis for real-time pseudodynamic and hybrid pseudodynamic testing with multiple sources of delay. *Earthquake Eng. Struct. Dyn.* 37, 1269–1293. doi: 10.1002/eqe.814
- Ou, G., Ozdagli, A. I., Dyke, S. J., and Wu, B. (2015). Robust integrated actuator control: experimental verification and real-time hybrid-simulation implementation. *Earthquake Eng. Struct. Dyn.* 44, 441–460. doi: 10.1002/eqe.2479
- Palacio-Betancur, A., and Gutierrez Soto, M. (2019). Adaptive tracking control for real-time hybrid simulation of structures subjected to seismic loading. *Mech. Syst. Signal Process.* 134, 106345. doi: 10.1016/j.ymssp.2019.106345
- Sarkka, S. (2013). Bayesian filtering and smoothing. New York, NY: Cambridge University Press. Available online at: <https://books.google.com/books?hl=en&lr=&id=5VlsAAAAQBAJ&oi=fnd&pg=PR9&dq=sarkka+bayesian+filtering&ots=OFPSDASW7B&sig=IYItSwUiS7VE04fK8IGDq4qWgxU#v=onepage&q=sarkka%20bayesian%20filtering&f=false>
- Silva, C. E., Gomez, D., Maghareh, A., Dyke, S. J., and Spencer, B. F. (2020). Benchmark control problem for real-time hybrid simulation. *Mech. Syst. Process.* 135:106381. doi: 10.1016/j.ymssp.2019.106381
- Slotine, J. E., and Li, W. (1991). *Applied Nonlinear Control*. Englewood Cliffs, NJ: Pearson Education.
- Su, W., and Song, W. (2019). A real-time hybrid aeroelastic simulation platform for flexible wings. *Aerospace Sci. Technol.* 95, 105513. doi: 10.1016/j.ast.2019.105513
- Tao, J., and Mercan, O. (2019). A study on a benchmark control problem for real-time hybrid simulation with a tracking error-based adaptive compensator combined with a supplementary proportional-integral derivative controller. *Mech. Syst. Signal Process.* 134:106346. doi: 10.1016/j.ymssp.2019.106346
- Wallace, M. I., Sieber, J., Neild, S. A., Wagg, D. J., and Krauskopf, B. (2005). Stability analysis of real-time dynamic substructuring using delay differential equation models. *Earthquake Eng. Struct. Dyn.* 34, 1817–1832. doi: 10.1002/eqe.513
- Wang, Z., Ning, X., Xu, G., Zhou, H., and Wu, B. (2019). High performance compensation using an adaptive strategy for real-time hybrid simulation. *Mech. Syst. Signal Process.* 133:106262. doi: 10.1016/j.ymssp.2019.106262
- Wu, T., and Song, W. (2019). Real-time aerodynamics hybrid simulation: wind-induced effects on a reduced-scale building equipped with full-scale dampers. *J. Wind Eng. Indus. Aerodyn.* 190, 1–9. doi: 10.1016/j.jweia.2019.04.005
- Xu, D., Zhou, H., Shao, X., and Wang, T. (2019). Performance study of sliding mode controller with improved adaptive polynomial-based forward prediction. *Mech. Syst. Signal Process.* 133:106263. doi: 10.1016/j.ymssp.2019.106263
- Xu, W., Chen, C., Guo, T., and Chen, M. (2019). Evaluation of frequency evaluation index based compensation for benchmark study in real-time hybrid simulation. *Mech. Syst. Signal Process.* 130, 649–663. doi: 10.1016/j.ymssp.2019.05.039
- Yang, J. H., and Lam, H. F. (2018). An efficient adaptive sequential Monte Carlo method for Bayesian model updating and damage detection. *Struct. Control Health Monitor.* 25, 6–11. doi: 10.1002/stc.2260
- Zarate, B. A., Caicedo, J. M., Yu, J., and Ziehl, P. (2012). Bayesian model updating and prognosis of fatigue crack growth. *Eng. Struct.* 45, 53–61. doi: 10.1016/j.engstruct.2012.06.012

Conflict of Interest: The authors declare that the research was conducted in the absence of any commercial or financial relationships that could be construed as a potential conflict of interest.

Copyright © 2020 Maghareh, Fu, Montoya, Condori, Wang, Dyke and Montoya. This is an open-access article distributed under the terms of the Creative Commons Attribution License (CC BY). The use, distribution or reproduction in other forums is permitted, provided the original author(s) and the copyright owner(s) are credited and that the original publication in this journal is cited, in accordance with accepted academic practice. No use, distribution or reproduction is permitted which does not comply with these terms.



Towards Data-Driven Real-Time Hybrid Simulation: Adaptive Modeling of Control Plants

Thomas Simpson, Vasilis K. Dertimanis* and Eleni N. Chatzi

Chair of Structural Mechanics & Monitoring, Institute of Structural Engineering, Department of Civil, Environmental and Geomatic Engineering, ETH Zürich, Zürich, Switzerland

OPEN ACCESS

Edited by:

Dimitrios Lignos,
École Polytechnique Fédérale de
Lausanne, Switzerland

Reviewed by:

Gaston A. Fernandois,
Federico Santa María Technical
University, Chile
Mettupalayam Veluswami Sivaselvan,
University at Buffalo, United States

*Correspondence:

Vasilis K. Dertimanis
v.derti@ibk.baug.ethz.ch

Specialty section:

This article was submitted to
Computational Methods in Structural
Engineering,
a section of the journal
Frontiers in Built Environment

Received: 09 June 2020

Accepted: 18 August 2020

Published: 25 September 2020

Citation:

Simpson T, Dertimanis VK and
Chatzi EN (2020) Towards
Data-Driven Real-Time Hybrid
Simulation: Adaptive Modeling of
Control Plants.
Front. Built Environ. 6:570947.
doi: 10.3389/fbuil.2020.570947

We present a method for control in real-time hybrid simulation (RTHS) that relies exclusively on data processing. Our approach bypasses conventional control techniques, which presume availability of a mathematical model for the description of the control plant (e.g., the transfer system and the experimental substructure) and applies a simple plug 'n play framework for tuning of an adaptive inverse controller for use in a feedforward manner, avoiding thus any feedback loops. Our methodology involves (i) a forward adaptation part, in which a noise-free estimate of the control plant's dynamics is derived; (ii) an inverse adaptation part that performs estimation of the inverse controller; and (iii) the integration of a standard polynomial extrapolation algorithm for the compensation of the delay. One particular advantage of the method is that it requires tuning of a limited set of hyper-parameters (essentially three) for proper adaptation. The efficacy of our framework is assessed via implementation on a virtual RTHS (vRTHS) benchmark problem that was recently made available to the community. The attained results indicate that data-driven RTHS may form a competitive alternative to conventional control.

Keywords: real-time hybrid simulation, adaptive signal processing, adaptive inverse control, feedforward, decorrelated LMS, DCT-LMS

1. INTRODUCTION

Whilst numerical simulation methods play an ever increasing role in the analysis and design of structures, these remain insufficient in the case of complex structural systems under extreme loading conditions. As such, physical tests cannot be fully removed from the analysis and assessment process. Hybrid testing (Takanashi and Nakashima, 1987; Mahin et al., 1989) can work complimentary with numerical modeling by allowing physical testing of those regions or components of greatest interest or complexity without incurring the high costs associated with physical testing of the whole system. The presence of significant non-linearities are often a motivation for the use of hybrid simulation due to the difficulties associated in properly modeling this behavior. Non-linear components can often exhibit considerable rate dependent behavior, with this rate-dependency often not adequately compensated by scaling. This motivates the use of RTHS as the “gold standard” of hybrid simulation. Real-time in this case implies that the time scales of the numerical and physical system are the same; this allows for tests which incorporate rate dependent non-linearities in the physical component and are hence more representative of the true system (Nakashima et al., 1992; Nakashima, 2001; Benson Shing, 2008).

The real-time aspect of RTHS brings significant difficulties in comparison to an increased time scale test or pseudo-dynamic testing (Bayer et al., 2005; Pegon, 2008). Notable challenges involve

the integration of the numerical system, which now must be executed in real-time, as well as enforcing robust and accurate actuator control. The ability of a hybrid simulation to recreate realistic testing conditions is reliant upon the accuracy of the applied boundary conditions. As such, the accurate recreation of the signals from the numerical substructure by the actuator are of paramount importance. With real-time testing, the accurate reproduction of these signals becomes more challenging. The dynamics of the actuation system and interaction with the test-piece can have significant effects on the reproduction of the reference signal as well as the effect of signal processing artifact. This results in two key control issues when implementing a RTHS scheme, namely, (i) the accurate reproduction (through the transfer system) of the reference signal that corresponds to the common boundaries between the experimental and the numerical substructure; and (ii) the suppression of the time delay, which is inevitably introduced by the transfer system (actuators, analog-to-digital and digital-to-analog converters, ADC and DAC, respectively, etc.) and possibly by the control scheme itself. The first issue is a typical control problem, while the second is a problem of prediction.

Initial control approaches implemented for RTHS focused on time domain approaches. The problem was first considered by Horiuchi et al. (1999), wherein a polynomial extrapolation method was used to reduce actuator delay. This method was further developed allowing for adaptation of the polynomial coefficients in Wallace et al. (2005). Further work exploited model-based control, wherein a model of the control plant is identified and used to make corrections to the reference signal for improving tracking (Carrion and B. F. Spencer, 2006; Chen and Ricles, 2009). Current state of the art methods focus on adaptive control schemes due to their superior robustness. Adaptive model based control schemes as in Najafi and Spencer (2019) demonstrate good performance, albeit present the drawback of requiring a mathematical model of the plant to be formulated. Ning et al. (2019) also demonstrate an adaptive method making use of an H_∞ filter for tracking error and a polynomial extrapolation for delay compensation. This method yields good performance but requires an offline identification stage in which a second order model form is assumed and identified to replicate the plant behavior.

Within the framework of methods for adaptive tracking control, a class of algorithms is exclusively based on data processing, rather than the integration of conventional control. As such, they require no prior knowledge on the dynamics of the transfer system, the experimental substructure and their interaction. Among other works, the adaptive time series compensator developed by Chae et al. (2013) has shown very good performance, but requires the careful prescription of user-defined limits on its hyper-parameters for ensuring the stability of test. Dertimanis et al. (2015a,b) apply adaptive signal processing concepts and succeed in reproducing reference signals with a high degree of efficacy. These algorithms can be applied online and in hard real-time, thus proving particularly beneficial in terms of robustness as the filters are adaptively optimized to the test conditions, even if these change between tests. However, although they have been experimentally validated, via a 10 Mgr

linear specimen on a shaking table, they have not yet been integrated into RTHS.

The present study extends the research conducted in Dertimanis et al. (2015a,b) and proposes a data-driven, adaptive inverse control (AIC) framework for RTHS. It proceeds by first formulating a set of specifications that data-driven control schemes should meet and then splits the adaptive process into two phases, which can be executed either simultaneously, or successively, both in online and offline mode. In the first phase, the decorrelated least mean square (LMS) algorithm is applied to the identification of the control plant, while in the second phase the discrete-cosine transform LMS (DCT-LMS) takes on the tuning of the inverse controller. It is shown that the cascade of the latter and the control plant closely approximates a perfect delay, allowing thus the signal of the numerical substructure to be driven to the experimental substructure with unaltered dynamics. Accordingly, the method adopts a polynomial extrapolation method (Horiuchi et al., 1999; Wallace et al., 2005) for the compensation of the time delay, ensuring thus the stability of the RTHS loop. A particular advantage of the developed scheme is its dependence to a very small number of hyper-parameters that must be provided by the uses, an important feature that favors robustness, safety, transparency, and ease of use.

We assess our AIC method via the recently established linear vRTHS benchmark problem of Silva et al. (2020). It must be emphasized that, whilst the benchmark problem dealt with herein considers the control of a linear plant, the AIC framework has previously been successfully extended to non-linear systems on multiple occasions. In Widrow and Plett (1996), it is discussed how the AIC framework for linear filters can be extended to take into account non-linear filtering. The demonstration of AIC to a theoretical non-linear plant then followed in Widrow et al. (1998), wherein the non-linear filters took the form of neural networks whereby the weights are updated with a gradient descent method. A full consideration of the non-linear AIC framework is given in Plett (2003). Alternative methods have made use of other regression techniques such as support vector machines for constructing non-linear filters (Yuan et al., 2008). Physical implementations of non-linear AIC have been demonstrated on piezo-electric actuators featuring hysteresis effects (Li and Chen, 2013), on a magnetic bearing system (Jeng, 2000) and in the control of an electronic throttle system (Xiaofang et al., 2010). Furthermore, the AIC method using linear filters has been applied to physical systems that are similar to those considered in this benchmark problem, i.e., electrohydraulic shaking table, and demonstrated success both in the case of conventional real-time dynamic tests (Shen et al., 2011; Dertimanis et al., 2015a).

The contributions of this study are (i) the treatment of RTHS in a purely data-driven fashion; (ii) the establishment of a set of specifications that such an approach should meet; (iii) the derivation of a simple, plug-n-play, adaptive modeling framework for the proper estimation of a feed-forward adaptive inverse controller for RTHS; and (iv) the assessment of our methodology via the vRTHS benchmark problem of Silva et al. (2020). The context is structured as follows: in section 2 the problem is formulated, along with the list of specifications and

a brief introduction to adaptive filtering is offered. Section 3 outlines the method, while section 4 contains the application study. Finally, in section 5 the outcomes of the study are summarized and directions for future research are given.

2. PROBLEM FORMULATION

Figure 1A illustrates a typical RTHS loop, where a structure is split into a numerical and an experimental part and their interaction is assured via the use of a *transfer system*. A minimal configuration of the latter contains a set of ADC and DAC devices, a controller and an actuator (oftentimes integrating an inner control loop) that is firmly attached to the experimental substructure. Inevitably, this firm attachment causes an evolution of dynamics along two paths: this is termed *controller-structure interaction* (CSI) in the literature and is represented by an additional feedback loop (not shown in **Figure 1**, refer to **Figure 1**). The *control plant* thus consists of the transfer system and the experimental substructure.

In more detail, it is assumed that an external excitation, $u[k]$ is applied to the numerical substructure and the kinematics at the boundary are calculated by applying an appropriate numerical integration scheme that solves the equations of motion (Shing, 2008). The calculated *reference signal*, $x_R[k]$, which can be in the

form of displacement, velocity, or acceleration, is then applied through the transfer system to the experimental substructure. The response of the latter is monitored and the dynamics at the boundary, usually in the form of a force, is fed back as additional input to the numerical substructure, in order to proceed to the next step of the loop.

For the effective implementation of a RTHS loop, two fundamental problems must be solved. The first corresponds to the dynamics of the control plant and is treated by introducing an additional controller (termed the RTHS controller in **Figure 1A**). The second problem pertains to the delay that the transfer path inherits, which is tackled via an appropriate delay compensation method. Under this enriched configuration, the reference signal is predicted Δ steps forward, where Δ is an estimate of the transfer path's *overall delay*, and then appropriately modified via the RTHS controller to form the *command signal* for the transfer system. A careful tuning of all the individual blocks results in an *achieved signal* at the experimental substructure that is equal to the reference one, e.g., $x_A[k] = x_R[k]$; this equality forms the hard constraint of any RTHS loop. Under this setting, the challenge that this study aims to tackle is summarized in the following question: is it possible to tune a RTHS controller and a delay compensation algorithm *without* any prior information on the dynamics of

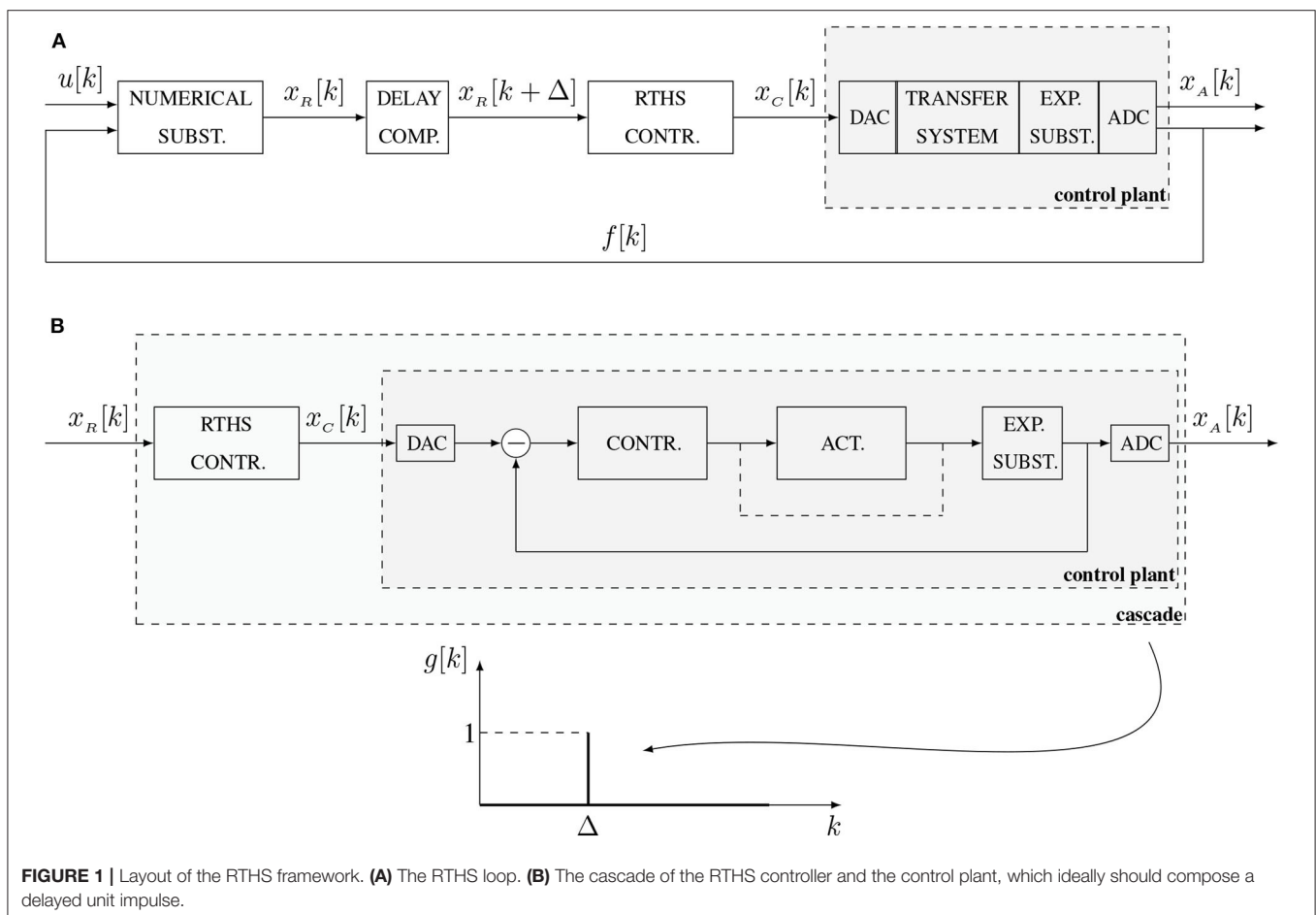


FIGURE 1 | Layout of the RTHS framework. **(A)** The RTHS loop. **(B)** The cascade of the RTHS controller and the control plant, which ideally should compose a delayed unit impulse.

the control plant, given *only* the availability of the reference and achieved signals?

Leaving out the delay problem for the moment, the *data-driven* attack to the establishment of a RTHS controller is illustrated in **Figure 1B** and reads as follows: under the availability of $x_R[k]$ and $x_A[k]$, a controller that forms the inverse of the control plant should be estimated, causing the cascade to perform as a perfect delay, e.g., $x_A[k] = x_R[k - \Delta]$. Then, the addition of the delay compensation method should result in fulfilling the hard constraint condition of the RTHS loop. In designing such a controller, Dertimanis et al. (2015a) described a set of specifications, which are herein reformulated and enriched. According to these, a controller should be:

1. **Data-driven:** no need for analytical models of individual components (valves, cylinders, etc.) and identification of system parameters (stiffness, damping, oil constants, flow rates, etc.)
2. **Feedforward-driven:** no need for additional feedback loops.
3. **Discrete-time oriented:** no need for discretization of continuous-time models. Everything should be digital.
4. **Minimally parametrized:** the number of parameters, henceforth referred to as *hyper-parameters*, required for the proper tuning of the controller should be kept as small as possible. The controller should not be “too sensitive” on these hyper-parameters.
5. **Of guaranteed stability:** exclusive use of finite impulse response (FIR) models (refer to section 2.1), instead of infinite impulse response models in order to enforce stability and safety during test.
6. **Robust:** the RTHS controller should compensate for all uncertainties of the control plant, as well as the CSI problem.
7. **Of minimum discrepancies:** the cascade frequency response should follow the zero dB line in the maximum possible frequency band. The phase delay should be constant within this band.
8. **Straightforward to implement to existing facilities:** the RTHS controller should be operational in conjunction with conventional fixed-gain controllers.
9. **Applicable to a wide range of transfer systems:** from small-scale actuators and light specimens, to shaking tables and specimens of several megagrams.
10. **Functional for all types of command signals:** both acceleration and displacement reference signals should be handled.
11. **Straightforward to realize-execute:** immediate implementation in commercial hardware and execution in real time. No need for sophisticated software design.

Our approach for establishing such an inverse controller utilizes the theory of adaptive signal processing (Widrow and Wallach, 2007; Diniz, 2008) and it can be implemented either online, or offline. Its effectiveness in modeling facilities for structural testing has already been demonstrated in Dertimanis et al. (2015a,b).

2.1. Brief Review of Adaptive Filtering

For convenience, this section offers a brief outline of the most fundamental concepts of adaptive signal processing. The

familiarized reader can safely skip this summary. A sound treatment to the topic is given in Diniz (2008), Hayes (1996), and Manolakis et al. (2005). Glentis et al. (1999) provide an excellent review on adaptive filters, including the presentation of a comprehensive review of associated algorithms.

Consider an unknown plant that can be effectively described by its impulse response $g[k]$ in the discrete-time domain, or by its transfer function $G(z)$ in the \mathcal{Z} -domain. The plant is driven by a wide-sense stationary input signal $u[k]$ and the response $x[k]$ is measured in a noise-corrupted fashion, under the assumption of an additive disturbance $d[k]$ at the plant's output, which is random and uncorrelated to $x[k]$. Using an FIR parametrization, we can represent the input-output dynamics as

$$x[k] = \sum_{i=0}^n g[i]u[k-i] + d[k] \quad (1)$$

with n corresponding to the model order. For $\mathbf{g} = [g[0] \ g[1] \ \dots \ g[n]]^T$ and $\mathbf{u}[k] = [u[k] \ u[k-1] \ \dots \ u[k-n]]^T$ Equation (1) can be cast into a regression form

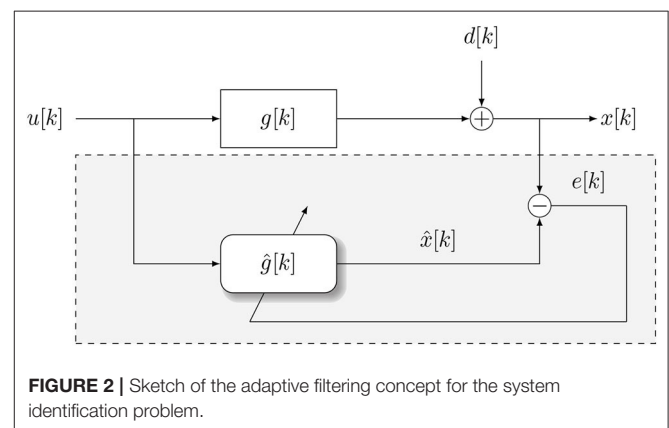
$$x[k] = \mathbf{u}^T[k]\mathbf{g} + d[k] \quad (2)$$

Suppose now that measurements of $u[k]$ and $x[k]$ are acquired and the aim is to estimate a FIR model of the plant. Our model reads

$$\hat{x}[k] = \sum_{i=0}^n \hat{g}[i]u[k-i] = \mathbf{u}^T[k]\hat{\mathbf{g}} \quad (3)$$

where $\hat{x}[k]$ is the model's output and $\hat{\mathbf{g}}$ the vector of unknown filter weights. This is a typical parametric identification problem, which can be solved by collecting measurements over a time interval and then solving a linear least-squares problem for recovering \mathbf{g} . Clearly, this *non-recursive* strategy cannot be applied in real-time, since it requires batch-processing of stored data.

An alternative approach is to proceed in a *recursive* estimation of the weights, whenever new data becomes available. The key idea, illustrated in **Figure 2**, is to update the weights via



the *stochastic approximation* of a deterministic optimization algorithm, in which the direction is calculated using unbiased estimates on the basis of the current time index. For example, consider the steepest descent algorithm

$$\hat{\mathbf{g}}[k+1] = \hat{\mathbf{g}}[k] - \mu \nabla V(\hat{\mathbf{g}}[k]) \quad (4)$$

where μ is the step size and $V(\hat{\mathbf{g}}[k])$ is the objective function, defined as the *instantaneous* mean square error (MSE)

$$V(\hat{\mathbf{g}}[k]) = E\{e^2[k]\} = E\{(\mathbf{x}[k] - \hat{\mathbf{x}}[k])^2\} \quad (5)$$

Plugging Equation (3) and differentiating with respect to $\hat{\mathbf{g}}[k]$ implies

$$\nabla V(\hat{\mathbf{g}}[k]) = -2E\{e[k]\mathbf{u}[k]\} \quad (6)$$

Approximating the expectation operator $E\{e[k]\mathbf{u}[k]\}$ as $e[k]\mathbf{u}[k]$ and substituting to Equation (4) yields

$$\hat{\mathbf{g}}[k+1] = \hat{\mathbf{g}}[k] + 2\mu e[k]\mathbf{u}[k] \quad (7)$$

This is the celebrated least mean square (LMS) adaptive filter developed by Widrow and Hoff (1960). Expectedly, the behavior of the algorithm depends on the step size. When $d[k]$ is wide-sense stationary and the unknown plant is time-invariant, the LMS filter converges in the mean to the optimal Wiener solution, provided that μ is bounded as

$$0 < \mu < \frac{1}{\lambda_{\max}} \quad (8)$$

where λ_{\max} is the largest eigenvalue of the input's autocorrelation matrix

$$\mathbf{\Gamma}_{uu} = \begin{bmatrix} \gamma_{uu}[0] & \gamma_{uu}[1] & \dots & \gamma_{uu}[n] \\ \gamma_{uu}[1] & \gamma_{uu}[0] & \dots & \gamma_{uu}[n-1] \\ \vdots & \vdots & \ddots & \vdots \\ \gamma_{uu}[n] & \gamma_{uu}[n-1] & \dots & \gamma_{uu}[0] \end{bmatrix} \quad (9)$$

for $\gamma_{uu}[h] = E\{u[k+h]u[k]\}$. The condition of Equation (8) does not, however, ensure stability. This is succeeded by

$$0 < \mu < \frac{1}{\text{tr}\{\mathbf{\Gamma}_{uu}\}} = \frac{1}{(n+1)\sigma_{uu}^2} \quad (10)$$

an expression that is widely used in practice, since it is based on the energy of the input signal, which is easier to calculate than the eigenvalues. Finally, maximum convergence speed is achieved when

$$\mu = \frac{1}{\lambda_{\min} + \lambda_{\max}} \quad (11)$$

with λ_{\min} denoting the smallest eigenvalue of $\mathbf{\Gamma}_{uu}$. Equation (11) indicates that the speed is controlled by the eigenvalue spread of $\mathbf{\Gamma}_{uu}$, e.g.,

$$\text{eigenvalue spread} = \frac{\lambda_{\max}}{\lambda_{\min}} \quad (12)$$

From Equations (11, 12) it is easy to conclude that convergence speed requires an eigenvalue spread close to one. When the input signal can be selected by the user, the best option is to let $u[k]$ being a realization of a zero-mean Gaussian white noise process, since $\mathbf{\Gamma}_{uu} = \sigma_{uu}^2 \mathbf{I}_{n+1}$ and the spread is equal to one.

2.2. The Problem of Inverse Identification

Assume that the control plant can be described by the following digital rational transfer function

$$G(z) = \frac{\theta(z)}{\phi(z)} = \frac{\theta_0 + \theta_1 z^{-1} + \theta_2 z^{-2} + \dots + \theta_{n_\theta} z^{-n_\theta}}{1 + \phi_1 z^{-1} + \phi_2 z^{-2} + \dots + \phi_{n_\phi} z^{-n_\phi}} \quad (13)$$

Then, the problem of identifying an inverse controller is reduced in approximating the inverse transfer function

$$G^{-1}(z) = \frac{1 + \phi_1 z^{-1} + \phi_2 z^{-2} + \dots + \phi_{n_\phi} z^{-n_\phi}}{\theta_0 + \theta_1 z^{-1} + \theta_2 z^{-2} + \dots + \theta_{n_\theta} z^{-n_\theta}} \quad (14)$$

If $G(z)$ is strictly minimum phase (e.g., poles and zeros inside the unit circle), then the problem has a straightforward solution, since $G^{-1}(z)$ will be also minimum phase, admitting a convergent expansion of the form

$$G^{-1}(z) = \sum_{i=0}^{\infty} g_i [i] z^{-i} \quad (15)$$

with $g_i[0] = 1$ and

$$\sum_{i=0}^{\infty} |g_i[i]| < \infty \quad (16)$$

Thus, by truncating the infinite sum up to an order n_i , it is possible to derive a FIR representation for the inverse controller. If, however, $G(z)$ is non-minimum phase, the poles of $G^{-1}(z)$ [e.g., the zeros of $G(z)$] are located outside the unit circle and the power expansion of Equation (15) diverges. To cope with this issue, recall that a digital transfer function admits two inverse \mathcal{Z} -transforms, a causal and a non-causal one, depending on the region of convergence (Oppenheim et al., 1999, Chapter 3). In the case of the non-minimum phase $G(z)$, the causal inverse transform is unstable, but the non-causal is stable. A stable, non-causal expansion of $G^{-1}(z)$ can be written as

$$G^{-1}(z) = \sum_{i=0}^{n_1} g_i[i] z^{-i} + \sum_{\ell=0}^{\infty} g_i[\ell] z^{\ell} \quad (17)$$

where, usually, the causal part is limited to very few terms (e.g., n_1 is small). If the weights of the non-causal part are significant, attempting to adapt an inverse controller would render quite poor results. However, if one would consider multiplying Equation (17) by a pure delay, $z^{-\Delta}$, it would cause Δ weights to jump from the non-causal to the causal part, increasing thus the accuracy of the inverse (Widrow and Wallach, 2007, Chapter 5).

To summarize, the adaptation of the inverse controller aims at satisfying the following equation

$$z^{-\Delta} G^{-1}(z)G(z) \longrightarrow 1 \quad (18)$$

In practice, this implies that the reference signal passes through a pure delay before being fed to the adaptation block. It is emphasized that, even if the continuous-time transfer function of a plant is minimum phase, its digital counterpart may oftentimes result non-minimum phase.

3. ADAPTIVE INVERSE CONTROL FOR RTHS

3.1. Description

The control strategy implemented herein essentially pertains to applying the adaptive filtering concepts previously outlined in identifying an appropriate inverse controller. The latter is then placed before the plant in the signal path, such that the cascade results ideally in a delayed unit impulse response. Accordingly, by integrating an appropriate delay compensation method, the achieved signal may follow the reference one with a reasonable accuracy, *at a certain frequency band*.

The strategy used for the adaptation of this inverse controller is based on the simple architecture shown at **Figure 3** and consists of two stages that are implemented in (hard) real-time:

- The *forward adaptation* stage, where an FIR estimate of $g[k]$, $\hat{g}_F[k]$, is obtained.
- The *inverse adaptation* stage, where an FIR estimate of the inverse of $g[k]$, $\hat{g}_I[k]$, is obtained, making use of $\hat{g}_F[k]$.

These two phases can either be performed successively or simultaneously, in the sense that it is not necessary to wait for the full convergence of the forward controller, in order to start the adaptation of the inverse one (Widrow and Wallach, 2007).

The adaptation process initiates by supplying a reference signal, $x_R[k]$, of favorable properties (see below), to the control plant. This signal, together with the noise-corrupted achieved

response of the plant, $x_A[k]$ are fed to the forward adaptation block, for estimating a FIR filter that describes the *end-to-end* reference-achieved signal dynamics. The term *end-to-end* herein implies that the path from the reference to the achieved signal contains *all* individual software/hardware components, including ADCs, DACs, signal conditioners, etc., besides the control plant.

When the forward and inverse adaptation are carried out simultaneously, e.g., in *synchronous mode*, the instantaneous estimate of the achieved response, $\hat{x}_A[k]$, together with a *delayed* version of the original reference signal, are fed to the inverse adaptation block and a FIR filter is tuned for describing the achieved-(delayed) reference signal dynamics. The output of this block is an estimate of $x_R[k - \Delta]$ (see **Figure 3**). The delay Δ is an algorithmic parameter (it is included in the set of method's *hyper-parameters*, listed in **Table 1**) and its size depends heavily on the qualitative characteristics of the control plant.

A key detail of the presented algorithm is that the inverse filter weights are not adapted by directly feeding the output of the control plant to the inverse block, in order to avoid the propagation of the disturbance. When both stages have been successfully executed and convergence has been achieved, the inverse FIR filter can be copied *before* the control plant and it is implemented as an inverse controller. Ideally, the cascade of the inverse controller and the control plant form a unit impulse that reproduces a delayed version of any reference signal. It is noted that more sophisticated algorithms can be implemented as adaptive inverse controllers, as the modified filtered-X one presented in the work of Dertimanis et al. (2015a).

3.2. Forward Adaptation

Our choice for the algorithm that implements the forward adaptation path is based on (i) the reported convergence rates; and (ii) the reduction of the required tuning parameters. Based on previous results (Dertimanis et al., 2015a,b) we apply the decorrelated LMS algorithm Doherty and Porayath (1997), which belong to the class of instrumental variable methods (Glentis

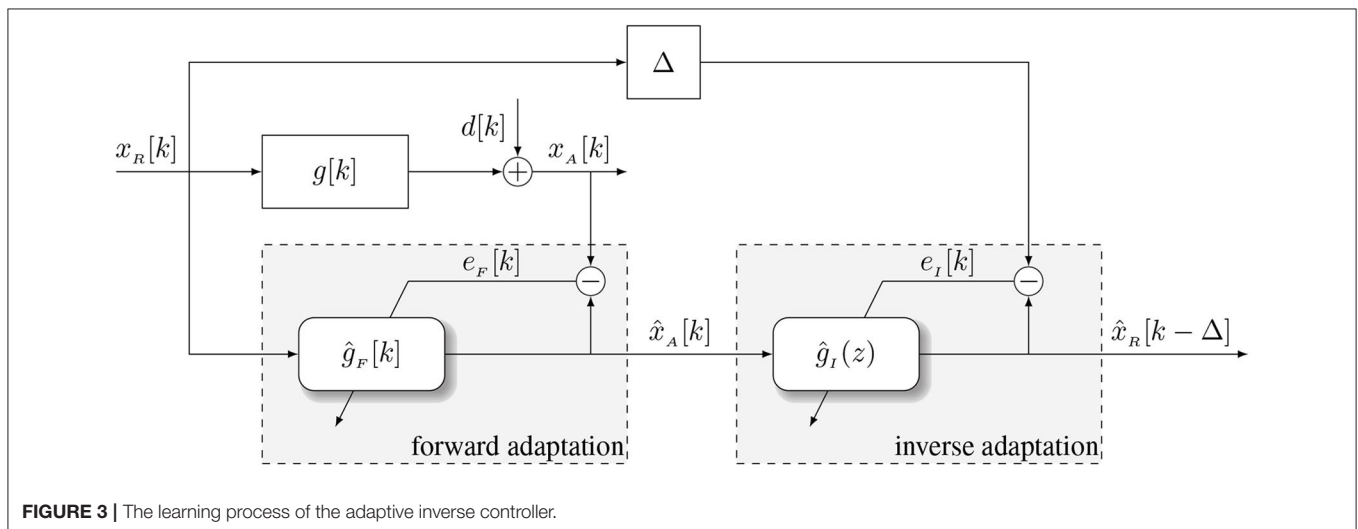


TABLE 1 | Method's hyper-parameters.

Parameter	Symbol	Default value	Comments
Order of the forward filter	n_F	-	Depends on control plant
Order of the inverse filter	n_I	-	Depends on control plant
Delay	Δ	$\frac{n_I}{2}$	
Order of polynomial extrapolation	n_p	3	
Coefficients of polynomial extrapolation	p_i	{4, -6, 4, -1}	when $n_p = 3$
Decorrelated LMS "stability" parameter	ϵ_F	$2.2044 \dots \times 10^{-16}$	
DCT-LMS "stability" parameter	ϵ_i	10^{-3}	
DCT-LMS power update factor	γ	0.95	
DCT-LMS step size	μ	$0 < \mu < \frac{2}{3n_I}$	Requires careful tuning

Boldface entries indicate the minimum required subset of hyper-parameters that must be supplied by the user.

et al., 1999). At each step, the adaptive filter's output is calculated as

$$\hat{x}_A[k] = \mathbf{x}_R^T[k] \mathbf{g}_F[k] \quad (19)$$

where

$$\mathbf{x}_R[k] = [x_R[k] \ x_R[k-1] \ \dots \ x_R[k-n_F]]^T \quad (20)$$

$$\hat{\mathbf{g}}_F^T[k] = [\hat{g}_F[k, 0] \ \hat{g}_F[k, 1] \ \dots \ \hat{g}_F[k, n_F]]^T \quad (21)$$

and n_F is the order of the filter. The coefficients are updated by

$$\hat{\mathbf{g}}_F[k+1] = \hat{\mathbf{g}}_F[k] + \mu[k] \mathbf{w}[k] \quad (22)$$

for a step size $\mu[k]$

$$\mu[k] = \frac{e_F[k]}{\mathbf{x}_R^T[k] \mathbf{w}[k] + \epsilon_F} \quad (23)$$

In Equation (23), ϵ_F is a small constant ("stability" parameter), $e_F[k] = x_A[k] - \hat{x}_A[k]$ is the error between the measured and the predicted signal and $\mathbf{w}[k]$ is the filter gradient, updated by

$$\mathbf{w}[k] = \mathbf{x}_R[k] - \alpha[k] \mathbf{x}_R[k-1] \quad (24)$$

with $\alpha[k]$ denoting the decorrelation coefficient

$$\alpha[k] = \frac{\mathbf{x}_R^T[k] \mathbf{x}_R[k-1]}{\mathbf{x}_R^T[k-1] \mathbf{x}_R[k-1]} \quad (25)$$

The properties of the decorrelated LMS algorithm are studied in Doherty and Porayath (1997). See also (Douglas et al., 1999; Rørtveit and Husøy, 2009). As an alternative to the decorrelated LMS, the normalized LMS algorithm (Diniz, 2008, Chapter 4) can be also applied to the forward adaptation path, at the cost of an additional hyper-parameter that controls the adaptation step.

3.3. Inverse Adaptation

The signal that arrives at the input of the inverse adaptation block, $\hat{x}_A[k]$ is, in general, highly correlated (e.g., colored), since it describes the dynamics of the control plant. Notice that when the reference signal is Gaussian-like, the inverse adaptation pertains essentially to a whitening process. This is because, the cascade of the inverse controller and the plant should give an achieved signal which is uncorrelated like the Gaussian input. As the convergence rate of the conventional LMS algorithm (including its normalized version) is adversely affected by correlated inputs, it cannot be considered as a competitive candidate. Instead, an effective solution to this problem is offered by *transform domain* methods, which utilize an orthogonal transformation to a space that is attributed with favorable properties (Beaufays, 1995; Diniz, 2008; Chergui and Bouguezal, 2017).

Setting temporarily $\hat{x}_R[k - \Delta] = y[k]$ for notational convenience (see **Figure 3**), the output of the inverse filter reads

$$y[k] = \sum_{i=0}^{n_I} \hat{g}_I[k, i] \hat{x}_A[k - i] = \hat{\mathbf{x}}_A^T[k] \hat{\mathbf{g}}_I[k] \quad (26)$$

For any orthogonal matrix $\mathbf{S} \in \mathbb{R}^{n_I}$, the regression form of Equation (26) can be written as

$$y[k] = \hat{\mathbf{x}}_A^T[k] \mathbf{S}^T \mathbf{S} \hat{\mathbf{g}}_I[k] = \mathbf{u}^T[k] \mathbf{c}[k] \quad (27)$$

for $\mathbf{u}[k] = \mathbf{S} \hat{\mathbf{x}}_A[k]$ and $\mathbf{c}[k] = \mathbf{S} \hat{\mathbf{g}}_I[k]$. The orthogonal transformation of the input can be considered as another type of decorrelation. However, it has small effects on the convergence rate. The latter is treated by normalizing the entries of the transformed input vector by the square root of their power via

$$v_i[k] = \frac{1}{\sqrt{P_i[k] + \epsilon_i}} u_i[k], \quad i = 0, 1, \dots, n_I \quad (28)$$

where ϵ_i is a small constant ("stability" parameter),

$$P_i[k] = \gamma P_i[k-1] + (1 - \gamma) u_i^2[k], \quad i = 0, 1, \dots, n_I \quad (29)$$

and $\gamma \rightarrow 1$ is the power update factor. The transformed weights are then updated by a typical LMS filtering operation

$$\mathbf{c}[k+1] = \mathbf{c}[k] + \mu e[k] \mathbf{v}[k] \quad (30)$$

with μ being the step size, $e_I[k] = x_R[k - \Delta] - y[k] = x_R[k - \Delta] - \hat{x}_R[k - \Delta]$ the inverse adaptation error and $\mathbf{v}[k] = [v_1[k] \ \dots \ v_{n_I}[k]]^T$.

There's a plenty of options for the selection of the orthogonal matrix \mathbf{S} , including the discrete Fourier transform (DFT), the discrete Hartley transform (DHT) and the discrete cosine transform (DCT). Herein, we adopt the third option and we construct the orthogonal matrix as

$$\mathbf{S} = \begin{bmatrix} Q_{0,0} & Q_{0,1} & \dots & Q_{0,n_I-1} \\ Q_{1,0} & Q_{1,1} & \dots & Q_{1,n_I-1} \\ \vdots & \vdots & \ddots & \vdots \\ Q_{n_I-1,0} & Q_{n_I-1,1} & \dots & Q_{n_I-1,n_I-1} \end{bmatrix} \quad (31)$$

where

$$Q_{p,q} = \sqrt{\frac{2}{n_l}} K_p \cos\left(\frac{p(q+1/2)\pi}{n_l}\right), \quad p, q = 0, 1, \dots, n_l - 1 \quad (32)$$

for

$$K_p = \begin{cases} \frac{1}{\sqrt{2}}, & p = 0 \\ 1, & p \neq 0 \end{cases} \quad (33)$$

Since the DCT transform is fully parametrized by the filter order, the orthogonal matrix \mathbf{S} can be formulated and stored prior to the adaptive modeling process. Further details on the performance of transform domain adaptive algorithms can be found in Zhao et al. (2009), Kim and Wilde (2000), Lee and Un (1986), and Narayan et al. (1983).

3.4. Delay Compensation and Method's Hyper-Parameters

The successful adaptive modeling of the control plant and its inverse forces, ideally, the cascade to behave as a delayed unit impulse. This implies that a reference signal is driven to the control plant with unaltered dynamics, but at a delay Δ . To compensate for this delay, we integrate a one-step ahead prediction method, which is based on polynomial extrapolation (Horiuchi et al., 1999; Darby et al., 2001; Wallace et al., 2005). The reference signal that is driven to the inverse

controller is

$$x_R[k + \Delta] = \sum_{i=0}^{n_p} p_i x_R[k - i\Delta] \quad (34)$$

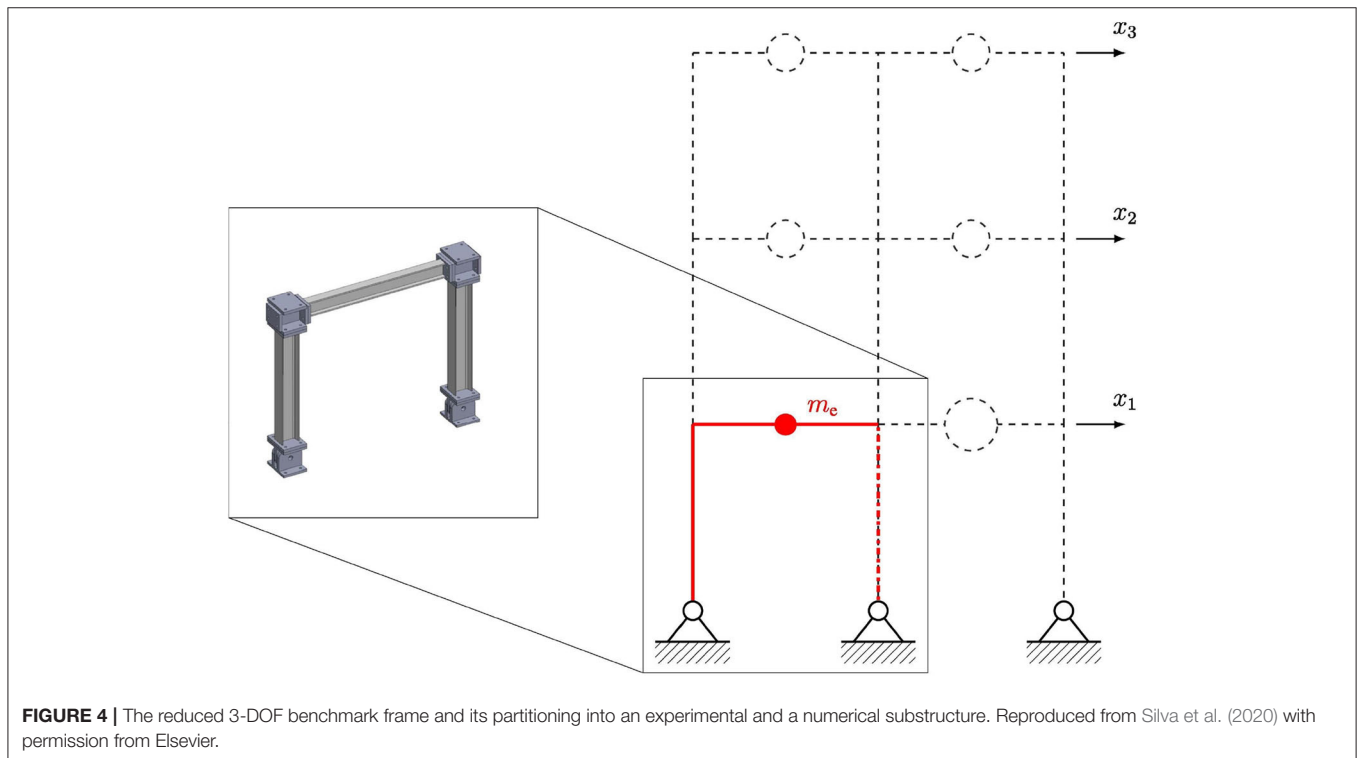
where n_p is the polynomial order and p_i the polynomial coefficients, which are calculated via the Lagrange basis function and are predefined for a given order.

Table 1 gathers all the hyper-parameters of the method. The most important of them pertain to the orders of the forward and the inverse adaptive filters, as well as to the step size of the DCT-LMS: these are essentially the quantities that the user has to decide for, every time a new experimental substructure is attached to a transfer system, composing thus the control plant. The default order of the polynomial extrapolation is sufficient, as long as the cascade is close to a pure delay. Higher orders do not, in general improve accuracy; actually they might oftentimes lead to instability, especially when Δ is large.

TABLE 2 | vRTHS partitioning cases.

Scheme	Floor mass (kg)	Modal damping (%)
Case 1	1,000	5
Case 2	1,100	4
Case 3	1,300	3
Case 4	1,000	3

Adapted from Silva et al. (2020) with permission from Elsevier.



4. APPLICATION STUDY

4.1. The vRTHS Benchmark Structure

In evaluating the performance of novel control schemes for RTHS in a safe manner, vRTHS offers a useful platform. VRTHS involves the implementation of a hybrid simulation fully in silico, whereby both the numerical substructure and the physical substructure are simulated. Crucially, vRTHS also involves recreation of the transfer functions associated with the actuation and signal artifacts associated to the actual physical implementation. The use of vRTHS can allow for rapid and safe assessment of various algorithms relating to the hybrid simulation procedure. The robustness of any algorithm can also be investigated by the introduction of uncertainty in the vRTHS.

The study of suitable control and delay compensation algorithms for RTHS has resulted in proposition of alternatives schemes, which have been investigated on disparate testing setups. However, hybrid simulation setups tend to be unique and hence it is difficult to fairly evaluate the relative performance of control schemes implemented on different setups. This provides the motivation for establishing benchmark problems, wherein the only variable is the control regime implemented.

Such a benchmark problem is recently proposed by Silva et al. (2020), who developed a vRTHS framework for the purpose of evaluating different control regimes on a unified system. This benchmark consists of a 2-bay, 3-story steel frame, in which the structural mass is concentrated on the floors, motion is allowed only horizontally on a single direction and damping is proportional. An originally 30-degrees of freedom (DOFs) linear elastic planar finite element model is reduced to a 3-DOF model, pinned at ground and excited on its base, which consists the reference structure (Figure 4). The benchmark is implemented in SIMULINK® and is created such that the controller block can easily be exchanged, whilst the rest of the system is left unchanged. This allows for the fair comparison of controllers. A number of uncertainties in the system parameters is also offered, to allow for analysis of controller robustness, along with a set of standardized performance metrics to aid comparison.

For the vRTHS tests the reference structure is partitioned into an “experimental” and a numerical substructure, with the former corresponding to a single bay of the ground floor and the latter consisting of the remainder of the structure (Figure 4). The structural properties of the experimental substructure are kept fixed, while the ones of the numerical substructure vary in accordance to the partition schemes of Table 2

The dynamics of the control plant (transfer system plus experimental substructure) are described as shown in Figure 5. The open-loop transfer function between the command and the achieved signals in continuous-time reads

$$G(s) = \frac{B_0}{A_5 s^5 + A_4 s^4 + A_3 s^3 + A_2 s^2 + A_1 s + A_0} \quad (35)$$

for

$$\begin{aligned} B_0 &= \alpha_1 \beta_0 A_0 = k_e \alpha_3 \beta_2 + \alpha_1 \beta_0 \\ A_1 &= k_e \alpha_3 \beta_1 + (k_e + c_3 \alpha_3 + \alpha_2) \beta_2 \\ A_2 &= k_e \alpha_3 + (k_e + c_3 \alpha_3 + \alpha_2) \beta_1 + (c_e + m_e \alpha_3) \beta_2 \\ A_3 &= (k_e + c_3 \alpha_3 + \alpha_2) + (c_e + m_e \alpha_3) \beta_1 + m_e \beta_2 \\ A_4 &= c_e + m_e \alpha_3 + m_e \beta_1 \\ A_5 &= m_e \end{aligned} \quad (36)$$

TABLE 3 | Parameter values for the control plant of Figure 5.

Parameter	Component	Nominal value	St. dev.	Units
$\alpha_1 \beta_0$	Servo-valve	2.13×10^{13}	-	m Pa/s
α_2	Actuator	4.23×10^6	-	m Pa
α_3	Actuator	3.3	1.3	1/s
β_1	Servo-valve	425	3.3	-
β_2	Servo-valve	10×10^4	3.31×10^3	1/s
m_e	Exp. sub.	29.1	-	kg
c_e	Exp. sub.	114.6	-	kg/s
k_e	Exp. sub.	1.19×10^6	5×10^4	N/m

Adapted from Silva et al. (2020) with permission from Elsevier.

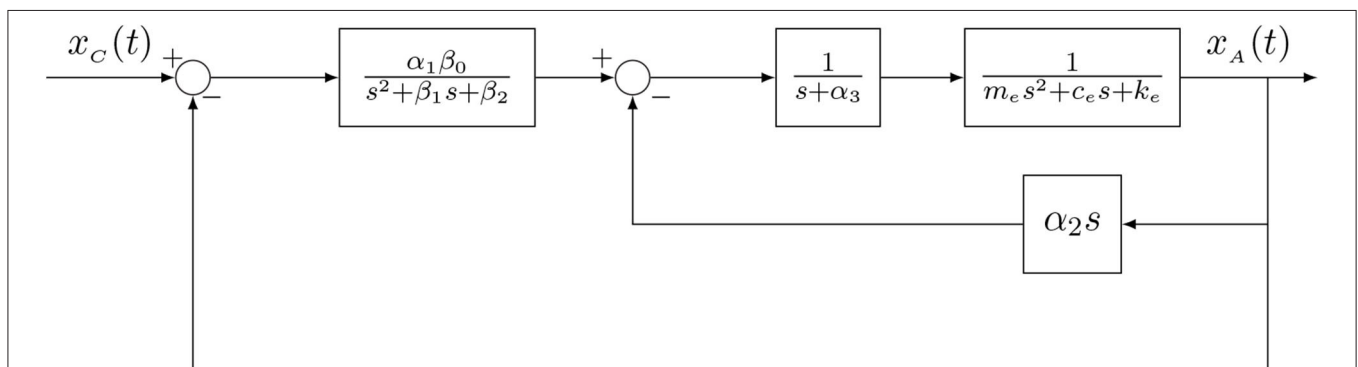
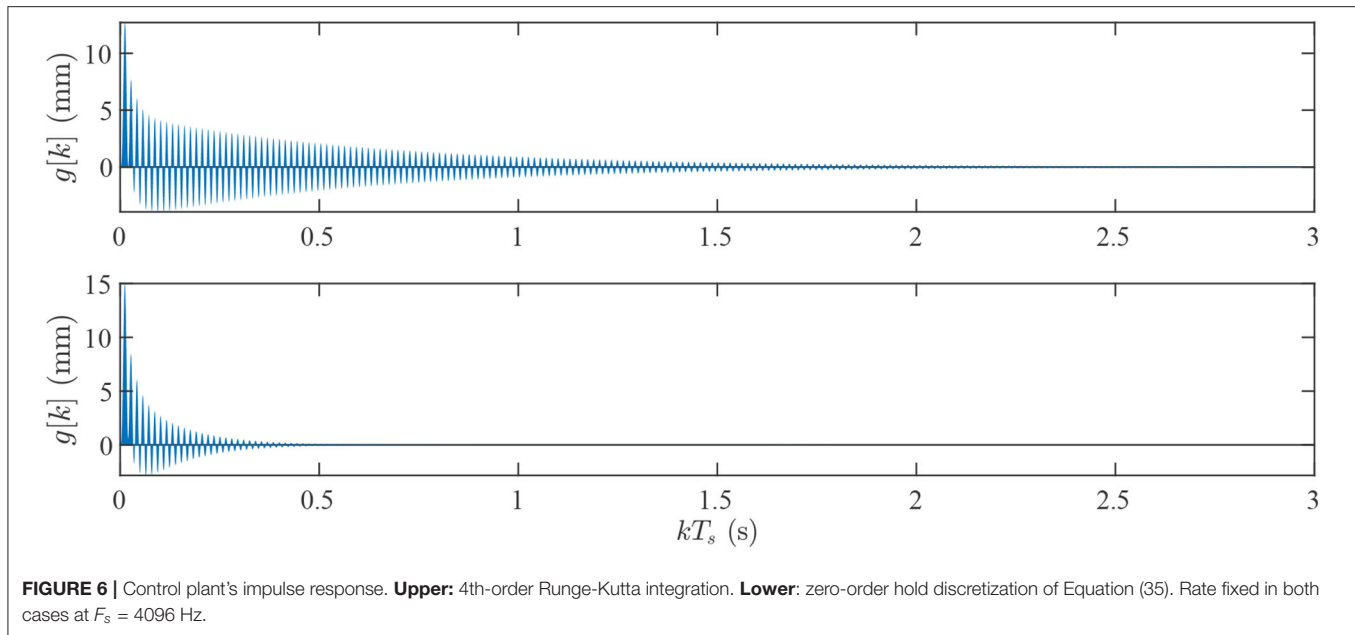


FIGURE 5 | Layout of the control plant. From left to right, the transfer functions on the upper branch correspond to the valve, actuator and experimental substructure dynamics, respectively, while the transfer function on the inner feedback loop corresponds to the control-structure interaction dynamics. Adapted from Silva et al. (2020) with permission from Elsevier.



The numerical values of all associated parameters are listed in **Table 3**. To incorporate a degree of uncertainty, for testing the robustness of a proposed controller, some parameters are defined as normally distributed random variables.

All vRTHS tests are conducted in SIMULINK[®] through the integration of the structural equations of motion via an explicit 4th-order Runge-Kutta numerical framework, at a fixed sampling rate $F_s = 4,096$ Hz. It is emphasized that the choice of the integration scheme has detrimental effects on the evolution of the dynamics and, consequently, on the behavior on the proposed adaptive modeling method. To demonstrate this, **Figure 6** displays the discrete-time impulse response of the control plant under two different discretization schemes: in the upper plot, $g[k]$ is calculated via the aforementioned integration, by applying a unit impulse excitation to the part of the SIMULINK[®] model that corresponds to **Figure 5**. In the lower part, the impulse response is obtained by the impulse-invariance transformation of Equation (35), e.g., $g[k] = T_s g(t = kT_s)$, where $g(t)$ is the continuous-time impulse response (the inverse Laplace transform of Equation 35). A quite different “damped” behavior is observed, which renders the integration-based impulse response attaining a much slower decay rate, necessitating the use of very high order FIR models for effective adaptive modeling of the control plant.

4.2. Adaptive Modeling

For generating the reference signal, a Markov-1 process of the form

$$u[k] + \phi_1 u[k-1] = e[k] \quad (37)$$

is adopted, where $e[k]$ is a zero-mean Gaussian white noise stochastic process of variance σ_{ee}^2 . In deciding for the values of ϕ_1 and σ_{ee}^2 , recall that the maximum and minimum eigenvalues of

Γ_{uu} are provided by the corresponding maximum and minimum of the power spectrum of $u[k]$, which is given by

$$S_{uu}(f) = \frac{1}{1 + 2 \cos\left(2\pi \frac{f}{F_s}\right) \phi_1 + \phi_1^2} \sigma_{ee}^2 \quad (38)$$

Thus,

$$\begin{aligned} \lambda_{\max} &= (1 - \phi_1)^2 \sigma_{ee}^2 \\ \lambda_{\min} &= (1 + \phi_1)^2 \sigma_{ee}^2 \end{aligned}$$

and the eigenvalue spread for Γ_{uu} is

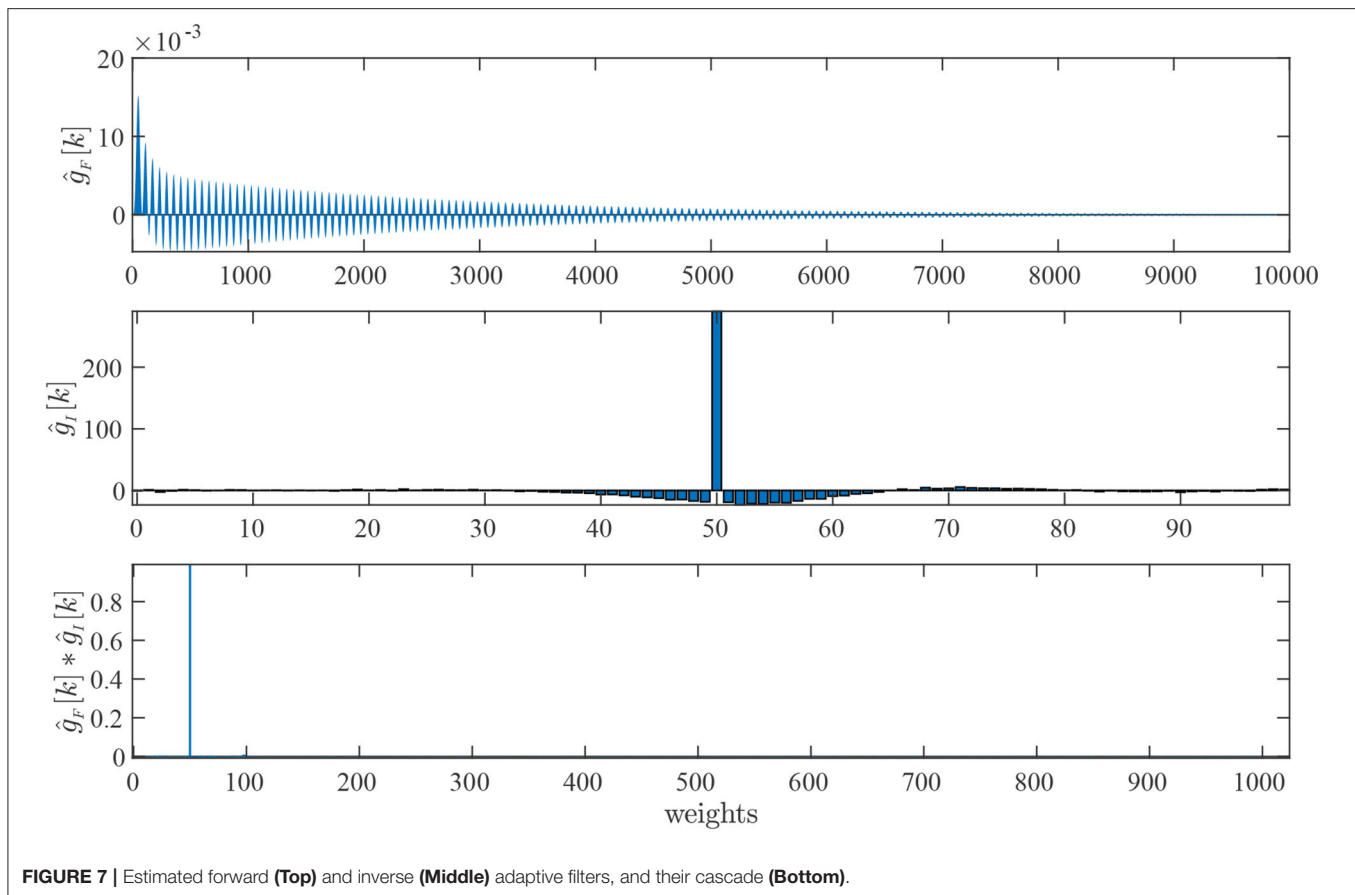
$$\text{eigenvalue spread} = \left(\frac{1 - \phi_1}{1 + \phi_1} \right)^2 \quad (39)$$

In order to maintain this number close to one, our choice is $\phi_1 = -0.01$ (the minus sign is adopted for attributing $S_{uu}(f)$ with low pass characteristics). The variance of $e[k]$ is then determined by first setting $2\sigma_{uu} = 0.01$, for constraining 95% of the input's amplitude within the ± 10 mm range. From the theoretical Markov-1 process variance

$$\sigma_{uu}^2 = \frac{1}{1 - \phi_1^2} \sigma_{ee}^2 \quad (40)$$

solving for σ_{ee}^2 leads to $\sigma_{ee}^2 \approx 2.5 \times 10^{-5}$.

The adaptation process is carried out *simultaneously*, that is, the forward and the inverse adaptation counterparts operate in synchronous mode. Having established the statistics of the reference signal, several trials are performed for the rest of the hyper-parameters of the method (e.g., the forward and inverse filter orders and the step size of the DCT-LMS), while the total adaptation time frame is fixed to 60 s. Some critical observations



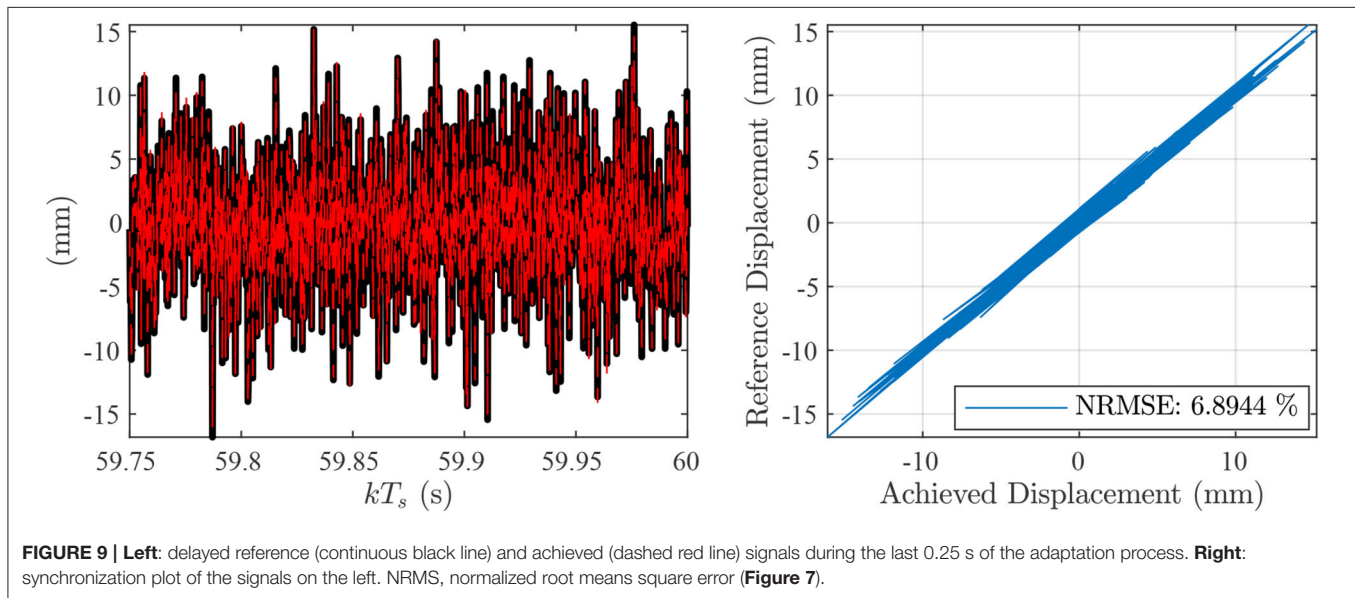
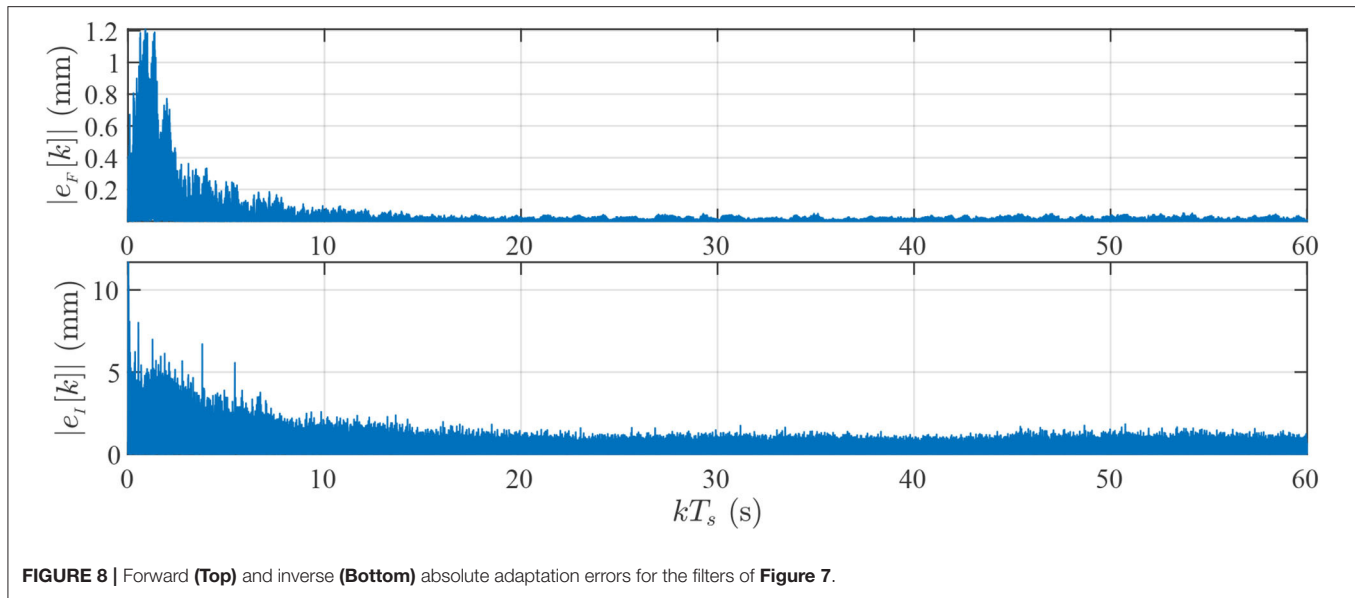
during the evolution of the whole adaptation process can be summarized by the following remarks:

- In all trials the convergence in synchronous mode is quite fast and robust against the DCT-LMS step size. The forward adaptation phase requires at least around 10–15 s for proper convergence.
- Within this time the DCT-LMS makes a rapid improvement, indicating that full convergence of the forward filter is not necessary for adapting the inverse.
- A proper selection of the DCT-LMS step size is important. In many cases, a quite fast convergence is observed, yet, the final result is not optimal in terms of cascade dynamics, as the corresponding impulse response returns “noisy.”
- It is noted that a fair number of trials is conducted by applying non-Markovian inputs, as well as other adaptive algorithms. Regarding the former, signals composed from filtering Gaussian white noise at cut-off frequencies equal to 100 Hz and $F_s/2$ are also tested. The result is a severe distortion in the filters’ weights, followed by inability to converge within the specified time frame. Very slow convergence is also observed in the case where the normalized LMS algorithm replaces the DCT-LMS one for the adaptation of the inverse filter. This is, though, an expected result, attributed to the inability of the algorithm to cope with colored inputs.

Aspects of these remarks can be visually validated from **Figures 7–10**, which display the results for $n_F = 10,000$ and $n_I = 100$ ($\Delta = 50$, $\mu = 5 \times 10^{-3}$), our final choice for the forward and inverse FIR filters. The fact that $\hat{g}_F[k]$ is very long (**Figure 7**, top) is explained by the high sampling rate of the simulation (4,096 Hz): in absolute times this impulse response evolves over 2.14 s (the settling time of the control plant’s step response is around 1 s). It is noted that when lower orders are considered (for example 8,000 and 9,000 weights), an apparent distortion around the last weights of the cascade is caused: in fact, this is a practical way of detecting that the forward filter requires higher orders. The absolute error (**Figure 8**, upper part) confirms that convergence has been succeeded already after 15–20 s.

In contrast, the inverse filter dynamics are expanded in a considerably smaller time frame (around 24 ms, **Figure 7**, middle). The dominant part of $\hat{g}_I[k]$ is located around the chosen delay (which is typical for inverse filters) and there exist many leading and trailing weights that could, potentially, be treated as zeros. However, adaptation at lower order/delay pairs (indicatively 80/40, 60/30, and 40/20), or at fixed order ($n_I = 100$) and lower delays (e.g., $\Delta = 40, 30$, and 20) does not improve the inverse controller. Thus, the 100/50 pair results as the lowest possible accurate choice for this plant.

The absolute adaptation error (**Figure 8**, bottom) exhibits fast convergence (after approximately 25–30 s), with longer time



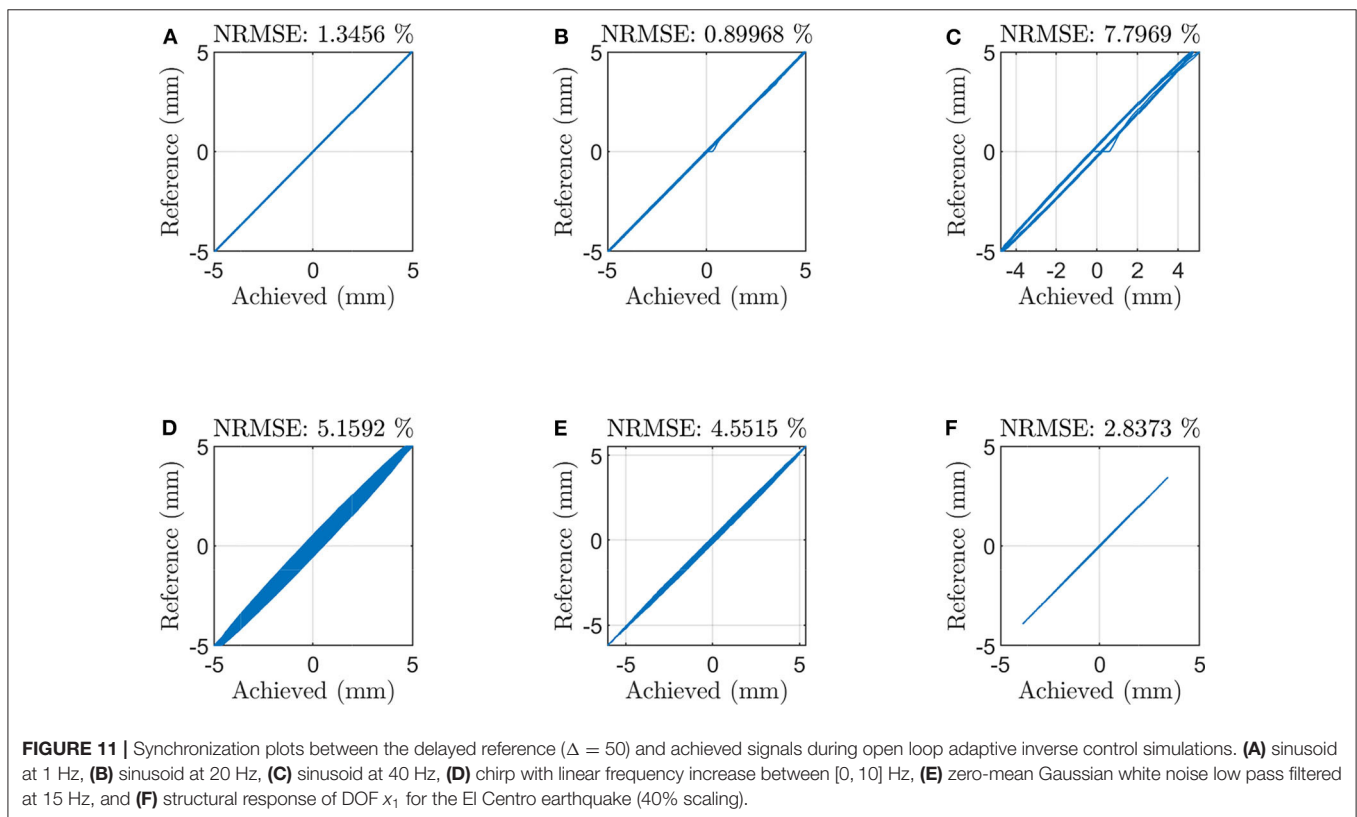
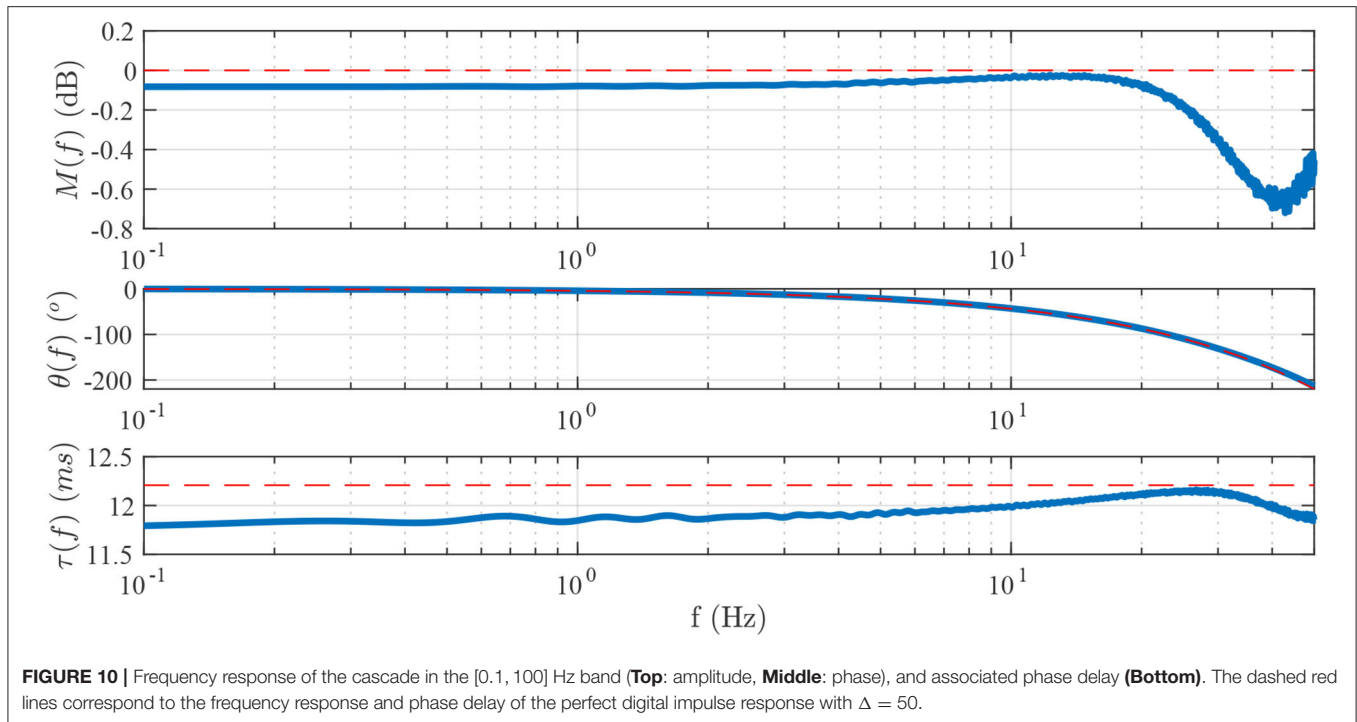
needed however for a finer tuning of the weights; it is observed that by reducing the adaptation time to half the fixed frame (e.g., 30 s) and keeping all other hyper-parameters unaltered leads to sub-par results. It is also worth mentioning that the converged values for $|e_I[k]|$ are higher in comparison to the ones of $|e_F[k]|$. This is also expected since, as already mentioned in section 3.3, the inverse adaptation performs as a whitening filter. Indicatively, **Figure 9** shows the synchronization plot between the delayed reference and the achieved signals for the last 0.25 s of the adaptation process. A normalized root-mean-square error, defined as

$$\text{NRMSE} = \sqrt{\frac{\sum_{k=1}^N (x_R[k] - \hat{x}_R[k])^2}{\sum_{k=1}^N x_R^2[k]}} \quad (41)$$

of approximately 7% is estimated.

The cascade of $\hat{g}_F[k]$ and $\hat{g}_I[k]$, the first 1,024 weights of which are plotted in **Figure 7**, bottom, depicts a very good approximation to a pure delay. This is verified in the frequency domain against the perfect digital impulse with $\Delta = 50$; as **Figure 10** displays, there is a quite close resemblance between the frequency responses and the associated phase delays between the estimated and the perfect delayed impulses. The highest distortion in amplitude, located around 40 Hz, is not more than -0.8 dB, whereas the largest difference in phase delay is approximately 0.5 ms.

In order to obtain a better insight on the effects of the observed distortions in the frequency domain, a number of open loop simulations is conducted with the adaptive inverse controller



placed before the control plant. Different signals are selected as references, including sinusoids at different frequencies, a chirp, low pass filtered Gaussian white noise, as well as the structural

response of DOF x_1 for the El Centro earthquake (40% scaling). The results of the simulations are again interpreted in terms of synchronization plots and are shown in **Figure 11**. Apart from

TABLE 4 | vRTHS evaluation criteria for the partitioning cases of **Table 2**.

Quantity	J_1 (ms)	J_2 (%)	J_3 (%)	J_4 (%)	J_5 (%)	J_6 (%)	J_7 (%)	J_8 (%)	J_9 (%)
Case 1									
Nominal	0.00	3.29	3.63	4.41	3.95	3.36	3.38	1.81	1.87
Mean	0.05	3.68	4.23	5.76	4.74	4.48	4.50	2.43	2.46
St. Dev.	0.16	0.57	0.91	2.06	1.19	2.31	2.31	1.20	1.21
Min.	0.00	2.98	3.01	3.13	2.96	0.59	0.60	0.47	0.45
Max.	0.70	5.10	6.46	9.62	6.85	8.90	8.92	4.65	4.61
Case 2									
Nominal	0.00	3.10	3.64	4.18	3.43	3.25	3.25	1.80	1.83
Mean	0.06	3.52	4.21	5.31	4.13	4.26	4.27	2.37	2.38
St. Dev.	0.19	0.49	0.80	1.42	0.72	1.62	1.62	0.88	0.88
Min.	0.00	2.69	2.70	3.59	2.87	2.36	2.37	1.33	1.35
Max.	0.70	4.49	5.65	9.22	5.84	8.70	8.71	4.77	4.73
Case 3									
Nominal	0.00	2.33	3.13	4.85	4.20	5.02	5.01	3.47	3.45
Mean	0.19	2.92	3.93	7.36	5.93	7.27	7.27	4.97	5.00
St. Dev.	0.38	0.75	1.06	4.37	3.05	4.73	4.73	3.22	3.23
Min.	0.00	1.85	2.13	2.09	2.10	1.37	1.37	0.96	0.99
Max.	1.00	4.38	6.02	15.81	11.72	16.50	16.48	11.24	11.34
Case 4									
Nominal	0.00	2.85	3.42	5.98	4.23	5.59	5.60	2.84	2.87
Mean	0.16	3.27	4.13	8.52	5.64	7.87	7.88	3.97	3.96
St. Dev.	0.30	0.55	0.79	3.97	1.98	4.06	4.06	2.01	2.00
Min.	0.00	2.53	3.09	3.63	3.18	2.86	2.87	1.49	1.48
Max.	1.00	4.28	5.52	17.20	9.95	16.66	16.69	8.31	8.32

the case of 40 Hz (**Figure 11C**), which returns a NRMSE value of approximately 8%, all other simulations produce achieved signals of good quality in a wide frequency range.

4.3. vRTHS

We are now almost ready to integrate the estimated adaptive inverse controller to the vRTHS closed loop. To this end, the delay compensation scheme outlined in section 3.4 is applied and the reference signal that is sent to the adaptive inverse controller is calculated from Equation (34) as

$$x_r[k+\Delta] = 4x_1[k] - 6x_1[k-\Delta] + 4x_1[k-2\Delta] - x_1[k-3\Delta] \quad (42)$$

where $x_1[k]$ is the displacement of the interface DOF calculated at time k and $\Delta = 50$, which corresponds to a cascade delay of 12.2 ms. The numerical substructure is excited by the El Centro earthquake at 40% intensity, while for each case of **Table 2** 20 individual simulations are executed. The results are presented in terms of the criteria J_1 to J_9 that are reported in Silva et al. (2020) and listed in **Table 4**.

The following points summarize the performance of the proposed data-driven method:

- The delay between the reference and the achieved displacement (e.g., J_1) is exactly zero in all nominal simulations, and very low in the perturbed simulations of all partitioning case studies. The statistics of the perturbed simulations are comparable, indicating robustness of the controller against uncertainty. It is noted that the total number of non-zero delay simulations are 3, 2, 5 and 5 in partitioning case studies 1 to 4, respectively. This is illustrated in **Supplementary Tables 1–4**.
- The NRMSE between the reference and the achieved displacement (e.g., J_2) is also kept quite low, ranging from 2.85 to 3.29% in the nominal simulations. These numbers are within the range of the NRMSEs shown at the synchronization plots of **Figure 11**. The mean values of the perturbed simulations follow closely the ones of their nominal counterparts, whereas the corresponding standard deviations are one order of magnitude lower.
- Expectedly, the normalized peak tracking error (e.g., J_3) returns a bit increased, compared to J_2 , but again is kept in very low levels.
- Criteria J_4 to J_6 calculate the NRMSEs between the relative displacements of the storys during vRTHSs and the ones during the simulation of the reference structure (e.g., without substructuring), while J_7 to J_9 the normalized peak tracking errors of the same quantities. The associated errors never exceed 6% in the nominal cases, whereas the mean values of the perturbed simulations are higher (reaching up to 8.52% in partitioning case study 4), followed by increased dispersions. It is, however, noted that in the offered benchmark problem, the simulation of the reference structure is accomplished via a different discretization scheme (either zero, or first order hold), to the one implemented for vRTHS (e.g., the explicit 4th-order Runge-Kutta integration) and, as shown in **Figure 6** there might be significant differences in the calculated structural responses.

We conclude that the efficacy and robustness of the adaptive inverse controller is quite competitive in all partitioning case studies. In comparing the method presented herein, the reader may refer to Silva et al. (2020), Wang et al. (2019), Najafi and Spencer (2019), Fernandois (2019), and Ning et al. (2019), where several alternative approaches for RTHS are developed and assessed through the same vRTHS benchmark problem.

5. CONCLUSIONS

In this study, we explore the possibility of conducting RTHS from a purely data-driven perspective. By setting a number of specifications that such a framework should fulfill, we demonstrate that this is indeed feasible and it is characterized by several potential advantages, including transparency, robustness and minimum tuning. Further improvements are possible, such as a more rigorous methodology for automating/adapting the selection of the method's hyper-parameters to the examined case study, the integration of the delay compensation to the adaptation process, as well as techniques for reducing the delay of the cascade's impulse and increasing the effective

frequency band of RTHS. These are left as objectives of future work together with the design and conduction of an extensive experimental campaign for the validation of the method.

DATA AVAILABILITY STATEMENT

The software and data developed for this study are available upon request to the corresponding author.

AUTHOR CONTRIBUTIONS

TS: methodology, conduction of simulations, and manuscript preparation. VD: conceptualization, methodology, conduction of simulations, and manuscript preparation.

REFERENCES

- Bayer, V., Dorka, U. E., Füllekrug, U., and Gschwilm, J. (2005). On real-time pseudo-dynamic sub-structure testing: algorithm, numerical and experimental results. *Aerospace Sci. Technol.* 9, 223–232. doi: 10.1016/j.ast.2005.01.009
- Beaufays, F. (1995). Transform-domain adaptive filters: an analytical approach. *IEEE Trans. Signal Process.* 43, 422–431. doi: 10.1109/78.348125
- Benson Shing, P. (2008). “Real-time hybrid testing techniques,” in *Modern Testing Techniques for Structural Systems*, eds O. S. Bursi and D. Wagg (Vienna: Springer), 259–292. doi: 10.1007/978-3-211-09445-7_6
- Carrion, J. E., and B. F. Spencer, J. (2006). “Real-time hybrid testing using model-based delay compensation,” in *4th International Conference on Earthquake Engineering* (Taipei), 299.
- Chae, Y., Kazemibidokhti, K., and Ricles, J. M. (2013). Adaptive time series compensator for delay compensation of servo-hydraulic actuator systems for real-time hybrid simulation. *Earthquake Eng. Struct. Dyn.* 42, 1697–1715. doi: 10.1002/eqe.2294
- Chen, C., and Ricles, J. M. (2009). Improving the inverse compensation method for real-time hybrid simulation through a dual compensation scheme. *Earthquake Eng. Struct. Dyn.* 38, 1237–1255. doi: 10.1002/eqe.904
- Chergui, L., and Bouguezel, S. (2017). A new pre-whitening transform domain LMS algorithm and its application to speech denoising. *Signal Process.* 130, 118–128. doi: 10.1016/j.sigpro.2016.06.021
- Darby, A. P., Blakeborough, A., and Williams, M. S. (2001). Improved control algorithm for real-time substructure testing. *Earthquake Eng. Struct. Dyn.* 30, 446–448. doi: 10.1002/eqe.18
- Dertimanis, V., Mouzakis, H., and Psycharis, I. (2015a). On the acceleration-based adaptive inverse control of shaking tables. *Earthquake Eng. Struct. Dyn.* 44, 1329–1350. doi: 10.1002/eqe.2518
- Dertimanis, V., Mouzakis, H., and Psycharis, I. (2015b). “On the control of shaking tables in acceleration mode: an adaptive signal processing framework,” in *Experimental Research in Earthquake Engineering: EU-SERIES Concluding Workshop*, eds F. Taucer and R. Apostolska (Cham: Springer International Publishing), 159–172. doi: 10.1007/978-3-319-10136-1_12
- Diniz, P. S. R. (2008). *Adaptive Filtering: Algorithms and Practical Implementation*, 3rd Edn. New York, NY: Springer.
- Doherty, J., and Porayath, R. (1997). A robust echo canceler for acoustic environments. *IEEE Trans. Circ. Syst. II Anal. Digit. Signal Process.* 44, 389–396. doi: 10.1109/82.580846
- Douglas, S. C., Cichocki, A., and Amari, S. (1999). Self-whitening algorithms for adaptive equalization and deconvolution. *IEEE Trans. Signal Process.* 47, 1161–1165. doi: 10.1109/78.752617
- Fernandois, G. A. (2019). Application of model-based compensation methods to real-time hybrid simulation benchmark. *Mech. Syst. Signal Process.* 131, 394–416. doi: 10.1016/j.ymssp.2019.05.041
- EC: methodology, supervision, manuscript preparation, and funding acquisition.
- ## FUNDING
- This work was carried out as part of the ITN project DyVirt and has received funding from the European Union’s Horizon 2020 research and innovation programme under the Marie Skłodowska-Curie grant agreement no. 764547.
- ## SUPPLEMENTARY MATERIAL
- The Supplementary Material for this article can be found online at: <https://www.frontiersin.org/articles/10.3389/fbuil.2020.570947/full#supplementary-material>
- Glentis, G.-O., Berberidis, K., and Theodoridis, S. (1999). Efficient least squares adaptive algorithms for fir transversal filtering. *IEEE Signal Process. Mag.* 16, 13–41. doi: 10.1109/79.774932
- Hayes, M. H. (1996). *Statistical Digital Signal Processing and Modeling*. New York, NY: John Wiley & Sons Ltd.
- Horiuchi, T., Inoue, M., Konno, T., and Namita, Y. (1999). Real-time hybrid experimental system with actuator delay compensation and its application to a piping system with energy absorber. *Earthquake Eng. Struct. Dyn.* 28, 1121–1141. doi: 10.1002/(SICI)1096-9845(199910)28:10<1121::AID-EQE858>3.0.CO;2-O
- Jeng, J.-T. (2000). Nonlinear adaptive inverse control for the magnetic bearing system. *J. Magnet. Magnet. Mater.* 209, 186–188. doi: 10.1016/S0304-8853(99)00683-6
- Kim, D. I., and Wilde, P. (2000). Performance analysis of the DCT-LMS adaptive filtering algorithm. *Signal Process.* 80, 1629–1654. doi: 10.1016/S0165-1684(00)00098-0
- Lee, J. C., and Un, C. K. (1986). Performance of transform-domain LMS adaptive digital filters. *IEEE Trans. Acoust. Speech Signal Process.* 34, 499–510. doi: 10.1109/TASSP.1986.1164850
- Li, W., and Chen, X. (2013). Compensation of hysteresis in piezoelectric actuators without dynamics modeling. *Sens. Actuat. A Phys.* 199, 89–97. doi: 10.1016/j.sna.2013.04.036
- Mahin, S. A., Shing, P. S. B., Thewalt, C. R., and Hanson, R. D. (1989). Pseudodynamic test method-current status and future directions. *J. Struct. Eng.* 115, 2113–2128. doi: 10.1061/(ASCE)0733-9445(1989)115:8(2113)
- Manolakis, D. G., Ingle, V. K., and Kogon, S. M. (2005). *Statistical and Adaptive Signal Processing*. Norwood, MA: Artech House, Inc.
- Najafi, A., and Spencer, B. F. (2019). Adaptive model reference control method for real-time hybrid simulation. *Mech. Syst. Signal Process.* 132, 183–193. doi: 10.1016/j.ymssp.2019.06.023
- Nakashima, M. (2001). Development, potential, and limitations of real-time online (pseudo-dynamic) testing. *Philos. Trans. R. Soc. Lond. Ser. A Math. Phys. Eng. Sci.* 359, 1851–1867. doi: 10.1098/rsta.2001.0876
- Nakashima, M., Kato, H., and Takaoka, E. (1992). Development of real time pseudodynamic testing. *Earthquake Eng. Struct. Dyn.* 21, 79–92. doi: 10.1002/eqe.4290210106
- Narayan, S. S., Narayan, S. S., Peterson, A. M., and Narasimha, M. J. (1983). Transform domain LMS algorithm. *IEEE Trans. Acoust. Speech Signal Process.* 31, 609–615. doi: 10.1109/TASSP.1983.1164121
- Ning, X., Wang, Z., Zhou, H., Wu, B., Ding, Y., and Xu, B. (2019). Robust actuator dynamics compensation method for real-time hybrid simulation. *Mech. Syst. Signal Process.* 131, 49–70. doi: 10.1016/j.ymssp.2019.05.038
- Oppenheim, A. V., Schaffer, R. W., and Buck, J. R. (1999). *Discrete-Time Signal Processing*, 2nd Edn. New Jersey, NJ: Prentice-Hall, Inc.
- Pegon, P. (2008). “Continuous PsD testing with substructuring,” in *Modern Testing Techniques for Structural Systems*, eds O. S. Bursi and D. Wagg (Vienna: Springer), 197–257. doi: 10.1007/978-3-211-09445-7_5

- Plett, G. L. (2003). Adaptive inverse control of linear and nonlinear systems using dynamic neural networks. *IEEE Trans. Neural Netw.* 14, 360–376. doi: 10.1109/TNN.2003.809412
- Rørtveit, Ø. L., and Husøy, J. H. (2009). “A new prewhitening-based adaptive filter which converges to the wiener-solution,” in *2009 Conference Record of the Forty-Third Asilomar Conference on Signals, Systems and Computers* (Pacific Grove, CA), 1360–1364. doi: 10.1109/ACSSC.2009.5469890
- Shen, G., Zheng, S.-T., Ye, Z.-M., Huang, Q.-T., Cong, D.-C., and Han, J.-W. (2011). Adaptive inverse control of time waveform replication for electrohydraulic shaking table. *J. Vibrat. Control* 17, 1611–1633. doi: 10.1177/1077546310380431
- Shing, P. B. (2008). “Integration schemes for real-time hybrid testing,” in *Hybrid Simulation: Theory, Implementation and Applications*, eds V. Saouma and M. V. Sivaselvan (London: Taylor and Francis), 25–45.
- Silva, C., Gomez, D., Maghareh, A., Dyke, S., and Spencer, B. Jr. (2020). Benchmark control problem for real-time hybrid simulation. *Mech. Syst. Signal Process.* 135:106381. doi: 10.1016/j.ymssp.2019.106381
- Takanashi, K., and Nakashima, M. (1987). Japanese activities on on-line testing. *J. Eng. Mech.* 113, 1014–1031. doi: 10.1061/(ASCE)0733-9399(1987)113:7(1014)
- Wallace, M., Wagg, D., and Neild, S. (2005). An adaptive polynomial based forward prediction algorithm for multi-actuator real-time dynamic substructuring. *Proc. R. Soc. A Math. Phys. Eng. Sci.* 461, 3807–3826. doi: 10.1098/rspa.2005.1532
- Wang, Z., Ning, X., Xu, G., Zhou, H., and Wu, B. (2019). High performance compensation using an adaptive strategy for real-time hybrid simulation. *Mech. Syst. Signal Process.* 133:106262. doi: 10.1016/j.ymssp.2019.106262
- Widrow, B., and Hoff, M. E. (1960). “Adaptive switching circuits,” in *IRE Wescon Conference Record* (Los Angeles, CA), 96–104. doi: 10.21236/AD0241531
- Widrow, B., Plett, G., Ferreira, E., and Lamego, M. (1998). Adaptive inverse control based on nonlinear adaptive filtering. *IFAC Proc. Vol.* 31, 211–216. doi: 10.1016/S1474-6670(17)42160-4
- Widrow, B., and Plett, G. L. (1996). “Adaptive inverse control based on linear and nonlinear adaptive filtering,” in *Proceedings of International Workshop on Neural Networks for Identification, Control, Robotics and Signal/Image Processing* (Venice), 30–38. doi: 10.1109/NICRSP.1996.542742
- Widrow, B., and Wallach, E. (2007). *Adaptive Inverse Control: A Signal Processing Approach*. New York, NY: John Wiley & Sons Ltd.
- Xiaofang, Y., Yaonan, W., Wei, S., and Lianghong, W. (2010). RBF networks-based adaptive inverse model control system for electronic throttle. *IEEE Trans. Control Syst. Technol.* 18, 750–756. doi: 10.1109/TCST.2009.2026397
- Yuan, X., Wang, Y., and Wu, L. (2008). Adaptive inverse control of excitation system with actuator uncertainty. *Neural Process Lett.* 27, 125–136. doi: 10.1007/s11063-007-9064-7
- Zhao, S., Man, Z., Khoo, S., and Wu, H. R. (2009). Stability and convergence analysis of transform-domain LMS adaptive filters with second-order autoregressive process. *IEEE Trans. Signal Process.* 57, 119–130. doi: 10.1109/TSP.2008.2007618

Conflict of Interest: The authors declare that the research was conducted in the absence of any commercial or financial relationships that could be construed as a potential conflict of interest.

Copyright © 2020 Simpson, Dertimanis and Chatzi. This is an open-access article distributed under the terms of the Creative Commons Attribution License (CC BY). The use, distribution or reproduction in other forums is permitted, provided the original author(s) and the copyright owner(s) are credited and that the original publication in this journal is cited, in accordance with accepted academic practice. No use, distribution or reproduction is permitted which does not comply with these terms.



Hybrid Test on a Simply Supported Bridge With High-Damping Rubber Bearings

Chengyu Yang¹, Xuesong Cai^{2*}, Ziqin Lai³ and Yong Yuan¹

¹ State Key Laboratory of Disaster Reduction in Civil Engineering, Tongji University, Shanghai, China, ² Department of Geotechnical Engineering, Tongji University, Shanghai, China, ³ Guangzhou Municipal Engineering Design and Research Institute, Guangzhou, China

OPEN ACCESS

Edited by:

Chia-Ming Chang,
National Taiwan University, Taiwan

Reviewed by:

Pei-Ching Chen,
National Taiwan University of Science
and Technology, Taiwan

Tao Wang,
China Earthquake Administration,
China

*Correspondence:

Xuesong Cai
caixuesong2009@163.com

Specialty section:

This article was submitted to
Earthquake Engineering,
a section of the journal
Frontiers in Built Environment

Received: 22 May 2020

Accepted: 27 July 2020

Published: 25 September 2020

Citation:

Yang C, Cai X, Lai Z and Yuan Y
(2020) Hybrid Test on a Simply
Supported Bridge With
High-Damping Rubber Bearings.
Front. Built Environ. 6:141.
doi: 10.3389/fbuil.2020.00141

In this study, hybrid simulation techniques are used to test earthquake excitation on a supported bridge with High-damping rubber (HDR) bearings, which are widely used in girder bridges. It is impractical to make a full-scale or large-scale test of a whole bridge in the laboratory and substructure hybrid simulation techniques can overcome these scale issues to some extent. Using the software framework OpenFresco, the study involved a continuous exchange of data between a numerical model and a physical specimen. An experimental bearing element is introduced to the HDR bearings, and the remainder of the structure is modeled with beam-column elements for numerical analysis. These hybrid simulation results match the analytical results under the designated earthquake excitation. Therefore, this technique reproduces the seismic performance of a simply supported bridge with HDR bearings. This series of dynamic hybrid simulations of a simply supported bridge provides useful insights into the selection of HDR bearings. The study analyses and discusses the mechanical properties of these HDR bearings when subject to earthquake excitations.

Keywords: hybrid simulation, seismic performance, simply supported bridge, high-damping rubber bearing, OpenFresco

INTRODUCTION

Earthquakes are among the most catastrophic natural hazards. They have caused tremendous loss of life and damage to infrastructure throughout history. Bridges are essential components of transportation infrastructure, and the damage to or collapse of these structures caused by earthquakes can not only cause casualties, it can also influence important public transportation systems, potentially hindering the life-saving services needed to respond to these disasters. Therefore, measures that reduce the seismic responses of bridge structures are of considerable importance. Seismic isolation achieves high seismic performance for the seismic safety of bridge structures (Yamamoto et al., 2009). Rubber bearings are standard components of these bridge isolation systems. Compared with conventional rubber bearings, high-damping rubber (HDR) bearings have advantages such as a high energy-dissipating capacity, low maintenance costs, and little residual deformation. Moreover, HDR bearings are not prone to shear and displacement failure, which may occur on other types of rubber bearings (Li et al., 2013), meaning they are

widely used in girder bridges. With the application of HDR-bearing isolators, there is a considerable decrease in the seismic responses of bridge structures. Thus, the characteristics of these HDR bearing isolators have a substantial influence on the vibration behavior of bridge structures.

With respect to the numerical modeling of bearings, Abe et al. (2004) have proposed a displacement-dependent elastoplastic model. The proposed bearing model could predict the bearing response in both one-dimensional and two-dimensional cases. Amin et al. (2006a) propose an HDR bearing constitutive model based on the multiplicative decomposition of the deformation gradient tensor. This type of model could describe the viscosity-induced rate-dependent effect. Yamamoto et al. (2012) have conducted multiaxial cyclic tests on three types of rubber bearings to study the equivalent stiffness and damping ratio. These results indicate that the effects of triaxial loading significant. Abe et al. (2004) conducted bidirectional loading tests on seven full-scale HDR bearing isolators. Based on the test results, an analytical model that simulates the restoring force under bidirectional loading was proposed in the OpenSEES platform. Chaudhary and Masato Abe Fujino (2001) utilized a method to identify the modal and structural parameters of a bridge with HDR bearings.

In cyclic tests on HDR bearings, test results do not capture an adequate description of the dynamic behavior of HDR bearings, especially under an earthquake loading pattern. Although shaking table tests can simulate the overall seismic behavior of a girder bridge in a more realistic way, they are limited by the scale ratio and the cost of the test. As a result, few full-scale girder bridge shaking table tests have been published.

In a girder bridge, the mechanical properties of the superstructure (generally referred to as the girder) and the substructure (generally referred to as pier) are relatively easy to model with the finite element (FE) method in terms of its structural nature as well as dynamic performance under common earthquake loading. However, HDR bearings are not easily studied using a proper numerical model, due to their nonlinear behavior and complex constitutive model. It is therefore important to develop hybrid simulations to study the mechanical properties of HDR bearings when subject to earthquakes, which could be of great value when applied to engineering.

Compared with traditional test methods and model identification methods, hybrid simulation techniques can to an extent reproduce the seismic process of structures. Hybrid simulation techniques take advantage of numerical modeling and test techniques. With hybrid simulation techniques, scale ratio issues existed in shake table test would be tackled. Given the lack of dynamic test results, this work studies HDR bearings using hybrid simulation techniques. HDR bearings are tested as the physical substructure, while the other components of the girder bridge are modeled as the numerical substructure. First, a hybrid simulation process of a simply supported bridge with HDR bearings is presented. Then, this article analyses a standard case study to verify the effectiveness and accuracy of substructure techniques. Finally, it presents the hybrid simulation test results for HDR bearings under three situations of earthquake excitation.

STRUCTURE AND MODELING APPROACH

As shown in **Figure 1**, the prototype structure analyzed in this study is a simply supported bridge with four steel piers. In order to meet the requirements of test loading equipment, the FE model is designed as a scaled model with a ratio of 1:3. Based on the dynamic equation and the Buckingham- π theorem, similitude ratios for the length and acceleration are chosen as the fundamental terms, and other scale factors include the parameters of the length, mass, time, stress, velocity, force, and stiffness, as shown in **Table 1**.

The scaled simply supported bridge model has a span length of 5.00 m. The bridge weighs 54.0 tons in total. The structural components of the simply supported bridge include the girder, the bridge deck, the counterweight, the HDR bearings, and the piers.

Structure Details

The details of the HDR bearings are shown in **Figure 2**. The sectional dimensions of the HDR bearing specimens used in the tests are 400 mm \times 400 mm. The total thickness of the HDR bearing is 140 mm.

According to the requirements of the *Standard for Design of Steel Structures*, the cover beams, the girders, and the piers are made of Q235 steel with a yield stress of 235.0 MPa (Ministry of Construction of the People's Republic of China, 2003). The sectional dimensions of the piers are 200 mm \times 200 mm, and the thickness of the bridge piers is 5 mm. The sectional dimensions of the cover beams are 700 mm \times 400 mm. The cover beams are used to connect the girders and the piers with bolts. The HDR bearings are located on top of the cover beams. The I-shaped section girder has a width of 650 mm and a height of 400 mm and is made of Q235 steel.

Ground Motions

The Imperial Valley record, North Ridge record, and Loma Prieta record are adopted as the input earthquake motions for the hybrid simulation process. **Figure 3** shows the seismic acceleration time histories and spectra. The time step of the aforementioned records is set to 0.01 s. The frequency content of the input motions are mainly below 10 Hz, and the dominant frequency ranges from 0.91 to 2.13 Hz based on the Fourier transformation results. The peak base accelerations (PBA) of the input motions, as mentioned earlier, are scaled to 1.2 g for the test. Both the physical and numerical components of the hybrid models are scaled in size by a length scale factor of 0.333 due to the cost and space limitations of the testing facility. Thus, the equations of motion are solved for the scaled models with the earthquake record time compressed by a time scale factor of 0.577.

Numerical Modeling

Due to the fact that a calculation efficiency was needed in the hybrid simulation process, the FE model of the simply supported bridge was simplified, as shown in **Figure 4**. The steel bridge deck had dimensions of 6100 mm \times 4100 mm \times 70 mm. The

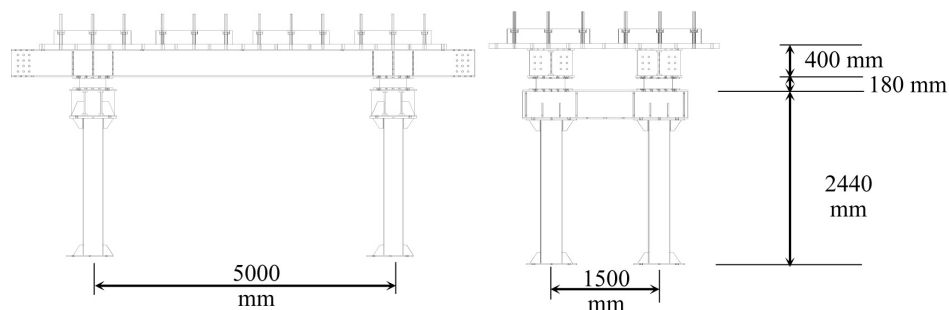


FIGURE 1 | Evaluation of the specimen.

TABLE 1 | Scale Factors between the prototype and scale models.

Dimension	Definition/in terms of S	Scale factor
Length	S	0.333
Mass	S^2	0.109
Time	$S^{0.5}$	0.577
Stress	1.0	1.0
Velocity	$S^{0.5}$	0.577
Acceleration	1.0	1.0
Force	S^2	0.109
Stiffness	S	0.333

bridge deck was modeled as a rigid body due to its mechanical properties. The sectional dimensions of the HDR bearings were set to 400 mm × 400 mm × 140 mm. The sectional dimensions of the piers were set to 200 mm × 200 mm × 2070 mm. The simply supported bridge piers were modeled with distributed plasticity Euler-Bernoulli beam elements, which had four Gauss-Legendre integration points (Feng et al., 2019). The Steel 02 model was utilized for the components of the simply supported bridge. The steel structural components had a density of 7800 kN/m³, Poisson's ratio of 0.3, Young's modulus of 200.0 GPa, and yield stress of 235.0 MPa. The hardening ratio was set to 0.01. The elastic rubber bearing elements were set between the pier top and the bridge deck. The shear stiffness was considered in the bearing element, while the bending stiffness was neglected. The bottom of the pier elements was fixed for all three degrees of freedom. The rotation degree was assumed to be restricted at the top point of the pier elements. The stiffnesses of the girders and the bridge deck were much larger than those of the piers. Therefore, the HDR bearings would present shear deformations in the hybrid simulation process.

HYBRID SIMULATION FRAMEWORK

With the help of substructuring hybrid simulation techniques, large-scale, or full-scale tests can be realized to study the seismic performance of the designated specimens (McCrumb and Williams, 2016). In this work, substructuring hybrid simulation techniques are utilized. HDR bearings are physically tested, while the other structural components are numerically modeled. In

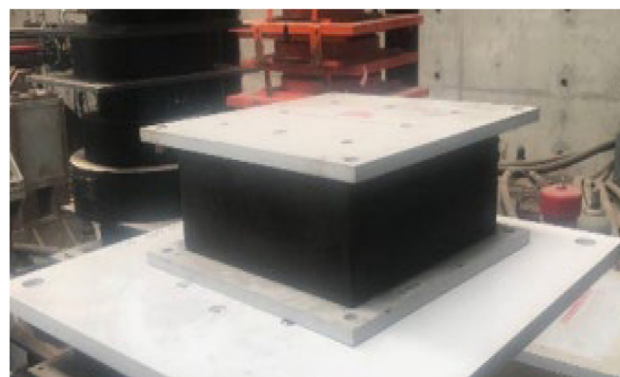


FIGURE 2 | Details of the specimen.

the numerical model, four bearings are assembled and modeled with one bearing element. To simplify the physical test and make it more feasible, two HDR bearings are arranged vertically as one specimen.

Substructure Division

The details of the physical and numerical substructure are illustrated in **Figure 5**. The HDR bearings are selected as the experimental elements. In the numerical model, it is assumed that the bridge deck is a rigid body, and the mechanical properties of the four bearings are the same. Therefore, the HDR bearings share the same deformation in the analysis.

As mentioned previously, two HDR bearings are vertically set as one in the physical specimen. The physical substructure and numerical substructure are combined and interact through the OpenFresco platform. The purpose of OpenFresco middleware is to build a bridge between the loading hardware and the computation hardware. In the substructuring process, interface nodes are used to connect the physical and numerical substructures, ensuring equilibrium, and compatibility (McKenna and Fenves, 2001; Maikol et al., 2015). At each data communication step, two times the value of the horizontal actuator feedback forces are transmitted back to the numerical substructure. The experimental bearing element is applied, which uses host FE analysis software to represent

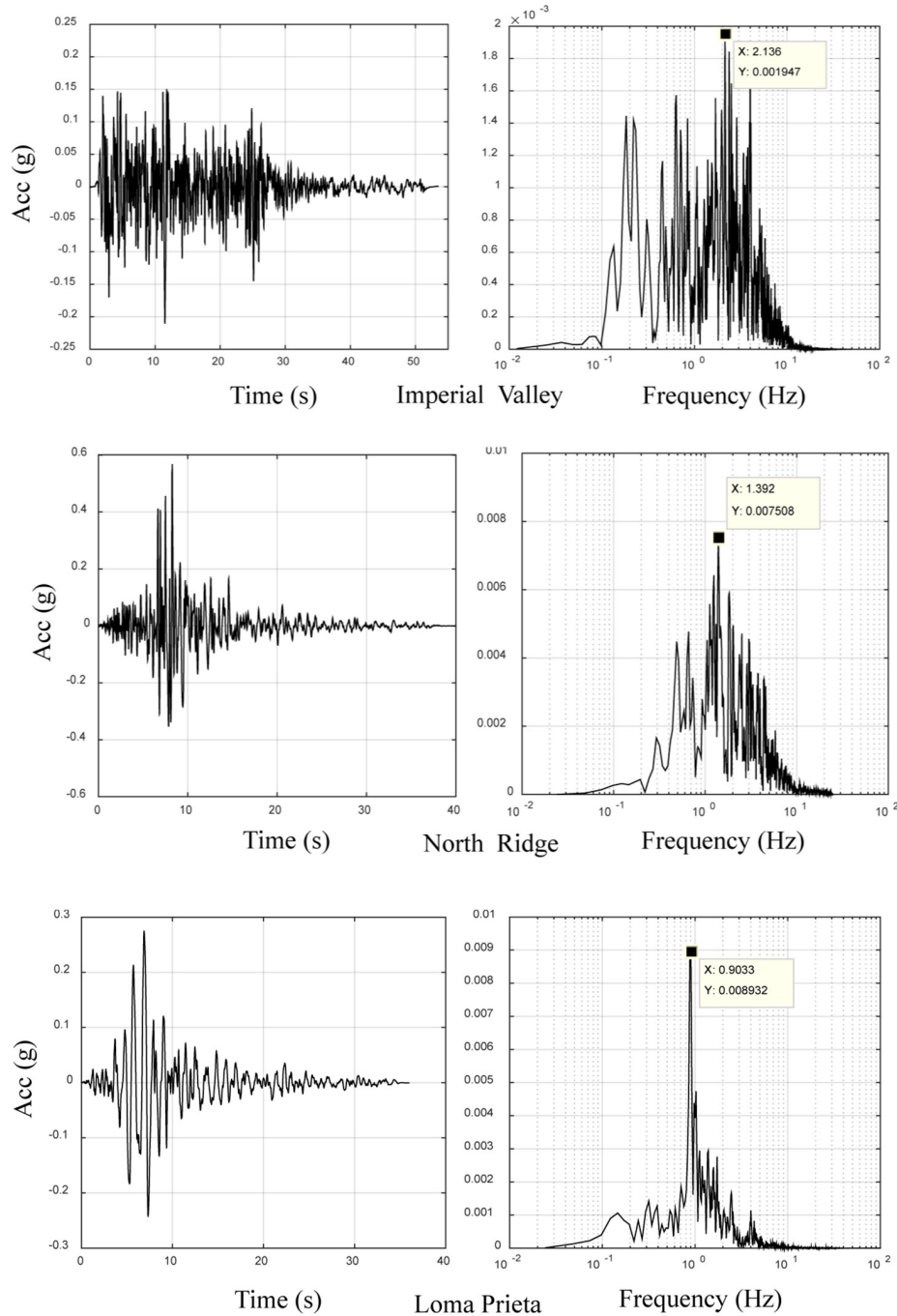


FIGURE 3 | Selected input motion.

a physical portion of a model (instead of a numerical one; Schellenberg et al., 2009).

The prototype structure has a total of four HDR bearings. As the stiffness of the bridge deck is much greater than that of the bearings, it is assumed that the upper structure will not undergo in-plane deformation. The FE model is simplified, and the four HDR bearings are modeled with one experimental bearing element in the OpenFresco platform.

The HDR bearing is then subjected to a direct shear test, and horizontal friction is introduced on the sliding surface. With the help of rollers and lubricants, friction is reduced to an extent. Because friction exists in the direct shear test with only one HDR bearing specimen, a double shear test is adopted to eliminate friction. In the double shear test pattern, two bearings are stacked together and fixed on a steel plate in the middle. The steel plate is driven by a horizontal actuator (shown in **Figure 6**).

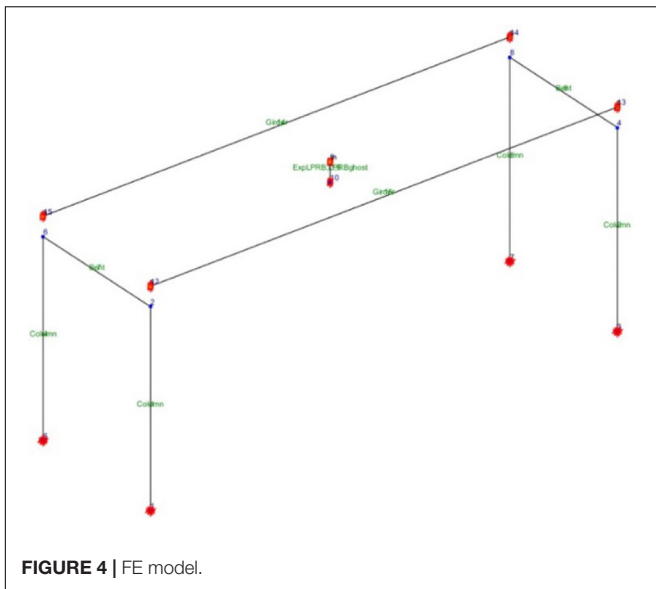


FIGURE 4 | FE model.

The restoring force measured by the actuator is the sum of the horizontal shear forces of the two HDR bearing specimens. No friction is introduced with such experimental settings.

To eliminate the influence of friction, the physical test uses two HDR bearings, stacked together with the horizontal actuator. The actuator is set in the middle part of the specimen to achieve the effect of a double shear test. In this way, the restoring force of the specimen comes from the two HDR bearings. To realize the boundary compatibility and equilibrium, two times the restoring force is transmitted back to the numerical substructure.

Experimental Test Setup

The physical hybrid simulation process was carried out in the multifunctional shaking tables laboratory of Tongji University.

The MTS hybrid simulation system consists of a 500.0 kN capacity high speed linear hydraulic actuator, the simulation Host PC, and a two-channel MTS 793 controller. As shown in **Figure 6**, the linear hydraulic actuator provides the horizontal force at the middle point of the specimen. The horizontal loading is carried out in displacement controlled mode, and the displacement command for the horizontal actuators is sent directly from the numerical substructure to the physical substructure. For the vertical load, the loading scheme is determined in open-loop control, and no axial forces or displacements are returned to the numerical simulation. The constant load provided by the vertical actuator is determined by the gravity of the structure, namely, 135.0 kN. The vertical force is measured by the load cell in the test process. The upper part of the HDR specimen is connected to the reaction frame. During the test, vertical loading is carried out in force-controlled mode. To keep the pressure constant, the vertical load is measured by the load cell. In the aforementioned loading pattern, the vertical actuator provides constant pressure during the test process.

Sano and Di proposed a rate-independent model of HDR bearings, which could present changes of stiffness and equivalent damping (Sano and Di Pasquale, 1995). Amin et al. (2006b) developed a hyperelasticity model that can reproduce the rate-independent response of HDR bearings under compression and shear force. According to previous research, the loading rate influences the performance of HDR bearings, but the mechanical properties of the high-damping bearing are more

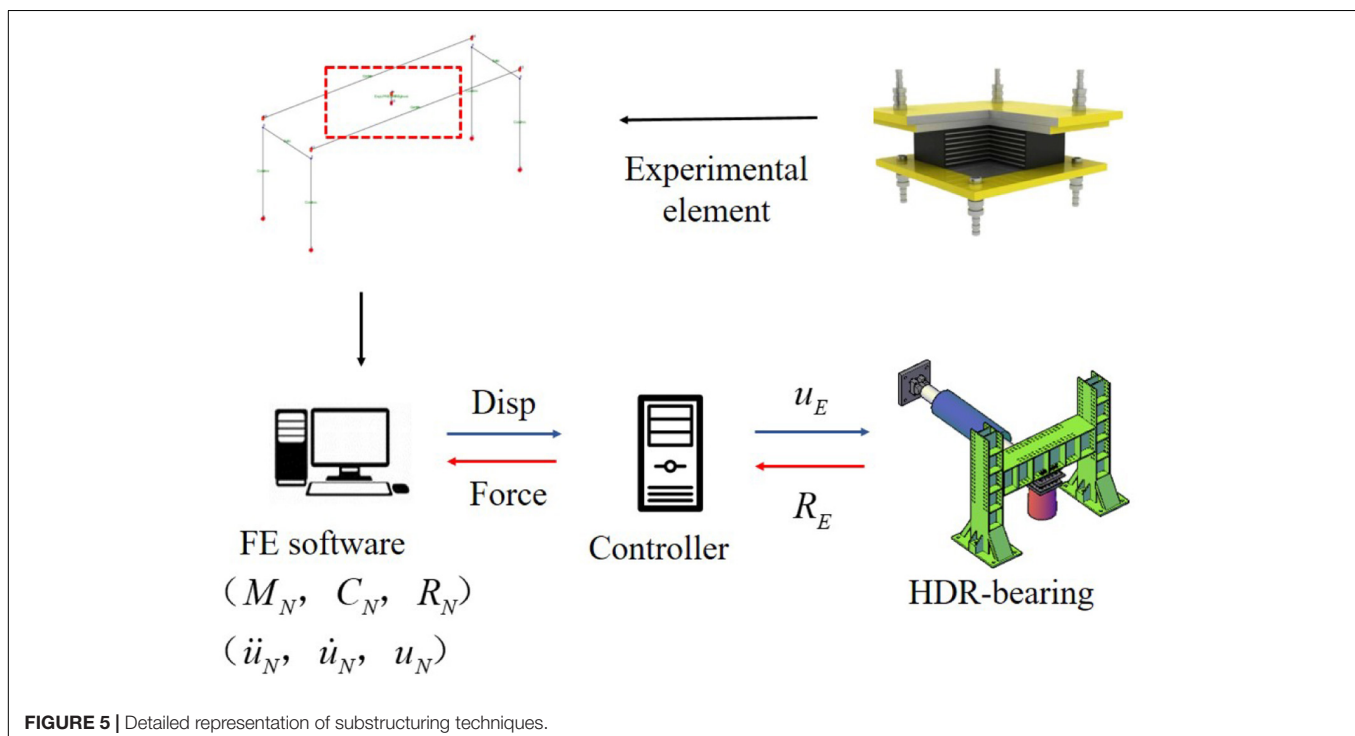


FIGURE 5 | Detailed representation of substructuring techniques.

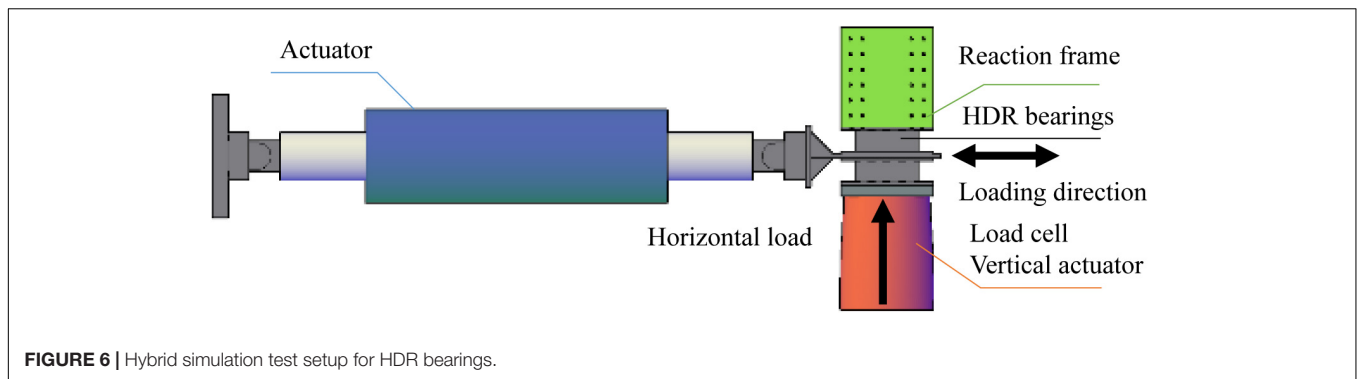


FIGURE 6 | Hybrid simulation test setup for HDR bearings.

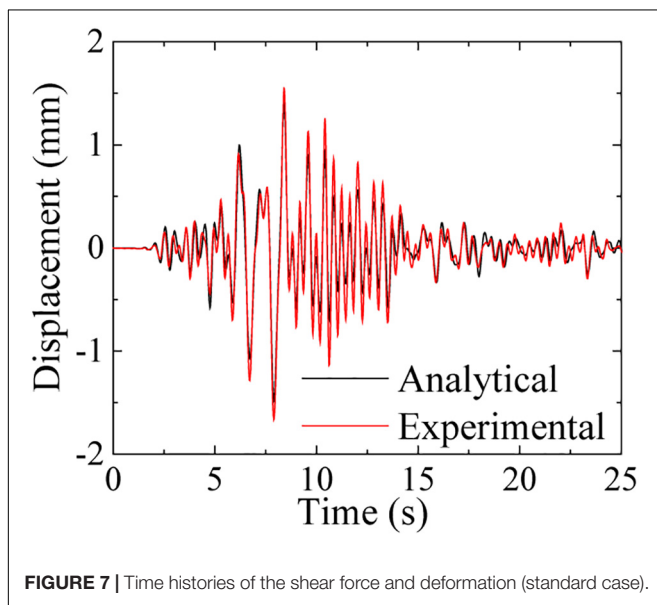


FIGURE 7 | Time histories of the shear force and deformation (standard case).

dependent on deformation. The hysteresis loop of HDR bearing is displacement-relevant, instead of velocity-relevant. Therefore, in this research paper, the hybrid simulation process of HDR bearings is conducted in a fast continuous loading pattern. The

ramp time is set to 0.1 s in the OpenFresco platform. The test duration is approximately five times the input record duration. The time span of a 40-s excitation hybrid simulation case is approximately 200 s.

The operator-splitting integration method was adopted to solve the numerical substructure. The “experimental bearing” element was introduced for the HDR bearings. The “MTSCsi” pattern, involving horizontal force and displacement, was applied as the control method for the test. As the boundary conditions of the physical substructure were simplified to one horizontal DOF, the “NoTransformation” experimental setup pattern was introduced.

HYBRID SIMULATION PROCESS

Standard Case

Before the series of hybrid simulations, the accuracy of the hybrid simulation process of HDR bearings could be verified by the results of a standard case. The PBA of the Loma Prieta record is scaled to 0.2 g as the input motion for the standard case. In the standard case, the HDR bearings are mainly within the elastic stage. As the HDR bearings are displacement-dependent, the displacement index is selected to evaluate the accuracy of the hybrid simulation framework. Figure 7 shows that the hybrid

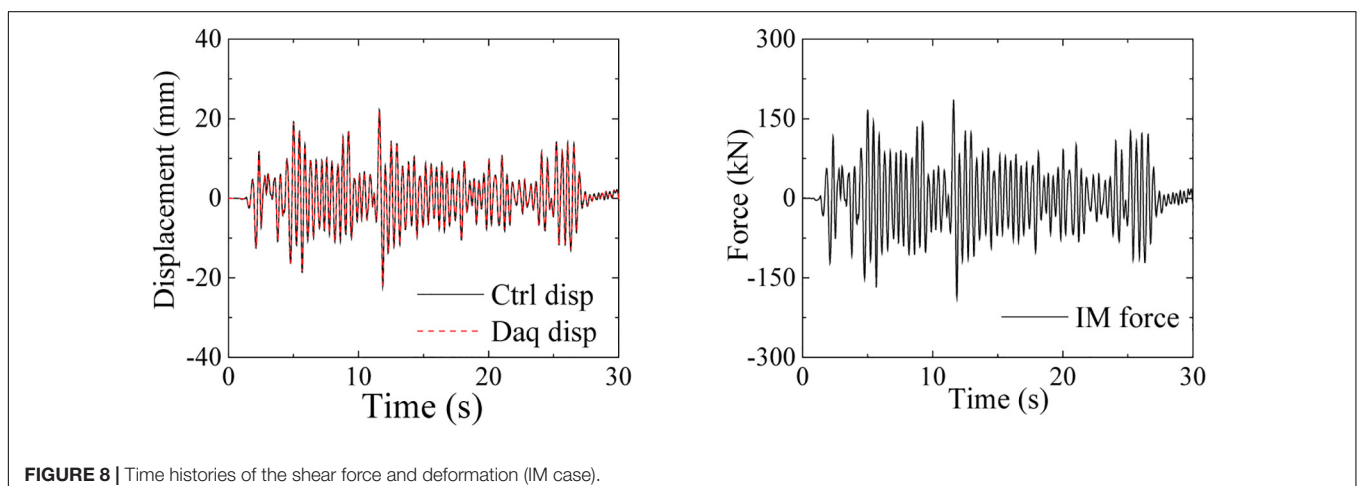


FIGURE 8 | Time histories of the shear force and deformation (IM case).

simulation results agree with the analytical results in terms of peak value and waveform. The correspondence between the results of the hybrid simulation and analytical model is shown in the elastic stage. In this study, the aforementioned hybrid simulation framework and numerical model can reproduce the seismic responses of HDR bearings.

Test Results

The IM case, NO case, and LO case were analyzed to evaluate the seismic responses of HDR bearings under different excitations.

Note that IM stands for the Imperial Valley record input motion (PBA = 1.2 g), NO stands for the North Ridge record input motion (PBA = 1.2 g), and LO stands for the Loma Prieta record input motion (PBA = 1.2 g).

Figure 8 shows the force histories and displacement histories of the HDR bearings under the Imperial Valley excitation. **Figure 9** shows the force histories and displacement histories of the HDR bearings under the North Ridge excitation. **Figure 10** shows the force histories and displacement histories of the HDR bearings under the Loma Prieta excitation.

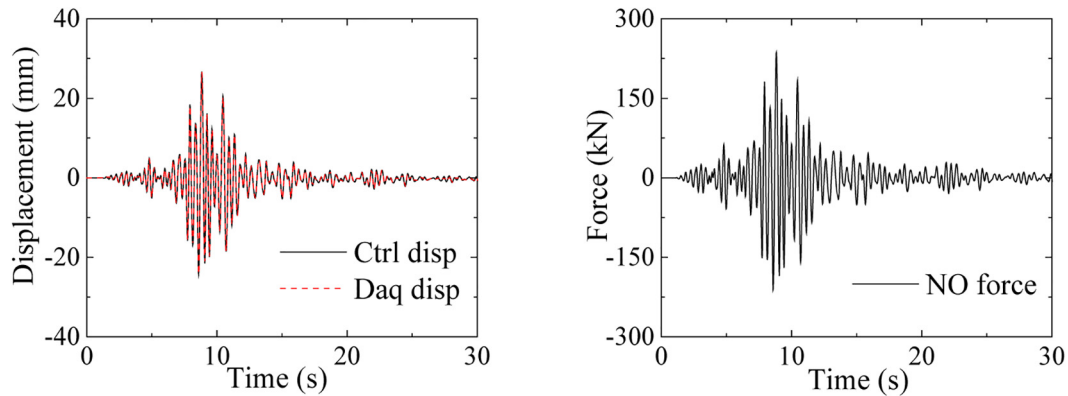


FIGURE 9 | Time histories of the shear force and deformation (NO case).

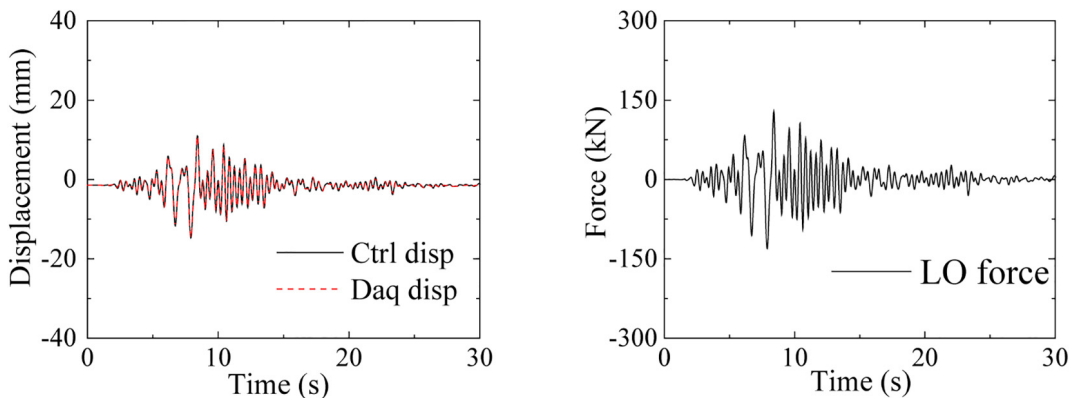


FIGURE 10 | Time histories of the shear force and deformation (LO case).

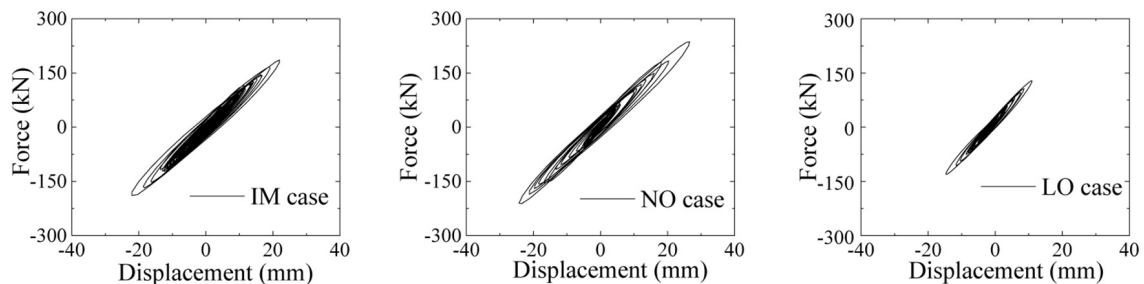


FIGURE 11 | Force-displacement hysteretic responses.

In these three figures, target displacement matches the measured horizontal actuator displacement, which proves that the actuator has good loading ability during the hybrid simulation process.

Discussion

Unlike the results of the standard case, the specimens enter the plastic stage in the IM case, NO case, and LO case. **Figure 11** shows the force-displacement hysteretic responses of the HDR bearings. The stiffness property under earthquake excitation is analyzed by introducing the parameter of the secant stiffness trend. The peak-to-peak secant stiffness of the load-displacement hysteretic response is applied to define the secant stiffness trend. This parameter is calculated as:

$$K_i = \frac{F_i^+ - F_i^-}{D_i^+ - D_i^-} \quad (1)$$

where K_i is the secant stiffness, F_i^+ , and F_i^- are peak loads in the positive and negative loading directions, respectively. D_i^+ and D_i^- are the corresponding displacements in the positive and negative loading directions, respectively. K_i decreases substantially during the hybrid simulation process. In the standard case, K_i is 14.6 kN/mm in the elastic stage. Compared to the standard case, the K_i of specimens IM, NO, and LO are lower than those of the standard case by 41.5, 39.7, and 30.8%, respectively. It should be noted that compared with other experimental studies on HDR bearings (Dall'Asta and Ragni, 2006; Xiudi et al., 2018; Khan et al., 2019), these cases showed a strong linearity.

Usually, the HDR bearings are modeled with a linear elastic constitutive model in the numerical FE model and it is hard to obtain a precise solution from such a numerical model. It is therefore necessary to conduct hybrid simulations to study the seismic behavior of simply supported bridges with HDR bearings.

The test results show that the deformation of the bearing is relatively small, and nonlinear behavior is not prominent. However, it can be seen from the hysteresis curve that the stiffness of the bearing decreases in both the IM and NO cases, as an obvious energy-consumption phenomenon appears at approximately 20.0 mm. The HDR bearings are not entirely in a linear elastic state.

This work introduces novel hybrid simulation techniques to study the seismic behavior of simply supported bridges with HDR bearings. This paper aims to verify the feasibility and

accuracy of the aforementioned hybrid simulation framework through the dynamic testing of HDR bearings. More work is needed to illustrate the high nonlinearities of HDR bearings for large deformations.

CONCLUSION

In this paper, the hybrid simulation process was used to test a simply supported bridge structure. The OpenSees-OpenFresco framework provides a tool for implementing this hybrid simulation procedure, with the use of a horizontal actuator. Once the test results were recorded and analyzed, we found that the hybrid simulation procedure reproduced the mechanical behavior of the simply supported bridge when subject to earthquake excitation. This hybrid simulation technique was able to capture both the mechanical properties and rate-dependent behavior of HDR bearings.

In summary, the proposed hybrid simulation architecture is a reliable method for studying the seismic performance of HDR bearings. In such a loading scheme, the HDR bearings did not exhibit large strain values. Future work should explore the hybrid simulation process of HDR bearings at larger strain values.

DATA AVAILABILITY STATEMENT

The raw data supporting the conclusions of this article will be made available by the authors, without undue reservation.

AUTHOR CONTRIBUTIONS

CY, ZL, and XC conceived the study and were responsible for the design and development of the data analysis. YY wrote the abstract and introduction part. XC and ZL helped perform the analysis with discussions. XC wrote the first draft of the article. All authors contributed to the article and approved the submitted version.

FUNDING

The research has been supported by the Shanghai Committee of Science and Technology (16DZ1200302).

REFERENCES

- Abe, M., Yoshida, J., and Fujino, Y. (2004). Multiaxial Behaviors of Laminated Rubber Bearings and Their Modeling. I: *Exp. Stud. J. Struct. Engin.* 130, 1119–1132. doi: 10.1061/(asce)0733-9445(2004)130:8(1119)
- Amin, A. F. M. S., Lion, A., Sekita, S., and Okui, Y. (2006a). Nonlinear dependence of viscosity in modeling the rate-dependent response of natural and high damping rubbers in compression and shear: Experimental identification and numerical verification. *Int. J. Plast.* 22, 1610–1657. doi: 10.1016/j.ijplas.2005.09.005
- Amin, A. F. M. S., Wiraguna, S. I., and Bhuiyan, A. R. (2006b). Hyperelasticity Model for Finite Element Analysis of Natural and High Damping Rubbers in Compression and Shear. *J. Engin. Mech.* 132, 54–64. doi: 10.1061/(asce)0733-9399(2006)132:1(54)
- Chaudhary, M. T. A., and Masato Abe Fujino, Y. (2001). Performance evaluation of base-isolated Yama-age bridge with high damping rubber bearings using recorded seismic data. *Engin. Struct.* 23, 902–910. doi: 10.1016/s0141-0296(00)00117-6
- Dall'Asta, A., and Ragni, L. (2006). Experimental tests and analytical model of high damping rubber dissipating devices. *Engin. Struct.* 28, 1874–1884. doi: 10.1016/j.engstruct.2006.03.025

- Feng, D. C., Xie, S. C., Ning, C. L., and Liang, S. X. (2019). Investigation of Modeling Strategies for Progressive Collapse Analysis of RC Frame Structures. *J. Perform. Construct. Facil.* 33:04019063. doi: 10.1061/(asce)cf.1943-5509.0001328
- Khan, A. K. M. T. A., Bhuiyan, M. A. R., and Ali, S. B. (2019). Seismic Responses of a Bridge Pier Isolated by High Damping Rubber Bearing: Effect of Rheology Modeling. *Int. J. Civ. Engin.* 17, 1767–1783. doi: 10.1007/s40999-019-00454-x
- Li, Y., Wang, J. J., and Liu, J. B. (2013). Seismic Performance of a Multi-Span RC Highway Bridge with High Damping Rubber Bearings. *Key Engin. Mater.* 540, 69–78. doi: 10.4028/www.scientific.net/kem.540.69
- Maikol, D. C. R., Mosqueda, G., and Javad Hashemi, M. (2015). Large-Scale Hybrid Simulation of a Steel Moment Frame Building Structure through Collapse. *J. Struct. Engin.* 14:04015086. doi: 10.1061/(asce)st.1943-541x.0001328
- Mccrum, D. P., and Williams, M. S. (2016). An overview of seismic hybrid testing of engineering structures. *Engin. Struct.* 118, 240–261. doi: 10.1016/j.engstruct.2016.03.039
- McKenna, F., and Fenves, G. L. (2001). *The OpenSees command language manual, version 1.2*. Berkeley: Pacific Earthquake Engineering Research Center.
- Ministry of Construction of the People's Republic of China. (2003). *GB50017-2003 Code for design of steel structures*. Beijing: China Communications Press.
- Sano, T., and Di Pasquale, G. (1995). A constitutive model for high damping rubber bearings. *J. Press. Vessel Technol.* 117, 53–57. doi: 10.1115/1.2842090
- Schellenberg, A., Kim, H. K., and Takahashi, Y. (2009). *OpenFresco Command Language Manual*. Berkeley: University of California.
- Xiudi, L., Huaiyuan, M., and Ke, X. (2018). A SHPB Experimental Study on Dynamic Mechanical Property of High-Damping Rubber. *Shock Vibr.* 2018, 1–10. doi: 10.1155/2018/3128268
- Yamamoto, M., Minewaki, S., and Yoneda, H. (2012). Nonlinear behavior of high-damping rubber bearings under horizontal bidirectional loading: full-scale tests and analytical modeling. *Earthqu. Engin. Struct. Dynam.* 41, 1845–1860. doi: 10.1002/eqe.2161
- Yamamoto, M., Minewaki, S., Yoneda, H., Higashino, M., and Wada, A. (2009). Full-scale tests and analytical modeling of high-damping rubber bearings under two horizontal directional loading. *J. Struct. Construct. Engin.* 74, 639–645. doi: 10.3130/aifs.74.639

Conflict of Interest: The authors declare that the research was conducted in the absence of any commercial or financial relationships that could be construed as a potential conflict of interest.

Copyright © 2020 Yang, Cai, Lai and Yuan. This is an open-access article distributed under the terms of the Creative Commons Attribution License (CC BY). The use, distribution or reproduction in other forums is permitted, provided the original author(s) and the copyright owner(s) are credited and that the original publication in this journal is cited, in accordance with accepted academic practice. No use, distribution or reproduction is permitted which does not comply with these terms.



Real-Time Hybrid Test Using Two-Individual Actuators to Evaluate Seismic Performance of RC Frame Model Controlled by AMD

Yoichi Mukai^{1*}, Ayaka Yokoyama¹, Kohiro Fushihara¹, Takashi Fujinaga² and Hideo Fujitani¹

¹ Department of Architecture, Graduate School of Engineering, Kobe University, Kobe, Japan, ² Research Center for Urban Safety and Security, Kobe University, Kobe, Japan

OPEN ACCESS

Edited by:

Wei Song,
University of Alabama, United States

Reviewed by:

Ge Ou,
The University of Utah, United States
Said Elias Rahimi,
University of Iceland, Iceland

*Correspondence:

Yoichi Mukai
ymukai@port.kobe-u.ac.jp

Specialty section:

This article was submitted to
Computational Methods in Structural
Engineering,
a section of the journal
Frontiers in Built Environment

Received: 31 May 2020

Accepted: 03 August 2020

Published: 04 November 2020

Citation:

Mukai Y, Yokoyama A, Fushihara K, Fujinaga T and Fujitani H (2020) Real-Time Hybrid Test Using Two-Individual Actuators to Evaluate Seismic Performance of RC Frame Model Controlled by AMD. *Front. Built Environ.* 6:145. doi: 10.3389/fbuil.2020.00145

The seismic responses of a single-story reinforced concrete (RC) frame building model under control using an active mass damper (AMD) are demonstrated through a real-time hybrid simulation (RTHS) method. In this study, the RTHS test is carried out by using a hydraulic actuator and a shaking table under synchronization. Most parts of the target RC frame model are provided as an analytical model for an online computer simulation, and only the single column of the first story is prepared as an experimental substructure. A hydraulic actuator deforms the actual RC column, and uncertainty or nonlinearity of the RC column's behavior is focused on in this RTHS test. At the same time, a control device of AMD is actually tested under a situation of installing it on the target building's floor. The floor response of the target building model is generated using a shaking table. A control motion of the AMD is manipulated based on an online simulation of the entire RC building model. Firstly, a time delay compensation of the hydraulic actuator is considered. Time delay parameters are identified using a combination model of a time lag and a first-order delay. A PID controller and a time series compensator are applied to improve actuator performances. Next, the reproducibility of the RTHS test using two-individual actuators is evaluated. The tracking of a restoring force and deformation of the actual RC column specimen generated by the hydraulic actuator and floor motion responses reproduced on the shaking table are investigated. To improve the online numerical simulation based on the measured force responses of the RC column specimen, a high-pass filter (HPF) is applied for a force correction to utilize its phase-lead property. The effect of this HPF force correction is evaluated in both a linear region and a strong nonlinear region of the actual RC column specimen. Finally, the RTHS test results are compared to fully numerical simulations and the control effect of the AMD to increase the damping effect for the target RC building model is also investigated.

Keywords: real-time hybrid simulation, shaking table, hydraulic actuator, active mass damper, time delay compensator, reinforced concrete structure

INTRODUCTION

The high demand for structural reinforcement to improve the seismic-resistant performance of existing buildings has been heightened, to reduce damage and risk against earthquakes in the near future, because of the lack of seismic-resistance capacity. Various methods are used for the seismic retrofitting of existing buildings; installations of viscous dampers, hysteresis dampers, or reinforcing frame members are the general construction methods for a seismic retrofitting (Wang and Zhao, 2018; Kazantzi and Vamvatsikos, 2020). A base isolation system is also adopted for seismic retrofitting of structures (Matsagar and Jangid, 2008; Cardone and Flora, 2016). Tuned mass dampers (TMD) are thought to have the potential for improving the wind and seismic behaviors of civil and building structures (Elias and Matsagar, 2017, 2019). Recently, actual installations of mass dampers to building structures have also been seen in the purpose of seismic retrofitting (Miyamoto et al., 2010; Nakai et al., 2019), in particular, a mass damper system can contribute effectively in reducing resonant vibration in low-damping buildings. Using a mass damper for a seismic retrofitting is thought to provide ease in installing because a mechanical performance of the mass damper can be theoretically adjusted. A TMD is sufficient to reduce the resonant vibration of the target buildings as far as the device is tuned to the optimal condition. However, once the tuned parameter deviates from the optimal value, the response control effects will be decreased. An active mass damper (AMD) system provides an advantage to this problem by a software compensator. An AMD can also reduce the volume of the additional mass to give an equivalent performance using a TMD.

Considering structural reinforcement or structural vibration control, the precise performance evaluation of the entire building systems installing these subsystems is a significant interest in the seismic design of the building structures. Although a numerical simulation is a general approach to estimate dynamic behaviors of buildings, it is necessary to identify all the structural elements accurately for response analysis. In particular, numerical simulations often give a considerable variation in the results of the maximum response or the residual displacement of the analysis model which has a strong non-linearity (Huff, 2016). A huge-scale shaking-table test using the entire specimen of a building is an effective way to observe practical structural responses, in a case where the properties of some structural parts cannot be clearly understood. However, entire-building tests cannot be placed as a standard structural performance estimation method without a reason for the test cost and/or a test-system capacity. The real-time hybrid simulation (RTHS) method is considered to be a useful way to respond to these limitations in numerical analyses or full-scale experimental tests. In an RTHS, a physical substructure of a structural member of the target building is generally proposed by a hydraulic actuator, and the actual force and deformation of the substructure are measured and fed back to online numerical simulations.

Various kinds of construction types for civil engineering structures have been tested by RTHS methods, and RC frame structures have also been focused on as test targets. For example, an RTHS test was carried out for the purpose of evaluating the

retrofitting effect of an old RC viaduct bridge using a sliding bearing. The scale-reduced mono-cock models of RC frame piers were provided as experimental substructures, and a built and isolated configuration of the piers were tested and compared (Abbiati et al., 2015). The difficulty of precise displacement control for rigid members is pointed to in RTHS tests for civil engineering structures because a servo-hydraulic actuator causes a large force error in the tests. Chae et al. proposed a two-span bridge structure for RTHS tests and conducted the test using an RC pier experimental substructure specimen. Displacement histories of the experimental specimen were evaluated under the test of slow time and real-time. The influence of variation of the axial stiffness during the test was investigated (Chae et al., 2017, 2018b). Mei et al. (2019) carried out RTHS tests to examine seismic behaviors of the tall-pier RC bridge using a substructure of an RC column specimen which was horizontally loaded by a hydraulic actuator. A novel hybrid simulation scheme was proposed with a method of online updating the concrete constitutive parameters.

In general, the test specimens of RC substructures include unevenness of quality or performance; therefore, high uncertainty and variation often exist in the structural test results. In this study, a test method to reflect the uncertainty of local structural elements was proposed for the performance evaluation of the entire RC building. This study aims to develop an RTHS system setup to generate a dynamic floor response for RC frame building structures while reflecting the actual structural feature of an RC substructure specimen. Mass damper's contribution to the response control of an RC frame building is investigated by using the proposed testing system. To put it into practice, an RTHS test system using two-individual actuators is proposed and developed. The test is carried out by using the high-speed hydraulic actuator and the shaking table at Kobe University. Unlike conventional RTHS tests performed with a single actuator, the developing RTHS test system can simulate the motions of different structural parts by using different test specimens under synchronization. The hydraulic actuator generates a partial deformation of a target model, and the shaking table imposes a partial dynamic action of a target model. The RTHS is focused on seismic responses of a single-story RC frame building model and response control effects using an AMD. A single column of the first story and a control device of AMD is provided as experimental substructures in this RTHS test.

This paper is composed as follows: the section "Literature Review" gives descriptions of time delay compensation schemes for an RTHS and tracking accuracy of servo-hydraulic actuators in an RTHS, demonstrations of an RTHS using a shaking table, and the use of the RTHS for performance evaluations of mass damper systems. The section "Experimental Substructure of RTHS" describes the detail of a test setup and configuration, and the design consideration of the SDOF model corresponding to the target RC frame building for the RTHS. The section "Time Delay Compensation Scheme for Hydraulic Actuator" considers a time delay compensation of the hydraulic actuator. A combination of a PID controller and a time series compensator (TSC) is applied to improve actuator performances. In this study, the RTHS tests

are conducted under the condition of insufficient time delay compensation; thus, the influence of residual time delay of the hydraulic actuator's displacement is investigated. In the section "RTHS Test Results," a force correction method using a high-pass filter (HPF) is introduced to improve an online numerical simulation based on the measured force-response of the actual RC column specimen. This operation is introduced as the simple phase-matching method between the simulation time of the computer model and the measurement data of generated force in the RTHS. The reproducibility of the RTHS test system using two-individual actuators is evaluated. Moreover, the RTHS test results are assessed by observing the restoring force vs. deformation of the actual RC column specimen and the equivalent damping effects under control motions of the AMD. The final section "Conclusion and Future Works" describes the summary of the results of the RTHS demonstrations and the discussion of the next steps for the research.

LITERATURE REVIEW

Existing works of literature regarding the state-of-the-art advances in the RTHS test are summarized in this section. The essential and relevant researches of the time delay compensation and displacement tracking methodology for a servo-hydraulic actuator, the execution of the RTHS using shaking table, and the practical demonstration of the RTHS for performance evaluation of mass damper systems are reviewed in the following.

Time Delay Compensation Methods for RTHS

The operation of a hydraulic actuator generally contains a time delay between the desired and generated displacements. In an online test such as an RTHS, a time delay compensation is an essential problem to improve the accuracy of the tests and to avoid unstable behaviors in online simulations. Horiuchi et al. (1999) proposed a delay time compensation method based on a displacement compensation using an acceleration prediction for an actuator motion delay. In an RTHS test, a time delay is usually identified and assumed as constant by the preliminary experiment; thus, the precise estimation of a time delay is essential for a time delay compensation. However, a time delay of a hydraulic actuator is varied during an RTHS test, considering the changing stiffness of an experimental specimen, such as a nonlinear structural response. By adopting the Horiuchi's method, a time delay compensator was proposed as a multiplication of proportional gains and the difference between the desired vs. the measured displacements (Darby et al., 2002). Carrion and Spencer (2006) and Carrion et al. (2009) proposed a model-based feedforward compensator as an online estimation method for the variable time delay. The predicted displacement was estimated by a linear acceleration prediction approach in this scheme. Phillips and Spencer (2013) reformulated the actuator tracking as a regulator problem and applied linear-quadratic-Gaussian (LQG) control theory to propose a systematic framework for a model-based servo-hydraulic tracking control method. Ahmadzadeh et al. (2008) proposed a delay estimator

of servo-hydraulic actuators, which required little or no prior information about a test specimen based on the method to directly use the desired and measured displacement histories. By considering the control of a servo-hydraulic system with non-linearities, an adaptive time series (ATS) compensator method was proposed to improve the performance of an RTHS. The ATS has the advantage that structural modeling for a test structure is unnecessary (Chae et al., 2013, 2018a). Liu et al. (2013) proposed an integrated compensation method for an RTHS test, which was developed by combining feedforward capabilities of an inverse compensation and the delay estimation characteristics of Darby's method. Chen and Tsai (2013) proposed a dual compensation strategy based on an inversed discrete transfer function and a force balance of the equation of motion. Chen and Tsai's strategy includes an adaptive second-order phase lead compensator (PLC) and an online restoring force compensator (RFC) to improve the stable margin of RTHS tests. Robust performance in terms of un-modeled dynamics and uncertainties of the physically testing system is focused, and H_{∞} strategy is introduced as a loop shaping feedback control to integrate the robust actuator control for the design flexibility, robustness, and tracking accuracy in RTHS (Gao et al., 2013; Ou et al., 2015).

RTHS Using Shaking Table

The expectation for RTHS tests increases because it can become an alternative experimental test for the seismic performance evaluation of the entire building system instead of full-scale tests. While considering seismic behaviors of a building structure, the observation point is put not only on deformations of the substructure but also on dynamic actions under the acceleration motion. An RTHS test using a shaking table was recently conducted to observe and demonstrate a substructure's response under inertia effects. An SDOF system was sub-structured such that a portion of the mass formed an experimental substructure and the remainder of the mass plus the spring and the damper, because of the experimental substructure, was adjusted to the capacity of shaking tables (Horiuchi et al., 2000; Neild et al., 2005). Lee et al. (2007) operated an RTHS test using a shaking table to evaluate a multi-stories model. The entire structure was separated into the experimental substructure of the upper parts and the numerical substructures of the lower part (Lee et al., 2007; Zhang et al., 2016). Shao et al. (2011) proposed a general formulation of an RTHS to test a substructure of any part of a multi-story system. While using a three-story structural model, RTHS tests were conducted to verify the concept of the proposed scheme. An RTHS test for SSI problems was intended to consider the radiation damping effect of a semi-infinite soil foundation. A numerical calculation of a soil part and a physical test of a superstructure were coupled and demonstrated on a shaking table (Wang et al., 2011; Zhang and Jiang, 2017). Mukai et al. (2018) provided numerical models of a structural foundation and a soil-ground as non-linear numerical models, and interactive motions with the experimental substructure of the superstructure of a building model were reproduced by RTHS tests using a shaking table.

RTHS for Mass Damper System

Real-time hybrid simulation tests to demonstrate a response control using an experimental substructure of a mass damper system were also carried out. Ito et al. (2018) operated an RTHS test of a structural system with a TMD. The top floor motion of a numerical building model was simulated by a shaking table. Yoshida et al. (2018) operated an RTHS test for the performance evaluation of an inter-story-isolated system. The lower part of the isolated story is numerically modeled, and the small-scaled building part upper than the isolation-story is provided and vibrated on a shaking table. Zhu et al. (2017) developed an RTHS framework to carry out full-scale experiments of tuned liquid column dampers (TLCD). An experimental substructure of TLCD is placed on a shaking table, and a simulated response with a numerical model of a structural system considering a soil-structure interaction was demonstrated.

The performance evaluation of an AMD was recently conducted by introducing an RTHS method. Xu et al. (2014) conducted an RTHS test using an AMD. The entire system was composed of an AMD as a physical subsystem and a target structure as a numerical subsystem. Interactions between the physical AMD and the numerical three-stories linear model were considered, but the AMD was placed on a fixed basement. Fushihara et al. (2020) developed an RTHS system using a shaking table to evaluate the seismic response control performance of an AMD. The test device of AMD was provided as an experimental substructure, and the overall target building structure was considered as a numerical simulation model. The RTHS test was proposed to observe the uncertainty of mechanical behaviors of the AMD, which was influenced by floor accelerations. The importance of serviceability requirements of civil and building structures are also considered in building design (Jaafari and Mohammadi, 2018), and a mass damper installation is also regarded as effective for improving occupants' comfort and protecting nonstructural elements. Goorts et al. proposed a novel concept of a deployable control system (DCS) with an AMD to apply the short-term vibration mitigation of a lightweight bridge. The floor response of the bridge was simulated by using a shaking table, and a device setup of DCS was placed on the shaking table. Real-time hybrid simulation tests were carried out for the physical DCS device and the numerical substructure, and the controlled performance was demonstrated (Goorts et al., 2017).

EXPERIMENTAL SUBSTRUCTURE OF RTHS

Test-System Configuration Using Two-Individual Actuators

An ordinary RC frame building model is an experimental target in this study to estimate its seismic performance. Moreover, AMD is installed as a damping device to generate control forces. The RTHS test is operated, while a high-speed hydraulic actuator

loads the single RC column specimen with an unidentified feature. At the same time, a shaking table generates a dynamic floor response of the target RC building model. All the other parts of the target RC building excepting the part of the single-column specimen are provided as an analytical model for online computer simulation in this RTHS test. **Figure 1** shows a conceptual diagram of the RTHS system using two-individual actuators. A single-story RC building model with an AMD installed on its top floor is assumed in this study. The single RC column placed at the first story is prepared as an actual test specimen, and a deformation of this column is given by the high-speed actuator. The shaking-table reproduces the top floor's acceleration responses of the target building model for providing the AMD which influences the top floor's behavior. In the operation of the RTHS test, an online time-history response analysis is performed in a digital signal processor (DSP) controller (AD5436: produced by A&D Co. Ltd.). Firstly, a ground acceleration \ddot{z} (m/s^2) of a seismic excitation is loaded into an internal numerical model, and the relative displacement of the first story x (m) is calculated. Then, the actual RC column specimen is deformed by the hydraulic actuator. At the same time, the shaking table reproduces an absolute displacement of the top floor $y = x + z$, (m) to apply the top floor's acceleration $\ddot{y} = \ddot{x} + \ddot{z}$ (m/s^2) to the AMD device on the shaking table.

Meanwhile, an actual displacement x_m (m) and a restoring force f_m (N) of the actual RC column specimen and an acceleration \ddot{x}_m (m) and a reacting force q_m (N) of the AMD are directly measured, and these interaction forces are reflected in the online model simulation. The internal model simulation determines the next target motion of the internal building model and the required control force of the AMD. The DSP controller gives a control signal to the AMD and drives instruction signals to the shaking table and the high-speed hydraulic actuator. These procedures are synchronized between the simulation part and the experimental substructures and are continued sequentially in real-time. This RTHS test is also required to synchronize the two actuators' motions. Since this RTHS test system uses two actuators, which are placed at different laboratories, two DSP controllers (master and slave) are prepared, and communication between these DSPs is performed via LAN cables. Control operations in the RTHS test are executed every 0.002 s, and a signal time delay between two DSPs is less than this control time interval.

Figure 2A shows an overview of the AMD device used in this study ($\omega\text{AD} - 50\text{ZZ1}$: produced by Tokkyokiki Co.), and **Figure 2B** depicts a schematic diagram of the AMD device composition. The AC servomotor of the AMD rotates a ball screw and drives an additional mass along with a liner guide in a horizontal direction. A control mode of the motor is set to a torque adjusting method. Specifications of the AMD device are shown in **Table 1**. As seen in **Figure 2**, the AMD is placed on a load measuring table, and a reacting force of the AMD can be directly measured by a load cell.

Outline of RC Column Specimen

Figure 3A depicts the configuration of the RC column specimen used in the RTHS test. The RC column specimen has a

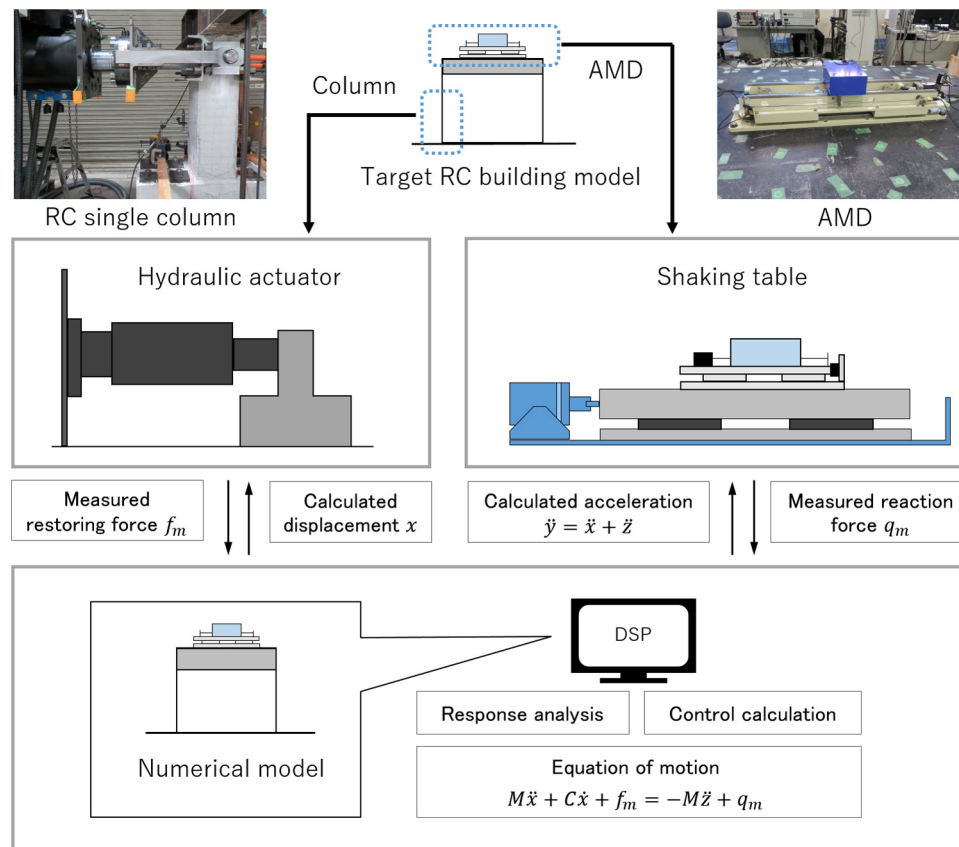


FIGURE 1 | Conceptual diagram of the RTHS test using two-individual actuators.

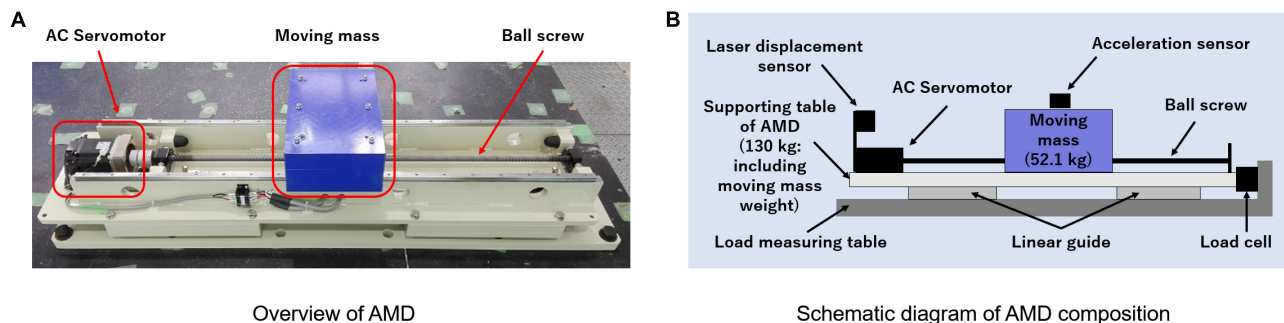


FIGURE 2 | Configuration outlook of the test device of AMD. (A) Overview of AMD. (B) Schematic diagram of AMD composition.

square cross-section of a width of 250 mm. A stub with a cross-section of 450 mm and a width of 350 mm is placed at the bottom of the specimen. Column height is 900 mm, and a loading point is set at the position of 750 mm from the top of the stub (or the bottom face of the column). Table 2 shows the material properties of rebar and the concrete cylinder test result for the RC column specimen. Stiffness of the column is calculated by considering a static loading test result. Figure 3B shows the relationship between lateral

forces and horizontal deformations of the RC column specimen. This horizontal loading test was conducted by installing an axial force (axial force ratio of 0.2) in a vertical direction. Deformations of the specimen are given until they reach the maximum value of 0.01 rad ($\delta_{max} = 7.5$ mm); a loading history is cyclic, having deformation steps by an increment of 1.5 mm from the original position ($\delta = 1.5, 3.0, 4.5, 6.0,$ and 7.5 mm). Each deformation step is repeated three times in the loading sequence.

TABLE 1 | Mechanical specification of the test device of AMD.

Item	Explanation
Weight of moving mass	52.1 kg
The total weight of AMD	130 kg
Motor control method	Torque-adjusting control
Available stroke length	± 408 mm (between stoppers)
Limit sensor position	Electrically shut off the motor at ± 395 mm
Drive mechanism	AC servomotor and ball screw (lead pitch 30 mm)
Maximum torque	1.5 kN *1
Maximum velocity	1.5 m/s *1
Driving force of AMD	260 N/V *2

*1 Conversion value for 30 mm ball screw lead, *2 Calculated from the sine-wave response test.

TABLE 2 | Material properties of rebar and cylinder test results of concrete used in the RC column specimen.

Material properties of rebar			
Rebar type	Yield stress (N/mm ²)	Tensile strength (N/mm ²)	Elongation (%)
D6	334	509	31
D10	365	516	27
D13	373	513	26
D22	381	566	20

Concrete cylinder test result	
Compressive strength (N/mm ²)	Tensile strength (N/mm ²)
36.5	2.98

Numerical Structural Model and Correspondence With the RC Column Specimen

Figure 4 shows the correspondence of the entire structural model and the experimental substructure (the actual RC column specimen) for the RTHS test. The actual RC column specimen is an extraction of a half part in the entire-length column; thus, its deformation δ (m) is also regarded as a half value of the entire-length column. Accordingly, the stiffness of the entire-length column k' is considered to be a half value of the stiffness of the test specimen k , as explained in **Figure 4A**. The RTHS test supposes a single-story frame model as the entire target building for computer simulation; thus, a floor mass of the model is considered to be supported by four columns, as shown in **Figure 4B**. The story stiffness K (N/m) is also considered to be four times the single entire-length column's stiffness and to be twice the actual RC column specimen's stiffness ($K = 4k' = 2k$). Every column is considered supporting

1/4 weight of the entire floor mass M (kg). The value of the floor's mass of the target structural model is determined by giving the specified natural period of the numerical model. The initial structural parameters for the RTHS in this study are supposed, as shown in **Table 3**. During the RTHS test, the axial force of the actual RC column specimen is applied using PC tendons.

TIME DELAY COMPENSATION SCHEME FOR HYDRAULIC ACTUATOR

Time Delay Evaluation

From a previous test, the hydraulic actuator, which is used for this RTHS test, is known to have a time delay of about 0.05 s between the time-histories of the desired displacement and the reproduced displacement depending on the hydraulic

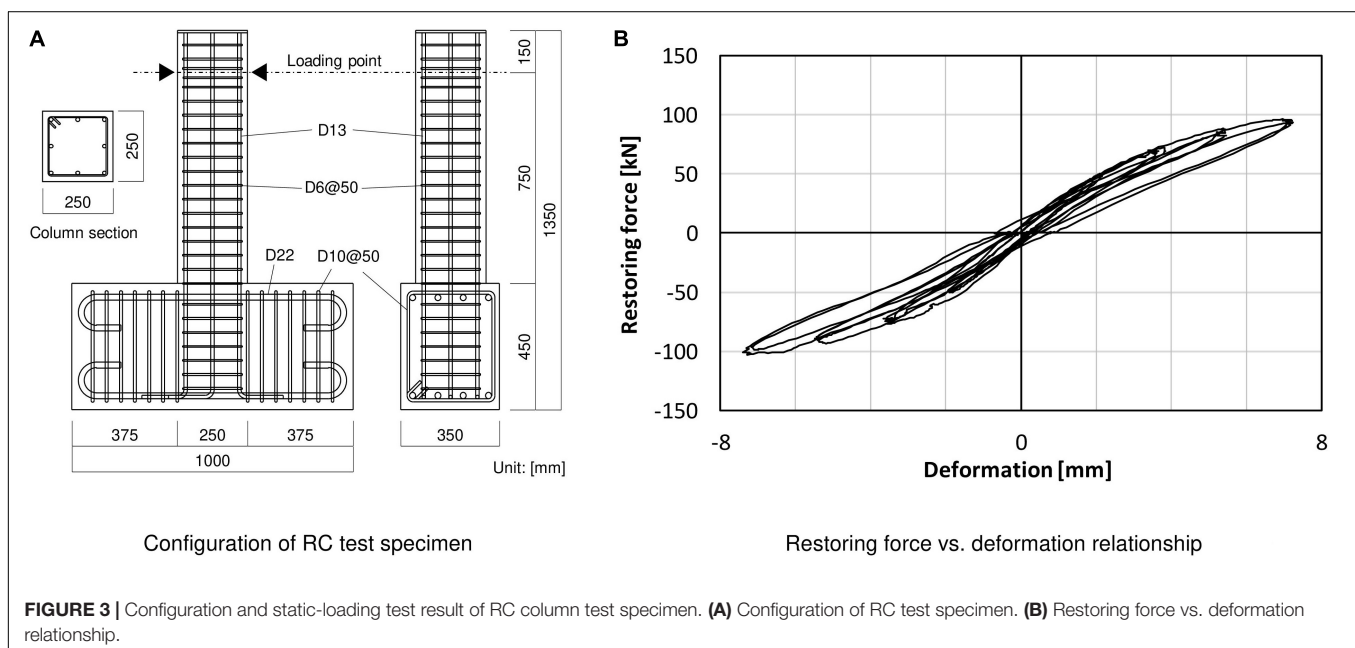


FIGURE 3 | Configuration and static-loading test result of RC column test specimen. **(A)** Configuration of RC test specimen. **(B)** Restoring force vs. deformation relationship.

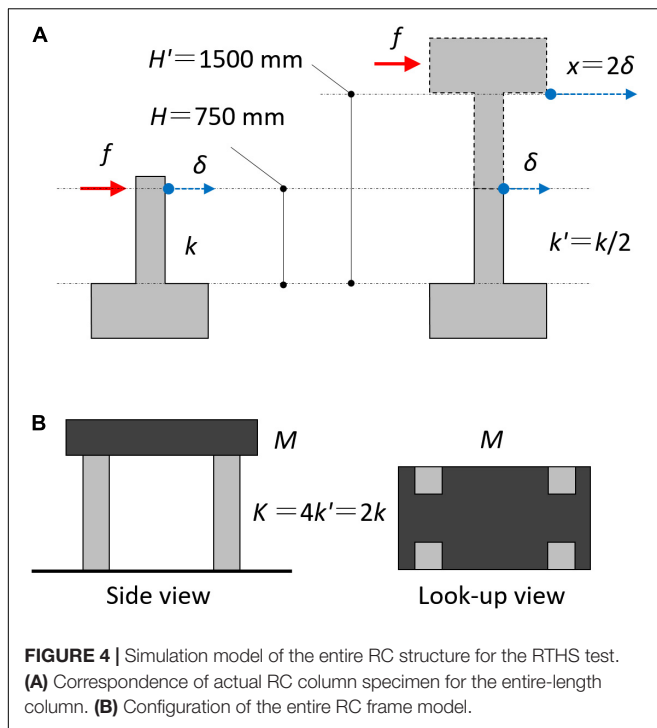


FIGURE 4 | Simulation model of the entire RC structure for the RTHS test. (A) Correspondence of actual RC column specimen for the entire-length column. (B) Configuration of the entire RC frame model.

TABLE 3 | Initial model parameters of the target structural model.

Design natural period (s)	Floor mass (kg)	Story stiffness (N/m)	Damping coefficient (Ns/m)
0.5	160,000	25,000,000*	200,000

*This value is evaluated approximately using an elastic-stiffness as the gradient observed from the static-loading test result.

mechanism. The natural period of the target structural model in this study is approximately 0.5 s. Thus, the time delay of the hydraulic actuator is thought to become a severe factor causing the RTHS test performance to become unstable, because the response delay may unexpectedly cause inaccurate results in the online simulation. Therefore, a time delay compensator is designed to improve the performance of the hydraulic actuator. Firstly, a step response method as the authorized manner is used to identify a time delay model. In which, a control target is modeled as a time lag system and a first-order delay system.

As seen in **Figure 5**, a unit step input is applied to the hydraulic actuator, and the unit step response is measured. Herein, the gray line indicates the commanded displacement, and the red line indicates the measured response displacement. A gradient at the inflection point while increasing the step response is depicted with a broken blue line, and the time at which the tangent intersects the time axis is determined as a time lag L (s). Then, a progress time interval by which the tangent intersects the line in the steady-state of the step response after the time lag L is determined as a time constant T (s). These parameters are calculated as $L = 0.014$ s and $T = 0.030$ s from this step response. When the gain of the

steady-state is α , the controlled object model, which includes the time delay, can be described by the transfer function in Eq. 1.

$$G(s) = \frac{\alpha}{Ts + 1} e^{-Ls} \quad (1)$$

Actuator Motion Compensation Using PID Control and Time Series Compensator

A PID control combines the three operations of a proportional operation, an integration operation, and a differential operation on a deviation signal $e(t)$ between an output $x(t)$ measured from a control target and a target value $r(t)$; $e(t) = x(t) - r(t)$. This way is considered to be a control method for determining an input $u(t)$ for compensating the control target output. By applying a PID control method, it is possible to make a slow rise in the time constant increase sharply. The compensating input based on a PID control can be expressed by Eq. 2. Eq. 3 expresses the Laplace transform of Eq. 2, and describes the transfer characteristic between input and output in the s -region (Ziegler and Nichols, 1942). A proportional constant $P = 1.93$ ($=0.9T/L$), an integration constant $I = 0.047$ ($=L/0.3$), and a differential constant $D = 0$ are used in this RTHS test to compensate for the hydraulic actuator motion.

$$u(t) = Pe(t) + I \int_0^t e(\tau) d\tau + D \frac{de(t)}{dt} \quad (2)$$

$$U(s) = \left(P + I \frac{1}{s} + Ds \right) E(s) \quad (3)$$

The PID controller is installed for the error correction between the target signal and the measured signal of the hydraulic actuator displacement. To improve the actuator motion more effectively, the compensator using a predictive response expressed by a time series is also introduced to the control operation of the hydraulic actuator (Chae et al., 2013). By evaluating the value of the time delay τ (s), the target input for the feedforward compensation related to the referential value after the time interval τ is considered. At the time t (s), the target displacement after the time interval τ can be expressed as $r(t + \tau)$. Using the Taylor series, this expression can be expanded to a power series of τ .

$$r(t + \tau) = r(t) + \dot{r}(t)\tau + \frac{1}{2!}\ddot{r}(t)\tau^2 + \dots \quad (4)$$

In this study, approximately considering the first-order term in the Taylor series, the following TSC is installed to drive the hydraulic actuator in parallel with the PID controller (Eq. 5). The block diagram, including these actuator motion compensators, is shown in **Figure 6**.

$$r(t + \tau) \cong r(t) + \dot{r}(t)\tau \quad (5)$$

In **Figure 7A**, the commanded value, the measured value under compensation, and the measured value without compensation are compared when a sinusoidal wave is used as an input. It was confirmed that the delay time, which was about

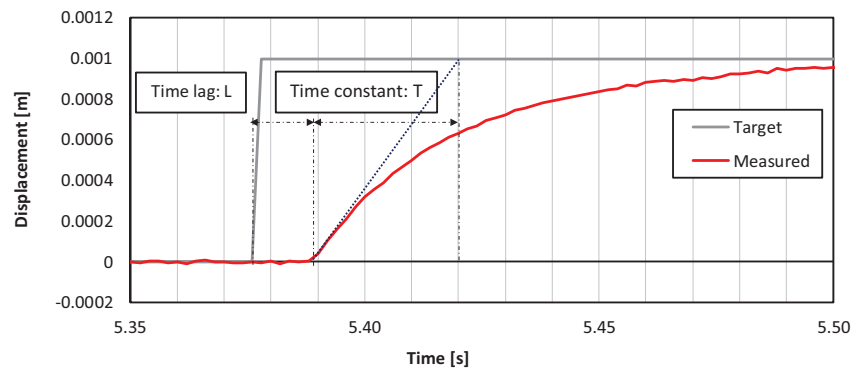


FIGURE 5 | Time delay between commanded vs. measured displacements of hydraulic actuator under a unit step input.

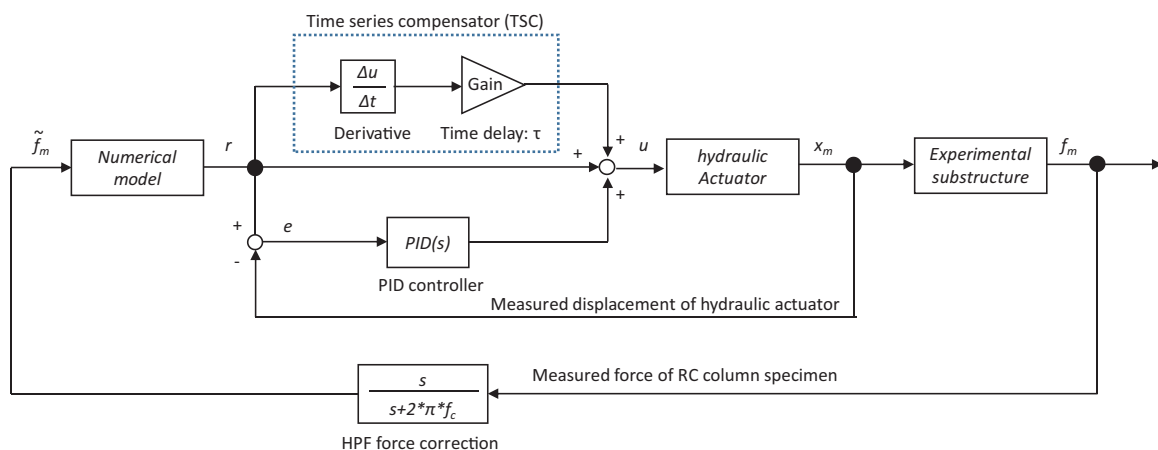


FIGURE 6 | Block diagram of actuator motion compensator and force correction.

0.046 s without compensation, is reduced to about 0.014 s with compensation. **Figure 7B** shows the commanded displacement and the measured displacement of the hydraulic actuator using the PID control and TSC when a random wave is applied. In this case, the time difference between the commanded displacement and the measured displacement is as small as about 0.014 s, and the effectiveness of the PID control and TSC can be confirmed. Although the PID and TSC blocks in **Figure 6** may work for reducing the permanent time delay of the servo-hydraulic actuator's displacement, the desired performance level of the RTHS compared to the general studies has not yet been achieved. Therefore, a phase-matching scheme between the simulation time of the computer model and the measurement data of the generated force is additionally considered to touch up the RTHS performance.

RTHS TEST RESULTS

Force Correction Method for the Online Simulation

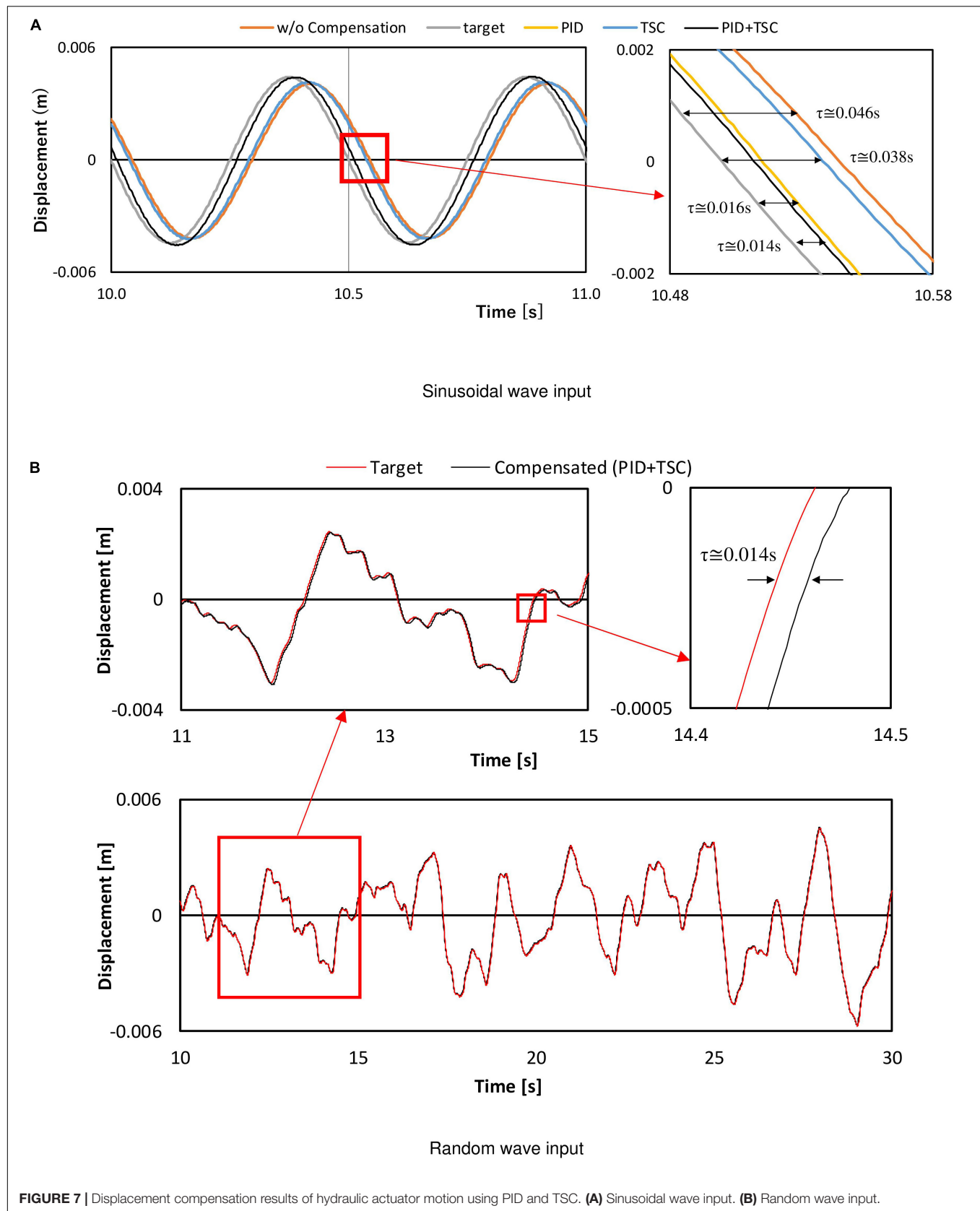
Through the previous investigation of displacement compensation, the time delay of the hydraulic actuator can

be shortened, but a small time delay has remained. In this study, the RTHS performance is improved using an alternative method based on a force correction scheme, which is installed to the force-response feedback signal from the hydraulic actuator. A single-pole HPF is applied to the phase-leading correction of the measured forces before the feedback to the internal numerical simulations. The formula of HPF force correction is expressed by the transform function of Eq. 6.

$$\text{HPF}(s) = \frac{s}{s + 2\pi f_c} \quad (6)$$

In which, f_c (Hz) is a cut-off frequency, which needs to adjust according to the system phase delay. This HPF has a phase-shift of $\pi/4$ at the cut-off frequency f_c . The RTHS setup in this study has kept a residual time delay of about 0.014 s in the displacement generation of the hydraulic actuator. In the following part, the method to compensate for this considerable time delay effect indirectly for the computer calculation of the RTHS is considered.

The block diagram of the force correction process is shown in **Figure 6**. **Figure 8** shows the restoring force vs. displacement relationship of the actual RC column, and **Figures 8A,B** are the results of applying the value of the cut-off frequency $f_c = 0.5$ and 0.2 Hz, respectively. The target structural model was designed



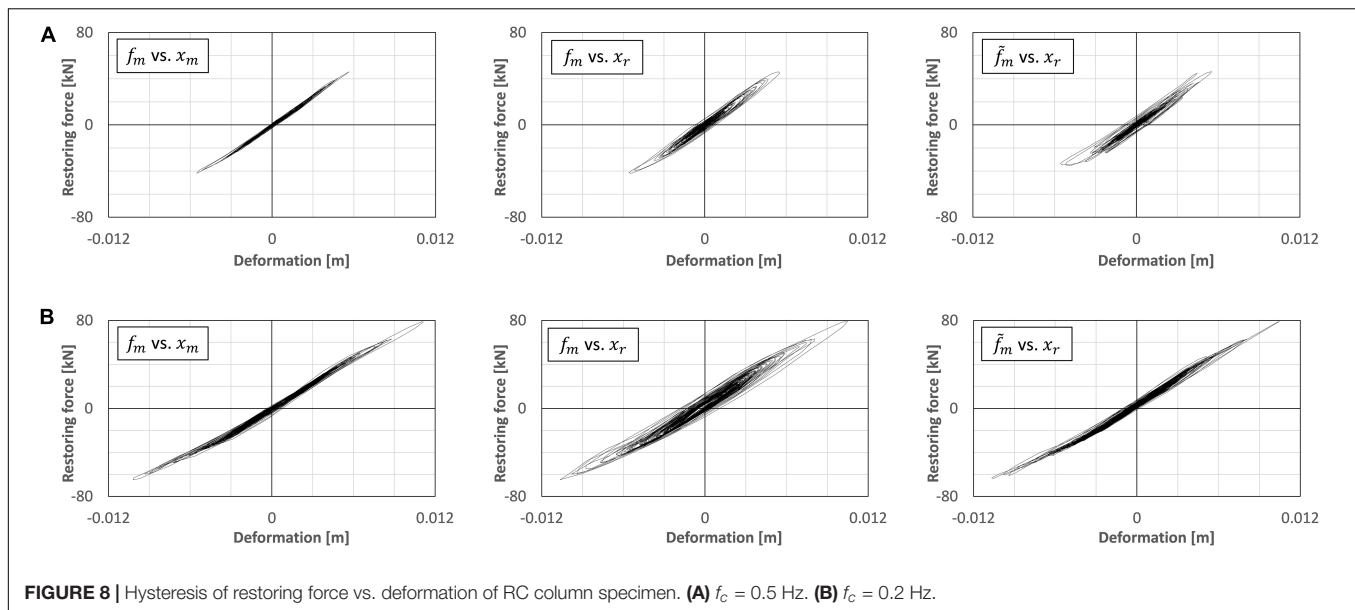


FIGURE 8 | Hysteresis of restoring force vs. deformation of RC column specimen. **(A)** $f_c = 0.5$ Hz. **(B)** $f_c = 0.2$ Hz.

TABLE 4 | Error indications of RTHS performance under different earthquake inputs.

Earthquake input	J_1 (mm)	J_2	J_3
El Centro 20% (w/o Control)	0.5656	0.1845	0.04360
El Centro 20% (Control)	0.3359	0.1877	0.03379
Takatori 10% (w/o Control)	0.5416	0.1770	0.04683
Takatori 10% (Control)	0.3733	0.1805	0.04412
JMA Kobe 7% (w/o Control)	0.6068	0.2035	0.04669
JMA Kobe 7% (Control)	0.3621	0.1895	0.03693

as the natural frequency of 2 Hz in this study, and the most predominant vibration response of the model must be caused around 2 Hz in the RTHS test. Thus, the angle of phase-lead can be calculated by $\varphi = \tan^{-1}(f_c/f)$ [rad] and a time-lead is given by $\Delta t = \varphi/2\pi f$ (s). When $f_c = 0.5$ and 0.2 Hz, the values of Δt are expected as about 0.020 and 0.008 s, respectively. In **Figure 8**, the figures on the left correspond to the measured force f_m vs. the measured displacement x_m , the figures in the middle correspond to the measured force f_m vs. the target displacement x_r , and the figures on the right correspond to the measured force with HPF \tilde{f}_m vs. the target displacement x_r , respectively. The input motion is El Centro NS of 20% scale factor; thus, the range of the RC column's response is regarded as mostly inside the linear region. In these test cases, the same RC column specimen is repeatedly used, the tangential stiffness of the specimen has been changing gradually through each test case. As seen in the figures in the middle of **Figure 8**, the hysteresis curve of the internal simulation draws a negative loop if the measured force signal was directly fed back to the simulation. However, as seen in the figures on the right in **Figure 8B**, the HPF can correct the phase delay of the force response, and the negative loop behavior can be effectively corrected. By comparing the figures on the left and the right in **Figure 8B**, the hysteresis curve of the HPF-filtered force \tilde{f}_m vs.

the target displacement x_r can be appropriately corresponded to the hysteresis curve of the measured force f_m vs. the measured displacement x_m , when the cut-off frequency f_c is selected at 0.2 Hz, in this test condition.

The error of displacement tracking is investigated in cases using different earthquake inputs. To evaluate the degree of tracking error in the RTHS, the following indications which are introduced by Ou et al. in their previous study (Ou et al., 2015) are used.

$$J_1 = \sqrt{\sum_n (D_m - D_d)^2 / n} = \text{RMS}(D_e), \quad (7)$$

$$J_2 = \sqrt{\sum_n (D_m - D_d)^2 / n} / \sqrt{\sum_n D_d^2 / n} = \text{RMS}(D_e) / \text{RMS}(D_d), \quad (8)$$

$$J_3 = \sqrt{\sum_n (D_m - D_d)^2 / n} / \max(D_d) = \text{RMS}(D_e) / \max(D_d), \quad (9)$$

where D_m is measured displacement, D_d is desired displacement, and $D_e = D_m - D_d$ is the tracking error. $\max(D_d)$ means the maximum of the absolute value of the desired displacement. **Table 4** lists the error indications for each case under Eqs 7–9. All cases were conducted under the cut-off frequency $f_c = 0.2$ Hz for the HPF. In this table, “Takatori” is the ground motion record observed at the JR Takatori Railway Station during the South Hyogo Prefecture Earthquake in 1995, and “JMA Kobe” is the ground motion record observed at the Kobe Local Meteorological Office of Japan Meteorological Agency (JMA) during the South Hyogo Prefecture Earthquake in 1995. The influence due to the residual time delay of the hydraulic actuator motion was observed in the values of error indications, especially, in the

value of J_2 . However, as seen in the overall results, the difference depending on the earthquake inputs is considered to be small among these test cases.

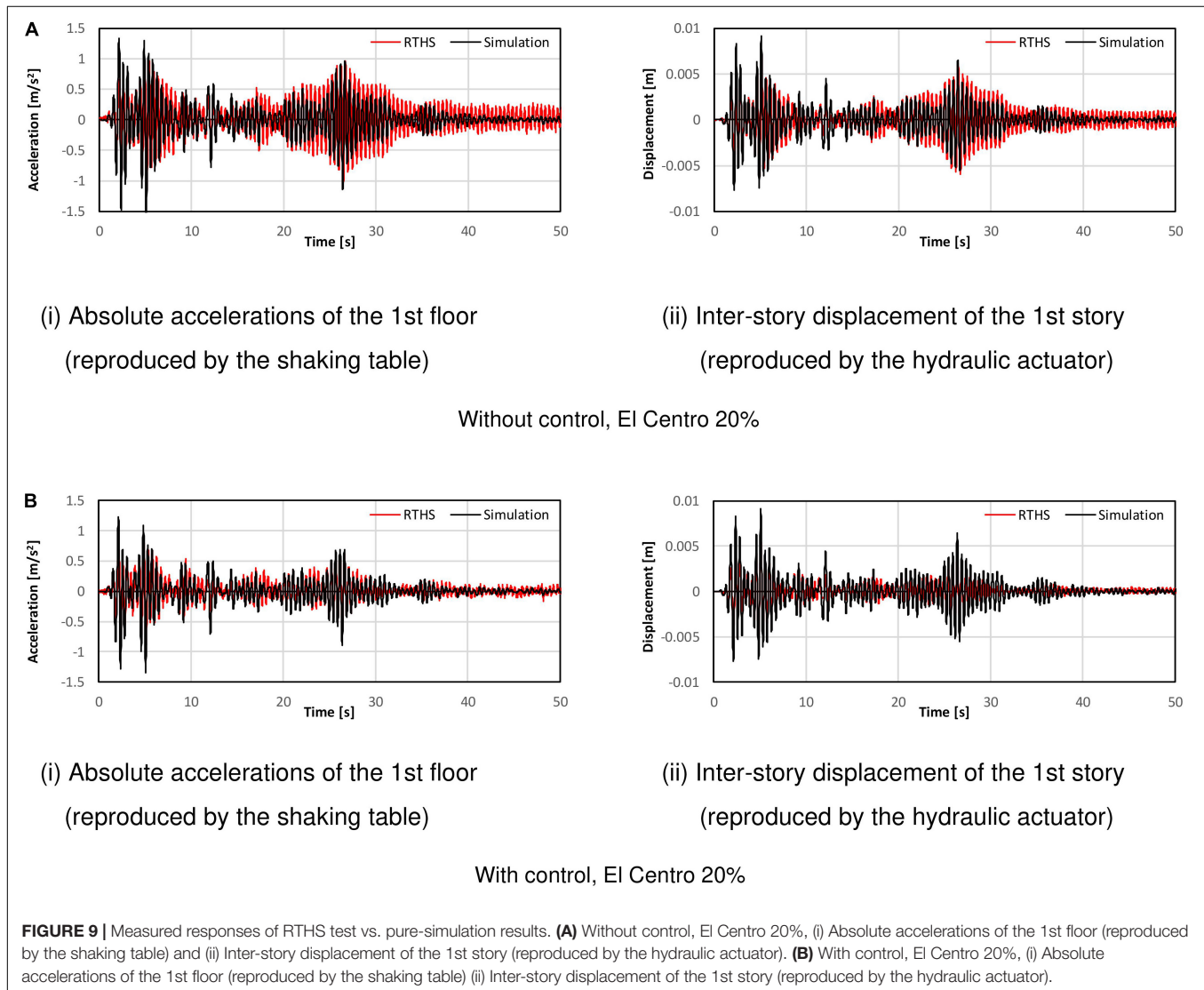
Comparison of RTHS Test and Numerical Analysis Results Without AMD

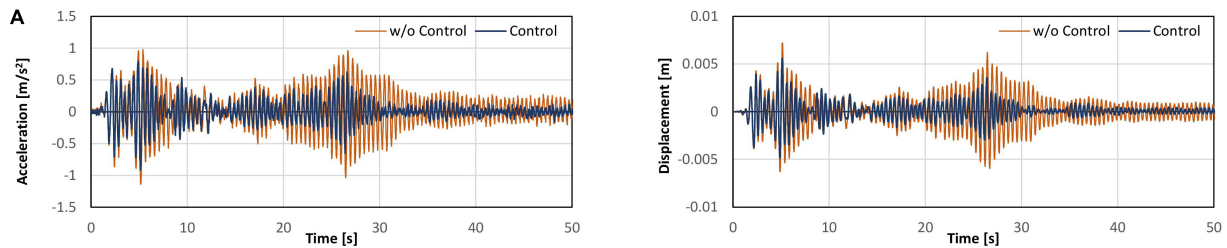
In the previous section, the effect of a compensator for the time delay of the hydraulic actuator was observed. In this section, the reproducibility of the RTHS test system is investigated. **Figure 9A** shows the comparison between the measured responses in the RTHS test and the pure-simulation results. The experimental data are processed through the low-pass filter to remove the high-frequency noise. The numerical simulation is conducted by supposing the linear model; thus, the stiffness of the simulation model is considered as the tangential ratio of the maximum restoring force for the maximum displacement of the RC column in the corresponding RTHS test case. As seen in these figures, it is found that the RTHS test results are slightly

larger than the numerical responses, but the phase correlation is assured between the RTHS and the pure-simulation results. These differences are increased in the shaking-table motion to reproduce a floor acceleration compared with the hydraulic actuator motion to reproduce an inter-story displacement. As the reason for this, it is considered that the negative damping effects caused by the residual time delay in the actuators influences the decrease of the damping effects of the entire system in the RTHS test.

Comparison of RTHS Test and Numerical Analysis Results Using AMD

Figure 9B shows the comparison of the responses under the velocity feedback control using the AMD. Control forces are given by the rule of the equivalent feedback gain $G = 120,000$ Ns/m, which is corresponding to the damping factor of about 3% for the target building model. As seen in these figures, it is found that the RTHS test results have

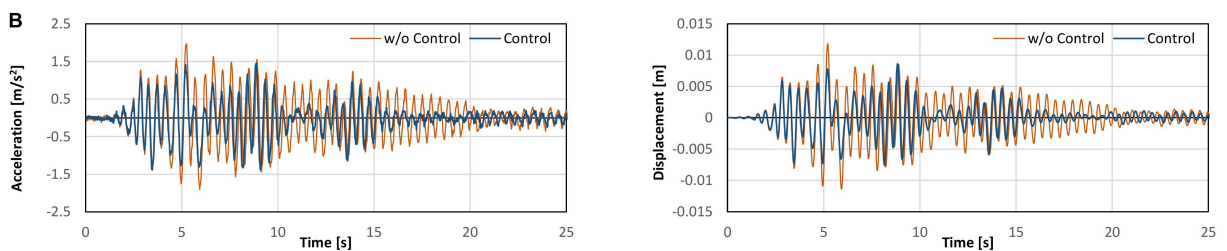




(i) Absolute accelerations of the 1st floor
(reproduced by the shaking table)

(ii) Inter-story displacement of the 1st story
(reproduced by the hydraulic actuator)

El Centro 20%



(i) Absolute accelerations of the 1st floor
(reproduced by the shaking table)

(ii) Inter-story displacement of the 1st story
(reproduced by the hydraulic actuator)

Takatori 10%

FIGURE 10 | Comparison of responses between with/without control in the RTHS test. **(A)** El Centro 20%, (i) Absolute accelerations of the 1st floor (reproduced by the shaking table) and (ii) Inter-story displacement of the 1st story (reproduced by the hydraulic actuator). **(B)** Takatori 10%, (i) Absolute accelerations of the 1st floor (reproduced by the shaking table) and (ii) Inter-story displacement of the 1st story (reproduced by the hydraulic actuator).

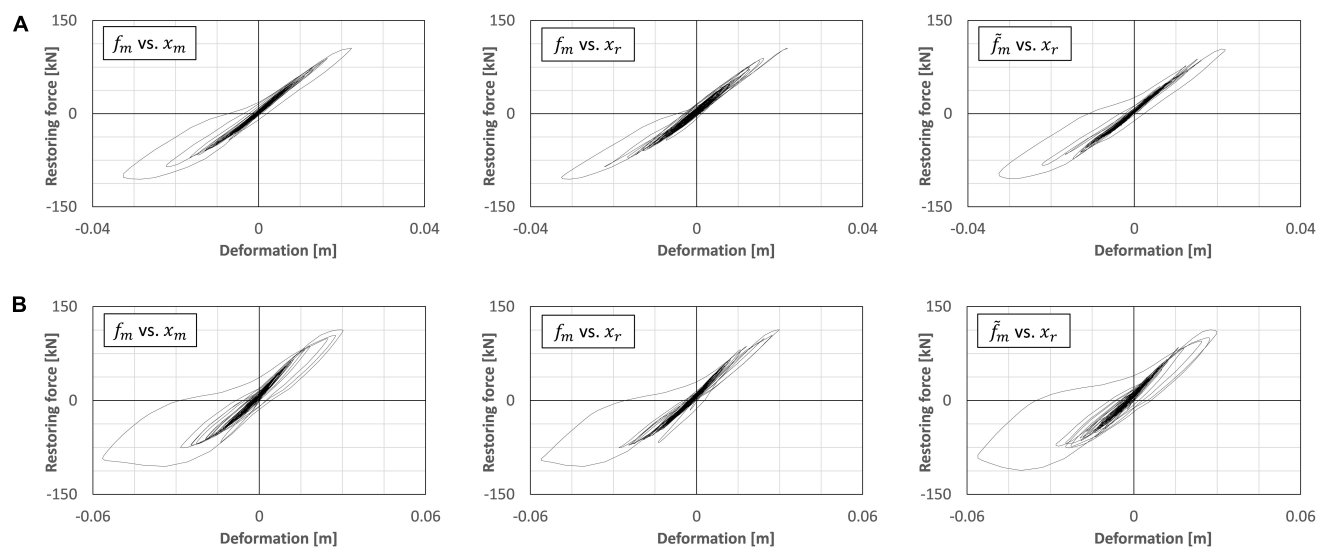


FIGURE 11 | Hysteresis of restoring force vs. deformation of RC column specimen. **(A)** $f_c = 0.2$ Hz, El Centro NS 50%. **(B)** $f_c = 0.2$ Hz, El Centro NS 80%.

moderate agreements with the pure-simulation results on both of the shaking table motion and the hydraulic actuator motion in the case under control using AMD. **Figure 10** shows the comparison of the RTHS test results of the controlled case using AMD and the case without control. **Figure 10A** corresponds to the case, the input motion is El Centro NS of 20% scale factor. **Figure 10B** corresponds to the case, the input motion is Takatori NS of 10% scale factor. By observing these figures, it is confirmed that the control performance of the AMD can be adequately reflected in the RTHS test results as the reduction of the inter-story displacement and the floor acceleration.

Imposed force-deformation relationships in the strong non-linear region of the actual RC column specimen are compared, as seen in **Figures 11A,B**. **Figures 11A,B** are the RTHS test results under the input motion of El Centro of 50 and 80% scale factors, respectively. The HPF with the cut-off frequency $f_c = 0.2$ Hz is applied to the force feedback signal in these test cases. In **Figure 11**, the figures on the left correspond to the measured force f_m vs. the measured displacement x_m , the figures on the middle correspond to the measured force f_m vs. the target displacement x_r , and the figures on the right correspond to the measured force with HPF \tilde{f}_m vs. the target displacement x_r , respectively. As seen in the figures on the left in **Figure 11**, the RC column has moved into the inelastic region, and the force-deformation relationships have drawn hysteresis loops. By comparing the figures on the left and the middle in **Figures 11A or B**, the hysteresis loops of the internal simulations draw different loops from the correct hysteresis loops. There is the time delay's influence on the hydraulic actuator as long as the measured force signal was directly fed back to the internal simulation. However, by comparing the figures on the left and the right in **Figures 11A or B**, the hysteresis loops of the HPF-filtered force \tilde{f}_m vs. the target displacement x_r correspond to the hysteresis loops of the measured force f_m vs. the measured displacement x_m in the non-linear region.

CONCLUSION AND FUTURE WORKS

In this study, an RTHS test using two-individual actuators was conducted. A high-speed hydraulic actuator was used to deform the RC column test specimen, and a shaking table was used to reproduce the acceleration response of the AMD-equipped floor. The findings of this study are summarized as follows.

1. To improve the system performance of the RTHS test, a time delay compensation of the hydraulic actuator was designed. The combination of the PID controller and the TSC method was installed for the operation of the hydraulic actuator. In this study's setup, the permanent time delay about 0.046 s could be shortened to about 0.014 s by the PID + TSC compensator. To achieve a stable performance of the RTHS test, the additional compensation scheme was required for eliminating the influence due to this residual time delay.

2. To improve a numerical simulation of the internal model in the RTHS under the existence of the residual time delay, the measured force to feedback to the simulation was corrected by using the HPF as an input signal. The filter parameter of HPF was considered as the phase-lead angle can be adjusted to eliminate the influence of the residual time delay during the steady oscillation depending on the natural period of the target structural model. By introducing the appropriate HPF, it was observed the force-displacement relationship in the internal simulations correspond moderately to the actual force-displacement relationship, which was directly measured in the actual test specimen.
3. The combination of the PID + TSC compensator for the displacement tracking and the simple phase-matching method using HPF for the measured force correction enabled the stable RTHS operation even if the considerable time delay remained. These results were confirmed not only in the linear region of the RC column specimen but also in the non-linear region in the range of this test setup.
4. The RTHS tests could be operated under synchronization between the hydraulic actuator and the shaking-table. Comparing the reproduced responses of the RTHS tests to the pure-simulation responses, there are moderate agreements, in particular for the case under control using AMD. A moderate difference between the RTHS tests and the pure-simulations was observed in the case without control. This considers that the negative damping effect depending on the residual time delay of the hydraulic actuator was rather sensitive in the low-damping condition of the internal model.

These findings have resulted from the limited test conditions and have not reached general conclusions yet. However, this approach of developing the RTHS test environment, which can generate the floor response of RC frame constructions, may contribute to potential users requiring rapid and simple test tools to conduct the performance evaluation of mass damper devices. Future work on the RTHS using two-individual actuators: the further improvement of the RTHS performance in the highly non-linear range of the RC substructure, the more test variations of the seismic inputs or the natural frequencies of the entire model, and the application to the multi-degree-freedom model, should be implemented while associating with the state-of-the-art methodologies of the RTHS.

DATA AVAILABILITY STATEMENT

The datasets supporting the conclusions of this article will be made available on request to the corresponding author.

AUTHOR CONTRIBUTIONS

YM supervised the research, conducted the RTHS experiment and data analysis, and wrote the manuscript. AY conducted the

RTHS experiment and data analysis. KF conducted the RTHS experiment and control program operation. TF discussed the results and prepared the actual RC column test specimens. HF discussed the results and supervised the research. All authors contributed to the article and approved the submitted version.

REFERENCES

- Abbiati, G., Bursi, O. S., Caperan, P., Sarno, L. D., Molina, F. J., Paolacci, F., et al. (2015). Hybrid simulation of a multi-span RC viaduct with plain bars and sliding bearings. *Earthqu. Engin. Struct. Dynam.* 44, 2221–2240. doi: 10.1002/eqe.2580
- Ahmadizadeh, M., Mosqueda, G., and Reinhorn, A. M. (2008). Compensation of actuator delay and dynamics for real-time hybrid structural simulation. *Earthqu. Engin. Struct. Dynam.* 37, 21–42. doi: 10.1002/eqe.743
- Cardone, D., and Flora, A. (2016). An alternative approach for the seismic rehabilitation of existing RC buildings using seismic isolation. *Earthqu. Engin. Struct. Dynam.* 45, 91–111. doi: 10.1002/eqe.2618
- Carrion, J. E., and Spencer, B. F. Jr. (2006). “Real-time hybrid testing using model-based delay compensation,” in *Proc. of the 4th International Conference on Earthquake Engineering, Taipei*, (Berlin: Springer), 1–11. doi: 10.1002/eqe.2189
- Carrion, J. E., Spencer, B. F. Jr., and Phillips, B. M. (2009). Real-time hybrid simulation for structural control performance assessment. *Earthqu. Engin. Struct. Dynam.* 37, 481–492. doi: 10.1007/s11803-009-9122-4
- Chae, Y. B., Kazemibidokhti, K., and Ricles, J. M. (2013). Adaptive time series compensator for delay compensation of servo-hydraulic actuator systems for real-time hybrid simulation. *Earthqu. Engin. Struct. Dynam.* 42, 1697–1715. doi: 10.1002/eqe.2294
- Chae, Y. B., Lee, J. H., Park, M. S., and Kim, C. Y. (2018a). Real-time hybrid simulation for an RC bridge pier subjected to both horizontal and vertical ground motions. *Earthqu. Engin. Struct. Dynam.* 47, 1673–1679. doi: 10.1002/eqe.3042
- Chae, Y. B., Rabiee, R., Dursun, A., and Kim, C. Y. (2018b). Real-time force control for servo-hydraulic actuator systems using adaptive time series compensator and compliance springs. *Earthqu. Engin. Struct. Dynam.* 47, 854–871. doi: 10.1002/eqe.2994
- Chae, Y. B., Park, M. S., Kim, C. Y., and Park, Y. S. (2017). Experimental study on the rate-dependency of reinforced concrete structures using slow and real-time hybrid simulations. *Engin. Struct.* 132, 648–658. doi: 10.1016/j.engstruct.2016.11.065
- Chen, P. C., and Tsai, K. C. (2013). Dual compensation strategy for real-time hybrid testing. *Earthqu. Engin. Struct. Dynam.* 42, 1–23.
- Darby, A. P., Williams, M. S., and Blakeborough, A. (2002). Stability and delay compensation for real-time substructure testing. *J. Engin. Mechan. ASCE* 128, 1276–1284. doi: 10.1061/(ASCE)0733-93992002128:121276
- Elias, S., and Matsagar, V. (2017). Research developments in vibration control of structures using passive tuned mass dampers. *Annu. Rev. Contr.* 44, 129–156. doi: 10.1016/j.arcontrol.2017.09.015
- Elias, S., and Matsagar, V. (2019). Seismic vulnerability of a non-linear building with distributed multiple tuned vibration absorbers. *Struct. Infrastruct. Engin. Mainten.* 15, 1–16. doi: 10.1080/15732479.2019.1602149
- Fushihara, K., Yokoyama, A., and Mukai, Y. (2020). “Real-time hybrid test system using shaking table for performance evaluation of active mass damper,” in *17th World Conference on Earthquake Engineering*, (Sendai: AEES), (2g-144) 1–9.
- Gao, X., Castaneda, N., and Dyke, S. J. (2013). Real time hybrid simulation: from dynamic system, motion control to experimental error. *Earthq. Engin. Struct. Dynam.* 42, 815–832. doi: 10.1002/eqe.2246
- Goorts, K., Ashasi-Sorkhabi, A., and Narasimhan, S. (2017). Deployable Active Mass Dampers for Vibration Mitigation in Lightweight Bridges. *J. Struct. Engin.* 143, 4017159–4017151. doi: 10.1061/(ASCE)ST.1943-541X.0001921
- Horiuchi, T., Inoue, M., and Konno, T. (2000). “Development of a real-time hybrid experimental system using a shaking table,” in *Proc. of the 12th World Conference on Earthquake Engineering, Auckland*, 1–8.
- Horiuchi, T., Inoue, M., Konno, T., and Namita, Y. (1999). Real-time hybrid experimental system with actuator delay compensation and its application to a piping system with energy absorber. *Earthqu. Engin. Struct. Dynam.* 28, 1121–1141. doi: 10.1002/(SICI)1096-9845(199910)28
- Huff, T. (2016). Estimating Residual Seismic Displacements for Bilinear Oscillators. *Pract. Period. Struct. Des. Construct.* 21:282. doi: 10.1061/(ASCE)SC.1943-5576.0000282
- Ito, M., Fujitani, H., Oknana, M., Nishikawa, K., and Mosqueda, G. (2018). “Real-time hybrid test of structures with a tuned mass damper using shaking table,” in *Proc. of the 7th World Conference on Structural Control and Monitoring*, (Qingdao: Wiley), 1263–1271.
- Jaafari, C., and Mohammadi, J. (2018). Floor Vibration Control as a Serviceability Requirement in Design Standards and Practices: Review. *Pract. Period. Struct. Des. Construct.* 23:07019001. doi: 10.1061/(ASCE)SC.1943-5576.000361
- Kazantzi, A. K., and Vamvatsikos, D. (2020). Seismic and Vibration Performance Rehabilitation for an Industrial Steel Building. *Pract. Period. Struct. Des. Construct.* 25:475. doi: 10.1061/(ASCE)SC.1943-5576.000475
- Lee, S. K., Park, E. C., Min, K. W., and Park, J. H. (2007). Real-time substructuring technique for the shaking table test of upper substructures. *Engin. Struct.* 29, 2219–2232. doi: 10.1016/j.engstruct.2006.11.013
- Liu, J., Dyke, S. J., Liu, H. J., Gao, X. Y., and Phillips, B. (2013). A novel integrated compensation method for actuator dynamics in real-time hybrid structural testing. *Struct. Contr. Health Monit.* 20, 1057–1080. doi: 10.1002/stc.1519
- Matsagar, V. A., and Jangid, R. S. (2008). Base Isolation for Seismic Retrofitting of Structures. *Pract. Period. Struct. Des. Construct.* 13, 175–185. doi: 10.1061/(ASCE)1084-0680200813:4(175)
- Mei, Z., Wu, B., Bursi, O. S., Xu, G. S., Wang, Z., Wang, T., et al. (2019). Hybrid simulation with online model updating: Application to a reinforced concrete bridge endowed with tall piers. *Mechan. Sys. Sign. Proc.* 123, 533–553. doi: 10.1016/j.ymsp.2019.01.009
- Miyamoto, H. K., Gilani, A. S. J., Garza, J., and Mahin, S. A. (2010). Seismic Retrofit of a Landmark Structure Using a Mass Damper, Structure Congress 2010. *ASCE Orlando* 19, 2291–2302. doi: 10.1061/41130(369)208
- Mukai, Y., Miki, Y., Uchida, S., Fujitani, H., and Ito, M. (2018). “Real-time hybrid simulator of soil-structure interaction system by using shaking table,” in *Proc. of 11th U.S. National Conference on Earthquake Engineering*, (California: Los Angeles), 1–11. doi: 10.1155/2017/1291265
- Nakai, T., Kurino, H., Yaguchi, T., and Kano, N. (2019). Control effect of large tuned mass damper used for seismic retrofitting of existing high-rise building. *Japan Architect. Rev.* 2, 269–286. doi: 10.1002/2475-8876.12100
- Neild, S. A., Stoten, D. P., Drury, D., and Wagg, D. J. (2005). Control issues relating to real-time substructuring experiments using a shaking table. *Earthq. Engin. Struct. Dynam.* 34, 1171–1192. doi: 10.1002/eqe.473
- Ou, G., Ozdagli, A. I., Dyke, S. J., and Wu, B. (2015). Robust integrated actuator control: experimental verification and real-time hybrid-simulation implementation. *Earthqu. Engin. Struct. Dynam.* 44, 441–460. doi: 10.1002/eqe.2479
- Phillips, B. M., and Spencer, B. F. Jr. (2013). Model-Based Feedforward-Feedback Actuator Control for Real-Time Hybrid Simulation. *J. Struct. Engin.* 139, 1206–1214. doi: 10.1061/(ASCE)ST.1943-541X.0000606
- Shao, X., Reinhorn, A. M., and Sivaselvan, M. V. (2011). Real time hybrid simulation using shake tables and dynamic actuators. *J. Struct. Engin. ASCE* 137, 748–760. doi: 10.1061/(ASCE)ST.1943-541X.0000314
- Wang, J., and Zhao, H. (2018). High Performance Damage-Resistant Seismic Resistant Structural Systems for Sustainable and Resilient City: A Review. *Shock Vibr.* 2018:8703697. doi: 10.1155/2018/8703697

FUNDING

Part of the present study was supported by the Grants-in-Aid for Scientific Research (JSPS KAKENHI No. 18H01587) and JSPS Grant No. R2904 in the program for Fostering Globally Talented Researchers.

- Wang, Q., Wang, J. T., Jin, F., Chia, F. D., and Zhang, C. H. (2011). Real-time dynamic hybrid testing for soil-structure interaction analysis. *Soil Dynam. Earthqu. Engin.* 31, 1690–1702. doi: 10.1016/j.soildyn.2011.07.004
- Xu, H. B., Zhang, C. W., Li, H., and Ou, J. P. (2014). Real-time hybrid simulation approach for performance validation of structural active control systems: a linear motor actuator based active mass driver case study. *Struct. Contr. Health Monit.* 21, 574–589. doi: 10.1002/stc.1585
- Yoshida, S., Fujitani, F., Mukai, Y., and Ito, M. (2018). Real-time hybrid simulation of semi-active control using shaking table: Proposal and verification of a testing method for mid-story isolated buildings. *Japan Architect. Rev.* 1, 221–234. doi: 10.1002/2475-8876.12034
- Zhang, C. X., and Jiang, N. (2017). A shaking table real-time substructure experiment of an equipment-structure-soil interaction system. *Adv. Mechan. Engin.* 9, 1–12. doi: 10.1177/1687814017724090
- Zhang, R. Y., Lauenstein, P. V., and Phillips, B. M. (2016). Real-time hybrid simulation of a shear building with a uni-axial shake table. *Engin. Struct.* 119, 217–229. doi: 10.1016/j.engstruct.2016.04.022
- Zhu, F., Wang, J. T., Jin, F., and Lu, L. Q. (2017). Real-time hybrid simulation of full-scale tuned liquid column dampers to control multi-order modal responses of structures. *Engin. Struct.* 138, 74–90. doi: 10.1016/j.engstruct.2017.02.004
- Ziegler, J. G., and Nichols, N. B. (1942). Optimum Settings for Automatic Controllers. *Transact. ASME* 64, 759–768.

Conflict of Interest: The authors declare that the research was conducted in the absence of any commercial or financial relationships that could be construed as a potential conflict of interest.

Copyright © 2020 Mukai, Yokoyama, Fushihara, Fujinaga and Fujitani. This is an open-access article distributed under the terms of the Creative Commons Attribution License (CC BY). The use, distribution or reproduction in other forums is permitted, provided the original author(s) and the copyright owner(s) are credited and that the original publication in this journal is cited, in accordance with accepted academic practice. No use, distribution or reproduction is permitted which does not comply with these terms.

Advantages of publishing in Frontiers



OPEN ACCESS

Articles are free to read
for greatest visibility
and readership



FAST PUBLICATION

Around 90 days
from submission
to decision



HIGH QUALITY PEER-REVIEW

Rigorous, collaborative,
and constructive
peer-review



TRANSPARENT PEER-REVIEW

Editors and reviewers
acknowledged by name
on published articles

Frontiers

Avenue du Tribunal-Fédéral 34
1005 Lausanne | Switzerland

Visit us: www.frontiersin.org

Contact us: info@frontiersin.org | +41 21 510 17 00



REPRODUCIBILITY OF RESEARCH

Support open data
and methods to enhance
research reproducibility



DIGITAL PUBLISHING

Articles designed
for optimal readership
across devices



FOLLOW US

@frontiersin



IMPACT METRICS

Advanced article metrics
track visibility across
digital media



EXTENSIVE PROMOTION

Marketing
and promotion
of impactful research



LOOP RESEARCH NETWORK

Our network
increases your
article's readership